

U.S. Department of Energy  
Fossil Energy  
Advanced Research and Technology Development

RECEIVED  
OCT 29 1996  
OSTI

**Proceedings  
of the  
Tenth Annual Conference  
On Fossil Energy Materials**

May 14-16, 1996  
Knoxville, Tennessee

**Fossil Energy AR&TD Materials Program**

OAK RIDGE NATIONAL LABORATORY  
MANAGED BY  
LOCKHEED MARTIN ENERGY RESEARCH CORP.  
FOR THE  
U.S. DEPARTMENT OF ENERGY  
UNDER CONTRACT DE-AC05-96OR22464

**MASTER**

*Fossil  
Energy  
Program*

This report has been reproduced directly from the best available copy.

Available to DOE and DOE contractors from The Office of Scientific and Technical Information, P. O. Box 62, Oak Ridge, TN 37831; prices available from (423) 576-8401.

Available to the public from the National Technical Information Service, U. S. Department of Commerce, 5285 Port Royal Rd., Springfield, VA 22161.

This report was prepared as an account of work sponsored by an agency of the United States Government. Neither the United States Government nor any agency thereof, nor any of their employees, makes any warranty, expressed or implied, or assumes any legal liability or responsibility for the accuracy, completeness, or usefulness of any information, apparatus, product, or process disclosed, or represents that its use would not infringe privately owned rights. Reference herein to any specific commercial product, process, or service by trade name, trademark, manufacturer, or otherwise, does not necessarily constitute or imply its endorsement, recommendation, or favoring by the United States Government or any agency thereof. The views and opinions of authors expressed herein do not necessarily state or reflect those of the United States Government or any agency thereof.



CONF-9605167  
ORNL/FMP-96/1

PROCEEDINGS OF THE TENTH ANNUAL CONFERENCE  
ON FOSSIL ENERGY MATERIALS

May 14-16, 1996  
Knoxville, Tennessee

Compiled by  
N. C. Cole and R. R. Judkins

Date Published: August 1996

Prepared by the  
Department of Energy  
Fossil Energy Office of Advanced Research  
and  
Oak Ridge Operations Office  
AA 15 10 10 0

Prepared by the  
OAK RIDGE NATIONAL LABORATORY  
Oak Ridge, Tennessee 37831-6285  
managed by  
LOCKHEED MARTIN ENERGY RESEARCH CORP.  
for the  
U. S. DEPARTMENT OF ENERGY  
under Contract DE-AC05-96OR22464

DISTRIBUTION OF THIS DOCUMENT IS UNLIMITED





## PREFACE

The Tenth Annual Conference on Fossil Energy Materials was held in Knoxville, Tennessee, on May 14-16, 1996. The meeting was sponsored by the U.S. Department of Energy's (DOE) Office of Fossil Energy through the Advanced Research and Technology Development (AR&TD) Materials Program. The objective of the AR&TD Materials Program is to conduct research and development on materials for longer-term fossil energy applications as well as for generic needs of various fossil fuel technologies. The management of the program has been decentralized to the DOE Oak Ridge Operations Office and Oak Ridge National Laboratory (ORNL). The research is performed by staff members at ORNL and by researchers at other national laboratories, universities, and in private industry. The work is divided into the following categories: (1) structural ceramics, (2) new alloys and coatings, (3) functional materials, and (4) technology development and transfer.

This conference is held each year to review the work on all of the projects of the program. The final program for the meeting is given in Appendix A, and a list of attendees is presented in Appendix B.

These proceedings have been published from camera-ready masters supplied by the authors. All of the contributions have been checked for errors but have not been subjected to peer reviews. However, most of the papers have already undergone technical review within the individual organizations before submission to the Program Office.

The successful completion of the conference and publication of the proceedings has required help from several people. The organizers wish to thank Judy Fair for her superb coordination work; Connie Tilley for her assistance with preparations for the conference; Gloria Donaldson and Judy for their excellent work at the registration desk; Thelma Bonfoey for her help in the many arrangements; and the numerous staff and support personnel associated with the conference. Finally, we express our sincere appreciation to the authors whose efforts are the very basis of the conference.



# **DISCLAIMER**

**Portions of this document may be illegible in electronic image products. Images are produced from the best available original document.**

## TABLE OF CONTENTS

PREFACE .....	iii
<b>SESSION I - CERAMIC COMPOSITES AND FUNCTIONAL MATERIALS</b>	
<i>Fabrication of Fiber-Reinforced Composites by Chemical Vapor Infiltration</i> T. M. Besmann, W. M. Matlin, D. P. Stinton, and P. K. Liaw .....	1
<i>Transport Properties of Ceramic Composites</i> T. L. Starr and N. Hablutzell .....	11
<i>Joining of SiC Ceramics And SiC/SiC Composites</i> B. H. Rabin .....	21
<i>Development of Nondestructive Evaluation Methods For Structural Ceramics</i> W. A. Ellingson, R. D. Koehl, H. P. Engel, J. A. Wilson, and J. B. Stuckey ..	27
<i>Effects of Flaws on Fracture Behavior of Structural Ceramics</i> J. P. Singh, D. Singh, and M. Sutaria .....	39
<i>Strength and Corrosion Behavior of SiC-Based Ceramics In Hot Coal Combustion Environments</i> K. Breder and R. J. Parten .....	53
<i>Corrosion And Its Effect On Mechanical Properties of Materials For Advanced Combustion Systems</i> K. Natesan, M. Freeman, and M. Mathur .....	63
<i>Interaction of Low-Expansion NZP Ceramics with Na<sub>2</sub>SO<sub>4</sub> at 1000 °C</i> W. Y. Lee, K. M. Cooley, D. P. Stinton, and D. L. Joslin .....	75
<i>Synthesis of Mullite Coatings by Chemical Vapor Deposition</i> Rao P. Mulpuri, Michael Auger, and Vinod K. Sarin .....	83
<i>Plasma Deposition of High Temperature Protective Coatings</i> O. R. Monteiro, Z. Wang, K.-M. Yu, P. Y. Hou, I. G. Brown, B. H. Rabin, and G. F. Kessinger .....	97
<i>Ceramic Membranes for High Temperature Hydrogen Separation</i> D. E. Fain and G. E. Roettger .....	107
<i>Mixed Oxygen Ion/Electron-Conducting Ceramics for Oxygen Separation</i> J. W. Stevenson, T. R. Armstrong, B. L. Srmstrong, J. L. Bates G. Hsieh, L. R. Pederson, and W. J. Weber .....	117

<i>Preparation and Evaluation of Coal Extracts As Precursors for Carbon and Graphite Products</i>	
J. W. Zondlo, A. W. Stiller, P. G. Stansberry, I. C. Lewis, R. T. Lewis, and H. K. Mayer .....	127
<i>A Novel Approach to the Removal of CO<sub>2</sub></i>	
T. D. Burchell, R. R. Judkins, M. R. Rogers, and A. M. Williams .....	135

## SESSION II - CERAMICS, NEW ALLOYS, AND FUNCTIONAL MATERIALS

<i>Oxidation-Resistant Interface Coatings for SiC/SiC Composites</i>	
D. P. Stinton, E. R. Kupp, J. W. Hurley, R. A. Lowden, S. Shanmugham, and P. K. Liaw .....	151
<i>Modeling of Fibrous Preforms for CVI Fabrication</i>	
D. Y. Chiang and T. L. Starr .....	161
<i>Fiber/Matrix Interfaces for SiC/SiC Composites: Multilayer SiC Coatings</i>	
H. Halverson and W. A. Curtin .....	171
<i>Conditions for Testing the Corrosion Rates of Ceramics in Coal Gasification Systems</i>	
J. P. Hurley and J. W. Nowok .....	181
<i>Fracture Behavior of Advanced Ceramic Hot-Gas Filters</i>	
J. P. Singh, S. Majumdar, M. Sutaria, and W. Bielke .....	193
<i>High Temperature Corrosion of Advanced Ceramic Materials For Hot Gas Filters and Heat Exchangers</i>	
C. E. Crossland, D. L. Shelleman, K. E. Spear, and R. E. Tressler .....	205
<i>Effect of Heat Treatment at 1150 °C on Creep-Rupture Properties of Alloy FA-180</i>	
C. G. McKamey and P. J. Maziasz .....	215
<i>The Influence of Composition on Environmental Embrittlement of Iron Aluminides</i>	
D. A. Alven and N. S. Stoloff .....	225
<i>Effects of Titanium and Zirconium on Iron Aluminide Weldments</i>	
R. P. Burt, G. R. Edwards, and S. A. David .....	237
<i>Evaluation of Iron Aluminide Weld Overlays for Erosion-Corrosion Resistant Boiler Tube Coatings In Low No<sub>x</sub> Boilers</i>	
J. N. DuPont, S. W. Banovic, and A. R. Marder .....	247
<i>Effects of Surface Condition on Aqueous Corrosion and Environmental Embrittlement of Iron Aluminides</i>	
R. L. Perrin and R. A. Buchanan .....	251

<i>Processing and Properties of Low-Aluminum Alloy FAPY</i> V. K. Sikka, C. R. Howell, F. Hall, and J. Valykeo .....	261
<i>Microstructural and Mechanical Characterization of Alumina Scales Thermally Developed On Iron Aluminide Alloys</i> K. Natesan, K. L. Klug, D. Renusch, M. Grimsditch, and B. W. Veal .....	273
<i>Overview of the Carbon Products Consortium</i> C. Irwin .....	281
<i>Carbon-Fiber Composite Molecular Sieves for Gas Separation</i> M. Jagtoyen and F. Derbyshire .....	291
<i>Stability of Solid Oxide Fuel Cell Materials</i> T. R. Armstrong, J. L. Bates, G. W. Coffey, L. R. Pederson, P. J. Raney, J. W. Stevenson, W. J. Weber, and F. Zheng .....	301
<i>Proton-Conducting Cerate Ceramics</i> L. R. Pederson .....	311
<i>Ceramic Catalyst Materials</i> A. G. Sault .....	319
<i>Nanoparticle Synthesis in Pulsed Low Temperature Discharges</i> R. J. Buss .....	329
<b>SESSION III - SUMMARIES OF WORKSHOP ON MATERIALS RESEARCH AND DEVELOPMENT NEEDS FOR THE SUCCESSFUL DEPLOYMENT OF ADVANCED POWER GENERATION TECHNOLOGIES .....</b>	<b>341</b>
<b>SESSION IV - NEW ALLOYS</b>	
<i>ODS Iron Aluminides</i> I. G. Wright, B. A. Pint, E. K. Ohriner, and P. F. Tortorelli .....	359
<i>The Influence of Processing on Microstructure and Properties of Iron Aluminides</i> R. N. Wright and J. K. Wright .....	373
<i>Weld Overlay Cladding With Iron Aluminides</i> G. M. Goodwin .....	381
<i>High-Temperature Corrosion Behavior of Coatings and ODS Alloys Based on Fe<sub>3</sub>Al</i> P. F. Tortorelli, B. A. Pint, and I. G. Wright .....	393



<i>Evaluation of the Intrinsic and Extrinsic Fracture Behavior of Iron Aluminides</i> B. S. Kang, Qizhou Yao, and B. R. Cooper .....	405
<i>The Mechanical Reliability of Alumina Scales and Coatings</i> K. B. Alexander, K. Prüßner, and P. F. Tortorelli .....	419
<i>Electro-Spark Deposition Technology</i> R. N. Johnson .....	429
<i>Investigation of Austenitic Alloys for Advanced Heat Recovery and Hot-Gas Cleanup Systems</i> R. W. Swindeman .....	439
<i>Microstructural And Weldability Evaluation of 310TaN</i> C. D. Lundin and C. Y. P. Qiao .....	445
<i>Fireside Corrosion Testing of Candidate Superheater Tube Alloys, Coatings, and Claddings - Phase II</i> J. L. Blough and G. J. Stanko .....	455
<i>Pack Cementation Coatings for Alloys</i> Yi-Rong He Minhui Zheng and R. A. Rapp .....	465
<i>Cr<sub>2</sub>Nb-Based Alloy Development</i> C. T. Liu, P. F. Tortorelli, J. A. Horton, D. S. Easton, and L. Heatherly ....	477
<i>Study of Fatigue and Fracture Behavior of Cr<sub>2</sub>Nb-Based Alloys and Intermetallic Materials: Phase Stability In NbCr<sub>2</sub>-Based Laves Phase Alloys</i> J. H. Zhu, P. K. Liaw, and C. T. Liu .....	491

**APPENDIX A. FINAL PROGRAM FOR THE TENTH ANNUAL  
CONFERENCE ON FOSSIL ENERGY MATERIALS**

**APPENDIX B. LIST OF ATTENDEES**

## **SESSION I**

# **CERAMIC COMPOSITES AND FUNCTIONAL MATERIALS**

---

**FABRICATION OF FIBER-REINFORCED COMPOSITES BY**  
**CHEMICAL VAPOR INFILTRATION**

T.M. Besmann,\* W.M. Matlin\*\*, D.P. Stinton,\* and P. K. Liaw\*\*

\*Oak Ridge National Laboratory, Oak Ridge, TN 37831

\*\*Department of Materials Science and Engineering, University of Tennessee  
Knoxville, TN 37996-2200

**ABSTRACT**

Processing equipment for the infiltration of fiber-reinforced composite tubes is being designed that incorporates improvements over the equipment used to infiltrate disks. A computer-controlled machine-man interface is being developed to allow for total control of all processing variables. Additionally, several improvements are being made to the furnace that will reduce the complexity and cost of the process. These improvements include the incorporation of free standing preforms, cast mandrels, and simpler graphite heating elements.

**INTRODUCTION**

Fiber-reinforced silicon carbide matrix composites are a candidate for a number of high temperature applications due to their high temperature strength, light weight, thermal shock resistance and damage tolerance. However, in the current commercial isothermal, isobaric chemical vapor infiltration process, thick parts are difficult to density. A leading alternative process is forced chemical vapor infiltration (FCVI). In FCVI, a preform is placed in a reactor, where one side is heated and the other side is cooled, resulting in a thermal gradient across the preform. As the reactant gases pass through the preform they undergo a surface reaction, resulting in the formation of a ceramic matrix and an effluent gas. In the case of SiC deposited from chlorosilanes, the effluent gas has a poisoning effect on the reaction rate. This poisoning,

combined with the depletion of the reactant, tends to slow down the deposition rate. However, since the gases are traveling toward the hot side of the preform their temperature increases, resulting in faster deposition rates due to the Arrhenius behavior of the deposition reaction. Control over deposition can thus be maintained by using the increase in temperature to offset reactant depletion and effluent gas buildup.

Work at the Oak Ridge National Laboratory (ORNL) has shown that the time to infiltrate 4.45 cm diameter disks 1.27 cm thick can be reduced from 24 hours to less than 15 hours by utilization of a two-step process [1]. This reduction in processing time is expected to result in lower processing cost, thereby making the process more industrially feasible [2]. Additionally, ORNL researchers have investigated the production of more industrially relevant shapes such as tubes. Initially, 2.54 cm diameter tubes were made using furnaces originally designed for the production of disks [3]. Based on the initial successes of the 2.54-cm inner diameter, 0.64-cm wall thickness tubes, a larger furnace was designed exclusively for the fabrication of tubes (Fig. 1). This furnace is designed to process tubes up to 10 cm in diameter and 30 cm in length. The new furnace, as well, will incorporate a number of improvements based on the experience of processing numerous disks and a few initial tubes.

## **PROCESS OPTIMIZATION THROUGH THE CONTINUAL CONTROL OF PROCESSING VARIABLES**

As demonstrated in the two-step FCVI process, significant time savings can be achieved through the proper control of thermal gradient, reactant concentration, total gas flow, and

pressure. The two-step process does not represent the end of process optimization, but an initial step. In the ideal case, processing conditions would be varied continuously in response to the continually changing pore structure within the preform. A LabView™-based process control system is being designed that will allow for the complete control of reactant and carrier gas flow rates as well as preform hot-side temperature. Each of these variables can be controlled as a function of time, thereby allowing the investigation of more complex process optimization schemes. Figure 2 is a schematic of the FCVI system and controls.

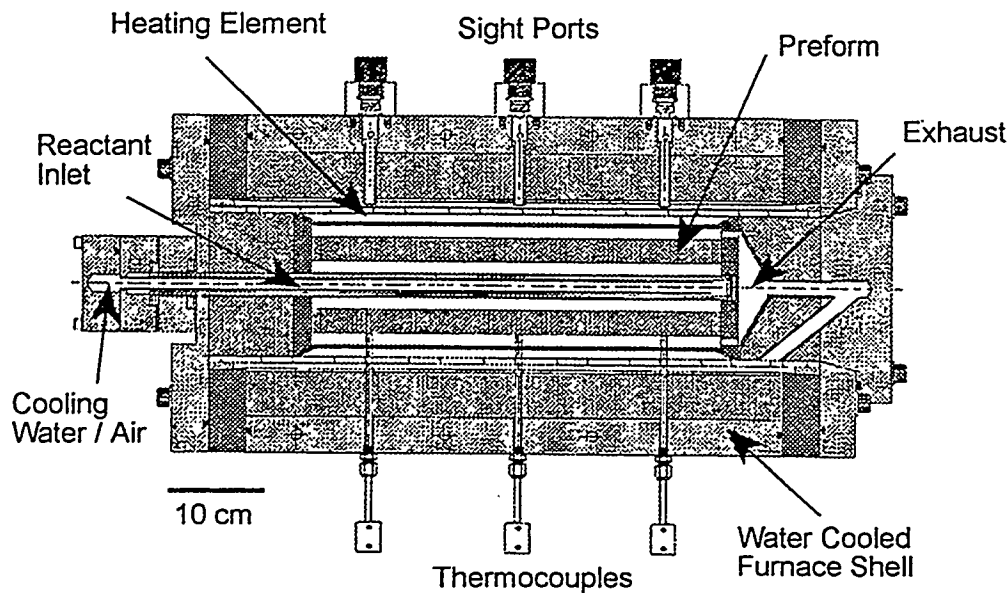


Figure 1. Scale-up furnace for the fabrication of tubular composites.

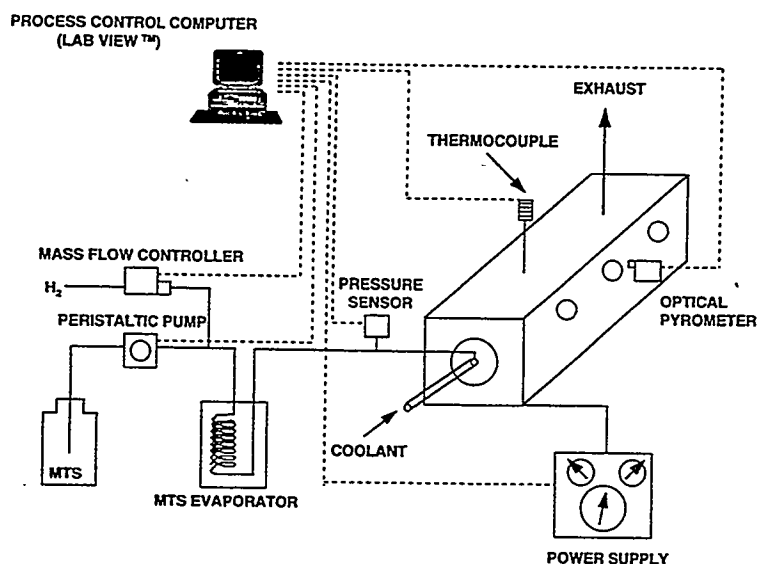


Figure 2. Flow diagram and controls for the scale-up FCVI system for preparing tubular composites.

At the heart of the system is a Power Macintosh 7100/80 containing a four port serial card and a Lab - NB data acquisition card running LabView 3.1.1. Carrier gas flow is controlled through the use of a serial connection between the LabView computer and mass flow controllers. Liquid methyltrichlorosilane ( $\text{CH}_3\text{SiCl}_3$  or MTS), at room temperature and pressure is pumped from a storage container to a vaporizer using a peristaltic pump. In a manner similar to the control of the carrier gas, LabView is used to send a set point to the peristaltic pump thereby controlling the flow of reactant into the system. As an additional method of control the MTS container is placed on a electronic balance with a serial port. In this way an accurate measurement of reactant flow can be maintained by continually monitoring the reduction in container weight using LabView.

The final area of control is preform temperature. The system has two methods for

controlling preform temperature. The first method is through the use of an Ircon Modline Plus optical pyrometer. Additional monitoring of preform temperature can be accomplished through a thermocouple which can be placed on the cool side of the preform to monitor the thermal gradient..

### **IMPROVEMENTS IN THE TUBE FURNACE DESIGN**

The transition from processing relatively simple shape preforms such as disks to more complicated shapes such as tubes requires alternate design furnace internals. In order to effectively infiltrate composites using FCVI, four criteria must be met; a pressure differential must be established across the preform, a thermal gradient must be established across the preform, reactant and carrier gases must be introduced to the high pressure, cool-side of the preform, and effluent gases must be removed from the low pressure hot side of the preform.

The pressure differential in the disk furnace is achieved by allowing a water-cooled injector to be pressed against the bottom of the preform holder. A graphite foil gasket is placed between the holder and the injector to ensure a relatively gas-tight seal. The holder is held in place by ridges inside the coating chamber. In addition to positioning the preform within the furnace, the coating chamber also serves to protect the heating element, which resides outside the coating chamber, from overcoating by SiC. A preform hot side temperature can be measured and controlled by sighting an optical pyrometer down the inside of the coating chamber and focusing on the top of the preform. Once the correct preform hot-side temperature is established the correct thermal gradient can be fixed by varying the materials and distance between the

preform and the water-cooled injector. The further away from the injector and the lower the thermal conductivity of the spacer material the higher the cool-side temperature. Finally, the reactant gases are directed to the cool-side of the preform by flowing them through the inside of the water-cooled injector.

Since this furnace design served the production of disks so well it was adapted for the production of tubes. However, the first tube infiltration revealed a number of areas which required improvement. In the production of disks the graphite holder became bonded by deposited SiC to the preform during the FCVI process. At completion, the holder must be machined from the part. While this works well in the case of disks where the preform is surrounded by the holder, it does not work as easily with tubes since the mandrel is surrounded by the preform. It is also difficult to form a gas-tight seal between the mandrel and the cooled injector. Without such a seal a pressure differential can not be imposed across the preform. Lack of a tight seal has two negative results. It becomes impossible to achieve high final preform densities and there is a large loss of reactant through deposition on the inner walls of the furnace and through exhaust from the furnace.

As a solution to these difficulties, methods of removing the graphite mandrel were investigated. Initially, the use of more easily machinable mandrel material, such as carbon bonded carbon fiber were investigated. However, it was recognized that the ideal situation would be being able to process the preform without the use of a mandrel. With the assistance of researchers at the 3M Company's Research and Development Center, a process for rigidizing tubular preforms was adapted for the current system. While originally developed as a method to



rigidize thin, hot gas filter preforms, the method works equally well for thicker preforms. In the 3M process, the preform is immersed in a dilute phenolic resin solution. The impregnated tube is then removed from the solution, dried, and cured, resulting in a rigid preform. When fired to FCVI process temperatures,  $800^{\circ}\text{C}$  -  $1200^{\circ}\text{C}$ , the phenolic resin pyrolyzes, leaving a thin carbon layer. It is speculated that this carbon layer bonds the individual fibers together where the fibers contact each other, thereby explaining the limited strength of the after fired tubes.

Without the use of a mandrel, another approach to forming of a gas tight seal is needed. Casting the preform to the cooled injector was attempted since it was simple, inexpensive, and likely effective. In this method a high-alumina castable refractory was used to fix the preform directly to the injector, thereby positioning the preform a specific distance from the injector and creating a gas tight seal. Tailoring the thermal gradient can still be achieved by positioning an insulating sleeve of material between the injector and the preform.

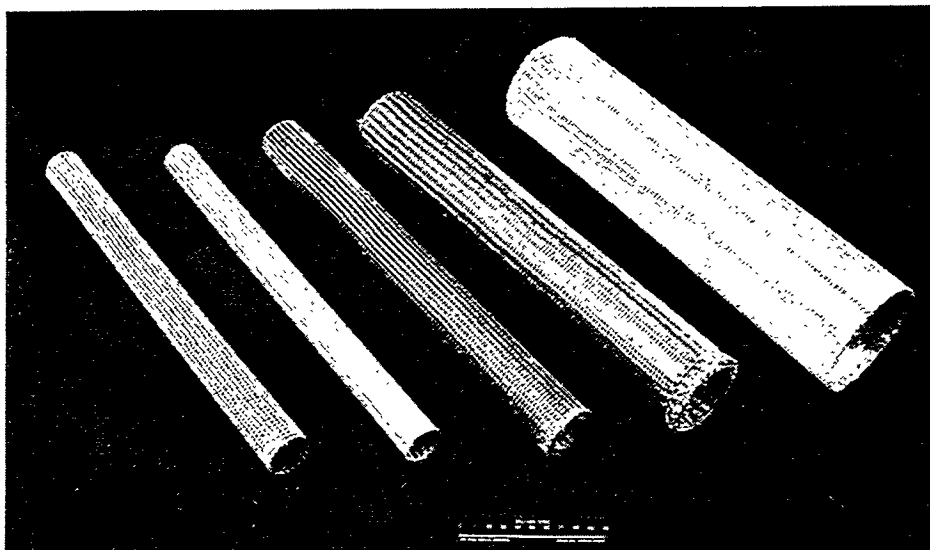


Figure 3. Various Nextel<sup>TM</sup> fiber tubes rigidized with phenolic resin.

Rather than supplying reactant to the cool-side of the preform by running the gases inside the injector, as is done in the smaller units for preparing disks, penetrations through the cast end caps were used to allow the reactant gases to be routed to the inside of the preform. This method greatly simplifies the injector design and eliminates any welds from being exposed to the highly corrosive environment within the furnace.

Finally, one of the most critical process parameters in FCVI is the thermal gradient, and therefore the cool- and hot-side temperatures. Hot-side temperatures are relatively easily controlled via power to the furnace. Cool-side temperature control is more problematic. Current efforts to improve control of the cool-side temperature in the scale-up tube furnace involve variability in the injector coolant. The injector system has been designed to allow for water, high-temperature oil (silicone), or air cooling. Previous experience in the smaller tube fabrication systems has indicated that maintaining a sufficiently high inner diameter temperature is difficult. It is thus expected that alternate cooling media will allow greater control over the thermal gradient and allow higher inner diameter temperatures to be used.

## REFERENCES

- [1] W.M. Matlin, D.P. Stinton, and T.M. Besmann, "Fabrication of Fiber-Reinforced Composites by Chemical Vapor Infiltration", Proceedings of the Ninth Annual Conference on Fossil Energy Materials, Oak Ridge National Laboratory Report ORNL/FMP-95/1, pp 157-165, (1995)
- [2] Y.G. Roman, D.P. Stinton, "The Preparation and Economics of Silicon Carbide Matrix Composites by Chemical Vapor Infiltration"; in Mat. Res. Soc. Symp. Proc. Vol. 365 Edited by R.A. Lowden, M.K. Ferber, J.R. Hellman, K.K. Chawla, S.G. DiPietro, Materials Research Society, Pittsburg, PA, pp. 343-350 (1994)

[3] D.P. Stinton, T.M. Besmann, W.M. Matlin, T.L. Starr, and W.A. Curtin, "Forced Chemical Vapor Infiltration of Tubular Geometries: Modeling, Design, and Scale-Up"; in Mat. Res. Soc. Symp. Proc. Vol. 365 Edited by R.A. Lowden, M.K. Ferber, J.R. Hellman, K.K. Chawla, S.G. DiPietro, Materials Research Society, Pittsburg, PA, pp. 317-324 (1994)



## TRANSPORT PROPERTIES OF CERAMIC COMPOSITES

T.L. Starr and N. Hablutzel

School of Materials Science and Engineering  
Georgia Institute of Technology  
Atlanta, Georgia 30332-0245

Instrumentation and procedures have been completed for measurement of gas permeability and mass diffusivity of fiber preforms and porous materials. Results are reported for composites reinforced with Nicalon fiber in cloth lay-up and 3-D weave and with Nextel fiber in multi-layer braid. Measured permeability values range from near 100 to less than 0.1 darcies. Mass diffusivity is reported as a structure factor relating the diffusion through the porous material to that in free space. This measure is independent of the diffusing species and depends only the pore structure of the material.

Measurements are compared to predictions of a node-bond model for gas transport. Model parameters adjusted to match measured transport properties relate to physical microstructure features of the different architectures. Combination of this transport model with the CVI process model offers a predictive method to evaluate the densification behavior of various fiber preforms.

### INTRODUCTION

The success of chemical vapor infiltration (CVI) for ceramic matrix composites is strongly controlled by the mass transport properties of the preform and of the partially densified composite. These properties include gas permeability and mass diffusivity (effective diffusion coefficient), and depend on the density and microstructure of the composite. While gas permeability is the critical factor for forced flow CVI, mass diffusivity is a controlling property for isothermal CVI and may be important for coating or finishing processes designed to produce oxidation resistance or gas tightness in ceramic composite components. This effort involves experimental measurement of transport properties and model development for prediction of these properties and of densification performance.

## MASS TRANSPORT MEASUREMENTS

The apparatus for measurement of gas permeability and mass diffusivity is shown schematically in Figure 1 and photographically in Figure 2. A specimen of preform or porous composite, mounted in an aluminum ring, is held in the specimen chamber with o-ring seals top and bottom. The two sides of a differential pressure (DP) gauge (MKS Instruments) are connected to the volumes above and below the specimen. Helium gas flows through a mass flowmeter (MKS Instruments) into the chamber below the specimen. The apparatus includes two different DP gauges (0-10 and 0-200 torr) and two different flow meters (0-20 and 0-200 sccm) to allow accurate measurements over a wide range of permeabilities. The 4-port valve v7 can be switched to connect together the two ends of the DP gauge to allow checking of the gauge zero point reading.

For permeability measurements, only valves v1-v3 are open. The helium gas flow rate is adjusted using the needle valve v1 and the differential pressure across the specimen is recorded for each flow level. The gas permeability is calculated from a linear fit to the flow vs. pressure data, the specimen dimensions and the viscosity of helium. A typical plot of measured data and the resulting fit is shown in Figure 3. The estimated standard error for these measurements, based on the goodness-of-fit, is often as low as 1-2% of the permeability value.

For mass diffusivity, valves v4-v6 are opened producing flow of a helium-10% methane mixture across the top face of the specimen and of pure helium across the bottom face. Any methane passing through the specimen is measured using the gas chromatography, thermal conductivity-type detector TC. Over a small range near zero differential pressure the concentration of methane through the detector depends on both convection and diffusion, proportional to the expression,

$$U \left( 1 + \frac{1}{\exp(P_e) - 1} \right)$$

where U is the linear velocity of the gas through the specimen which is calculated from the known gas permeability and the pressure difference,  $P_e$  is the Peclet number  $UL/D$ , L is the

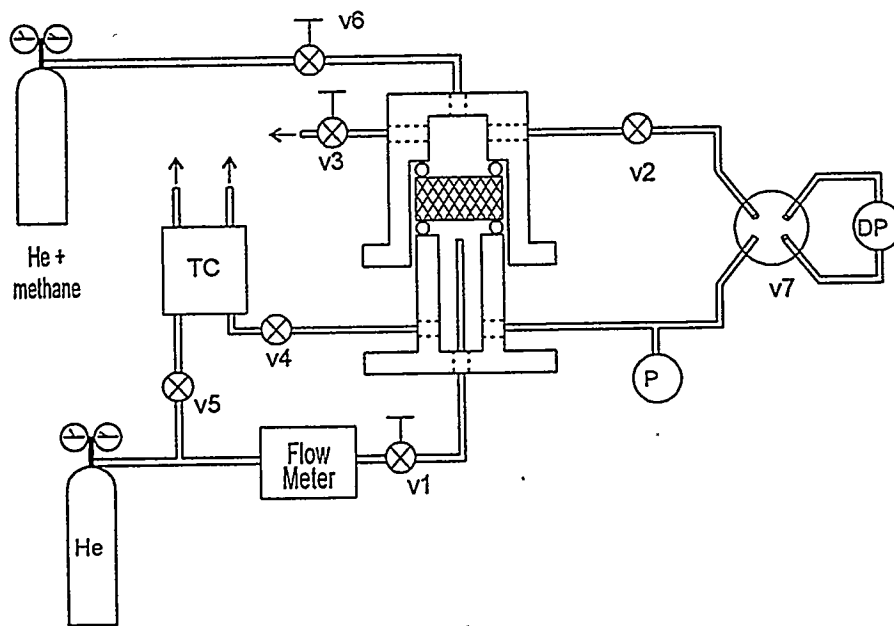


Figure 1. Apparatus for measuring gas permeability and mass diffusivity.

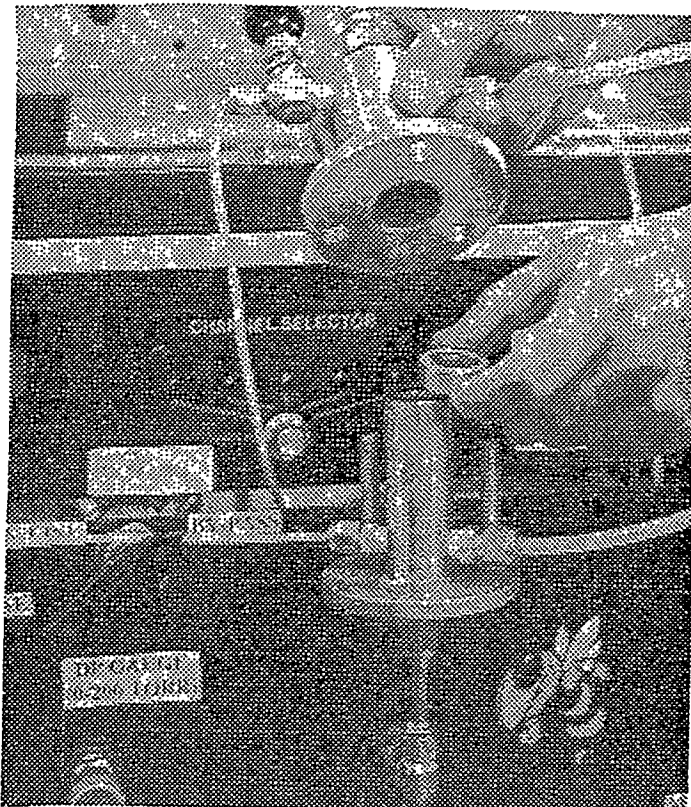


Figure 2. Permeability specimen is mounted in aluminum ring and placed in chamber.

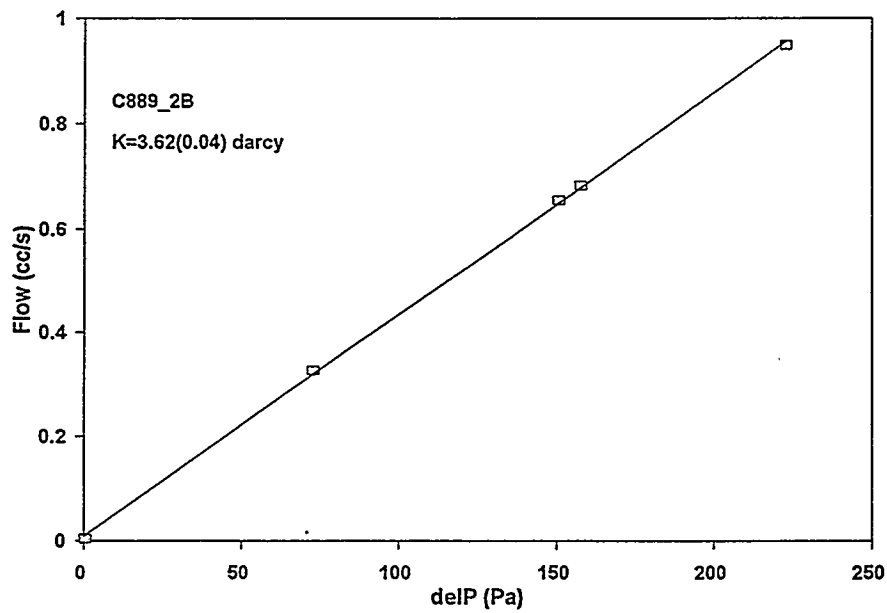


Figure 3. Gas permeability is calculated from linear fit to measured flow versus differential pressure.

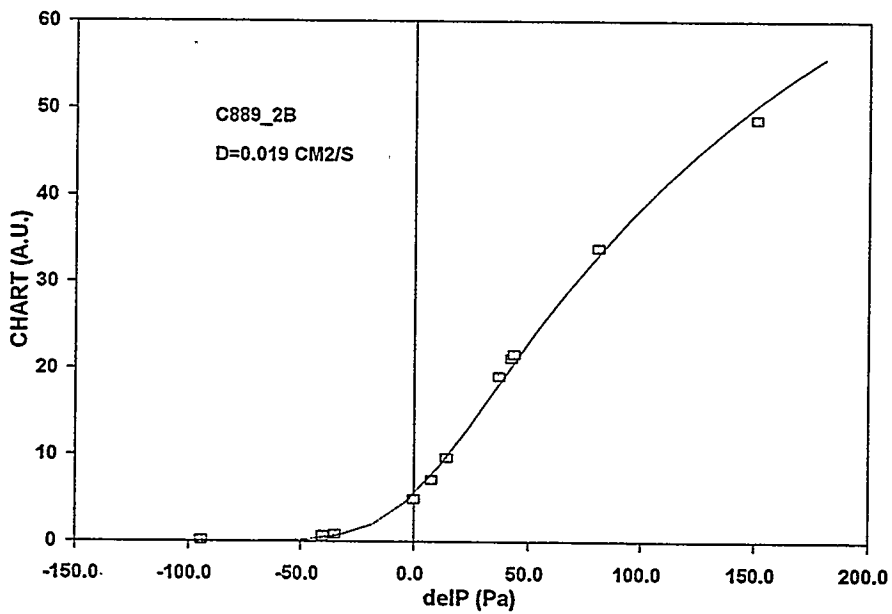


Figure 4. Mass diffusivity is calculated from fit to measured methane concentration versus pressure differential across specimen.



thickness of the specimen and  $D$  is the mass diffusivity ( $\text{cm}^2/\text{s}$ ). Fitting this curve to the measured data gives the mass diffusivity (Figure 4). This value is converted to a dimensionless diffusion factor by dividing by the handbook value of the free space diffusion coefficient for methane in helium<sup>1</sup>,  $0.748 \text{ cm}^2/\text{s}$ . This diffusion factor relates to the amount and tortuosity of the open porosity in the specimen. Recent measurements include Nicalon fiber cloth layup and 3-D weave, and Nextel fiber braid. Values of gas permeability and diffusion factor for these materials are given in Table 1.

Table 1. Measurements of permeability and mass diffusivity.

specimen		density		permeability (darcy)	diffusion factor
ID	description	( $\text{g}/\text{cm}^3$ )	(fraction)		
Ni30-1	Nicalon 0/30/60 layup	1.02	0.40	12.0	.047
Ni45-1	Nicalon 0/45 layup	1.02	0.40	9.1	.031
Ni90-1	Nicalon 0/90 layup	1.02	0.40	11.7	.047
Ni90-3	Nicalon 0/90 layup	1.02	0.40	8.2	.044
C885-1	CVI Nic 0/30/60	1.89	0.65	1.86	.0026
C885-2	CVI Nic 0/30/60	1.93	0.67	1.30	.0053
C885-3	CVI Nic 0/30/60	1.89	0.65	1.70	.0026
C889-2	CVI Nic 0/30/60	2.09	0.72	3.54	.024
C227a	CVI Nic 0/30/60	1.96	0.68	2.66	.002
C227c	CVI Nic 0/30/60	2.45	0.85	3.19	nd
C559g	CVI Nic 3-D weave	2.04	0.70	0.50	.0094
C559-1	CVI Nic 3-D weave	2.29	0.79	(0)	(0)
C559-3	CVI Nic 3-D weave	2.23	0.77	(0)	(0)
Nex-1	Nextel braid	0.99	0.37	25.3	.056
Nex-2	Nextel braid	0.89	0.33	19.0	.063

1 darcy =  $10^{-8} \text{ cm}^2$  ; nd= not determined; (0) = no flow detected through specimen

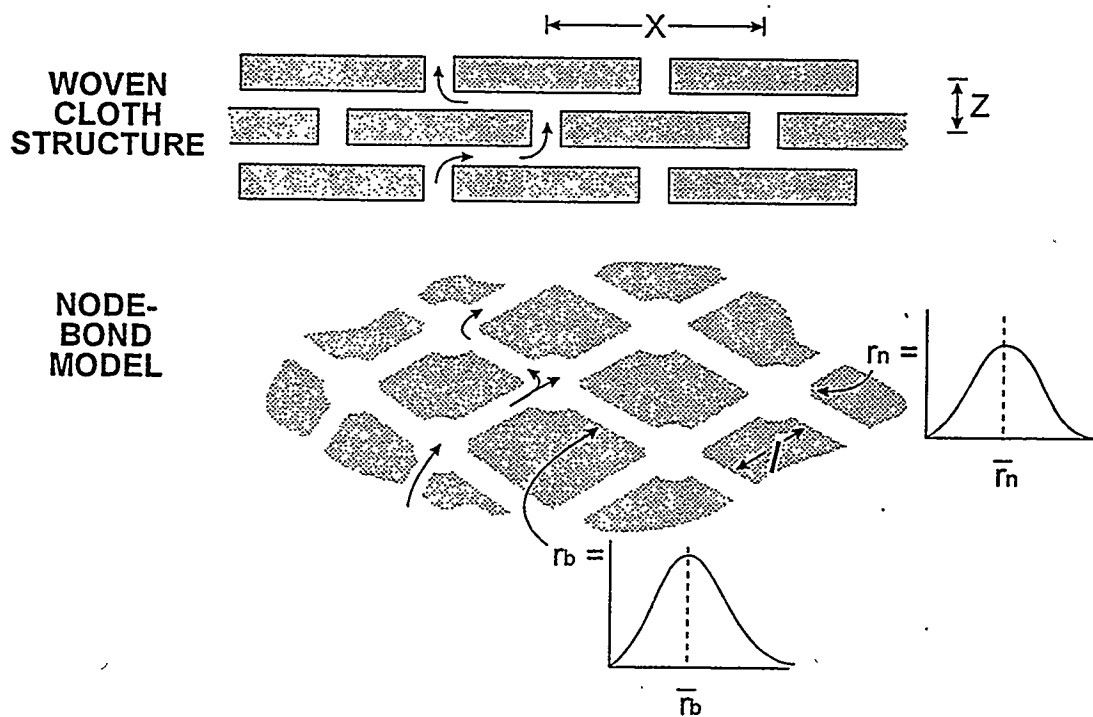


Figure 5. Node-bond model approximates structure of woven fiber preform.

## MODELING OF MICROSTRUCTURE AND MASS TRANSPORT

In order to better understand the relationship between transport properties and fiber architecture we have developed a node-bond model<sup>2</sup>. Woven and braided fiber structures are constructed using tows or yarns of 500-5000 individual filaments. While the fine porosity between filaments in the tows constitutes approximately half of the total porosity, it is the coarser porosity between tows that carries the gas flow through the composite. We model this structure as a network of nodes and bonds as shown in Figure 5. The average dimensions of the nodes and bonds, and their variability are determined by the weave structure. These dimensions are used to calculate permeability and diffusivity of the network. During CVI the pores fill in a progressive manner with increasing deposit thickness. When a particular fraction of the bonds are closed - the percolation limit - mass transport through the structure cannot continue and the composite has reached its ultimate density.

By selecting values for the bond and node dimensions, this model fits experimental measurements of gas permeability for cloth layup and 3-D weave preforms and composites

(Figures 6 and 7). The dimensions in the model for the cloth layup preform are consistent with microstructure measurements using high resolution X-ray computed tomography<sup>3</sup>. The 3-D weave becomes impermeable at a lower density than the cloth layup due to its initially lower fiber volume fraction (32%) and to the relatively large size of the "holes" at tow crossings.

## DENSIFICATION PERFORMANCE OF PREFORMS

In addition to the transport properties, the model gives the composite density as a function of matrix deposit thickness. For different preforms the deposit thickness needed to reach the percolation limit is a relative measure CVI processing times. For the cloth layup and 3-D weave preforms above the maximum deposit thicknesses are 85 and 120  $\mu\text{m}$  respectively. Thus under similar process conditions the 3-D weave preform will require approximately 50% greater processing time. This result is consistent with the limited experience at ORNL in densification of 3-D weave preforms.

It is desirable to use this model to predict the densification performance of new, untried preforms. Of current interest is a multilayer braid of Nextel fiber used to make free-standing tube preforms<sup>4</sup>. Our approach involves three steps: 1) select model parameters based on examination of the tow and layer spacings in the preform, 2) confirm model parameters by comparison with experimental permeability measurements on the preform, and 3) predict densification performance using these model parameters. This procedure, combining modeling and experimental measurement, may offer a reliable method for quickly testing the densification performance of various preform architectures prior to infiltration experiments.

Initial application of this method to the Nextel braid fiber architecture indicates densification behavior similar to that of the 3-D weave, i.e. longer processing times than for cloth layup preforms. Additional permeability measurements - particularly for the 3-D weave preform - are needed to fully tested this predictive approach.

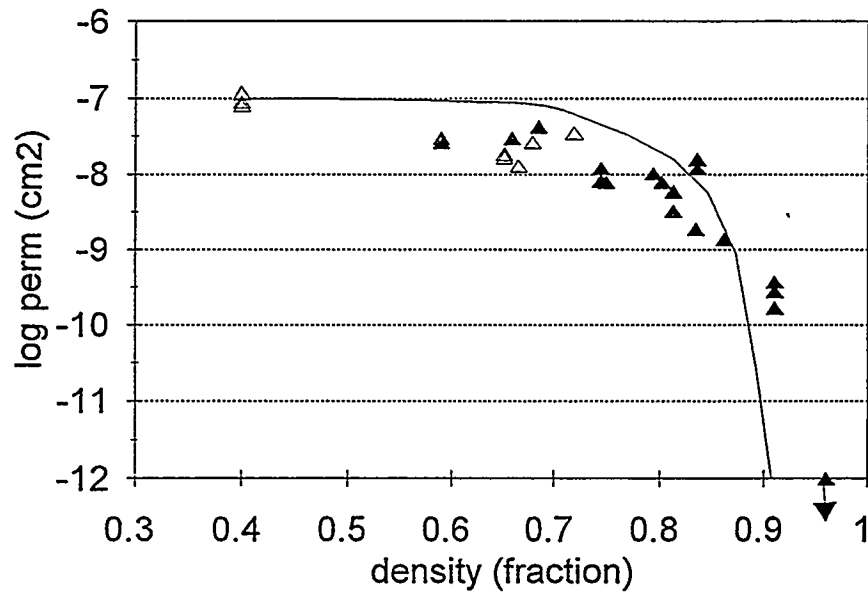


**Figure 6.** Model shows good agreement with experimental permeability for cloth layup composites. Open triangles are new measurements.

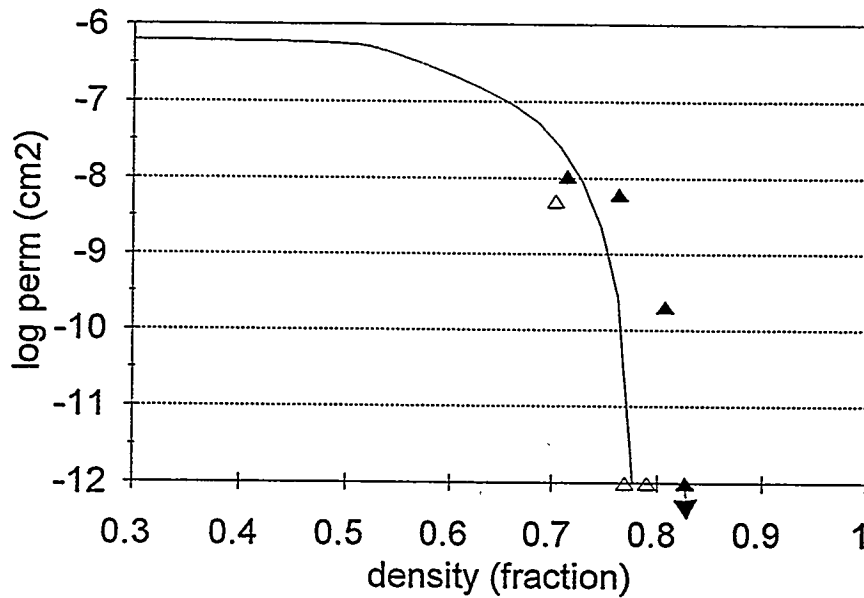


**Figure 7.** Model shows good agreement with experimental permeability for 3-D weave composites. Open triangles are new measurements.

## SUMMARY

Instrumentation and procedures have been completed for measurement of gas permeability and mass diffusivity of fiber preforms and porous materials. Permeability results for composites reinforced with Nicalon fiber in cloth lay-up and 3-D weave architectures are consistent with a node-bond model. Measured permeability values range from near 100 to less than 0.1 darcies. Mass diffusivity is reported as a structure factor relating the diffusion through the porous material to that in free space. These values clearly are correlated closely with the permeability values.

Measured values of gas permeability for the fiber preforms can be used to validate the parameters in the transport property model. In turn, the model can be used to predict the densification behavior of new, untried preforms. Additional measurements are needed to confirm this predictive approach to CVI performance.

## REFERENCES

1. Handbook of Chemistry and Physics 68th edition, R. C. Weast, ed., (CRC Press, Boca Raton, Florida) 1988
2. T. L. Starr "Gas transport model for chemical vapor infiltration" J. Mater. Res. 10(9) 2360-2366 (1995).
3. S-B. Lee, S.R. Stock, M.D. Butts, T.L. Starr, T.M. Breunig and J.H. Kinney, " Pore Geometry in Woven Fiber Structures: 0°/90° Plain-weave Cloth Layup Preforms," J. Mat. Res., submitted for publication (1996); S-B. Lee, "Nondestructive Examination of Chemical Vapor Infiltration of 0°/90° SiC/Nicalon Composites," Ph.D. Thesis, Georgia Institute of Technology, December 1993.
4. T.L. Starr, D.Y. Chiang, T.M. Besmann, D.P. Stinton, J.C. McLaughlin and W.M. Matlin, "Rapid Fabrication of Ceramic Composite Tubes using Chemical Vapor Infiltration," Ceramic Transactions, accepted for publication (1996)



## JOINING OF SiC CERAMICS AND SiC/SiC COMPOSITES

B. H. Rabin

Idaho National Engineering Laboratory  
P.O. Box 1625  
Idaho Falls, ID 83415-2218

### ABSTRACT

This project has successfully developed a practical and reliable method for fabricating SiC ceramic-ceramic joints. This joining method will permit the use of SiC-based ceramics in a variety of elevated temperature fossil energy applications. The technique is based on a reaction bonding approach that provides joint interlayers compatible with SiC, and excellent joint mechanical properties at temperatures exceeding 1000°C. Recent emphasis has been given to technology transfer activities, and several collaborative research efforts are in progress. Investigations are focusing on applying the joining method to sintered  $\alpha$ -SiC and fiber-reinforced SiC/SiC composites for use in applications such as heat exchangers, radiant burners and gas turbine components.

### INTRODUCTION

SiC ceramics have considerable potential as elevated temperature structural materials in fossil energy applications. Ceramic-to-ceramic joining methods are needed to allow the fabrication of large or complex shaped parts, and ceramic-to-metal joining methods are needed to allow integration of ceramic components into existing engineering systems. Although considerable efforts have been devoted to understanding the processing, microstructures and properties of SiC-based structural materials, joining remains largely an unresolved issue, particularly with respect to elevated temperature applications. Ideally, joined components should exhibit mechanical properties (including reliability), elevated temperature capabilities and environmental resistance comparable to the base material. Furthermore, the joining method should be practical, cost effective and applicable to different types of SiC ceramics, including SiC fiber-reinforced composites.

This project has successfully developed a reaction processing method for fabricating SiC ceramic-to-ceramic joints [1,2]. The processing method involves tape casting thin sheet SiC+C interlayer precursors, clamping the tape between the SiC parts, and infiltrating the joint with molten Si to form a reaction bonded silicon carbide (RBSC) joint interlayer. This method is attractive since the interlayer material is compatible with SiC, and excellent room and elevated temperature mechanical properties can be achieved.

In addition, as with brazing, external pressure is not required, thus making the process inexpensive and practical compared to alternative joining methods. Details of the joining procedure as well microstructural and mechanical property characterization results have been described previously [1,2]. This paper reports on recent laboratory efforts to improve the joining process, as well as the status of technology transfer efforts.

## PROGRESS STATUS

### Laboratory Joining Studies

The applicability of the joining method for producing a variety of joint geometries has been demonstrated in previous work [3]. Figure 1 shows examples of several joined structures that were fabricated from sintered  $\alpha$ -SiC using the laboratory scale localized induction heating apparatus at INEL. Of particular interest is the ability to fabricate tube-to-tube joints, since long ceramic tube structures are required in applications such as heat exchangers and radiant burners.

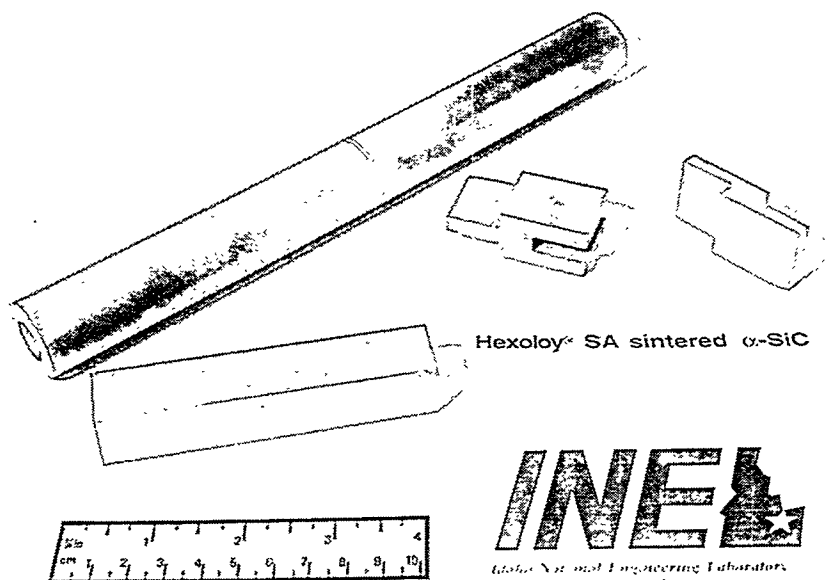


Figure 1. Examples of joined  $\alpha$ -SiC structures produced using the reaction processing method developed under this project.



Recently, laboratory experiments have been directed at (1) improving the tape casting formulation to minimize the free Si content of the SiC+Si interlayer joints, and (2) using Si-Mo alloyed melts to produce SiC+MoSi<sub>2</sub> joint interlayers containing little or no free Si.

A variety of different tape cast formulations have been prepared wherein the ratio of SiC-to-C powder was varied, as well as the binder content. As in the case of commercial bulk RBSC fabrication [4,5], it is necessary to optimize particle packing so that, after binder burnout, the density of the mixture is close to the calculated theoretical value that results in complete densification, no dimensional change, and minimum free Si content after the Si+C reaction is complete. In general, the processing of defect-free SiC+C tape cast products typically requires higher binder contents than the extrusion of SiC+C mixtures used in commercial RBSC manufacturing. Through careful control of particle sizes, and use of appropriate surfactants and dispersion techniques, suitable tapes can be produced. Currently, the new tape cast formulations being investigated are considered proprietary.

Si-Mo alloys containing 3 wt.% and 6 wt.% Mo were prepared by arc melting. The ingots were crushed in 1-3 mm pellets and used to infiltrate the standard SiC+C tape cast precursor. The presence of MoSi<sub>2</sub> in the joints was confirmed using x-ray diffraction (XRD) and energy dispersive spectrometry (EDS), demonstrating that MoSi<sub>2</sub> can be formed in joints, as has previously been demonstrated in bulk RBSC ceramics [6,7]. However, the volume fraction of MoSi<sub>2</sub> obtained in the joints was well below that required to eliminate all free Si from the interlayer. This is a direct result of the excess quantity of free Si present in these joints. It is expected that this problem will be eliminated through optimization of the tape casting process to minimize the Si content in joints produced without Si-Mo melts.

#### Technology Transfer Activities

Table 1 lists the ongoing active industrial collaborations and the associated applications being explored for the use of the SiC joining technology developed in this research program.

industrial partner	material	potential applications	project status
DuPont Lanxide Composites, Inc.	CVI SiC/SiC	gas turbine components, heat exchangers, radiant burners	initial specimens joined and tested, detailed studies in progress
Allied-Signal Aerospace	$\alpha$ -SiC	ceramic air heater for HITAF	Phase I completed, Phase II approved for scale-up demonstration
Stone & Webster	$\alpha$ -SiC	ethylene cracking, steam reforming	equipment modifications in progress,
Amercom, Inc.	SiC/SiC	gas turbine components, heat exchangers, radiant burners	investigating applicability to the material
Textron Specialty Materials, Inc.	NBSC	gas turbine components, heat exchangers, radiant burners	investigating applicability to the material
Dow Corning	SiC/SiCN	gas turbine components, chemical pump	investigating applicability to the material

Table 1. Active Industrial Collaborations and Potential Uses for SiC Joining Technology

Cooperative work with DuPont Lanxide Composites, Inc. is in progress to apply the joining technique to CVI SiC/SiC composites. Preliminary shear lap joints were fabricated from both coated and uncoated specimens, and room temperature mechanical testing was carried out. In some joints failure initiated within the excess free Si adjacent of the joint, and crack propagation occurred through the composite material. Failure did not occur at the interface, indicating excellent bond strength was achieved. Joint strengths were ~35 MPa, approximately half the value expected for the composite material. Work is in progress to determine if the joining process significantly degrades composite properties, and additional mechanical testing and failure analysis are in progress. A presentation describing these results was recently given at the 26th Annual Conference on Composites and Structures held in Cocoa Beach, FL, January 14-17, 1996.

Phase II activities have been defined in collaboration with Allied Signal Aerospace Corp., a subcontractor to Foster Wheeler Development Corp., involved in the development of the Ceramic Air Heater for the DOE High Temperature Advanced Furnace. The Phase II work, funded under the High Performance Power Systems Program through DOE-PETC, is expected to begin in the near future. This work will involve fabrication and elevated temperature high pressure testing of  $\alpha$ -SiC tube-to-tube

joints, and demonstration of the ability to fabricate a subscale tube-manifold assembly in cooperation with Carborundum.

Work has recently been initiated in cooperation with Stone & Webster Engineering Corporation to investigate fabrication of long  $\alpha$ -SiC tube assemblies for use in ethylene cracking applications. Preliminary testing of joints in simulated cracking environments will be conducted in collaboration with ORNL. Subsequently, actual tubular assemblies will be fabricated for pilot testing by Stone & Webster.

## SUMMARY

Reaction processing methods have been developed for fabricating SiC-to-SiC joints for potential use at elevated temperatures. Laboratory studies are focusing on optimizing the tape casting process to produce joints containing a minimum of free Si, and on producing SiC+MoSi<sub>2</sub> interlayers using alloyed Si-Mo melts. Technology transfer activities are continuing.

## REFERENCES

1. B. H. Rabin and G. A. Moore, "Microstructure and Properties of SiC-to-SiC Joints Produced by Reaction Bonding," Silicon-Based Structural Ceramics, B. Sheldon (ed.), The American Ceramic Society, Westerville, OH, 1993.
2. B. H. Rabin and G. A. Moore, "Reaction Processing and Properties of SiC-to-SiC Joints," *Mat. Res. Soc. Symp. Proc.*, Vol. 314, 1993, pp. 197-203.
3. B. H. Rabin "Joining of SiC Ceramics and SiC/SiC Composites," ORNL/FMP-95/1, Oak Ridge National Laboratory, August 1995, pp. 41-44.
4. P. Popper, "The Preparation of Dense Self-Bonded Silicon Carbide," Special Ceramics, Heywood, London, p. 209, 1960.
5. C. W. Forrest, P. Kennedy and J. V. Shennan, "The Fabrication and Properties of Self-Bonded Silicon Carbide Bodies," Special Ceramics 5, P. Popper (ed.), British Ceramic Research Association, Stoke-on-Trent, p. 99, 1972.
6. R. P. Messner and Y-M. Chiang, "Processing of Reaction-Bonded Silicon Carbide Without Residual Silicon Phase," *Ceram. Eng. Sci. Proc.*, 9(7-8), pp. 1052-1060, 1988.
7. R. P. Messner and Y-M. Chiang, "Liquid-Phase Reaction-Bonding of Silicon Carbide Using Alloyed Silicon-Molybdenum Melts," *J. Amer. Ceram. Soc.*, 73(5), pp. 1193-1200, 1990.



DEVELOPMENT OF NONDESTRUCTIVE EVALUATION METHODS  
FOR STRUCTURAL CERAMICS

W. A. Ellingson, R. D. Koehl, H. P. Engel,<sup>†</sup>  
J. A. Wilson and J. B. Stuckey

Energy Technology Division  
Argonne National Laboratory  
Argonne, IL 60439

<sup>†</sup>Heaviside Science, Inc.  
Melbourne, FL 32934

ABSTRACT

Nondestructive evaluation (NDE) methods using three-dimensional microfocus X-ray computed tomographic imaging (3DXCT) were employed to map axial and radial density variations in hot-gas filters and heat exchanger tubes. 3D XCT analysis was conducted on (a) two 38-mm-OD, 6.5-mm wall, SiC/SiC heat exchanger tubes infiltrated by CVI; (b) eight 10 cm diam. oxide/oxide heat exchanger tubes; and (c) one 26-cm-long Nextel fiber/SiC matrix hot-gas filter. The results show that radial and axial density uniformity as well as porosity, can be assessed by 3D XCT. NDE methods are also under development to assess thermal barrier coatings which are under development as methods to protect gas-turbine first-stage hot section metallic substrates. Further, because both shop and field joining of CFCC materials will be necessary, work is now beginning on development of NDE methods for joining.

INTRODUCTION

Nondestructive evaluation (NDE) technology is being developed to advance the reliable application of ceramic materials to fossil energy systems for improved efficiency and better environmental control. Advanced materials systems under development for fossil energy applications include continuous fiber ceramic matrix composites for hot-gas filters and heat-exchangers and thermal barrier coatings for high gas-firing temperature turbines.

## DISCUSSION OF CURRENT ACTIVITIES

### Hot Gas Filters and Heat Exchangers

#### (a) Hot Gas Filters

For hot-gas filter and heat exchanger studies, high spatial resolution 3DXCT methods have been explored.<sup>(1-3)</sup>

One 38 mm O.D. nextel fiber/SiC matrix hot-gas filter supplied by 3M, was examined at 25 mm intervals along the 26 cm length with data acquired using the ANL 3DCT scanner<sup>(2)</sup>. The CT images were reconstructed in a 687 x 687 matrix, using 1053 projections with a pixel size of 85  $\mu\text{m}$  x 85  $\mu\text{m}$ , and six rows were averaged or a slice thickness of .51 mm. At each 25 mm section 14 slices were reconstructed. Image reconstructions were done using a newly installed 133 MHz dual pentium computer which has allowed faster reconstruction times. The 32-bit reconstruction files are rescaled to 8-bit scaled data for input to a 3D image display software, IDL, from Research Systems, Inc. This runs on Windows 95 in a separate 150 MHz pentium. However, a software package was written which speeds the input to the IDL software so that density related information can be determined.

Using these methods, hot gas filters have been analyzed for axial density variations as shown in Fig. 1. These data were obtained by using an in-house written software package which allows the average grayscale for each CT slice to be computed. A typical individual CT cross-section is shown in Fig. 2.

Once the 3D data sets (image and histograms) are obtained, the grayscale threshold can be set to allow any particular part of the filter tube viewed in 3D. This could allow quantification of 3D density variations by looking at before and after operation data. Examples are shown in Fig. 3. Figure 3 shows: a) the image of the outer mesh of the 3M hot gas filter; b) the internal wall (refer to Fig. 2a; white inner ring).

By such analysis, volumetric analysis of trapped material in hot gas filters may be accomplished.

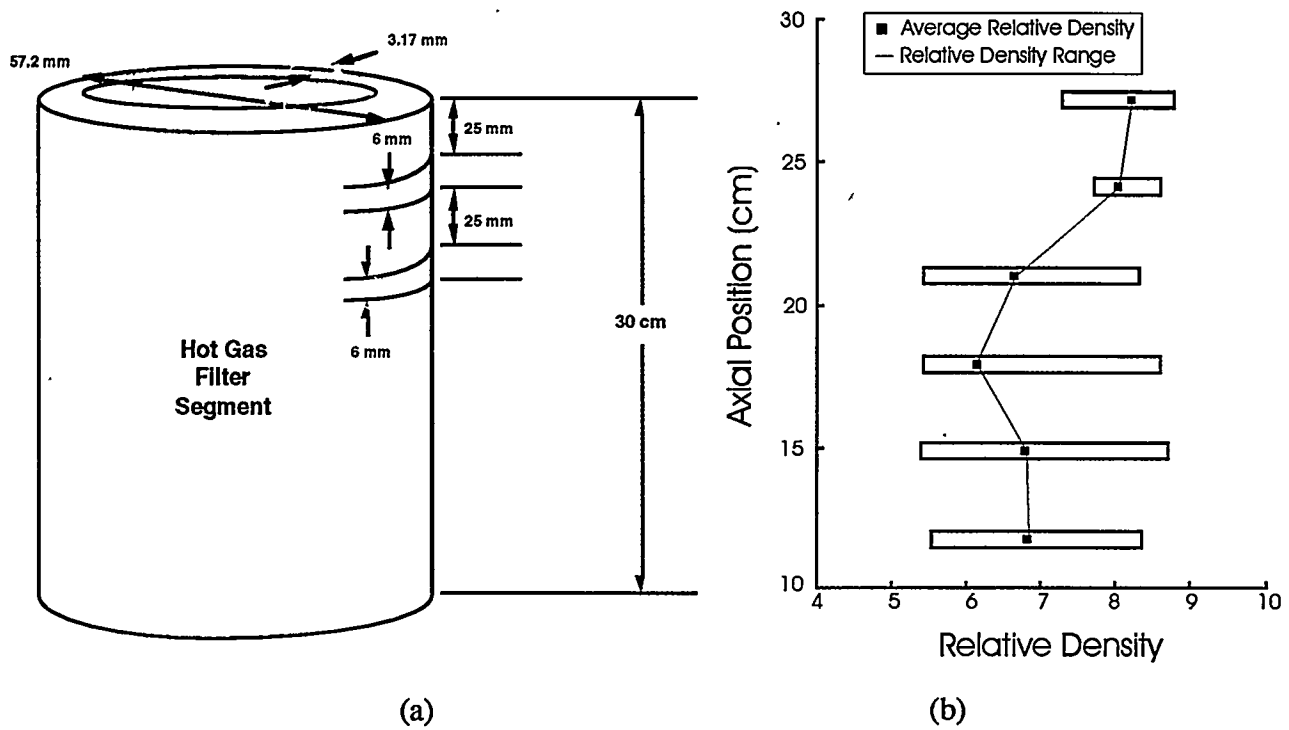


Fig. 1. Axial density variations for 3M hot-gas filter. (a) Schematic showing data locations. (b) Axial density profile

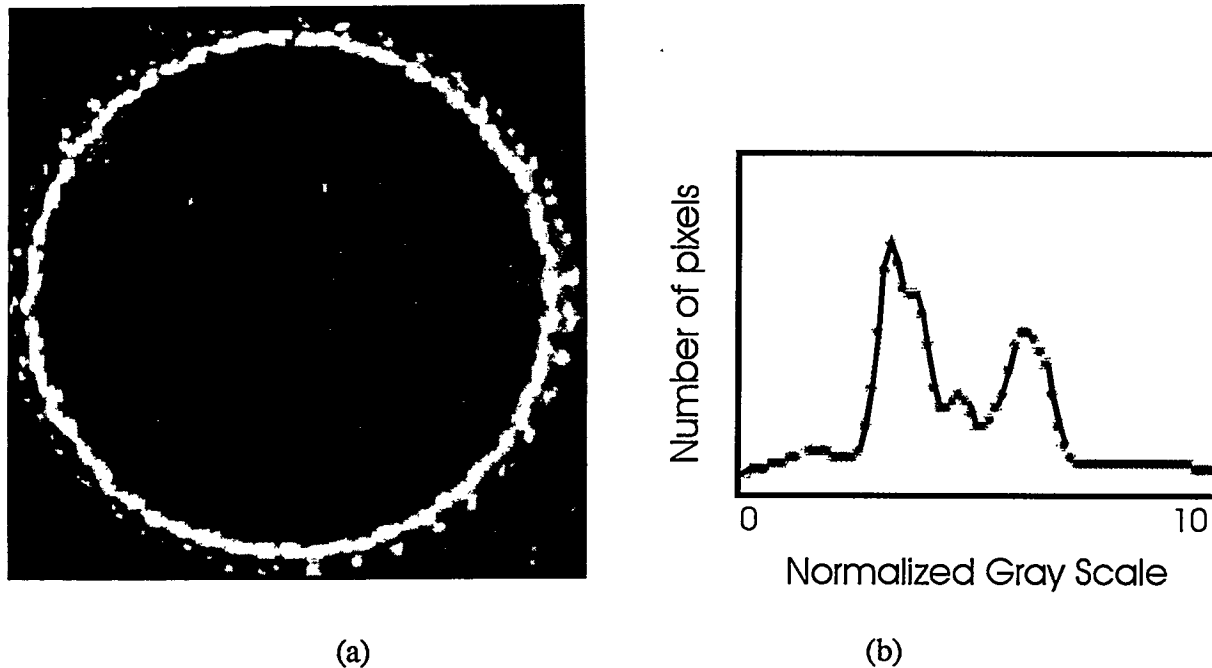


Fig. 2. Typical X-ray CT cross section through the 3M hot-gas filter and corresponding gray-scale histogram. Note the high-density inner fabric. (a) CT image. (b) Histogram.

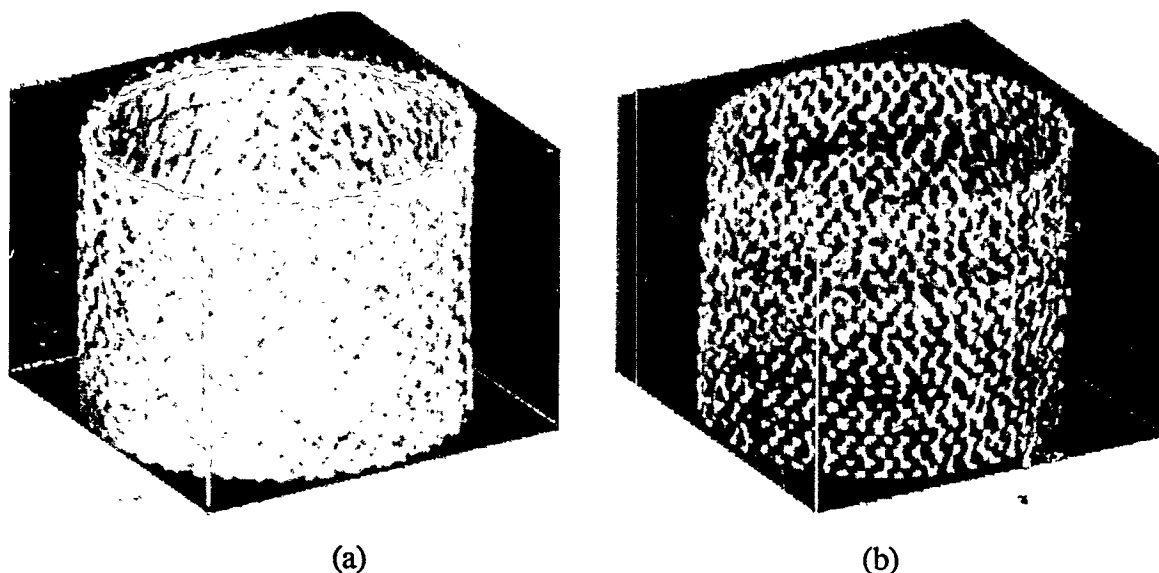


Fig. 3. Volumetric 3D X-ray CT analysis of 3M hot gas filter. a) Verification of detection of outer mesh. b) Inner surface.

#### b) Heat Exchangers

For the heat exchanger studies, 3DXCT methods were again explored. Two sets of specimens were available: set 1 consisted of eight 10 cm diam. by 10 cm long specimen provided by Oak Ridge National Laboratory (ORNL). These heat exchanger tubes were provided to ORNL by Babcock & Wilcox and had been exposed to conditions used in the E. I. DuPont hazardous waste incinerator. The specimens for NDE had been cut from 1.5 m long tubes. These specimens are identified in Table 1. Note that specimen AR is an as-received (unexposed) specimen. Set two (see Table 2) consisted of 2 CVI SiC/SiC specimens provided by Virginia Polytechnic Institute (VPI) with considerably different fiber architecture. Tube I appears to be a 3D weave. Tube II appears to be a 2D layup with 45° rotations between plys.

While the NDE work conducted so far consisted of analysis using X-ray CT data acquisition, future work will evaluate air-coupled ultrasonic methods and thermal imaging.

#### Throughwall Density Variations Including Delamination Detection

3DXCT data were acquired at various locations along the axial length of each of the 10 cm long sections from Set 1. At various azimuthal locations at any axial position, through-wall "line plots" were taken to establish the extent of throughwall density variations.



Table 1. Ceramic Heat Exchanger Tubes Used in NDE Study

Tube ID	Diam (in)	Wall Thickness (mm)	Exposure Position	Visual Observations	Materials	Manufacturer	Exposure Period
1	4	3.2	Right side Front row	Helically wound fibers	Nextel 610 fibers zirconia matrix	B&W	8 weeks
3	"	6.35	Center of Center row	Hoop wound fibers on surfaces, helically wound internal fibers, thermocouples on tube	Almax fibers zirconia matrix	B&W	27 weeks
4	"	"	Center of Rear row	Hoop wound fibers on surfaces, helically wound internal fibers, some unbonded layers visible	PRD166 fibers zirconia matrix	B&W	27 weeks
5	"	"	Left side Rear row	Hoop wound fibers on surfaces, helically wound internal fibers, some unbonded layers visible	PRD166 fibers zirconia matrix	B&W	27 weeks
6	"	"	Right side Center row	No evidence of fibers	SiC particles alumina matrix	DLC	27 weeks
7	"	"	Right side Rear row	Appears to be helically wound fibers, ~3/8" repeat	Type B mixed oxides	DLC	8 weeks
9	"	"	Left side Center row	Appears to be helically wound fibers, ~3/8" repeat	Type B mixed oxides	DLC	8 weeks
AR	"	"	Unexposed	Hoop wound fibers, some unbonded layers	PRD166 fibers zirconia matrix	B&W	None

DLC = DuPont Lanxide Composites

B&W = Babcock & Wilcox

This includes detection of delaminations. A delamination, clearly visible by inspection, was detectable. 3DXCT analysis, see Fig. 4, shows (see position b) that the visible crack is clearly detected whereas "c" position show only a slight density variation.

Table 2. CVI SiC/SiC Heat Exchanger Tubes for NDE

Tube ID (ANL)	Diam (mm)	Wall Thickness (mm)	Length (cm)	Remarks
I	38	6.35	18.9	Appears to be a 3D braided fiber architech
II	38	6.35	20.3	Appears to be 2D layup 45° interlayer rotation

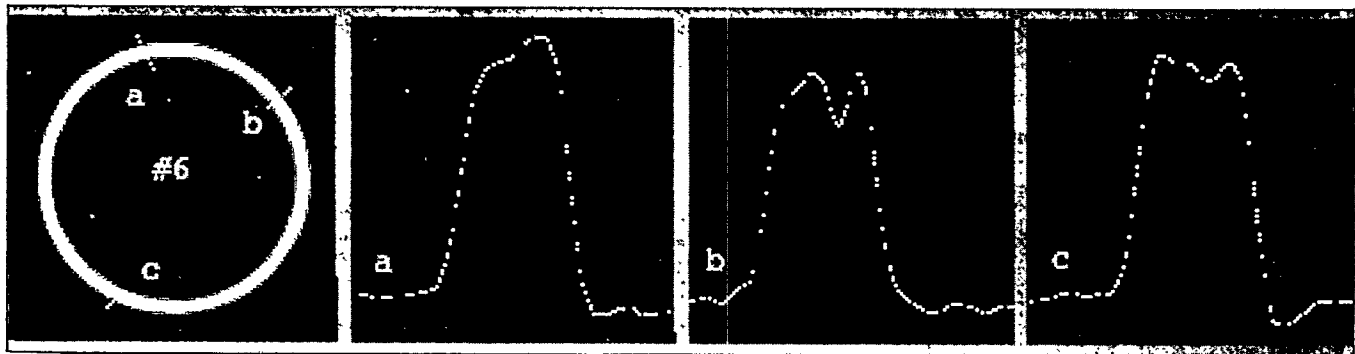


Fig. 4. X-ray CT analysis of heat exchanger tube 6, showing throughwall density profiles at 3 azimuthal positions. Note the delamination detection at location "b".

We conducted similar analysis of the as-received PRD66 hoopwound fiber specimen and again detected delaminations in the wall.

A software package was also developed which allows study of the density variation at any location through the wall using CT axial cross-sections. An example is shown in Fig. 5 for tube 1. Note that at each radial position a 360° density map is determined. The density variations are very small for this particular example.

#### Axial Density Variations

To establish axial density variations along the tubes, the new software package was used which allows total average density for any CT cross section as a function of axial

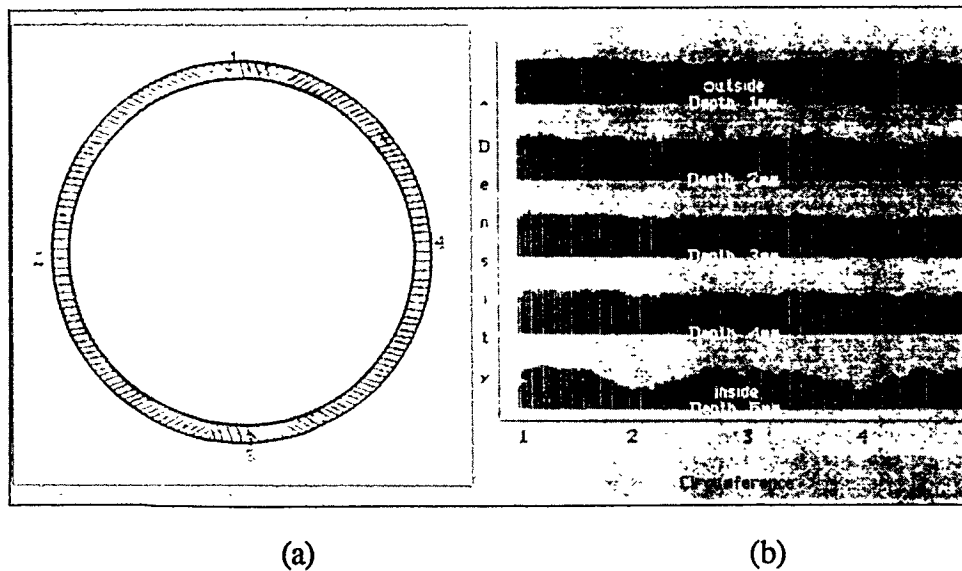


Fig. 5. X-ray CT sectional image of tube 1 and corresponding 360° density profiles at any position through the wall thickness. a) X-ray CT cross-sectional image. b) five 360° density plots at 0.95, 1.90, 2.85, 3.80 and 4.75 mm from the outer wall.

position to be obtained. Thus density as a function of axial position can be plotted for any CT data set obtained. The axial density analysis is shown in Fig. 6 for the two CFCC specimens of Set 2. The density range for the 3D braid is 1.98 to 2.29 g/cc with a mean of 2.15 g/cc while the 2D laminate is 1.87 to 2.50 with a mean of 2.35 g/cc.

Argonne has a new CT facility which will allow 2-2.5 m long tubes to be studied by CT. In addition, a new air coupled ultrasonic system is now being studied for detection sensitivity for CFCC materials part of the CFCC program. This NDE method will also be examined for applicability to hot-gas filter and heat exchanger tubes.

### Thermal Barrier Coatings

Thermal barrier coatings (TBCs) are a key materials element to allow upgrading of turbine gas-firing temperatures and subsequent hot-stage sections for evolutionary turbine materials such as superalloys. The mechanical integrity of these TBC's depends on careful control of the microstructure as well as the bond coat which is used to join the TBC to the alloy substrate.

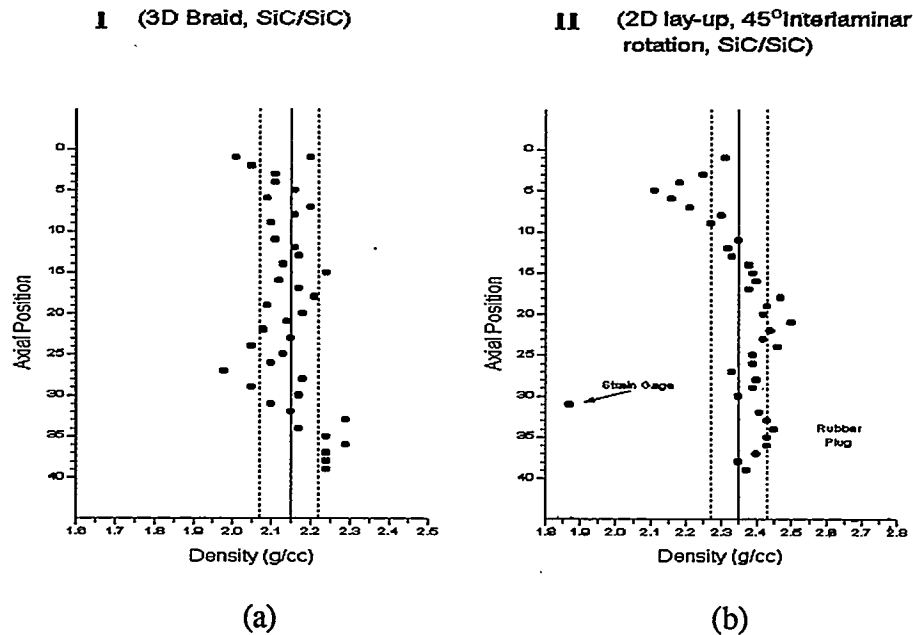


Fig. 6. Axial density profiles for two CVI SiC/SiC CFCC heat exchanger tubes. (a) 3D weave. (b) 2D laminate.

For fossil energy applications, e.g., coal-gas-fired turbines, high temperatures and long-term exposures increases the likelihood of spallation of the TBC and subsequent turbine blade failure. Key development issues for TBCs include: a) reliability of bond coat interface, b) thermal expansion characteristics of the TBC and c) thermal conductivity across the TBC thickness.

For the thermal barrier coating studies, this NDE work initially concentrates on two methods: a) a non-contact, non-invasive method called Time-Resolved-Infrared-Radiometry (TRIR).<sup>(4,5)</sup> and b) elastic optical scatter.<sup>(6)</sup> In the TRIR method (see Fig. 7), a thermal excitation source and a high sensitivity, high frame rate infrared camera are located on one side of the thermal barrier coating. The thermal excitation source can be a high energy flash lamp (we have a 1.6 KJ lamp) or a scanning laser. The thermal pulse applies a heat source which penetrates the TBC and reflects off the bond-coat (may reflect off bond coat-substrate interface depending on wave-length of excitation). The reflected thermal "pulse" is then time-dependent recovered by the infrared camera and the individual full-field thermal frames are

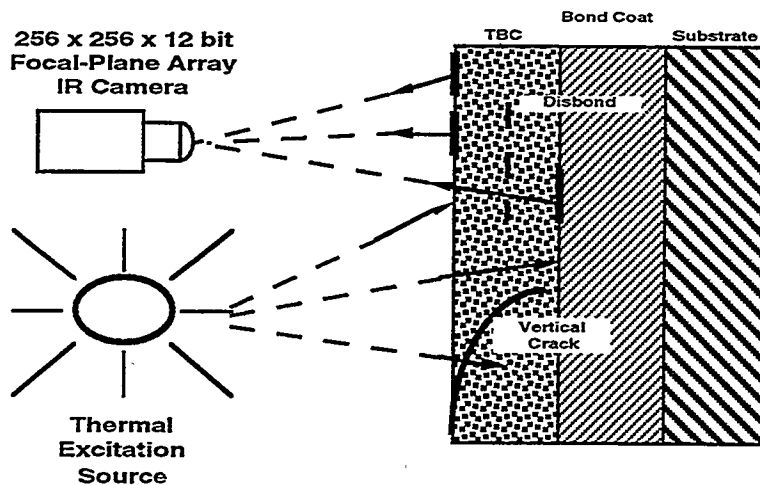


Fig. 7. Schematic diagram of one-sided time-resolved-infrared radiometry method. Note: Schematic shows two defect types: a) disbond, b) vertical crack.

stored in a digital computer. For a disbond of the coating, the temperature rise detected by the camera is much higher as the input heat pulse is not absorbed in the substrate.

### Joining

Ceramic-to-ceramic joining methods are usually necessary both for shop fabrication of complex shaped parts and for field repair. There are several potential joint architectures as shown in Fig. 8. These include lap joints, socket flange, straight socket and conical joints.<sup>(7)</sup>

Rabin et al.<sup>(8,9)</sup> of Idaho National Engineering Laboratory (INEL), have been developing joining methods as part of this program. They have been primarily focusing on tape casting sheets of SiC + C precursor, clamping the tape between the parts to be bonded, and then infiltrating with molten Si to form a reaction bonded silicon carbide (RBSC) joint interlayer.

Regardless of the method used for joining, NDE methods are necessary to establish the completeness and quality of the joint. The development of NDE methods to study joint quality is the focus of this part of the NDE work.

For the SiC/SiC NDE joining studies, efforts are concentrating on CFCC materials and this work is being conducted in cooperation with the CFCC program. Cooperative efforts have been established with DuPont Lanxide Composites (DLC) as well as Dow-Corning and with INEL.

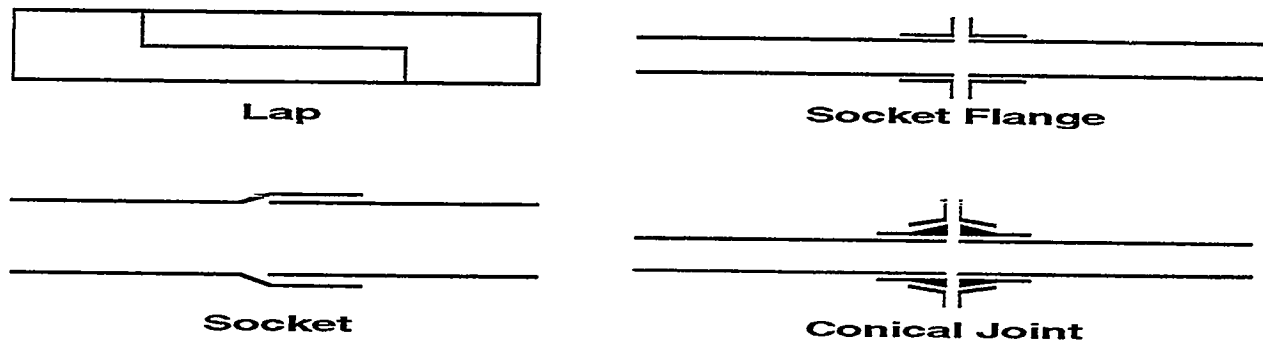


Fig. 8. Schematic diagrams of several possible CFCC joint configurations.

Lap-joint specimens have been received from DLC as noted in Table 3 below.

Table 3. Lap joint CVI CFCC SiC/SiC specimens for NDE

Specimen Number	Specimen Length	Specimen Thickness	Comments
4U-1B-1	41 mm	3 mm	Lap joint at midpoint length Lap joint = 15 mm long
3C-1B-1	43 mm	3 mm	Center lap joint Lap joint = 14 mm long
3C-2A-1	42 mm	3 mm	Center lap joint unknown Lap joint length: estimate 13-14 mm
2A-C	42 mm	3 mm	Center lap joint unknown Lap joint length: estimate 13-14 mm
3U-2A-5	42 mm	3 mm	Center lap joint Lap joint = 13 mm long

Metallic Si flashing on the specimens was removed by a diamond grit grinding wheel. Several NDE studies will be conducted on these and subsequently mechanical property data will be obtained. NDE studies will include, thermal infrared studies, air-coupled through-transmission ultrasonic studies, pulsed multi-frequency eddy-current and microfocus through-transmission X-ray imaging. As field repairs will be part of joining, NDE methods are being developed which have field application potential.

## REFERENCES

1. W. A. Ellingson, M. W. Vannier and D. P. Stinton, "Application of X-ray Computed Tomography to Ceramic/Ceramic Composites," in Chara. of Adv. Mat., E. Henneke, ed., Plenum Press, N.Y., 1991, pp. 9-25.
2. E. A. Sivers, P. A. Holloway and W. A. Ellingson, "Obtaining High-Resolution Images of Ceramics from 3D X-ray Microtomography by Region-of-Interest Reconstruction in Cer. Eng. on Sci., Proc. Vol. 14, No. 17-18, 1993, pp. 463-472.
3. E. A. Sivers, "Use of Multiple CT Scans to Accommodate Large Objects and Stretch Dynamic Range of Detectability in Nuc. Inst. and Methods in Phy. Res. B., Vol. 99, 1995, pp. 761-764.
4. J. C. Murphy, J. W. Maclachlin-Spicer, R. Osiander, W. D. Kevas and L. C. Aamudt, "Quantitative Nondestructive Evaluation of Coatings by Thermal Wave Imaging" in Rev. of Prog. in Quan. Non. Dest. Eval., Vol. 13, 1994, pp. 417-425, eds. D. O. Thompson and D. E. Chimenti, Plenum Press, N.Y., No. 7.
5. J. C. Murphy, L. C. Aamodt and J. W. M. Spicer, "Principles of Photothermal Detection in Solids," in Prog. in Photothermal and Photoacoustic Science and Technology, Vol. 1: Principles and Perspectives of Photothermal and Photoacoustic Phenomena, A. Mandelis, ed., 1992, pp. 41-94, Elsevier, North Holland.
6. J. S. Steckenrider and W. A. Ellingson, "Application of Laser Scattering to the Detection of Surface and Subsurface Defects in  $\text{Si}_3\text{N}_4$  Ceramics," Cer. Eng. and Sci. Proc., Vol. 15, No. 4, 1994, pp. 382-389.
7. Private communication, B. F. Goodrich-Supertemp, January 1996.
8. B. H. Rabin, "Joining of SiC Ceramics and SiC/SiC Composites," in Proc. of the Ninth Annual Conf. on Fossil Energy Materials, Oak Ridge National Laboratory Report, ORNL/FMP-95/1, 1995, pp. 41-44.
9. B. H. Rabin and G. A. Moore, "Joining of SiC Ceramics and SiC/SiC Composites," in Proc. of Seventh Annual Conf. on Fossil Energy Materials, Oak Ridge National Laboratory Report ORNL/FMP-93/1, 1993, pp. 33-42.





## EFFECTS OF FLAWS ON FRACTURE BEHAVIOR OF STRUCTURAL CERAMICS

J.P. Singh, D. Singh, and M. Sutaria

Energy Technology Division  
Argonne National Laboratory  
Argonne, Illinois 60439

### ABSTRACT

We evaluated the effects of fiber coating thickness, fiber orientation, and elevated temperature on flaw morphology and mechanical properties of Nicalon-fiber-reinforced SiC matrix composites with fiber cloth lay-up sequences of  $0^\circ/45^\circ$ ,  $0^\circ/20^\circ/60^\circ$ , and  $0^\circ/40^\circ/60^\circ$  and fiber coating thicknesses of 0.2 and 0.4  $\mu\text{m}$ . For the three fiber cloth lay-up sequences ( $0^\circ/45^\circ$ ,  $0^\circ/20^\circ/60^\circ$ , and  $0^\circ/40^\circ/60^\circ$ ), mechanical property (first matrix cracking stress, ultimate stress, and work of fracture) initially increase with coating thickness and reach peak values at a coating thickness of 0.2  $\mu\text{m}$ . A further increase in coating thickness does not result in further improvements in mechanical properties; this is related to the role of coatings in protecting fibers from damage during composite processing. Measured values of strength and work-of-fracture of the above composites at elevated temperatures increased with temperature up to  $1200^\circ\text{C}$ , but decreased at higher temperatures. This decrease is correlated to in-situ fiber strength and fiber/matrix interface degradation.

Correlations between model prediction and measured room-temperature ultimate strength of composites with  $0^\circ/45^\circ$  and  $0^\circ/40^\circ/60^\circ$  lay-up sequences were established by using in-situ fiber strength characteristics.

The failure modes and degradation mechanisms in hot-gas filters and ceramic composite joints are being characterized by the mechanical and fractographic evaluation techniques established thus far. Correlation of these results with those of nondestructive evaluation can provide critical information for improved quality control.

### INTRODUCTION

Continuous fiber-reinforced ceramic matrix composites (CFCCs) are being pursued as materials for structural applications in various industries, including automotive, aerospace,

and utilities, chiefly because of their combination of high strength and toughness at both room and elevated temperatures.<sup>1,2</sup> It has now become clear that the mechanical response of CFCCs, for a fixed fiber content, is largely controlled by intrinsic composite parameters, including strengths of the reinforcing fibers and matrix,<sup>3,4</sup> fiber/matrix interface characteristics,<sup>5,6</sup> and fiber architecture. Therefore, effort is continuing on the evaluation of the effects of fiber cloth lay-up sequence, fiber/matrix interface, and high-temperature environments on flaw generation and resulting mechanical properties of reinforcing fibers and composites.

### SPECIMEN FOR FRACTURE STUDIES

To evaluate the effects of fiber cloth lay-up sequence and elevated-temperature service environments on flaw generation and resulting mechanical properties, Nicalon-fiber-reinforced SiC matrix composites fabricated by chemical vapor infiltration (CVI) with various cloth lay-up sequences and fiber coating thicknesses were obtained from Ceramic Composites, Inc. (MD). To date, composites with fiber lay-up sequences of 0°/45°, 0°/20°/60°, and 0°/40°/60° and with carbon coating thicknesses of 0-0.4  $\mu\text{m}$  have been evaluated. Fiber content in the final composite was  $\approx 40$  vol.%. These composites were received in plate form and used to machine rectangular bars ( $\approx 3 \times 4 \times 40$  mm). The tensile edges of the test bars were bevelled to eliminate stress concentrations and thus avoid edge failures. Density was measured by the Archimedes principle. Approximately five specimens were tested per condition.

### ROOM- AND ELEVATED TEMPERATURE MECHANICAL PROPERTY EVALUATIONS AND CORRELATIONS WITH FIBER ARCHITECTURE

Flexure testing in a four-point-bend mode was used to evaluate mechanical properties of the composites at room and elevated temperatures. This method was chosen because of its relatively low cost and ease of use. For room-temperature tests, flexural bars ( $2.9 \times 4.2 \times 25.4$  mm) were tested with loading and support spans of 9.5 and 19.0 mm, respectively. All tests were conducted at a crosshead speed of 1.27 mm/min at ambient conditions on a universal testing machine.

High-temperature flexure tests were conducted at 1000, 1200, and 1300°C. The composite bars ( $2.9 \times 4.2 \times 28.0$  mm) were similar to those tested at room temperature, except for an additional SiC surface coating ( $\approx 100$   $\mu\text{m}$  thick) to prevent oxidizing the exposed carbon

coating on the fiber surfaces. SiC fixtures with loading and support spans of 12.7 and 25.4 mm, respectively, were used, and crosshead speed was 1 mm/min. All specimens were loaded perpendicular to the mat layers. At least three specimens were tested under each set of conditions.

The first matrix cracking stress, or onset of permanent damage to the composites, was determined from the load at which first deviation from the linear variation in the load-vs.-displacement plots was observed. Nominal ultimate stress was determined from the peak load value. Composite work-of-fracture (WOF) was estimated from the total area under the load-specimen displacement plots normalized on the basis of unit cross-sectional area of the fractured composites. True specimen displacement was obtained by subtracting system displacement from total displacement (system displacement was determined by measuring system compliance with a stiff alumina piece).

## ANALYTICAL BACKGROUND

Mechanical response of continuous fiber-reinforced ceramic matrix composites with increasing stress levels is dependent on in-situ fiber strength and its distribution. Based on the weakest-link-principle (i.e., failure occurs at the most severe flaw), strength distribution of fibers can be represented by the Weibull distribution function as follows:

$$F(\sigma) = 1 - \exp \left[ - \frac{L}{L_0} \left( \frac{\sigma}{\sigma_0} \right)^m \right], \quad (1)$$

where  $F(\sigma)$  is the cumulative failure probability at an applied stress  $\sigma$ ,  $\sigma_0$  is the scale parameter signifying a characteristic fiber strength at a fiber gauge length,  $L_0$ , and  $m$  is referred to as the Weibull modulus that characterizes flaw distribution in the material. Thus, by using the Weibull distribution function as given by Eq. 1, it is possible to estimate Weibull scale parameter at some standard gauge length,  $L$ , with the following expression:

$$\sigma = \sigma_0 \left( \frac{L_0}{L} \right)^{\frac{1}{m}}, \quad (2)$$

The in-situ fiber strength distribution parameters,  $\sigma_c$  and  $m$ , can be evaluated by measuring mirror sizes on fractured fibers. Figure 1 shows typical flaw morphology and

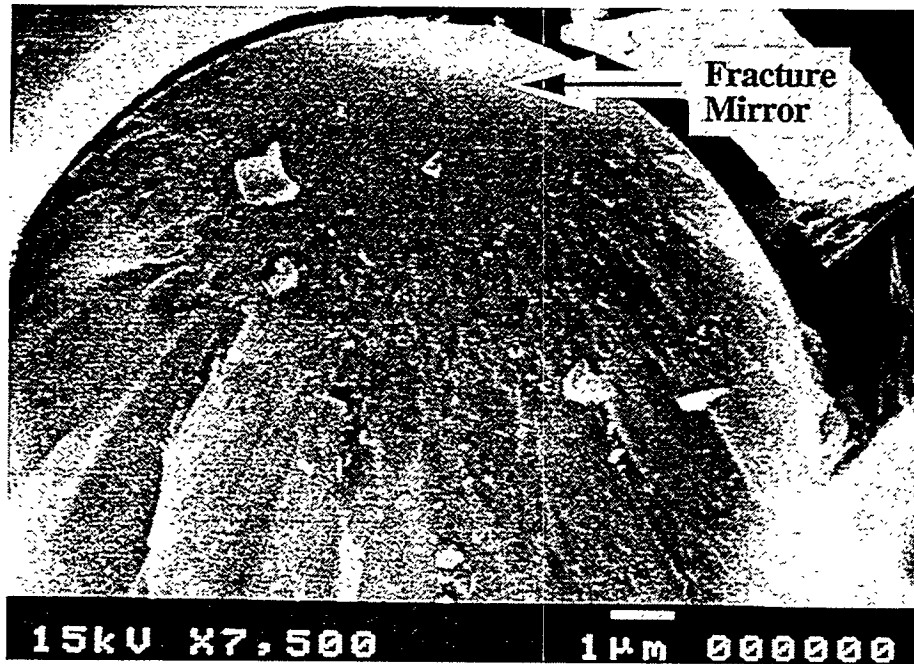


Fig. 1. Fracture surface morphology of SiC (Nicalon) fiber.

associated fracture features such as mirrors (smooth regions) and hackles (regions of multiple fracture planes) on a Nicalon fiber in a composite tested at room temperature. For brittle materials such as glasses and ceramics, it is possible to correlate sizes of fracture features to fracture stress with empirical relationships. For example, fracture stress,  $\sigma_f$ , of the fibers can be obtained from mirror-size measurements with the following relationship:<sup>7</sup>

$$\sigma_f = \frac{3.5K_f}{\sqrt{r_m}}, \quad (3)$$

where  $r_m$  is the mirror radius and  $K_f$  is the fracture toughness of the fiber. This semiempirical relationship is applicable for mirror sizes much smaller than the fiber diameter.

Based on the fiber fragmentation theory,<sup>8</sup> the resulting value of scale parameter,  $\sigma_c$ , from fracture mirror evaluations is at a gauge length,  $L_c$ , that is controlled by fiber/matrix interfacial shear strength and fiber strength. An average value for the gauge length for in-situ fractured fibers can be written as

$$L_c = r \frac{\sigma_c}{\tau}, \quad (4)$$

where  $r$  is the fiber radius and  $\tau$  is the fiber/matrix interfacial shear strength.

The fiber/matrix interfacial shear strength can be determined from average fiber pullout length measurement,  $h$ , as<sup>4,8</sup>

$$\tau = \frac{\lambda(m) r \sigma_c}{4h}, \quad (5)$$

where  $\lambda(m)$  is a nondimensional function and is dependent on fiber fracture statistics.

In-situ fiber strength distribution parameters ( $\sigma_c$  and  $m$ ) can be correlated to the ultimate strength,  $\sigma_{UTS}$ , of the composite as follows:<sup>8</sup>

$$\sigma_{UTS} = f_l \sigma_c \left[ \frac{2}{m+2} \right]^{1/m+1} \left[ \frac{m+1}{m+2} \right], \quad (6)$$

where  $f_l$  is the fiber volume fraction parallel to the loading direction.

## RESULTS AND DISCUSSION

As shown in Table 1, mechanical properties of composites are dependent on both fiber coating thickness and fiber cloth lay-up sequence. For sequences of  $0^\circ/45^\circ$  and  $0^\circ/20^\circ/60^\circ$ , mechanical properties (first matrix cracking stress, ultimate stress, and work of fracture) initially increase with coating thickness and reach peak values at a coating thickness of  $0.2 \mu\text{m}$ . Further increases in coating thickness do not result in further improvements in mechanical properties; this is believed to be related to the role of coating in protecting fibers from damage during processing and in service.<sup>9</sup> These results indicate an optimal coating thickness of  $0.2 \mu\text{m}$  for fibers in the composites. Similar results have been obtained for CVI SiC/SiC composites obtained from Oak Ridge National Laboratory.<sup>9</sup>

Table 1. Room-temperature mechanical property data for SiC/SiC CFCC with various fibercloth lay-up sequences

Fiber Architecture	Coating Thickness ( $\mu\text{m}$ )	Composite Density ( $\text{g}/\text{cm}^3$ )	First Matrix Cracking Stress ( $\text{MPa}$ )	Ultimate Stress ( $\text{MPa}$ )	Work-of-Fracture ( $\text{kJ}/\text{m}^2$ )
0°/45°	0.0	-	-	105 $\pm$ 28	0.16
	0.2	-	95.0	321 $\pm$ 131	17.8 $\pm$ 6
	0.4	2.25	86 $\pm$ 23	153 $\pm$ 41	9.8 $\pm$ 2
0°/20°/60°	0.0	2.43	-	93 $\pm$ 12	0.25 $\pm$ 0.6
	0.2	2.31	223 $\pm$ 15	319 $\pm$ 41	12.7 $\pm$ 2.3
	0.4	2.40	115 $\pm$ 25	287 $\pm$ 48	15.7 $\pm$ 4
0°/40°/60°	0.4	2.46	116 $\pm$ 28	312 $\pm$ 28	14.4 $\pm$ 4

For a given fiber coating thickness, mechanical properties of composites with 0°/20°/60° and 0°/40°/60° fiber lay-up sequences were similar in magnitude, whereas composites with a fiber sequence of 0°/45° had relatively lower values. The decrease in mechanical properties for composites with the 0°/45° sequence is believed to have two causes: first, composites with a fiber lay-up sequence of 0°/45° had a lower density (2.25  $\text{g}/\text{cm}^3$ ) than composites with other fiber lay-up sequences (Table 1); the second cause could be related to the smaller fiber fraction in the loading direction for 0°/45° composites relative to that of composites with other fiber lay-up sequences. This will be discussed in more detail in the following sections.

Figure 2 shows typical load-displacement behavior obtained from flexure tests conducted on SiC(f)/SiC composites with the 0°/40°/60° fiber lay-up sequence, at both room and elevated temperatures. Similar variations in load displacement were observed for the 0°/45° composites, and gradual failure was observed in all tests. However, the area under the curve increased somewhat in tests at elevated temperatures. It is recognized here that because of the generation of matrix crack(s) and the shift in the neutral axis, use of the simple beam theory to assess ultimate stresses gives a semiquantitative estimate of ultimate strength. However, the purpose of estimating these values is to compare the relative load-bearing properties of the composites under specific fiber orientations and test conditions.

Figure 3 shows the variation of ultimate strength for the three sets of composites (0.4  $\mu\text{m}$  coating thickness) as a function of temperature. At 1000°C, strength of the 0°/40°/60° composites was similar to its room-temperature value. No 0°/45° specimens were available for tests at 1000°C. Beyond 1000°C, the ultimate strengths of both sets of composites increased dramatically over their room-temperature values, probably because of matrix-softening effects at elevated temperatures. Such behavior is well documented in monolithic ceramics and CFCCs.<sup>10</sup> In general, at elevated temperatures, the 0°/40°/60° composites had higher strengths than those of the 0°/45° composites. However, at 1300°C, strengths of both sets of composites dropped to  $\approx 270$  MPa. This decrease above 1200°C is believed due to degradation in strength of the reinforcing fibers.<sup>11-13</sup> For the 0°/20°/60° composites, strength remained relatively unchanged up to 1300°C, except for a slight decrease at 1200°C.

Observed WOF variation with test temperature of two sets of composites (0°/45° and 0°/40°/60°) was similar (see Fig. 4). With increasing test temperature, WOF increased to a maximum at 1200°C because of matrix-softening effects, but dropped rapidly above 1300°C. This drop is related to physical changes in the in-situ Nicalon fibers in composites tested at elevated temperatures; formation of silica at the fiber surface is a distinct possibility at elevated temperatures and can lead to degradation of fiber/matrix interfacial properties. This oxidation can minimize the effective fiber pullout during fracture of the composites, thus accounting for low WOF values.<sup>14</sup>

However, for 0°/20°/60° composites, the WOF remained relatively unchanged up to 1300°C, except for a slight decrease at 1200°C. This behavior is consistent with the observed strength behavior. The difference in mechanical behavior of 0°/20°/60° composites from that of 0°/40°/60° and 0°/45° composites is probably due to specimen-related variations.

To establish the large difference in room-temperature strengths of 0°/40°/60° and 0°/45° composites, we measured their in-situ fiber strengths and correlated them to the composite strengths. In-situ fiber strength measurements by fractography were made on the two sets of composites samples fractured at room temperature. In most fibers, fractures originated at surface flaws, as shown in Fig. 1. Using mirror size measurements and a value of 1 MPa $\sqrt{\text{m}}$  as the Nicalon fiber fracture toughness,<sup>4</sup> we estimated fiber strengths from Eq. 3; these values were then used to construct linearized Weibull plots with Eq. 1.

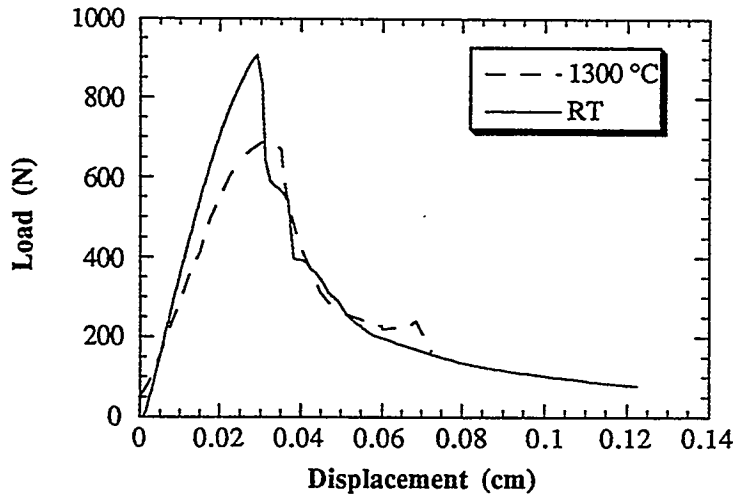


Fig. 2. Typical Load Displacement Observed for 0°/40°/60° Composites Tested at Room Temperature and 1300°C.

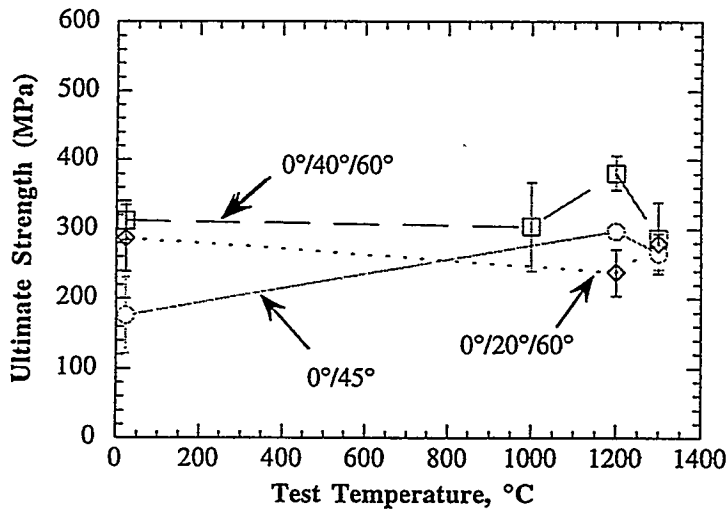


Fig. 3. Variation of ultimate strength with test temperature for SiC(f)/SiC composites with different fiber lay-up sequences.

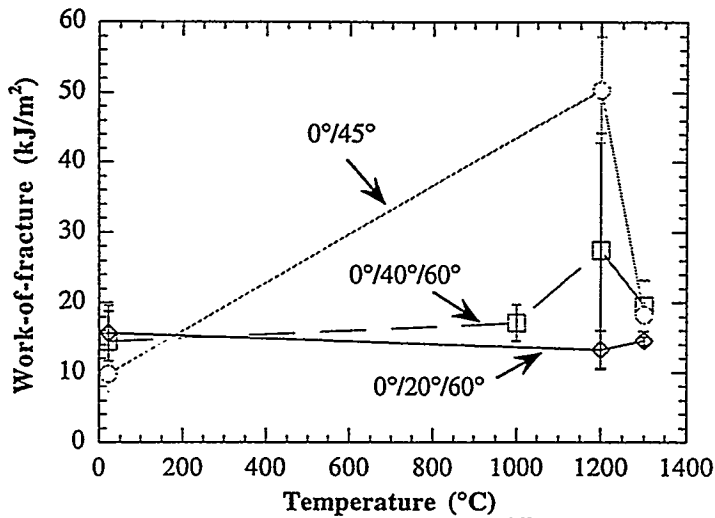


Fig. 4. Variation of work-of-fracture with test temperature for SiC(f)/SiC composites with different fiber lay-up sequences.



The linearized Weibull plots (not shown) of in-situ fibers in  $0^\circ/40^\circ/60^\circ$  and  $0^\circ/45^\circ$  composites tested at room temperature were used to estimate the scale parameter and Weibull modulus. These values for the  $0^\circ/40^\circ/60^\circ$  composites were 2.42 GPa and 4.9, respectively, while those for the  $0^\circ/45^\circ$  composites were 2.38 GPa and 4.9, respectively. Associated average fiber pullout lengths were 160  $\mu\text{m}$  for the  $0^\circ/45^\circ$  and 200  $\mu\text{m}$  for the  $0^\circ/40^\circ/60^\circ$  composites.

For comparison purposes, the scale parameters for fractured fibers in the  $0^\circ/40^\circ/60^\circ$  and  $0^\circ/45^\circ$  composites tested at room temperature were evaluated at a standard gauge length of 1 mm. This was done by first estimating the gauge length,  $L_c$ , for the fractured fibers in the composites tested with the two fiber lay-up sequences, based on the average fiber pullout lengths and the scale parameters (Eq. 4). Fiber radius was assumed to be 8  $\mu\text{m}$ , and  $\lambda$  was taken as 2.1 for fibers tested in both  $0^\circ/40^\circ/60^\circ$  and  $0^\circ/45^\circ$  composites.<sup>8</sup> The corresponding values for the gauge lengths of fractured fibers were estimated as 381 and 305  $\mu\text{m}$  for the  $0^\circ/40^\circ/60^\circ$  and  $0^\circ/45^\circ$  composites, respectively. Subsequently, these fiber gauge lengths were used in conjunction with Eq. 2 to estimate scale parameters for the in-situ fibers at a gauge length of 1 mm. The resulting scale parameters at a gauge length of 1 mm for in-situ fractured fibers in the  $0^\circ/40^\circ/60^\circ$  and  $0^\circ/45^\circ$  composites tested at room temperature were 2 and 1.87 GPa, respectively. These values were then used to plot Weibull distribution curves (Fig. 5). Similarity in the Weibull strength distribution plots suggests that there are no differences in in-situ fiber strength characteristics for the two sets of composites.

Equation 6 was used to determine the ultimate strengths of the  $0^\circ/40^\circ/60^\circ$  and  $0^\circ/45^\circ$  composites tested at room temperature. As a first approximation, the fraction of fibers along the loading direction (i.e.,  $0^\circ$ ) are accounted for in the calculations. Therefore, values of  $f_l$  for the  $0^\circ/40^\circ/60^\circ$  and  $0^\circ/45^\circ$  composites are 0.07 and 0.1, respectively. Based on these values and the Weibull parameters, predicted ultimate strengths for the  $0^\circ/40^\circ/60^\circ$  and  $0^\circ/45^\circ$  composites are 117 and 165 MPa. The predicted strength for the  $0^\circ/45^\circ$  composites agrees well with the observed room-temperature strength of  $\approx 153$  MPa, while for the  $0^\circ/40^\circ/60^\circ$  composites, there is a large discrepancy. It is possible that in the  $0^\circ/40^\circ/60^\circ$  composites, fibers in the lay-ups oriented at  $40^\circ$  and  $30^\circ$  (in  $60^\circ$  oriented mats) may be contributing to the mechanical response of the composite. If the contribution of these fibers is included in the model, the predicted strength for the  $0^\circ/40^\circ/60^\circ$  is  $\approx 334$  MPa; this is in accordance with the observed strength of  $\approx 312$  MPa. Thus, from this work it seems that fibers oriented off-axis by more than  $40^\circ$  do not contribute significantly to the ultimate strength of the composites. However, if they are

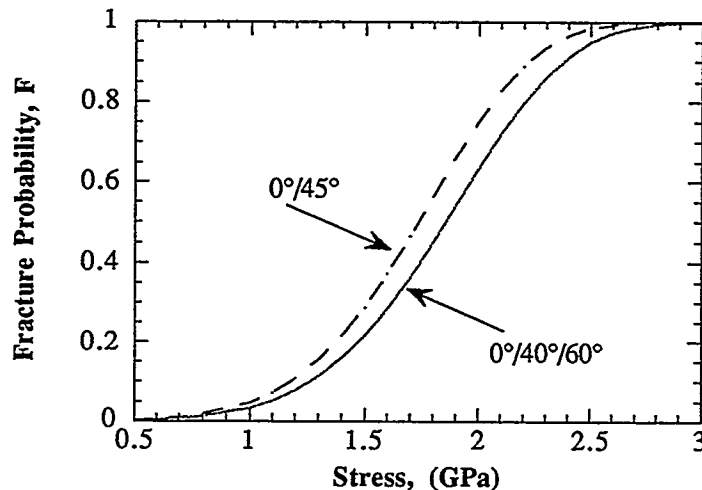


Fig. 5. Weibull strength distribution of in-situ Nicalon fibers in  $0^\circ/40^\circ/60^\circ$  and  $0^\circ/45^\circ$  composites at gauge length of 1 mm.

oriented  $<40^\circ$  from the loading direction, they do influence composite strength. Realistically, the contribution of the off-axis fibers to composite strength is expected to change gradually with the off-axis angle and needs to be further quantified. In addition to the fiber fraction available to sustain the applied loads, there may also be a change in the failure mechanism as the fiber lay-up sequence changes in the composites.

## ENGINEERING APPLICATIONS

These techniques are currently being used to provide insight into the effects of in-situ fiber strength, fiber coating, and fiber architecture on mechanical performance of engineering composites in service environments. We have begun to investigate engineering components and processes being developed for commercial applications. Specifically, damage evaluation of composite hot-gas filters exposed to service environments and composite joints has been conducted.

### Composite Hot-Gas Filters

O-ring compression tests on samples machined from composite hot-gas filters in as-fabricated condition showed an ultimate strength of  $19.7 \pm 2$  MPa. The corresponding value for the ultimate strength of a filter exposed in the Tidd demonstration plant for  $\approx 1100$  h was  $7.7 \pm 1$  MPa. This represents a strength loss of 60% during filter exposure. Based on observations in other studies,<sup>9,11</sup> we believe that the reduced ultimate strength is related to the degradation of in-situ fiber strength. Therefore, we evaluated the in-situ strength of reinforcing fibers in as-fabricated and exposed filters by using the fractographic technique

discussed above. Figure 6 shows the distribution of in-situ fiber strengths in composite filters in both as-fabricated and exposed conditions. The average fiber strength in as-fabricated filters is  $\approx 1.7$  GPa, while that in exposed composite filter is  $\approx 0.8$  GPa. Thus, fiber strength reduction during exposure is  $\approx 60\%$ , in agreement with the strength degradation of the filters themselves. This confirms that filter strength degradation is related to fiber damage.

### Composite Joining

An evaluation of in-situ fiber strength in an as-fabricated composite (SiC/SiC) and in a lap joint made of the same composite showed significant fiber strength degradation in the joint section. This is consistent with the observed strength degradation of composite joints. These results validate the use of in-situ fiber strength evaluation for damage evaluation that leads to process optimization of engineering composite components.

### ACKNOWLEDGMENTS

The work was supported by the U.S. Department of Energy, Office of Fossil Energy, Advanced Research and Technology Materials Program [DOE/FE AA 15 10 10 0, Work Breakdown Structure Element ANL-1], under Contract W-31-109-Eng-38. The authors thank

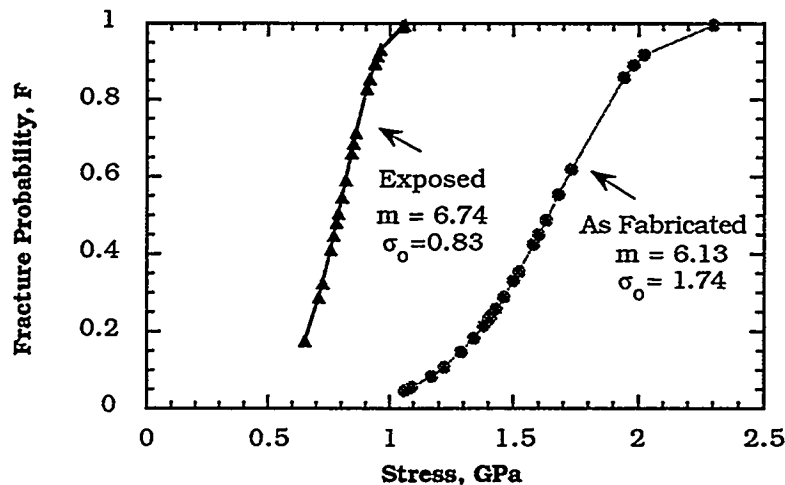


Fig. 6. Weibull strength distribution of in-situ fibers in composite hot gas filters before and after exposure in Tidd demonstration plant.

D. J. Pysher, B. L. Weaver, and R. G. Smith of the 3M Company for providing filter specimens, and James K. Weddell from DuPont Lanxide for providing the composite joint specimen.

## REFERENCES

1. A. G. Evans and D. B. Marshall, "The Mechanical Behavior of Ceramic Matrix Composites," Overview No. 85, *Acta Metall.*, **37** [10] 2567-2583 (1989).
2. E. Y. Luh and A. G. Evans, "High-Temperature Mechanical Properties of a Ceramic Matrix Composite," *J. Am. Ceram. Soc.*, **70** [7] 466-69 (1987).
3. T. Mah, M. G. Mendiratta, A. P. Katz, R. Ruh, and K. S. Mazdiasni, "Room-Temperature Mechanical Behavior of Fiber-Reinforced Ceramic-Matrix Composites," *J. Am. Ceram. Soc.*, **68** [1] C-27-C-30 (1985).
4. M. D. Thouless, O. Sbaizero, L. S. Sigl, and A. G. Evans, "Effect of Interface Mechanical Properties on Pullout in a SiC-Fiber-Reinforced Lithium Aluminate Silicate Glass Ceramic," *J. Am. Ceram. Soc.*, **72** [4] 525-32 (1989).
5. H. C. Cao, E. Bishcoff, O. Sbaizero, M. Ruhle, A. G. Evans, D. B. Marshall, and J. J. Brennan, "Effect of Interfaces on the Properties of Fiber-Reinforced Ceramics," *J. Am. Ceram. Soc.*, **73** [6] 1691-99 (1990).
6. R. N. Singh, "Fiber-Matrix Interfacial Characteristics in a Fiber-Reinforced Ceramic-Matrix Composite," *J. Am. Ceram. Soc.*, **72** [9] 1764-67 (1989).
7. R. W. Rice, *Treatise on Materials Science and Technology*, Vol. II, pp. 199, Academic Press, New York, 1978.
8. W. A. Curtin, "Theory of Mechanical Properties of Ceramic-Matrix Composites," *J. Am. Ceram. Soc.*, **74** [11] 2837-45 (1991).
9. J. P. Singh, D. Singh, and R. A. Lowden, "Effect of Fiber Coating on Mechanical Properties of Nicalon Fibers and Nicalon-Fiber/SiC Matrix Composites," *Ceram. Eng. Sci. and Proc.*, **15** [4] 456-464 (1994).
10. D. P. Stinton, R. A. Lowden, and R. H. Krabill, "Mechanical Property Characterization of Fiber-Reinforced SiC Matrix Composites," in *Proc. 4th Annual Conf. on Fossil Energy Materials, Fossil Energy AR&TD Materials Program, ORNL/FMP-90/1*, 3-13 (1990).
11. D. Singh, J. P. Singh, and M. Wheeler, "Mechanical Behavior of SiC(f)/SiC Composites and Correlation to In-Situ Fiber Strength at Room and Elevated Temperatures," to appear in *Journal of the American Ceramic Society*.
12. T. J. Clark, R. M. Arons, and J. B. Stamatoff, "Thermal Degradation of Nicalon SiC Fibers," *Ceram. Eng. Sci. Proc.*, **6** [7-8] 576-588 (1985).

13. D. J. Pysher, K. C. Goretta, R. S. Hodder, and R. E. Tressler, "Strengths of Ceramic Fibers at Elevated Temperatures," J. Am. Ceram. Soc., **72** [2] 284-88 (1989).
14. R. A. Lowden and D. P. Stinton, "Interface Modification in Nicalon/SiC Composites," Ceram. Eng. Sci. Proc., **9** [7-8] 705-722 (1988).



## **STRENGTH AND CORROSION BEHAVIOR OF SiC - BASED CERAMICS IN HOT COAL COMBUSTION ENVIRONMENTS**

Kristin Breder and Randy J. Parten  
High Temperature Materials Laboratory  
Oak Ridge National Laboratory  
Oak Ridge, TN 37831 - 6069

### **ABSTRACT**

As part of an effort to evaluate the use of advanced ceramics in a new generation of coal-fired power plants, four SiC-based ceramics have been exposed to corrosive coal slag in a laboratory furnace and two pilot scale combustors. Initial results indicate that the laboratory experiments are valuable additions to more expensive pilot plant experiments. The results show increased corrosive attack with increased temperature, and that only slight changes in temperature may significantly alter the degree of strength degradation due to corrosive attack. The present results are part of a larger experimental matrix evaluating the behavior of ceramics in the coal combustion environment.

### **INTRODUCTION**

A new generation of coal fired power plants with increased efficiency, fewer emissions and lower costs are currently being developed.<sup>1, 2</sup> Large improvements in efficiencies will require a change to gas turbines (Brayton Cycle) instead of exclusive reliance on steam turbines (Rankine Cycle). Extremely high temperature working fluid is required to boost the efficiency, and the result is that the power plant sub-systems will be exposed to much more corrosive environments than in the present systems. The uses of ceramic heat exchangers are being investigated for those new power plants because of the potential for producing a clean, hot working fluid for the gas turbine.

The leading candidate materials for ceramic heat exchangers are silicon carbide-based materials in the form of sintered SiC, siliconized SiC, or a composite containing SiC. The thermal conductivity of this group of ceramics is good, and the retention of mechanical properties, as well as the thermal shock resistance, is presumed to be adequate for the application. However, relatively little is known about the behavior of these ceramics in the corrosive coal combustion environment, and in order to achieve the desired lifetimes of up to 20 000 h this needs to be determined. Some early studies indicated severe corrosion problems in a coal/oil burning rig,<sup>3-6</sup> and basic coal chemistries were found to be more corrosive than acidic chemistries. More recently modern SiC and a new SiC-particulate reinforced Al<sub>2</sub>O<sub>3</sub> composite have been tested in a coal ash environment.<sup>7-11</sup>

## EXPERIMENTAL PROCEDURE

The coal ash exposure experiments were carried out using ceramic tubes. NT230 siliconized silicon carbide (SiSiC) from Saint Gobain Norton Industrial Ceramics contained free silicon metal (8 vol%) and some residual porosity. Lanxide DIMOX SiC<sub>p</sub> reinforced Al<sub>2</sub>O<sub>3</sub> from DuPont Lanxide Composites Inc. was manufactured by the Lanxide Direct Oxidation process (DIMOX) and contained 48 vol% SiC<sub>p</sub>, 38 vol% Al<sub>2</sub>O<sub>3</sub> and 13 vol% Al-alloy, and some residual porosity. Two sintered SiC were tested; β-SiC from Coors Ceramics Co., and Hexoloy sintered α-SiC from Carborundum Co. The SiSiC and sintered SiC ceramics were tested as machined while the Lanxide DIMOX was reoxidized by the manufacturer after machining.

The tubes were nominally 50 mm (2") OD and 38 mm (1.5") ID and were cut into 150 mm (6") long sections for exposure. A thorough description of the materials have been given previously.<sup>7</sup>

The slags for the exposure experiments were gathered from the taps of three cyclone-fired utility boilers. Two types of Illinois #6 bituminous coals were used. One was from coal burned at the Central Illinois Public Service Coffeen Plant (labeled Coffeen) and was produced from a low sulfur producing mine. The low sulfur (in the form of low FeS<sub>2</sub> content) leads to high viscosity of the slag, so therefore 1.5% limestone was added at the power plant to reduce the viscosity. The second Illinois #6 coal was from the Illinois Power Company Baldwin Plant (labeled Baldwin) and was a mixture of Illinois #6 and Illinois #5 coals, resulting in a typical slag with less Ca and more Fe than the batch from



the Coffeen plant. The third slag came from coal burned at the Northern States Power Riverside Plant, and was produced from the Rochelle mine, Wyoming (labeled Rochelle). Approximately 3% petroleum coke was added at the power plant.

Each slag was analyzed at the University of North Dakota Energy and Environmental Research Center (UNDEERC)<sup>12</sup> and was split from the main barrel according to ASTM D 2013 "Standard Method of Preparing Coal Samples for Analysis." The chemical compositions of the three coal ashes are given in Table 1.

Table 1. Chemical composition of the coal ashes.

Oxide, wt%	Coffeen	Baldwin	Rochelle
SiO <sub>2</sub>	52.5	53.4	47.0
Al <sub>2</sub> O <sub>3</sub>	16.3	18.6	18.6
Fe <sub>2</sub> O <sub>3</sub>	13.5	17.6	5.3
TiO <sub>2</sub>	0.7	0.7	1.4
P <sub>2</sub> O <sub>5</sub>	0.2	0.0	0.6
CaO	13.1	7.1	19.7
MgO	1.2	0.9	5.7
Na <sub>2</sub> O	0.8	0.0	0.9
K <sub>2</sub> O	1.6	1.7	0.4
SO <sub>3</sub>	0.1	0.0	0.4

The test temperatures were 1090°C to produce a condition of sintered ash, 1260°C for a viscous molten ash, and 1430°C for a fluid molten ash. The tube-sections were placed in a box furnace; an initial layer of coal slag was added; and the furnace was brought up to temperature in 2 h. In order to replenish the coal slag 75 ml was added to each tube length every 48 h through the top of the furnace. Total exposure time was 500 h after which the furnace was slowly cooled to room temperature. After inspection each tube was cut into 14 C-ring specimens for strength testing. The C-rings were placed in a mechanical test system containing a box furnace, re-heated to the exposure temperature and loaded in compression to failure at a fast loading rate (45 N/s). The strength was evaluated using the appropriate formula for C-rings in compression.<sup>13</sup> Three tubes were cut into C-rings

and tested in the as-received condition in order to provide base-line strength data at each test temperature. The strength data were analyzed using Weibull statistics<sup>14,15</sup> and fractography was performed.

One 300 mm long tube section of each material were exposed in a pilot scale combustor in order to tie the laboratory experiments to systems testing. The combustor was a 220 kW (750 000 Btu/h) pilot scale combustor at UNDEERC burning the same type of Illinois #6 coal from the Baldwin plant as described above.<sup>16</sup> The tube was placed in the coal stream in a section at a temperature between 1340°C and 1370°C and the total run was 100 h. One tube of the SiC<sub>p</sub> reinforced Al<sub>2</sub>O<sub>3</sub> material was placed in the radiant section at the Combustion and Environmental Research Facility (CERF) at (PETC) at a temperature between 1050°C and 1250°C. The CERF is a 150 kW (500 000 Btu/h) pilot scale combustor, and the tube was exposed in the combustor for 1000 h while miscellaneous eastern bituminous coals were burned for other experimental applications.<sup>17</sup> Both these tubes were sectioned into C-rings and strength tested at 1260°C as described above.

#### Exposure in the Laboratory Furnace

Following are descriptions of the tubes after 500 h exposure in the laboratory furnace. The visual appearance did not vary much between the materials, but varied between the coal slags and temperatures. Of a test matrix of 9 conditions for each material two are remaining at the present time.

At 1090°C the Baldwin slag was lightly sintered together but did not stick to the surface of the tubes except in certain small spots. The surface of the SiC<sub>p</sub> reinforced Al<sub>2</sub>O<sub>3</sub> was discolored gray-brown from its original gray color, but did not show any obvious surface damage. The surfaces of the other three ceramics remained essentially unchanged with the exception of a few spots of sintered slag stuck on to them.

At 1090°C the Coffeen slag was also lightly sintered together, and a layer was loosely sintered onto the tubes. When the slag was peeled off, there was no obvious surface damage, but some brown discoloration from this darker slag was observed. The viscosity for the two coal slags was similar at 1430°C, but the temperature where the slag starts to solidify was somewhat higher for the Baldwin than the Coffeen slag, and this may explain the difference in appearance at this temperature. Details pertaining to the different viscosities will be included with detailed microprobe work later in the project.

The Rochelle slag was also just loosely sintered on to the tubes after exposure to 1090°C. The slag was yellow-brown in color, but had not caused any discoloration of the tubes.

At 1260°C the Baldwin slag was fused onto the tubes. The slag was brown and had a shiny glazed appearance on the side of the tubes, and was black with large bubbles on the top surface where the slag had been applied.

At 1260°C the Coffeen slag was also well fused onto the tubes, but the appearance was less glazed and the color was uniformly matte brown. There were small bubbles in the slag, but fewer large bubbles at the surface.

At 1430°C the Baldwin slag was very well fused onto the tubes in a thinner layer than for 1260°C. The color was generally matte brown.

At 1430°C the Coffeen slag was very well fused onto the tubes in a thin brown layer. Few bubbles had developed, and it was obvious that the slag had been very fluid at that temperature.

#### Exposure in Coal Combustors

The tubes which had been exposed in the UNDEERC combustor at a temperature between 1340°C and 1370°C (Baldwin slag), had a highly glazed, even brown slag layer fused onto them. There was some slag build-up on one side, containing areas with large bubbles under the surface. Some material loss was observed on one side of the tubes, this was more pronounced for the  $\text{SiC}_p$  reinforced  $\text{Al}_2\text{O}_3$  ceramic than for any of the other specimens. Each of the C-rings were measured and the dimensions will be compared to the as-received dimensions. The appearance of the slag on these tubes was very similar to the appearance of the slag on the tube from the laboratory furnace, (Baldwin slag at 1260°C) indicating a similar temperature level. However, the wall recession was in some cases more severe, indicating that the combustor environment, in which there is rapidly moving combustion gases passing over the tube, would be more severe than the furnace environment.

The slag on the  $\text{SiC}_p$  reinforced  $\text{Al}_2\text{O}_3$  tube exposed at PETC at a temperature between 1050°C and 1250°C, was less sintered, which confirmed that the exposure temperature had been under the temperature for creating molten slag. The slag was discolored, was lightly sintered together, and was well attached to the tube. There did not seem to be a serious wall recession for this tube.

## Strength Testing

Figure 1 shows the average strengths for the as received C-rings as well as the average strength measured after exposure at the UNDEERC and PETC pilot scale combustors. Testing of C-rings from the tubes exposed in the laboratory furnace is ongoing, and will not be discussed here. C-rings from the tubes exposed in both the pilot scale combustors were strength tested at 1260°C. From the ranges of temperatures given, this was in the high-end for the tube exposed at PETC and in the low end for the tubes exposed at UNDEERC; however, the temperature was chosen as a common denominator, and for ease of comparisons to the as-received data.

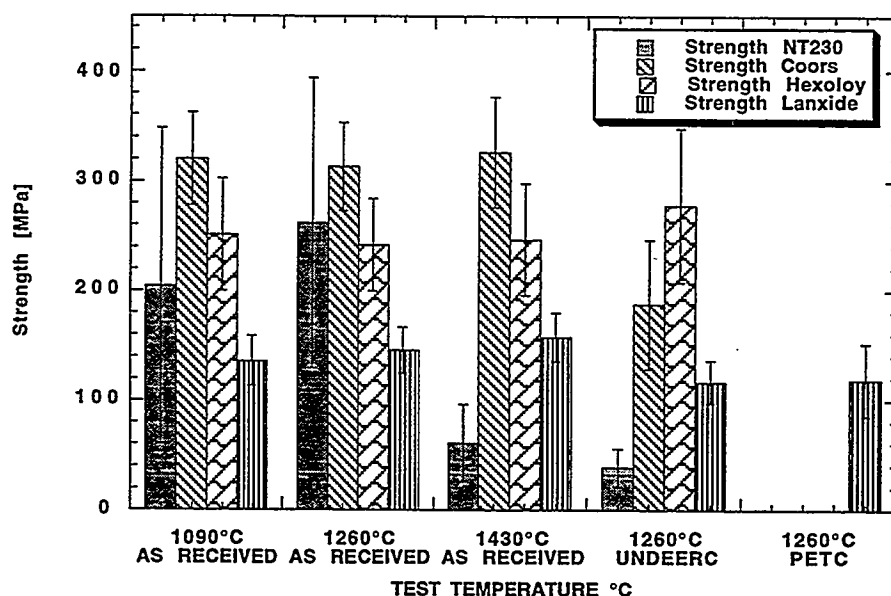


Figure 1. Comparison of strength of C-rings before and after exposure in pilot scale combustor.

Statistical analysis of the strength results for the NT230 SiSiC material showed that there was a significant drop in strength for the specimens tested at 1430°C. This is to be expected as the melting point for Si is 1410°C. The residual strength of the NT230 after the 100 h exposure in the UNDEERC combustor was significantly reduced compared to

the as-received strength measured at 1260°C. The exposed specimens showed some reduction in wall thickness, and the preliminary fractography indicated that fracture generally was initiated from corrosion pits generated during the exposure. The overall variability in the strengths measured for this material was large (high standard deviation and low Weibull modulus), similar to what was observed previously in flexure testing of this material.<sup>7</sup>

The strength of the Coors  $\beta$ -SiC material remained the same over the entire temperature range, but a significant reduction in strength was observed after exposure in the UNDEERC combustor. The preliminary fractography for these specimens indicated a predominance of failure from surface pits or pores, probably related to the exposure. Detailed Scanning Electron Microscopy (SEM) work is needed to determine the extent of these pits.

The strength of the Hexoloy  $\alpha$ -SiC was unaffected by the temperature or the exposure at UNDEERC. The exposed specimens failed mostly from pores, but in contrast to the  $\beta$ -SiC the pores in these specimens were mostly in the volume near the surface, and as such unaffected by the exposure. The as-received specimens failed from similar types for pores throughout, consistent with the constant stress level.

The strength of the Lanxide SiC<sub>p</sub> reinforced Al<sub>2</sub>O<sub>3</sub> ceramic remained unaffected by the elevated temperatures, however, these were all lower than the room temperature strength for this material. After exposure in the two pilot scale combustors there was a slight but significant reduction in strength for this material. However, the strengths of the specimens from the two combustor runs were not significantly different, in spite of the fact that there was an order of magnitude difference in the exposure times for these tubes. This result indicates that the exposure temperature plays a very important role, and that significant differences in life-times may occur for only moderate changes in material exposure temperature. Further, the results indicate that it is important to investigate the influence of the coal chemistries. Also, microprobe studies of the reaction layers will give important additional information on the difference observed for the different slags.

## SUMMARY

Four SiC-based ceramics were exposed to three different coal slags in a laboratory furnace. The materials were also exposed in a 100 h pilot scale combustor using one of the same coals. Comparison of the strengths of SiC - based ceramics in the as-received condition to the strength after exposure to coal slag in a pilot-scale combustor indicates that the slag will act as a strong corrodent and reduce the strength of some of the ceramics. There are, however, clear indications that the time for significant strength reduction to occur may vary considerably with only slight variations in temperature. Further work on the corrosion mechanisms, surface damage and strength degradation will be performed in order to determine the boundary conditions for a possible successful implementation of this type of ceramics in the proposed application.

## ACKNOWLEDGMENTS

Research sponsored by the U.S. Department of Energy, Office of Fossil Energy, Pittsburgh Energy Technology Center, Advanced Combustion Technology Program, DOE/FE AA 20 10 00 0, under contract DE-AC05-96OR22464 with Lockheed Martin Energy Research Corp.

## REFERENCES

1. J. M. Klara, "HIPPS: Beyond State-of-the-art. Part 1," *Power Eng.* 12 37-39 (1993).
2. J. M. Klara, "HIPPS can Compete with Conventional PC Systems, Part 2," *Power Eng.* 1 33-36 (1994).
3. M. K. Ferber, and V. J. Tennery, "Evaluation of Tubular Ceramic Heat Exchanger Materials in Basic Coal Ash from Coal-Oil-Mixture Combustion," *Ceram. Bull.* 63 [7] 898 (1984).

4. M. K. Ferber, and V. J. Tennery, "Evaluation of Tubular Ceramic Heat Exchanger Materials in Acidic Coal Ash from Coal-Oil-Mixture Combustion," *Ceram. Bull.* **62** [2] 236 (1983).
5. M. K. Ferber, J. Ogle, V. J. Tennery, and T. Henson, "Characterization of Corrosion Mechanisms Occurring in a Sintered SiC Exposed to Basic Coal Slags," *J. Am. Ceram. Soc.* **68** [4] 191 (1985).
6. P. F. Becher, "Strength Degradation in SiC and Si<sub>3</sub>N<sub>4</sub> Ceramics by Exposure to Coal Slags at High Temperatures," *J. Mater. Sci.* **19** 2805 (1984).
7. K. Breder and V. J. Tennery, "Materials Support for HITAF, Final Report for Phase I," ORNL/TM-12815, Oak Ridge Nat. Laboratory, Oak Ridge, TN, 1995.
8. T. M. Strobel, J. P. Hurley, K. Breder, and J. E. Holowczak, "Coal Slag Corrosion and Strength Degradation of Silicon Carbide/Alumina Composites," *Cer. Eng. Sci. Proc.*, **15** [4] 579-86 (1984).
9. T. M. Strobel, J. P. Hurley, K. Breder, and J. E. Holowczak, "Coal Slag Corrosion and Strength Degradation of Siliconized Silicon Carbide," *Cer. Eng. Sci. Proc.*, **16** [5] 911-18 (1985).
10. K. Breder, V. J. Tennery, T. M. Strobel, J. P. Hurley, and J. E. Holowczak, "Strength Measurements of Monolithic SiC and Al<sub>2</sub>O<sub>3</sub>/SiC Composites After Exposure to Coal Slag," *J. Am. Cer. Soc.* **78** [10] 2837-40 (1995).
11. P. F. LaRue, "An Evaluation of the Strength of a SiC<sub>(p)</sub> / Al<sub>2</sub>O<sub>3</sub> Ceramic Matrix Composite Exposed to Coal Slag at Elevated Temperature," M.S. Thesis, University of Tennessee, Knoxville, 1995.
12. J. P. Hurley, "Support Services for Ceramic Fiber-Ceramic Matrix Composites" ORNL/Sub/94-SS112/01, Oak Ridge National Laboratory, Oak Ridge, TN 1995.
13. O. M. Jadaan, D. L. Shelleman, J. C. Conway, Jr. J. J. Mecholsky, Jr., and R. E. Tressler, "Prediction of the Strength of Ceramic Tubular Components: Part1 - Analysis," *Journal of Testing and Evaluation*, **19** [3] 181-91 (1991).
14. W. Weibull, "A Statistical Theory for the Strength of Materials," Ingeniörsvetenskapsakademien, Handligar, No. 151 (1939).
15. S. Duffy and E. Baker, Manual for Spread Sheet Macro for Estimation of Weibull Parameters Based on the Maximum Likelihood Method, Civil Eng. Dep., Cleveland State University, Cleveland Ohio, 1995.

16. T. M. Strobel, J. P. Hurley and J. R. Gunderson, "Pilot-Scale Testing of Silicon-Based Ceramics," to be published in *Cer. Eng. Sci Proc.* **17** [4-5] 1996.

17. K. Natesan, M. Freeman, and M. Mathur, "Corrosion Performance of Materials for Advanced Combustion Systems," pp. 71-83 in Proceedings of the Ninth Annual Conference on Fossil Energy Materials, N. C. Cole and R. R. Judkins, Eds. U. S. Department of Energy, Oak Ridge, 1995.



CORROSION AND ITS EFFECT ON MECHANICAL PROPERTIES OF MATERIALS FOR  
ADVANCED COMBUSTION SYSTEMS\*

K. Natesan

Argonne National Laboratory  
Argonne, IL 60439

and

M. Freeman and M. Mathur  
Pittsburgh Energy Technology Center  
Pittsburgh, PA 15236

ABSTRACT

Conceptual designs of advanced combustion systems that utilize coal as a feedstock require high-temperature furnaces and heat transfer surfaces that can operate at temperatures much higher than those prevalent in current coal-fired power plants. The combination of elevated temperatures and hostile combustion environments necessitates development and application of advanced ceramic materials in these designs. The objectives of the present program are to evaluate (a) the chemistry of gaseous and condensed products that arise during combustion of coal; (b) the corrosion behavior of candidate materials in air, slag, and salt environments for application in the combustion environments; and (c) the residual mechanical properties of the materials after corrosion. The program emphasizes temperatures in the range of 1000-1400°C for ceramic materials and 600-1000°C for metallic alloys. Coal/ash chemistries developed on the basis of thermodynamic/kinetic calculations, together with slags from actual combustors, are used in the program. The materials being evaluated include monolithic silicon carbide from several sources: silicon nitride, silicon carbide in alumina composites, silicon carbide fibers in a silicon carbide-matrix composite, and some advanced nickel-base alloys. The paper presents results from an ongoing program on corrosion performance of candidate ceramic materials exposed to air, salt, and slag environments and their effect on flexural strength and energy absorbed during fracture of these materials.

INTRODUCTION

Coal is a complex and relatively dirty fuel that contains varying amounts of sulfur and a substantial fraction of noncombustible mineral constituents, commonly called ash. Conceptual designs of high-performance power systems (HIPPS) that utilize coal as a feedstock require high-temperature furnaces and heat transfer surfaces capable of operating at higher temperatures than those used in current coal-fired power plants. The combination of elevated temperatures and hostile combustion environments necessitates the use of ceramic materials at least in the first few passes of the heat exchangers in these designs.

The HIPPS concept would employ a combined cycle that uses a gas turbine driven by a working fluid (air) that is separately heated in a high-temperature advanced furnace, in addition to conventional steam turbines.<sup>1</sup> The ultimate goal is to produce electricity from coal with an overall thermal efficiency of 47% or higher (compared with  $\approx 35\%$  for current systems) and to reduce CO<sub>2</sub> emissions by 25 to 30%. The pulverized-coal high-temperature advanced furnace (HITAF) in the HIPPS concept will heat air to an intermediate temperature of  $\approx 1000^\circ\text{C}$  and burn supplemental clean fuel to boost the temperature of air to the

---

\*Work supported by the U.S. Department of Energy, Office of Fossil Energy, Advanced Research and Technology Development Materials Program, Work Breakdown Structure Element ANL-4, under Contract W-31-109-Eng-38.

turbine inlet temperature of  $\geq 1300^{\circ}\text{C}$ . Use of supplemental fuel can be reduced as the HITAF technology evolves to permit air to be heated to higher temperatures in the furnace. HITAF represents a major departure from conventional pulverized-coal-fired boilers in which only steam is raised to a maximum of  $530\text{--}620^{\circ}\text{C}$ . The purpose of the HITAF is to heat the clean working fluid – air – to the required turbine inlet temperatures. At the elevated temperatures of the HITAF, transfer of heat from the combustion gases to the working fluid will be dominated by radiative heat transfer, and the design of the heat transfer surface will be critical for success of the system. Several concepts are under development for the design of the heat transfer surfaces in the HITAF system.<sup>2</sup>

For any of the concepts to be viable for a commercial-scale HIPPS, the heat transfer surfaces will be exposed to much higher temperatures than are prevalent in conventional coal-fired steam-turbine systems. For temperatures of  $1000\text{--}1300^{\circ}\text{C}$ , conventional metallic materials do not possess adequate strength properties and/or corrosion resistance for long-term service. In addition, an important difference between the conventional boiler system and the HIPPS is seen in the chemical and physical characteristics of the ash layers that can deposit on the heat transfer surfaces. These deposits are likely to be dominated by alkali sulfates and coal slags in HIPPS, rather than by pyrosulfates or alkali-iron-trisulfates (which are prevalent in conventional pulverized coal-fired boilers), and by the increased mobility of corrosion-accelerating agents in the deposit layers due to the much higher temperature of the heat transfer surfaces in HIPPS. A major challenge is to develop methods to combat severe deposition, erosion, and corrosion (DEC) of heat transfer surfaces exposed to higher-than-normal temperatures. These methods could include fuel selection, cleaning of aggressive contaminants from coal, fine grinding of coal, use of additives, and selection of advanced corrosion-resistant ceramic materials, coatings, and advanced alloys for vulnerable heat transfer sections.

The objectives of the present program are to evaluate (a) the chemistry of gaseous and condensed products that arise in combustion of coal and (b) candidate materials for application in the combustion environments. Chemistry calculations determine the types and amounts of combustion products over the wide temperature range of  $700\text{--}1700^{\circ}\text{C}$  and at 1 atm pressure. The experimental program on heat exchanger materials will develop mechanistic information on the roles of material composition, ash constituents, combustion deposits, chlorine, alkali sulfates, and sulfur sorbents in the corrosion process. The program emphasizes corrosion evaluation of materials in air, salt, and coal/ash environments at temperatures between  $1000$  and  $1400^{\circ}\text{C}$ , as well as measurement of residual fracture properties of the materials after corrosion. Coal/ash chemistries synthesized on the basis of thermodynamic/kinetic calculations, together with slags from actual combustors, are used in the program.

Thermodynamic calculations were used to evaluate the chemistries of gaseous and condensed phases that occur during combustion of coals.<sup>2,3</sup> Based on the results of these calculations, the general behavior of the solution phase under oxidizing conditions can be described as follows. A liquid solution phase, consisting mostly of silicates of aluminum, calcium, sodium, magnesium, and iron, is present at  $1730^{\circ}\text{C}$ . The mole fraction of  $\text{Na}_2\text{SO}_4$  phase in the liquid is  $<0.01$  above  $1280^{\circ}\text{C}$ .  $\text{Na}_2\text{SO}_4$  concentration rises rapidly as the temperature decreases and becomes a major component of the solution at  $980^{\circ}\text{C}$ . The mole fraction of  $\text{Na}_2\text{SO}_4$  may increase to 0.9 or more at  $980^{\circ}\text{C}$ . These compositional changes can have implications for the

corrosive behavior of the liquid condensates. In the temperature range of interest in HIPPS, the predominant deposits are either mullite or Ca-rich aluminosilicates. The silicate liquid may be even more corrosive and have worse fouling tendencies than sulfates because of (a) high-temperature conditions, (b) adhesive behavior of the silicates, and (c) solubility of ceramic materials, which are probably higher in silicate melts than in sulfate melts.

## EXPERIMENTAL PROCEDURE

**Laboratory Experiments.** The materials selected for the laboratory experimental program include advanced metallic alloys, monolithic ceramic materials, and ceramic-matrix ceramic composites; they are listed in Table 1, together with their manufacturers. Hexoloy SA is a sintered form of alpha silicon carbide with >98% of theoretical density. It has a very fine grain structure (8  $\mu\text{m}$ ) for excellent wear resistance, contains no free silicon, and has been reported to be chemically resistant in both oxidizing and reducing environments. SiC (p) in  $\text{Al}_2\text{O}_3$  material was fabricated by Du Pont-Lanxide by a direct metal oxidation process and has an  $\text{Al}_2\text{O}_3$  matrix containing dispersed SiC particulates. The material also exhibited some free Al in the matrix. Siliconized SiC material (identified as NT 230) made by Norton/TRW. SiC Fiber/SiC Matrix material is made by Du Pont with a chemical vapor infiltration process. It is recommended for service requiring high strength, high-temperature properties, and light weight. The material exhibits creep deformation at temperatures >1200°C, contrary to the behavior of Hexoloy SA and NT 230, in which creep was virtually absent. The material consisting of SiC in an Si matrix is made by INEX, Inc., and has been used in tubes for natural-gas-fired heat exchangers. The material containing SiC fibers in Si carbide was also fabricated by Oak Ridge National Laboratory.

Coupon specimens measuring 2 cm x 2 cm x 2-3 mm were prepared from several of the above-listed materials for salt- and slag-exposure experiments. Dimensions and initial weights of the specimens were measured prior to exposure. Salt tests were conducted at 1000 and 1200°C for 168 h in the presence of  $\text{Na}_2\text{SO}_4$  or a mixture of  $\text{Na}_2\text{SO}_4$  and NaCl. Tests in the presence of three different slags were conducted at 1200°C for a test time of 200 h. Table 2 lists the compositions of slags and the coals that were combusted to obtain these slags. Analysis shows that the slag obtained from Illinois #6 coal was richer in  $\text{Fe}_2\text{O}_3$  and leaner in CaO and MgO, while the reverse is seen for slag from the Rochelle coal. Slags #43 and XX typify the slags derived from coals in the eastern U.S. while slag #47 is typical of that from western coals.

Table 1. Ceramic materials selected for corrosion tests

Material	Manufacturer
Hexoloy SA	Carborundum
SiC (p) in alumina	Du Pont/Lanxide
Siliconized SiC (NT 230)	Norton/TRW
Silicon nitride (NT 154)	Norton/TRW
SiC in Si matrix	INEX, Inc.
SiC fibers in SiC matrix	Du Pont
SiC fibers in SiC matrix	ORNL

Table 2. Compositions of slags for laboratory study

Compound	Slag 43/ Illinois #6	Slag 47/ Rochelle	Slag XX/ Illinois #6
SiO <sub>2</sub>	52.9	47.1	53.3
Al <sub>2</sub> O <sub>3</sub>	16.6	18.8	18.6
Fe <sub>2</sub> O <sub>3</sub>	12.9	5.2	17.6
CaO	13.0	19.6	7.2
MgO	1.3	5.8	1.0
Na <sub>2</sub> O	0.8	0.9	0
K <sub>2</sub> O	1.6	0.3	1.7
SO <sub>3</sub>	0.1	0.3	0

In addition, the effect of air oxidation, salt exposure, and exposures to slag from Illinois #6 and Rochelle coals on the flexural strength of four of the candidate materials were evaluated by preexposure to the specific environment and postexposure four-point testing of the specimens in vacuum. For these specimens, the temperature was maintained at 1200°C for both the preexposure and mechanical test. The flexural test involved bending a specimen of rectangular cross section until fracture. The specimen dimensions were 1.0 x 0.188 x 0.064 and the salt/slag exposed surface was maintained under tension during the test. The data on the load that caused fracture and the area under the load-displacement curves were used to calculate the flexural strength of the material and the energy absorbed to complete the fracture.

**Combustor Experiments.** High-temperature materials were tested by exposing samples of several ceramic materials in the CERF at the Pittsburgh Energy Technology Center.<sup>3</sup> The CERF is a state-of-the-art, 0.5 million Btu/h pilot-scale combustion facility designed to achieve similarity with full-scale utility and industrial boilers. It is designed to closely duplicate typical full-scale specifications for solid fuel fineness or liquid fuel atomization quality, burner relative mass flow (fuel and air) and velocities, furnace temperature distributions, radiant furnace residence time, and convective section gas velocity. Material exposures in CERF are being conducted in a piggyback mode, whereby normal CERF testing would proceed in terms of evaluating combustion of various coals and coal blends. With this approach, comparative assessments of many materials at different locations could be made economically before pursuing dedicated-materials CERF tests that would require continuous operation of the facility for 1000 h or more. To minimize thermal stresses during exposure, samples were placed in the CERF prior to the start of each test and removed after the CERF was cooled to room temperature. Coupon samples of several of the ceramic materials were mounted on a water-cooled, high-temperature materials testing probe that uses welded clips and pins to hold the samples. Ceramic specimens were exposed during several 100-h runs in which Pittsburgh coal and a blend of Alaskan/Russian coal were burned. The compositions of the coals used in CERF runs were similar to those that generated slags for the laboratory test program.<sup>3</sup>

## EXPERIMENTAL RESULTS

### Oxidation in Air

Oxidation of ceramic materials such as monolithic and composite SiC, Si<sub>3</sub>N<sub>4</sub>, and SiC-dispersed Al<sub>2</sub>O<sub>3</sub> involves reaction of carbide and nitride phases to Si-rich oxides. Oxidation rate is generally influenced

by porosity of the material and exposure temperature. Figure 1 shows the weight changes for several of the materials exposed to air at 1200°C. It is evident that most of the SiC and Si<sub>3</sub>N<sub>4</sub> materials oxidize at a low rate at 1200°C. The two exceptions are SiC(p) in Al<sub>2</sub>O<sub>3</sub> and SiC(f)/SiC made by ORNL. In the former, the increase in weight in the early stage of exposure is due to oxidation of free Al in the surface region of the sample. After ≈100 h exposure, the oxidation rate slows but is still higher than that of other materials, indicating oxidation of free Al in the interior of the material, but dictated by the diffusion of oxygen. The increased rate of oxidation for the latter material can be attributed only to lack of formation of glass phase at the grain boundaries, in contrast with the Du Pont made material which has additives that lead to glassy phase formation. Oxidation can occur via either the passive mode in which a solid SiO<sub>2</sub> phase forms and can offer protection against further oxidation, or via active oxidation in which the SiO phase forms and can volatilize, resulting in accelerated oxidation of the material. Figure 2 shows the regions of active and passive oxidation as functions of temperature and pO<sub>2</sub>.<sup>4</sup> Experiments conducted with these materials at temperatures of 1000-1400°C in a dry air environment showed that the materials undergo passive oxidation.

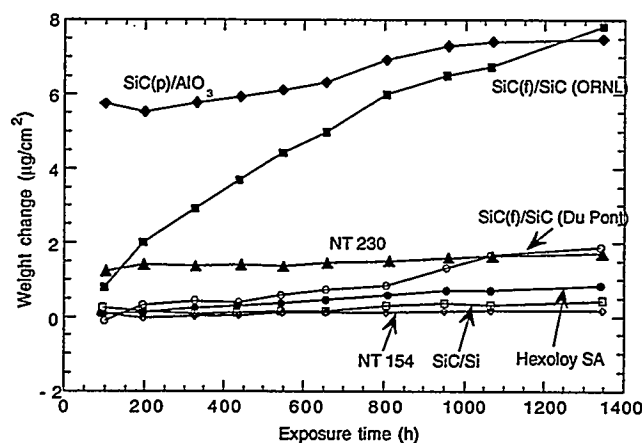


Fig. 1. Oxidation behavior of several ceramic materials in dry air at 1200°C

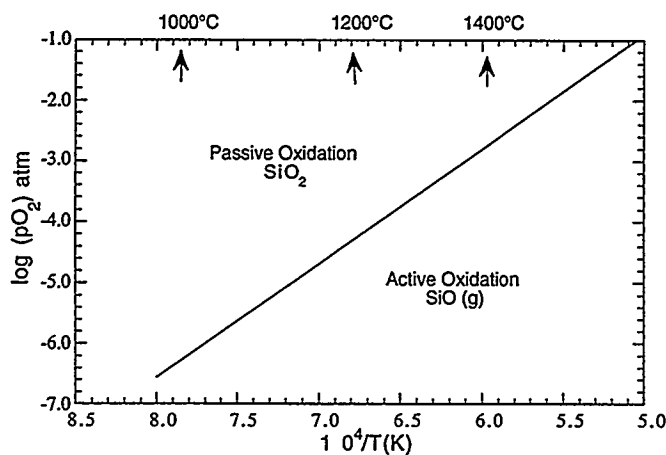


Fig. 2. Regions of active and passive oxidation of SiC in dry air

## Exposure to Salt Environment

Salt-induced degradation of these materials involves reactions between the ceramic materials and alkali sulfates such as  $\text{Na}_2\text{SO}_4$  and  $\text{K}_2\text{SO}_4$  and alkali chlorides such as  $\text{NaCl}$  and  $\text{KCl}$ . In the combustion gas environment, the concentrations of oxygen and of sulfur as  $\text{SO}_2$  and  $\text{SO}_3$  determine the sodium oxide activity via the reaction  $\text{Na}_2\text{SO}_4 = \text{Na}_2\text{O} + \text{SO}_3$ . Subsequently, the silica phase that forms on the ceramic materials can react with  $\text{Na}_2\text{O}$  to form compounds such as  $\text{Na}_2\text{O} \cdot \text{XSiO}_2$ , where X can be 0.5, 1, 2, or 4. This mode of degradation of ceramic materials requires that  $\text{Na}_2\text{O}$  activity be sufficiently high and is usually possible in gas turbine systems where slag constituents are virtually absent. In such instances, the liquid phase can dissolve the protective  $\text{SiO}_2$  scale and also result in penetration of the liquid reaction products into the substrate ceramic material, thereby mechanically weakening the material. To examine the effect of salt deposit, specimens were exposed for 168 h at  $1200^\circ\text{C}$  to a gas stream of 1 vol.%  $\text{SO}_2$ -air was passed over  $\text{Na}_2\text{SO}_4$  salt maintained at temperatures between 700 and  $1400^\circ\text{C}$ . The materials selected for these tests were Hexoloy SA,  $\text{SiC(p)}/\text{Al}_2\text{O}_3$ , NT 230, and NT 154. Figure 3 shows the specimen weight change after 168 h at different salt temperatures.  $\text{Na}_2\text{SO}_4$  has a melting temperature of  $884^\circ\text{C}$ , and the samples exposed to solid salt at 700- $900^\circ\text{C}$  did not exhibit significant corrosion. The weight increase of the  $\text{SiC(p)}/\text{Al}_2\text{O}_3$  is primarily due to oxidation of free Al in the material. Even at a salt temperature of  $1000^\circ\text{C}$ , the vapor pressure of  $\text{Na}_2\text{SO}_4$  is low enough to prevent significant corrosion of the exposed materials. At salt temperatures of  $1200^\circ\text{C}$  and higher, corrosion of the SiC-based materials was evident, while the  $\text{SiC(p)}/\text{Al}_2\text{O}_3$  was resistant to salt-induced corrosion. In the absence of  $\text{Al}_2\text{O}_3$ , the monolithic and composite SiC and  $\text{Si}_3\text{N}_4$  materials oxidize to form  $\text{SiO}_2$ , which reacts with  $\text{Na}_2\text{SO}_4$  to form compounds of compositions  $\text{Na}_2\text{O} \cdot \text{XSiO}_2$  and melting temperatures of  $875$ - $1110^\circ\text{C}$ ; these compounds lead to enhanced corrosion. The presence of  $\text{Al}_2\text{O}_3$  in the Du Pont/Lanxide material leads to formation of mullite ( $\text{Na}_2\text{O} \cdot \text{Al}_2\text{O}_3 \cdot 2\text{SiO}_2$ ) with a melting temperature of  $1526^\circ\text{C}$  resulting in low corrosion, if any, at temperatures of 1200 and  $1400^\circ\text{C}$  in the present investigation. In coal-fired combustion systems, the presence of slag constituents determine the thermodynamic activity of various deposit constituents, and alkali-sulfate-induced corrosion is generally not dominant.

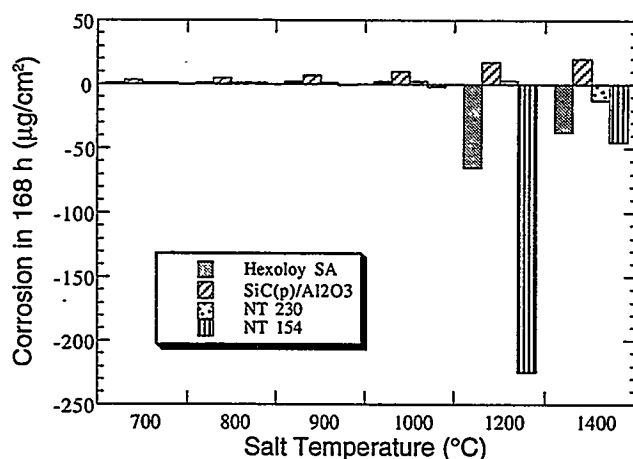


Fig. 3. Effect of sodium sulfate salt condensate on corrosion behavior of several ceramic materials at  $1200^\circ\text{C}$

## Corrosion in Slag Environments

In laboratory slag tests, the materials behaved differently than in salt tests. The specimen showed significant surface cracking but the slag itself did not seem to penetrate the sample, as evidenced by energy-dispersive X-ray (EDX) analysis of specimen cross sections. Because  $\text{Na}_2\text{O}$  activity in the slag is relatively low, the deposit did not melt, but significant bubbling of the slag was noted, probably due to formation of  $\text{SiO}$  vapor in a reducing condition established locally by entrapped carbon in slag. All three slags exhibited similar appearance after testing and also all three specimens exposed to different slags appeared similar, indicating that coal slag chemistry has little influence in these short exposures. In the CERF exposure conducted with Pittsburgh coal, the specimen exhibited a thin layer of deposit after  $\approx 100$  h of testing. X-ray diffraction analysis of the deposit indicated predominantly mullite ( $3\text{Al}_2\text{O}_3 \cdot 2\text{SiO}_2$ ), with some ordered albite  $[(\text{Na},\text{Ca})\text{Al}(\text{Si},\text{Al})_3\text{O}_8]$  and traces of hematite. No significant degradation of the sample was observed in scanning electron microscopy (SEM) and EDX analysis. In the CERF exposure conducted with Alaskan/Russian coal, the dominant phases were anorthite ( $\text{CaO} \cdot \text{Al}_2\text{O}_3 \cdot 2\text{SiO}_2$ ), calcium aluminum silicate ( $\text{CaO} \cdot \text{Al}_2\text{O}_3 \cdot \text{SiO}_2$ ), and ordered sodium anorthite  $(\text{Ca},\text{Na})(\text{Al},\text{Si})_2\text{Si}_2\text{O}_8$ . These Ca-rich silicates also have melting temperatures  $>1400^\circ\text{C}$ , and reactions between the coal ash deposit and the ceramics occur predominantly in the solid state. The experimental results also indicate that  $\text{Na}_2\text{O}$  activities in the deposits (with combustion of coals containing  $\text{Fe}_2\text{O}_3$  and  $\text{CaO}$ ) are sufficiently low to form liquid sodium silicates of various types in coal-fired systems. This may qualitatively indicate that the material may be susceptible to cracking at elevated temperatures by particle impingement.

## Baseline Mechanical Properties

Four-point bend tests were conducted on Hexoloy SA, NT 230, SiC in Si matrix, and SiC(f) in SiC matrix materials at 1000, 1200, and  $1400^\circ\text{C}$ . The load to cause fracture measured in the test is used to calculate the flexural strength for the materials using the expression

$$\sigma = \frac{3(L_1 - L_2)P}{2t^2w},$$

where  $\sigma$  is flexural strength in MPa,  $L_1$  and  $L_2$  are distance between support points and load points, respectively,  $P$  is load, and  $t$  and  $w$  are thickness and width of the specimen, respectively. The test technique produces a nonuniform stress distribution with the maximum tensile stress in the outer skin of the specimen. Figure 4 shows the flexural strength of the materials as a function of temperature. The results show that Hexoloy SA maintains fairly high strength (in the range of 350–400 MPa) at up to  $1400^\circ\text{C}$ . Flexural strength of NT 230 is somewhat higher than that of Hexoloy SA up to  $1200^\circ\text{C}$  and seems to drop to  $\approx 300$  MPa at  $1400^\circ\text{C}$  and  $\approx 180$  MPa at  $1450^\circ\text{C}$ . The material SiC in Si matrix had a relatively lower strength of 100–120 MPa up to  $1200^\circ\text{C}$  and dropped to  $\approx 70$  MPa at  $1300^\circ\text{C}$ . The material SiC(f) in SiC matrix exhibited strength values comparable to those of Hexoloy SA at temperatures up to  $1200^\circ\text{C}$  but the values dropped at temperatures above  $1200^\circ\text{C}$  and comparable to those observed for NT 230. The load-displacement curves from these baseline tests were also used to calculate the area under the curves, which is indicative of the absorbed energy during fracture. The absorbed energy values can differentiate between the monolithic and composite

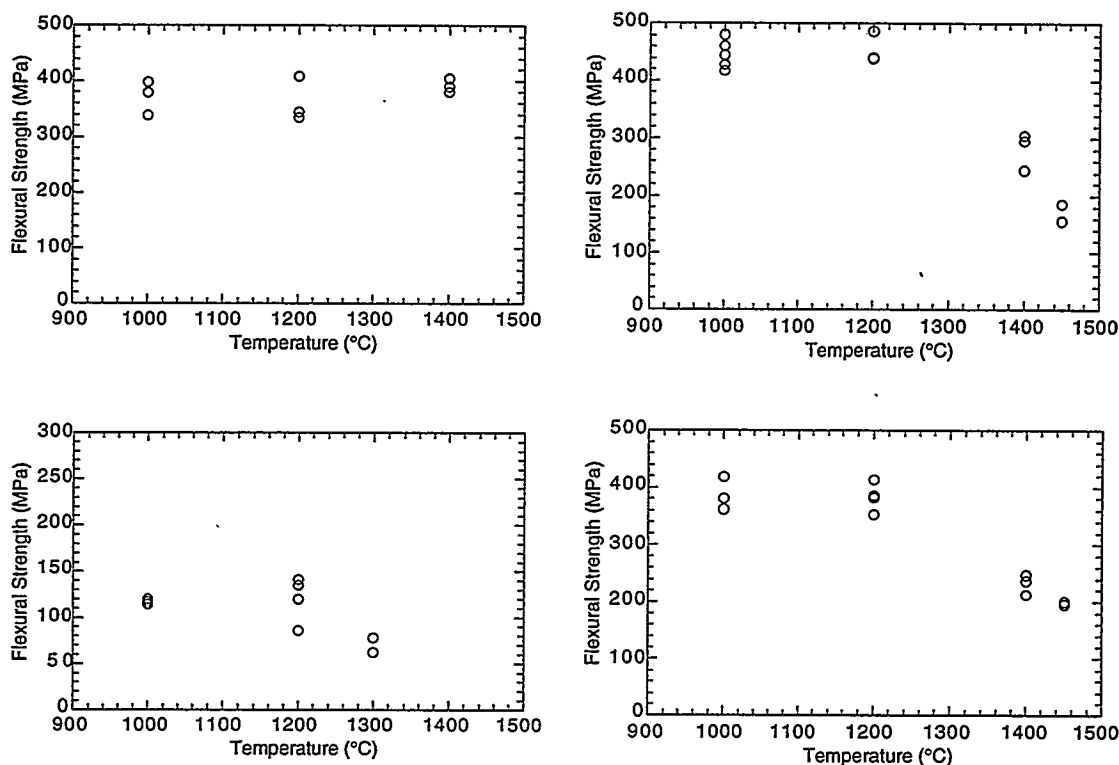


Fig. 4. Flexural strength data as a function of temperature for Hexoloy SA (top left), NT 230 (top right), SiC in Si matrix (bottom left), and SiC(f) in SiC matrix (bottom right) at 1200°C

materials because monolithic materials (such as Hexoloy SA) rarely exhibit creep prior to fracture while composites, such as SiC(f)/SiC, generally exhibit significant creep deformation prior to fracture. The fracture energy values for the materials will be presented in the next section, along with data obtained for the materials after exposure to corrosive environments.

#### Effect of Corrosion on Mechanical Properties

To examine the role of exposure environment several specimens of the four ceramic materials such as Hexoloy SA, NT 230, SiC in Si matrix, and SiC(f) in SiC matrix were preexposed for 200 h at 1200°C to dry air, Na<sub>2</sub>SO<sub>4</sub> salt, 75wt.% Na<sub>2</sub>SO<sub>4</sub>-25 wt.% NaCl mixture, and three different coal slags, identified as 43, 47, and XX. After exposure, the specimens were mechanical tested in vacuum at 1200°C. In these tests, the specimen surfaces exposed to the salt and slag environments were on the support side of the fixture, ensuring a tensile mode of loading for the surfaces exposed to corrosive environments.

Figure 5 shows the flexural strength for the four materials under baseline condition and after exposure to different environments. It is evident that exposures of 200 h in different environments had very little influence on the strength of Hexoloy SA material. Analysis of fracture surfaces of exposed specimens showed formation of thin layers of silica in air exposure, and virtually no salt or slag penetration of the



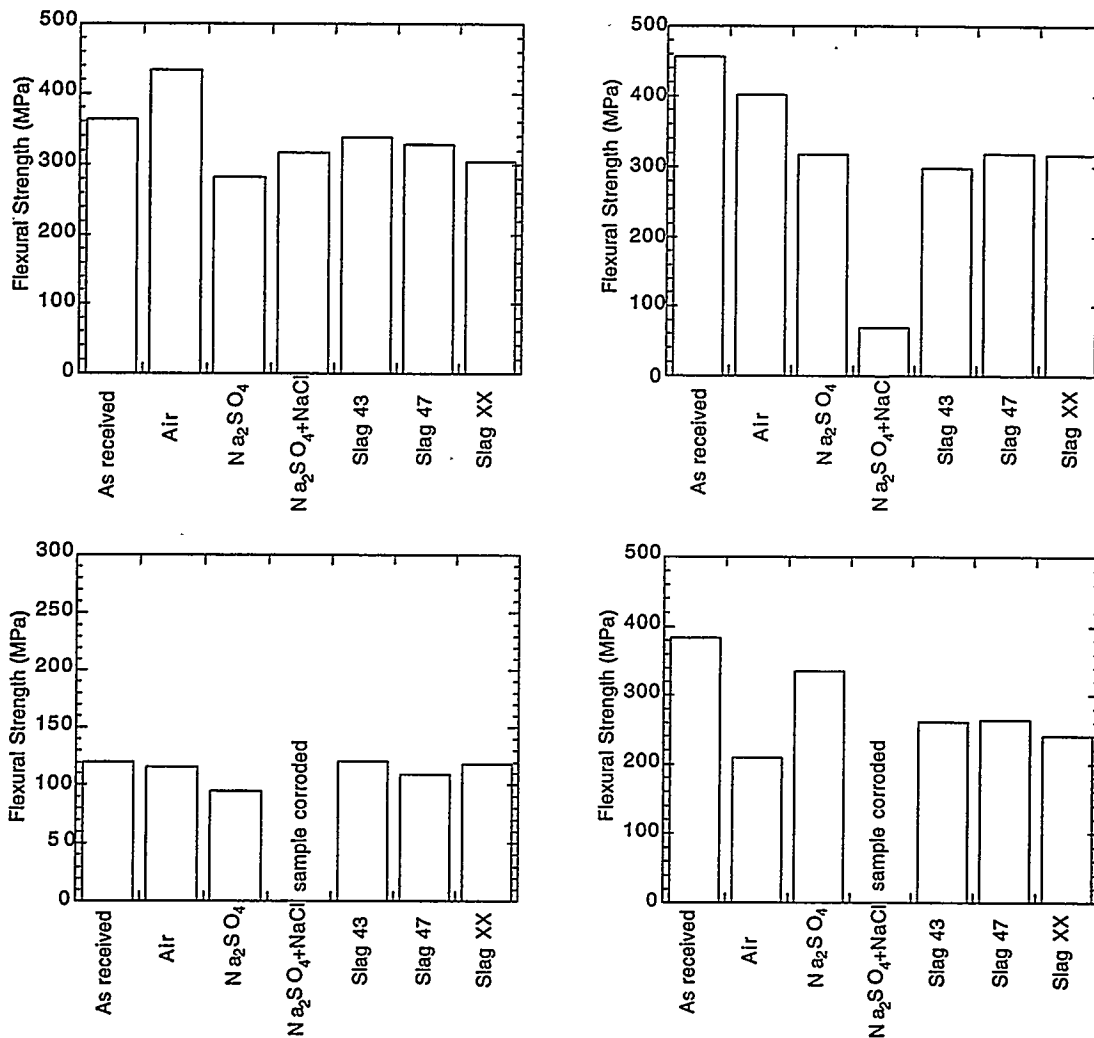


Fig. 5. Effect of exposure 200 h exposure at 1200°C on flexural strength for Hexoloy SA (top left), NT 230 (top right), SiC in Si matrix (bottom left), and SiC(f) in SiC matrix (bottom right)

specimens. Because of the high density of this material, influence of corrosive attack on this material may require longer exposure times or higher temperatures. The NT 230 exhibited fairly good strength after air exposure but had a significant loss in strength after exposure to salt that contained NaCl. On the other hand, the presence of slags at 1200°C had very little effect on the strength of the NT 230. The SiC in Si matrix was fairly porous and the sample became fully corroded in the presence of the salt containing NaCl but did not exhibit significant loss in strength in the presence of other deposits. The composite SiC(f) in SiC matrix also was subjected to accelerated corrosion in the presence of salt containing NaCl but behaved fairly well in other environments.

Figure 6 shows the absorbed energy per unit area for the four materials after 200 h exposure at 1200°C to different environments. The absorbed energy values for Hexoloy SA are 0.15-0.20 J/cm<sup>2</sup> after exposure in air and slag environments. The low value, which is an average of three tests conducted at

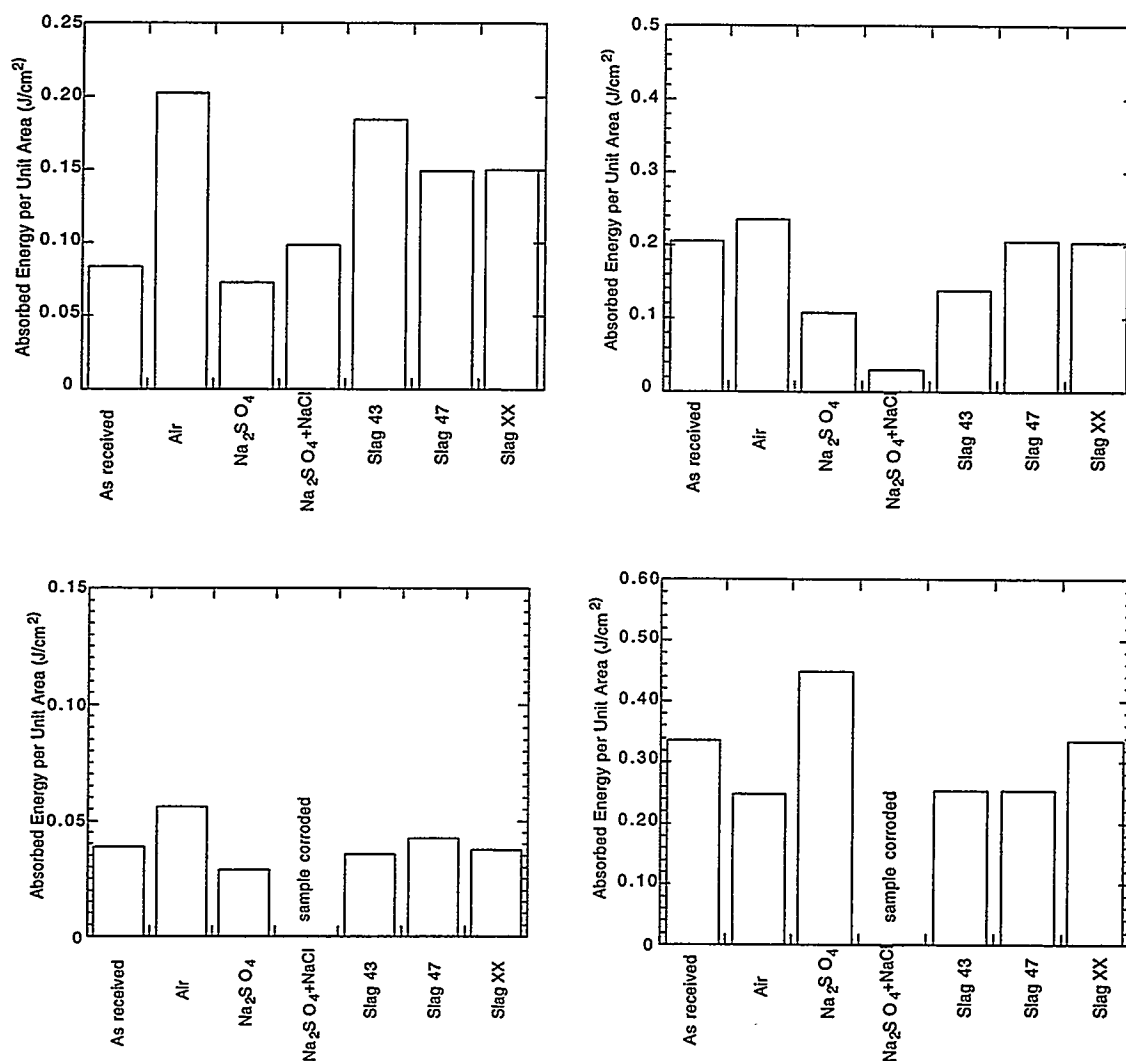


Fig. 6. Effect of exposure 200 h exposure at 1200°C on absorbed energy per unit area for Hexoloy SA (top left), NT 230 (top right), SiC in Si matrix (bottom left), and SiC(f) in SiC matrix (bottom right)

1200°C, for the as-received material cannot be explained at present. The lower values for the salt-exposed specimens may indicate some intergranular prenatration of salt, which was not obvious from SEM analysis of specimen cross sections. Absorbed energy values for the as-received, air-exposed, and slag-exposed specimens of NT 230 were comparable, indicating that these environments are benign from the corrosion standpoint after 200 h of exposure at 1200°C. The slag-exposed specimens showed lower absorbed energy values similar to those of Hexoloy SA. Specimens of SiC in Si matrix had inherently a low value for energy to fracture and were not significantly affected after exposure in air and slag environments. The presence of sulfate salt seems to lower the fracture energy. The composite material SiC(f) in SiC matrix had the highest value (0.25-0.40 J/cm²) for fracture energy among the four materials tested. The results also indicate that the salt environments have degrading effects on the strength properties of these materials but the presence of slag

(simulating either Eastern or Western U.S. coals) had a minimal effect at 1200°C in 200 h exposures.

### SUMMARY

Several ceramic materials have been examined to evaluate performance after exposure to dry air, salt environments that contained Na<sub>2</sub>SO<sub>4</sub> or 75 wt.% Na<sub>2</sub>SO<sub>4</sub>-25 wt.% NaCl mixture, and to three different coal slags that simulate slags obtained from combustion of coals from Eastern and Western U.S. The results showed that the materials exposed to an air environment undergo passive oxidation of SiC to SiO<sub>2</sub>. Exposure of these materials to salt environments can lead to catastrophic corrosion, especially if the condensed salt is high in sodium activity, which can lead to low-melting corrosion products. On the other hand, exposure of the materials to slags obtained from typical coal ash had very little effect on the corrosion performance of the materials, especially at 1200°C under which the reactions do not involve formation of liquid corrosion products. Four-point bend tests conducted on several of the materials after exposure to dry air, salt, and slag environments indicated that sodium salts (both sulfates and chlorides) have the most degrading effect on properties, while exposure to air and slag environments had minimal effect on properties at 1200°C.

### ACKNOWLEDGMENTS

The authors thank the ceramics manufacturers for supplying specimen materials. D. L. Rink assisted in the corrosion and four-point bend tests and microstructural analysis of exposed specimens.

### REFERENCES

1. L. A. Ruth, "Combustion 2000," PETC Review, Issue 4, p. 4, Fall 1991.
2. K. Natesan, M. Yanez-Herrero, and C. Fornasieri, "Corrosion Performance of Materials for Advanced Combustion Systems," Argonne National Laboratory Report ANL/FE-93/1, Dec. 1993.
3. K. Natesan, M. Freeman, and M. Mathur, "Corrosion Performance of Materials for Advanced Combustion Systems," Proc. 9th Annual Conf. on Fossil Energy Materials, CONF-9505204, ORNL/FMP-95/1, 1995.
4. S. C. Singhal, "Thermodynamic Analysis of the High-Temperature Stability of Silicon Nitride and Silicon Carbide," *Ceramurgia Intl.*, 2(3) (1976) 123-130.



# INTERACTION OF LOW-EXPANSION NZP CERAMICS WITH $\text{Na}_2\text{SO}_4$ AT 1000°C

W. Y. Lee, K. M. Cooley, D. P. Stinton, and D. L. Joslin

Oak Ridge National Laboratory  
P. O. Box 2008  
Oak Ridge, TN 37831-6063

## ABSTRACT

The interaction between several low-expansion NZP materials and  $\text{Na}_2\text{SO}_4$  at 1000°C in pure  $\text{O}_2$  was studied.  $\text{Ba}_{1.25}\text{Zr}_4\text{P}_{5.5}\text{Si}_{0.5}\text{O}_{24}$  experienced extensive cracking and delamination upon reaction with  $\text{Na}_2\text{SO}_4$ . On the other hand,  $\text{Ca}_{0.5}\text{Sr}_{0.5}\text{Zr}_4\text{P}_6\text{O}_{24}$  remained intact in terms of visual appearance, and had no significant weight loss or gain. However, the ion exchange between  $\text{Na}^+$  ions and  $\text{Ca}^{+2}$  ions was observed to be sufficiently rapid to allow the penetration of the  $\text{Na}^+$  ions into the test specimens in 100h. The segregation of Ca to the specimen surface was observed due to the ion exchange.  $\text{Ca}_{0.6}\text{Mg}_{0.4}\text{Zr}_4\text{P}_6\text{O}_{24}$  was also tested, but its stability could not properly be assessed because the as-received specimens contained a significant amount of  $\text{MgZr}_4\text{P}_6\text{O}_{24}$  as an impurity phase.

## INTRODUCTION

A new class of ceramic materials with low and tailorable thermal expansion characteristics has been developed for potential use in a variety of high temperature applications [1-3]. They are commonly referred to as NZP and named after the parent composition ( $\text{NaZr}_2\text{P}_3\text{O}_{12}$ ) which was discovered to exhibit high cationic conductivity and low-expansion characteristics. Although the thermal expansion behavior of most NZP materials is generally anisotropic, some NZP compositions such as  $\text{Ba}_{1+x}\text{Zr}_4\text{P}_{6-2x}\text{Si}_{2x}\text{O}_{24}$  (where  $0 < x < 1$ ),  $\text{Ca}_{1-x}\text{Sr}_x\text{Zr}_4\text{P}_6\text{O}_{24}$ , and  $\text{Ca}_{1-x}\text{Mg}_x\text{Zr}_4\text{P}_6\text{O}_{24}$  can be tailored to obtain isotropic expansion characteristics [2-4]. The Young's modulus of these NZP materials is reported to be rather low for a ceramic (~70 GPa) [3]. Another interesting property of these materials is their low thermal conductivity (~1 W/mK for slip-cast materials [3]) which is essentially as low as that of air plasma sprayed yttria stabilized zirconia coatings currently used as thermal barrier coatings in advanced gas turbines.

In addition to their potential use as bulk materials, the NZP ceramics could also be considered for thermal barrier and corrosion resistant coating applications. For example, Si-based materials such as  $\text{Si}_3\text{N}_4$  and SiC are known to be susceptible to major strength reduction

in certain corrosive environments containing condensible deposits such as  $\text{Na}_2\text{SO}$  and  $\text{Na}_2\text{CO}_3$  [5,6]. Thus, the need for developing a coating system which protects the surface of the Si-based materials from the corrosive environments has been recognized [7,8]. Unfortunately, progress in developing such a coating system has been limited because of many challenging thermochemical and thermomechanical requirements. From a thermomechanical point of view, the use of the NZP materials as protective coatings for Si-based ceramics may be advantageous because of the low thermal expansion and compliance of the NZP materials relative to most Si-based materials. However, the thermochemical stability of these complex material systems has not been explored except for the recent work of Li et al. [9]. They prepared a thin  $\text{Ca}_{0.6}\text{Mg}_{0.4}\text{Zr}_4\text{P}_6\text{O}_{24}$  coating on  $\text{Si}_3\text{N}_4$  and SiC substrates using a sol-gel method. The coated substrates were exposed to several environments containing  $\text{Na}_2\text{CO}_3$  at  $1000^\circ\text{C}$  for 50h, and yet no major change in the flexural strength of the  $\text{Si}_3\text{N}_4$  substrates was observed. This suggested that the coating was effective in protecting the  $\text{Si}_3\text{N}_4$  substrates from the corrosive environments. In order to further assess the potential of NZP materials for use as corrosion-resistant coatings, the present study is aimed at examining the intrinsic stability of several NZP bulk forms in a  $\text{Na}_2\text{SO}_4$ -containing atmosphere.

## EXPERIMENTAL

Three slip-cast NZP materials were evaluated:  $\text{Ba}_{1.25}\text{Zr}_4\text{P}_{5.5}\text{Si}_{0.5}\text{O}_{24}$  (BS25,  $x=0.25$ , LoTEC, Salt Lake City, UT),  $\text{Ca}_{0.6}\text{Mg}_{0.4}\text{Zr}_4\text{P}_6\text{O}_{24}$  (CM40,  $x=0.4$ , Golden Technologies, Golden, CO), and  $\text{Ca}_{0.5}\text{Sr}_{0.5}\text{Zr}_4\text{P}_6\text{O}_{24}$  (CS50,  $x=0.5$ , LoTEC). These particular compositions were chosen because they possess high strength while exhibiting low thermal expansion anisotropy and hysteresis [2,3]. Two specimens (1 cm x 0.4 cm x 0.3 cm) were tested for each material. The specimens were typically loaded with about 5 to 10  $\text{mg}/\text{cm}^2$  of  $\text{Na}_2\text{SO}_4$  using a procedure described elsewhere [8]. Prior to applying the layer of  $\text{Na}_2\text{SO}_4$ , the specimens were cleaned with distilled water, methanol, and acetone. The  $\text{Na}_2\text{SO}_4$  loaded specimens were placed on an  $\text{Al}_2\text{O}_3$  holder and exposed for 100h to a flowing oxygen environment (200  $\text{cm}^3/\text{min}$ ) at 101 kPa in a quartz tube heated to  $1000^\circ\text{C}$  using an electric resistance furnace. It is noted that  $\text{Na}_2\text{SO}_4$  has a relatively low rate of evaporation at these temperature and pressure conditions ( $\sim 0.016 \text{ Mg}/\text{cm}^2/\text{h}$ ) [10]. Thus, the premature loss of  $\text{Na}_2\text{SO}_4$  due to evaporation was not expected to occur for the test duration used in this study. Each NZP composition was

tested in separate batches to avoid any sample cross-contamination. A Scintag V x-ray diffractometer (XRD) and a JEOL Superprobe 733 electron microprobe analyzer (EMPA) were used for characterization. Both as-received and reacted specimens were mounted in epoxy and polished using kerosene as a lubricant to examine the formation of any reaction products and resulting surface microstructures. One of the two specimens exposed to the reaction treatment was washed in warm water using an ultrasonic bath to remove any water-soluble or weakly bonded phase(s) from the reacted surface.

## RESULTS

Table I shows that BS25 lost significant weight after reacting with  $\text{Na}_2\text{SO}_4$  for 100h. In reference to the initial weight before  $\text{Na}_2\text{SO}_4$  loading, Sample # BS25-1 lost 33.7 mg (or  $27.2 \text{ mg/cm}^2$ ) after the reaction and washing steps. It was visually evident that both unwashed and washed BS25 specimens were structurally disintegrated. Severe surface recession due to cracking and delamination were observed particularly along the corners and edges of the specimens' top surface. The formation of  $\text{NaZr}_2\text{P}_3\text{O}_{12}$  was detected by XRD as a minor phase in both unwashed and washed specimens. In addition, the BS25 diffraction peaks were observed to be somewhat randomly shifted by small amounts as a result of the reaction step.

Table I

Weight (g) of low-expansion ceramic specimens (dimensions; 1 cm x 0.4 cm x 0.3 cm) measured after  $\text{Na}_2\text{SO}_4$  loading, reaction, and washing in warm water. Net weight change ( $\Delta m$ ) = Final weight after washing - Initial sample weight. CM40 specimens could not be washed because they were fractured into pieces after reaction.

Sample Initial	$\text{Na}_2\text{SO}_4$		Reacted	Washed	$\Delta m$
BS25-1	0.3745	0.3859	0.3644	0.3414	-0.0337
BS25-2	0.3519	0.3652	0.3087	-	-
CM40-1	0.3875	0.3945	0.3725	-	-
CM40-2	0.3774	0.3879	-	-	-
CS50-1	0.3151	0.3203	0.3162	0.3145	-0.0006
CS50-2	0.3225	0.3308	0.3242	-	-

CM40 specimens also significantly cracked, and were actually fractured into several pieces after reacting with  $\text{Na}_2\text{SO}_4$ . However, it appeared from the XRD analysis that the as-received CM40 specimens contained a significant amount of  $\text{MgZr}_4\text{P}_6\text{O}_{24}$  as an impurity phase. The XRD pattern of the reacted specimens indicated the formation of  $\text{NaZr}_2\text{P}_3\text{O}_{12}$  and/or  $\text{CaZr}_4\text{P}_6\text{O}_{24}$  along with an unknown phase(s). Note that  $\text{NaZr}_2\text{P}_3\text{O}_{12}$  and  $\text{CaZr}_4\text{P}_6\text{O}_{24}$  are difficult to distinguish by XRD because of their similar lattice parameters.

Unlike the BS25 and CM40 samples, the weight of the CS50 specimens decreased only slightly after the reaction and washing steps ( $0.5 \text{ mg/cm}^2$  for Sample# CS50-1 in Table I). No significant recession due to cracking and delamination was visually detected. However, as shown in Figure 1, an EMPA analysis of the polished cross-section of the reacted specimen (Sample # CS50-1) shows that the ion exchange between  $\text{Na}^+$  ions from  $\text{Na}_2\text{SO}_4$  and  $\text{Ca}^{+2}$  ions from CS50 was fairly extensive during the 100h reaction period. The presence of Na was observed throughout the entire cross-section of the reacted sample. In contrast, as-received CS50 samples did not contain any Na detectable to the EMPA technique. The segregation of Ca toward the surface was observed as shown in Figure 1. It appeared that the Ca-enriched surface layer was weak since it was somewhat damaged by polishing as evidenced by some delamination in this region. There was no apparent change in the Ca-enriched surface layer after washing. The presence of sulfur was not detected by the EMPA technique in the reacted and washed samples. In comparing the XRD patterns of the as-received, corroded, and washed samples, the appearance of some new, unindexable diffraction peaks was observed after the reaction step. The new peaks did not disappear after the specimen was washed.

## DISCUSSION

The experimental observations suggested that the BS25 specimens became structurally as well as chemically unstable when reacted with  $\text{Na}_2\text{SO}_4$  at  $1000^\circ\text{C}$  for 100h in  $\text{O}_2$ . The formation of the  $\text{NaZr}_2\text{P}_3\text{O}_{12}$  phase was observed as a reaction product from the BS25 samples. The  $\text{NaZr}_2\text{P}_3\text{O}_{12}$  phase is known to exhibit highly anisotropic thermal expansion behavior, and consequently microcracks extensively. Also, the formation of  $\text{NaZr}_2\text{P}_3\text{O}_{12}$  can induce undesired volume changes since the unit-cell volume of  $\text{NaZr}_2\text{P}_3\text{O}_{12}$  ( $1527.83 \text{ \AA}^3$ ) is smaller



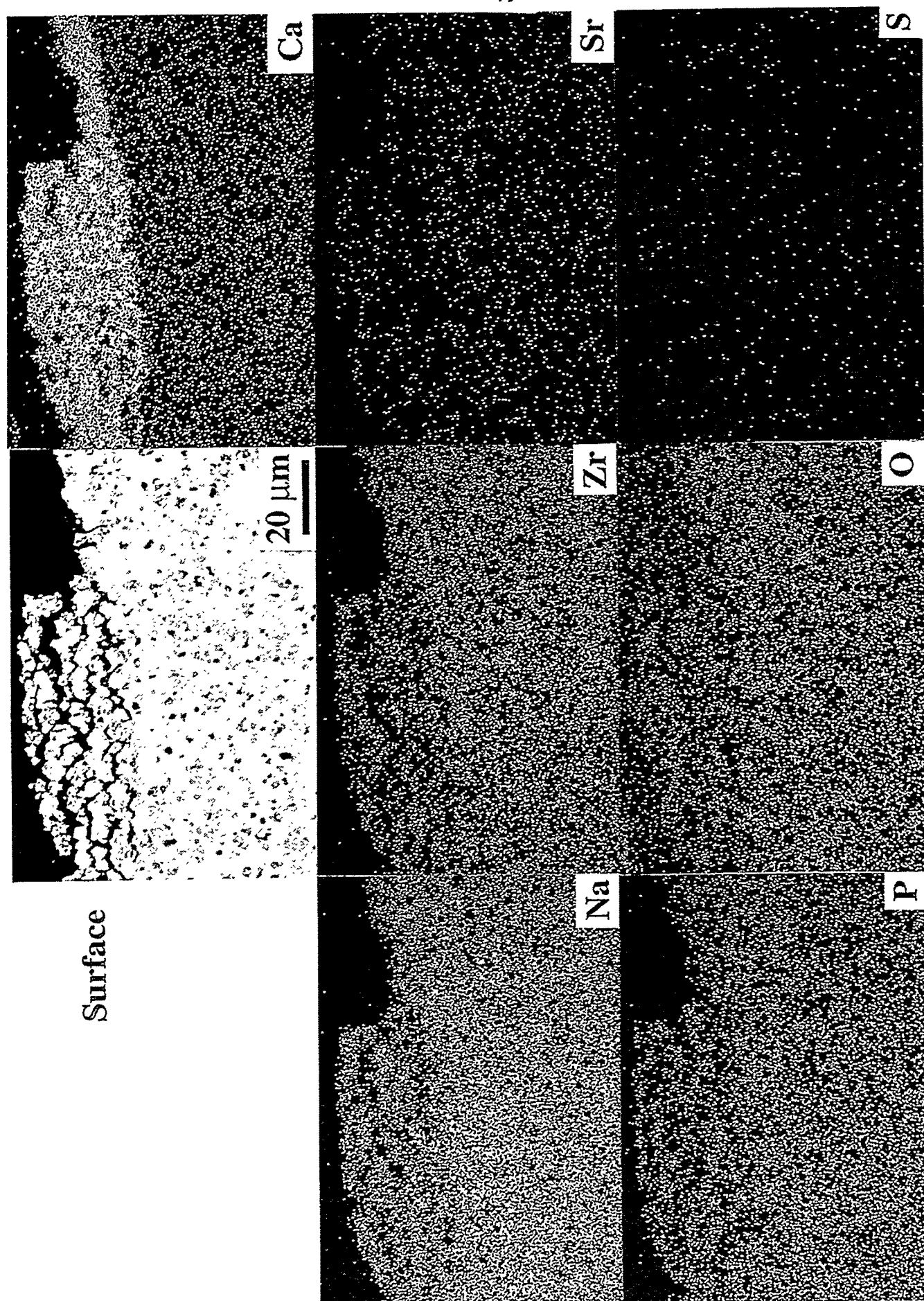


Figure 1. Backscattered image and x-ray elemental maps of CS50 after reaction with  $\text{Na}_2\text{SO}_4$  at  $1000^\circ\text{C}$  for 100 h in pure  $\text{O}_2$ .

than that of BS25 ( $1559.94 \text{ \AA}^3$  [11]). Therefore, the formation of the  $\text{NaZr}_2\text{P}_3\text{O}_{12}$  phase appears to be responsible for the observed cracking and delamination of the reacted BS25 samples.

The stability of CM40 with respect to  $\text{Na}_2\text{SO}_4$  could not be assessed from this study, because the starting material contained a significant amount of  $\text{MgZr}_4\text{P}_6\text{O}_{24}$  as an impurity phase. Nevertheless, the observed cracking and delamination of these specimens after reaction with  $\text{Na}_2\text{SO}_4$  could be explained by the relatively large volume change anticipated from the transition of  $\text{MgZr}_4\text{P}_6\text{O}_{24}$  to  $\text{NaZr}_2\text{P}_3\text{O}_{12}$  and/or  $\text{CaZr}_4\text{P}_6\text{O}_{24}$ . The unit-cell volume of monoclinic  $\text{MgZr}_4\text{P}_6\text{O}_{24}$  ( $977.52 \text{ \AA}^3$ ) is considerably smaller than that of rhombohedral  $\text{NaZr}_2\text{P}_3\text{O}_{12}$  and  $\text{CaZr}_4\text{P}_6\text{O}_{24}$  ( $1527.83$  and  $1516.01 \text{ \AA}^3$ , respectively). Because of the  $\text{MgZr}_4\text{P}_6\text{O}_{24}$  impurity phase, the results from this study could not directly be compared to those reported by Li et al. [9]. As mentioned earlier,  $\text{Si}_3\text{N}_4$  substrates coated with a sol-gel CM40 coating did not show any strength degradation after exposure to several corrosive environments containing  $\text{Na}_2\text{CO}_3$  at  $1000^\circ\text{C}$  for 50h. In future work, pure CM40 specimens are needed to determine their intrinsic stability in the corrosive environments.

In terms of visual appearance and weight loss, the CS50 samples appeared to have remained relatively intact after reaction with  $\text{Na}_2\text{SO}_4$ . However, at a microscopic level, the EMPA results clearly indicated that the ion exchange between the  $\text{Na}^+$  and  $\text{Ca}^{+2}$  ions was sufficiently rapid for the  $\text{Na}^+$  ions to penetrate the entire CS50 specimens during the 100h exposure. The presence of sulfur was not detected at least within the sensitivity of the EMPA technique. Therefore, it seems that the CS50 material promotes the dissociation of  $\text{Na}_2\text{SO}_4$  while releasing  $\text{SO}_3$  and/or  $\text{SO}_2$  as gaseous byproducts. The significance of these observations relative to the potential of the CS50 material as a corrosion resistant coating for Si-based ceramics is not yet clear. A further study is needed to assess the effects of Na penetration through a CS50 coating structure in protecting Si-based substrates. Also, the thermochemical compatibility between the CS50 and Si-based ceramics must be addressed.

#### ACKNOWLEDGMENTS

The authors acknowledge their gratitude to Santosh Limaye for providing the BS25 and CS50 samples, Tom Geer for metallography, and Y. W. Bae for x-ray diffraction.

## REFERENCES

1. C.-Y. Huang, D.K. Agrawal, H.A. McKinstry, and S.Y. Limaye, "Synthesis and Thermal Expansion Behavior of  $\text{Ba}_{1+x}\text{Zr}_4\text{P}_{6-2x}\text{Si}_{2x}\text{O}_{24}$  and  $\text{Sr}_{1+x}\text{Zr}_4\text{P}_{6-2x}\text{Si}_{2x}\text{O}_{24}$  Systems," *J. Mater. Res.*, 9, 2005 (1994).
2. D.A. Hirschfeld, S.M. VanAken, T.K. Li, Y.P. Yang, and J.J. Brown, "Development of Ultra-Low-Expansion Ceramics: Synthesis, Thermal Expansion, and Thermal Conductivity of  $(\text{Ca}_{1-x}\text{Mg}_x)\text{Zr}_4(\text{PO}_4)_6$ ," pp. 239-244 in the Proceedings of the Annual Automotive Technology Development Contractors' Meeting, Dearborn, MI, October 22-25, 1990. Published by the Society of Automotive Engineers, Inc., Warrendale, PA, 1991.
3. S.Y. Limaye and R. Nageswaran, "Development of NZP Ceramic Based "Cast-In-Place" Diesel Engine Port Liners," Final Report, LoTEC, Inc., West Valley City, UT, November 1994.
4. T.B. Jackson, S.Y. Limaye, and W.D. Porter, "The Effects of Thermal Cycling on the Physical and Mechanical Properties of [NZP] Ceramics," pp. 63-80 in Ceramics Transactions Vol. 52: Low-Expansion Materials. Edited by D.P. Stinton and S.Y. Limaye, The American Ceramic Society, Westerville, OH, 1995.
5. N.S. Jacobson, "Corrosion of Silicon-Based Ceramics in Combustion Environments," *J. Am. Ceram. Soc.*, 76, 3 (1993).
6. Components to Erosion and Hot Corrosion/Oxidation Attack," p. 36-1 in Proceedings of Advisory Group for Aerospace and Research & Development Symposium on Erosion, Corrosion, and Foreign Object Damage Effects in Gas Turbines. Printed by Canada Communication Group, Quebec, Canada, November 1994.
7. K.N. Lee, N.S. Jacobson, and R.A. Miller, "Refractory Oxide Coatings on SiC Ceramics," *MRS Bulletin*, 35, (October 1994).
8. W.Y. Lee, Y.W. Bae, and D.P. Stinton, " $\text{Na}_2\text{SO}_4$  Induced Corrosion of  $\text{Si}_3\text{N}_4$  Coated with Chemically Vapor Deposited  $\text{Ta}_2\text{SO}_5$ ," *J. Am. Ceram. Soc.*, 78, 1927 (1995).
9. T.K. Li, D.A. Hirschfeld, and J.J. Brown, "Thin Film Coatings of  $(\text{Ca}_{1-x}\text{Mg}_x)\text{Zr}_4(\text{PO}_4)_6$  on  $\text{Si}_3\text{N}_4$  and SiC," *J. Mater. Res.*, 9, 2014 (1994).
10. N.S. Jacobson and D.S. Fox, "Molten-Salt Corrosion of Silicon Nitride: II, Sodium Sulfate," *J. Am. Ceram. Soc.*, 71, 139 (1988).
11. S. Shanmugham, D.P. Stinton, O.B. Calvin, C.R. Hubbard, and S.Y. Limaye, "Synthesis and Cell Refinement of  $\text{Ba}_{0.5+x/2}\text{Zr}_2\text{P}_{3-x}\text{Si}_x\text{O}_{12}$  with  $x=0.25$  and  $x=0.375$ ," *J. Mater. Sci. Lett.*, 13, 1326 (1994).



## SYNTHESIS OF MULLITE COATINGS BY CHEMICAL VAPOR DEPOSITION

Rao P. Mulpuri, Michael Auger, Vinod K. Sarin

Boston University  
Department of Manufacturing Engineering  
Boston, MA 02215

### ABSTRACT

Formation of mullite on ceramic substrates via chemical vapor deposition was investigated. Mullite is a solid solution of  $\text{Al}_2\text{O}_3$  and  $\text{SiO}_2$  with a composition of  $3\text{Al}_2\text{O}_3 \cdot 2\text{SiO}_2$ . Thermodynamic calculations performed on the  $\text{AlCl}_3$ - $\text{SiCl}_4$ - $\text{CO}_2$ - $\text{H}_2$  system were used to construct equilibrium CVD phase diagrams. With the aid of these diagrams and consideration of kinetic rate limiting factors, initial process parameters were determined. Through process optimization, crystalline CVD mullite coatings have been successfully grown on  $\text{SiC}$  and  $\text{Si}_3\text{N}_4$  substrates. Results from the thermodynamic analysis, process optimization, and effect of various process parameters on deposition rate and coating morphology are discussed.

### INTRODUCTION

Silicon-based ceramics such as  $\text{Si}_3\text{N}_4$  and  $\text{SiC}$  are currently the leading candidate materials for high temperature applications due to their unique combination of high strength and thermal conductivity, low thermal expansion, good high temperature stability and oxidation resistance. However, their susceptibility to high temperature corrosion and damage due to contact stress considerably limit their utilization. For example, corrosion can occur at elevated temperatures as a result of the combined effect of the oxygen plus gaseous, condensed, or particulate impurities induced via the gas stream in a turbine engine. [1] In addition, contact stress damage at ceramic/ceramic

interfaces has been projected as a major failure mode for ceramic components in advanced heat engines. [2] It has been established that the application of a coating on silicon based substrates is an effective technique to minimize or overcome these problems. [3,4] Several coating systems have been developed, but none to date have been able to meet all the requirements due to the severity of these applications. [5,6] Mullite ( $3\text{Al}_2\text{O}_3 \cdot 2\text{SiO}_2$ ) due to its unique properties such as thermal expansion match with  $\text{Si}_3\text{N}_4$  and  $\text{SiC}$ , stability, and significantly superior corrosion resistance at high temperatures, [7,8] is considered a prime candidate coating material.

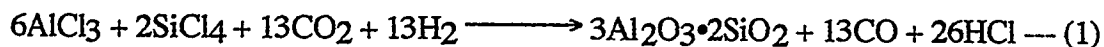
Mullite is a solid solution of  $\text{Al}_2\text{O}_3$  and  $\text{SiO}_2$  and is the only stable crystalline compound in the  $\text{Al}_2\text{O}_3$ - $\text{SiO}_2$  system. Although it is popularly quoted with an  $\text{Al}_2\text{O}_3$ : $\text{SiO}_2$  ratio of 3:2, mullite is known to have a range of solid solubilities. After several years of research, there are still controversies regarding the melting behavior and the solid-solution range of mullite. However, it has been observed that the solid solubility is dependent on the method of synthesis. Attempts to grow mullite coatings by various processing techniques have met with limited success. [4] Deposition of plasma sprayed mullite coatings was reported, [9] however the coatings exhibited problems such as non-uniformity and microcracks which are characteristic of the plasma spray process. To overcome these deficiencies, formation of mullite via CVD has been investigated. The CVD process generally results in dense coatings that can be synthesized well below the melting or sintering temperatures of the material, with the possibility of microstructural and morphological optimization through variation in process parameters. Although the deposition of CVD  $\text{Al}_2\text{O}_3$  and  $\text{SiO}_2$  is now well established, [10-14] to our knowledge mullite coatings have never before been grown from the vapor phase.

## THERMODYNAMIC ANALYSIS

Equilibrium thermodynamic analysis was performed on the  $\text{AlCl}_3$ - $\text{SiCl}_4$ - $\text{CO}_2$ - $\text{H}_2$  system in order to establish equilibrium reaction products at various operating conditions. It has been common practice to use thermodynamic analysis to predict the possible outcome of a CVD reaction. [15-22] A computer program [23] utilizing minimization of Gibbs free energy was used to perform the thermodynamic analysis. This was based on

earlier work to calculate the composition and heat condition of an equilibrium mixture. [24] The results of several calculations at each set of process conditions were presented in the form of binary and ternary CVD phase diagrams. Chemical equilibrium is rarely achieved under most CVD flow conditions. [25] Therefore, results from these diagrams can only be used to establish guidelines in the form of trends rather than to predict the exact phases that would be actually present. Most importantly, thermodynamic analysis did not include the rate-controlling factors in the CVD process such as reaction kinetics, mass transport of the gaseous species, and depletion of the reactant gases. Thus, an actual CVD experiment does not necessarily conform with predictions of the thermodynamic analysis. However, such phase diagrams can be used to project the influence of process variables such as temperature, pressure, and inlet gas concentrations on the phase assemblage stoichiometry of the deposit, the equilibrium deposition efficiency, and the concentration of the molecular species in the exhaust gas. The thermodynamic equilibrium state of the CVD system can be calculated for (i) partial pressures of all the gaseous species, (ii) the identification of the condensed phase, (iii) equilibrium deposition rates possible and (iv) their theoretical efficiencies. Such calculations provide limiting criteria and aid in establishing rate-limiting gaseous species. The reliability of these calculations is, of course, dependent on the availability and accuracy of thermochemical data as well as identification of all the critical vapor and condensed phases. Information from such phase diagrams can be used to help determine the range of input conditions which would produce mullite and other compounds at equilibrium.

The reaction yielding mullite from  $\text{AlCl}_3$  and  $\text{SiCl}_4$  is hypothesized to be as follows:



For the purpose of the equilibrium calculations, it was assumed that mullite is a line compound, and of  $3\text{Al}_2\text{O}_3:2\text{SiO}_2$  composition. The calculations were based on thermodynamic data obtained from Ref [26]. Several calculations were performed on the  $\text{AlCl}_3$ - $\text{SiCl}_4$ - $\text{CO}_2$ - $\text{H}_2$  system at different process parameters at each set of deposition conditions. Figure 1 shows a sample ternary CVD phase diagram of  $\text{AlCl}_3$ - $\text{SiCl}_4$ - $\text{CO}_2$ - $\text{H}_2$  system at 1000 °C and 75 torr. This diagram represents, for a set of reaction conditions and input reactant concentrations, all the possible phases that would be present during equilibrium conditions equilibrium.

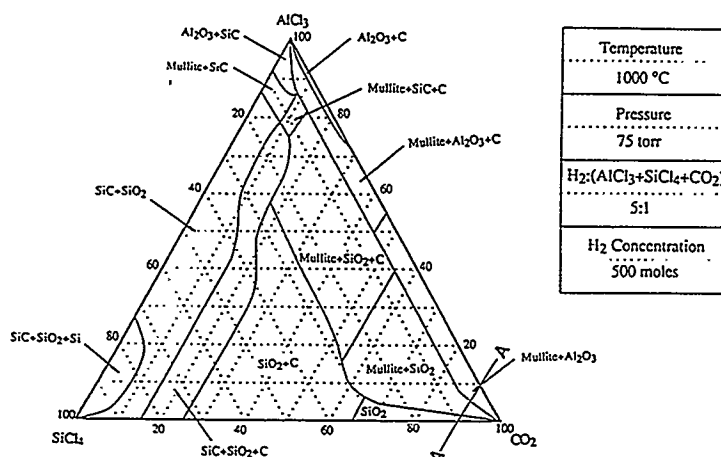


Figure 1: CVD phase diagram of  $\text{AlCl}_3$ - $\text{SiCl}_4$ - $\text{CO}_2$ - $\text{H}_2$  system at  $1000^\circ\text{C}$  and 75 torr

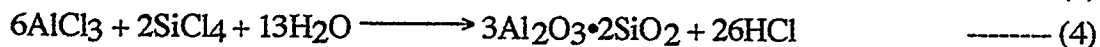
Details of an extensive thermodynamic analysis were discussed in an earlier publication. [27] It was concluded that low concentrations of the chlorides need to be used in order to obtain high deposition efficiency, and carbon-free deposits. It was also found that there were no underlying benefits to using bromides and fluorides as alternative halide sources.

### KINETIC CONSIDERATIONS

As mentioned earlier, an understanding of thermodynamics alone is not sufficient to establish the CVD process parameters. Reaction kinetic limitations to a great extent have a major effect on the deposition characteristics. The relative importance of thermodynamic and kinetic considerations depends on the particular system of interest and the specific process conditions. Since no data was available to predict the mechanism of formation of mullite from  $\text{AlCl}_3$  and  $\text{SiCl}_4$ , it was assumed that the CVD formation of mullite follows the same reaction path associated with the formation of  $\text{Al}_2\text{O}_3$  from  $\text{AlCl}_3$ . It is well established that the formation of  $\text{Al}_2\text{O}_3$  necessitates the formation of  $\text{H}_2\text{O}$  through the water-gas-shift reaction, thus making it the rate-limiting step. It is also important to note that the formation of  $\text{SiO}_2$  from  $\text{SiCl}_4$  does not require an intermediate reaction such as  $\text{H}_2\text{O}$  formation to occur. Keeping this in mind, the



assumed reaction steps during the formation of mullite can be expressed using the following set of intermediate reactions:



Initial process parameters were chosen based on the information obtained through equilibrium thermodynamic analysis, and consideration of kinetic factors such as the influence on the water-gas-shift reaction. At this stage, it was unclear how the water-gas-shift reaction influenced the formation of CVD mullite.

## EXPERIMENTAL METHODS

A CVD unit consisting of a vertical hot wall reactor with a resistively heated furnace was used for the experiments. Polished bars of 3x4x20 mm size of monolithic SiC and Si<sub>3</sub>N<sub>4</sub> were used as substrates. In general, low chloride concentrations were chosen for experimentation. AlCl<sub>3</sub> was formed in-situ by flowing Cl<sub>2</sub> with Ar carrier gas through densely packed Al wire cuttings maintained at a constant temperature. SiCl<sub>4</sub> was evaporated from liquid stage at room temperature. AlCl<sub>3</sub> and SiCl<sub>4</sub> were mixed in appropriate ratios prior to entering the CVD reactor. H<sub>2</sub> and CO<sub>2</sub> were used via the water-gas-shift reaction in order to form H<sub>2</sub>O in-situ in the CVD reactor. There was always excess hydrogen present in the system to ensure all the chlorides were properly reduced to HCl before leaving the reactor.

## RESULTS AND DISCUSSION

A unique CVD process was developed for deposition of crystalline mullite coatings on silicon based substrates. [28] Figure 2 shows the surface morphology and cross-section of a typical mullite coating deposited on Si<sub>3</sub>N<sub>4</sub> at 950 °C and 75 torr for 2

hours. As is evident, the coating was dense, uniform in thickness (approximately  $6\text{ }\mu\text{m}$ ), and had a fine grained (around  $2\text{ }\mu\text{m}$ ) equiaxed structure. X-ray and electron diffraction analyses confirmed that the only crystalline phase present in the coating was mullite. To further characterize the coating structure on a microscopic level, TEM was performed. A more detailed microstructural analysis clearly shows that the coating starts with very fine grains and grows into larger grains as the growth process continues. Further characterization through energy dispersive spectroscopy shows that the Al/Si ratio gradually increased as the coating grew. Figure 3 shows a transmission electron micrograph and a typical change in the Al/Si ratio of the coating on SiC.

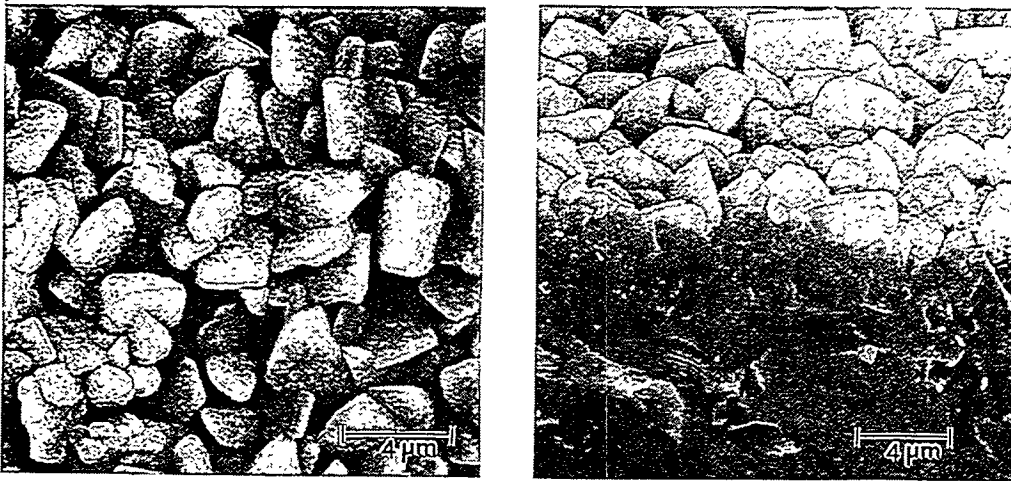


Figure 2: Scanning Micrograph of mullite coating on SiC a) surface, b) cross-section

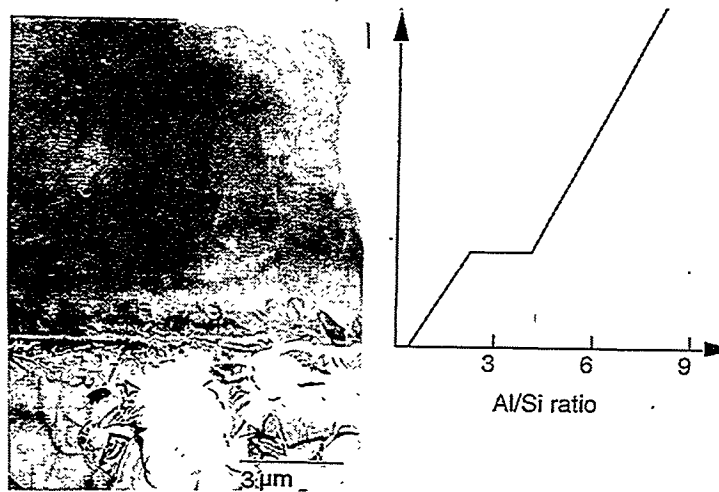


Figure 3: Transmission Electron Micrograph of mullite on SiC, b) change in Al/Si ratio throughout the coating

### Effect of Temperature

The effect of temperature on the deposition rate is shown in Figure 4. The mullite deposition rate decreased from 800 °C to 850 °C and then increased beyond that. Figure 5 shows the Arrhenius plot corresponding to an activation energy of 7.4 kcal/mol. Although this activation energy is characteristic of a mass-transport limited process, the result should be interpreted with caution since a variation in Al/Si ratio was observed in the coating. In addition, the extent of crystallinity was also a variable, making it even more complicated. Figure 6 shows the coating surface morphology at various process temperatures. At 800 °C, the coating has a globular morphology and is amorphous according to X-ray analysis. This is in agreement with the thermodynamic analysis that mullite is not predicted to form at 800 °C. At 850 °C, the coating remained globular with small crystallite formation. X-ray diffraction also shows a small amount of mullite detected. As the temperature was increased beyond 1000 °C, large clusters of crystals were formed resulting in cracking of the coating.

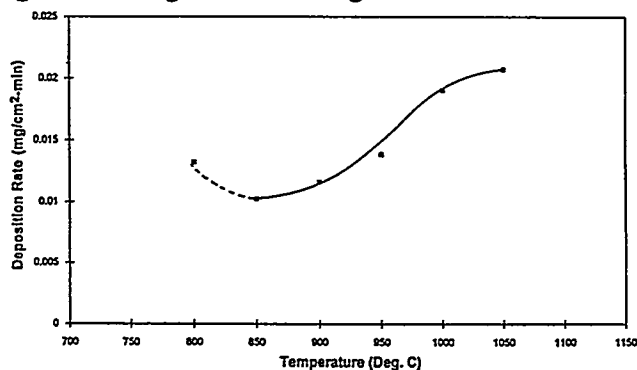


Figure 4: Effect of Temperature on Deposition Rate

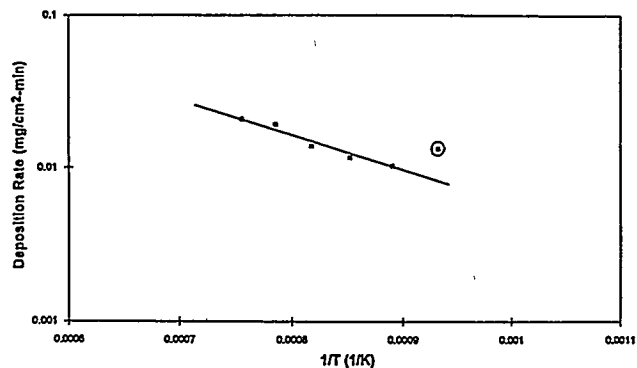


Figure 5: Arrhenius plot of mullite deposition at 75torr

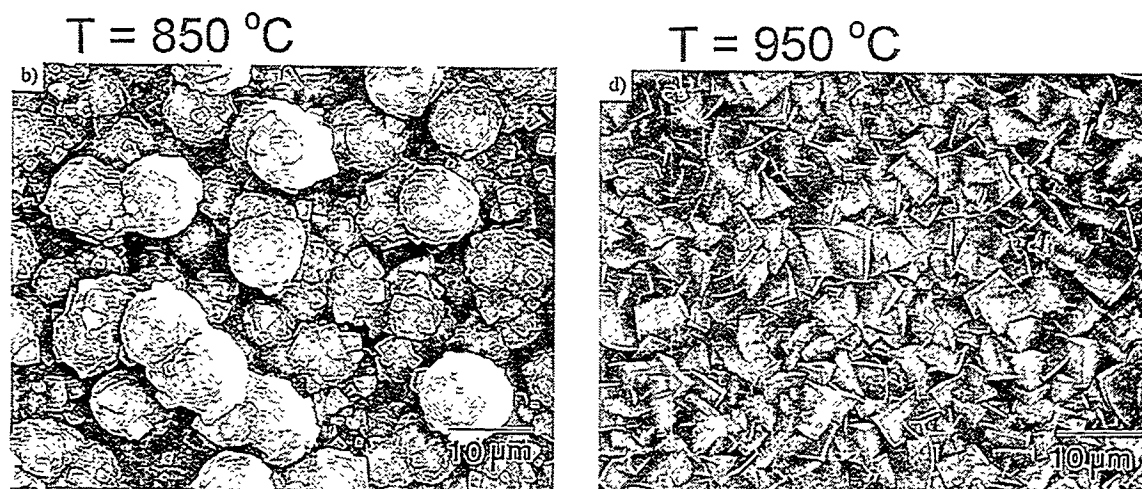


Figure 6: Surface morphology of mullite grown at various temperatures

### Effect of Total System Pressure

The effect of total system pressure on deposition rate is shown in Figure 7. The deposition rate increased almost linearly at low system pressures; however, with a further increase in the system pressure, the rate of increase was reduced, with a subsequent reduction in the deposition rate. This effect can be attributed to the depletion of reactants with increase in pressure due to the hot wall configuration of the system. Figure 8 shows the variation in coating surface morphology with total system pressure. The grain size increased with an increase in the pressure to a certain extent. The grain size at the 200 torr condition was actually smaller than that at the 150 torr condition. In addition, it was observed that the coating was porous at higher pressures. This variation is again, believed to be a result of the depletion of reactants.

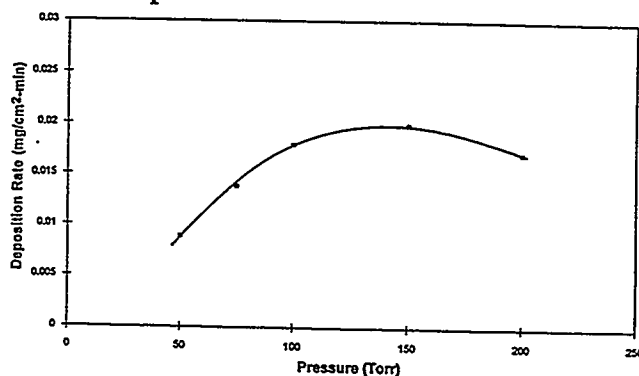


Figure 7: Effect of total system pressure on mullite deposition rate at  $950\text{ }^{\circ}\text{C}$

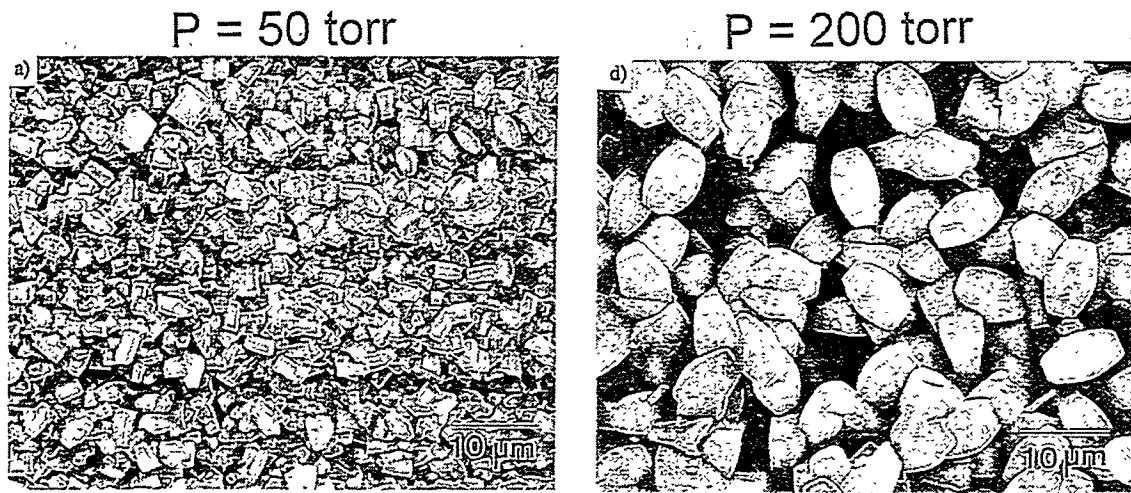


Figure 8: Surface morphology variation of mullite with change in total system pressure

#### Effect of Input Gas Stoichiometry

The effect of the input gas stoichiometry in the form of Al/Si ratio was investigated. The Al/Si ratio was varied from 0 to 4. Figure 9 shows the variation in deposition rate with respect to Al/Si ratio in the input gas composition. At Al/Si ratio of zero (pure  $\text{SiO}_2$  deposit), a high growth rate was observed. As the Al/Si ratio was increased, the deposition rate decreased rapidly to a certain level and then increased. This implies that the addition of a small amount of Al species to  $\text{SiCl}_4$  in the formation of mullite reduces the deposition rate considerably. This also points to a possible shift in the deposition mechanism with the addition of Al species. There is insufficient data available at this stage to understand this phenomenon completely. Figure 10 shows the variation in coating surface morphology with the Al/Si ratio. The size of the mullite crystals increased with an increase in the Al/Si ratio in the input gas composition. This variation corresponds to the finding that the grain size increased with the coating growth along with an increase in Al/Si ratio in the coating.

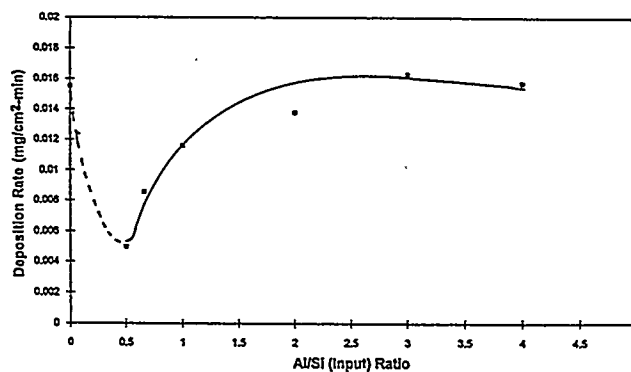


Figure 9: Variation in deposition rate with respect to input Al/Si ratio at 950°C, 75torr

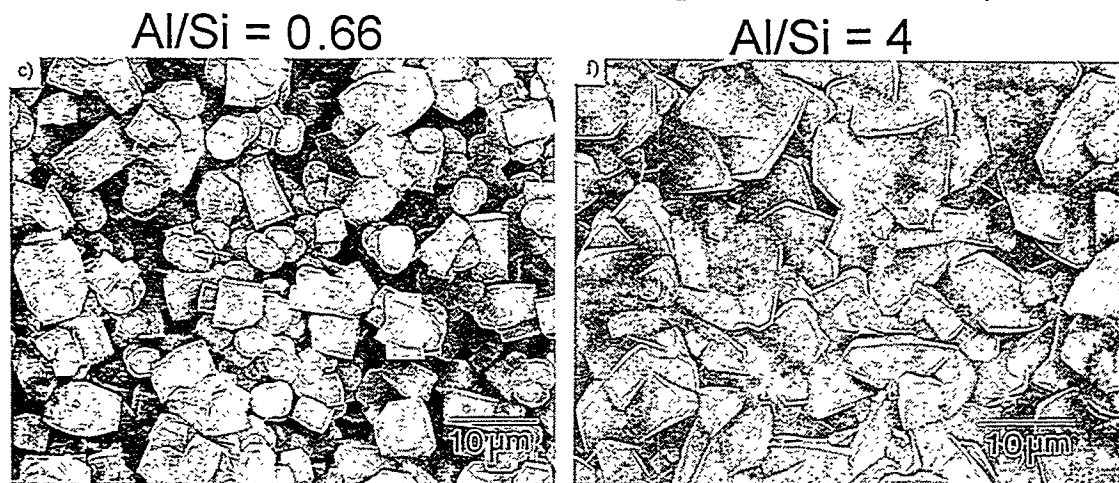


Figure 10: Surface morphology variation with respect to Al/Si input ratio

Comparison of the growth rates at various levels in the reactor and the reactant depletion effects suggest that the formation of mullite does not require the formation of  $H_2O$  through the water-gas-shift reaction. Instead, oxygen from  $CO_2$  is utilized for the formation of the oxide(s). Reactant depletion effects in the hot wall system make it difficult to separate the effect of parameters such as temperature and pressure independently. Further experimentation is necessary in order to understand the exact mechanisms involved.

Results from the initial corrosion resistance evaluations at Oak Ridge National Laboratory look very promising. Mullite coated  $Si_3N_4$  samples loaded with  $Na_2SO_4$  were heated to temperatures over 1000 °C in an oxygen environment. Electron microprobe analysis of the treated samples as well as x-ray diffraction analysis before and after the corrosion testing show that there were no reactions and formation of corrosion products between mullite and  $Na_2SO_4$ .

## CONCLUSIONS

Equilibrium thermodynamic analysis was performed on the  $\text{AlCl}_3\text{-SiCl}_4\text{-CO}_2\text{-H}_2$  system which pointed out that low concentrations of the chlorides were necessary in order to obtain high deposition efficiency, and carbon-free deposits. Information from the phase diagrams and kinetic rate-limiting considerations was effectively used to identify the initial process parameters for the growth of mullite. Based on these results, a new process for depositing crystalline mullite coatings on  $\text{Si}_3\text{N}_4$  and SiC based substrates was developed. The coatings were dense, and increased in Al content from the substrate to the surface of the coating. Preliminary testing projects mullite as a promising coating material for corrosion protection of SiC and  $\text{Si}_3\text{N}_4$ .

## ACKNOWLEDGMENT

The authors wish to acknowledge Mr. D.P. Stinton of Oak Ridge National Laboratory (ORNL) for his helpful insights throughout this research. The authors also wish to acknowledge the help from Mr. D. Doppalapudi, and Dr. S.N. Basu with the TEM analysis, and Dr. W.Y. Lee of ORNL with the corrosion resistance evaluation. Research sponsored by the U.S. Department of Energy, Assistant Secretary for Energy Efficiency and Renewable Energy, Office of Transportation Technologies, as part of the Ceramic Technology Project of the Propulsion System Materials Program, and Fossil Energy AR&TD Materials Program under contract numbers DE-AC05-84OR21400 and SC-19X-SS110C with Martin Marietta Energy Systems, Inc.

## REFERENCES

1. N.S. Jacobson, *J. Am. Ceram. Soc.*, **76** [1] 3-28 (1993)
2. D.W. Richerson, W.D. Carruthers, and L.J. Lindberg, *Materials Science Research*, Vol. 14, pp 661-676, J.A. Pask, and A. Evans, Eds. Plenum Press, NY (1981)
3. K.N. Lee, R.A. Miller, and N.S. Jacobson, *Ceramic Transactions*, Vol. 38, pp 565-575, N.P. Bansal, Ed. The American Ceramic Society, Westerville, OH (1993)
4. J. Schienle, and J. Smyth, Final Report, ORNL/Sub/84-47992/1 (1987).
5. W.J. Lackey, D.P. Stinton, G.A. Cerny, L.L. Fehrenbacher, and A.C. Schaffhauser, ORNL/TM-8959 (1984).
6. W.J. Lackey, D.P. Stinton, G.A. Cerny, L.L. Fehrenbacher, and A.C. Schaffhauser, *Advanced Ceramic Materials*, Vol. 2, No. 1 (1987).
7. J.I. Federer, *Adv. Ceram. Mater.*, **3** [1] 56 (1988).
8. I.A. Aksay, and J.A. Pask, *J. Am. Ceram. Soc.*, **58** [11-12] 507 (1975).
9. K.N. Lee, N.S. Jacobson, and R.A. Miller, *MRS Bulletin*, Vol. 19, No. 10, pp 35-38, (1994)
10. R. Colmet, and R. Naslain, *Wear*, **80**, pp 221-231 (1982)
11. C.S. Park, J.G. Kim, and J.S. Chun, *J. Vac. Sci. Technol. A* **1** (4) pp 1820-1824 (1983)
12. J. Oroshnik, J. Kraitichman, *J. Electrochem. Soc.*, Vol. 155, No. 6, pp 649-652 (1968)
13. W. Hanni, H.E. Hintermann, D. Morel, and A. Simmen, *Surface and Coatings Technology*, Vol. 36 pp 463-470 (1988)
14. A.C. Adams, and C.D. Capio, *J. Electrochem. Soc.*, Vol. 126, No. 6, pp 1042-1046 (1979)
15. K.E. Spear, Proceedings of the 7th International Conference on CVD, T.O. Sedgwick, and H. Lydtin, eds. Electrochemical Society, Pennington, NJ, pp 1-16 (1979)
16. T.M. Besmann, Proceedings of the First International Conference on Surface Modification Technology, pp 311-325, 17th TMS Annual Meeting, T.S. Sudarshan, and D.G. Bhat, eds., Phoenix, AZ January 25-28, (1988)
17. A.I. Kingon, and R.F. Davis, pp. 317-328, in Conference on Emergent Process Methods for High-Technology Ceramics, R.F. Davis, H. Palmour III, and R.L. Porter, eds., Raleigh, NC (1982)



18. L. Vandenbulcke, J. Electrochem. Soc. Vol. 128, No. 7, pp 1584-1587 (1981)
19. T.S. Moss, J.A. Hanigofsky, and W.J. Lackey, J. Mater. Res., Vol. 7, No. 3 pp 754-764 (1992).
20. F. Teyssandier, M. Ducarrior, and C. Bernard, Journal of the Less-Common Metals, 78 pp 269-274 (1981)
21. C. Bernard, Proceedings of the 8th International Conference on CVD, Gouvieux, France, The Electrochemical Society, Pennington, NJ, pp 3-16 (1981)
22. H.E. Rebenne, and V.K. Sarin, Proceedings of the 25th Automotive Technology Development Contract Coordinators Meeting, SAE, pp 199-206 (1987)
23. T.M. Besmann, ORNL/TM-5775, Oak Ridge National Laboratory, Oak Ridge, TN(1989).
24. G. Eriksson, Acta Chem. Scand. 25, No. 7, pp 2651-2658 (1971)
25. K.F. Jensen, Microelectronics Processing: Chemical Engineering Aspects, D.W. Hess and K.F. Jensen, eds., American Chemical Society, Washington, DC, p. 199 (1989)
26. D.R. Stull, and H. Prophet, JANAF Thermochemical Tables, Third Edition, Parts I and II, American Institute of Physics, U.S. Government Printing Office, Washington, DC (1986)
27. R. Mulpuri, and V.K. Sarin, 19th Annual Cocoa Beach Conference and Exposition on Engineering Ceramics, Cocoa Beach, FL, The American Ceramic Society, Westerville, OH, January 1995
28. R. Mulpuri, and V.K. Sarin, US Patent Application Filed, Serial Number 08/368,814, January 1995.



## PLASMA DEPOSITION OF HIGH TEMPERATURE PROTECTIVE COATINGS

O.R. Monteiro<sup>1</sup>, Z. Wang<sup>1</sup>, K.-M. Yu<sup>1</sup>, P.Y. Hou<sup>1</sup>, I.G. Brown<sup>1</sup>, B.H. Rabin<sup>2</sup> and G.F. Kessinger<sup>2</sup>

<sup>1</sup>Lawrence Berkeley National Laboratory, University of California, Berkeley, CA 94708

<sup>2</sup>Idaho National Engineering Laboratory, P.O. Box 1625, Idaho Falls, ID 83415-2218

### ABSTRACT

Oxide ceramic films can be made using a vacuum arc based technique in which a metal plasma is formed in an oxygen background, with ion energy controlled by the application of a repetitive pulse bias to the substrate throughout the deposition. High ion energy early in the process produces atomic mixing at the film-substrate interface while lower but optimized ion energy later in the deposition can control the structure and morphology, and films that are adherent and dense can be formed in this way. We have investigated the formation of films of aluminum-silicon oxide on silicon carbide substrates by mixed aluminum and silicon plasmas produced from separate plasma sources. The Al to Si ratio was controlled by the plasma gun parameters and the guns were pulsed simultaneously so as to mix the plasma streams before deposition; a magnetic plasma homogenizer device was used to further blend the two plasmas. Films with Al:Si ratios from 2:1 to 8:1 were produced (Al:Si is 3:1 for mullite), and the oxygen content in the films was controlled by varying the oxygen partial pressure during deposition. We have also compared some of the characteristics of alumina films plasma deposited on iron aluminide substrates with films produced by e-beam evaporation of  $\text{Al}_2\text{O}_3$  using oxygen ion beam assisted deposition onto unheated or heated substrates. Here we outline the film synthesis techniques and describe the characterization results obtained to-date.

### INTRODUCTION

The formation of thin films by plasma deposition is a versatile technique with a wide range of different embodiments. The version that we've developed and used has the important feature that the ion energy can be controlled widely. Highly adherent, dense films of metals, alloys (including non-equilibrium alloys) and other conducting materials, and their oxides and nitrides, can be formed. In the early stages of the process the ion energy is held in the keV range so as to produce atomic mixing at the film-substrate interface, and in the latter stages of deposition the energy is reduced so as to optimize the film structure and morphology.

In this method, which we call Mepioid (*Metal plasma immersion ion implantation and deposition*), the object to be implanted is immersed in a plasma of the desired species and repetitively pulse-biased to a negative voltage<sup>1-6</sup>. A high voltage sheath rapidly forms at the substrate-plasma boundary, and plasma ions are accelerated through the sheath and into the substrate, thereby accomplishing implantation into the substrate of plasma ions at an energy determined by the bias voltage. Because of the surface retention of condensed metal plasma, the plasma immersion process in a metal plasma is quite different from in a gaseous plasma. Ions that are accelerated from the plasma into the substrate during the high voltage bias pulse suffer collisions with previously-deposited neutral metal atoms on the substrate surface and thus also produce recoil implantation. By varying the proportions of the direct and recoil implantation parts of the

cycle (ie, the duty cycle of the pulse biasing) one can tailor the shape of the profile, and the range can be tailored by the amplitude of the applied pulse voltage. The whole operation can be time-varied throughout the processing duration, starting for example with a high energy phase so as to create a deep buried layer of the implanted species and slowly changing to a low energy phase whereby a surface film is built up by plasma deposition. By controlling the plasma ion energy we acquire control over two very important features to the deposition process: the interface width can be tailored, and the film morphology and structure can be controlled. In this way one can synthesize a surface metallic film of precisely controllable thickness having a well-determined and controllable atomically mixed interface with the substrate, and the parameters of the film and the interface can be tailored over a wide range. For purely metallic films, the process is carried out at a vacuum in the  $10^{-6}$  Torr range; oxides and nitrides can be formed by doing the deposition at the appropriate background pressure of oxygen or nitrogen, typically a few tens of microns. The technique has been developed by us and others, and put to a range of laboratory applications.

In prior work we have shown that highly adherent films can be formed in this way. We have produced near-stoichiometric alumina films of thickness  $\sim 0.5 \mu$  on substrates of FeAl (containing  $\sim 0.1\%$  Zr); the films were amorphous prior to heat treatment and showed an  $\alpha$ -alumina phase after heat treating at  $1000^\circ\text{C}$  for up to 16 hours<sup>7,8</sup>. The film substrate adhesion was typically greater than  $\sim 70$  MPa prior to heating, and the adhesion was maintained after repetitive cycling in temperature between ambient and  $1000^\circ\text{C}$ .

We report here on the extension of this work in two directions. We have explored the plasma synthesis of aluminum-silicon oxide films on silicon carbide substrates by mixing together separately produced plasmas of aluminum and silicon. The Al to Si ratio was controlled by the plasma gun parameters and the plasmas blended together in a magnetic multipole plasma homogenizer device. Deposition was done onto appropriately positioned SiC substrates. Separately, we have compared the characteristics of alumina films plasma deposited on iron aluminide substrates with films produced by e-beam evaporation of  $\text{Al}_2\text{O}_3$  using oxygen ion beam assisted deposition onto unheated or heated substrates. We outline here the film synthesis techniques and describe the results obtained to-date.

## PLASMA PROCESSING

The vacuum arc is a high current discharge between two electrodes in vacuum in which metal plasma is produced in abundance<sup>9-12</sup>. We have made a number of different embodiments of vacuum arc plasma guns. For the work described here we used a small, repetitively pulsed version operated at a pulse length of 5 ms and repetition rate about 1 Hz, and arc current in the range 100 – 300 A. Along with the metal plasma that is generated, a flux of macroscopic droplets of size in the broad range 0.1 - 10 microns is also produced<sup>9-14</sup>. In general it is desirable to remove the solid particulate contamination and this can be done using a curved 'magnetic duct' which stops line-of-sight transmission of macroparticles while allowing the transmission of plasma<sup>15,16</sup>. The overall plasma deposition system thus consists of the repetitively pulsed plasma gun in conjunction with the  $90^\circ$  bent magnetic filter. Plasma exits the filter and deposits on the substrate.

Metal oxides can be formed by carrying out the deposition not in a high vacuum environment but in a somewhat higher pressure ambient of oxygen gas; we have found empirically that a pressure in the range 1 - 100 mTorr is suitable for most purposes. In the present work the oxygen background pressure was 5 to 25 mTorr. The oxygen is both entrained in the plasma stream, ionized, and deposited in the plasma state, as well as reacting at the freshly-deposited metallic surface to form aluminum oxide or silicon dioxide. In either case, for the optimal oxygen pressure a near-stoichiometric film of the metal oxide is formed.

Ion energy of the depositing plasma flux is controlled by repetitively pulse biasing the substrate. Typically the pulse duration might be  $\sim 10 \mu\text{s}$  and the duty cycle  $\sim 10 - 50\%$ . Pulsing of the bias voltage is necessary (for all but the lowest bias voltages) because a high-voltage dc bias would cause an electrical discharge between the substrate and the vessel or the plasma gun; the plasma would be grossly perturbed (because the plasma sheath would expand from the substrate to large distances). The solution is to switch off the bias before a discharge can occur (to limit the sheath expansion to modest distances), let the plasma recover, and then repeat the process; ie, to do the biasing in a repetitively pulsed mode. For the early stages of the deposition process the pulse bias is held at a relatively high voltage of 2.2 kV. The mean aluminum ion energy is then 3.75 keV, because the mean ion charge state of the aluminum plasma is 1.7 and  $E_i = QV$ ; for silicon the mean charge state is 1.4 and the mean ion energy 3.1 keV; (the charge state spectra of vacuum arc produced plasmas have been discussed in detail in refs. 17,18). At this energy ions are implanted into the substrate to a depth of up to  $\sim 100 \text{ \AA}$ . The film thus grows on the SiC substrate from a highly mixed interface. When a film thickness of just a few tens of angstroms has accumulated, the pulse bias voltage is reduced, since intermixing with the substrate is no longer a factor and the higher ion energy would sputter away the already-deposited film. Moreover, it is known from a large body of work on ion assisted deposition that a modest ion energy can be highly advantageous for controlling such characteristics as the density, morphology and structure of the film. For the bulk of the plasma deposition process the pulse amplitude is kept at 200 volts.

For synthesis of the mixed aluminum-silicon oxide films we firstly tried a plasma gun cathode that was formed of mixed Al-Si in 3:1 atomic ratio – mullite has composition  $3\text{Al}_2\text{O}_3 \cdot 2\text{SiO}_2$  for an Al:Si atomic ratio of 3:1 – but we found that the deposited film composition ratio did not reflect the cathode composition ratio closely enough. Thus we went to an alternative approach making use of an additional plasma gun/filter for forming a Si plasma that was added to the original Al:Si plasma stream. The two streams are then fed through a special 'plasma homogeneizer', which further mixes and spreads out the plasma stream. The plasma homogeneizer is a magnetic multipole plasma confinement geometry, well known in the plasma community and made here using a number of high-field-strength rare-earth permanent magnets. The utility of this kind of arrangement, in particular the novel use of the homogeneizer as a tool for blending the two vacuum arc plasmas, has been explored in prior work in our laboratory<sup>19,20</sup>. The precise Al:Si atomic mix can then be tuned via the plasma guns (pulse width or arc current). Films with Al:Si ratios varying from 1:1 to 8:1 were formed. A simplified schematic of the overall system is shown in Figure 1.

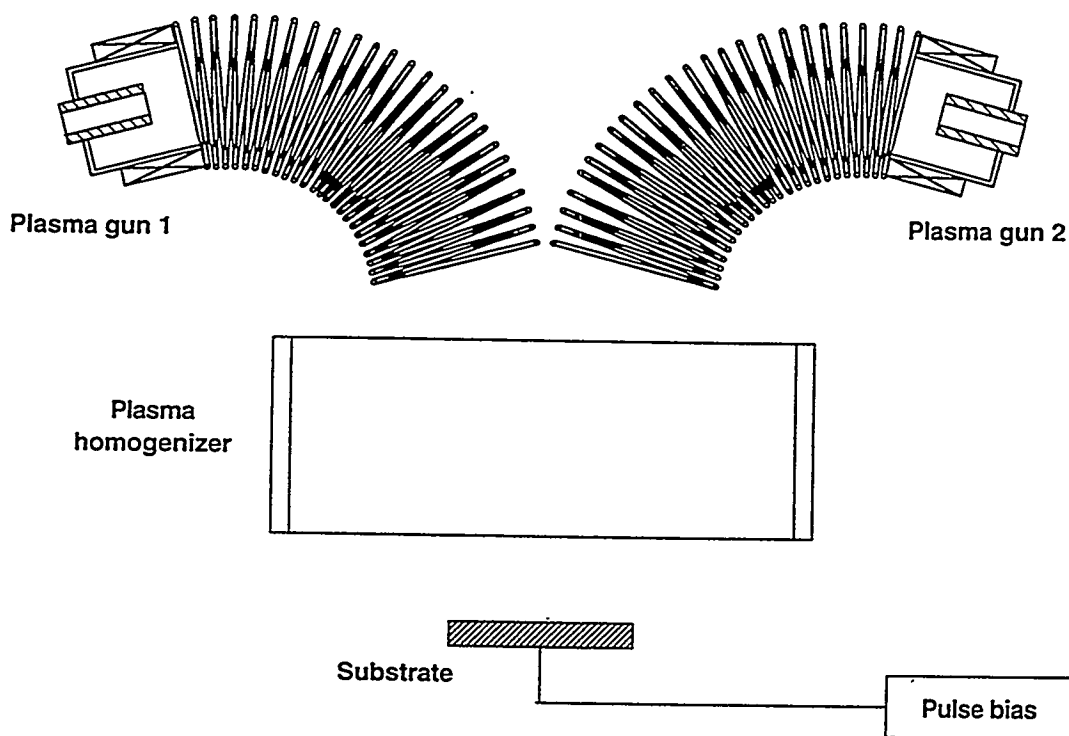


Fig. 1. Schematic of the overall dual-gun deposition system

## EXPERIMENTAL RESULTS

### Aluminum-Silicon Oxides (Mullite)

Two types of SiC substrate material were used; one was sintered at LBNL from commercially available SiC powders, and the other was a commercial SiC (Hexalloy 5) from Carborundum Industries. The material produced at LBNL contained 94.4% SiC, 3% Al, 2% C, and 0.6% B. The surface was ground and polished to a mirror finish prior to the deposition. Scanning electron microscopy of the polished surface of an uncoated piece of LBNL silicon carbide showed the presence of a second phase, appearing as dark grains that are Al-rich particles.

Control of the stoichiometry of the silicon-aluminum oxide films was achieved by varying the duration of the plasma pulses and the oxygen partial pressure during deposition. The deposition rate of each individual source was determined for all oxygen partial pressures used by measuring the thickness of the deposited films after one thousand pulses of 5 ms duration each. These individual deposition rates were then used to deposit films with desired Al:Si ratios.

An advantage of the MePiiid process is the high degree of atomic mixing achieved; thus here the duration of the pulses used was always below the time required for the formation of monolayers of silica or alumina, and both sources were triggered simultaneously so as to prevent stratification of alumina or silica. A previous attempt to synthesize mullite coatings by depositing alternate layers of silica and alumina by CVD and subsequent annealing failed due to brittleness resulting from the transformation of silica into cristoballite that takes place during the high temperature annealing required to homogenize the multilayer film<sup>21</sup>. Here we wanted to ensure that complete mixing happened during the deposition.

Table 1 shows the composition of several aluminum-silicon oxides films deposited on SiC under various experimental conditions. The content of each element in the films was determined by Rutherford Backscattering Spectroscopy (RBS) and normalized to the Si content. The accuracy of these measurements is  $\pm 15\%$ . Elemental composition of mullite is also included in the table for comparison.

Table 1. Composition of as-deposited films.

Deposition	Al-Si pulse (ms)	Si pulse (ms)	Pressure (mTorr)	Al content	Si content	O content	Thickness (nm)
#1	5	5	25	4.4	1	10.4	240
#2	5	2.5	25	6.7	1	16	230
#3	5	10	25	1.2	1	5.3	240
#4	5	0	25	8	1	19.5	220
#5	5	0	5	7.4	1	13	240
#6	5	5	25	4.2	1	10.4	1250
Mullite				3	1	6.5	

X-ray diffraction indicates that the deposited films were amorphous. No evidence of crystalline structure or phase separation was observed. A feature in the films produced was the high oxygen content when deposition was carried out at 25 mTorr. An analysis of the compositions shown in Table 1 indicates that films produced at this pressure consist of mixtures of  $\text{Al}_2\text{O}_{3+x}$  and  $\text{SiO}_{2+y}$  with a good match being achieved for  $x = 2$  and  $y = 0$ .  $\text{Al}_2\text{O}_5$  is not a stable oxide for our deposition conditions, and therefore this composition must be a consequence of oxygen ion bombardment. Such high oxygen content has been found previously in pure alumina films produced by MePiiid at 26 mT<sup>7</sup>. At lower pressures, oxygen implantation appears to decrease in importance and the films are basically mixtures of  $\text{Al}_2\text{O}_3$  and  $\text{SiO}_2$ .

Annealing of the films at 1100°C in air for 2 hours resulted primarily in the formation of crystalline mullite. The alumina-silica binary phase diagram indicates that the only stable phases in the silica-alumina system at the pressures used in this investigation are silica, alumina and mullite. To achieve the mullite stoichiometry, excess oxygen present in the as-deposited films had to be lost to the environment or react with the SiC substrate to form silicon oxide and/or carbon dioxide. X-ray diffraction indicates mullite as

the main crystalline phase after annealing (Fig. 2). The low intensity of the diffraction peaks is mostly due to the small film thickness. Another silicon-aluminum oxide known as sillimanite ( $\text{Al}_6\text{Si}_3\text{O}_{15}$ ) can also be fitted to the peaks in the diffractogram but was discarded because the ratio of intensities of the diffraction peaks was closer to that expected from mullite. Little difference was observed in the diffraction patterns of the samples #1 through #5, indicating that after annealing at  $1100^\circ\text{C}$ , in all cases the main crystalline phase formed was mullite. In the films with very low Al:Si ratio we were expecting that silicon dioxide would be present as well, and in the films with very high Al:Si ratio, peaks from crystalline alumina were expected. However, neither of these phases, silica or alumina, could be identified from the diffraction patterns of samples #1 through #5. Further sample preparation and characterization is in progress.

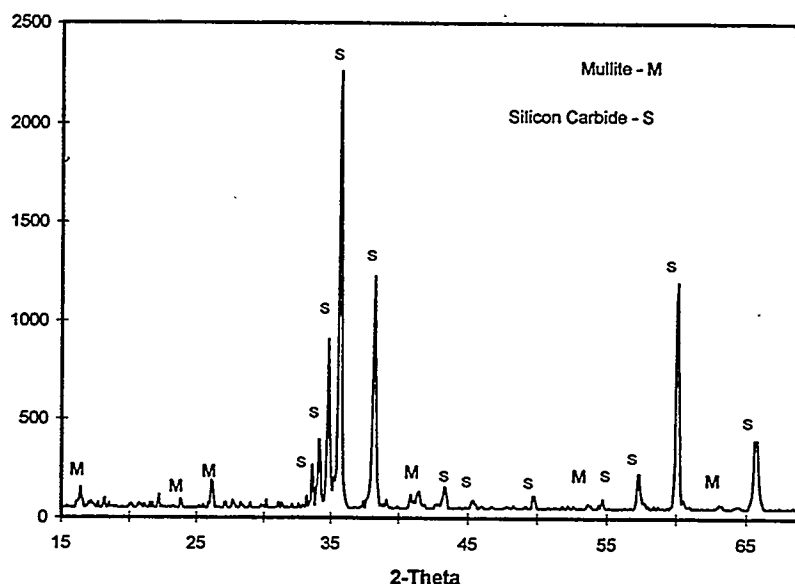


Fig. 2. X-ray diffraction pattern of coated SiC (#1) annealed at  $1100^\circ\text{C}$  for 2h in air.

Table 2. Adhesion of as-deposited and annealed films:

Deposition	Adhesion as-deposited (MPa)	Adhesion annealed (MPa)	Al content (pre-anneal)	Si content (pre-anneal)	O content (pre-anneal)	Thickness (nm)
#1	9	70	4.4	1	10.4	240
#2	38	57	6.7	1	16	230
#3	31	63	1.2	1	5.3	240
#4	31	57	8	1	19.5	220
#5	9	65	7.4	1	13	240

Adhesion test results for the as-deposited and the annealed films are shown in Table 2. The instrumental limit of our pull-tester before epoxy failure occurs is  $\sim 70$  MPa, and all of the post-annealing samples show an adhesion strength that is within experimental uncertainty of this instrumental limit.



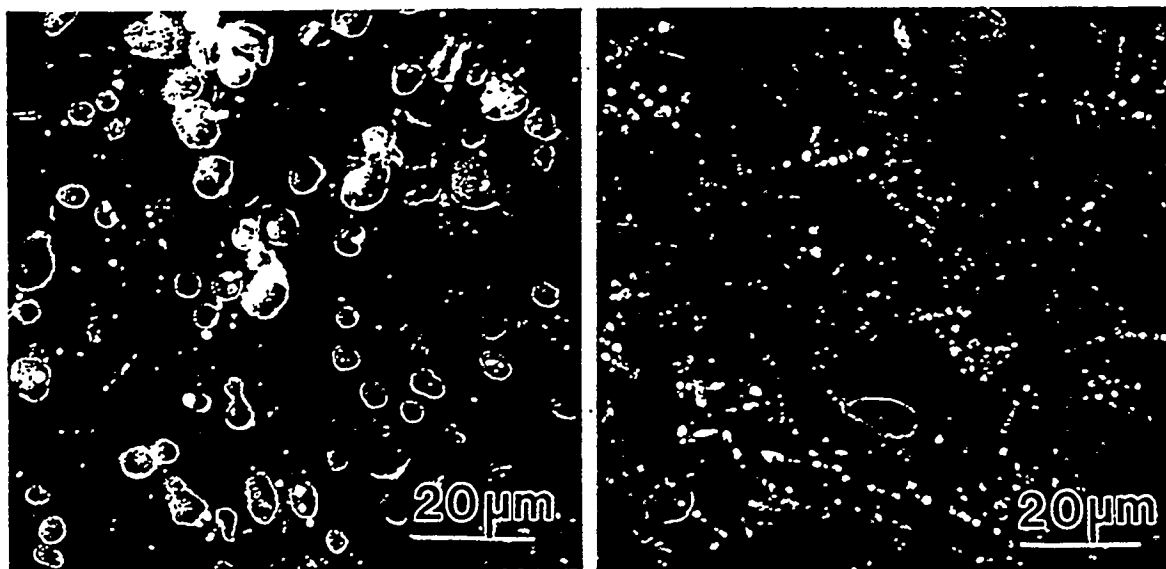


Fig. 3 SEM of a SiC sample with an aluminum-silicon oxide coating after being tested for adhesion. (a) area which had the film removed; (b) area from where the film was still present.

When the aluminum content of the coating was too high, e.g. samples #2, #4 and #5, both the as-deposited and the annealed films had a high concentration of microstructural features that looked like micro-bubbles. The mechanism of formation of these bubbles is not clear to us yet, but their concentration seems to be directly related to the deviation of the Al content from the ideal mullite stoichiometric ratio (i.e. the higher the Al content, the higher the density of voids). These bubbles are clearly seen in the micrographs shown in Fig. 3. Figs 3(a) and 3(b) are SEM images from sample #4 after annealing and after the adhesion test; Fig 3(a) is from an area from which the film has been removed by the adhesion pull-test measurement, and Fig 3(b) is from an area which still has the film intact. The delamination left the voids exposed, suggesting that these voids were either at the SiC/oxide interface or in the SiC but near to the interface. Upon annealing, very few of these bubbles appear to have broken through the coating, but in the regions where the film delaminates due to the pull-test, these voids have been exposed. Subsurface bubbles (voids) have been observed to form in the silicon carbide used here when subjected to high temperature oxidation.

It is clear from the results presented here that annealing of the deposited aluminum-silicon oxides helps greatly to improve the adhesion of the film. Stoichiometry seems to play a role in the adhesion of the as-deposited (pre-annealing) film. An extensive analysis of microstructure of the coatings is under way, and the role of the Al-Si stoichiometry and of oxygen content on the as-deposited adhesion strength should become clear.

### Aluminum Oxides

In this section we describe the initial results of the characterization of the properties of aluminum oxide films deposited on iron aluminides (Zr-containing) by two different ion beam assisted techniques.

The first technique, Mepioid, is as described above except that instead of two plasma sources only an aluminum source was used, in oxygen. All depositions were done at room temperature. The as-deposited alumina films were amorphous, and with an oxygen content that depended on the oxygen partial pressure. At a pressure of 12 mTorr the film composition was  $\text{Al}_2\text{O}_{3.3}$ , whereas at 25 mTorr the composition was  $\text{Al}_2\text{O}_5$ . Such a high oxidation state of aluminum has been observed previously in Mepioid produced films<sup>7</sup>. The  $\text{Al}_2\text{O}_5$  produced here is believed to be a direct result of the simultaneous implantation that our plasma method provides. Annealing of the amorphous  $\text{Al}_2\text{O}_5$  and  $\text{Al}_2\text{O}_{3.3}$  films at 1100°C in air for two hours led to their crystallization into  $\alpha\text{-Al}_2\text{O}_3$ . Adhesion of these films has been reported previously to exceed 70 MPa in the as-deposited amorphous condition as well as after annealing<sup>7</sup>.

The second set of aluminum oxide films was prepared using ion-beam assisted (IBAD) deposition according to the following procedure. The substrate was initially ion-milled with 1 kV  $\text{Ar}^+$  ions at an ion current of 0.15 mA. Then  $\text{Al}_2\text{O}_3$  was deposited at a rate of 0.5 nm/s to a total thickness of 500 nm. During the initial 10 - 15 nm, a 1 kV oxygen ion beam (0.25 mA) simultaneously bombard the substrate, and for the remainder of the deposition the energy of the incident oxygen ions was reduced to 0.4 kV. Depositions were done at two different temperatures, 825 K and 605 K. Cooling of the substrate to room temperature after deposition was done in vacuum.

The films have been characterized by X-ray diffraction, and the results are presented in Figure 4. Post-deposition heat treatments are presently under way. The e-beam + IBAD films produced at low temperature were predominantly amorphous, while the film deposited at 825K contain microcrystalline aluminum oxides, as evidenced in the X-ray diffractogram. The specific alumina phase present could not be uniquely determined and a mixture of several phases is likely. In addition some amorphous materials may also be present since the deposition temperature was still much lower than the recrystallization temperature, and the diffraction peaks are somewhat diffuse. The film deposited at 825K had a grainy appearance whereas the films produced at 600K looked more homogeneous, similar to the ones deposited by Mepioid.

The ion energies used in the IBAD and the Mepioid process are similar. In the early stages of the IBAD process, oxygen ions are accelerated through 1kV, and for the remainder of the deposition the accelerating voltage is reduced to 0.4 kV. In Mepioid, aluminum ions are responsible for the plasma formation and subsequent ionization of the oxygen. The accelerating voltages used for Mepioid are 2kV during the first tens of nanometer and 0.2kV for the remainder of the deposition. Characterization for their adhesion and corrosion resistance properties and comparison of films prepared in the two different but related ways described above is continuing, and we will report on this work as the results become available.

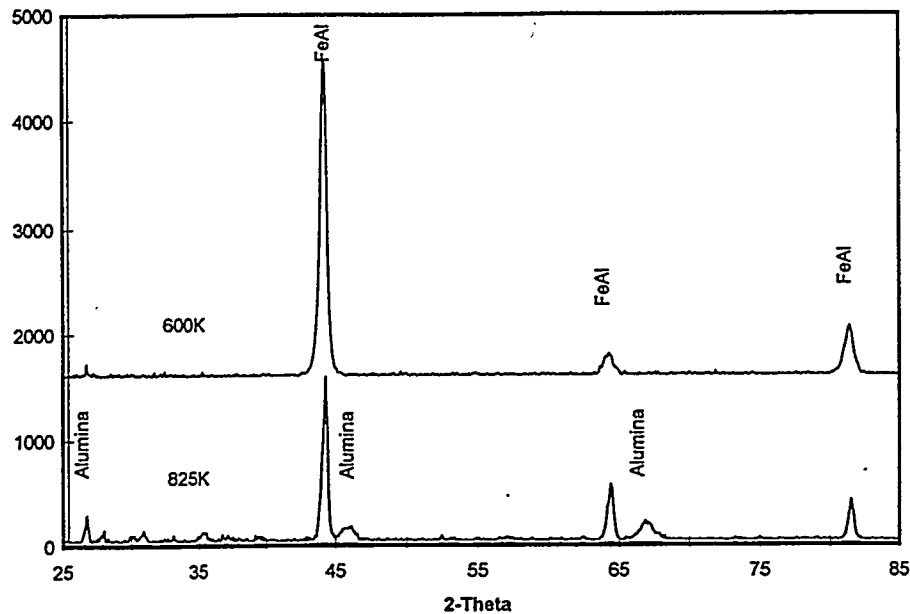


Fig. 4 Diffraction pattern of the as-deposited alumina films produced by e-beam evaporation + ion-beam assisted deposition. The deposition temperatures are indicated.

### CONCLUSION

A novel technique for the plasma synthesis of high temperature protective coatings for metallic and ceramic structural materials (*Metal plasma immersion ion implantation and deposition, Mepioid*) has been applied to deposit aluminum-silicon oxides on silicon carbide, and aluminum oxide on iron aluminides. Post-annealing adhesion of the aluminum-silicon oxide films was good. When the Al:Si ratio increases, adhesion between the oxide and the SiC is weakened because of the presence of voids at or immediately below the interface. Our plasma method allows convenient and simple control of the "quasi-mullite" film stoichiometry.

Aluminum oxides on iron aluminides were also produced by Mepioid and by e-beam evaporation + IBAD. Depositions below 300°C resulted in films which are amorphous by both techniques. Deposition at higher temperatures with e-beam + IBAD led to the formation of a mixture of micro-crystalline aluminum oxides. Annealing at 1000°C for 16h in air of the Mepioid film resulted in a coating that is predominantly  $\alpha$ -Al<sub>2</sub>O<sub>3</sub>. Further work is underway to continue the comparison between the films produced by these two techniques.

## ACKNOWLEDGMENTS

We are indebted to Bob MacGill and Mike Dickinson for their support of the LBNL experimental equipment. This work was supported by the U.S. DOE, Office of Advanced Research, Fossil Energy, under Contract Number DE-AC03-76SF00098.

## REFERENCES

1. I.G. Brown, X. Godechot and K.M. Yu, Appl. Phys. Lett. 58, 1392 (1991).
2. I.G. Brown, A. Anders, S. Anders, M.R. Dickinson, I.C. Ivanov, M.A. MacGill, X. Yao and K.M. Yu, Nucl. Instrum. Meth. Phys. Res. B80/81, 1281 (1993).
3. Ian Brown, in *Plasma Synthesis and Processing of Materials*, edited by K. Upadhyaya (pub. TMS, Warrendale, PA, 1993).
4. A. Anders, S. Anders, I.G. Brown and I.C. Ivanov, Mat. Res. Soc. Symp. Proc. 316, 833 (1994).
5. A. Anders, S. Anders, I.G. Brown, M.R. Dickinson and R.A. MacGill, J. Vac. Sci. Tech. B12, 815 (1994).
6. See the proceedings of the First International Workshop on Plasma-Based Ion Implantation, J. Vac. Sci. Tech. B12, 815-998 (1994).
7. Ian Brown and Zhi Wang, "Plasma Synthesis of Alumina Films on Metal and Ceramic Substrates", 9th Annual Conference on Fossil Energy Materials, Oak Ridge, TN, May 16-18, 1995, Proceedings of conference (U.S. Dept. of Energy, Conf-9505204, ORNL/FMP-95/1), p. 239.
8. P.Y. Hou, K.B. Alexander, Z. Wang and I.G. Brown, "The Effect of Plasma Synthesized Alumina Coatings on the Oxidation Behavior of Iron Aluminides", TMS Annual Meeting, Symposium on High Temperature Coatings, Anaheim, CA, Feb 4 - 8, 1996.
9. J.M. Lafferty (ed.), *Vacuum Arcs - Theory and Application*, Wiley, New York, 1980.
10. R.L. Boxman, P. Martin and D. Sanders (eds), *Vacuum Arc Science and Technology*, Noyes, New York, 1995.
11. For a most impressive and comprehensive bibliography of the vacuum arc literature see H.C. Miller, *A Bibliography and Author Index for Electrical Discharges in Vacuum (1897 - 1986)*, pub. by the General Electric Co., document No. GEPP-TIS-366e (UC-13), March 1988; also published in part in IEEE Trans. Elec. Insul. 25(5), 765 (1990) and 26(5), 949 (1991).
12. See the Special Issues on Vacuum Discharge Plasmas in IEEE Trans. Plasma Sci. These issues contain selected papers from the biennial International Symposium on Discharges and Electrical Insulation in Vacuum, (usually in the October issues in odd-numbered years).
13. D.T. Tuma, C.L. Chen and D.K. Davies, J. Appl. Phys. 49, 3821 (1978).
14. J.E. Daalder, Physica 104C, 91 (1981).
15. I.I. Aksenov, A.N. Belokhovostikov, V.G. Padalka, N.S. Repalov and V.M. Khoroshikh, Plasma Physics and Controlled Fusion 28, 761 (1986).
16. A. Anders, S. Anders and I.G. Brown, Plasma Sources Sci. & Technol. 4, 1 (1995).
17. I.G. Brown and X. Godechot, IEEE Trans. Plasma Sci. PS-19, 713 (1991).
18. I.G. Brown, Rev. Sci. Instrum. 10, 3061 (1994).
19. S. Anders, S. Raoux, K. Krishnan, R.A. MacGill and I.G. Brown, "Application of a Magnetic Multicusp to a Cathodic Arc Deposition System", J. Appl. Phys. (1996), to be published.
20. S. Anders, R.A. MacGill, S. Raoux and I.G. Brown, "Modification of Cathodic Arc Deposition Profiles by Magnetic Multicusp", to be presented at the XVIIth Int. Symp. on Discharges and Electrical Insulation in Vacuum, Berkeley, CA, July 21-26, 1996.
21. D. Doppalapudi, R. Mulpuri, S.N. Basu and V.K. Sarin, "Phase Transformations in Multilayered CVD Mullite Coatings", Mat. Res. Soc. Symp. Proc. 363, 95 (1995).

CERAMIC MEMBRANES FOR HIGH TEMPERATURE  
HYDROGEN SEPARATION

D. E. Fain and G. E. Roettger

Oak Ridge K-25 Site\*  
P. O. Box 2003  
Oak Ridge, TN 37831-7271

ABSTRACT

Ceramic gas separation membranes can provide very high separation factors if the pore size is sufficiently small to separate gas molecules by molecular sieving and if oversized pores are adequately limited. Ceramic membranes typically have some pores that are substantially larger than the mean pore size and that should be regarded as defects. To assess the effects of such defects on the performance of ceramic membranes, a simple mathematical model has been developed to describe flow through a gas separation membrane that has a primary mode of flow through very small pores but that has a secondary mode of flow through undesirably large pores. This model permits separation factors to be calculated for a specified gas pair as a function of the molecular weights and molecular diameters of the gases, the membrane pore diameter, and the diameter and number of defects. This model will be described, and key results from the model will be presented.

The separation factors of our membranes continue to be determined using a permeance test system that measures flows of pure gases through a membrane at temperatures up to 275°C. A primary goal of this project for FY 1996 is to develop a mixed gas separation system for measuring the separation efficiency of membranes at higher temperatures. Performance criteria have been established for the planned mixed gas separation system and design of the system has been completed. The test system is designed to measure the separation efficiency of membranes at temperatures up to 600°C and pressures up to 100 psi by separating the constituents of a gas mixture containing hydrogen. The system will accommodate our typical experimental membrane that is tubular and has a diameter of about 9 mm and a length of about 23 cm. The design of the new test system and its expected performance will be discussed.

INTRODUCTION

The goal of this project is to develop methods for fabricating ceramic membranes that will efficiently separate hydrogen from gasified coal at temperatures of 1,000°F or higher. Previous work has demonstrated that high separation factors can be achieved with ceramic membranes if the mean pore size is sufficiently small to separate gas molecules by molecular sieving.<sup>1</sup> Since ceramic membranes typically

---

\*The Oak Ridge K-25 Site is managed by Lockheed Martin Energy Systems, Inc. for the U.S. Department of Energy under contract No. DE-AC05-84OR21400.

have some pores that are substantially larger than the mean pore size, recent modeling work has sought to determine the effects of oversized pores on separation factors. The separation factors of our membranes have been measured to date using a permeance test system that measures the flows of pure gases through a membrane at temperatures up to 275°C. An important current objective of the project is to develop a mixed gas separation system that will measure the separative performance of membranes with gas mixtures at temperatures up to 600°C.

## DISCUSSION OF CURRENT ACTIVITIES

### Model for Free Molecule Flow Through an Inorganic Gas Separation Membrane Containing Leaks

Inorganic membranes typically have some pores that are substantially larger than the mean pore size and that should be regarded as leaks or defects. A means to determine the effects of such leaks on the performance of inorganic membranes has been needed. To meet this need, a simple mathematical model has been developed to describe free molecule gas flow through an inorganic membrane containing some undesirable large pores, which will be referred to as leaks. The model was developed to study the effects of leaks on the performance of inorganic gas separation membranes that have small pores and that would be operated at high temperatures. For this case, the equation for free molecule diffusion of a gas through a circular capillary will be used as a starting point. This equation is usually expressed as

$$F = \frac{1}{12} \bar{v} \pi d^3 \frac{T_o \Delta P}{TP_o \ell}, \quad (1)$$

where

- F = flow rate in standard cc per second,
- $\bar{v}$  = mean molecular velocity of the gas molecules,
- d = mean capillary diameter
- T<sub>o</sub> = standard temperature,
- ΔP = pressure difference across the capillary,
- T = temperature,

$P_o$  = standard pressure, and  
 $\ell$  = capillary length.

Equation (1) approximates the gas transport through the capillary so long as the pore diameter is large compared to the diameter of the gas molecules. If the effective pore diameter approaches the size of the gas molecules, as is the case with a molecular sieve gas separation membrane, then the size of the gas molecule should be taken into account. If we consider a circular capillary with rigid, smooth walls as a model, then the distance of closest approach of the center of a gas molecule to a wall is the radius of the molecule. Therefore, the effective diameter of the capillary for transport is the difference between the capillary diameter and the molecule diameter. As discussed elsewhere,<sup>2</sup> Eq. (1) then becomes

$$F = \frac{1}{12} \bar{v} \pi (d - \sigma)^3 \frac{T_o \Delta P}{TP_o \ell}, \quad (2)$$

where  $\sigma$  is the diameter of the gas molecule.

Equation (2) may be used to describe flow through a gas separation membrane that has a primary mode of flow through very small pores but that has a secondary mode of flow through undesirably large pores, or leaks. Consider a representative section of the membrane containing one leak of diameter  $d_L$  and a related number,  $n$ , of small pores having mean diameter of  $d_P$ . The total gas flow through this representative section of the membrane can be expressed using Eq. (2) as follows

$$F_{total} = \frac{n}{12} \bar{v} \pi (d_P - \sigma)^3 \frac{T_o \Delta P}{TP_o \ell} + \frac{1}{12} \bar{v} \pi (d_L - \sigma)^3 \frac{T_o \Delta P}{TP_o \ell}, \quad (3)$$

where  $n$  is the ratio of the number of small pores per one leak.

Equation (3) may be simplified and expressed as

$$F_{total} = \frac{1}{12} \pi \frac{T_o \Delta P}{TP_o \ell} \bar{v} [n(d_P - \sigma)^3 + (d_L - \sigma)^3]. \quad (4)$$

The ideal separation factor,  $\alpha$ , of a membrane for a binary gas mixture is the ratio of the specific flows (the flow rate per unit pressure difference) of the individual gases. Thus, using Eq. (4), the ideal separation factor can be expressed as

$$\alpha = \frac{\bar{v}_1}{\bar{v}_2} \left[ \frac{n(d_P - \sigma_1)^3 + (d_L - \sigma_1)^3}{n(d_P - \sigma_2)^3 + (d_L - \sigma_2)^3} \right] \quad (5)$$

where

$\bar{v}_1, \bar{v}_2$  = mean molecular velocities of gas 1 and gas 2, and

$\sigma_1, \sigma_2$  = molecular diameters of gas 1 and gas 2.\*

Since the ratio of the molecular velocities is equivalent to the inverse ratio of the square root of molecular weights, Eq. (5) may be expressed in the more convenient form

$$\alpha = \left( \frac{M_2}{M_1} \right)^{0.5} \left[ \frac{n(d_p - \sigma_1)^3 + (d_L - \sigma_1)^3}{n(d_p - \sigma_2)^3 + (d_L - \sigma_2)^3} \right], \quad (6)$$

where  $M_1, M_2$  are the molecular weights of gas 1 and gas 2.

Equation (6) is appropriate assuming  $d_p \geq \sigma_1$  and  $\sigma_2$ . In other words, the pore diameter is as large or larger than the molecular diameter of both gas 1 and gas 2, such that both gases will flow through the pores.

If  $d_p < \sigma_2$ , then there is no flow of the larger gas molecules (gas 2) through the pores. Gas 2 would flow only through the leaks. Thus, for  $\sigma_1 < d_p < \sigma_2$

$$\alpha = \left( \frac{M_2}{M_1} \right)^{0.5} \left[ \frac{n(d_p - \sigma_1)^3 + (d_L - \sigma_1)^3}{(d_L - \sigma_2)^3} \right]. \quad (7)$$

If  $d_p < \sigma_1$ , then there is no flow of either gas through the pores. The gases can flow only through the leaks. Thus, for  $d_p < \sigma_1$  and  $\sigma_2$

$$\alpha = \left( \frac{M_2}{M_1} \right)^{0.5} \left[ \frac{(d_L - \sigma_1)^3}{(d_L - \sigma_2)^3} \right]. \quad (8)$$

The above equations permit ideal separation factors to be calculated for a specified gas pair as a function of the molecular weights and molecular diameters of the gases, the membrane mean pore diameter, and the diameter and frequency of leaks. The frequency of leaks is expressed by  $n$ , the number of pores per each leak. Obviously, a higher value of  $n$  represents a lower frequency of leaks.

Finally, for the special case of a membrane that has no leaks, an equation for the ideal separation factor can be derived readily from Eq. (2) as discussed elsewhere.<sup>2</sup> For a membrane having no leaks,

---

\*In this model,  $\sigma_1$  denotes the smaller gas molecule and  $\sigma_2$  the larger gas molecule.



$$\alpha = \left( \frac{M_2}{M_1} \right)^{0.5} \left[ \frac{(d_p - \sigma_1)^3}{(d_p - \sigma_2)^3} \right]. \quad (9)$$

In studying a gas separation membrane containing leaks, it is also useful to determine how much of the gas flow through the membrane occurs through the small pores (as contrasted to the leaks). For a particular gas flowing through a membrane having  $n$  small pores per each leak, the ratio of (flow through pores)/(total flow through pores plus leaks) can be readily determined using Eq. (2). Expressed as a percentage rather than a fraction, this percentage for gas 1 is given by

$$\% \text{ of flow through pores} = \frac{100 \, n (d_p - \sigma_1)^3}{n (d_p - \sigma_1)^3 + (d_L - \sigma_1)^3}. \quad (10)$$

This equation applies when  $d_p \geq \sigma_1$ . When  $d_p < \sigma_1$ , there is no flow through the small pores and the above ratio is zero. The ratio shown in Eq. (10) is illustrated for gas 1 having molecular diameter of  $\sigma_1$ . Clearly, the value of the ratio would be different for gas 2 having a larger molecular diameter,  $\sigma_2$ .

### Results from Model Studies

The mathematical model described above permits ideal separation factors to be calculated for inorganic gas separation membranes containing leaks. The model has been used to study the effects of leak size and frequency on the separation factors of membranes having various mean pore sizes. Several examples of model results are presented below for the helium/carbon tetrafluoride ( $\text{He}/\text{CF}_4$ ) gas pair, which we commonly use to test membranes.

Separation factors calculated from the model are presented in Fig. 1 as a function of the membrane mean pore size for membranes containing leaks of 2,000 Å (0.2 µm) arbitrary diameter. Plots are shown for a leak frequency ( $n$ ) of  $10^9$  pores per leak and  $10^7$  pores per leak and contrasted with results for a membrane containing no leaks. For the membrane containing no leaks, the separation factor increases continually with declining pore size, and the separation factor becomes infinite when the pore size becomes smaller than the larger gas molecule (4.7 Å for  $\text{CF}_4$ ) but larger than the smaller gas molecule. For the membrane containing  $10^9$  pores per each 2,000 Å leak, the separation factor is severely limited to

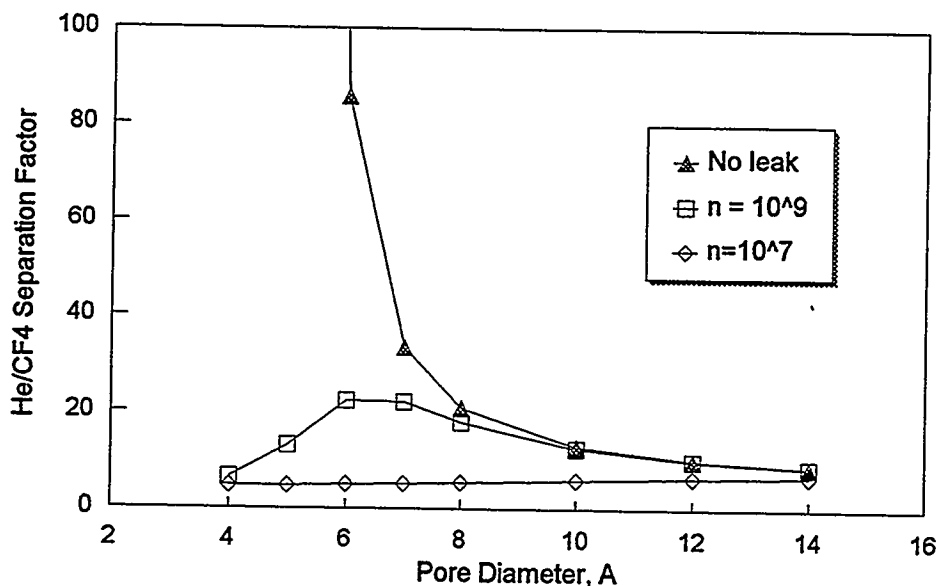


Fig. 1. Model calculated separation factors for He/CF<sub>4</sub> as a function of membrane mean pore size showing the effects of leak frequency ( $n$ ) for 2,000 Angstrom diameter leaks.

a maximum value of about 22 at a pore size of about 6 Å. Further reduction of pore size below 6 Å actually results in lower separation factors because an increasingly larger fraction of the flow occurs through the leaks as the “good” pores are reduced in size. Calculations using Eq. (10) show 16.6% of the flow through leaks for the 6 Å membrane, and 73.4% of the flow through the leaks for the 4 Å membrane. For the membrane containing only  $10^7$  pores per each 2,000 Å leak, the separation factor continually declines with decreasing pore size. In this case, 34.8% of the flow is through leaks for the 14 Å membrane, increasing to 99.64% of the flow through leaks for the 4 Å membrane.

Separation factors calculated from the model are presented in Fig. 2 as a function of the membrane mean pore size for membranes containing an arbitrary leak frequency of  $10^8$  pores per leak. Plots are shown for leak diameters of 2,500 Å, 1,000 Å, and 500 Å, and are contrasted with results for a membrane containing no leaks. The results show that the separation factor achievable by reducing pore size can be severely limited if the size of leaks is large.

Model results presented in Fig. 3 show the effect of leak diameter on separation factor for a membrane having a pore diameter of 6 Å and a leak frequency of  $10^8$  pores per leak. The results show that the separation factor can be dramatically increased by reducing the leak diameter from 2,500 Å to

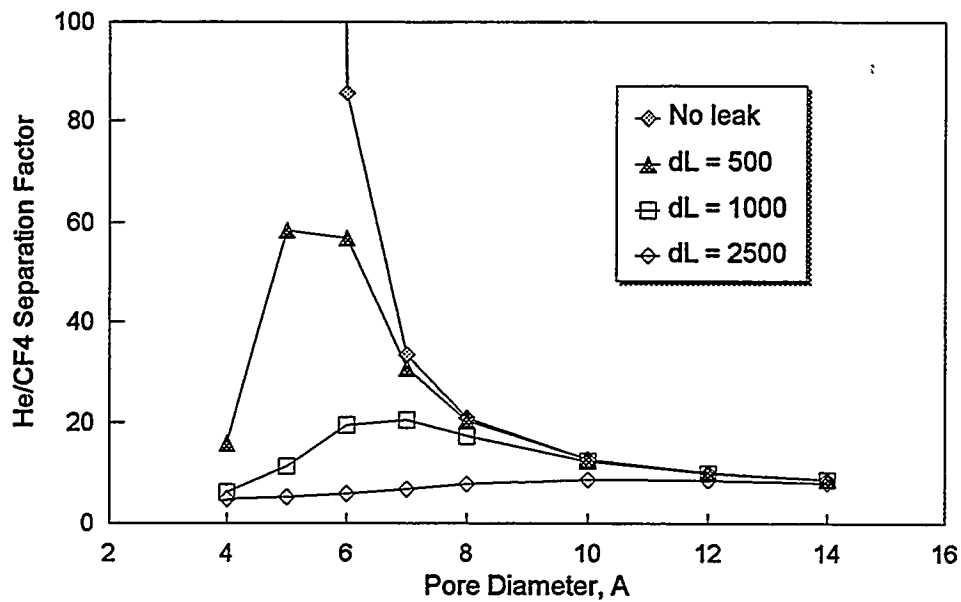


Fig. 2. Model calculated separation factors for He/CF<sub>4</sub> as a function of membrane mean pore size showing the effects of leak diameter (dL) for a leak frequency of 10<sup>8</sup> pores per leak.

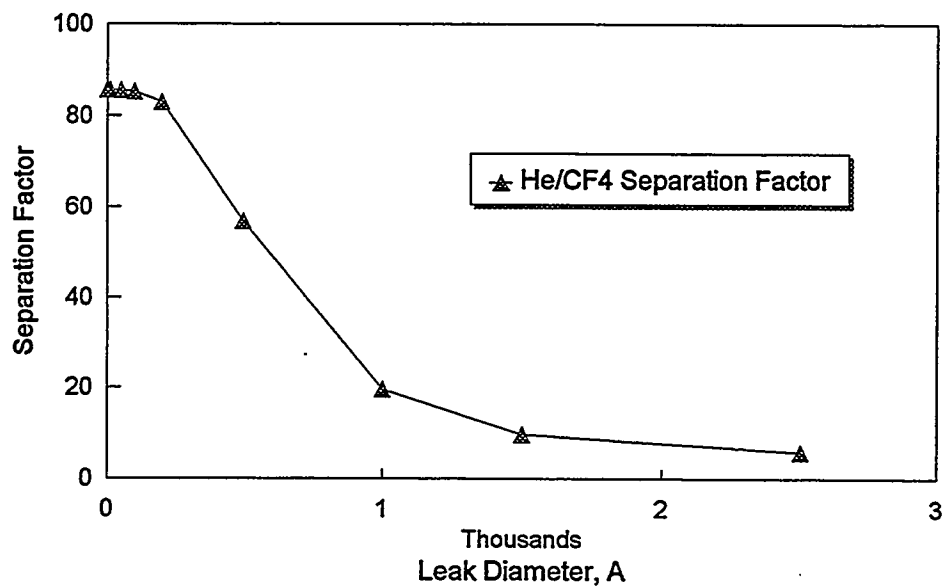


Fig. 3. Model calculated separation factors for He/CF<sub>4</sub> as a function of leak diameter for a membrane having a leak frequency of 10<sup>8</sup> pores per leak and a pore diameter of 6 Å.

about 200 Å. Further reducing the size of the leaks below 200 Å results in only a slight additional increase in separation factor. Various studies performed with the model generally indicate that reducing the size of leaks (in contrast to completely eliminating them) can be a very effective means of increasing separation factors.

### Mixed Gas Separation System

The separative performance of our membranes has been determined to date using a permeance test system that measures flows of pure gases through a membrane at temperatures up to 275°C. Using these data, the separation factor of the membrane for a particular gas pair is determined from the ratio of the pure gas specific flows.

An important goal for FY 1996 is to develop a mixed gas separation system for measuring the separation efficiency of membranes at higher temperatures. Performance criteria have been established for the planned mixed gas separation system. The test system will measure the separation efficiency of membranes at temperatures up to 600°C and pressures up to 100 psi by separating the constituents of a gas mixture containing hydrogen. The system will accommodate our typical experimental membrane that is tubular and has a diameter of about 9 mm and a length of about 23 cm. Design of this test system has been completed, and specifications have been developed for system components. A diagram of the system is shown in Fig. 4. The test system has been designed to operate with binary gas mixtures such as hydrogen/methane or hydrogen/carbon dioxide. The mixed gas will be fed into the tubular membrane at pressures up to 100 psi, and the membrane will separate the gas mixture into a permeate stream and a raffinate stream. The membrane will be sealed in a holder mounted in a split tube furnace to permit membrane separations to be evaluated at temperatures up to 600°C. The compositions of the three gas streams will be measured with a gas chromatograph equipped with a thermal conductivity detector. Other variables to be measured include the flow rate of the feed gas stream and the temperatures and pressures of all three of the gas streams. These data taken over a range of flows and pressures will permit the separation efficiency to be determined as a function of the operating conditions and from these data the separation factor can be evaluated.

One of the significant technical challenges involved in designing the test system was to establish a method for sealing a tubular alumina membrane into a metal holder to provide an assembly that would tolerate heating to 600°C. A method has been developed that involves joining a tubular section of a low-thermal-expansion metal alloy to the ends of the porous alumina tube using a glass glazing technique as

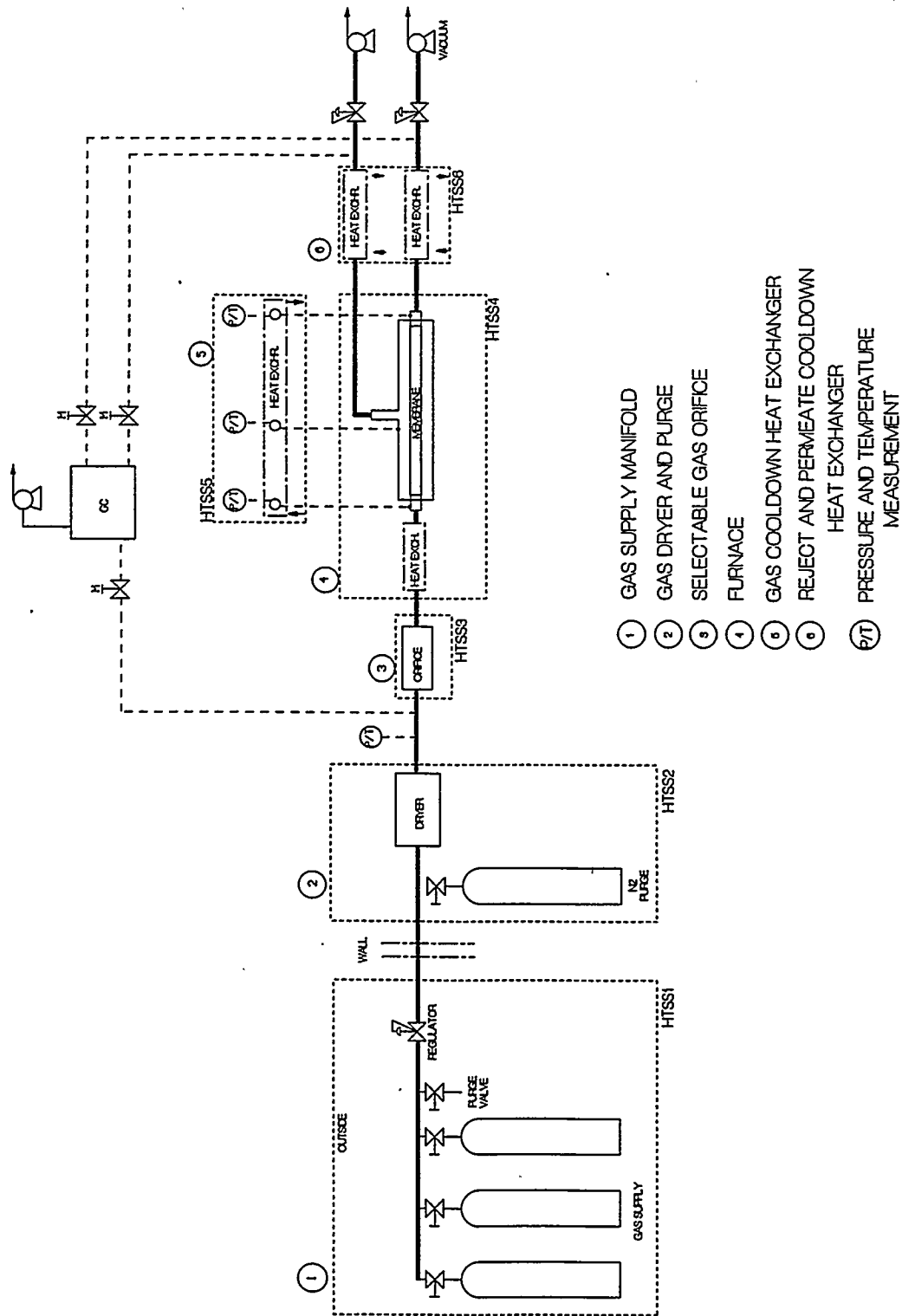


Fig. 4. Diagram of the mixed gas separation system being developed to measure the separation efficiency of membranes at temperatures up to 600°C.

shown in Fig. 5. Several test assemblies have been prepared with the alloy tubing glazed to the end of the ceramic membrane. These glazed assemblies have been thermally cycled to 600°C and back to room temperature as many as six times. The test assemblies have remained leak free following such thermal cycling, indicating that this sealing method should be suitable for use in the test system.

#### REFERENCES

1. D. E. Fain and G. E. Roettger, "High Temperature Inorganic Membranes for Separating Hydrogen," in *Proceedings of the Ninth Annual Conference on Fossil Energy Materials*, Oak Ridge, Tennessee, May 16-18, 1995, pp. 185-193.
2. D. E. Fain and G. E. Roettger, "Coal Gas Cleaning and Purification with Inorganic Membranes," *Transactions of the ASME*, 115 (3), pp. 628-633 (July 1993).

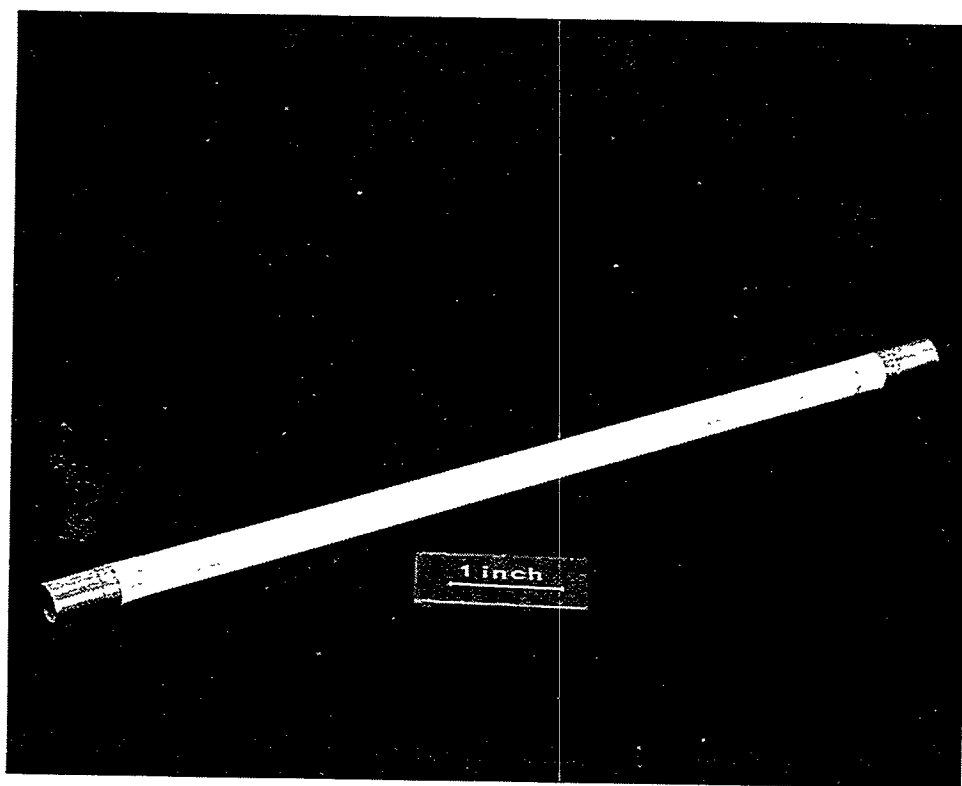


Fig. 5. Metal end pieces glazed to ends of a porous alumina tube.

# MIXED OXYGEN ION/ELECTRON-CONDUCTING CERAMICS FOR OXYGEN SEPARATION<sup>1</sup>

J. W. Stevenson, T. R. Armstrong, B. L. Armstrong, J. L. Bates,  
G. Hsieh, L. R. Pederson, and W. J. Weber

Pacific Northwest National Laboratory  
P.O. Box 999  
Richland, WA 99352

## ABSTRACT

Mixed oxygen ion and electron-conducting ceramics are unique materials that can passively separate high purity oxygen from air. Oxygen ions move through a fully dense ceramic in response to an oxygen concentration gradient, charge-compensated by an electron flux in the opposite direction. Compositions in the system  $\text{La}_{1-x}\text{M}_x\text{Co}_{1-y-z}\text{Fe}_y\text{N}_z\text{O}_{3-\delta}$ , perovskites where  $\text{M}=\text{Sr}, \text{Ca}, \text{ and Ba}$ , and  $\text{N}=\text{Mn}, \text{Ni}, \text{Cu}, \text{Ti}, \text{ and Al}$ , have been prepared and their electrical, oxygen permeation, oxygen vacancy equilibria, and catalytic properties evaluated. Tubular forms, disks, and asymmetric membrane structures, a thin dense layer on a porous support of the same composition, have been fabricated for testing purposes. In an oxygen partial gradient, the passive oxygen flux through fully dense structures was highly dependent on composition. An increase in oxygen permeation with increased temperature is attributed to both enhanced oxygen vacancy mobility and higher vacancy populations. Highly acceptor-doped compositions resulted in oxygen ion mobilities more than an order of magnitude higher than yttria-stabilized zirconia. The mixed conducting ceramics have been utilized in a membrane reactor configuration to upgrade methane to ethane and ethylene. Conditions were established to balance selectivity and throughput in a catalytic membrane reactor constructed from mixed conducting ceramics.

## INTRODUCTION

Mixed oxide compositions in the  $(\text{La}, \text{Sr})(\text{Co}, \text{Fe})\text{O}_{3-\delta}$  system ( $\text{ABO}_3$  perovskite structure) are known to exhibit substantial ionic and electronic conductivity at elevated temperatures.<sup>1-5</sup> This behavior makes them attractive candidate materials for many important applications, including solid oxide fuel cell cathodes, oxygen separation membranes, and membrane reactors for synthesis gas production (carbon monoxide and hydrogen) and the partial oxidation of hydrocarbons. While the ionic conductivity in these materials frequently accounts for less than 1% of the overall electrical conductivity, the magnitude of the ionic conductivity can be quite large relative to other oxygen ion conductors such as yttria-stabilized zirconia. A spontaneous flux of oxygen through fully dense, mixed conducting

---

<sup>1</sup> Research sponsored by the U. S. Department of Energy, Fossil Energy AR&TD Materials Program. Pacific Northwest National Laboratory is operated by Battelle for the U. S. Department of Energy under Contract DE-AC06-76RLO 1830.

specimens will occur when these materials are placed in an oxygen partial pressure gradient at elevated temperatures. The ionic current resulting from this flux of oxygen ions is compensated internally by an electronic current, so that no electrodes or external circuitry are required for the oxygen flux through the membrane to occur. Passive oxygen flux through a fully dense, mixed conducting ceramic membrane is shown schematically in Figure 1.

In this study, perovskite compositions in the system  $\text{La}_{1-x}\text{M}_x\text{Co}_{1-y-z}\text{Fe}_y\text{N}_z\text{O}_{3-\delta}$ , where  $\text{M}=\text{Sr}, \text{Ca}, \text{ and Ba}$ , and  $\text{N}=\text{Mn}, \text{Ni}, \text{Cu}, \text{Ti}, \text{ and Al}$ , have been prepared and their electrical, oxygen permeation, oxygen vacancy equilibria, and catalytic properties evaluated.

The purpose of this work is to develop compositions and forms that support a high oxygen flux, yet retain sufficient chemical and mechanical stability to enable the use of this class of materials as oxygen separation membranes, as membrane reactors operating in dual oxidizing and reducing environments, and as the cathode in a fuel cell operating at intermediate temperatures.

## EXPERIMENTAL METHODS

Compositions within the system  $\text{La}_{1-x}\text{M}_x\text{Co}_{1-y-z}\text{Fe}_y\text{N}_z\text{O}_{3-\delta}$  ( $\text{M}=\text{Sr}, \text{Ba}, \text{Ca}$ ;  $0.4 \leq x \leq 0.8$ ;  $0.2 \leq y \leq 0.8$ ;  $\text{N}=\text{Mn}, \text{Ni}, \text{Cu}, \text{Ti}, \text{ and Al}$ ) were prepared using the glycine-nitrate combustion synthesis technique.<sup>6</sup> After mixing metal nitrate solutions in the appropriate proportions, glycine was added as a fuel and complexant. The resulting mixtures were then heated in stainless steel beakers on a hot plate to the point of combustion. The resulting ash was calcined at  $850^\circ\text{C}$  for 12 h in air. The calcined powders were compacted using uniaxial pressure (55 MPa) and then pressed isostatically (138 MPa). The pressed compacts were sintered in air in a  $\text{MoSi}_2$  furnace using a heating rate of  $5^\circ\text{C}/\text{min}$  and a cooling rate of  $2^\circ\text{C}/\text{min}$ ; typical sintering conditions to achieve relative densities  $\geq 90\%$  were  $1150\text{--}1250^\circ\text{C}$  for 2–4 h.

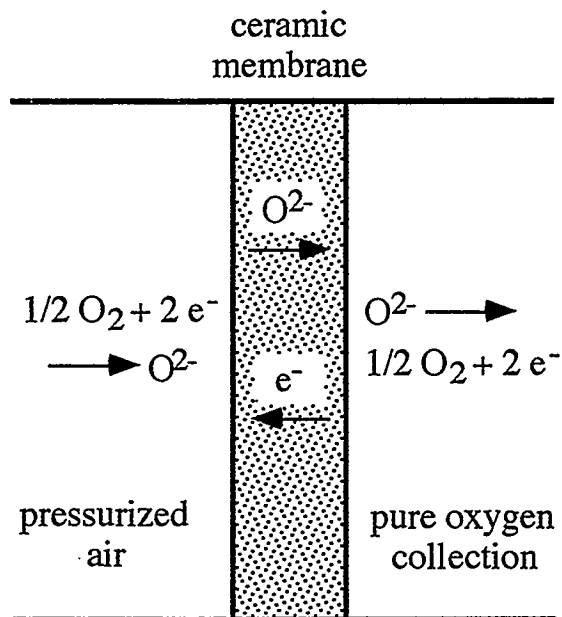


Figure 1. Schematic of oxygen separation using mixed electron and ion-conducting ceramic membranes.



Electrical conductivities of sintered bars were measured as a function of temperature (25-1100°C) in air by a 4-point pulsed dc method using platinum electrodes and a heating and cooling rate of 1.6°C/min. Thermogravimetric analyses (TGA) were performed on calcined powder specimens using a heating rate of 5°C/min and a cooling rate of 2°C/min. The TGA measurements were performed in several different atmospheres (dry air; 10,000, 1,000, and 100 ppm O<sub>2</sub> in N<sub>2</sub>). Passive (i.e., no applied field) oxygen permeation measurements were performed between 720 and 950°C using sintered disc specimens (nominal dimensions: 20 mm dia. x 2 mm thick) sealed in an alumina test cell with gold gaskets. Oxygen or air was used as the source gas with nitrogen as the carrier gas. An oxygen sensor and mass spectrometer were used in calculating the oxygen fluxes. Phase development was determined by x-ray diffraction analysis using Cu K $\alpha$  radiation. Semi-quantitative analysis of phase concentrations was based on comparison of observed peak heights after background subtraction. Room temperature oxygen stoichiometries of calcined powder specimens were determined by iodometric titration.<sup>7</sup>

## RESULTS AND DISCUSSION

### Phase Development

Phase development after calcination in air at 850°C and sintering in air at 1200°C were determined by x-ray diffraction analysis for each of the compositional series. The (LaSr)(CoFe)O<sub>3- $\delta$</sub>  compositions were essentially single-phase perovskite solid solutions after heating to 850°C, while the calcium and barium-containing compositions typically required higher temperature treatment to yield a high proportion ( $\geq 95$  wt %) of the desired perovskite phase. In the (LaCa)(CoFe)O<sub>3- $\delta$</sub>  materials, additional phases observed included Ca<sub>2</sub>Fe<sub>2</sub>O<sub>5</sub>, Ca<sub>2</sub>Co<sub>2</sub>O<sub>5</sub>, CaFe<sub>3</sub>O<sub>5</sub>, and CoO. Compositions of (LaBa)(CoFe)O<sub>3- $\delta$</sub>  with a Ba content  $\geq 0.6$  mole fraction contained multiple perovskite-type phases, as well as other phases (e.g., Ba<sub>5</sub>Fe<sub>14</sub>O<sub>26</sub>, BaCO<sub>3</sub>), after the 850°C calcination. After heat treatment at 1200°C, they were nearly single-phase perovskites, with small quantities of additional phases (e.g., BaFe<sub>2</sub>O<sub>4</sub>, Ba<sub>2</sub>Fe<sub>2</sub>O<sub>5</sub>, and Ba<sub>3</sub>Fe<sub>2</sub>O<sub>6</sub>).

### Oxygen Stoichiometry

All of the materials studied exhibited a substantial reversible weight loss when heated in air. This weight loss upon heating was due to a partial loss of lattice oxygen, so that the

oxygen stoichiometry,  $3-\delta$ , decreased with increasing temperature. The magnitude of the oxygen loss during heating was highly dependent on composition, and tended to increase with increasing acceptor (Sr,Ba,Ca) content. The temperature at which oxygen loss began to occur was also highly dependent on the composition, with oxygen loss beginning to occur at lower temperatures as the acceptor content increased. Coupled with iodometric titration results, the oxygen stoichiometry ( $3-\delta$ ) could be determined. Results for  $(\text{LaSr})(\text{CoFe})\text{O}_{3-\delta}$  are given in Figure 2. Compositions in the series  $(\text{LaBa})(\text{CoFe})\text{O}_{3-\delta}$  tended to exhibit a higher degree of oxygen non-stoichiometry. Lower oxygen loss found for compositions high in cobalt compared to those compositions high in iron indicate that cobalt is more resistant to oxidation than iron in the perovskite structure. The absence of hysteresis in the TGA results during heating and cooling at different rates indicates that the materials were close to their equilibrium oxygen contents during the measurements.

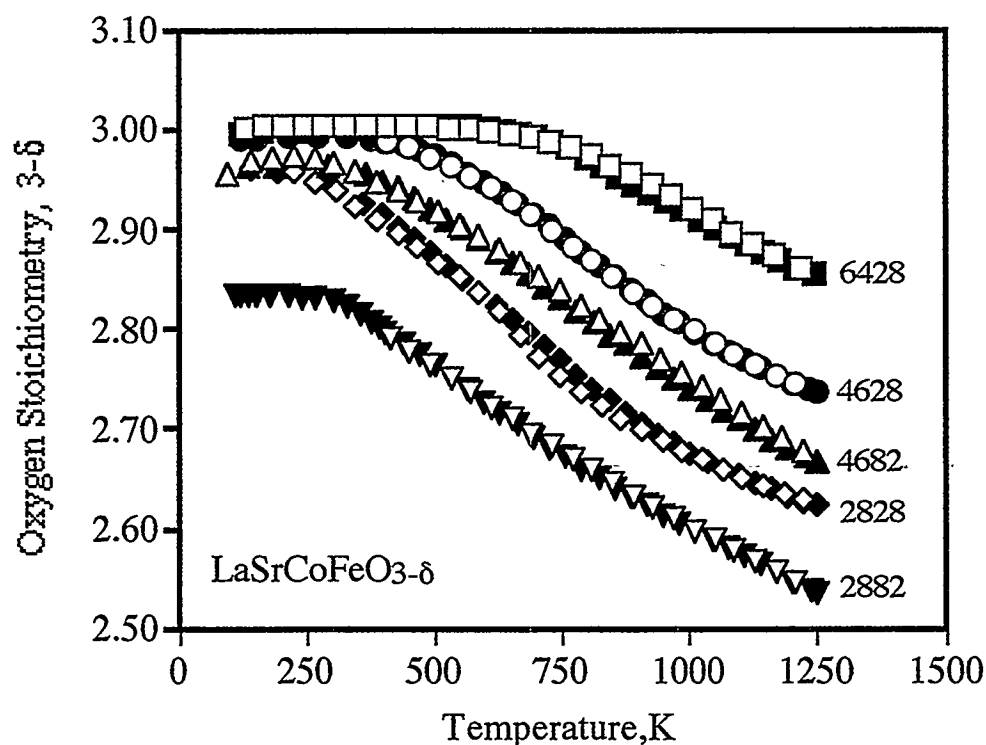


Figure 2. Oxygen stoichiometry as a function of temperature for the indicated  $\text{LaSrCoFeO}_{3-\delta}$  compositions, measured in air. Open symbols refer to heating data; closed symbols refer to cooling data.

### Electrical Conductivity

Electrical conductivities for each compositional series were determined as a function of temperature using the 4-probe dc method. Because the ionic transport number in these compositions is low (typically less than 1%), the bulk conductivities obtained by these dc 4-probe measurements were representative of the electronic conductivity of the materials. The conductivity was enhanced by increasing the Co content; this result is consistent with previous studies on acceptor-doped  $\text{LaFeO}_3$  and  $\text{LaCoO}_3$ .<sup>8, 9</sup> Activation energies ranged from 0.03-0.29 eV. This behavior is consistent with small polaron conduction, with localized electronic carriers having a thermally activated mobility.

At higher temperatures, a substantial decrease in electronic conductivity with increasing temperature was observed. When a divalent acceptor (e.g., Sr) is substituted for trivalent La, electroneutrality requires that the effective negative charge of the Sr cations be compensated by an increase in valence of some of the B-site cations (electronic compensation) and/or the formation of oxygen vacancies (ionic compensation). Electronic compensation results in an increase in the average valence of the transition metal cations, while ionic compensation reduces the oxygen stoichiometry. At low temperatures, the charge compensation for  $\text{La}_{0.6}\text{Sr}_{0.4}\text{Co}_{0.2}\text{Fe}_{0.8}\text{O}_{3-\delta}$  is primarily electronic, with a substantial fraction of B-site cations being converted from the trivalent to the tetravalent state due to the presence of the acceptor cations. At higher temperatures, ionic compensation becomes significant, while the electron hole population is lowered.

### Oxygen Permeation and Ionic Conductivity

Oxygen permeation rates through sintered specimens of several  $(\text{LaSr})(\text{CoFe})\text{O}_{3-\delta}$  compositions are shown as a function of temperature in Figure 3. The specimen thickness was  $\approx 2$  mm. Oxygen or air was the source gas on the high  $P(\text{O}_2)$  side, with nitrogen being used as the carrier gas. In the  $(\text{LaSr})(\text{CoFe})\text{O}_{3-\delta}$  compositions, the oxygen flux increased significantly with increasing Sr content. Oxygen flux also increased with increasing temperature, attributed to an increase in the mobility of the lattice oxygen vacancies (the hopping of vacancies from site to site is thermally activated), as well as the increase in the concentration of lattice oxygen vacancies. Fluxes for the  $(\text{LaCa})(\text{CoFe})\text{O}_{3-\delta}$  compositions were much lower than for the  $(\text{LaSr})(\text{CoFe})\text{O}_{3-\delta}$  compositions. Barium-substituted compositions gave oxygen fluxes comparable to those containing a like concentration of Sr, and higher fluxes than those containing Ca.

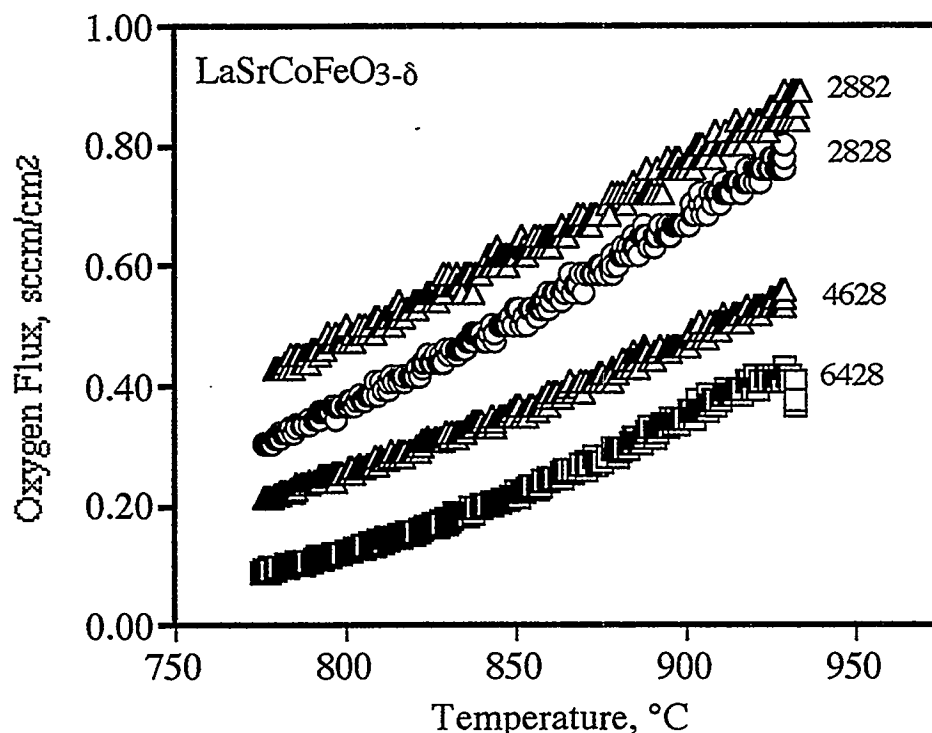


Figure 3. Oxygen permeation as a function of temperature through sintered specimens of the indicated  $\text{LaSrCoFeO}_{3-\delta}$  composition. The membrane thickness was approximately 2 mm for each composition, while the oxygen partial pressure gradient was approximately 10.

The oxygen flux through the bulk of a mixed conducting membrane should be inversely proportional to the thickness of the membrane. Thus, to maximize oxygen flux, the membrane thickness should be minimized. Very thin, self-supporting membranes of this type are mechanically very weak and of little practical importance. When thin films were prepared on a porous  $\text{MgO}$  or  $\text{Al}_2\text{O}_3$  support, differences in thermal expansion behavior resulted in membrane cracking. A promising alternative approach is to fabricate an asymmetric membrane structure, consisting of a thin, dense membrane on a porous support of the same composition, by tape calendering. An organic phase was included in the ceramic powder plus plasticizer mixture that formed a porous structure during burnout. The porous support allowed relatively free transport of oxygen to the dense membrane surface, and provided much needed mechanical support. Because the support and dense membrane consisted of the same composition, there was no thermal expansion mismatch. A micrograph

of a cross-section of an  $\text{LaSrCoFeO}_{3-6428}$  membrane is given in Figure 4. Molecular oxygen fluxes as a function of temperature for an approximately 2 mm thick and an approximately 15  $\mu\text{m}$  thick asymmetric membrane are given in Figure 5, along with calculated fluxes for different membrane thicknesses. An improvement of approximately two orders of magnitude was realized for the 15  $\mu\text{m}$  thick membrane compared to the 2 mm thick membrane.

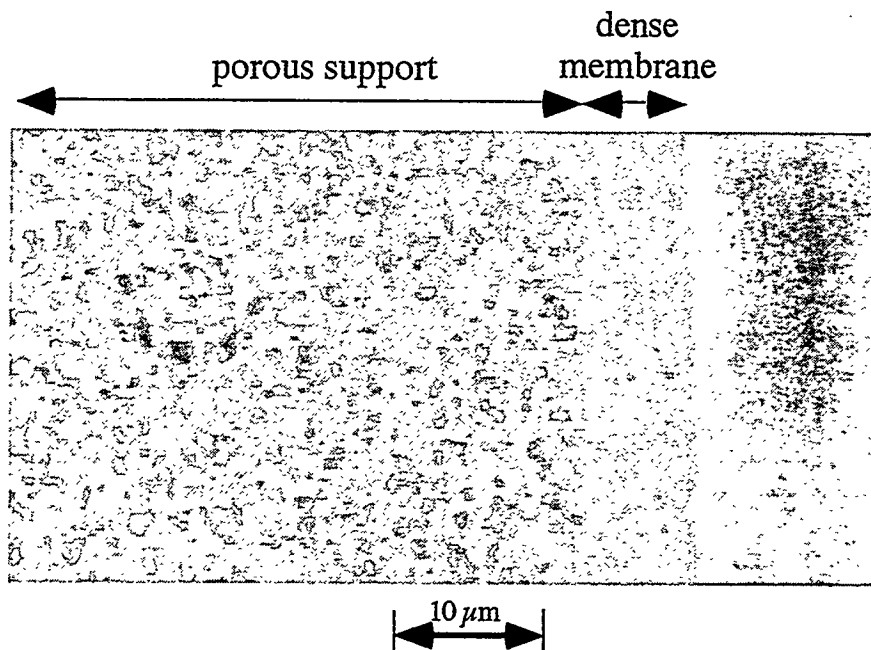


Figure 4. Asymmetric membrane structure consisting of a fully dense layer on a porous support of the same composition, made by tape calendering.

At some point, however, surface exchange kinetics will become rate limiting, so that any further reduction in membrane thickness will not result in an increase in the oxygen flux. Bouwmeester et al.<sup>10</sup> calculated the characteristic thickness of various membrane compositions, below which oxygen permeation is controlled by surface exchange kinetics. The characteristic thickness for Sr-doped  $\text{LaCoO}_3$  and  $\text{LaFeO}_3$  varied from 20 to 500  $\mu\text{m}$  at 900°C.

If a material is to be a successful candidate for oxygen membrane applications, it must exhibit long-term phase stability under the membrane operating conditions. In general, the perovskite systems evaluated in this study do not exhibit high stability towards reducing atmospheres at elevated temperatures, typical of membrane reactor applications. These materials are stable under oxidizing conditions, typical of oxygen separation devices. A

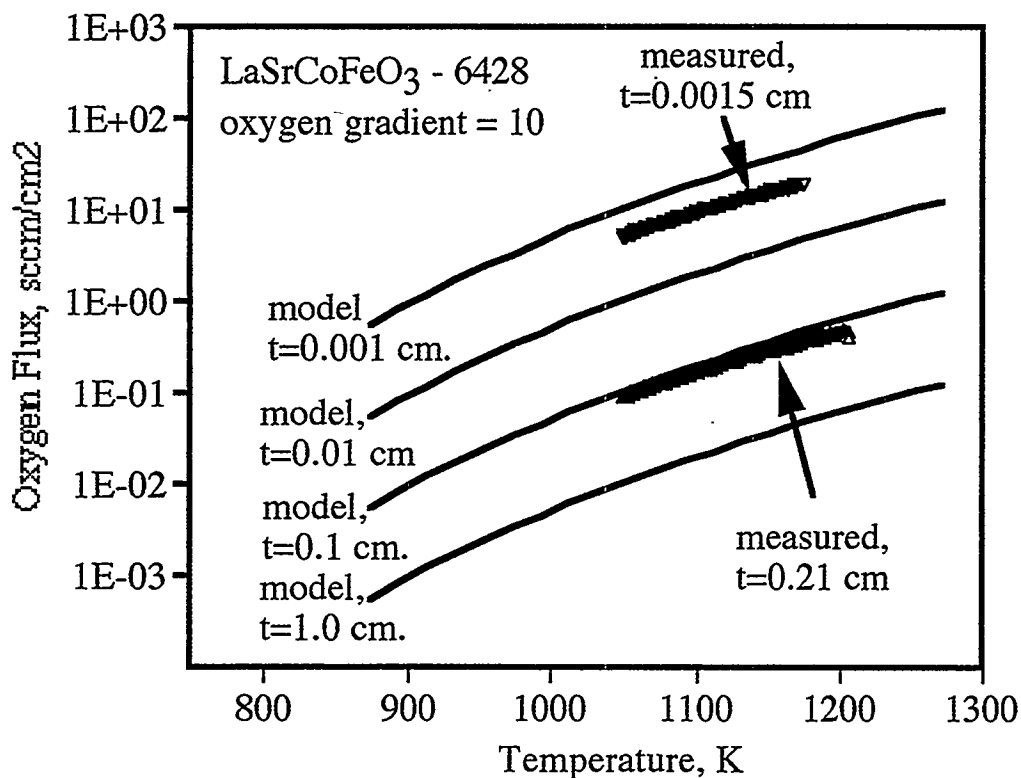


Figure 5. Oxygen flux versus temperature for two different thicknesses of the composition  $\text{LaSrCoFeO}_3\text{-6428}$ . Oxygen flux is inversely proportional to membrane thickness, to a limit imposed by surface processes.

membrane of composition  $\text{La}_{0.2}\text{Sr}_{0.8}\text{Co}_{0.2}\text{Fe}_{0.8}\text{O}_{3-\delta}$  operated for 340 h in an oxygen gradient of 10 at  $775^\circ\text{C}$  with minimal decrease in oxygen flux ( $<5\%$ ), as given in Figure 6. Similarly,  $\text{La}_{0.6}\text{Sr}_{0.4}\text{Co}_{0.2}\text{Fe}_{0.8}\text{O}_{3-\delta}$  gave an essentially constant flux at  $800^\circ\text{C}$  for nearly 1400 h. These observations are in contrast to the results of a study by Kruidhof et al.<sup>11</sup> for a related composition ( $\text{La}_{0.6}\text{Sr}_{0.4}\text{CoO}_{3-\delta}$ ) at a slightly lower temperature,  $750^\circ\text{C}$ . The observed long-term stability indicates that the oxygen fluxes measured during the oxygen permeation trials in this study were true fluxes through the membrane rather than false transient fluxes resulting from oxygen depletion of the perovskite lattice.

From the rates of oxygen permeation, membrane thicknesses, and oxygen partial pressure gradients, oxygen ion conductivities were calculated. Activation energies for oxygen ion conductivities varied from approximately 0.6 to 1.8 eV, depending on composition, as given in Table 1. The activation energies reflect not only the mobility of oxygen ions in the solid, but also the formation of oxygen vacancies at elevated temperatures.

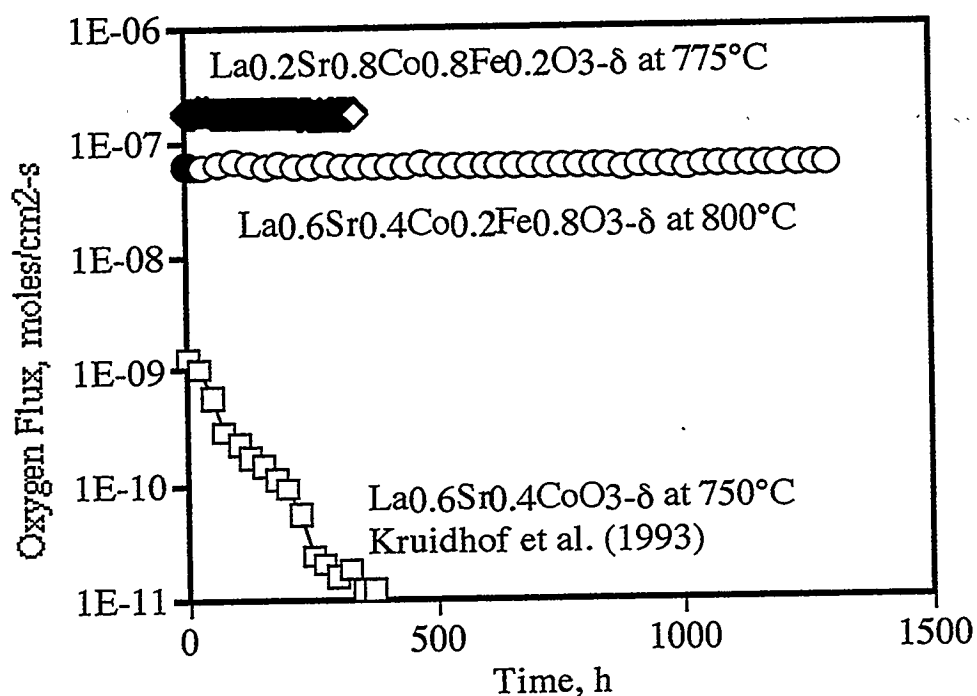


Figure 6. Long-term oxygen flux measurements for several mixed conductor compositions.

Table 1. Ion Conductivities at 900°C and Activation Energies for Oxygen Ion Conduction for Mixed Electron and Ion-Conducting Membranes

Composition	Ionic Conductivity at 900°C (ohms-cm)	Activation Energy (eV)
$\text{La}_{0.6}\text{Sr}_{0.4}\text{Co}_{0.2}\text{Fe}_{0.8}\text{O}_{3-\delta}$	0.23	1.30
$\text{La}_{0.4}\text{Sr}_{0.6}\text{Co}_{0.2}\text{Fe}_{0.8}\text{O}_{3-\delta}$	0.40	0.95
$\text{La}_{0.2}\text{Sr}_{0.8}\text{Co}_{0.2}\text{Fe}_{0.8}\text{O}_{3-\delta}$	0.62	0.85
$\text{La}_{0.2}\text{Sr}_{0.8}\text{Co}_{0.8}\text{Fe}_{0.2}\text{O}_{3-\delta}$	0.87	0.66
$\text{La}_{0.4}\text{Ca}_{0.6}\text{Co}_{0.2}\text{Fe}_{0.8}\text{O}_{3-\delta}$	0.03	0.70
$\text{La}_{0.4}\text{Ca}_{0.6}\text{Co}_{0.8}\text{Fe}_{0.2}\text{O}_{3-\delta}$	0.01	1.80
$\text{La}_{0.6}\text{Ba}_{0.4}\text{Co}_{0.2}\text{Fe}_{0.8}\text{O}_{3-\delta}$	0.01	1.64
$\text{La}_{0.4}\text{Ba}_{0.6}\text{Co}_{0.2}\text{Fe}_{0.8}\text{O}_{3-\delta}$	0.33	0.90
$\text{La}_{0.2}\text{Ba}_{0.8}\text{Co}_{0.2}\text{Fe}_{0.8}\text{O}_{3-\delta}$	0.37	0.65
$\text{La}_{0.6}\text{Sr}_{0.4}\text{Co}_{0.2}\text{Fe}_{0.6}\text{Al}_{0.2}\text{O}_{3-\delta}$	0.15	0.83
$\text{La}_{0.6}\text{Sr}_{0.4}\text{Co}_{0.2}\text{Fe}_{0.6}\text{Cr}_{0.2}\text{O}_{3-\delta}$	0.03	1.63
$\text{La}_{0.6}\text{Sr}_{0.4}\text{Co}_{0.2}\text{Fe}_{0.6}\text{Cu}_{0.2}\text{O}_{3-\delta}$	0.10	1.34
$\text{La}_{0.6}\text{Sr}_{0.4}\text{Co}_{0.2}\text{Fe}_{0.6}\text{Ni}_{0.2}\text{O}_{3-\delta}$	0.10	0.84
$\text{La}_{0.6}\text{Sr}_{0.4}\text{Co}_{0.2}\text{Fe}_{0.6}\text{Ti}_{0.2}\text{O}_{3-\delta}$	0.04	1.34

## SUMMARY

Perovskite ceramics in the system  $\text{La}_{1-x}\text{M}_x\text{Co}_{1-y-z}\text{Fe}_y\text{N}_z\text{O}_{3-\delta}$ , where  $\text{M}=\text{Sr}, \text{Ca}$ , and  $\text{Ba}$ , and  $\text{N}=\text{Mn}, \text{Ni}, \text{Cu}, \text{Ti}$ , and  $\text{Al}$ , have been prepared and their electrical, oxygen permeation, oxygen vacancy equilibria, and catalytic properties evaluated. These materials exhibit mixed electron and oxygen ion conductivity, and are useful as oxygen separation membranes, fuel cell cathodes, and membrane reactors. Highly acceptor-doped compositions resulted in oxygen ion mobilities more than an order of magnitude higher than yttria-stabilized zirconia. An asymmetric membrane structure was fabricated by tape calendering, consisting of a fully dense, thin layer on a porous support of the same composition. This arrangement provided a high molecular flux, yet was mechanically robust. Little degradation in molecular flux was found for times up to approximately 2 months for most compositions.

## REFERENCES

1. T. Ishigaki, S. Yamauchi, K. Kishio, J. Mizusaki, and K. Fueki, *J. Solid State Chem.* **73**, 179 (1988).
2. Y. Teraoka, H. Zhang, K. Okamoto, and N. Yamazoe, *Mat. Res. Bull.* **23**, 51 (1988).
3. Y. Teraoka, T. Nobunaga, K. Okamoto, N. Miura, and N. Yamazoe, *Solid State Ionics* **48**, 207 (1991).
4. J. W. Stevenson, T. R. Armstrong, R. D. Carneim, L. R. Pederson, and W. J. Weber, *J. Electrochem. Soc.* (1996, in press).
5. U. Balachandran, S. Morissette, J. Picciolo, J. Dusek, and R. Peoppel, Proc. International Gas Research Conference, Ed. H. Thompson, Government Institutes, Rockville, MD, p. 565 (1992).
6. L.A. Chick, L.R. Pederson, G.D. Maupin, J.L. Bates, L.E. Thomas, and G.J. Exarhos, *Materials Letters* **10**, 6 (1990).
7. R. Nadalin and W. Brozda, *Analytica Chimica Acta* **28**, 282 (1963).
8. J. Mizusaki, T. Sasamoto, W. Cannon, and H. Bowen, *J. Am. Ceram. Soc.* **66**, 247 (1983).
9. J. Mizusaki, J. Tabuchi, T. Matsuura, S. Yamauchi, and K. Fueki, *J. Electrochem. Soc.* **136**, 2082 (1989).
10. H. Bouwmeester, H. Kruidhof, and A. Burggraaf, *Solid State Ionics* **72**, 185 (1994).
11. H. Kruidhof, H. Bouwmeester, R. v. Doorn, and A. Burggraaf, *Solid State Ionics* **63-65**, 816 (1993).



**PREPARATION AND EVALUATION OF COAL EXTRACTS  
AS PRECURSORS FOR CARBON AND GRAPHITE PRODUCTS**

J. W. Zondlo, A. W. Stiller, and P. G. Stansberry  
West Virginia University, Department of Chemical Engineering  
P. O. Box 6101  
Morgantown, WV 26506-6101

I. C. Lewis, R. T. Lewis, and H. K. Mayer  
UCAR Carbon Company Inc.  
P. O. Box 6116  
Cleveland, OH 44101

**ABSTRACT**

A coal extraction process coupled with coal hydrotreatment has been shown capable of producing suitable precursors for a variety of commercially important carbon and graphite products. The N-methylpyrrolidone (NMP) extracts of hydrotreated coals have been analytically and chemically characterized and shown to have properties acceptable for use as binder and impregnation pitch. Mesophase formation studies have demonstrated their capability for producing both needle and anode grade coke as well as precursors for mesophase pitch fibers. A graphite artifact has been produced using a coal extract as a binder and coke derived from the extract as a filler. Further evaluation of the extract materials is being carried out by industrial members of the Carbon Products Consortium.

**I. WVU Extraction Process and Preparation of Coal Extracts**

For the past eight years, workers in the Chemical Engineering Department at West Virginia University have been developing a technique based on solvent extraction of coal whereby significant quantities of the organic material in coal can be separated from the inorganic contaminants<sup>(1)</sup>. The process employs a novel class of organic compounds known as dipolar aprotic solvents. When bituminous coal is treated with these solvents at their normal boiling point, much of the carbonaceous material in the coal is solubilized and the inorganic matter remains as an undissolved solid. Through simple filtration the solution is separated from

the residual inorganic solids and the organic material is reconstituted by evaporation of the solvent. Through efficient use of evaporative technologies, virtually all of the solvent is recovered and recycled in the process.

It has been found that for most bituminous coals indigenous to the Appalachian region, extract yields in the range of 30 to 50% by weight of the original coal can be realized. Moreover, if the raw coal is first treated by mild hydrogenation, extract yields high as 80% can be achieved. Most importantly, by adjusting processing conditions and/or blending extracts. A variety of extracts with different properties can be obtained.

A successful program was completed for the U. S. Department of Energy in which cokes produced from the solvent extraction process were utilized as feedstocks for the production of fine-grained, isotropic, graphite<sup>(2)</sup>. Furthermore, the program demonstrated that precursors suitable for a number of other carbon products could be produced from the process.

The objective of this present program was to establish the suitability of the extracts as precursors for commercially significant carbon products including the following: binder pitch, impregnating pitch, needle coke for electrodes, anode grade coke, carbon/carbon matrices, and a precursor for mesophase pitch. The ultimate evaluation of materials would be made by Industrial Partners of a Consortium formed for investigation of coal-based precursors for carbon products.

This study reports results for materials prepared by the extraction of hydrotreated coals with N-methylpyrrolidone (NMP) solvent. Two different sub-bituminous West Virginia coals were employed in the process. Initially, the coals were hydrogenated in a one-liter autoclave using 2,000 psi hydrogen and temperatures of 350-450 in both the presence and absence of a catalyst. Tetralin was employed as a hydrogen donor.

The hydrogenated coal was transferred to a rotary evaporator to remove unreacted tetralin. After tetralin removal, N-methylpyrrolidone was added to the mixture and agitated at 140°C for 1 hour. The NMP-hydrogenated-coal slurry was then transferred to a centrifuge to separate the solids. Finally, NMP soluble coal extract was isolated from the NMP by rotary evaporation and then vacuum dried. Larger-size samples were produced using 1-gallon autoclaves. Typically, 600g of powdered coal and 1.8L tetralin were placed into the stirred reactor and pressurized to 2,000 psig, initial cold hydrogen pressure. Between 3 and 4 hours were required to reach final temperature after which several more hours were needed to reach ambient temperature. The extract separations were performed similarly to the small-scale samples.

## **II. Characterization of Coal Extracts**

The NMP extracts prepared at WVU from hydrotreated coals were characterized by a variety of analytical techniques including: elemental C, H, N, O, S, analysis, thermogravimetric analysis (TGA), Proton NMR, solvent extraction with toluene and trichlorobenzene (TCB), Mettler softening point measurement, determination of modified Conradson carbon content (MCC), and Gel Permeation Chromatography (GPC) for evaluation of molecular weight distribution (MWD). Mesophase formation studies were also carried out by direct observation on the microscope hot stage and by separate heat treatment for subsequent examination by polarized light microscopy. Although these evaluations were performed for a variety of extract materials, prepared using different reaction conditions, results are reported here only for NMP extracts from coal hydrotreated at 450°C. These products were found to be the most suitable for the wide variety of carbon products encompassed by the Consortium Team.

Two different West Virginia bituminous coals designated as WVGS-13421 and WVGS-13423 were hydrotreated at 450°C for 2 hours without use of a catalyst. The NMP extracts obtained in 70-85% yields were then characterized in detail. The analytical results are summarized in Table I.

**Table I**  
**Properties for NMP Coal Extracts of Hydrotreated Coals**

	450°C - 2 Hrs. Coal 13421	450°C - 2 Hrs. Coal 13423
SP, °C	104.7	115.3
MCC %	52.9	51.7
TGA Yd%	34	31
C, %	88.9	89.6
H, %	5.85	5.78
C/H Ratio	1.28	1.30
N, %	2.20	1.90
O, %	2.74	2.49
S, %	0.45	0.33
Ar H %	45	48
Mn (GPC)	367	389
Mesophase (μ)	272	136

The Mettler softening points and carbon yield (MCC) values are in the range of commercially produced binder and impregnant pitches. However, in addition to being solids free, these extracts differ in a number of properties from conventional pitches. The very low aromatic hydrogen contents from NMR, reflect the extensive hydrogenation of aromatic ring systems during the coal pretreatment. The extracts also have substantially higher N and O contents than standard coal tar or petroleum-derived pitches. The molecular weight distributions are comparable to those of commercial pitches.

### III. Mesophase Evaluation of Coal Extracts

The nature of the formed mesophase is a suitable guide for the applicability of these extracts for many different carbon precursors. The extracts were heat treated for mesophase domain size evaluation using a published technique<sup>(3)</sup>. The results are listed in Table I and as can be seen, the WVGS-13421 gave a substantially larger domain size than the WVGS-13423 extract. The large domain size of 272 $\mu$  is comparable to that found for needle coke precursors for high-performance graphite electrodes and is in the range of materials suitable for mesophase pitch fibers. This large domain size is surprising in view of the high-oxygen content of the extract. A high-oxygen content has been believed to be detrimental for mesophase formation in coal extracts.

### IV. Fabrication of Graphite Artifacts from Hydrotreated Coal Extracts

We produced a graphite artifact using coke derived from the WVGS-13421 extract as the filler and the coal extract itself as the binder. The raw coke was prepared at WVU and then calcined to 1,100°C by T. Burchell at the Oak Ridge Laboratory. The calcined coke was mixed with 1/3 by weight of the coal extract binder and then extruded to produce 19mm-diameter rods. The rods were baked and graphitized to 3,000°C. The properties measured for the graphitized rods were the following:

Coefficient of Thermal Expansion (CTE) =  $0.26 \times 10^{-6}/^{\circ}\text{C}$

Specific Resistance = 9.55 micro-ohm-meters

Density = 1.38/gcc

The very low CTE value of 0.26 is similar to that measured for electrode graphite derived from petroleum needle coke.

## V. Activation of Coal Extraction Residues

The economics of the coal extraction process would be improved if the extraction residues also had some value. For this purpose, we attempted to activate these materials to produce a high surface area carbon. We obtained samples of the NMP extraction residue of raw coal WVGS-13421, as well as the extraction residue of the coal hydrotreated at 450°C for 2 hours. Both materials were activated in an H<sub>2</sub>O/N<sub>2</sub> mixture at 900°C using a tumbling furnace.

After activation, the measured surface area for the activated residue from the untreated coal was 770 m<sup>2</sup>/gm while that for the hydrotreated coal was 212 m<sup>2</sup>/gm. The lower surface area of the hydrotreated residue is expected since it would have a greater ash content than the residue from the untreated coal.

## VI. Conclusions

Our evaluation studies have demonstrated that the coal extraction process coupled with hydrotreatment can produce materials that are suitable for use as pitches, coke precursors, or mesophase raw materials. We have also demonstrated that coke derived from hydrotreated coal extract can be used to produce graphite with a low coefficient of thermal expansion, a requisite for graphite electrodes. By altering the processing conditions and the use of blends, it would be possible to produce graphites with varying degrees of anisotropy. Additionally, the extraction residue can

be activated to produce an activated carbon. No other known process has the flexibility for producing this range of carbon materials.

### REFERENCES

1. K. Renganathan, J. W. Zondlo, E. A. Mintz, P. Kneisl, and A. H. Stiller, Fuel Proc. Tech., 18, p. 273 (1988).
2. Coal-Based Nuclear Graphites for the NP Gas-Cooled Reactors, USDOE Contract DE-FG02-91NP00159.
3. R. T. Lewis, I. C. Lewis, R. A. Greinke, and S. L. Strong, Carbon 25, 289 (1987).





## A NOVEL APPROACH TO THE REMOVAL OF CO<sub>2</sub>

T. D. Burchell, R. R. Judkins, M. R. Rogers, and A. M. Williams

Oak Ridge National Laboratory  
P.O. Box 2008  
Oak Ridge, TN 37831-6088

### ABSTRACT

The removal of CO<sub>2</sub> from gas streams is becoming increasingly significant in the field of energy production. A porous monolithic activated carbon material (CFCMS) has been developed that is both strong and rigid, yet is permeable, and thus offers little resistance to the free-flow of fluids. The material has a unique combination of properties, including reasonable compressive strength, electrical conductivity, a large micropore volume, and a large CO<sub>2</sub> adsorption capacity. At 30°C and atmospheric pressure, CFCMS has a CO<sub>2</sub> uptake >100 mg/g. The uptake is reduced at elevated temperatures, dropping to ~40 mg/g at 100°C. However, the CO<sub>2</sub> uptake increases substantially with pressure, such that at 25°C and 58 bar the mass of CO<sub>2</sub> adsorbed is >490 mg/g. The ability of CFCMS to selectively remove CO<sub>2</sub> from a CO<sub>2</sub>/CH<sub>4</sub> gas mixture is demonstrated in a series of breakthrough experiments. The unique combination of properties of CFCMS has been exploited to effect the rapid desorption of CO<sub>2</sub> under the influence of a low applied dc voltage.

### INTRODUCTION

The removal of CO<sub>2</sub> is of significance in several energy applications. The combustion of fossil fuels, such as coal or natural gas, releases large volumes of CO<sub>2</sub> to the environment. Several options exist to reduce CO<sub>2</sub> emissions, including substitution of nuclear power for fossil fuels, increasing the efficiency of fossil plants, and capturing the CO<sub>2</sub> prior to emission to the environment. All of these techniques have the attractive feature of limiting the amount of CO<sub>2</sub> emitted to the atmosphere, but each has economic, technical, or societal limitations. In the production of natural gas, the feed stream from the well frequently contains contaminants and diluents which must be removed before the gas can enter the pipeline distribution system. Notable amongst these diluent gasses is CO<sub>2</sub>, which has no calorific value. Currently, the pipeline specification calls for <2 mol % CO<sub>2</sub> in the gas. Gas separation is thus a relevant technology in the field of energy production. A novel separation system based on a parametric swing process

has been developed that utilizes the unique combination of properties exhibited by our carbon fiber composite molecular sieve (CFCMS).

The CFCMS is a monolithic activated carbon composed of petroleum pitch-derived carbon fiber and a phenolic resin-derived binder<sup>1-3</sup>. Routinely, fiber microporosity with surface areas  $>1000 \text{ m}^2/\text{g}$  are obtained using pitch fibers. The binder phase content is quite low and provides a monolithic structure by bonding the fibers at contact points only, thus rendering the CFCMS macroporous. The CFCMS offers, therefore, a highly adsorbent material with very little resistance to bulk gas flow. Experiments conducted at ORNL have shown the CFCMS to have a high affinity for carbon dioxide compared to zeolites and conventional granular activated carbons. The CFCMS also allows certain equipment variations not possible with granular materials. It can be molded into almost any shape, i.e., shape is constrained only by the ability to fabricate molds, where constraints appear to be minimal. The CFCMS can be machined by skilled operators using conventional tooling. These features permit the activated carbon to be formed to a desired shape to meet process equipment constraints as opposed to conventional filling of vertically-oriented vessels with granular carbon. Granular carbon systems are also subject to attrition due to abrasive wear in service, and channeling of the gas being processed as a result of inhomogeneous packing in the beds. Use of the CFCMS would permit the employment of, for example, horizontally-oriented vessels with controlled flow of the natural gas with the contaminants/diluents to be adsorbed through the adsorbent without risk of channeling and bypass flows.

The CFCMS is, as a result of the continuity of the fiber-matrix unit, electrically conductive. Advantage has been taken of this property to develop a novel desorption process we have termed electrical (or voltage) swing adsorption. On saturation of the CFCMS with, for example, carbon dioxide, immediate desorption can be accomplished by application of very low voltages (in our experiments we have used 0.5-1 volt) across the adsorbent. There are many important operational implications of this desorption process. The system pressure and temperature do not have to be altered as they do in other parametric swing processes such as pressure swing adsorption (PSA) or temperature swing adsorption (TSA). The electrical swing adsorption process is extremely fast in comparison to PSA or TSA. It is an inherently low-energy process compared to the energy requirements of PSA or TSA processes. All of these features suggest a great deal of system and operational simplicity. We present below the results of several experiments which demonstrate the performance of the CFCMS and the electrical swing adsorption process.

## EXPERIMENTAL

The CFCMS material used in this study was fabricated using a process initially developed by the U. S. Department of Energy (USDOE) for the production of thermal insulators for NASA space missions<sup>4</sup>. The CFCMS synthesis route has been described in detail previously<sup>1</sup>. Isotropic pitch-derived carbon fibers are mixed with powdered phenolic resin to form a water slurry. The slurry is transferred to a molding tank and the water drawn through a porous screen under vacuum. The resultant green artifact is dried, cured at 60°C in air, and stripped from the mold screen. The composite is cured at ~150°C in air prior to carbonization at 650°C in an inert gas. The final synthesis stage involves activation of the composite in moisture saturated He in the temperature range 800-950°C.

Porosity characterization was performed using nitrogen adsorption and mercury intrusion. Nitrogen adsorption isotherms were measured at 77 K using our Autosorb-1 instrument. Micropore size analysis used a variety of methods, including the Brunauer, Emmett, and Teller (BET)<sup>5</sup> method for surface area and the Dubinin-Astakhov (DA)<sup>6</sup> method for micropore radius and the t-method for micro-pore volume. CO<sub>2</sub> and CH<sub>4</sub> adsorption isotherms for CFCMS were also obtained using the Autosorb-1 apparatus over the pressure range 0.1 to 760-mm Hg and at temperatures of 30, 60, and 100°C. High pressure CO<sub>2</sub> and CH<sub>4</sub> adsorption data (850 psi max.) were obtained using a gravimetric apparatus, courtesy of Westvaco Corporation.

A schematic diagram of our experimental breakthrough apparatus is shown in Fig. 1. The feed gas flows through a CFCMS sample (25.4-mm diameter and 76.2-mm long) to a vent. A sample of the downstream gas is fed to a mass spectrometer allowing on-line monitoring of the exit gas composition. Flowmeters (F1 & F2) are positioned either side of the CFCMS sample. Electrical leads are connected to each end of the sample creating an electric circuit through the sample which allows an electric current to flow. On saturation of the CFCMS with, for example, carbon dioxide, immediate desorption can be accomplished by application of very low voltages (in our experiments we have used 0.5-1 volt) across the adsorbent.

## RESULTS AND DISCUSSION

Our previous gravimetric studies of CO<sub>2</sub> adsorption indicated that at 25°C and atmospheric pressure CFCMS can adsorb >100 mg of CO<sub>2</sub> per gram of CFCMS<sup>7,8</sup>. Here we

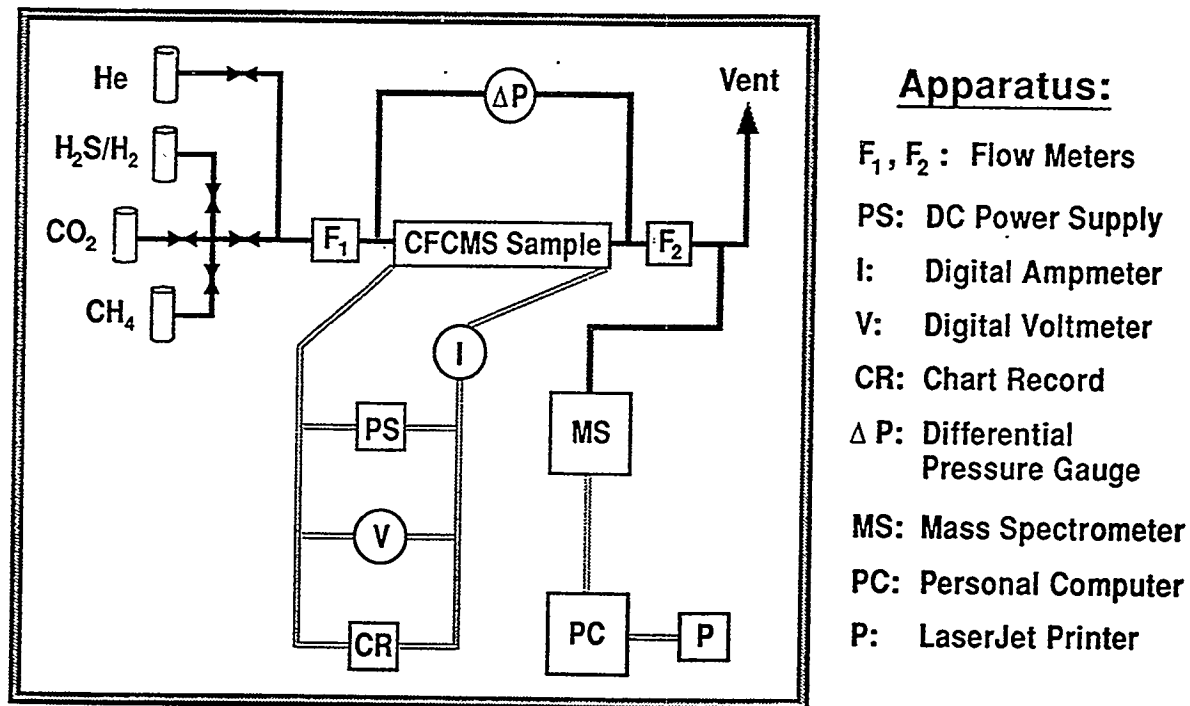


Fig. 1. Schematic drawing of our experimental breakthrough apparatus.

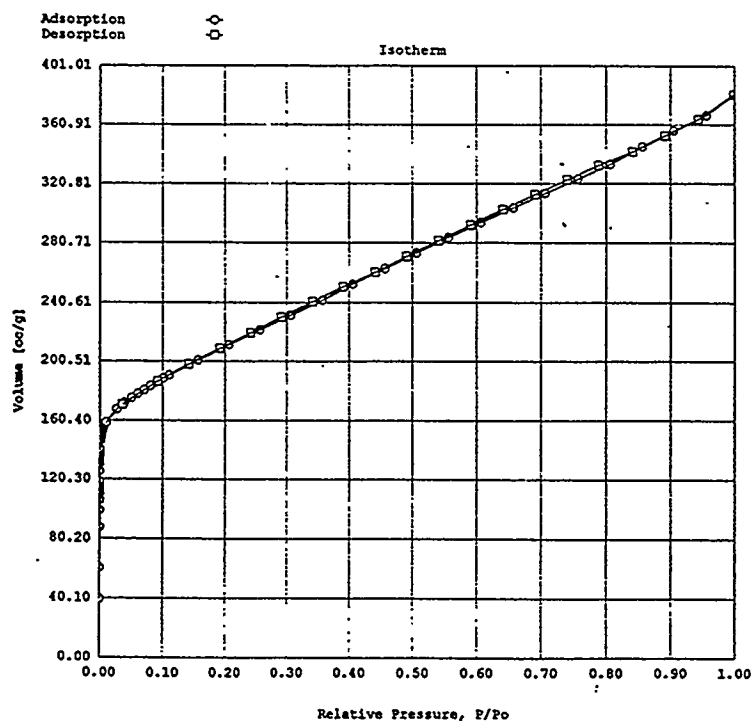


Fig. 2. Nitrogen adsorption isotherm at 77K on CFCMS activated to 9% burn-off.

report the extension of our CO<sub>2</sub> adsorption data to higher temperatures and pressures. Moreover, breakthrough experiments were conducted to determine the efficacy of CFCMS at separating CO<sub>2</sub> from CH<sub>4</sub>.

### Micropore Structure Analysis

A series of CFCMS cylinders was prepared and activated to burn-offs ranging from 9 to 36% and the BET surface area and micropore size/volume determined from the N<sub>2</sub> adsorption isotherms. Table 1 reports the mass and average burn-off for each of the four cylinders (25-mm diameter x 75-mm length), and their BET surface area, micropore volume (t-method), and mean micropore radius (DA method). Samples were taken from the top (T) and bottom (B) of each cylinder for analysis. Where the measured BET surface areas were widely different between the top and bottom of the cylinders a repeat measurement was performed.

Table 1. Micropore analysis data for activated CFCMS samples.

Specimen	Mass (g)	Burn-off (%)	BET Area (m <sup>2</sup> /g)	Pore Volume [t-method] (cm <sup>3</sup> /g)	DA Pore Radius (nm)
21-11 T	11.96	9	485	-	0.70
21-11 B	11.96	9	540	0.212	0.65
21-2B T	11.01	18	770	0.282	0.72
21-2B B	11.01	18	1725	0.603	0.70
21-2B B (repeat)	11.01	18	961	0.328	0.71
21-2D T	9.86	27	939	0.305	0.75
21-2D B	9.86	27	2470	0.866	0.75
21-2D B (repeat)	9.86	27	2477	0.791	0.75
21-2C T	8.86	36	923	0.235	0.87
21-2C B	8.86	36	2323	0.723	0.75
21-2C B (repeat)	8.86	36	856	0.270	0.75

The BET surface area increases with burn-off, approaching 2500 m<sup>2</sup>/g at >25% burn-off. The micropore size (DA pore radius) is apparently less sensitive to burn-off (Table 1) and increases only slightly over the weight loss range reported here. The pore volume (t-method) varies with the BET surface area, increasing with burn-off. The observed variations in BET surface area and micropore volume and radius are in agreement with our previous data<sup>8</sup>. In addition to the data reported above, a density function theory (DFT) analysis was performed on the N<sub>2</sub> adsorption isotherm for sample 21-11B. The isotherm (Fig. 2) is a "type I" isotherm<sup>9</sup>, as were all the isotherms obtained for our CFCMS materials. Figure 3 shows the DFT analysis results, which indicate a micropore (<2-nm width) distribution centered at approximately 0.4-0.5-nm radius. This value is somewhat smaller than DA pore radii reported in Table 1, but agrees well with our previously published DR method pore width data for CFCMS with similar burn-offs<sup>8</sup>. The pore volume attributable to the micropores is also shown in Fig. 3. Summing the volume elements for pore half widths <10Å yields a micropore volume of approximately 0.16 cm<sup>3</sup>/g, which is in reasonable agreement with the "t-method" micropore volume data in Table 1 for CFCMS samples 21-11 B and T.

#### CO<sub>2</sub>/CH<sub>4</sub> Adsorption Studies

Adsorption isotherms were obtained at temperatures of 30, 60, and 100°C at pressures up to one atmosphere for CO<sub>2</sub> and CH<sub>4</sub> (Figs. 4 and 5). Both of the CFCMS samples analyzed (21-11 and 21-2B) adsorbed less CO<sub>2</sub> at 60 and 100°C than at 30°C. At 100°C the amount of CO<sub>2</sub> adsorbed was approximately one third that adsorbed at 30°C. Both CFCMS specimens displayed similar trends with respect to CH<sub>4</sub> adsorption. CFCMS has a greater uptake of CO<sub>2</sub> compared to CH<sub>4</sub> at all of the temperatures studied here. For example, at 30°C approximately 50 cm<sup>3</sup>/g of CO<sub>2</sub> was adsorbed whereas only approximately 27 cm<sup>3</sup>/g of CH<sub>4</sub> was adsorbed at one atmosphere pressure. Figure 6 shows the variation of the amount of gas adsorbed (CO<sub>2</sub> or CH<sub>4</sub>) at one atmosphere pressure with temperature for two CFCMS specimens. The greater selectivity of specimen 21-11 at 30°C is apparent. However, the selectivity of the two specimens is very similar at 60 and 100°C.

Figure 7 shows CO<sub>2</sub> adsorption isotherms for CFCMS specimens 21-11 and 21-2B over the pressure range 0.5-59 bar (8-850 psi), and CH<sub>4</sub> adsorption isotherms for the same specimens over the pressure range 0.5-39 bar (8-560 psi). The measured volumetric (Fig. 6) and gravimetric (Fig. 7) adsorption capacities at one atmosphere for both CH<sub>4</sub> and CO<sub>2</sub> are in good agreement

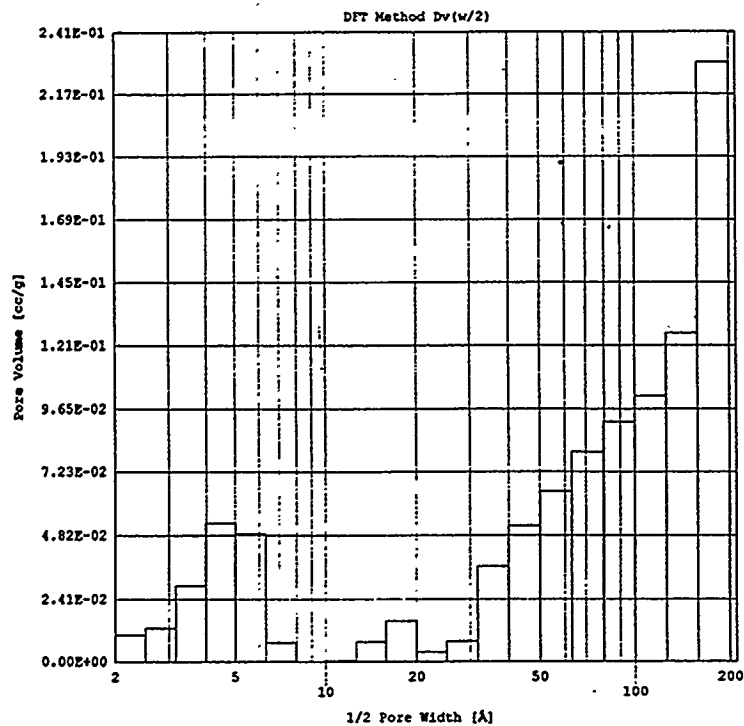


Fig. 3. DFT micropore size analysis of nitrogen adsorption isotherm at 77K on CFCMS (9% burn-off).

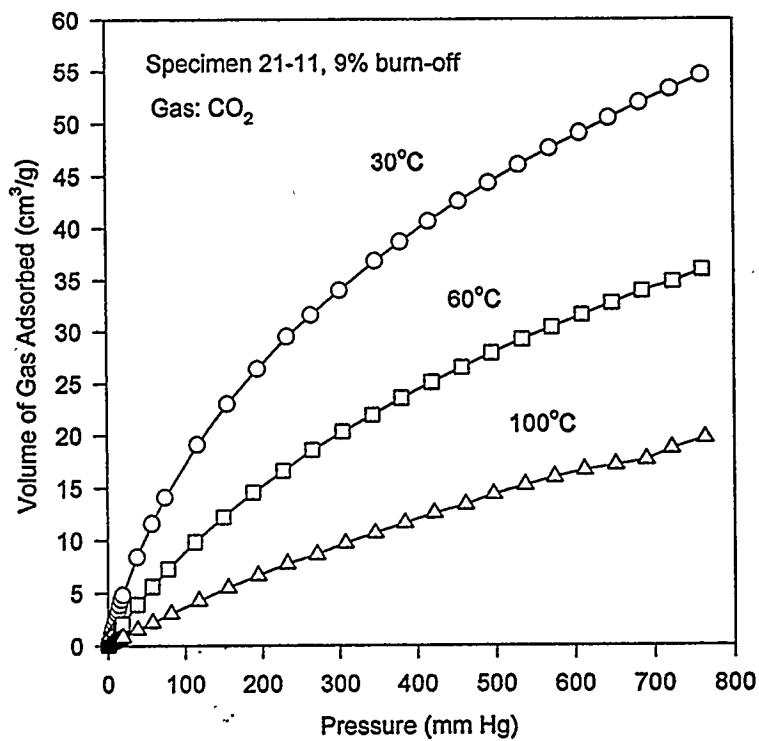


Fig. 4. Carbon dioxide adsorption isotherms at 30, 60, and 100°C on CFCMS (9% burn-off).

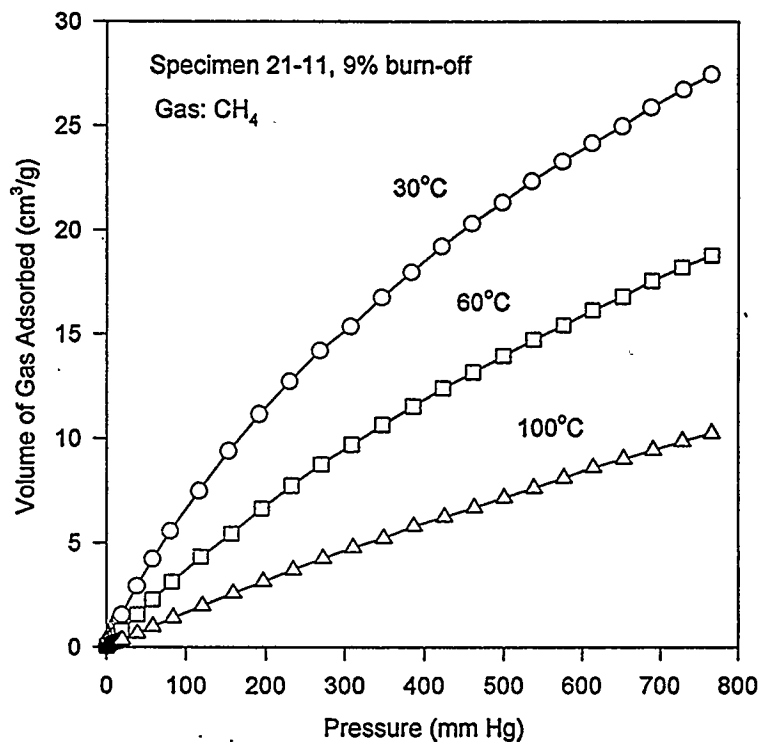


Fig. 5. Methane adsorption isotherms at 30, 60, and 100°C on CFCMS (9% burn-off).

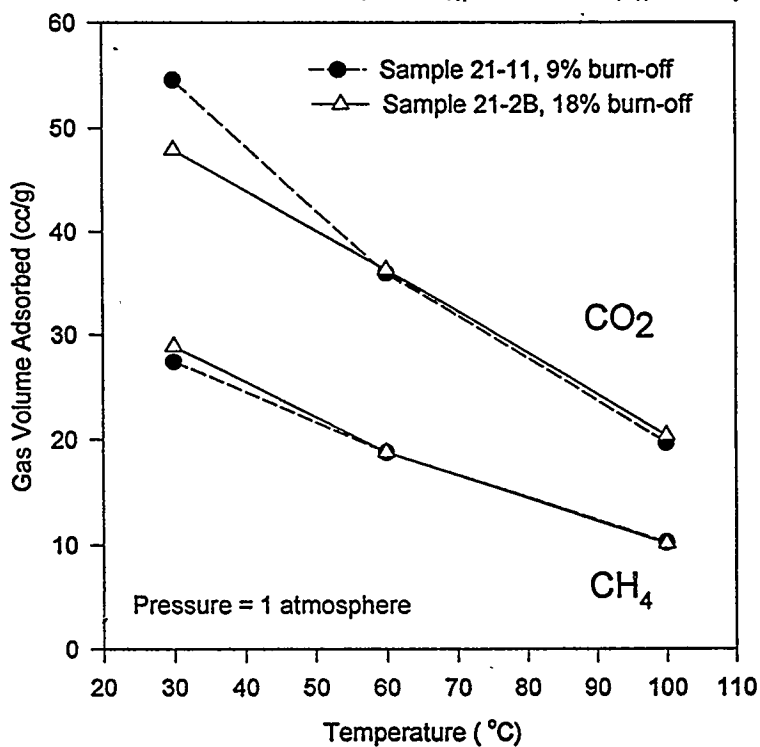


Fig. 6. A comparison of CO<sub>2</sub> and CH<sub>4</sub> gas adsorption for CFCMS at different burn-offs as a function of adsorption temperature.



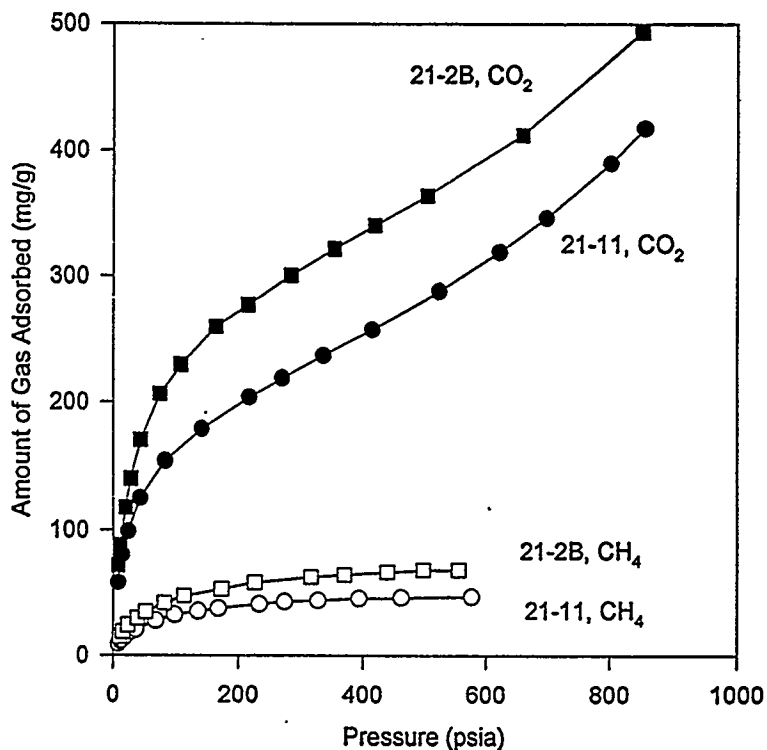
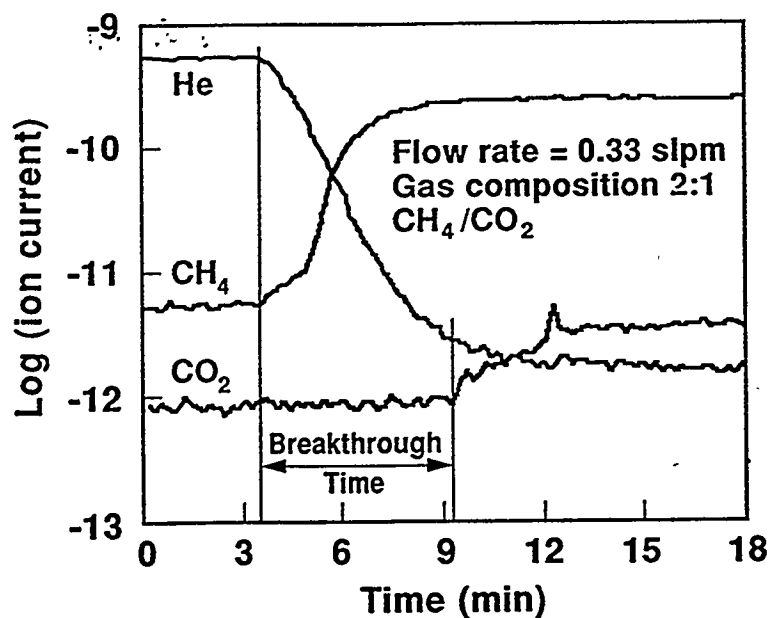


Fig. 7. High pressure  $\text{CO}_2$  and  $\text{CH}_4$  adsorption isotherms on CFCMS.



CFCMS sample 21-11

9% burn-off

BET SA =  $512 \text{ m}^2/\text{g}$

$\text{CO}_2$  adsorption  
capacity: =

Flow rate x  
breakthrough time  
x volume fraction  
of ads. gas

Fig. 8. Typical  $\text{CO}_2/\text{CH}_4$  breakthrough plots on CFCMS sample 21-11 (9% burn-off).

for the CFCMS specimens. At one atmosphere, approximately 100 mg of  $\text{CO}_2$  per g of CFCMS and approximately 19 mg of  $\text{CH}_4$  per g of CFCMS were adsorbed. The quantities of gas adsorbed rose to  $>490$  mg/g ( $\text{CO}_2$  on specimen 21-2B) and  $>67$  mg/g ( $\text{CH}_4$  on specimen 21-2B). Moreover, the  $\text{CO}_2$  isotherms are still increasing with pressure whereas the  $\text{CH}_4$  isotherms have flattened (i.e., the CFCMS has become saturated with  $\text{CH}_4$ ). However, the data in Fig. 7 clearly shows that CFCMS exhibits selective adsorption of  $\text{CO}_2$  over  $\text{CH}_4$ .

The  $\text{CO}_2$  adsorption data discussed above suggests that CFCMS might provide for the effective separation of  $\text{CO}_2$  from  $\text{CH}_4$ . To determine the efficacy of CFCMS for this purpose, several steam activated samples were tested in the breakthrough apparatus (Fig. 1) described previously. A typical breakthrough plot for a  $\text{CH}_4/\text{CO}_2$  mixture is shown in Fig. 8. Any entrained air is initially driven out with a He purge. The input gas is then switched to a 2:1 mixture of  $\text{CH}_4/\text{CO}_2$  at a flow rate of 0.33 slpm. The outlet stream He concentration decreases and the  $\text{CH}_4$  concentration increases rapidly (i.e.,  $\text{CH}_4$  breaks through). Adsorption of  $\text{CO}_2$  occurs and, therefore, the  $\text{CO}_2$  concentration remains constant at a low level for approximately six minutes before the  $\text{CO}_2$  concentration begins to increase, i.e., "breakthrough" occurs. Table 2 reports data from our preliminary study of  $\text{CO}_2$  separation.  $\text{CO}_2$  capacities are reported as determined from pure  $\text{CO}_2$  and  $\text{CO}_2/\text{CH}_4$  mixtures on each specimen examined. The reported  $\text{CO}_2$  capacities are the means of several repeats of the breakthrough experiments, and the BET surface areas are the means of the data reported in Table 1. Two of the CFCMS samples (lowest burn-off) had  $\text{CO}_2$  adsorption capacities of almost one liter on 0.037 liters of adsorbent, and only a small capacity reduction was observed in the  $\text{CO}_2/\text{CH}_4$  gas mixture. The  $\text{CO}_2$  adsorption capacity decreases with increasing burn-off, in agreement with the isotherm data.

#### A Novel Gas Separation System

CFCMS has a continuous carbon skeleton which imparts electrical conductivity to the material. The carbon fibers used in the synthesis of CFCMS have, according to their manufacture, an electrical resistivity of 5 milliohm.cm. Figure 9 is a plot of the current-voltage characteristics of a 2.5-cm diameter, 7.5-cm long CFCMS cylinder. The plot is linear, indicating that in CFCMS electrical conduction obeys ohm's law. At an applied dc potential of one volt, approximately 5 amps flows through the CFCMS. The CFCMS samples electrical resistance is thus 0.2 ohm and the resistivity is 131 milliohm.cm. This resistivity is considerably greater than that of the fibers, and is attributed to contact resistance and the lower electrical conductivity of

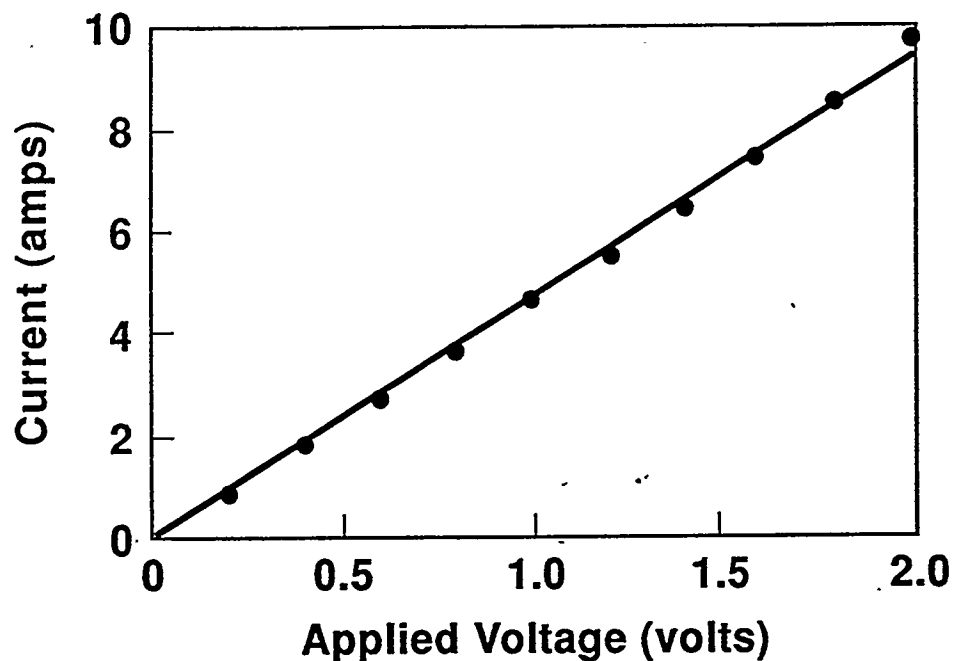


Fig. 9. The current-voltage relationship for CFCMS (sample 21-2B, 18% burn-off, 25-mm diameter x 76-mm length)

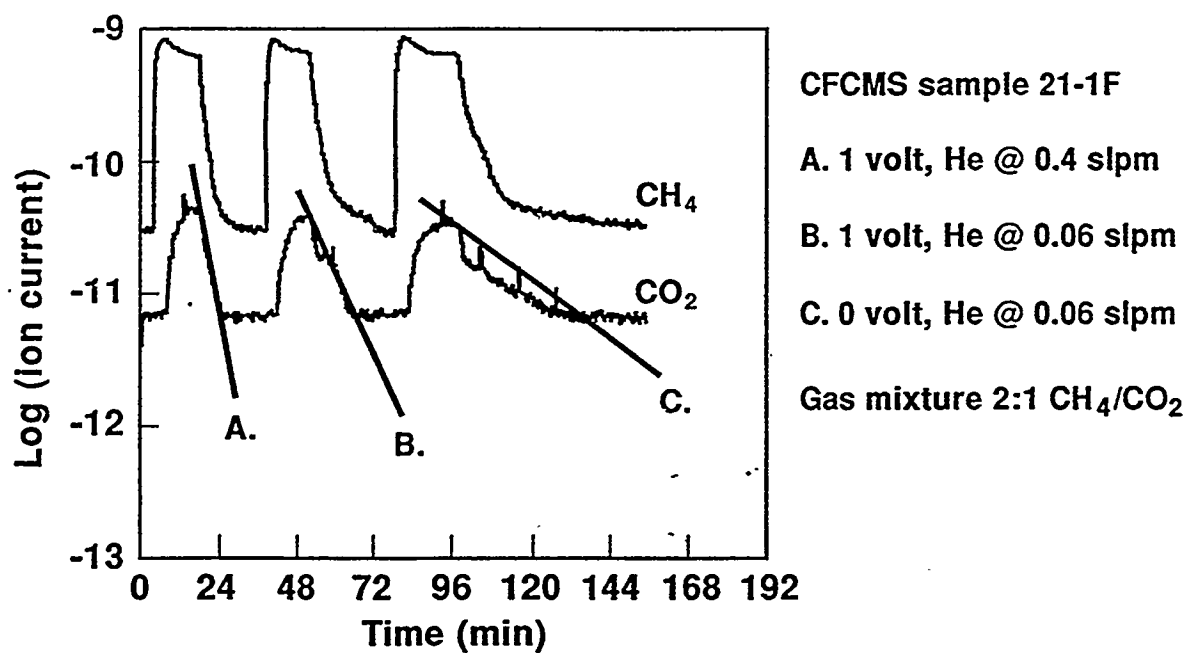


Fig. 10. CO<sub>2</sub>/CH<sub>4</sub> breakthrough plots on CFCMS showing the benefit of electrically enhanced desorption.

the phenolic resin derived carbon binder. A consequence of the passage of an electric current through the CFCMS is a heating effect, which causes the CFCMS to increase in temperature to approximately 50-60°C.

Table 2. CO<sub>2</sub> separation data from our CO<sub>2</sub> and CO<sub>2</sub>/CH<sub>4</sub> breakthrough experiments.

Specimen No.	Burn-off (%)	BET Surface Area (m <sup>2</sup> /g)	CO <sub>2</sub> Capacity (Liters)	
			CO <sub>2</sub> /CH <sub>4</sub>	CO <sub>2</sub> only
21-11	9	512	0.73	0.97
21-2B	18	1152	0.45	0.98
21-2D	27	1962	0.39	0.80
21-2C	36	1367	0.35	0.80

We have utilized the electrical properties of CFCMS to effect a rapid desorption of adsorbed gases in our breakthrough apparatus. The process has been named electrically enhanced desorption, and the benefit of this technique is shown in Fig. 10 where the CO<sub>2</sub> and CH<sub>4</sub> gas concentrations in the outlet gas stream of our breakthrough apparatus (Fig. 2) are shown as a function of time. Three adsorption/desorption cycles are shown in Fig. 10. In the first and second cycles (A and B in Fig. 10) desorption is caused by the combined effect of an applied voltage (1 volt) and a He purge gas. In the third cycle (C in Fig. 10) desorption is caused only by the He purge gas. A comparison of cycles B and C indicated that the applied voltage reduces the desorption time to less than one third of that for the He purge gas alone (cycle C). Clearly, the desorption of adsorbed CO<sub>2</sub> can be rapidly induced by the application of an electric potential. We postulate two explanations for this effect. First, the passage of an electric current through the CFCMS causes an increase in the materials temperature, which in turn thermally excites the adsorbed gas, effecting the desorption. Second, the flow of electrons through the CFCMS disrupts the weak dispersion or polar attractive forces which bind the gas in the micropores. The ability of CFCMS to selectively adsorb CO<sub>2</sub> from a CH<sub>4</sub>/CO<sub>2</sub> mixture, combined with the electrically enhanced desorption of the CO<sub>2</sub>, allow for a gas separation system where the separation is effected by electrical swing, rather than the more conventional pressure or temperature swings.

## CONCLUSIONS

A porous monolithic activated carbon material (CFCMS) has been developed that is strong, rigid, and which overcomes problems associated with operation using granular adsorbents. The open structure of CFCMS results in a permeable material which offers little resistance to the free-flow of fluids. The material has a unique combination of properties, including reasonable compressive strength, electrical conductivity and a large micropore volume.

CO<sub>2</sub> and CH<sub>4</sub> isotherms have been obtained for samples of CFCMS both volumetrically and gravimetrically. At 30°C and atmospheric pressure the CFCMS material has a CO<sub>2</sub> uptake of >50 cm<sup>3</sup>/g (>100 mg/g). The CO<sub>2</sub> uptake is reduced at elevated temperature, and falls to approximately 20 cm<sup>3</sup>/g (40 mg/g) at 100°C. However, the adsorption of CO<sub>2</sub> increases with increasing pressure such that at 58 bar the mass of CO<sub>2</sub> adsorbed increases to >490 mg/g. Similar trends were observed for CH<sub>4</sub> adsorption on CFCMS, except that the adsorption capacity was much less.

A series of breakthrough experiments was performed on CFCMS specimens and their ability to selectively remove CO<sub>2</sub> demonstrated. The unique combination of properties of CFCMS has been exploited to effect the rapid desorption of CO<sub>2</sub> from the materials. It has been shown that for adsorbent configuration reported here a 4-5 amp current flowing under an applied dc voltage of one volt causes a rapid desorption of the CO<sub>2</sub>.

## REFERENCES

1. T. D. Burchell. Carbon Fiber Composite Molecular Sieves, In *Proceedings of Eighth Annual Conference on Fossil Energy Materials*, Oak Ridge, Tennessee, U.S.A., May 1994. ORNL/FMP-94/1, CONF-9405143, pp. 63-70. Pub. Oak Ridge National Lab, U.S.A., August 1994.
2. T. D. Burchell, C. E. Weaver, F. Derbyshire, Y. Q. Fei, and M. Jagtoyen. Carbon Fiber Composite Molecular Sieves: Synthesis and Characterization, In *Poc. Carbon '94*, Granada, Spain, July 3-8, 1994. Pub. Spanish Carbon Group, July 1994.
3. F. Derbyshire, Y. Q. Fei, M. Jagtoyen, G. Kimber, M. Matheny, and T. Burchell, Carbon Fiber Composite Molecular Sieve for Gas Separation. "New Horizons for Materials". *Advances in Science and Technology*, 4. P. Vincenzini (Ed.), pp. 411-417 (1995). Pub. Techna Srl, Faenza, Italy, 1995.

4. G. C. Wei and JM Robbins, Carbon-Bonded Carbon Fiber Insulation for Radioisotope Space Power Systems, *Ceramic Bulletin*, Vol. 64, No. 5, p. 691 (1985).
5. S. Brunauer, P. H. Emmett and E. Teller, *J. Am. Chem. Soc.*, Vol. 60, p. 309 (1938).
6. R. C. Bansal, J-B Donnet and F. Stoeckli, *Active Carbon*, Pub. Marcell Dekker, Inc., New York (1988).
7. T. D. Burchell, J. W. Klett and C. E. Weaver, A Novel Carbon Fiber Based Porous Carbon Monolith, In *Proceedings of Ninth Annual Conference on Fossil Energy Materials*, Oak Ridge, Tennessee, U.S.A., May 1995. ORNL/FMP-95/1, CONF-9505204, pp. 447-456. Pub. Oak Ridge National Lab, U.S.A., August 1995.
8. T. D. Burchell and R. R. Judkins, *Energy Convers. Mgmt* Vol. 37, Nos. 6-8, pp. 947-954, 1996.
9. S. J. Gregg and K. S. W. Sing, *Adsorption, Surface Area and Porosity, 2nd Edition*, Pub. Academic Press, San Diego, CA (1982).

## SESSION II

# CERAMICS, NEW ALLOYS, AND FUNCTIONAL MATERIALS





OXIDATION-RESISTANT INTERFACE COATINGS FOR SiC/SiC COMPOSITES

D. P. Stinton, E. R. Kupp, J. W. Hurley and R. A. Lowden

Oak Ridge National Laboratory  
P. O. Box 2008  
Oak Ridge, TN 37831-6063

S. Shanmugham and P. K. Liaw

University of Tennessee  
427b Dougherty Engineering  
Knoxville, TN 37922

### ABSTRACT

The characteristics of the fiber-matrix interfaces in ceramic matrix composites control the mechanical behavior of these composites. Finite element modeling (FEM) was performed to examine the effect of interface coating modulus and coefficient of thermal expansion on composite behavior. Oxide interface coatings (mullite and alumina-titania) produced by a sol-gel method were chosen for study as a result of the FEM results. Amorphous silicon carbide deposited by chemical vapor deposition (CVD) is also being investigated for interface coatings in SiC-matrix composites. Processing routes for depositing coatings of these materials were developed. Composites with these interfaces were produced and tested in flexure both as-processed and after oxidation to examine the suitability of these materials as interface coatings for SiC/SiC composites in fossil energy applications.

### INTRODUCTION

Continuous fiber ceramic matrix composites require fiber/matrix interfaces which allow load transfer from the matrix to the fibers when the composite materials are stressed. Crack deflection and fiber pullout are also necessary components of the mechanical behavior of composites. Fiber/matrix interfaces are currently one of the weak links in continuous fiber ceramic matrix composites materials for applications in the oxidative environments which are typical of fossil energy applications. Pyrolytic carbon performs well as an interfacial coating for Nicalon fiber-reinforced silicon carbide-matrix composites, however its use in fossil energy applications may be limited because of its poor oxidation resistance. If stressed above the point where the matrix cracks, air can penetrate into the composites and oxidize the fiber/matrix interfaces. After very short times the composite's mechanical properties suffer and eventually the material becomes brittle.<sup>1</sup> Alternate interface coatings need to be developed that are chemically stable with respect to the fiber and matrix materials, and thermally stable and oxidation resistant at use temperatures.

Shanmugham et al<sup>2</sup> conducted FEM analysis and reported that a low modulus interfacial coating will be effective in reducing the radial stresses that result on cooling to room temperature from processing temperature. Further, for interfacial materials with the same modulus, a material with

a higher thermal expansion coefficient than that of the fiber and the matrix may be more effective in reducing the radial stresses than a material with a lower thermal expansion coefficient. These FEM results were similar to the analytical modeling results of Hsueh et al<sup>3</sup>. In order to investigate the above hypothesis, mullite and aluminum titanate were chosen as candidate interface materials for further study.

Another approach being investigated is to deposit a modified form of SiC in the interface. This idea was described previously by Lowden et al<sup>4</sup>. In a SiC fiber/SiC matrix composite, such an interface would be chemically and mechanically stable and as thermally stable as the other components of the composite. The modified SiC, amorphous in this case, would have a relatively low modulus to encourage crack propagation at the fiber/matrix interface.

### EXPERIMENTAL PROCEDURE

Composite preforms were prepared by stacking discs of ceramic-grade Nicalon<sup>TM</sup> plain-weave cloth (Nippon Carbon Company, Tokyo, Japan) in a 0/30/60 sequence in graphite holders. After immersing the preforms in acetone to remove the fiber sizing they were ready for interface coating deposition. The oxide interface coatings were deposited by a sol-gel process described previously<sup>5</sup>. Thin CVD carbon films were deposited on most samples on the fibers and/or on the interface coating prior to matrix infiltration. These films were not thick enough to act as effective interface coatings, but their purpose is simply to protect the samples from the corrosive CVD environment. Carbon deposition conditions were:

Temperature: 1100°C  
 Pressure: ~1-2 kPa  
 Time: 15 min  
 Gas flows: 25 cm<sup>3</sup>/min C<sub>3</sub>H<sub>6</sub>  
 500 cm<sup>3</sup>/min Ar.

The amorphous SiC interface coatings were also deposited by CVD, but at varying conditions. Only the pressure was held constant, at atmospheric pressure (101 kPa). The reaction gases in this case were methane (CH<sub>4</sub>), methylsilane (CH<sub>3</sub>SiH<sub>3</sub>) and Ar.

The composites were infiltrated using forced flow chemical vapor infiltration. In this process, described in detail by Stinton et al<sup>6</sup>, the gases are forced to flow through the preform under temperature and pressure gradients. When the pressure gradient reaches 200 kPa, the furnace automatically shuts off and the gas flows are stopped. The reactants used are 0.3 cm<sup>3</sup>/min methyltrichlorosilane (MTS, CH<sub>3</sub>SiCl<sub>3</sub>) and 500 cm<sup>3</sup>/min hydrogen. The top temperature of the preform holder is maintained at 1200°C and the pressure downstream of the part is 101 kPa.

## RESULTS AND DISCUSSION

### Sol-Gel Oxide Interface Coatings

Mullite and aluminum titanate precursor sols were developed for coating applications. The high temperature X-ray diffraction (HTXRD) study conducted on the precursor gels revealed that mullite and aluminum titanate formed at 1050°C and 1400°C, respectively. Based on the HTXRD results, it could be concluded that the aluminum titanate formation temperature is too high and would degrade Nicalon fibers. Since mullite forms at 1050°C, it was predicted that a mullite coating could be obtained on Nicalon fibers without damaging the fibers.

The developed mullite and aluminum titanate precursor sols were utilized for coating Nicalon tows and fabrics. Nicalon tows dipcoated in the mullite precursor sol and heat treated at 1000°C for 10 h, and cooled to room temperature broke easily during handling. In contrast, Nicalon tows dipcoated in the aluminum titanate precursor sol and heat treated similarly were relatively easy to handle. It should be noted that only an alumina and titania mixture would form on Nicalon fibers at 1000°C. Since alumina-titania did not damage the Nicalon fibers, it was considered as an interface material for further investigation.

A Nicalon/SiC composite with a mullite interface was fabricated, with the mullite (50 nm thick) interface deposited by a sol-gel process. However, the composite exhibited brittle fracture, and this could be attributed to the degradation of the Nicalon fibers during the sol-gel processing of mullite. In order to avoid damage to the fibers during the sol-gel processing of the oxide, the need to apply a thin carbon coating (inner carbon layer) prior to the deposition of an oxide coating deposition was recognized. Thermodynamic modeling studies indicated that oxide coatings would be attacked by HCl, a by-product of the SiC matrix formation reaction. It was surmised that a thin carbon coating (outer carbon layer) deposited on the oxide coating prior to the SiC matrix infiltration may help prevent the HCl attack. It should be noted that these carbon coatings are too thin to act as effective interfaces on their own.

In order to get a better understanding of the type of interface that would be appropriate to pursue, Nicalon/SiC composites with the following interfaces were considered: An oxide/C interface and a C/oxide/C interface. The composite with an oxide/C interface would identify the degradation of Nicalon fibers, if any, that might occur during the sol-gel processing of the oxide, because the oxide coating is directly applied on the fibers in this case. The composite with a C/oxide/C interface is likely to have better mechanical properties than a composite with a C/oxide interface, since the likelihood of the fiber degradation taking place during the sol-gel processing of the oxide is reduced due to an inner carbon layer.

The flexure strength results of Nicalon/SiC composites with four different interfaces are summarized in Table 1. The standard deviation of the flexure strength measurements for all the cases

was less than 25%. For the first two cases, it should be noted that there was no inner carbon layer, while the last two composites had an inner carbon layer between the fiber and the oxide. Twenty four flexure bars of approximately 2.5 x 3.0 x >33 mm dimensions were cut from each of the composites. The four-point bend testing was conducted either with inner and outer spans of 10 mm and 20 mm, or 10 mm and 30 mm, respectively. Twelve flexure bars of each of the composites were tested in the as-processed condition. For composites with low strength (< 150 MPa) in the as-processed condition, the remaining 12 bars were oxidized at 1000°C for 24 h in air, and subsequently tested at room temperature. In the case of composites with moderate or high strength (> 225 MPa) in the as-fabricated condition, the remaining 12 bars were oxidized at 1000°C in air as follows: 6 bars for 24 h, 3 bars for 200 h, and 3 bars for 500 h.

From Table 1, it is evident that composites with out an inner carbon layer had low flexure strength (< 122 MPa). The composite with a mullite/C interface had low flexure strengths (< 80 MPa) both in the as-processed and oxidized condition, and underwent brittle failure (no damage-tolerance). In contrast, the composite with an  $\text{Al}_2\text{O}_3$ - $\text{TiO}_2$ /C interface had an average flexure strength of 122 MPa in the as-processed condition, and did not undergo any significant strength reduction on oxidation. Moreover, it displayed damage-tolerant behavior in both the cases.

Table 1. Flexure strength results of Nicalon/SiC composites with four different interfaces

ID#	Interface	Strength (MPa)‡				Fracture Type
		As	Oxidized at 1000°C in air			
		Processed	24 h	200 h	500 h	
1	Mullite/C	64	80	~**	-	Brittle
2	AT*/C	122	112	-	-	Composite
3	C/Mullite/C	304	286	221	217	Composite
4	C/AT/C	255	189	TBT***	TBT	Composite

‡ standard deviation < 25 %

AT\* -  $\text{Al}_2\text{O}_3$ - $\text{TiO}_2$

\*\*\* - not tested

TBT\*\*\*- to be tested

The composite with a C/mullite/C interface had a moderate flexure strength of around 304 MPa as-processed condition and did not have any significant strength reduction after 24 h oxidation. However, the strength dropped to 221 MPa after 200 h oxidation and remained at that level even after 500 h oxidation. In contrast to a composite without an inner carbon layer (mullite/C interface), this composite (with an inner carbon layer) had damage-tolerant behavior in the as-processed condition

and sustained this characteristic even after 500 h oxidation. Fig. 1 shows the load vs displacement curve for samples in the as-processed and after 200 h oxidation for a composite with a C/mullite/C interface. It is evident from the figure that even after 200 h oxidation, the sample displayed a non-catastrophic mode of failure.

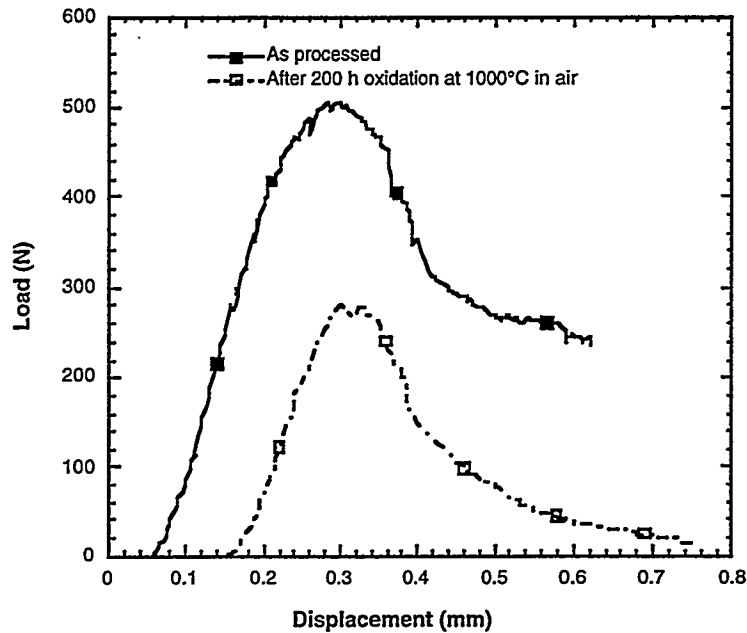


Figure 1. Composite with a Nicalon/C/mullite/C interface exhibit damage-tolerant behavior even after 200 h oxidation at 1000°C in air, but with reduced flexure strength

In the as-fabricated condition, the composite with a C/Al<sub>2</sub>O<sub>3</sub>-TiO<sub>2</sub>/C interface had a higher flexure strength (255 MPa) than the composite with an Al<sub>2</sub>O<sub>3</sub>-TiO<sub>2</sub>/C interface (120 MPa). This situation prevailed even after oxidation for 24 h (200 h and 500 h oxidized samples are to be tested). Similar to the composite with an Al<sub>2</sub>O<sub>3</sub>-TiO<sub>2</sub>/C interface, this composite also exhibited non-catastrophic failure.

Preliminary fracture surface examination revealed that the composite which underwent catastrophic failure showed very little pullout. In contrast, the samples which displayed non-catastrophic failure showed considerable amount of pullout. Scanning auger spectrometer analysis is underway and should identify where the debonding occurred (fiber-coating interface or coating-matrix interface) and the interface coating thickness.

### Amorphous SiC Interface Coatings

Previous work with a modified SiC interface coating in SiC/SiC composites yielded promising oxidation-resistance, but the coatings were generally non-uniform within the part. The primary goal of much of the recent work involving this interface material was to optimize the interface deposition uniformity. Other objectives were to repeat promising processing conditions to assess the reproducibility of the process and run longer term oxidation tests to further assess the stability of the materials in high temperature oxidative environments.

A series of experiments was performed in which the amorphous SiC deposition temperature was varied from 880 to 1000°C. The intent of these runs was to increase the interface coating uniformity by lowering the thermal gradient across the preform. The results of these tests were inconclusive since the flexure strengths were not statistically different in samples coated at different temperatures (see Table 2), although the variability in strengths was generally decreased as the temperature decreased. The load-displacement curves were indicative of materials showing good composite behavior in all cases. Another matrix of experiments was initiated at a deposition temperature of 1000°C in which the total flow of gases as well as the methylsilane and methane concentrations were varied to study their effects on composite uniformity. Increasing the total gas flow and/or concentrations of  $\text{CH}_3\text{SiH}_3$  and  $\text{CH}_4$  appeared to produce composites with less uniform coatings (high standard deviations for strengths and densities). At low flow/low concentration conditions, the composite properties (density, flexure strength and graceful failures) were promising. Strength retention after exposure to air for 24 hours at 1000°C was also good.

Table 2. Density and flexure strength data for composites with amorphous SiC interfaces deposited at temperatures between 880 and 1000°C.

Sample	Deposition Temperature (°C)	Density (g/cc)			Flexure Strength (MPa)		
		Top	Middle	Bottom	Top	Middle	Bottom
CVI947	880	2.63	2.58	2.36	144.2±28.5	334.3±22.1	248.1±35.4
CVI946	925	2.56	2.46	2.25	164.2±71.7	207.9±90.4	221.3±10.3
CVI950	1000	2.60	2.56	1.84	123.1±5.4	229.7±75.8	98.4±4.3

The following set of processing conditions was determined to be optimum after further refinement of the process, combining the best conditions from each set of experiments and additional tests of deposition time:

Temperature - 900°C  
 Pressure - 101 kPa  
 Time - 1 hr  
 Gas flows - 40 cm<sup>3</sup>/min CH<sub>3</sub>SiH<sub>3</sub>  
                   500 cm<sup>3</sup>/min CH<sub>4</sub>  
                   500 cm<sup>3</sup>/min Ar

The optimization was based on the magnitudes and uniformity of density, coating thickness and mechanical behavior (flexure strength and load-displacement curve shape) throughout the parts. Density is a measure of the degree of infiltration, which may be affected by the distribution of the interface coating. Non-uniform distribution may lead to portions of the part sealing before they are fully dense. Flexure testing is used not only as an assessment of the strength and damage tolerance of a material, but also to determine the extent of damage caused by oxidation. The flexure behavior of samples with an amorphous SiC interface coating deposited using the above conditions is illustrated in Figure 2. The composite retained 75% of its strength after being exposed to air at 1000°C for 100 hours. Some of the damage tolerance, or composite-like behavior, was lost during oxidation as evidenced by a faster decline in load-bearing capability past the peak load (i.e. the tail of the curve drops over a smaller displacement). In addition to the optimization of properties at this set of deposition conditions, the composite characteristics were reproducible using these conditions.

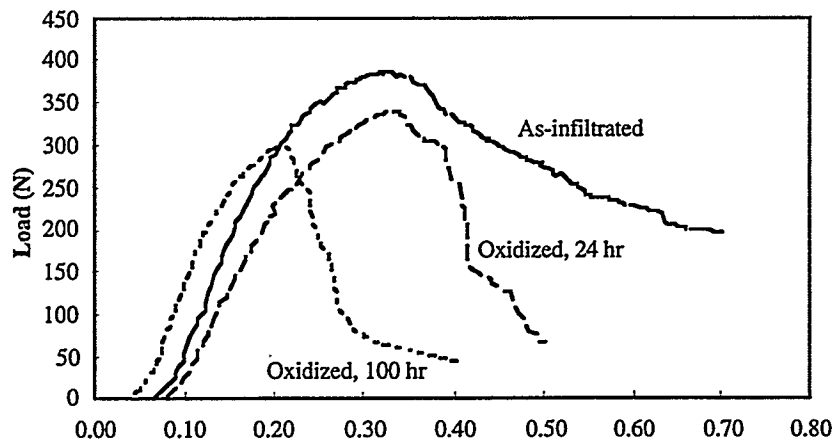


Figure 2. Flexure curves for a SiC/SiC composite (CVI993), with an amorphous SiC interface coating, as-processed and after oxidation for 24 and 100 hours at 1000°C in air.

Additional evidence that the SiC interface coating is effective even after oxidation is seen in Figure 3. This figure contains micrographs of the fracture surfaces of as-infiltrated and oxidized

composite samples. Considerable pullout is apparent in both images, indicating that the interface coating is still acting as the weak point and crack deflection is occurring at the interface.

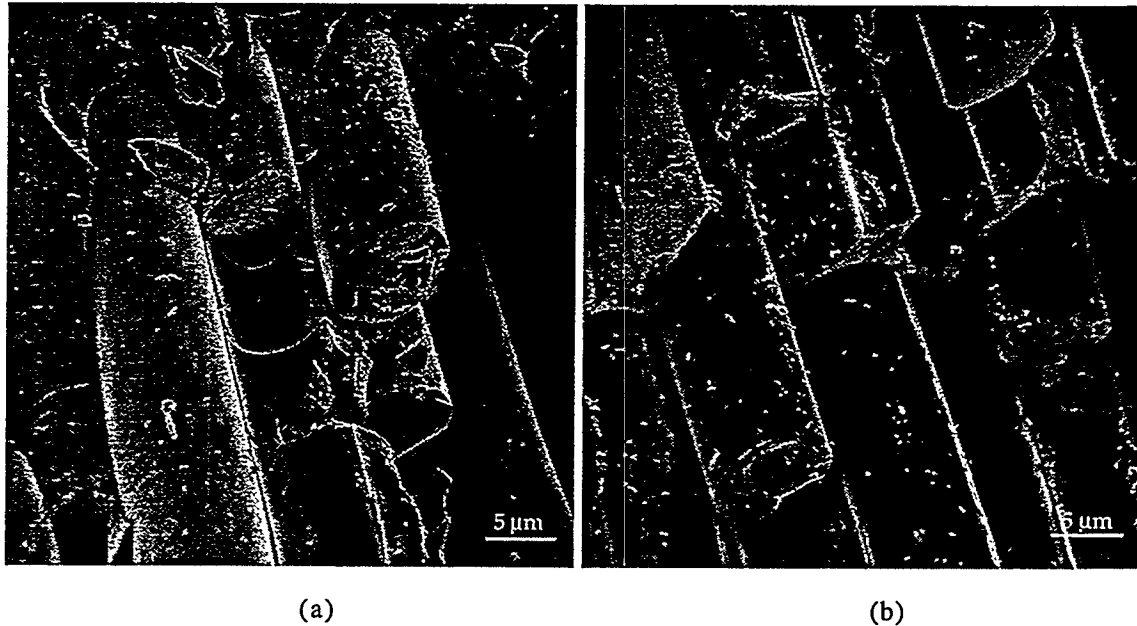


Figure 3. Scanning electron micrographs of a SiC/SiC composite with an amorphous SiC interface coating showing extensive pullout in both (a) as-infiltrated and (b) oxidized (100 hr, air, 1000°C) states.

### CONCLUSIONS

Composites with C/oxide/C interfaces exhibited higher flexure strengths than those of composites with oxide/C interfaces. Among the composites investigated, the composite with a C/mullite/C interface had the highest flexure strength and retained damage tolerant behavior even after 500 h oxidation. Both C/mullite/C and C/ $\text{Al}_2\text{O}_3$ - $\text{TiO}_2$ /C interfaces have good potential as interface materials for Nicalon/SiC composites and long-term oxidation tests need to be conducted to ascertain their potential.

Amorphous SiC also shows potential as an oxidation-resistant interface material in SiC/SiC composites. The deposition process has been optimized to yield a composite that is fairly uniform from top to bottom in terms of density and mechanical behavior. Flexure strengths of 350-400 MPa have been achieved. These materials also exhibit graceful failures characteristic of composite behavior even after oxidation, although a portion of the strength and damage tolerance are lost during oxidation.



## REFERENCES

1. P. F. Tortorelli, S. Nijhawan, L. Riester and R. A. Lowden, "Influence of Fiber Coatings on the Oxidation of Fiber-Reinforced SiC Composites," *Ceram. Eng. Sci. Proc.*, 14 [7-8], 358-366 (1993).
2. S. Shanmugham, D. P. Stinton, F. Rebillat, A. Bleier, T. M. Besmann, E. Lara-Curzio, and P. K. Liaw, "Oxidation-Resistant Interfacial Coatings for Continuous Fiber Ceramic Composites," *Ceram. Eng. Sci. Proc.*, 16 [4], 389-99 (1995).
3. C. H. Hsueh, P. F. Becher, and P. Angelini, "Effects of Interfacial Films on Thermal Stresses in Whisker-Reinforced Ceramics," *J. Am. Ceram. Soc.*, 71 [11], 929-33 (1988).
4. R. A. Lowden, O. J. Schwarz and D. P. Stinton, "Development of Oxidation-Resistant Interface Coatings," pp. 105-116 in the *Proceedings of the Eighth Annual Conference on Fossil Energy Materials*, ed. by N. C. Cole and R. R. Judkins, Oak Ridge, TN, May 10-12, 1994.
5. S. Shanmugham, P. K. Liaw, D. P. Stinton, T. M. Besmann, K. L. More, A. Bleier, W. D. Porter and S. T. Mixture, "Development of Sol-Gel Derived Coatings for Nicalon<sup>TM</sup>/SiC Composites," to be published in *Ceram. Eng. Sci. Proc.*, 17 (1996).
6. D. P. Stinton, A. J. Caputo and R. A. Lowden, "Synthesis of Fiber-Reinforced SiC Composites by Chemical Vapor Infiltration," *Amer. Ceram. Soc. Bull.*, 65 [2], 347-350 (1986).

## ACKNOWLEDGMENTS

"Research sponsored by the U. S. Department of Energy, Office of Fossil Energy, Advanced Research and Technology Development Materials Program and by the U. S. Department of Energy, Assistant Secretary for Energy Efficiency and Renewable Energy, Office of Industrial Technologies, Industrial Energy Efficiency Division and Continuous Fiber Ceramic Composites Program, under contract DE-AC05-96OR22464 with Lockheed Martin Energy Research Corporation"



## MODELING OF FIBROUS PREFORMS FOR CVI FABRICATION

D.Y. Chiang and T.L. Starr

School of Materials Science and Engineering  
Georgia Institute of Technology  
Atlanta, Georgia 30332-0245

The purpose of this program is to alter our existing CVI model to account for configuration changes made to ORNL's tubular forced-flow, thermal gradient CVI. Once these changes are made, the optimal parameters for this configuration are determined to produce high density, gas-tight tubes with short process time. Experimental validation could not be performed due to lack of experimental data because of problems encountered in running the new configuration. Alternative flow patterns show the promise of simpler fixturing and comparable results

### INTRODUCTION

Ceramic matrix composites are very promising materials for future fossil fuel generation technology due to their excellent elevated temperature properties such as strength, thermal shock resistance and thermal conductivity. Many of the applications of ceramic matrix composites in this technology are in the form of tubular shaped elements such as heat exchanger tubes or hot-gas filters. Previous attempts at fabricating these tubes using the forced-flow, thermal gradient chemical vapor infiltration (FCVI) technique developed at Oak Ridge National Laboratory (ORNL) discovered many significant problems. The tube furnace and related fixturing has been redesigned and altered to alleviate some of these problems. The purpose of this program is to alter the existing process model to account for the revised configuration and then to use the model to find sets of optimal processing conditions. Also, an alternative processing scheme, the isothermal, alternating flow configuration is explored.

### SYSTEM CONFIGURATION FOR FREE-STANDING TUBES

The previous ORNL configuration was modeled and reported in the past. [1] Significant changes were made from this configuration because of problems that surfaced

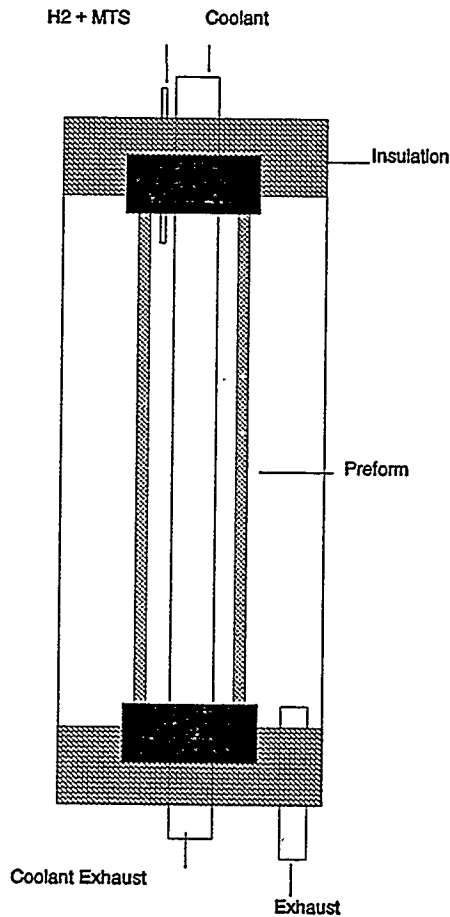


Figure 1: The new ORNL tube CVI configuration utilizes a free standing preform.

during operation. One of the most prominent problems in the original configuration was leakage of the feed gas due to poor fits between the various pieces of graphite fixturing used to hold the preform in place. Also during processing, the tube was cemented to the graphite mandrel used to hold the preform in place. To alleviate these problems, the new configuration shown in Figure 1 is used. This configuration consists of 8 layers of Nextel 312 braided fiber preform that have been rigidized with a phenolic resin to form a free standing preform, eliminating the need for the graphite mandrel. The ends of this preform along with the gas inlet tube and coolant tube are all set into an alumina castable to seal the tube and explicitly define the gas path through the reactor. The inner diameter of the preform is 2 inches with a thickness of 1/4" and a length of approximately 12.6 inches. The control temperature is a

pyrometer that views the outside of the preform. Heating of the reactor is achieved by using small resistively heated graphite rods instead of a large heating element as used previously. The use of the small graphite rods simplified the system by allowing the removal of the reaction chamber that protected the larger heating element from the by-product and waste gases of the reaction.

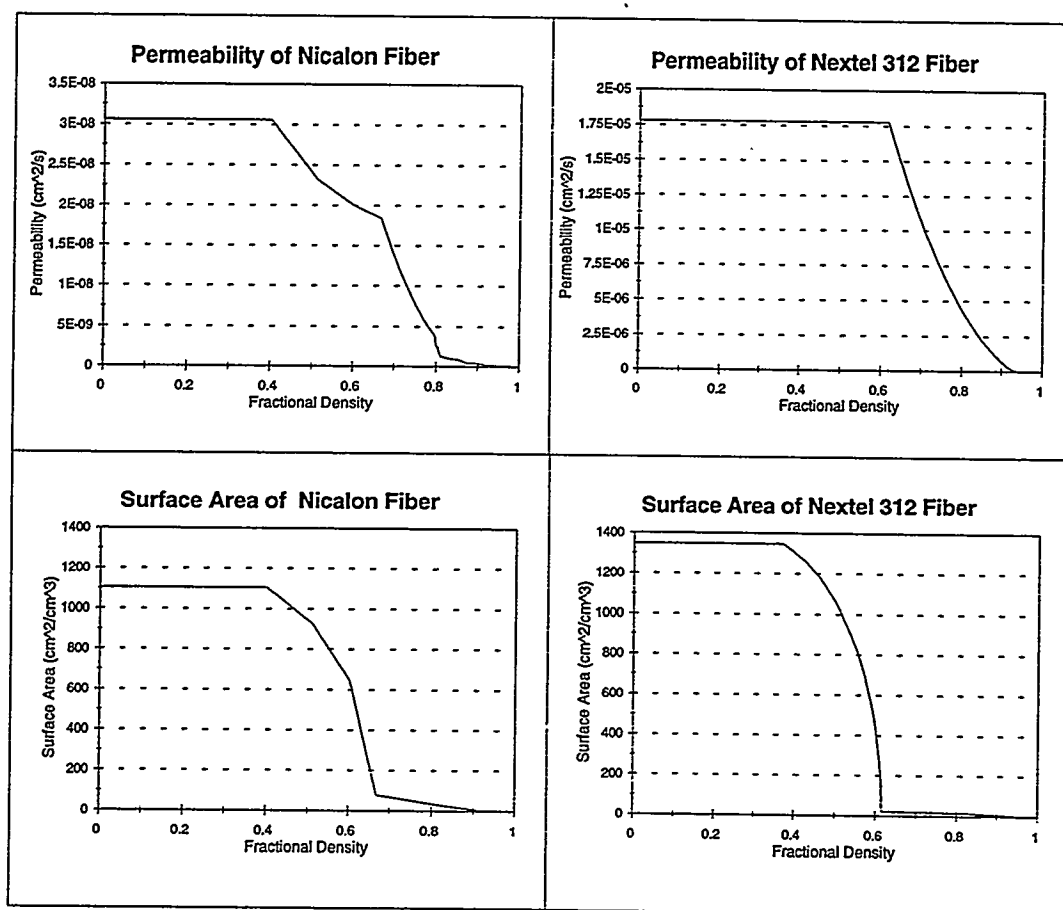


Figure 2: Gas permeability and surface area of Nextel 312 braided preforms are different than those of Nicalon square weave (Note the differences in scale for permeability)

The model used for this optimization process is GTCVI which has been described in previous reports.[2] GTCVI is a first principles based 3-dimensional finite volume process modeling program developed at the Georgia Institute of Technology. A pseudo-steady state model, GTCVI uses the conservation of mass, momentum and energy to solve for temperature, pressure, reactant concentration and densification as functions of time.

To account for the changes in experimental configuration, corresponding changes in the model were performed. First, a model with the corrected dimensions was generated. Then significant changes were made in the preform file to account for the different fiber type and preform construction used. The Nextel 312 fiber has different thermal properties than the Nicalon fibers used in previous experiments. Also, the braided structure of the preform produces different transport properties and surface area curves which are accounted for in the preform file. These differences can be seen in figure 2. Also, due to the change in the location of the control temperature, the model was simplified by moving the boundary condition from the outside of the reactor wall to the outside of the preform. To

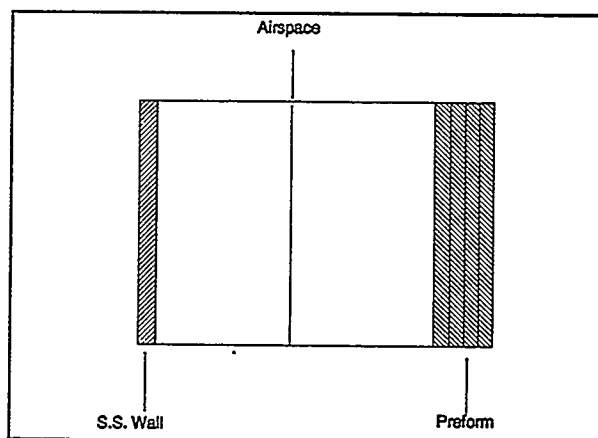


Figure 3: Simplified 1-D model is used for rapid evaluation of a range of process conditions

facilitate initial modeling, only a 1-d slice from the middle of the tube was used. To the extent that the furnace system maintains uniform temperature along the length of the tube, this model is expected to be representative of the whole tube with less computation time.

The model consists of a 1-d, 7 element grid incorporating a stainless steel wall (1 element), airspace (2 elements), and the preform (4 elements) as shown in Figure 3. The inlet gas flows through one end of the reactor at while the exhaust gas flows out the outside diameter of the preform. The controllable variables are the temperatures on the outside of the preform, temperature on the inside of the cooling jacket (stainless steel wall), the total inlet gas flow rate ( $H_2 + MTS$ ) and the MTS concentration in the inlet flow stream.

## PROCESS OPTIMIZATION FOR FCVI

In order to establish optimal conditions for FCVI, a measure of merit was established. The variables of importance are considered to be average density, density gradient, total process time and reagent usage. A process that results in high average density, low density gradient, low total process time and high reagent usage is deemed as optimal. The average density was calculated using a weighted mean to account for differences in volumes of each control volume due to the cylindrical shape of the preform. The density gradient is simply the maximum density minus the minimum density. This was determined to be a sufficient representation of the density gradient since all runs in this design matrix have an almost linear density gradient with the hot side as the maximum and the cool side as the minimum densities. The reactant usage was found by dividing the amount of reactant depleted by the amount input to the system at each time step. An average value over the entire run is used. It is not possible to optimize the system for all of these measures of merit simultaneously; there are inherent tradeoffs among the process characteristics. Different applications may warrant different "optimal" process conditions. For example, if a high mechanical strength is required by the application, then a longer process time can be tolerated. On the other hand, if it is possible to use a lower density part in another application, then significant economic advantages can be gained in process time and efficient reagent usage with a different set of process parameters. Because of this, we have optimized the process for three different situations. In case I high mechanical properties are required so high density and good uniformity are the priorities. Case II emphasizes economical processing with sacrifices made in mechanical strength. Case III is a balance of all four with high density, reagent usage and uniformity, and low process time.

To find the optimal conditions, a 2 level, 4 factor full factorial set of experiments were established. The outside temperature ranged from a high of 1200 °C (the upper limit of fiber stability) to a low of 1000 °C. It was decided that temperatures below 1000 °C would not result in sufficiently rapid densification. Inside temperature ranged from 300-50 °C which corresponds to the use of different cooling media through the center of the reactor such as water, ethylene glycol or air. The total molar flow rate ranged from 1E-6 to 1E-4 (0.8-80 L/min) and the molar concentration of MTS ranged from 5% to 15%. A high concentrations

of MTS may deposit some elemental silicon instead of stoichiometric silicon carbide. The coding and actual values of the different levels used in this matrix of experiments are shown in Table 1. Note that  $F$  = total gaseous flow rate in L/min,  $T(o)$  = temperature on the outside of the preform in  $^{\circ}\text{C}$ ,  $T(i)$  = temperature on the inside of the cooling tube in  $^{\circ}\text{C}$ , and  $C$  = concentration of MTS in the inlet stream in molar percent.

Table 1: Coded Levels and Actual Values

Variable	-	0	+
T (outside) ( $^{\circ}\text{C}$ )	1000	1100	1200
T (inside) ( $^{\circ}\text{C}$ )	50	175	150
Flow Rate (moles/cm <sup>2</sup> s)	800	8000	80000
Concentration (molar %)	0.05	0.10	0.15

## RESULTS

The results from the factorial set of model runs are shown in Table 2 along with the appropriate variable levels used. According to our modeling results, there are no advantages to running at the lower temperature of 1000  $^{\circ}\text{C}$

CASE I: For the highest mechanical strength, the highest density and lowest density gradient through the part are desired. For the range of experimental conditions explored, this results in a high outside temperature and high inside temperature, combined with a low flow rate and low concentration. These conditions result in the highest average density in the test matrix (0.9413%) and the lowest density gradient (0.0092%). The high temperatures allows



Table 2: Modeling Results

T(o) T(i) F C	Time	$\rho$ (avg)	$\rho$ (max)	usage
+ + + +	11.5	0.9155	0.0747	14.7
+ - + +	13	0.9041	0.1020	13.4
+ + - +	38	0.9326	0.0341	40.2
+ - - +	40	0.9316	0.0391	36.5
+ + + -	23	0.9073	0.0909	15.5
+ - + -	25.5	0.9080	0.1008	16.5
+ + - -	83	0.9413	0.0092	54.1
+ - - -	71	0.9219	0.0677	52.5
- + + +	65	0.9246	0.0511	6.5
- - + +	55	0.8887	0.1395	6.0
- + - +	188	0.9363	0.0216	13.6
- - - +	192	0.9240	0.0684	12.8
- + + -	138	0.9312	0.0335	7.8
- - + -	103	0.8913	0.1350	7.1
- + - -	363	0.9310	0.0384	19.0
- - - -	313	0.9287	0.0412	17.9
0 0 0 0	63	0.8983	0.0271	22.8

for a high reaction rate while the low flow rates allows for depletion to balance the temperature gradient through the part resulting in a uniformly densified part. Another advantage of running under these conditions is the low concentration coupled with the high temperature reduces the chance of codeposition of silicon with the SiC matrix. [3] The runtime under these conditions is a fairly long 83 hours.

CASE II: Process optimization from an economic standpoint involves two competing factors. Depending on the relative cost of running a reactor versus reagent costs, the optimal parameters are quite different. If, for example, reagent costs or reagent removal from the waste stream costs are very high, then utilization is the dominant factor in the economic analysis. In this case, conditions should be at high temperatures (inside and out) and low flow rates and concentrations which also gives the most thoroughly densified and uniform part but requires 83 hours to complete. If runtime is more important (factors such as reactor run costs and product throughput), then very aggressive high temperatures, flow rate and concentration can give a 92% dense tube in under 12 hours but results in a low reagent usage rate of 14.7% and a 7X increase in density gradient. Additional runs at even higher flow rates ( $1\text{E-}3$  moles/cm<sup>2</sup> s) produce even faster tube seal-off but results in an extremely large density gradient. These higher flow rates can cut the densification time in half (about 5 hours) but the average density drops to 0.8579% and the gradient is a very large 0.2145%.

Case III balances all factors of interest, optimizing with respect to physical properties as well as economic concerns. The best balance between high density and uniformity as well as low runtime and good reagent usage is high temperatures and concentration while keeping a low flow rate. This results in a 0.9326% dense tube in only 38 hours with a 3X higher density gradient than in case I. Usage is also very good at over 40%.

Also of interest is the effect of the internal temperature. In the past, cooling water at approximately 50 °C has been used to produce the temperature gradient in the part. Other options are using alternative cooling media such as ethylene glycol or air to control the magnitude of the gradient. At the higher preform temperatures (1200 °C), an increase in internal temperature causes an increase in final average density as well as decreases in process time and density gradient. A change from 50 to 300 °C in the internal side of the cooling chamber causes the temperature gradient to drop approximately 35 °C across the preform. The resulting increase in temperature allows for more uniform deposition (decrease in gradient of 0.059%) and higher average densities (increase of 0.019%) at the extremes of flow rate and concentration (high flow and concentration or low flow and concentration). If the hot-side temperature is lowered to 1000 °C and high flow rates are used, the result is more dramatic allowing a significantly higher average density part (increase up to 0.0399%) and a large decrease in the density gradient (decrease up to 0.1015%). It has been shown that the internal

temperature can be quite significant in densification results and should be explored more thoroughly through experimentation.

### ALTERNATING FORCED FLOW CONFIGURATION

In an effort to simplify fixturing and processing of the tubular CVI, an alternative configuration is explored. This configuration is a reversible forced-flow, isothermal process. The idea behind this processing scheme is to isothermally densify the part in one direction which results in a density gradient due to reactant depletion. To compensate for this density gradient, the flow is reversed mid-way through the process. In theory, this should allow for another density gradient in the opposite direction resulting in a uniformly densified part and significant economic savings due to less fixturing and ease of operation.

Table 3: Alternating Forced Flow Results

Process	Time (hrs)	$\rho_{avg}$ (%)	$\rho_{gradient}$ (%)	Usage (%)
Isothermal	24	0.8694	0.1150	55.1
Alternating-isothermal	28	0.9240	0.0366	33.7
Thermal Gradient	38	0.9326	0.0341	40.2

The conditions of case III (high temperatures and concentration, low flow rate) were used. The reactor was set up so that the entire reactor was isothermal at 1200 °C and both the inlet path and outlet were of the same volume. The inlet and outlet were set at diagonally opposed ends. The same molar flow rate was used through both paths which is the same flow rate used in the thermal gradient process. The process was run in the same direction as the thermal gradient configuration for 13 hours, then the direction of the inlet flow was reversed, until completion. As can be seen in Table 3, the alternating flow isothermal process can lead to significant reduction in process time with a small sacrifice in average density and almost no change in the density gradient. Not only does the alternating flow isothermal process reduce

process time, it can significantly decrease cost due to the simplicity of fixturing and the eliminated need for cooling. Because of the ease and cost savings of an isothermal process, the alternating flow scheme has the potential to produce well densified, economic tube shaped CVI parts competitive or even superior to the thermal gradient process.

### SUMMARY

Changes were made to the process model to reflect configuration alterations in ORNL tubular forced-flow thermal gradient CVI process. The optimal conditions for different sets of criteria were determined. It was also determined that a change of cooling fluid which would allow a smaller temperature gradient in the preform can result in higher average densities and better uniformity. A alternative processing configuration, the alternating flow, isothermal process, shows promise in producing high density uniform tubes with short process times and simplified fixturing.

### REFERENCES

1. Starr, T.L., Chiang, D.Y. "Modeling of Fibrous Preforms for CVI Fabrication" Proceedings of the Ninth Annual Conference on Fossil Energy Materials, May 16-18, 1995.
2. Starr, T.L. and Smith, A.W., "Modeling of Forced Flow/ Thermal Gradient Chemical Vapor Infiltration", Oak Ridge National Laboratory Report /ORNL/sub/85-55901/03 (September 1993).
3. Lowden, R.A., et al. "Effect of Infiltration Conditions on the Properties of SiC/Nicalon Composites", Oak Ridge National Laboratory Report /ORNL/TM-10403 (May 1987).

FIBER/MATRIX INTERFACES FOR SiC/SiC COMPOSITES:  
MULTILAYER SiC COATINGS

H. Halverson and W. A. Curtin

Departments of Engineering Science & Mechanics and Materials Science & Engineering  
Virginia Polytechnic Institute and State University  
Blacksburg, VA 24061

ABSTRACT

Tensile tests have been performed on composites of CVI SiC matrix reinforced with 2-d Nicalon fiber cloth, with either pyrolytic carbon or multilayer CVD SiC coatings [Hypertherm High-Temperature Composites Inc., Huntington Beach, CA.] on the fibers. To investigate the role played by the different interfaces, several types of measurements are made on each sample: (i) unload-reload hysteresis loops, and (ii) acoustic emission. The pyrolytic carbon and multilayer SiC coated materials are remarkably similar in overall mechanical responses. These results demonstrate that low-modulus, or compliant, interface coatings are *not* necessary for good composite performance, and that complex, hierarchical coating structures may possibly yield enhanced high-temperature performance. Analysis of the unload/reload hysteresis loops also indicates that the usual "proportional limit" stress is actually slightly below the stress at which the 0° load-bearing fibers/matrix interfaces slide and are exposed to atmosphere.

INTRODUCTION

The performance and long-term durability of ceramic matrix composites for use in Fossil Energy applications relies on the stability of specifically designed fiber/matrix interfacial coatings. Carbon coatings provide the necessary interface properties for low temperature applications, but readily oxidize at elevated temperatures and limit overall composite life. There is thus a critical need for the development of new coatings and coating structures to provide high-temperature performance. Here, the results of tensile tests performed on composites of CVI SiC matrix reinforced with 2-d Nicalon fiber cloth, with either pyrolytic carbon or multilayer CVD SiC coatings<sup>1</sup> on the fibers, are described. To investigate the role and properties of the different interfaces, two types of

measurements are made on each sample: (i) unload-reload hysteresis loops are measured at a sequence of applied loads, and (ii) acoustic emission events are detected during loading. A comparison of the pyrolytic carbon ( $0.4\mu\text{m}$ ) and multilayer SiC coated materials shows the overall mechanical responses to be remarkably similar in detail. The multilayer coatings, which have only very thin intermediary carbon layers, provide the same interfacial debonding and sliding as the standard thicker carbon layers. Careful analysis of the unload/reload hysteresis loops also indicates that the "proportional limit" stress does not correspond to the point at which the  $0^\circ$  load-bearing fibers are exposed to atmosphere, which occurs at a higher stress level. These results also demonstrate that low-modulus, or compliant, interface coatings are not necessary for good composite performance and that complex, hierarchical coating structures may be a direction for development of enhanced high-temperature performance in ceramic composites.

## PHYSICAL AND MECHANICAL PROPERTIES

The materials investigated here are SiC/SiC composites fabricated using ceramic grade Nicalon plain weave fiber mats in a matrix of SiC deposited by a Chemical Vapor Infiltration technique. The differences between materials lies in the specific fiber/matrix "coatings" used. One set of samples has fibers coated with  $0.4\mu\text{m}$  of pyrolytic CVD-deposited Carbon, which is the "standard" coating for SiC/SiC composites; these samples will be designated as PyC. A subsequent CVI deposition of the remaining SiC matrix material is performed after the coating deposition. The other set of samples has multilayer coatings consisting of alternating layers of SiC and PyC. The PyC layers are only  $\approx 0.02\mu\text{m}$  in thickness while the SiC layers begin at  $0.125\mu\text{m}$  at the inner (fiber) radius and increase in thickness by a factor of 1.25 as successive coatings are applied; these samples will be designated as ML. The graded "coatings" extend continuously outward until the material is fully densified; the "matrix" is thus a sequence of concentric annuli of SiC separated by very thin layers of Carbon. The fiber loadings and densities of the two sets of materials are shown in Table I.

The samples described above were supplied as tensile bar specimens of approximately 5 inches in length (aligned with one of the two orthogonal fiber directions),  $1/2$ " inches in width, with a thickness of about  $1/8$ ". Fiberglass end tabs were applied with epoxy and strain gauges mounted in the center of an approximately 1" gauge section. The

samples were then subjected to interrupted tensile tests; samples were loaded in tension to peak stresses of 10, 15, 20, 25, and 30 ksi, and then unloaded and reloaded to measure the hysteretic response at each load level. Acoustic emission signals were detected using a standard AE transducer set-up and an attenuator.

The results of the tension tests are partially summarized in Table I. The initial small-strain Young's moduli of the ML materials are smaller than those of the PyC materials, but this is largely attributable to the lower density and higher fiber loading, since the fibers are less stiff than the CVI-SiC matrix. The "proportional limit", or matrix-cracking point, is estimated by using an 0.005% offset stress and is also shown in Table I. The ML materials have a lower offset stress, suggesting a lower matrix cracking threshold; however, we will discuss carefully below the onset of matrix cracking in the 0° fiber tows. The tangent modulus near failure is observed to be larger for the ML materials. Since after matrix cracking the modulus is fiber-dominated, this result is generally consistent with the higher fiber longitudinal loading of the ML materials, although even after normalization by  $V_f/2$  the ML materials are stiffer. The additional stiffness could stem from incomplete "matrix cracking" or reduced fiber damage at failure; the former is more likely the reason, as will be seen by other comparisons. The ultimate tensile strengths (UTS) of the two materials are very nearly equal when normalized by  $V_f/2$ , indicating that the in-situ strengths of the as-processed fibers are essentially comparable. However, the failure strains of the ML materials are generally larger by about 10%, while equal fiber strengths would suggest that the failure strain should be consistent with the failure strength.

Table I. Physical and mechanical property data for SiC/SiC composites with pyrolytic carbon (PyC) and multilayer SiC (ML) fiber coatings, respectively.

	Dens g/cc	Fiber loading $V_f$	Youngs modulus $E_c$ (Msi)	Final Tan modulus $E_t$ (Msi)	Tensile Strength $\sigma_{uts}$ (ksi)	$2\sigma_{uts}/V_f$ (ksi)	Failure Strain (%)	.005% Offset Stress
PyC	2.55	0.30	35	3.2	$\approx 30$	200.0	$\approx 0.4$	15.5
ML	2.45	0.36	30	4.4	$\approx 35$	194.4	$\approx 0.45$	11.0

Figures 1a,b show the tensile stress-strain curves and hysteresis loops obtained for two specific but representative samples of the ML and PyC materials. These curves

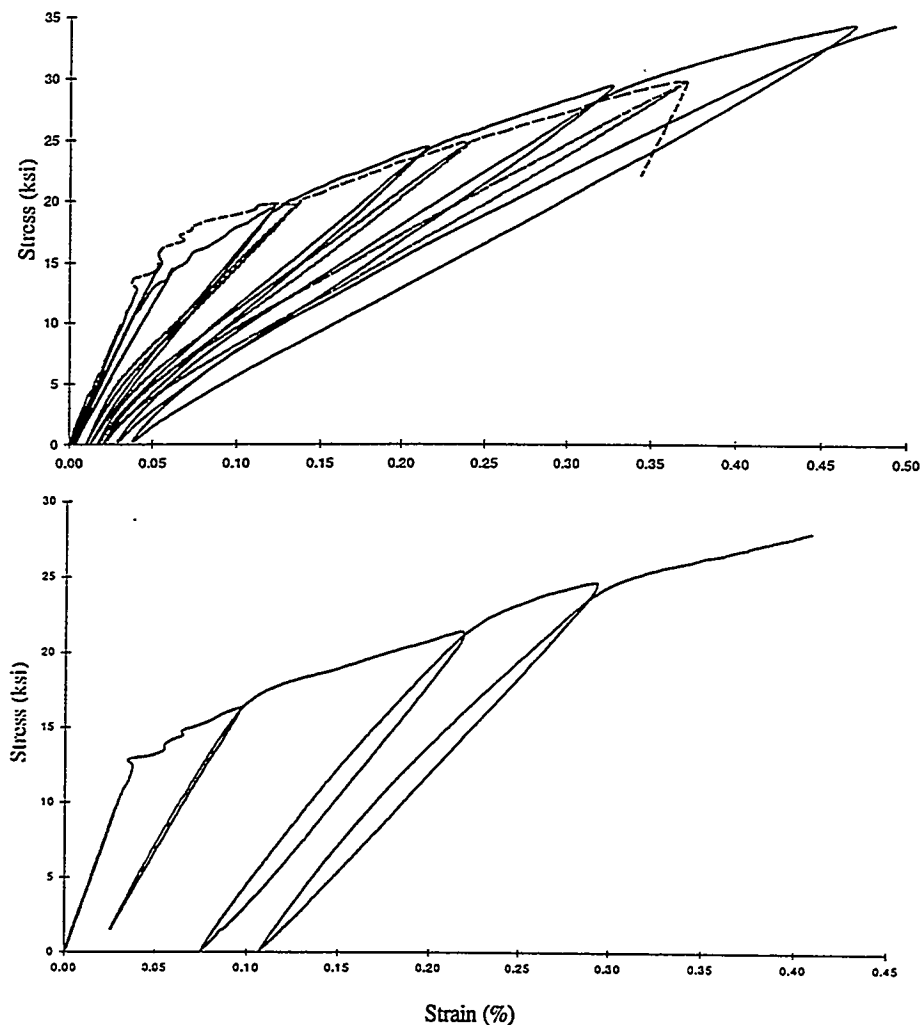


Figure 1. Stress-strain and hysteresis loops for SiC/SiC composites. Solid line - ML; dashed line - PyC Type I; dotted line - PyC Type II.

exhibit some of the general features discussed above and tabulated in Table I. However, they also show other features of interest. In particular, the PyC materials appear to fall into two classes, depending entirely on the hysteretic behavior. In one class (Type I; Figure 1a), the hysteresis loops are fairly narrow and the residual strain on complete unloading is small. In the other class (Type II; Figure 1b), the hysteresis loops are much broader and the residual strain is much larger; this behavior is more similar to that described recently by Lamon and coworkers for SiC/SiC materials.<sup>2</sup> The hysteretic behavior is an indicator of both extent of cracking and (irreversible) interfacial sliding between fibers and coating (or coatings and matrix) and thus highlights qualitative



differences in the interfacial behavior that are not evident from the stress-strain loading curves alone. The ML samples are almost all of the Type I class, with narrow hysteresis loops and small residual strains. The agreement in mechanical response between the PyC Type I materials and the ML materials is quite remarkable, given the rather different interface coatings in the two systems.

### MATRIX CRACKING THRESHOLDS

The onset of matrix cracking and "debonding" of the fibers from the matrix or coating is of critical importance in applications of CMCs wherein chemical attack/oxidation of the exposed interfaces can rapidly degrade mechanical properties. The use stress at temperature is thus considered to be below the matrix cracking threshold. Superficially, it would appear that the ML materials are inferior in this regard because the 0.005% offset stress is rather lower than that for the PyC materials. However, what is really of importance is the exposure of the 0° fiber interfaces and not the macroscopic non-linear deformation represented by the offset stress. In fact, early non-linear behavior can be beneficial in toughening or notch resistance of CMCs, as a mechanism of stress redistribution around stress concentrators. Here, we take a more careful look at the mechanical response around the matrix cracking threshold.

The onset of non-linearity can be associated with (i) pure crack formation in the matrix material and not in the fiber tows, or (ii) crack penetration into the fiber tows, followed by debonding at one of the coating interfaces. To assess which mechanism might be operative at a particular stress level, one must examine the hysteretic behavior of the material to look for irreversible response. Matrix cracking alone will lead to increased composite strain and a decreased composite modulus but will not yield either a residual strain (aside from very small relieved thermal residual strains) or hysteretic response associated with irreversible energy dissipation mechanisms such as interfacial sliding. Debonding at the fiber coating and subsequent fiber sliding does lead to both permanent strains and irreversible sliding and hysteresis. In fact, the hysteretic behavior is now regularly used to determine the fiber/matrix interfacial sliding resistance in unidirectional composites.<sup>3</sup>

Figure 2 shows the permanent offset or residual strain as function of applied load for both ML and PyC materials. Figure 3 shows the hysteresis loop area as a function of applied load for both ML and PyC materials. At the lowest stress of 10 ksi, the ML materials exhibit essentially no residual strain although there has been some non-linear deformation. The ML materials also exhibit essentially zero hysteresis, as measured by the loop area, at 10 ksi. Only at 15 ksi and above is there measurable residual strain and hysteresis. In comparison to the PyC materials, the ML materials are nearly identical to the Type I PyC materials at all applied loads, whereas the Type II materials show the rapid increase in residual strain and hysteresis evident in the typical stress-strain curve of Figure 1. The presence of non-linearity in the deformation of the ML materials at 10 ksi is therefore attributed matrix material cracking external to the  $0^\circ$  fiber tows, which would not expose those fibers and the interfaces to potential degrading atmospheres. The enhanced matrix damage at such low stresses probably arises from the multilayer nature of the ML "matrix" material. Additional flaws in the multilayer structure plus the blunting or deflection of matrix cracks at matrix interfaces generated by the ML matrix structure can cause enhanced "microcracking" in the matrix alone at low stresses. Only at elevated stresses do the more traditional matrix cracks extending into the  $0^\circ$  fiber tows appear, which gives rise to the residual strain and hysteresis behavior.

From the detailed comparison between ML and Type I PyC samples, we conclude that these two materials have nearly identical interfacial sliding characteristics, at least to the extent that such characteristics impact the macroscopic material mechanical response. This conclusion is rather surprising. It is well established that composite behavior in SiC/SiC materials with PyC coatings is not obtained when only thin coatings are utilized; coatings greater than about  $0.25\mu\text{m}$  are necessary to obtain debonding, sliding, and tough behavior. One of the prevailing arguments for the need for a minimum thickness is that the low-modulus PyC coating reduces the thermal and processing clamping stresses between fibers and matrix, which also then reduces the friction stress between fiber and matrix. Composites with high friction and/or debond stresses, as measured by pushout experiments for example, can be particularly brittle. The present results indicate that substantial amounts of PyC are *not* necessary for obtaining good composite behavior. The present ML materials have multiple layers of very thin carbon coatings, but at ever increasing radii, and these coatings in total are insufficient to mimic the effects of one thick PyC coating of  $0.4\mu\text{m}$ . At 60% fiber fraction in the tows and a fiber radius of  $7.5\mu\text{m}$ , 8 layers of increasing SiC coating are needed to densify the tow and the total carbon

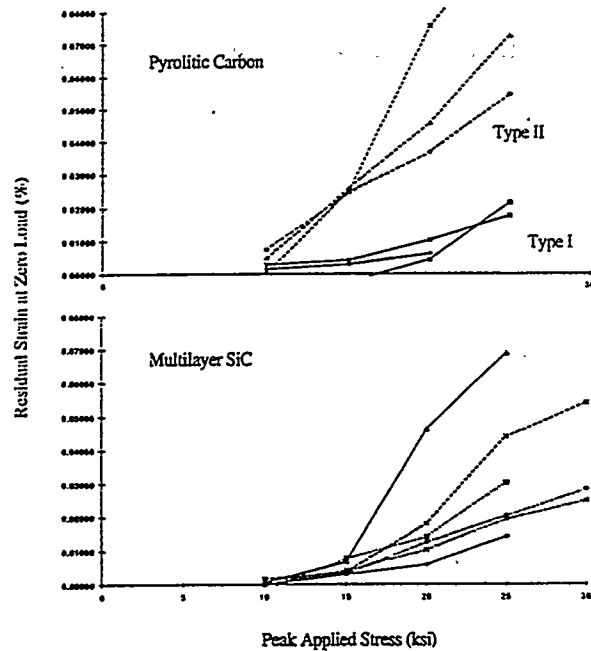


Figure 2. Residual strain at zero load versus peak applied load, for both ML and PyC SiC/SiC composites. Note the absence of residual strain in the ML samples at 10 ksi, and close similarity of ML and PyC Type I data.

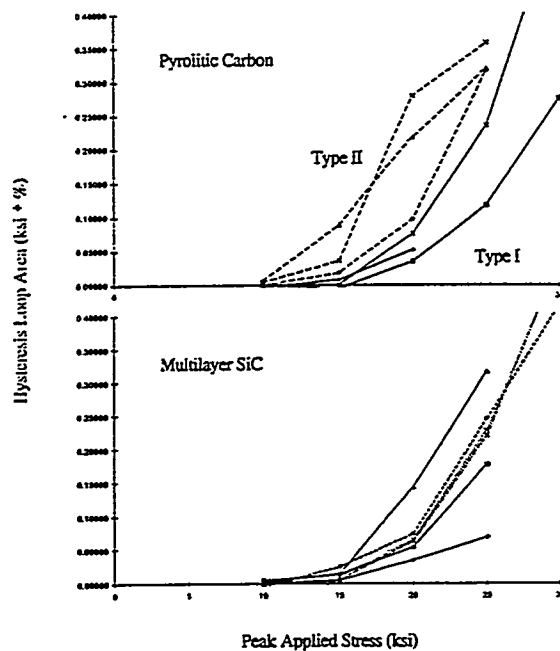


Figure 3. Hysteresis loop area versus peak applied load, for both PyC and ML SiC/SiC composites. Note the complete absence of hysteresis in the ML samples at 10 ksi despite non-linearity in the stress-strain curve prior to this stress.

deposition is then approximately  $0.16\mu\text{m}$ . Hypertherm High-Temperature Composites Inc. has reported similar composite performance results for ML systems with only 2 or 4 SiC layers prior to a full densification infiltration, as well.<sup>4</sup> *The conceptual mechanism of reduced clamping stress from a low-modulus coating may be a sufficient design principle for coating structures but is not necessary for good composite performance. Complex coating structures can accomplish the needed goals of crack debonding and acceptable sliding resistance without low modulus.* These conclusions are consistent with recent multilayer SiC coating developments for the SEP SiC/SiC materials, which have been reported to exhibit composite behavior by Lamon et al. and others.<sup>2</sup>

### ACOUSTIC EMISSION

We have monitored the acoustic emission from samples during loading, unloading, and reloading. Results for the number of emission events (hits) versus applied strain are shown in Figure 4 for a PyC Type II and a ML material, along with the associated stress-strain behavior. The ML materials show much greater acoustic activity than the PyC materials, starting at very low loads. The large amount of activity at low loads is consistent with the conceptual picture of extensive microcrack formation in the matrix prior to full matrix crack development. The AE signals are attributable to the matrix cracking, and it is evident that the peak AE coincides quite well with the dominant knee in the stress-strain curves, where considerable matrix cracking is driving the increasing strain in the material. In the ML materials, the peak in AE events occurs in the range of 15-20 ksi and then falls off gradually, but AE events are detected all the way up to failure in nearly all cases. In the PyC samples, the AE peak is at lower stresses, again around the knee in the stress-strain curve, but the AE events then die away rapidly with further loading, indicating a saturation of cracking. The rapid attainment of a nearly linear stress-strain curve in the PyC materials and the more gradual approach to a constant tangent modulus in the ML materials is consistent with the occurrence of broadly distributed matrix cracking in the ML materials. The greater number of events in the ML materials is attributable to the complex matrix/coating structure which favors the blunting of larger cracks in favor of a multiplicity of smaller cracks in the layered structure. The precise

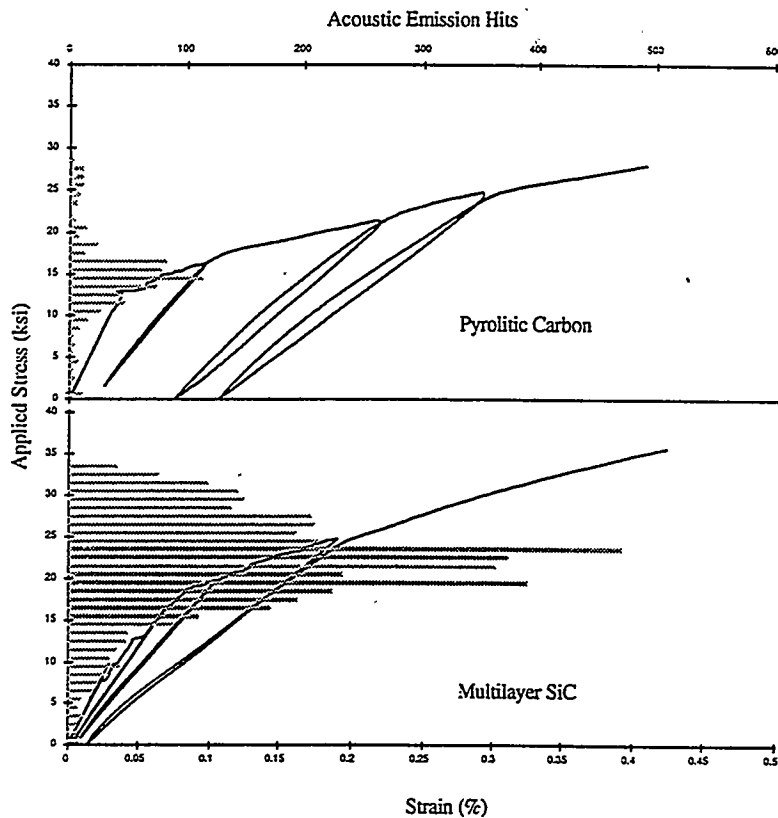


Figure 4. Acoustic emission counts versus strain, with superimposed stress-strain behavior, for typical ML and PyC Type II samples.

nature and number of AE events does not appear to have large effects on the overall deformation history, but is of interest in comparing different materials.

We have attempted to analyze the AE signals in detail to distinguish between matrix cracking and fiber breakage. However, all correlations between signal characteristics such as rise time, amplitude, duration, and energy are the same over the entire loading history. There are no simple signatures in the AE signals which suggest matrix cracking at lower loads giving way to fiber breakage at elevated loads.

Lastly, essentially all of the AE activity occurs on loading of the samples. On unloading and reloading no further AE events are detected until the load is increased beyond the prior peak load. This demonstrates the absence of any pronounced fatigue crack propagation during the measurement of the hysteresis behavior.

## SUMMARY

In summary, we have presented experimental data on the mechanical response of SiC/SiC composites with novel multilayer SiC coatings, and compared their response to that of standard composites with pyrolytic Carbon coatings. The mechanical response is nearly identical in the two cases, including subtle aspects such as hysteretic unload/reload behavior. The early onset of non-linearity in the ML materials is not attributed to full matrix cracking, with exposure of fiber/matrix interfaces, and hence the use of a simple proportional limit stress for assessing composite use stress is probably conservative. Detailed study of the hysteretic behavior appears to help identify the onset of fiber/matrix sliding behavior. The data on ML materials demonstrates that thick low modulus coatings are not necessary for obtaining composite behavior in SiC/SiC materials, which opens new avenues for the development of potential oxidation-resistant, high temperature coatings.

## REFERENCES

1. Generously supplied by Hypertherm High Temperature Composites Inc., Huntington Beach, CA.
2. C. Droillard and J. Lamon, J. American Ceramic Society 79, 849 (1996).
3. E. Vagaggini, J. M. Domergue, and A. G. Evans, "Relationships between Hysteresis Measurements and the Constituent Properties of Ceramic Matrix Composites: I, Theory", J. Am. Cer. Soc. 78, 2709 (1995); J. M. Domergue, E. Vagaggini, and A. G. Evans, "Relationships between Hysteresis Measurements and the Constituent Properties of Ceramic Matrix Composites: II, Experimental Studies on Unidirectional Materials", J. Am. Cer. Soc. 78, 2721 (1995).
4. Private communication, Hypertherm High Temperature Composites Inc.

CONDITIONS FOR TESTING THE CORROSION RATES OF CERAMICS  
IN COAL GASIFICATION SYSTEMS

John P. Hurley and Jan W. Nowok

Energy & Environmental Research Center  
University of North Dakota  
PO Box 9018  
Grand Forks, ND 58202-9018

ABSTRACT

Coal gasifier operating conditions and gas and ash compositions affect the corrosion rates of ceramics used for construction in three ways: 1) through direct corrosion of the materials, 2) by affecting the concentration and chemical form of the primary corrodents, and 3) by affecting the mass transport rate of the primary corrodents. To perform an accurate corrosion test on a system material, the researcher must include all relevant corrodents and simulate conditions in the gasifier as closely as possible. In this paper, we present suggestions for conditions to be used in such corrosion tests. Two main types of corrosion conditions are discussed: those existing in hot-gas cleanup systems where vapor and dry ash may contribute to corrosion and those experienced by high-temperature heat exchangers and refractories where the main corrodent will be coal ash slag.

Only the fluidized-bed gasification systems such as the Sierra Pacific Power Company Piñon Pine Power Project system are proposing the use of ceramic filters for particulate cleanup. The gasifier is an air-blown 102-MWe unit employing a Westinghouse™ ceramic particle filter system operating at as high as 1100°F at 300 psia. Expected gas compositions in the filter will be approximately 25% CO, 15% H<sub>2</sub>, 5% CO<sub>2</sub>, 5% H<sub>2</sub>O, and 50% N<sub>2</sub>. Vapor-phase sodium chloride concentrations are expected to be 10 to 100 times the levels in combustion systems at similar temperatures, but in general the concentrations of the minor primary and secondary corrodents are not well understood. In the case of high-temperature slag corrosion of heat exchangers or refractories that will occur in entrained-flow gasifiers or advanced power systems such as the Combustion 2000 High-Performance Power System, slag corrosiveness will depend on its composition as well as viscosity. For a laboratory test, the slag must be in a thermodynamically stable form before the beginning of the corrosion test to assure that no inappropriate reactions are allowed to occur. Ideally, the slag would be flowing, and the appropriate atmosphere must be used to assure realistic slag viscosity. However, as is the case for the hot-gas cleanup systems, the influence of specific gas stream components on slag properties is poorly understood at this time.

## INTRODUCTION

Many advanced power systems will combine two energy cycles to reach efficiencies as high as 47% in converting the chemical energy in coal into electrical energy. The energy cycles always include a typical steam or Rankine cycle, which usually produces 60%–80% of the electric power. The second cycle usually involves one of three possibilities. In an oxidizing system such as a pressurized fluidized-bed combustor (PFBC), one possibility is to clean the hot gas, then directly expand it in a gas turbine. In another concept, the turbine is indirectly fired by using a very high-temperature heat exchanger to transfer the energy to a clean noncondensing working fluid, such as air, which is then expanded in the turbine. The third possibility is to gasify the coal, clean the coal gas, then fire the gas directly into a gas turbine. A steam cycle combined with a gasification cycle is commonly called an integrated coal gasification combined cycle (IGCC).

Ceramics are suggested for constructing structures in these advanced energy systems because of their resistance to corrosion and high-temperature strength. At the highest temperatures, up to 1650°C, refractories are used to protect structural components and reduce heat loss from the system. Dense structural ceramics are proposed for use in heat exchangers, which may be used at temperatures as high as 1425°C. Both monolithic and composite ceramics are used to construct hot-gas filters to remove ash from the gas stream at temperatures up to 900°C. To improve the acceptability of these ceramic subsystems, a better understanding of their long-term performance is required.

The University of North Dakota Energy & Environmental Research Center (EERC) is providing technical assistance and test materials to the U.S. Department of Energy Advanced Research and Technology Development (AR&TD) Materials Program investigating ceramic corrosion in fossil energy systems. During 1994–1995, suggestions and materials for testing the corrosion resistance of ceramics in combustion systems were developed and proposed.<sup>1</sup> This year, the focus is on gasification systems. The main activities for are to perform thermochemical equilibrium calculations to develop recommendations for appropriate test conditions and to gather materials such as gasifier slag and ash that can be used by other researchers in performing ceramic corrosion tests.

This paper describes gas, ash, and operational factors that affect the corrosion rates of structural ceramics in coal gasification systems and provides suggestions for appropriate laboratory test conditions. Particular attention is focused on two subsystems: hot-gas particulate filtration and high-temperature refractories and heat exchangers, especially those constructed of silicon- and alumina-based ceramics.



The objective is not to present specific data on rate factors, but to help experimentalists measuring these factors to better design their corrosion tests.

## BACKGROUND

Approximately a dozen inorganic elements in the products of coal combustion affect the corrosion rates of silicon-based ceramics used to construct subsystems. These elements, including H, O, Na, Mg, Al, Si, P, S, Cl, K, Ca, and Fe, affect corrosion rates in three ways: as primary corrodents forming reaction products with the material, as secondary corrodents affecting the activity of the primary corrodents, or by influencing the rate of mass transfer of the primary corrodents. Although many of the elements function as more than one type of corrodent, they are listed here under what is believed to be their most active role.

The primary corrodents of silicon-based ceramics in coal-fired combustion systems include O, Mg, Ca, and Fe (refs. 2-6). These elements form silicates or silicides that are stable in the presence of the other constituents of the ash in contact with the ceramic surface. When ash is not present, such as downstream of a filter, vapor-phase Na can also be a primary corrodent of silicate ceramics, forming a sodium-enriched reaction layer through which oxygen can more rapidly diffuse than through a pure silica layer.<sup>7</sup> When ash is present, the more stable form of sodium is as a sodium aluminosilicate in the ash, rather than sodium silicate scale on the silicon carbide.

In contrast to the primary corrodents, the secondary corrodents have not been observed to form corrosion products with silica- or alumina-based ceramics. They are known, however, to affect the activities of some of the primary corrodents. The main elements acting in this role are H, Al, S, and Cl. Hydrogen is most important in gasification conditions, because it affects the concentration of O; in combustion conditions, it helps to form volatile hydroxides such as  $\text{Si(OH)}_4$  or  $\text{NaOH}$ , which will affect corrosion rates when no other ash is present. Similarly, S and Cl affect the vapor-phase concentrations of  $\text{Na}_2\text{SO}_4$  and  $\text{NaCl}$ , which will affect corrosion rates when ash is not present. In addition, Al affects the activity of Na, Mg, and Ca. Since these elements are more stable in an aluminosilicate phase than in a silicate corrosion product, they are less corrosive to silicate ceramics when aluminum is present in the ash.

The major role of several other elements is their effect on the transport rate of the primary corrodents. These elements include Na, Si, P, and K. Most important are their effects on the viscosity of a melt and on the rate of ion diffusion in a glass. These elements have not been observed to form

corrosion products with silicon- or alumina-based ceramics in coal fueled energy systems, except in minor roles.

Because the concentrations of many of these elements affect the activities of the primary corrosives, the surest experimental design to determine all of the interdependencies is the full factorial matrix, where the concentration of each element in the system is varied dependently on the others. However, the number of tests in such a matrix would involve  $x^n$  tests, where  $x$  is the number of variations possible for each element, and  $n$  is the number of different elements. For three variations (low, medium, and high concentrations) of each of 12 elements, the number of tests is 531,441 for a single temperature and pressure condition. The numbers can be partially reduced by using a fractional factorial test matrix, but the most cost-effective way to perform corrosion tests is to base them on realistic system conditions.

The best way to obtain appropriate test conditions is to expose the material in an operating coal-fueled system. This can be expensive, since a 100-hour pilot-scale test may cost \$100,000. As the scale of the test is reduced, so are the costs, but the accuracy of the conditions may also be compromised. To improve the accuracy of laboratory-scale test conditions and allow similar tests performed in different labs to be more comparable, the EERC has been surveying the literature and holding discussions with interested researchers and industry representatives to develop appropriate baseline test conditions. In addition, ash and slag samples are being collected from operating systems and are available in quart or gallon quantities to materials researchers by contacting the lead author. Thermochemical equilibrium calculations are also being performed to determine approximate gas-phase concentrations of some of the elements. The conditions suggested for testing are harsh yet realistic (i.e., not accelerated) and should include all of the primary and secondary corrosives. The ceramic subsystems that are the focus of the research are hot-gas particulate filters and high-temperature heat exchangers/refractories under both combustion and gasification conditions. Conditions for testing under combustion conditions are presented in an earlier paper, so only gasification conditions will be described here.<sup>1</sup>

Gasification conditions are much more difficult to simulate in the laboratory than combustion conditions because of the wide range of gas temperatures and compositions possible in the various systems and because the gas is poisonous and explosive. During gasification, coal is heated in the presence of insufficient oxygen to completely burn. Carbon monoxide and hydrogen are among the major product gases. Variations in system pressure and temperature strongly affect the concentrations of the gases in the product. Also, to keep the calorific value of the gas as high as possible, some gasifiers operate with pure oxygen rather than air, so that the gas is not diluted with nitrogen. This is especially true in the first IGCC systems because at the time of their design, low-Btu gas burners were

not reliable. However, advances in burner design over the last decade will permit air-blown product gas to be burned efficiently in future IGCC systems. These will include the Sierra Pacific Piñon Pine Power Project and the Foster Wheeler carbonizer to be used in the Four Rivers Energy Modernization Project and in the Combustion 2000 High-Performance Power System (HiPPS).

Three main types of coal gasifiers are currently in use: entrained-flow systems such as the pressurized Shell, Texaco, and Dow gasifiers and the atmospheric Koppers-Totzek gasifier; fluidized-bed systems such as the Winkler or Kellogg-Rust-Westinghouse™ (KRW) gasifiers; and a fixed-bed system used by Lurgi. The range of measured operating temperatures and product gas compositions for these three types of gasifiers as reported by Watkinson and others are summarized in Table 1. The coals used range in rank from lignite to bituminous, and all systems shown are oxygen-blown.<sup>8</sup>

TABLE 1

Typical Operating Conditions for the Main Types of Oxygen-Blown Gasifiers

	Entrained Flow		Fluidized Bed		Fixed Bed		Fixed Bed (dry ash)	
	Avg.	Range	Avg.	Range	Avg.	Range	Avg.	Range
Temp, °F		2150–2500		1700–1890		2280–2880		1440–1510
Pressure, psia		15–610		15–370		310–360		390–450
Gas Composition								
CO	54	41–62	37	26–51	57	56–58	17	16–18
H <sub>2</sub>	32	30–35	39	32–45	28	27–28	39	39–40
CO <sub>2</sub>	6.4	2–10	19	10–39	3.8	3.3–4.3	31	30–32
CH <sub>4</sub>	0.1	0–0.3	3.0	1.8–5.0	6.6	6.5–6.7	10	9–11
N <sub>2</sub>	1.9	0.8–4.7	0.7	0.5–0.9	2.4	0.6–4.3	1.2	0.8–1.5
H <sub>2</sub> S	1.1	0.3–1.8	1.4 <sup>a</sup>		1.3	0.6–2.0	1.4 <sup>a</sup>	
COS	0.1 <sup>a</sup>		0.0 <sup>b</sup>		0.0 <sup>b</sup>		0.0 <sup>b</sup>	
H <sub>2</sub> O	4.4 <sup>c</sup>		0.0 <sup>b</sup>		0.0 <sup>b</sup>		0.0 <sup>b</sup>	
No. of Systems		4		5		2		2

<sup>a</sup> 1 in estimate. <sup>b</sup> No data, values estimated. <sup>c</sup> Calculated by difference because of lack of data.

The wide range of gasifier designs and operating conditions makes it difficult to choose one set of conditions for baseline testing of ceramic materials. As in combustion, two main subsystems should be addressed: hot-gas particle filters where corrosion is caused by dry ash and gas and heat exchangers/refractories where the corrosion is caused by molten slag.

## HOT-GAS FILTERS

In most of the new oxygen-blown gasifier systems such as the Tampa Electric (Texaco), Wabash River (Dow), and Buggenum, Netherlands (Shell), projects, particulate cleanup will be performed in relatively cool gas at around 500°F, so ceramic corrosion should not be a problem. The Tampa project will include some hot-gas particulate cleanup at 1000°F, but they are proposing to use metal filters. Therefore, our recommendation is to run ceramic particle filter gasification corrosion studies in conditions that will be experienced in the Sierra Pacific Power Company Piñon Pine Power Project fluidized-bed gasifier. The gasifier is an air-blown 102-MWe unit employing a Westinghouse ceramic particle filter system operating at as high as 1100°F at 300 psia. Bed temperatures are expected to reach a maximum of 1850°F. Expected gas compositions in the filter will be approximately 25% CO, 15% H<sub>2</sub>, 5% CO<sub>2</sub>, 5% H<sub>2</sub>O, and 50% N<sub>2</sub>. Vapor-phase sodium chloride concentrations are expected to be 10 to 100 times the levels in combustion systems at similar temperatures, but in general the concentrations of the minor primary and secondary corrodents have not been measured. In addition, a hot-gas cleanup system to remove sulfur will be situated upstream of the filter system, and its effects on the minor species in the gas stream is not well understood.

In order to calculate approximate vapor concentrations of possible corrodents, the FACT program (Facility for the Analysis of Chemical Thermodynamics) developed by C.W. Bale, A.D. Pelton, and W.T. Thomson from Ecole Polytechnique de Montréal, was employed. It permits the calculations of stable phases in an ash-gas system over a broad range of temperatures through the minimization of free energy for the system. The FACT code is simple to implement because only chemical formulas of possible products and the mole fractions of the elements are needed. A multiple linear-regression technique estimates what stable phases are formed by minimizing errors for individual phases.

In simulating Piñon Pine gas compositions, we used a system pressure of 20 atmospheres and the design coal for the system (Utah SUFCo bituminous). The chlorine concentration in the coal is not known, so it was assumed for these calculations to be 100 ppmw, a relatively high figure. Table 2 shows the partial pressures of some corrodents in the gas stream. Concentrations are shown for two temperatures, 1110°F, the approximate maximum operating temperature of the filter vessel, and 1340°F, a temperature between that of the vessel and that of the fluid bed. Since the effects of the hot-gas cleanup system (sulfur removal) on the concentrations of minor corrodents is not known, they were not included in these calculations. Therefore, the data in Table 2 are a better simulation of conditions when the sulfur removal system is not on-line.

TABLE 2

Calculated Partial Pressures of Minor Corrodent Gas Species in the Piñon Pine System		
Minor Species	1110°F	1340°F
H <sub>2</sub> S	$2200 \times 10^{-6}$ atm	$3600 \times 10^{-6}$ atm
COS	$280 \times 10^{-6}$ atm	$260 \times 10^{-6}$ atm
HCl	$76 \times 10^{-6}$ atm	$300 \times 10^{-6}$ atm
NaCl	$2.6 \times 10^{-6}$ atm	$72 \times 10^{-6}$ atm
(NaCl) <sub>2</sub>	$1.5 \times 10^{-6}$ atm	$34 \times 10^{-6}$ atm
NaOH	$0.00012 \times 10^{-6}$ atm	$0.018 \times 10^{-6}$ atm

At 1110°F, the partial pressures of sodium species are quite low. However, at 1340°F, a temperature between that of the filter vessel and the fluid bed, concentrations are approximately 25 times higher, indicating that the sodium species may rapidly condense as the gas cools on the way to the hot-gas filter. Since equilibrium may not be reached by the time the gas reaches the filter vessel, the concentration of sodium vapor species in the filter vessel may be much above the equilibrium concentration. Therefore, we suggest that gaseous corrosion tests under hot-gas filtration conditions be run with a gas stream saturated with NaCl vapor by providing an excess of sodium chloride to the system. We suggest that this be done by adding a mixture of HCl and NaCl to water that is dripped into the hot corrosion test reactor. The mixture should be added at a rate to give HCl and NaCl vapors at somewhat higher concentrations than those at equilibrium in the filter vessel. We suggest the concentrations at 1340°F (1000 K) should be used. We acknowledge that this is a somewhat arbitrary value, but believe that these values will provide a harsh, yet realistic concentration of corrodents, which will serve as a benchmark for further parametric tests. Since the correct partial pressures of major gas species cannot be obtained in a 1-atmosphere reactor, we suggest that they be added in concentrations equal to their concentrations in the full-scale system. The suggested total gas stream concentrations for these tests should be 25% CO, 15% H<sub>2</sub>, 5% CO<sub>2</sub>, 5% H<sub>2</sub>O, 300 ppm HCl, and 75 ppm NaCl, with a balance of nitrogen. We suggest that the benchmark tests be run at 1100°F, with other, lower temperatures added in parametric tests.

In addition to vapor species, the ash may also corrode system components. The ash used for corrosion tests should be approximately at equilibrium at the start of the tests to prevent any unrealistic corrosion reactions from occurring as the ash attempts to reach equilibrium test conditions. Unfortunately, the Piñon Pine system is not expected to operate under standard conditions to supply ash to corrosion researchers until sometime in 1997. Therefore, the EERC is making available to corrosion researchers ash collected from the filter vessel of the EERC pilot-scale transport reactor development

unit (TRDU) from a test run performed in April 1996. The system is designed to operate under conditions similar to those at Piñon Pine, although a coal from the Belle Ayr Mine, Powder River Basin, Wyoming, was used for the tests rather than the Utah coal that is the design coal for the Piñon Pine system. The Belle Ayr ash has the advantage for corrosion tests in that it is well characterized, is available as a standard ash free of charge, and the coal will also be used at the Southern Company Services Wilsonville hot-gas filter test facility, which will also be operating fully by 1997.

### MOLTEN SLAG CORROSION

At the high operating temperatures to which some heat exchangers and refractories will be exposed, the ash will be very sticky, if not molten, and therefore will coat the subsystems and prevent direct gaseous corrosion of the materials. However, the composition of the gas in the corrosion reactor will still play an important role in the test, since the atmosphere directly affects the viscosity and therefore the erosiveness and corrosiveness of the slag. Figure 1 shows the viscosity versus temperature curves of a slag prepared from ash made by burning coal in the laboratory. The coal is from the Rochelle mine of the Wyoming Powder River Basin and is considered to have a relatively high calcium content. The three curves show the changes in viscosity caused by changes in the surrounding atmosphere. The fundamental reasons for the changes in viscosity are not completely clear, but are believed to be caused by the breakup of O-Si bonds and the creation of nonbridging hydroxyl groups, which will lower viscosity (reducing gas), but may also act as a mineralizer and increase the temperature at which crystallization occurs (air+water). These effects are especially strong for the more basic coal slags because water vapor is usually more soluble in more basic silicate glasses, even dissolving in a molecular form.<sup>9</sup> We suggest an overall gas composition of approximately 30% H<sub>2</sub>, 45% CO, and 25% CO<sub>2</sub> to which 10% water vapor is added. Because of equilibrium reactions at this temperature, we have calculated that the concentrations of CO may reach as high as 49%, H<sub>2</sub>O as high as 18%, CO<sub>2</sub> as low as 13%, and H<sub>2</sub> as low as 20% at 1400°C. SO<sub>2</sub> and H<sub>2</sub>S may cause changes in melt structure similar to those caused by water vapor, but because they are present in much lower concentrations, the sulfur-containing gases are expected to have a lesser effect, although this assumption must still be tested.

In addition to use of the correct atmosphere in slag corrosion tests, the slag should be in a relatively stable thermodynamic form at the beginning of the test. This can be best assured by producing the slag under realistic operating conditions or by collecting the slag from a large-scale operating facility.

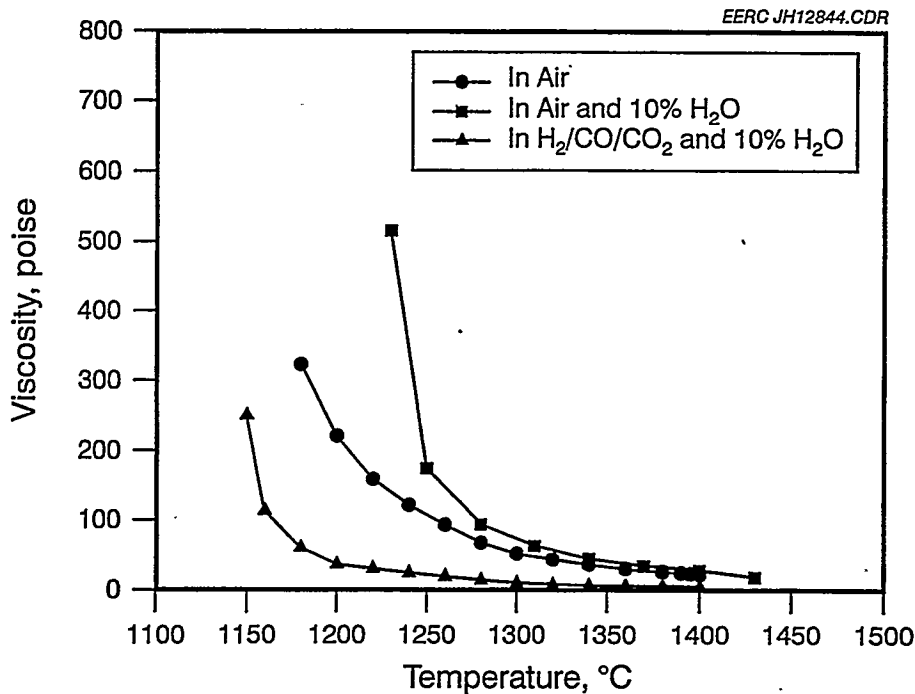


Figure 1. Viscosity versus temperature for Rochelle Mine coal ash slag under 3 atmospheres.

Unfortunately, most gasifier manufacturers and operators are very secretive about their operations, so it can be very difficult to obtain gasifier slag. However, the EERC has available coal slag donated for corrosion testing by three power plants burning economically important coals. The slags are produced in boilers fired with cyclone burners and are therefore in a mildly reduced state. High-calcium subbituminous coal slag was provided by the Northern States Power Company Riverside Plant, which was burning a coal from the Powder River Basin in Wyoming. Illinois No. 6 bituminous coal slag was provided by the Central Illinois Public Service Coffeen Plant. Analysis of the Coffeen slag showed abnormally high calcium concentrations owing to limestone additions to reduce slag viscosity, so another drum of more "pure" Illinois No. 6 slag was obtained from the Illinois Power Company Baldwin Plant. The compositions of the slags as well as the TRDU ash that can be used for corrosion tests at lower temperatures are shown in Table 3. Suggested temperatures for high-temperature slag corrosion testing are 2000°F for sintered ash conditions, 2300°F for viscous molten ash, and 2600°F for running ash. The slag layer thickness should be approximately 1 millimeter at 2600°F and 5 millimeters at 2300°F to ensure appropriate gas transport through the slag. The slag should be replenished often enough that it does not become overly concentrated with corrosion products.

TABLE 3

Chemical Compositions of Standard Ashes				
Oxide, wt%	TRDU Ash	Riverside Slag	Coffeen Slag	Baldwin Slag
SiO <sub>2</sub>	52.7	47.0	52.5	53.4
Al <sub>2</sub> O <sub>3</sub>	21.7	18.6	16.3	18.6
Fe <sub>2</sub> O <sub>3</sub>	1.5	5.3	13.5	17.6
TiO <sub>2</sub>	0.8	1.4	0.7	0.7
P <sub>2</sub> O <sub>5</sub>	0.8	0.6	0.2	0
CaO	13.4	19.7	13.1	7.1
MgO	7.2	5.7	1.2	0.9
Na <sub>2</sub> O	0.8	0.9	0.8	0.0
K <sub>2</sub> O	0.0	0.3	1.6	1.7
SO <sub>3</sub>	1.1	0.3	0.1	0.0

## SUMMARY

For a given temperature, the rate of corrosion of ceramic materials in advanced coal-fired energy systems is affected by the composition of the gas and condensed species in contact with the material. Approximately 12 elements affect the corrosion rates of silicon- and alumina-based ceramics in coal-fueled systems: O, Mg, Ca, Fe, and Na (when no ash is present) are primary corrodents in that they have been observed to form corrosion products with silicon carbides. Secondary corrodents—H, Al, S, and Cl—have not been observed to form corrosion products but do affect the activity of the primary corrodents. The other major elements, including Na, Si, P, and K, affect the rate of transport of the primary corrodents by affecting slag viscosity and ion mobility. In general, very little work has been done under reducing conditions, so the primary and secondary corrodents in gasifier systems are not well understood at this time.

To improve the accuracy of laboratory-scale combustion test conditions and assure comparability between testing groups, the EERC has assembled 55-gallon drums of coal ash and slag from large-scale coal-fueled systems that are approximately in equilibrium for mildly reducing conditions. For hot-gas filter testing, ash from the EERC TRDU hot-gas filter is available. The suggested total gas stream concentrations suggested for these tests should be 25% CO, 15% H<sub>2</sub>, 5% CO<sub>2</sub>, 5% H<sub>2</sub>O, 300 ppm HCl, and 75 ppm NaCl, with a balance of nitrogen. We suggest that the benchmark tests be run at 1100°F, with other, lower temperatures added in parametric tests.

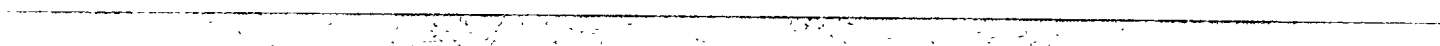
To simulate the type of ash that will strike a high-temperature heat exchanger in a combustion system upstream of ash removal devices, slags produced under slightly reducing conditions are available from utility cyclone-fired boilers. Suggested initial conditions for slag testing are 2000°F for sintered



ash conditions, 2300°F for viscous molten ash, and 2600°F for runny molten ash. We suggest an overall gas composition of approximately 30% H<sub>2</sub>, 45% CO, and 25% CO<sub>2</sub> to which 10% water vapor is added. To assure appropriate gas transport, the slag layer thickness in a static test should be approximately 1 millimeter for runny slag and 5 millimeters for viscous slags. The slag should be changed often enough to prevent it from becoming overly concentrated in corrosion products, since in a commercial system the slag will be constantly replenished.

## REFERENCES

1. J.P. Hurley, "Support Services for Ceramic Fiber-Ceramic Matrix Composites," ORNL/Sub/94-SS112/01, 1995.
2. M.K. Ferber and V.J. Tennery, "Behavior of Tubular Ceramic Heat Exchanger Materials in Acidic Coal Ash from Coal-Oil Mixture Combustion," *Ceram. Bull.*, 62 (2), pp. 236-243, 1983.
3. M.K. Ferber, V.J. Tennery, "Behavior of Tubular Ceramic Heat Exchanger Materials in Basic Coal Ash from Coal-Oil Mixture Combustion," *Ceram. Bull.*, 63 (7), pp. 898-904, 1984.
4. T.M. Strobel, J.P. Hurley, C.L. Senior, J.E. Holowczak, "Coal Slag Corrosion of Silicon Carbide-Based Ceramics in a Combustion Environment," *In Proceedings of the Symposium on Silicon Carbide-Based Structural Ceramics; American Ceramic Society PAC RIM Meeting, Honolulu, HI, Nov. 7-10*; pp. 327-334, 1993.
5. T.M. Strobel, J.P. Hurley, K. Breder, J.E. Holowczak, "Coal Slag Corrosion and Strength Degradation of Silicon Carbide-Alumina Composites," *In Ceramics Engineering & Science Proceedings*, 15 (4), pp. 579-586, 1994.
6. C.L. Senior, G.A. Moniz, J.P. Hurley, T.M. Strobel, "Corrosion of Silicon Carbides by Ash and Vapor in a Coal Combustion Environment," *In Proceedings of the Symposium on Silicon Carbide-Based Structural Ceramics; American Ceramic Society PAC RIM Meeting, Honolulu, HI, Nov. 7-10*, pp. 335-342, 1993.
7. Z. Zheng, R.E. Tressler, K.E. Spear, "A Comparison of the Oxidation of Sodium Implanted CVD Si<sub>3</sub>N<sub>4</sub> with the Oxidation of Sodium-Implanted SiC Crystals," *Corrosion Science*, 33 (4), pp. 569-580, 1992.
8. A.P. Watkinson, J.P. Lucas, C.J. Lim, "A Prediction of Performance of Commercial Coal Gasifiers," *Fuel*, 70, pp. 519-527, 1991.
9. J.E. Shelby, *Handbook of Gas Diffusion in Solids and Melts*, p. 223, 1996.



## FRACTURE BEHAVIOR OF ADVANCED CERAMIC HOT-GAS FILTERS

J. P. Singh, S. Majumdar, M. Sutaria, and W. Bielke

Energy Technology Division  
Argonne National Laboratory  
Argonne, Illinois 60439

### ABSTRACT

We have evaluated the microstructural/mechanical, and thermal shock/fatigue behavior and have conducted stress analyses of hot-gas candle filters made by various manufacturers. These filters include both monolithic and composite ceramics. Mechanical-property measurement of the composite filters included diametral compression testing with O-ring specimens and burst testing of short filter segments using rubber plug. In general, strength values obtained by burst testing were lower than those obtained by O-ring compression testing.

During single-cycle thermal-shock tests, the composite filters showed little or no strength degradation when quenched from temperatures between 900 and 1000°C. At higher quenching temperatures, slow strength degradation was observed. The monolithic SiC filters showed no strength degradation when quenched from temperatures of up to  $\approx 700$ -900°C, but displayed decreased strength at a relatively sharp rate when quenched from higher temperatures. On the other hand, a recrystallized monolithic SiC filter showed higher initial strength and retained this strength to higher quenching temperatures than did regular SiC filters. This may be related to the difference in strength of grain boundary phases in the two cases. In thermal cycles between room temperature and 800-1000°C, both monolithic and composite filters show a small strength degradation up to three cycles, beyond which the strength remained unchanged.

Results of rubber-plug burst testing on composite filters were analyzed to determine the anisotropic elastic constants of the composite in the hoop direction. When these results are combined with the axial elastic constants determined from axial tensile tests, the composite can be analyzed for stress due to mechanical (e.g., internal pressure) or thermal loading (thermal shock during pulse cleaning). The stresses can be compared with the strength of the composite to predict filter performance.

### INTRODUCTION

Hot-dirty gas exiting from a gasifier or an advanced combustor contains sufficient particulates to make the gas undesirable for direct utilization in gas turbines and heat engines. Today's hot-dirty gas cleanup systems, such as cyclones, can remove only the fraction

containing the larger particulates. Smaller particulates can be removed only by cooling and filtering the gas. The resulting enthalpy loss causes a significant decrease in overall system efficiency. Thus, there is a critical need for cleaning hot-dirty gas with little or no cooling.

This project supports the development of candle ceramic/composite filters for cleanup of hot-dirty gases. Effort has been directed toward developing materials qualification technology needed to ensure satisfactory performance of filters in hot-dirty gas streams. To predict the long-term performance of such filters, it is important to understand and evaluate fracture behavior of these filters in service environments. Mechanical properties should be evaluated to establish baseline data. Thermal-shock resistance should be measured to predict filter performance in the service environment.<sup>1</sup> Failure modes must be identified and failure mechanisms must be established.

### SPECIMENS FOR FRACTURE STUDY

The filters examined in this study were obtained from 3M (Nextel/SiC composite filters), DuPont Lanxide (PRD-66 filters), Babcock & Wilcox (oxide composites), Industrial Filter and Pump Mfg. Co. (IFPM) (regular monolithic SiC with high alumina binder and binderless recrystallized SiC filters) and Pall Corp. (monolithic SiC). The 3M filters consist of layered composite structures; a tubular filter element is sandwiched between two Nextel/SiC composite tubes. Bonding between the Nextel/SiC composite tubes and the filter layer is achieved by the chemical vapor infiltration (CVI) of SiC. The inner and outer diameters of these filters are  $\approx 5.08$  and  $\approx 5.72$  cm, respectively. Filters were obtained in both as-fabricated and exposed (in the Tidd demonstration plant for  $\approx 1100$  h) conditions. The PRD-66 is an all-oxide ceramic consisting of layered microstructure of alumina, mullite, cordierite, and amorphous material; the inner and outer diameters are  $\approx 4.52$  and  $\approx 5.96$  cm, respectively. The Babcock & Wilcox filter is made by a sol-gel technique and consists of an oxide composite with chopped and continuous Nextel fibers. The inner and outer diameters of the filters are  $\approx 5.00$  and  $\approx 5.96$  cm, respectively. Both of the monolithic SiC filters consist primarily of SiC grains; inner and outer diameters of the filters are  $\approx 4.52$  and  $\approx 5.96$  cm, respectively.

## EVALUATION OF STRENGTH AND THERMAL-SHOCK AND FATIGUE RESISTANCE

Filter strength was evaluated by both diametral compression testing of O-ring specimens and by burst testing of short filter segments with rubber plugs.

### O-Ring Compression Testing

One-inch-wide O-ring specimens were machined from each of the filters and then loaded to failure in a diametral compression mode at a crosshead speed of 0.13 cm/min. Maximum stress develops at the inner diameter across the load points, which simulates the thermal-shock stresses developed during a pulse-cleaning cycle. The fracture stress  $\sigma_f$  is given by Eq. 1.<sup>2</sup>

$$\sigma_f = \frac{PK}{\pi bl}, \quad (1)$$

where  $P$  is the fracture load,  $K$  is a function of the ratio of inner and outer diameters,<sup>2</sup>  $b$  is the outer radius of the specimen, and  $l$  is the length of the tube. Load displacement plots for the filter specimens in as-fabricated condition indicated a nonbrittle failure mode for all composites and brittle failure for the monolithic filters. A limited number of O-ring specimens machined from one of the composite filters exposed in the Tidd demonstration plant for  $\approx 1100$  h were tested in compression mode; strength was  $7.72 \pm 1.13$  MPa. The corresponding strength of the unexposed filter was  $19.47 \pm 2.11$  MPa. This represents a strength loss of 60% during filter exposure, which correlates very well with the strength loss of the reinforcing fibers and may be related to in-situ fiber damage during filter exposure.<sup>3</sup>

### Burst Testing

Burst testing was performed on 1-in.-wide O-ring specimens machined from a Nextel/SiC composite filter in as-fabricated condition. As shown in Fig. 1, uniform radial loading was applied to the O-rings through a rubber plug (slightly smaller in diameter than O-ring) that was compressed between two aluminum plates. Figure 2 shows a typical load-displacement plot for a specimen in as-fabricated condition.

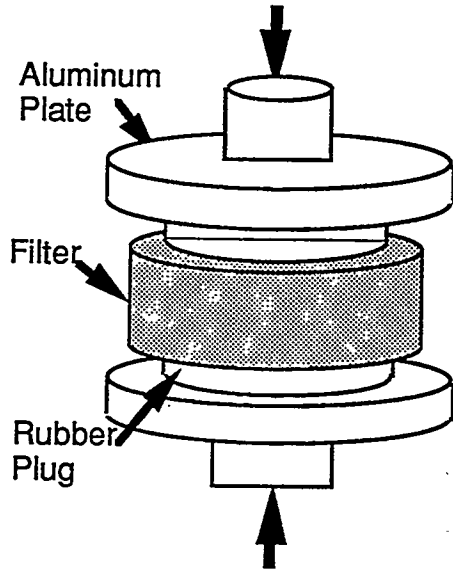


Fig. 1. Schematic diagram of burst test.

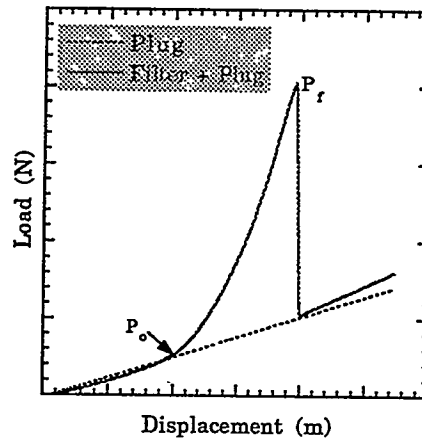


Fig. 2. Typical load-displacement plot for Nextel/SiC filter specimen.

The maximum hoop stress ( $\sigma_t$ ) occurs at the inner wall and is given by Eqs. 2 and 3:4,5

$$\sigma_t = p^L \left( \frac{r_o^2 + r_i^2}{r_o^2 - r_i^2} \right) \quad (2)$$

$$p^L = \frac{\nu}{(1 - \nu)} \frac{(P_f - P_o)}{\pi r_i^2} \quad (3)$$

where  $p^L$  is the radial pressure on the inner wall of the filter;  $r_o$  and  $r_i$  are the outer and inner radii of the filter, respectively;  $P_f$  is the maximum applied load at fracture,  $P_o$  is the load at which the rubber plug makes radial contact with the filter; and  $\nu$  is the Poisson's ratio (value taken to be 0.5). The fracture load  $P_f$  and contact load  $P_o$  were obtained from the load-displacement plot. To date, a limited number of specimens have been evaluated by burst testing to compare the strength data with those obtained by O-ring compression testing. For the Nextel/SiC composite filter specimens, burst strength was  $6.4 \pm 0.22$  MPa, a lower value than that obtained by O-ring tests. This difference is believed to be due to the larger specimen volume subjected to high stresses during burst testing than that in O-ring compression testing.

### Thermal-Shock Testing

Thermal-shock testing was performed on 1-in.-wide ring specimens machined from the filters. The ring specimens were insulated on the outer surface to simulate the heat transfer conditions in service. These specimens were heated to preselected temperatures (25-1100°C) in an electric furnace. Subsequently, the specimens were quenched in silicone oil at room temperature ( $\approx 25^\circ\text{C}$ ). Thermal-shock damage was estimated by measuring the strength of ring specimens by O-ring compression testing before and after thermal quenching.

The results of the thermal-shock experiments are given in Fig. 3, which shows the retained strength of specimens subjected to varying degrees of thermal quench ( $\Delta T$ ). Vertical bars represent the standard deviation when three or four specimens were tested. Other data points represent values for single specimens.

Results obtained so far indicate that the composite filters show little or no strength degradation when quenched from  $\approx 900$ -1000°C. At higher quenching temperatures, slow strength degradation was observed. The regular monolithic SiC filters showed no strength degradation when quenched from  $\approx 700$ -900°C. At higher temperatures, strength decreased at a relatively sharp rate. On the other hand, as seen in Fig. 3b, the recrystallized monolithic SiC filter specimens showed higher initial strength that was retained to higher quenching temperatures than in the regular SiC filter specimens. This may be related to differences in strengths of grain boundary phases in the two cases.

### Evaluation of Thermal-Fatigue Behavior

Thermal-fatigue testing of both monolithic and composite filters was performed on 1-in.-wide ring specimens machined from the filters. These specimens were thermally cycled between room temperature and preselected elevated temperatures of 800-1000°C. The elevated temperatures were close to the critical quenching temperature observed in the single-cycle thermal quenching experiments. The ring specimens were insulated on their outer surfaces, as before, to simulate heat transfer conditions in service. Thermal-fatigue damage was estimated by measuring strength (in O-ring compression tests) of the specimens before and after thermal cycling.

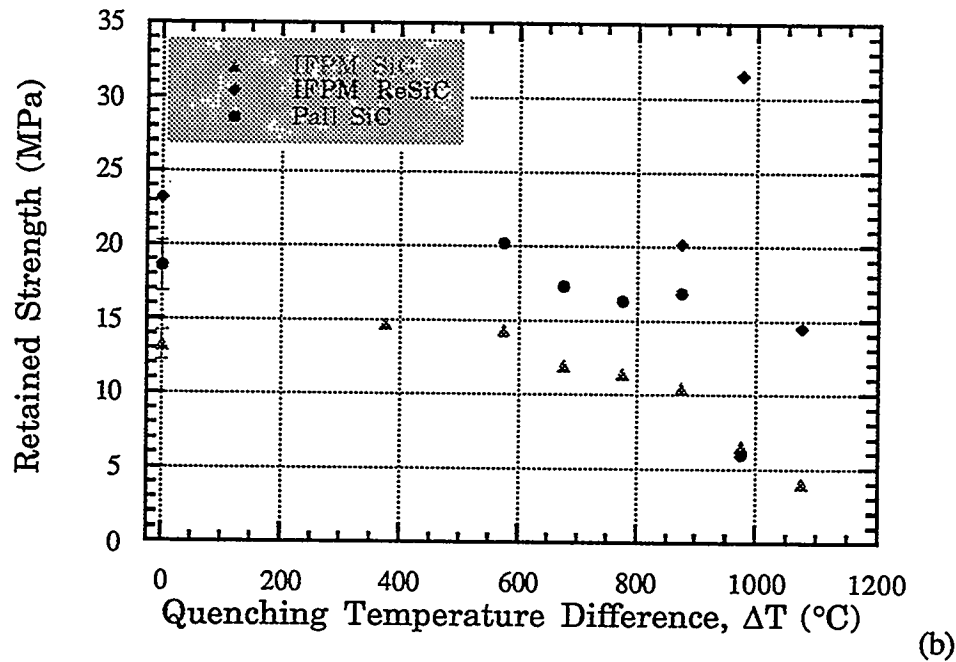
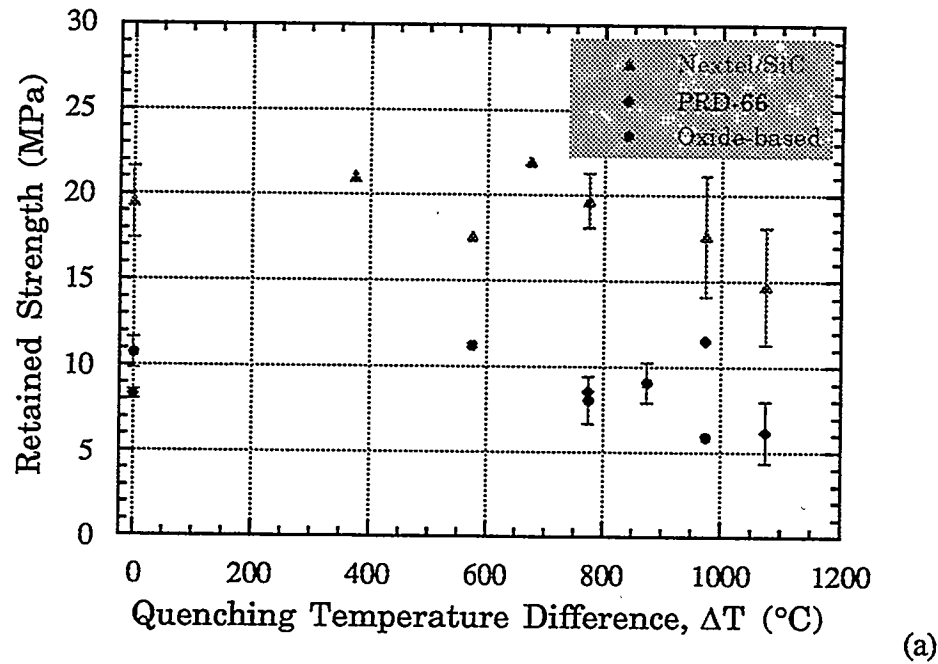


Fig. 3. Dependence of retained strength of ring specimens on quenching temperature difference ( $\Delta T$ ): (a) 3M Nextel/SiC, DuPont Lanxide PRD-66, and Babcock & Wilcox oxide-based composite filters; (b) IFPM monolithic SiC, IFPM monolithic recrystallized SiC, and Pall monolithic SiC filters.



The results of the thermal-fatigue experiments are given in Fig. 4, which shows retained strength of filter specimens as a function of thermal cycles. Vertical bars represent the standard deviation when three or four specimens were tested. Other data points represent values for single specimens.

In thermal cycling between room temperature and 800-1000°C, Nextel/SiC, PRD-66, and Babcock & Wilcox composite filters show a small strength degradation (18-24%) up to three cycles, beyond which strength remained unchanged. Similar behavior was observed for the monolithic filters that were thermally cycled between room temperature and 800°C; initially, strength decreased by 15-28% up to about three cycles, beyond which the strength remained constant. On the other hand, in thermal cycling between room temperature and 900°C, a large drop in strength was observed for the Pall monolithic filter; the reason for this behavior is currently under investigation to determine if the drop is just a scatter in data. Only one specimen was tested per condition because of limited filter. As expected, both the monolithic and the composite filters showed a slight decrease in strength when thermally cycled at higher temperatures. Microstructural evaluations are in progress to evaluate the failure modes and mechanisms; the results will be used for analytical modeling to predict filter performance in service.

## STRESS ANALYSIS OF O-RING BURST TESTS

Recently, a series of burst tests were conducted on the composite filters by using an internal plug. This section summarizes an analysis of the results conducted in order to deduce the elastic stiffness properties of the composite materials.

### Geometry

The geometry and loading of the composite O-ring burst tests are shown in Fig. 5. Radial pressure loading is achieved by an internal rubber plug that has an initial radial clearance at the inner diameter (ID) of the composite. The rubber plug is loaded axially in an Instron machine. Initially, the O-ring does not see any load, but after the radial gap between the O-ring and the composite is closed by lateral expansion of the plug (due to Poisson's ratio effect), the composite experiences a radial pressure loading.

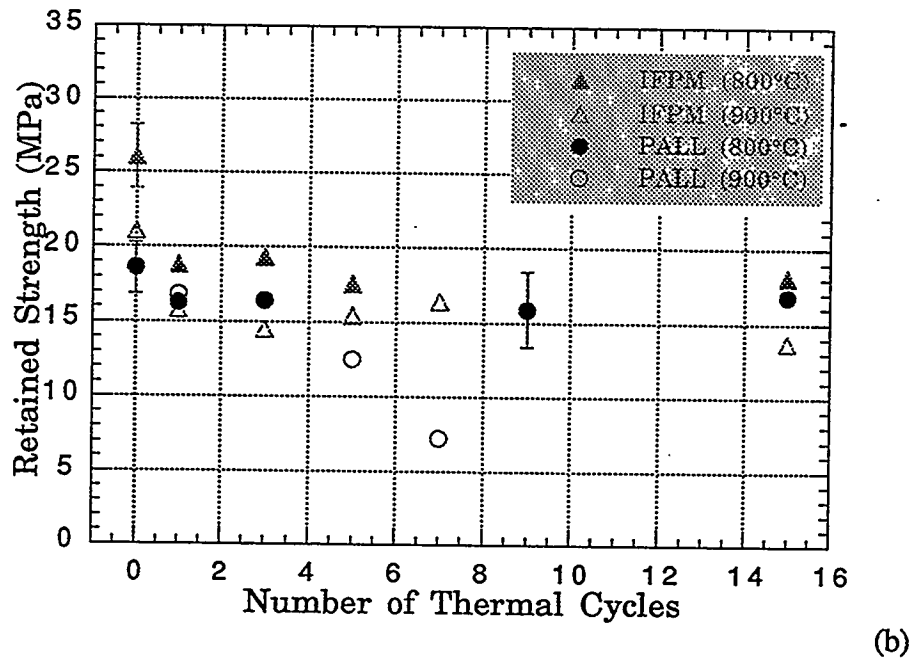
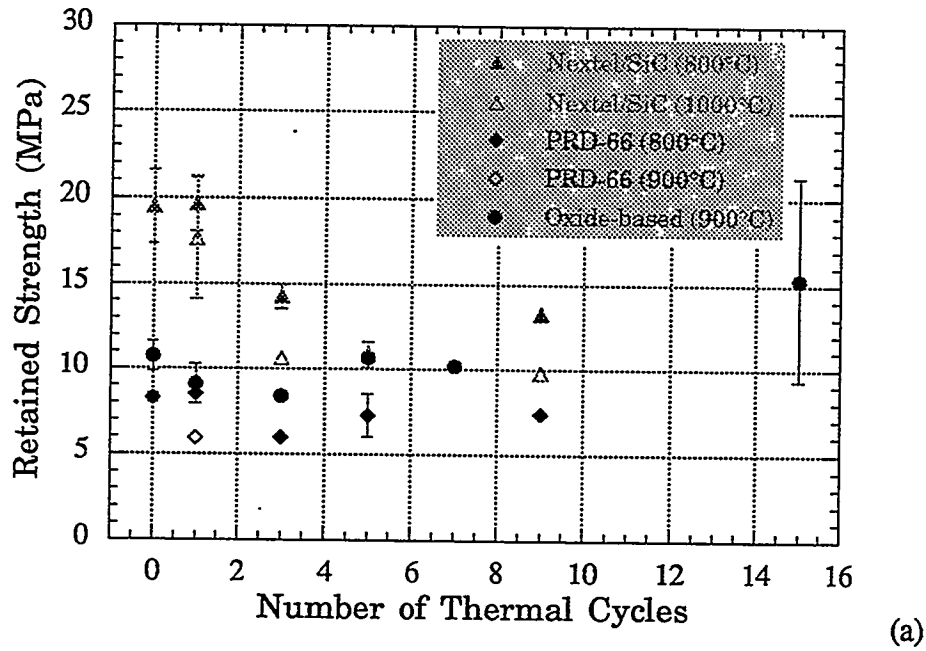


Fig. 4. Dependence of retained strength on number of thermal cycles: (a) 3M Nextel/SiC, DuPont Lanxide PRD-66, and Babcock & Wilcox oxide-based composite filters; (b) IFPM monolithic SiC and Pall monolithic SiC filters.

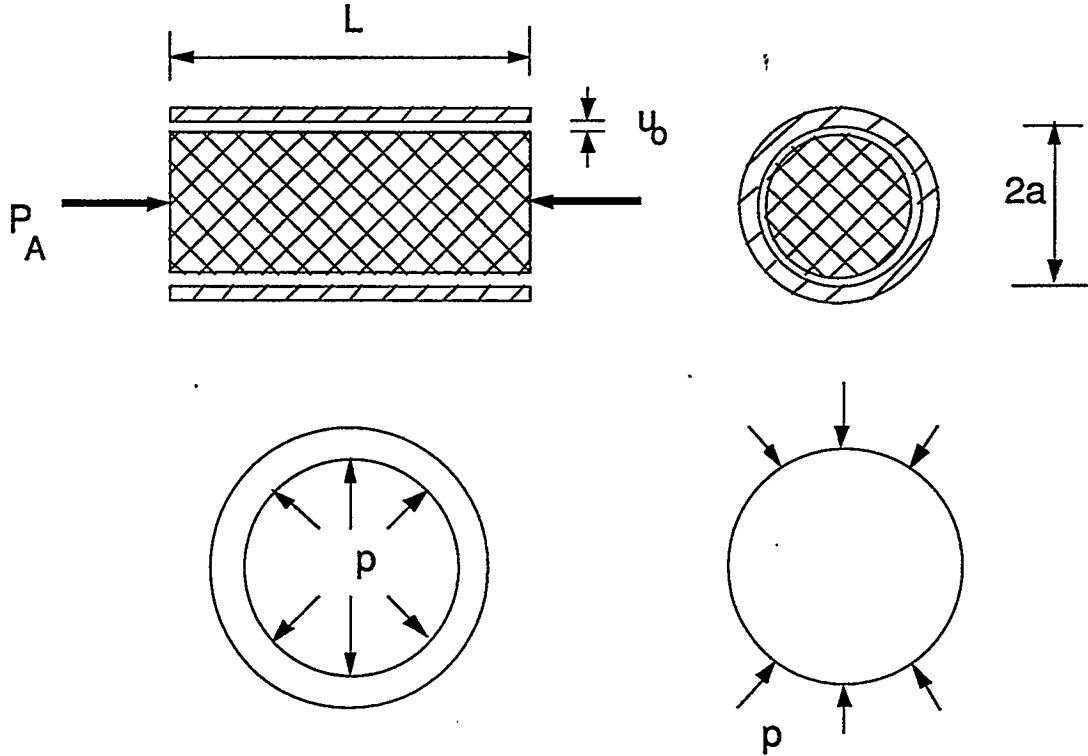


Fig. 5. Typical setup for O-ring burst test. Interfacial pressure  $p = 0$  until radial clearance  $u_0$  is closed at axial pressure  $p_{A0} = P_{A0}/\pi a^2$ .

### Analysis

The in-plane stress resultants in the composite are related to the membrane strains by the stiffness coefficients  $K_x$ ,  $K_y$ , and  $K_{xy}$  as follows:

$$N_x = K_x \varepsilon_x + K_{xy} \varepsilon_y \quad (4a)$$

$$N_y = K_{xy} \varepsilon_x + K_y \varepsilon_y, \quad (4b)$$

where  $N$  and  $\varepsilon$  are the stress resultants and strains, respectively; and subscripts  $x$  and  $y$  denote the axial and circumferential directions, respectively. We assume that the friction effects at the interface between the rubber plug and the composite O-ring are negligible, so that after contact, the composite experiences hoop stress only, i.e.,  $N_x = 0$ . In such a case, the above stress-strain relationship reduces to:

$$N_y = E_y \varepsilon_y = \left( K_y - \frac{K_{xy}^2}{K_x} \right) \varepsilon. \quad (4c)$$

The radial clearance  $u_o$  between the plug and the O-ring is closed at an axial pressure of  $p_{Ao}$ , where

$$p_{Ao} = E \varepsilon_{Ao} = \frac{E \varepsilon_o}{\nu}, \quad (5)$$

where  $\varepsilon_o = u_o/a$ , and  $E$  and  $\nu$  are the Young's modulus and Poisson's ratio of the plug, respectively. Assuming the rubber plug to be incompressible ( $\nu = 0.5$ ), the interfacial pressure  $p$  beyond the initial contact at an axial pressure  $p_A$  is derived by:

$$p = \frac{p_A - p_{Ao}}{1 + \frac{2Ea}{E_y}} = \left( 1 - \frac{E}{E_1} \right) (p_A - p_{Ao}), \quad (6)$$

where

$$E_1 = \frac{p_A - p_{Ao}}{\varepsilon_A - \varepsilon_{Ao}} = E \left( 1 + \frac{E_y}{2Ea} \right). \quad (7)$$

In Eqs. 6 and 7,  $E$  and  $E_1$  are the slopes of the axial stress-strain curve of the rubber plug before and after contact with the O-ring, respectively (Fig. 6).

An estimate for the stiffness of the O-ring can be obtained by solving Eq. 7 as

$$E_y = 2a(E_1 - E). \quad (8)$$

Therefore, the hoop stress resultant corresponding to any axial pressure  $p_A$  is given by

$$N_y = pa = \frac{E_y}{2E_1} (p_A - p_{Ao}) = \left[ 1 - \frac{E}{E_1} \right] (p_A - p_{Ao})a. \quad (9)$$

### O-Ring Burst Test

In an ideal O-ring burst test (Fig. 6) starting at O, the plug contacts the O-ring at a stress  $p_{Ao}$  and strain  $\varepsilon_{Ao}$  (point A), after which the load-displacement curve follows the steep curve

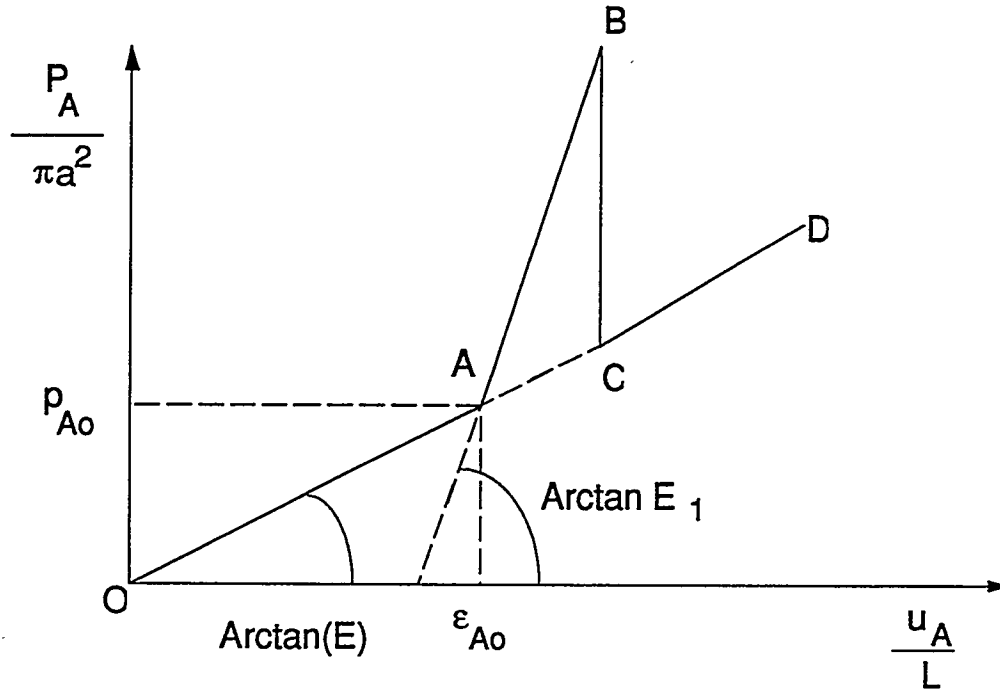


Fig. 6. Calculated idealized load-displacement curve.

AB with slope  $E_1$ . After bursting of the ring at B, the load rapidly drops to C and follows the original load-displacement curve for the plug along CD. In reality, the discontinuous changes in slopes are replaced by gradual changes.

The measured values of the slopes, based on three tests are

$$E = (2.455 \pm 0.136) \text{ MPa}$$

$$E_1 = (27.67 \pm 1.097) \text{ MPa}$$

Using Eq. 8, we find that

$$E_y = (1.2703 \pm 0.037) \text{ MN/m.}$$

The stiffness properties ( $E_x$ ,  $E_y$ , etc.) of the composite substrate tube (without filter layer) can be estimated from the measured values of the matrix and fiber properties. With known values of stiffness ( $E_y$ ) for the composite filter (composite tube and filter layer) and composite substrate alone, elastic properties of the filter layer can be estimated. These

properties will be used to analyze global stresses (thermal stresses, etc.) in composite filters to predict filter performance.

### ACKNOWLEDGMENTS

The work was supported by the U.S. Department of Energy, Office of Fossil Energy, Advanced Research and Technology Materials Program [DOE/FE AA 15 10 10 0, Work Breakdown Structure Element ANL-1A], under Contract W-31-109-Eng-38. The authors thank D. J. Pysher, B. L. Weaver, and R. G. Smith of the 3M Company, J. A. Chambers of DuPont Lanxide Composites, Inc., P. Eggerstedt and J. Zievers of the Industrial Filter & Pump Manufacturing Company, R. A. Wagner and R. W. Goettler of Babcock & Wilcox, and John Sawyer of Pall Corporation for providing filter specimens and for their helpful discussions.

### REFERENCES

1. J. P. Singh, S. Majumdar, A. S. Wagh, T. Wenzel, and R. B. Poeppel, "Materials Qualification Technology for Ceramic Cross-Flow Filters," Argonne National Laboratory Report ANL/FE-91/1 (July 1991).
2. E. A. Ripperger and N. Davis, "Critical Stress in Circular Ring," Trans. Amer. Soc. Civ. Engr., Paper No. 2308, pp. 619-35 (1948).
3. J. P. Singh, D. Singh, and M. Sutaria, "Effects of Flaws on Fracture Behavior of Structural Ceramics," in this Proceedings.
4. M. G. Stout and J. J. Petrovic, "Multiaxial Loading Fracture of  $\text{Al}_2\text{O}_3$  Tubes: I, Experiments," J. Am. Ceram. Soc., 67[1] 14-18 (1984).
5. O. M. Jaddan, D. L. Shelleman, J. C. Conway, Jr., J. J. Mecholsky, Jr., and R. E. Tressler. "Prediction of the Strength of Ceramic Tubular Components: Part I-Analysis," J. Testing and Evaluation, 19 [3] 181-191 (1991).

HIGH TEMPERATURE CORROSION OF ADVANCED CERAMIC  
MATERIALS FOR HOT GAS FILTERS AND HEAT EXCHANGERS

C. E. Crossland, D. L. Shelleman, K. E. Spear and R. E. Tressler  
The Pennsylvania State University  
226 Steidle Bldg  
University Park, PA 16802

ABSTRACT

A vertical flow-through furnace has been built to study the effect of corrosion on the morphology and mechanical properties of ceramic hot gas filters. Sections of 3M Type 203 and DuPont Lanxide SiC-SiC filter tubes were sealed at one end and suspended in the furnace while being subjected to a simulated coal combustion environment at 870°C. X-ray diffraction and electron microscopy is used to identify phase and morphology changes due to corrosion while burst testing determines the loss of mechanical strength after exposure to the combustion gases. Additionally, a thermodynamic database of gaseous silicon compounds is currently being established so that calculations can be made to predict important products of the reaction of the environment with the ceramics. These thermodynamic calculations provide useful information concerning the regimes where the ceramic may be degraded by material vaporization.

To verify the durability and predict lifetime performance of ceramic heat exchangers in coal combustion environments, long-term exposure testing of stressed (internally pressurized) tubes must be performed in actual coal combustion environments. We have designed a system that will internally pressurize 2" OD by 48" long ceramic heat exchanger tubes to a maximum pressure of 200 psi while exposing the outer surface of the tubes to coal combustion gas at the Combustion and Environmental Research Facility (CERF) at the Pittsburgh Energy and Technology Center (PETC). Water-cooled, internal o-ring pressure seals were designed to accommodate the existing 6" by 6" access panels of the CERF. Tubes will be exposed for up to a maximum of 500 hours at temperatures of 2500 and 2600°F with an internal pressure of 200 psi. If the tubes survive, their retained strength will be measured using the high temperature tube burst test facility at Penn State University. Fractographic analysis will be performed to identify the failure source(s) for the tubes.

INTRODUCTION

This project consists of two separate study areas. Part 1 details the corrosion and resulting changes in the mechanical properties of candidate hot gas filters exposed to a flow-through type combustion environment. Additionally, thermochemical modeling will be employed in an effort to predict system responses under various environments. ChemSage<sup>1</sup> can be used to study the phase equilibrium of systems over numerous pressure and temperature ranges. The objective for Part 2 of this program is to access the long-term (500 hours) durability of candidate ceramic heat exchangers subjected to the combined effects of stress (internal gas pressure of 200 psi) and hot corrosion via coal combustion environment.

## EXPERIMENTAL PROCEDURE

Based on results from earlier flow-over tests on 3M's Type 203 filters (SiC matrix-Nextel fiber composite) and DuPont Lanxide's SiC-SiC composite filters with Nicalon fibers, a reactor was developed to allow for flow-through experiments on 18" sealed sections of filters coated with ash collected at the Tidd plant. The vertical flow-through reactor (Figure 1) consists of a 6 inch I.D. SiC furnace tube fixed at the exhaust end by a stainless steel cylinder to support the filter sections. The inlet gas flow of 30% O<sub>2</sub>, 15% H<sub>2</sub>O, 3300 ppm SO<sub>2</sub>, 1100 ppm HCl, 10 ppm NaCl and 55% air is forced to flow through the filter material. These tests are carried out with the inlet gas flow rate between 1 and 5 slm at temperatures up to 870°C and time periods of 50, 100 and 200 hours. After exposure to the corrosive environment, any phase or morphological changes will be studied with x-ray diffraction and scanning electron microscopy. The residual strength of the filters will be measured by internal pressurized burst testing.

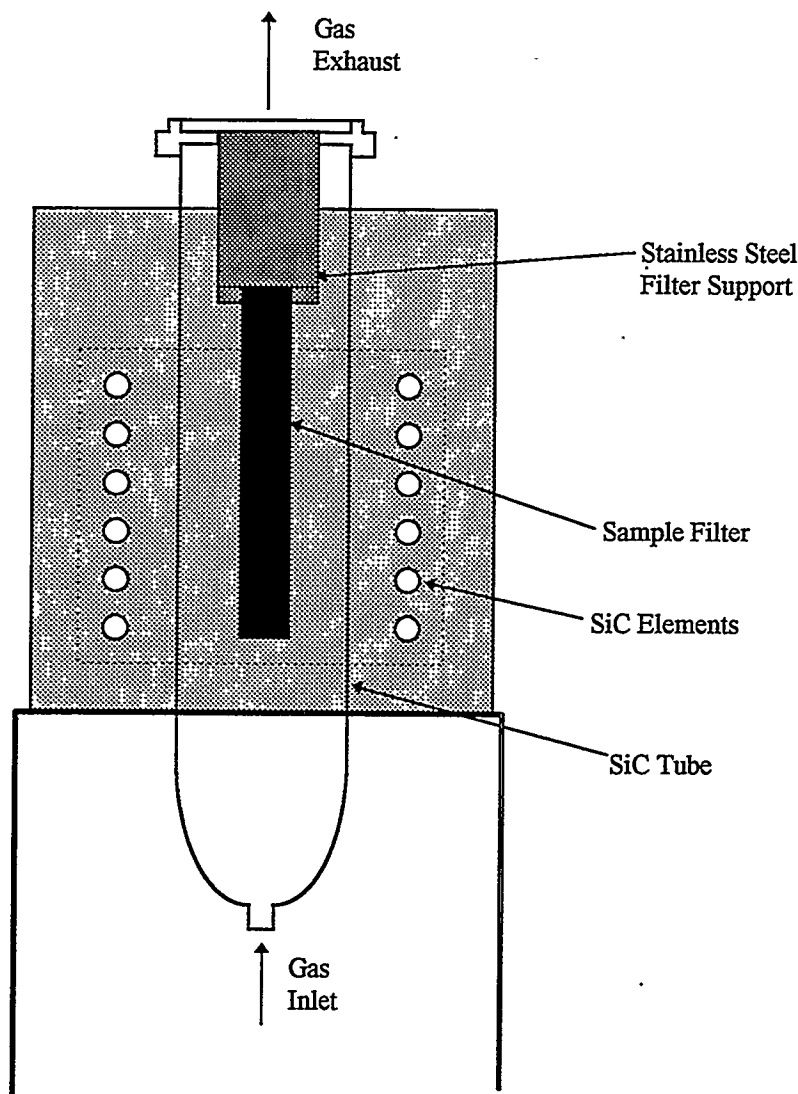


Figure 1: Vertical flow-through reactor designed for corrosion studies of ceramic filters



A database has been set up for the Si-O-H-Cl-Na-C-N-Ar system by incorporating thermodynamic data from MICROTHERM<sup>2</sup> and Allendorf et al.<sup>3</sup> By utilizing this database with ChemSage, the reaction of SiC with oxidizing and reducing atmospheres can be predicted over a range of temperatures and at extended pressures not easily duplicated by experiment.

Part II of this program began in February of this year. The objective of the program is to assess the durability of candidate ceramic heat exchangers subjected to the combined effects of stress and hot corrosion. This will be accomplished by designing a system that will internally pressurize ceramic tubes while the outer surface is exposed to coal combustion gases. A pressure system has been designed to fit the existing 6" by 6" access panels of the Combustion and Environmental Research Facility (CERF) at the Pittsburgh Energy and Technology Center (PETC) (see Figure 2). Two open-ended tubes (2" OD by 1.625" ID by 48" in length) will be exposed at the same time for a maximum of 500 hours at temperatures ranging from 2200 to 2600°F with an internal pressure of 200 psig N<sub>2</sub>. If the tubes survive the exposure to coal combustion, their retained strength will be measured using the Tube Burst Test Apparatus<sup>4</sup> at Penn State University. Fractographic analysis will be performed on the tube fragments to identify, if possible, the source(s) of failure for the tubes.

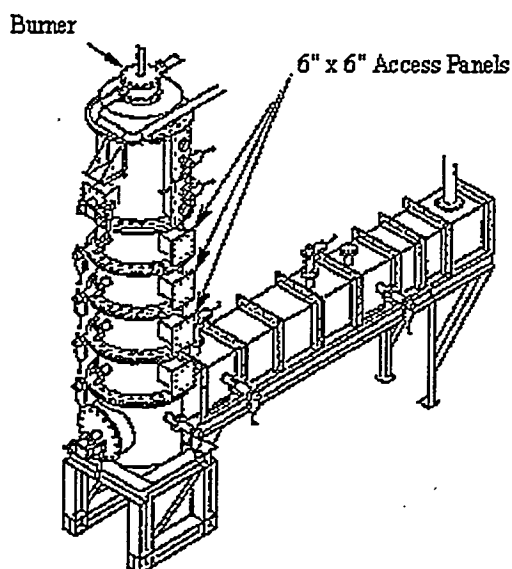


Figure 2: A system is being designed to fit the existing 6" by 6" access panels of the CERF at PETC to internally pressurize (200 psig of N<sub>2</sub> gas) 2" OD by 48" long ceramic tubes while the outer surface is exposed to coal combustion gases at temperatures ranging from 2200 to 2600°F for up to 500 hours

## RESULTS

Work thus far can be separated into two sections: 1) experimental results from initial flow-through test and 2) thermochemical modeling of pressurized fluidized bed combustors (PFBC). The results from the flow-through test include x-ray diffraction, scanning electron microscopy and internal pressurized burst testing. The corrosion of SiC was studied in oxidizing, reducing and carbonizing conditions by thermochemical modeling of existing PFBCs.

### Flow-Through Test

An initial flow-through test has been conducted on a section of 3M Type 203 filter at 870°C and 5 slm for 50 hours. Figure 3 contains a scanning electron micrograph of the inner surface of the filtering layer of the as-received 3M filter. The filtering layer consists of a mat of chopped Nextel 312 fibers with a CVI layer of SiC. The fiber surfaces appear smooth with spherical features on the order of 5 microns. Figure 4 shows the inner surface of the filtering layer after exposure. The mat now consists of 1 micron diameter fibrils extending from the chopped fiber surface.

Constant volume x-ray powder diffraction of the filtering layer of the as-received 3M filter revealed the presence of alpha SiC. The SiC is likely a mix of polytypes but the x-ray pattern most closely matches that of the 15R polytype (JCPDS file number 39-1196). X-ray on the exposed 3M filtering layer revealed an amorphous or glassy component and several low-angle peaks in addition to the SiC peaks found in the as-received 3M filter (Figure 5). The low-angle peaks seem to indicate the presence of trace amounts of tridymite.



Figure 3: Filtering Layer of 3M Type 203 Filter As-Received

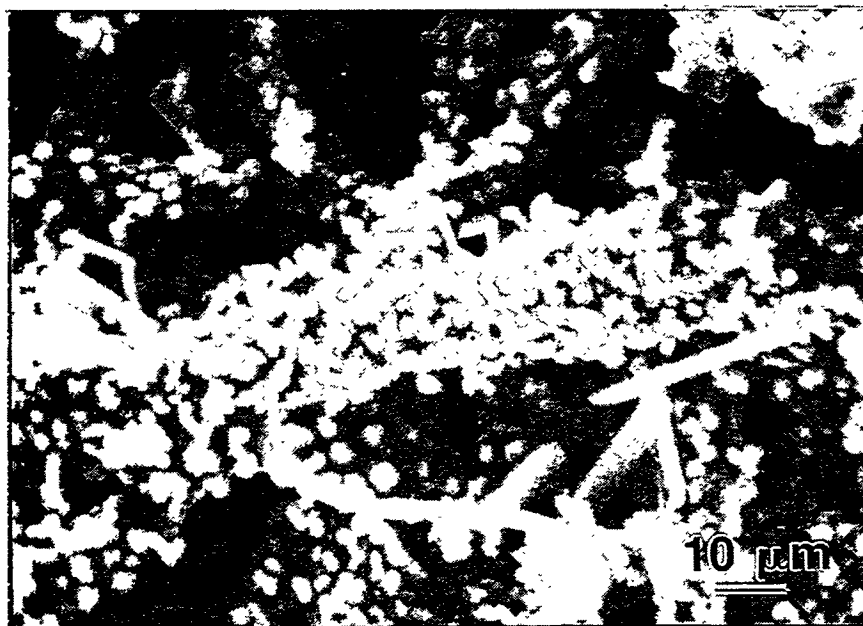


Figure 4: Filtering Layer of 3M Type 203 Filter After Exposure at 870°C for 50 Hours

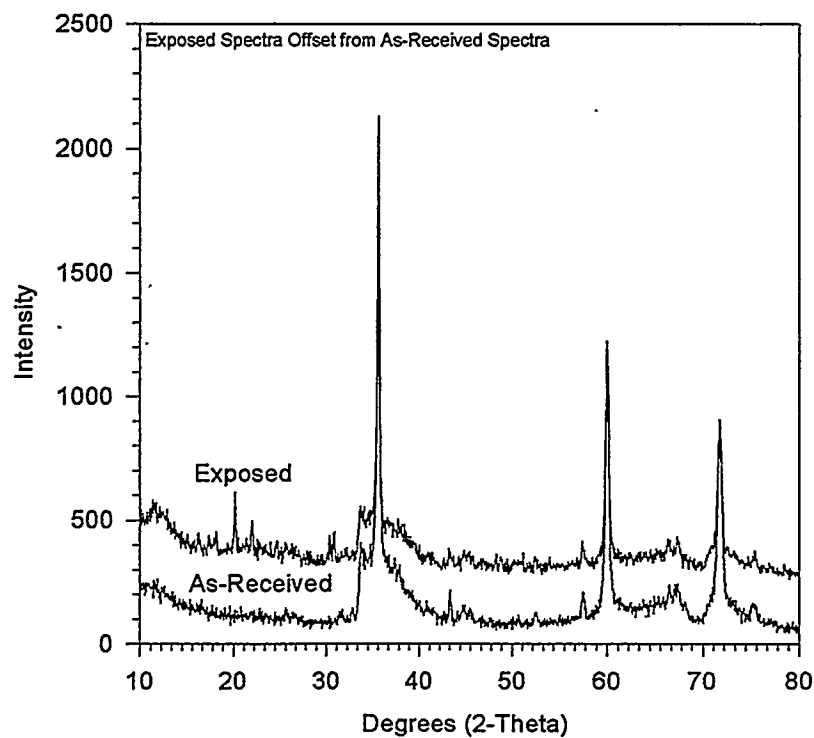


Figure 5: X-ray Diffraction of As-Received and Exposed Filtering Layer from 3M Type 203 Filter

As-received and exposed 3M filter materials were cut into 4" sections for internal pressurized burst testing. To pressurize the tubes from these materials, 3 inch rubber plugs were made and centered 0.5 inches from each end to minimize edge effects. The ends of the plugs were then compressed at a crosshead speed of 5 mm/min until the tube sections failed. Results indicate that the exposed filter maintained approximately 85 % of its initial strength.

### Thermochemical Modeling

Previous investigations have studied and analyzed the Si-O-H system over a range of temperatures and pressures.<sup>5-8</sup> They proposed that temperature, pressure and H<sub>2</sub>O (g) partial pressure would be the biggest determinants as to which silicon species would dominate in the gaseous phase. Si(OH)<sub>4</sub>, Si<sub>2</sub>O(OH)<sub>6</sub>, SiO(OH) and SiO(OH)<sub>2</sub> are among the silicon gases believed to be present in appreciable amounts over a broad temperature (600 - 1675 K) and pressure range (1 - 9000 atm). Among these, Si(OH)<sub>4</sub> (g) is thought to be the most dominate over the temperature and pressure ranges that combustion systems typically operate.

Six combustion systems were examined with ChemSage under normal operating conditions as summarized in Table 1. ChemSage calculates the equilibrium of products based upon the initial input of temperature, pressure and reactant species composition. A series of calculations were made to simulate the conversion of SiC to SiO<sub>2</sub>. Figure 6 is a schematic of the reaction routes which can occur during corrosion of SiC, SiC/SiO<sub>2</sub> and SiO<sub>2</sub> (top of Figure 6). Regions I, II and III are the equilibrium conditions that can exist after the reaction is complete (bottom of Figure 6). SiC, SiO<sub>2</sub>, carbon and the product gases are in equilibrium in Region I. This equilibrium can be reached by an initial system of SiC or SiC/SiO<sub>2</sub>. In Region II, all of the SiC has been removed at equilibrium and only carbon, SiO<sub>2</sub> and the product gases remain. This region is only reached by an initial SiC/SiO<sub>2</sub> system. Region III consists of 100 % silica. All of the SiC and carbon have been removed from the system. An SiC/SiO<sub>2</sub> or pure SiO<sub>2</sub> system can reach this equilibrium. Figures 7 through 12 have the equilibrium regions labeled at the top of each graph. The x-axis on each figure represents the initial percentage of SiC and SiO<sub>2</sub>. The far left of each graph represents 100 % SiC while the far right indicates 100 % SiO<sub>2</sub>. Each data point is equal to a decrease of 5 % SiC and a corresponding increase of 5 % SiO<sub>2</sub>.

Figures 7 through 12 show the predicted equilibrium for each system as SiC is converted to SiO<sub>2</sub>. In all of the systems, Si(OH)<sub>4</sub> (g) is the dominant silicon gas present after a layer of silica has formed on the SiC. This agrees with the previous studies<sup>5,6,8</sup>. However, there is no appreciable Si(OH)<sub>4</sub> (g) product when SiC is still present. Active oxidation of SiC results in the formation of SiO<sub>2</sub> and the removal of silicon by SiO, SiS and SiH<sub>4</sub> gases. The presence of sulfur seems to have a great impact on the removal of silicon from the system. Even a small amount of sulfur (20 ppm) as in the Pinon Pine combustor (Figures 10 and 11) can seriously affect the removal of silicon from SiC. The Argonne National Laboratory reducing combustor (Figure 8) is the only system studied that does not include sulfur. As a result, the partial pressure of the dominant silicon containing gas (SiO) in region "A" is several orders of magnitude lower than any silicon containing gas in the other systems. Also of significance is the prediction of free carbon formation in all of the systems under conditions where SiC is still present. This is due to the reducing atmosphere encountered in all of the systems after the conversion of SiC to SiO<sub>2</sub>.

The Pinon Pine system is of particular interest since the reducing conditions are the same except for the difference in pressure. When SiC is still present in the system at equilibrium, an increase in pressure from 1 to 10 atm causes a jump in SiH<sub>4</sub> (g) production by two orders of magnitude overtaking SiS (g) as the dominant silicon gas. However, the total removal of silicon only increases by approximately one order of magnitude assuming the gas phase reaches equilibrium. However, once a layer of silica forms, the Si(OH)<sub>4</sub> gas jumps three orders of magnitude for the same pressure increase.

	<u>Argonne National Lab</u>	<u>Argonne National Lab</u>	<u>Penn State</u>	<u>Pinon Pine</u>	<u>Pinon Pine</u>	<u>Wilsonville Facility</u>
Condition	Oxidizing	Reducing	Oxidizing	Reducing	Reducing	Carbonizing
Temperature	850°C	650°C	870°C	750°C	750°C	816°C
Pressure	1 atm	1 atm	1 atm	1 atm	10 atm	11.6 atm
N <sub>2</sub>	72.4 %	50 %	-	48.66 %	48.66 %	52.60 %
CO <sub>2</sub>	13.5 %	6.9 %	-	5.45 %	5.45 %	23.7 %
CO	-	8.8 %	-	23.89 %	23.89 %	6.8 %
O <sub>2</sub>	3.7 %	-	30 %	-	-	-
H <sub>2</sub> O	10.5 %	24 %	15 %	5.51 %	5.51 %	12.5 %
H <sub>2</sub>	-	9.4 %	-	14.57 %	14.57 %	0.5 %
SO <sub>2</sub>	250 ppm	-	3300 ppm	-	-	-
H <sub>2</sub> S	-	-	-	20 ppm	20 ppm	0.08 %
NaCl	50 ppm	50 ppm	10 ppm	-	-	30 ppm
CH <sub>4</sub>	-	-	-	1.35 %	1.35 %	1.6 %
NH <sub>3</sub>	-	-	-	0.02 %	0.02 %	0.08 %
Other	-	-	HCl - 1100 ppm Air - Balance	Ar - 0.56 %	Ar - 0.56 %	COS - 0.015 % C <sub>2+</sub> - 2.1 %

Table 1: Operating Conditions and Gas Compositions for Combustion Systems

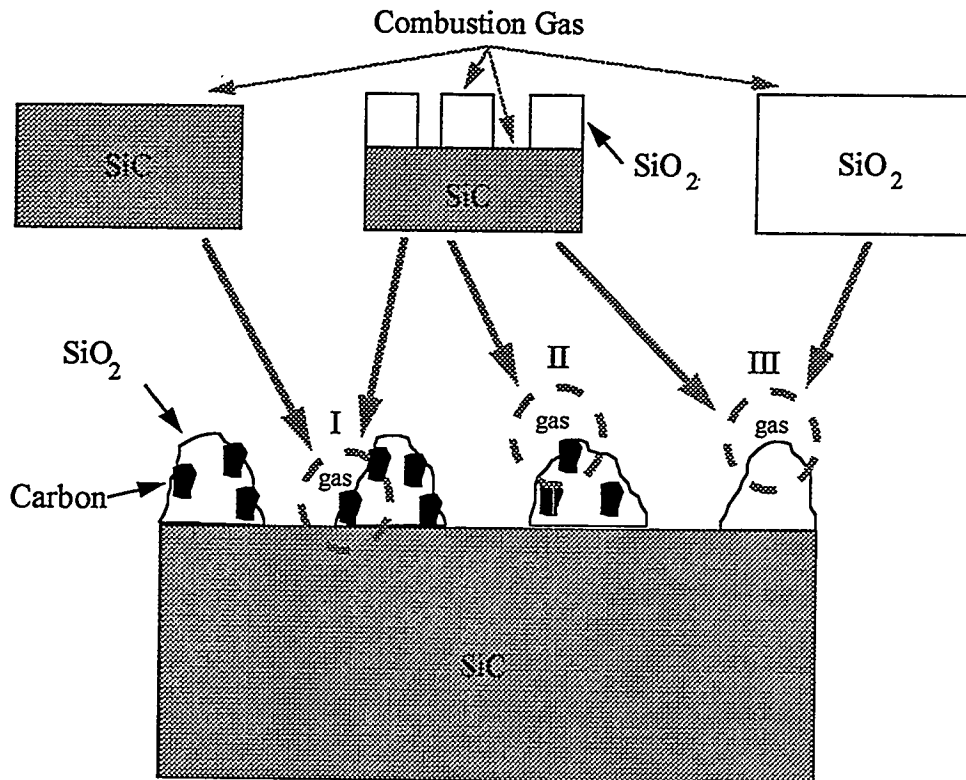


Figure 6: Schematic of Reaction Routes for Combustion Gas with SiC, SiC/SiO<sub>2</sub> and SiO<sub>2</sub>

## CONCLUSIONS

Flow-through tests on candidate ceramic filters are underway and preliminary results indicate that the filtering layer of the 3M Type 203 SiC material undergoes a morphological change as well as the formation of a glassy phase. Internal pressurized burst testing reveals a decrease in the strength of the filter of approximately 15 %.

Thermochemical modeling of this and other combustion systems in use suggests that Si(OH)<sub>4</sub> gas is the primary source of silicon loss once a scale of silica has formed on the SiC. This should not discount the fact that significant silicon transport may also occur directly from the SiC body by SiO (g), SiH<sub>4</sub> (g) and particularly SiS (g) when sulfur is present. Further work needs to be done both experimentally and theoretically to fully understand the transport of silicon from the SiC/SiO<sub>2</sub> system.

Simulating a combustion system with thermochemical modeling gives us the opportunity to study three areas in particular. First, it allows us to determine the dominant gaseous species of a system. Second, oxide (SiO<sub>2</sub>) and nonoxide (SiC) phases can be easily compared. Third, we can vary the pressure to decide how to simulate a high pressure run (10 atm) at 1 atmosphere.

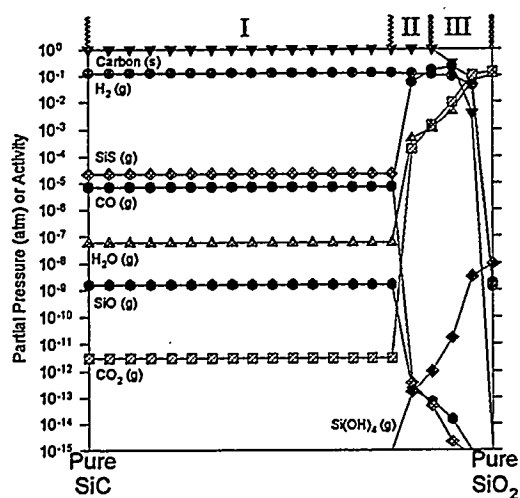


Figure 7: Predicted Partial Pressures and Activities of Product Species During Reaction of SiC with an Oxidizing Environment at 850°C and 1 atm (Argonne National Laboratory)

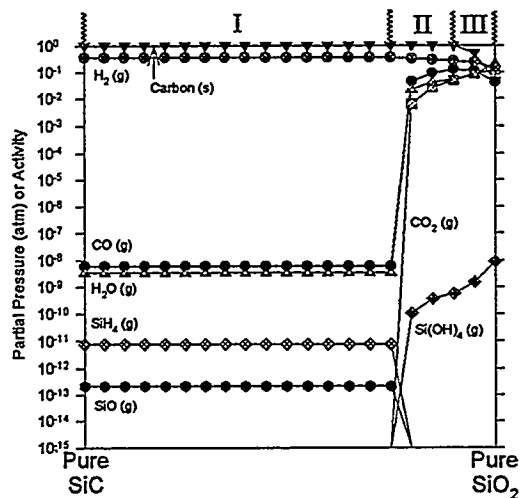


Figure 8: Predicted Partial Pressures and Activities of Product Species During Reaction of SiC with a Reducing Environment at 650°C and 1 atm (Argonne National Laboratory)

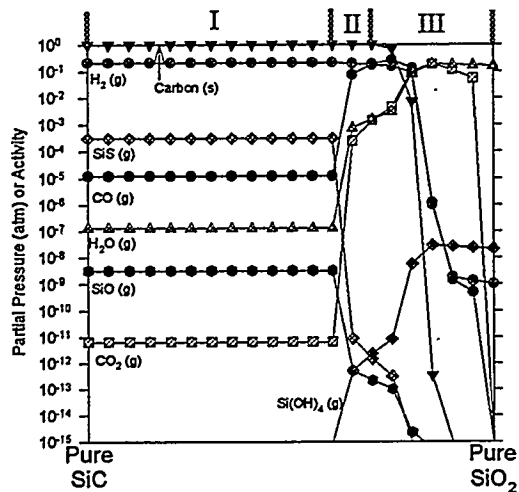


Figure 9: Predicted Partial Pressures and Activities of Product Species During Reaction of SiC with an Oxidizing Environment at 870°C and 1 atm (Penn State)

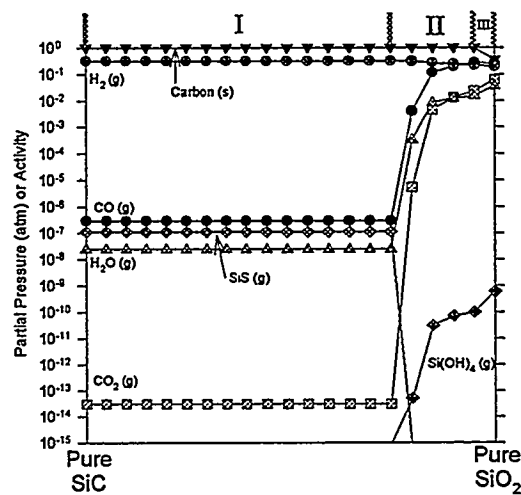


Figure 10: Predicted Partial Pressures and Activities of Product Species During Reaction of SiC with a Reducing Environment at 750°C and 1 atm (Pinon Pine)

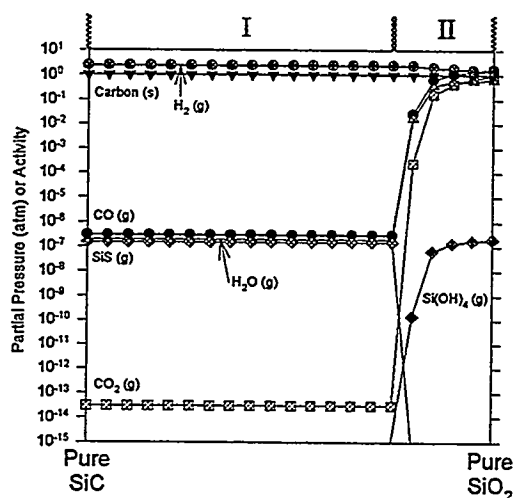


Figure 11: Predicted Partial Pressures and Activities of Product Species During Reaction of SiC with a Reducing Environment at 750°C and 10 atm (Pinon Pine)

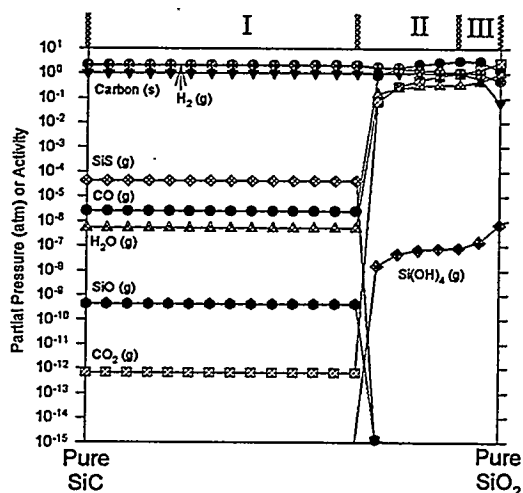


Figure 12: Predicted Partial Pressures and Activities of Product Species During Reaction of SiC with a Carbonizing Environment at 816°C and 11.6 atm (Wilsonville Facility)

1. G. Eriksson, ChemSage Application Software for Thermochemical Calculations, Version 3.0.1, © GTT TECHNOLOGIES, 1994.
2. B. Cheynet, MICROTHERM Thermodynamic Databank System for Inorganic Substances, © Thermodata, 1989.
3. M.D. Allendorf, C. F. Melius, P. Hoo, M. R. Zachariah, "Theoretical Study of the Thermochemistry of Molecules in the Si-O-H System," *Journal of Physical Chemistry*, Vol. 99, pp. 15285 (1995).
4. D.L. Shelleman, O.M. Jadaan, D.P. Butt, R.E. Tressler, J.R. Hellmann, and J.J. Mecholsky, Jr., "High Temperature Tube Burst Test Apparatus," *Journal of Testing and Evaluation*, JTEVA, Vol. 20, No. 4, July 1992, pp. 275-284.
5. O. H. Krikorian, "Thermodynamics of the Silica-Steam System," Symposium on Engineering with Nuclear Explosives, 14-16 January 1970, Las Vegas, NV 1970 (Unpublished), Vol. 1, pp. 481.
6. A. Hashimoto, "The Effect of H<sub>2</sub>O Gas on Volatilities of Planet-Forming Major Elements: I. Experimental Determination of Thermodynamic Properties of Ca-, Al-, and Si-Hydroxide Gas Molecules and its Application to the Solar Nebula," *Geochimica et Cosmochimica Acta*, Vol. 56, pp. 511-532 (1992).
7. D. L. Hildenbrand and K. H. Lau, "Thermochemistry of Gaseous SiO(OH), SiO(OH)<sub>2</sub>, and SiO<sub>2</sub>," *Journal of Chemistry and Physics*, Vol. 101, No. 7, pp. 6076-6079 (1994).
8. E. J. Opila and R. E. Hann, Jr., "Paralinear Oxidation of CVD SiC in Water Vapor," submitted to the *Journal of the American Ceramic Society*, January 1996.



EFFECT OF HEAT TREATMENT AT 1150°C ON CREEP-RUPTURE  
PROPERTIES OF ALLOY FA-180

C. G. McKamey and P. J. Maziasz

Metals and Ceramics Division  
Oak Ridge National Laboratory  
Oak Ridge, TN 37831-6115

ABSTRACT

The alloy FA-180, with a composition of Fe-28Al-5Cr-0.5Nb-0.8Mo-0.025Zr-0.05C-0.005B (at.%), is of interest because of its improved creep-rupture resistance when compared to alloy FA-129 (Fe-28Al-5Cr-0.5Nb-0.2C). At a temperature of 593°C and under a stress of 207 MPa, the creep-rupture life of FA-129 heat treated for 1 h at 750°C is about 20 h while the FA-180 alloy lasts approximately 100 h. Heat treatment at 1150°C has been shown to further improve the creep life of FA-180 and creep-rupture lives of approximately 2000 h have been attained. This strengthening was attributed to the presence of fine matrix and grain boundary Zr-rich MC precipitates that were produced by the heat treatment. The current study continues our investigation of the effect of heat treatment at 1150°C on the improvement of creep-rupture life in alloy FA-180. As part of our effort to understand the strengthening mechanisms involved with heat treatment at 1150°C, transmission electron microscopy was used to correlate the microstructure with the improved creep resistance. Results indicate that heat treatment at 1150°C for 1 h, followed by rapid quenching in water or mineral oil, produces even further improvements in the creep-rupture life of this alloy. A specimen being tested at 593°C and 207 MPa was stopped after over 6000 h of life, while another specimen lasted over 1600 h at 650°C and 241 MPa. The microstructure of the oil-quenched specimen contained many dislocation loops which were not present in the air-cooled specimens. These loops pinned dislocations during creep testing at temperatures of 593-700°C, resulting in a stabilized deformation microstructure and increased creep-rupture strength.

INTRODUCTION

Past studies have shown that binary Fe<sub>3</sub>Al possesses low creep-rupture strength compared to many other alloys, with creep-rupture lives of less than 5 h being reported for tests conducted at 593°C and 207 MPa.<sup>1,2</sup> The combination of poor creep resistance and low room-temperature tensile ductility due to a susceptibility to environmentally-induced dynamic hydrogen embrittlement<sup>3-5</sup> has limited use of these alloys for structural applications despite their generally excellent corrosion behavior.<sup>6</sup> With regard to the ductility problem, alloy development efforts have produced significant improvements, with ductilities of 10-20% and tensile yield strengths as high as 500 MPa being reported.<sup>7,8</sup> Likewise, initial improvements in creep resistance have been realized through small additions of Mo, Nb, and Zr.<sup>1,9-13</sup>

In recent years, further creep strengthening has been produced by using heat treatments to control the microstructure.<sup>14,15</sup> As shown in Fig. 1, for an Fe-28Al-5Cr (at.%) alloy containing additions of Mo, Nb, Zr, C, and B (designated alloy FA-180), a 1-h 1150°C heat treatment produced creep lives of over 2000 h for tests conducted at 593°C and 207 MPa. Especially interesting is the sharp dependence of creep strength on heat treating temperature, which is illustrated by the data in Fig. 1. In earlier studies, transmission electron microscopy revealed the presence of fine precipitates which appeared to pin dislocations.<sup>14</sup> This, together with an activation energy for creep of approximately 150 kcal/mole (a value which is about twice that obtained earlier<sup>1</sup> for the binary alloy heat treated at 750°C) and high creep exponents of 7-12 (ref. 15), indicated that the observed strengthening was being produced by a precipitation mechanism. The general conclusion was that the 1150°C heat treatment resulted in the dissolution of coarse particles remaining from the melting and casting process, and then reprecipitation of finer Zr-based precipitates during cooling or the early stages of creep produced the strengthening.

The current research effort is focused on reaching a better understanding of the relationship between microstructure and strengthening mechanism(s) for this alloy and heat treatment. This paper summarizes those efforts.

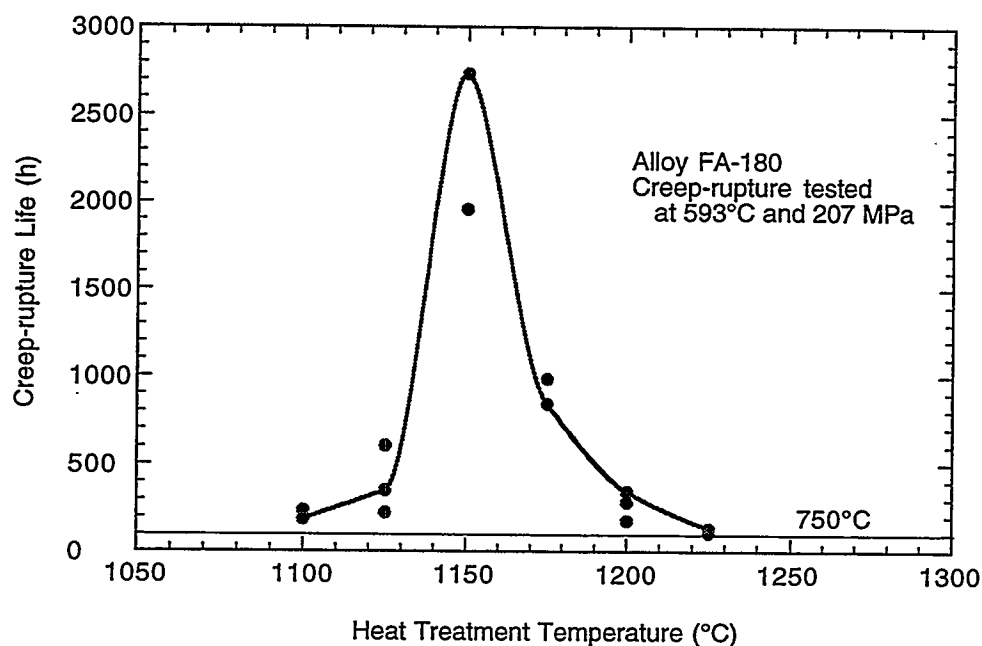


Fig. 1. Creep-rupture life as a function of heat treatment temperature (for 1 h anneals) for tests conducted on alloy FA-180 at 593°C and 207 MPa.

## EXPERIMENTAL PROCEDURES

The alloy composition used in this study was Fe-28Al-5Cr (at.%) with 0.5% Nb, 0.8% Mo, 0.025% Zr, 0.05% C, and 0.005% B (Oak Ridge National Laboratory designation FA-180). It was prepared by arc-melting and drop-casting into a chilled copper mold. Fabrication to 0.8-mm-thick sheet was accomplished by hot-rolling, beginning at 1000°C and finishing at 600-650°C. After a stress relief heat treatment of 1 h at 700°C, flat tensile specimens (0.8 x 3.18 x 12.7 mm) were mechanically punched from the rolled sheet. Before creep-rupture testing, specimens were further annealed in air for 1 h at 1150°C and then were either air cooled to room temperature or were quenched in oil or water.

Creep-rupture tests were performed in air at temperatures between 593 and 750°C under stresses of 138 to 276 MPa (20-40 ksi). In order to obtain creep exponents and activation energies, minimum creep rates (MCR) were measured as the slope of the linear portion of the test curve and the data were plotted to a power-law equation. The results for quenched specimens were compared to earlier published data on air-cooled specimens.<sup>15</sup>

Optical metallography and scanning electron microscopy (SEM) were used to study the microstructures and fracture modes. Analytical electron microscopy (AEM) using either a Philips CM30 (300 kV) or a CM12 [120 kV, with ultra-thin-window x-ray energy dispersive spectrometry (XEDS) detector] electron microscope was performed on samples cut from the gage portion of selected test specimens.

## RESULTS AND DISCUSSION

Creep-rupture tests were conducted on specimens cooled by different methods from the 1150°C heat treatment temperature and the data are presented in Table I. The creep-rupture lives of the rapidly cooled specimens are compared in Fig. 2 with the life of a specimen that had been cooled in air from the 1150°C heat treatment temperature and then tested at 593°C. The more rapidly cooled specimens (oil or water quenched) exhibited the best resistance to creep. Even though the air-cooled specimen had exhibited a very good rupture life of approximately 1959 h when tested at 593°C and 207 MPa, a specimen that had been quenched in oil showed no signs of rupturing (no increase in the very low, steady-state creep rate) after 6480 h, at which time the test was stopped. Likewise, the water quenched specimen that was tested at 650°C under a stress of 241 MPa ruptured after 1637 h, while another specimen that had been cooled more slowly in air and tested at the same conditions lasted less than 3 h. The strengthening mechanism, therefore, appears to be different for quenched versus air

Table I. Creep-Rupture Data for Alloy FA-180 as a Function of the Method Used for Cooling from the 1150°C Heat Treatment

Method of Cooling	Creep-rupture Test Conditions	Life (h)	Elongation (%)	MCR (/s)
air	593°C, 207 MPa	1959	10	$8.3 \times 10^{-7}$
oil quench	593°C, 207 MPa	>6480	5	$2.8 \times 10^{-8}$
air	650°C, 241 MPa	2.7	42	$2.2 \times 10^{-3}$
water quench	650°C, 241 MPa	1637	9	$2.2 \times 10^{-7}$

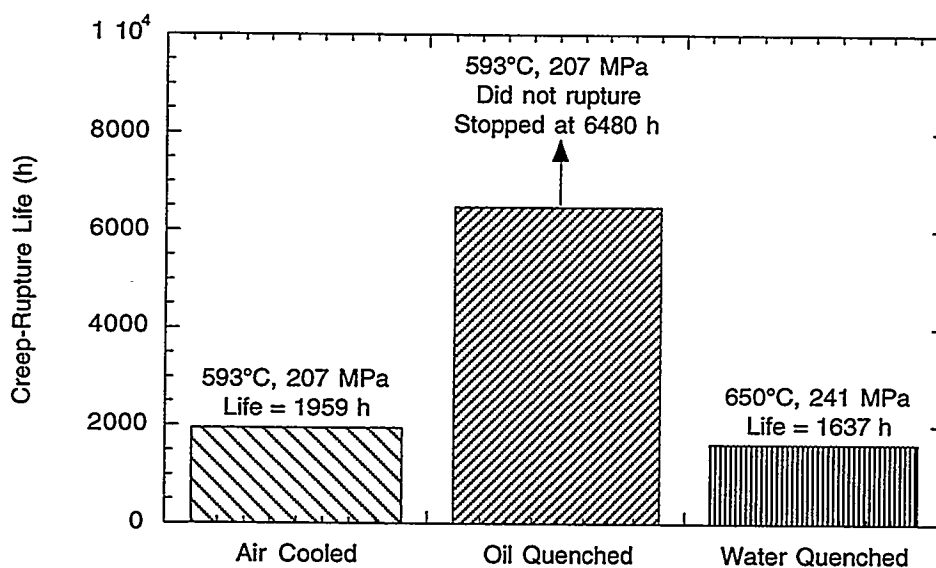


Fig. 2. Creep-rupture life of air-cooled versus quenched specimens of alloy FA-180.

cooled specimens, although the quenching medium itself does not appear to be the cause of that effect.

Creep tests were conducted as a function of temperature and stress in order to determine if the activation energies for creep ( $Q$ ) and the creep exponents ( $n$ ) were the same in both the air-cooled and oil-quenched conditions. The results are shown in Figs. 3 and 4. At a stress of 207 MPa (30 ksi), the activation energy for creep in the oil-quenched specimens was determined to be 76.6 kcal/mole, compared to a  $Q$  of 141.1 kcal/mole for air-cooled specimens. (The value of  $Q$  reported here for the air cooled specimens is slightly different from that reported earlier<sup>15</sup> because it was derived from more data points.) This significant difference in activation energy suggests that a

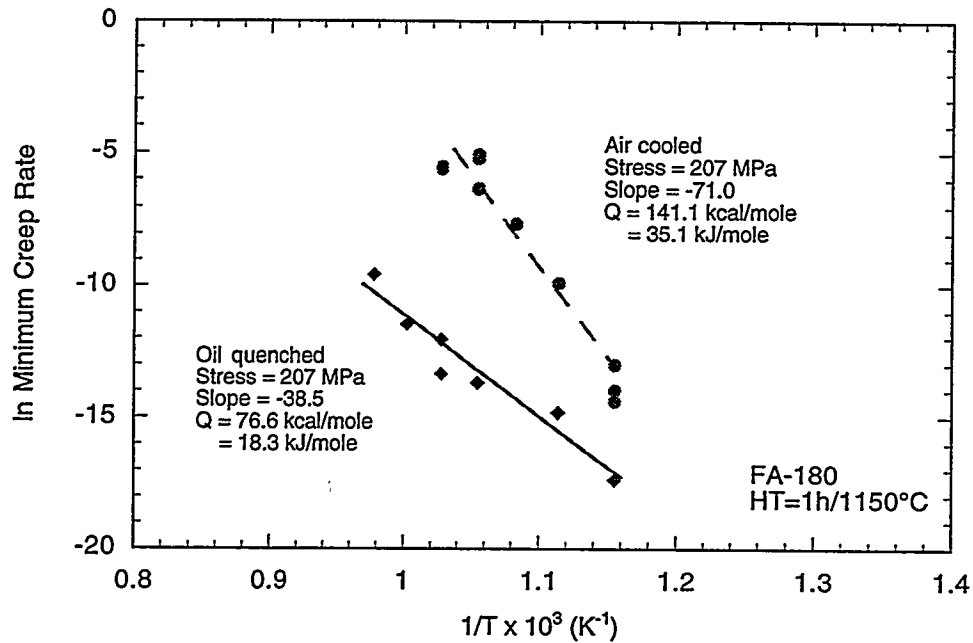


Fig. 3. Minimum creep rate versus temperature data for air cooled versus oil quenched specimens of alloy FA-180 heat treated at  $1150^\circ\text{C}$ . All tests were conducted at a stress of 207 MPa (30 ksi).

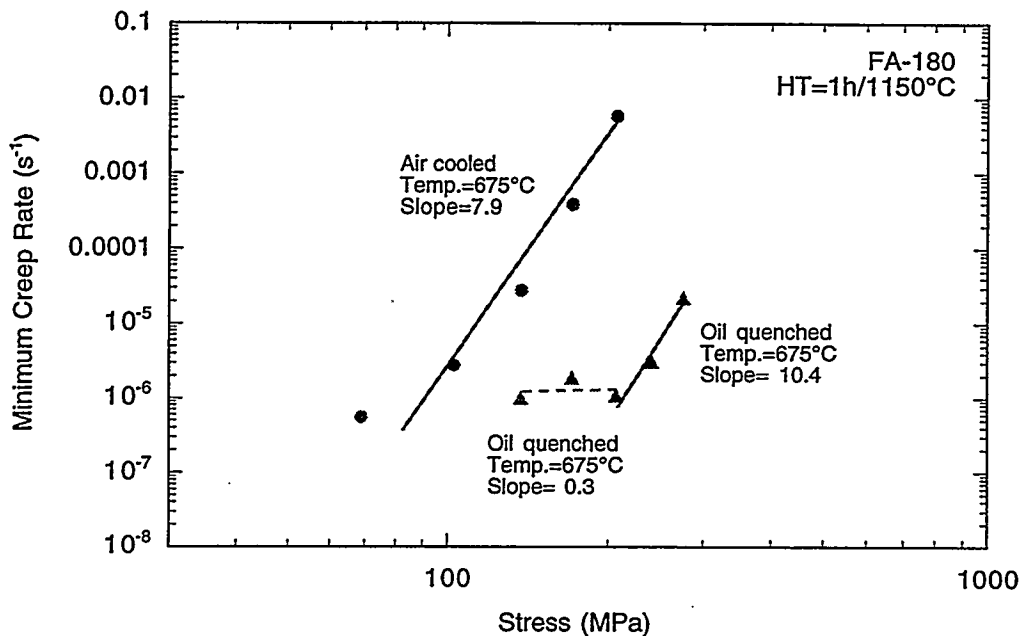


Fig. 4. Minimum creep rate versus stress data for air cooled versus oil quenched specimens of alloy FA-180 heat treated at  $1150^\circ\text{C}$ . All tests were conducted at  $675^\circ\text{C}$ .

different rate-controlling mechanism is active in the oil-quenched specimens. A plot of minimum creep rate versus stress (Fig. 4) shows a distinct break at approximately 200 MPa, with the creep exponent increasing at higher stresses. This behavior is indicative of a change in the rate-controlling creep mechanism with stress and is common in the data for many precipitate-hardened alloys.<sup>16,17</sup> The creep exponent of 10.4 shown in Fig. 4 for the oil-quenched specimens and the creep exponent for the air cooled specimens, which was earlier calculated to be 7.9 (ref. 15), are both indicative of alloys which have been hardened by precipitates or some other dislocation-pinning mechanism.<sup>18,19</sup>

Transmission electron microscopy was used to study the microstructure of the oil-quenched specimen that had been tested for 6480 h at 593°C. The micrograph in Fig. 5 shows that the creep-tested specimen contained networks of two-fold dislocations and many dislocation loops. At a higher magnification (Fig. 6), a few fine precipitates were also visible. Closer examination of the loops (Fig. 7) indicated that they were square or rectangular in shape and were restricted to the orthogonal habit planes (either  $\langle 110 \rangle$  or  $\langle 100 \rangle$ ). Additionally, the dislocation segments in the loops appeared to be single rather than 2-fold and the four segments of each loop were of the same Burgers vector. For comparison, Fig. 8 shows the microstructure of a specimen in the as-heat-treated-and-oil-quenched (untested) condition. The dominant features are the B2 ordered domains and many black dots visible by black-white strain contrast imaging. In this case, by rotating the specimen through several diffracting conditions, most of the black dots visible in the microstructure in Fig. 8 were identified as vacancy dislocation loops, not precipitates. It therefore appears that these fine loops were created in the microstructure as a result of the rapid quench from the 1150°C annealing temperature. This is in contrast to the results from air-cooled specimens reported earlier in which fine Zr-based precipitates that formed during cooling were found to provide some measure of strengthening during creep.<sup>14</sup> Since it is known that vacancies are created in the Fe-Al system by quenching from high temperatures, especially for the B2 structure,<sup>20,21</sup> the identification of these dislocation loops as being vacancy loops is not unreasonable. Vacancy loop nature would also be consistent with their growth during further heat treatment or creep testing. During creep-rupture testing at the temperatures used in this study, the loops provided strengthening by pinning dislocations and grew in size in the process (as indicated by the larger loop size in the as-tested specimen, Fig. 5).

## CONCLUSIONS

In earlier studies the creep-rupture strength of Fe<sub>3</sub>Al-based alloy FA-180 (Fe-28Al-5Cr-0.5Nb-0.8Mo-0.025Zr-0.05C-0.005B, at.%) was shown to be improved



Fig. 5. TEM micrograph of FA-180 oil-quenched from a heat treatment at 1150°C and creep tested at 593°C for 6480 h.



Fig. 6. Higher magnification of Fig. 5 showing presence of fine precipitates.



Fig. 7. Higher magnification TEM micrograph of dislocation loops visible in Fig. 5.

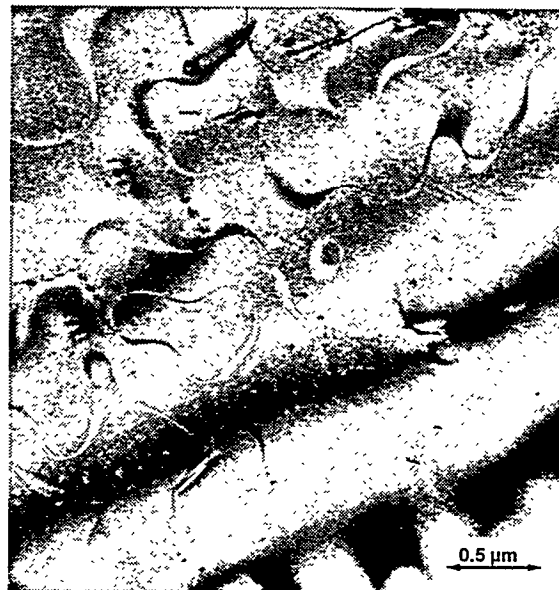


Fig. 8. TEM micrograph of alloy FA-180 showing B2 domains and fine dislocation loops (black dots) produced by oil-quenching from a heat treatment at 1150°C.

significantly by heat treating for 1 h at 1150°C. This strengthening was attributed to the dissolution at 1150°C of coarse particles left over from the melting and casting process and reprecipitation during cooling or during testing at 593°C of fine Zr-based matrix and grain boundary precipitates. In this study, creep-rupture tests were conducted on specimens of FA-180 that had been cooled quickly (oil or water quenched) from the 1150°C heat treatment. The results were compared to the previous data on specimens that were cooled more slowly in air. The more rapidly cooled specimens exhibited the best resistance to creep. This additional strengthening was attributed to the formation of dislocation loops as a result of the rapid quench. These loops pinned dislocations and grew slowly during testing at temperatures of 593-700°C, resulting in a stabilized deformation microstructure.

### ACKNOWLEDGEMENTS

This research was sponsored by the U.S. Department of Energy, Office of Fossil Energy, Advanced Research and Technology Development Materials Program, and by the Assistant Secretary for Energy Efficiency and Renewable Energy, Office for Industrial Technologies, Advanced Industrial Materials Program, under contract DE-AC05-96OR22464 with Lockheed Martin Energy Research Corp.

### REFERENCES

1. C. G. McKamey, P. J. Maziasz, and J. W. Jones, *J. Mater. Res.*, **7**(8) (1992), 2089-2106.
2. C. G. McKamey, J. H. DeVan, P. F. Tortorelli, and V. K. Sikka, *J. Mater. Res.*, **6**(8) (1991), pp. 1779-1805.
3. C. T. Liu, C. G. McKamey, and E. H. Lee, *Scripta Metall. Mater.*, **24**(2) (1990), 385-90.
4. C. T. Liu and C. G. McKamey, *High Temperature Aluminides and Intermetallics*, ed. S. H. Whang, C. T. Liu, D. P. Pope, and J. O. Stiegler, (TMS, Warrendale, PA, 1990), pp. 133-151.
5. C. G. McKamey and C. T. Liu, *Proceedings of ADVMAT/91, First International Symposium on Environmental Effects on Advanced Materials*, edited by R. D. Kane, (Houston, TX: NACE, 1992), paper no. 17-1.
6. P. F. Tortorelli and J. H. DeVan, in *Processing, Properties, and Applications of Iron Aluminides*, edited by J. H. Schneibel and M. A. Crimp (TMS, Warrendale, PA, 1994), pp. 257-70.
7. V. K. Sikka, *SAMPE Quart.*, **22**(4) (1991), 2-10.
8. V. K. Sikka, S. Viswanathan, and C. G. McKamey, *Structural Intermetallics*, eds. R. Darolia, J. J. Lewandowski, C. T. Liu, P. L. Martin, D. B. Miracle, and M. V. Nathal, (Warrendale, PA: The Metallurgical Society, 1993), 483-91.
9. P. J. Maziasz and C. G. McKamey, *Mater. Sci. & Eng.*, **A152** (1992), 322-34.
10. D. M. Dimiduk, M. G. Mendiratta, D. Banerjee, and H. A. Lipsitt, *Acta Metall.*, **36** (1988), 2947-58.
11. P. J. Maziasz, C. G. McKamey, and C. R. Hubbard, *Alloy Phase Stability and*



*Design*, eds. G. M. Stocks, D. P. Pope, and A. F. Giamei (MRS, Pittsburgh, PA, 1990), pp. 349-55.

12. C. G. McKamey, P. J. Maziasz, G. M. Goodwin, and T. Zacharia, *Mat. Sci. & Eng.*, **A174** (1994), 59-70.

13. D. G. Morris, M. Nazmy, and C. Nosedo, *Scripta Metall. Mater.* **31**, 173 (1994).

14. C. G. McKamey and P. J. Maziasz, in *Processing, Properties, and Applications of Iron Aluminides*, edited by J. H. Schneibel and M. A. Crimp (TMS, Warrendale, PA, 1994), pp. 147-58.

15. C. G. McKamey, Y. Marrero-Santos, and P. J. Maziasz, in *High Temperature Ordered Intermetallic Alloys VI*, edited by J. A. Horton, I. Baker, S. Hanada, R. D. Noebe, and D. S. Schwartz (MRS, Pittsburgh, 1995), pp. 249-254.

16. O. D. Sherby and P. M. Burke, *Prog. Mater. Sci.* **13**, 325 (1968).

17. R. Lagneborg and B. Bergman, *Met. Sci. J.* **10**, 20 (1976).

18. K. Sadananda, H. Jones, C. R. Feng, and A. K. Vasudevan, in *High Temperature Ordered Intermetallic Alloys IV*, edited by L. A. Johnson, D. P. Pope, and J. O. Stiegler (MRS, Pittsburgh, 1991), pp. 1019-25.

19. I. Jung, M. Rudy, and G. Sauthoff, *High Temperature Ordered Intermetallic Alloys II*, edited by N. S. Stoloff, C. C. Koch, C. T. Liu, and O. Izumi (MRS, Pittsburgh, 1987), pp. 263-74.

20. P. Nagpal and I. Baker, *Metall. Trans.* **21A**, 2281 (1990).

21. A. Ball and R. E. Smallman, *Acta Metall.* **16**, 233 (1968).



The Influence of Composition on Environmental  
Embrittlement of Iron Aluminides

D. A. Alven and N. S. Stoloff  
Rensselaer Polytechnic Institute  
Troy, New York 12180-3590

Abstract

The effects of water vapor in air and hydrogen gas on the tensile and fatigue crack growth behavior of  $\text{Fe}_3\text{Al}$  alloys has been studied at room temperature. Fe-28a%Al-5a%Cr alloys to which either Zr alone or Zr and C have been added have been tested in controlled humidity air environments as well as in 1.3 atm hydrogen or oxygen gas and in vacuum. As with other  $\text{Fe}_3\text{Al}$  alloys, oxygen produces the lowest crack growth rates as well as the highest critical stress intensities and tensile ductility in each of the alloys tested. However, while Zr lowers crack growth rates in the Paris regime, there is no apparent beneficial effect on crack growth thresholds. Hydrogen gas also produces unusual results. While crack growth rates are very high in hydrogen in the Paris regime for all alloys, hydrogen only lowers the crack growth threshold relative to air in ternary Fe-28Al-5Cr; it does not lower the threshold in the Zr-containing alloys. Fracture path tends to be transgranular in all alloys and environments. The results will be discussed in the light of possible effects of Zr on oxide formation.

Introduction

Iron aluminides are currently being considered for use in applications where excellent corrosion resistance, moderate strength at temperatures up to 500°C, and low cost are desired. Binary iron aluminides do not possess high ductility at room temperature in air; however, when tested in vacuum or gaseous oxygen environments iron aluminides have demonstrated ductility of greater than 10% (1, 2, 3). This indicates that  $\text{Fe}_3\text{Al}$  is an inherently ductile material and the low ductility in air is due to an environmental interaction.

The purpose of this research was to examine the changes in mechanical properties of several  $\text{Fe}_3\text{Al}$ , Cr intermetallic alloys in various environments. The tensile behavior and fatigue crack growth resistance were examined and the resulting data will be discussed in the light of the role of hydrogen in embrittlement of the iron-aluminum alloys.

## Experimental Procedure

### *Alloy Composition and Heat Treatment*

The composition of the alloys examined in this study are shown in Table 1. All alloys were fabricated at the Oak Ridge National Laboratory (ORNL) by vacuum induction melting, extrusion, and in the case of plate material either hot or warm rolling to the final thickness. The annealing parameters for B2 order consisted of a 700°C anneal for 1 hour with a mineral oil quench, which was then repeated.

Table 1. Composition of Iron Aluminide Alloys (Atomic %)

	ternary	1%ZrC	0.5%ZrC	0.5%Zr
Fe	67.0	65.95	66.45	66.5
Al	28.0	28.0	28.0	28.0
Cr	5.0	5.0	5.0	5.0
Zr	-	1.0	0.5	0.5
C	-	0.05	0.05	-
Grain Size	180 $\mu$ m	Partially recrystallized	Partially recrystallized	Partially recrystallized

### *Tensile Tests*

Tensile specimens were either cylindrical with a 12.7mm long by 5.7mm diameter gauge section or sheet with a 5mm by 1.2mm by 0.5mm gauge section. All tension specimens were polished to a 0.3 $\mu$ m finish and ultra-sonically cleansed in acetone prior to testing. Testing was carried out in a servo-hydraulic MTS machine fitted with a vacuum chamber or a screw-driven Instron. The strain rate used in all test was  $3 \times 10^{-4}$ /sec. All test were conducted at room temperature.

When testing in oxygen or hydrogen gas, the environmental chamber was first evacuated to  $< 6.6 \times 10^{-4}$  Pa using a diffusion pump fitted with a cold trap. The appropriate gas was then admitted to the chamber at a pressure of 2300 Pa over atmospheric pressure for 1 hour prior to testing.

### *Fatigue Crack Growth Tests*

Fatigue crack growth tests were performed at room temperature in air, hydrogen, oxygen gas, and vacuum. When testing in an environment the evacuation procedure was the same as with the tensile tests. For constant humidity tests the chamber was first evacuated then compressed air was bubbled through a closed beaker containing an aqueous solution of potassium acetate, which produced 21%RH.

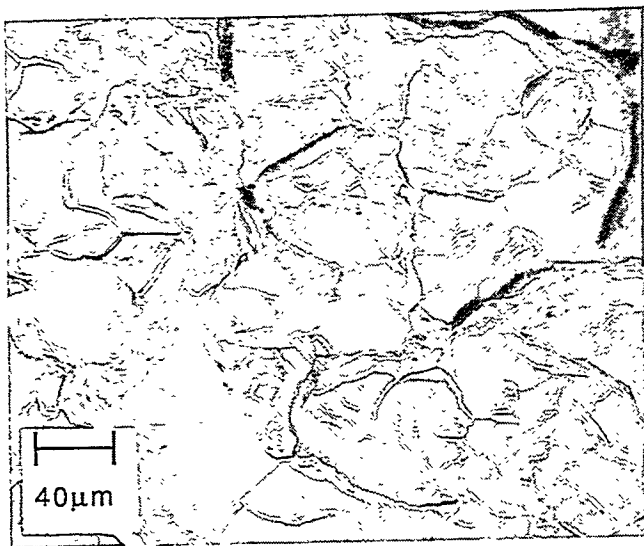
Compact tension specimens were used in all fatigue tests and were cut by electro discharge machining such that the crack propagation direction was perpendicular to the rolling direction. The ternary, 0.5%Zr, and 0.5%ZrC specimens were 31.75mm x 30.5mm x 4.8mm thick, while the 1%ZrC specimens were 28.7mm x 27.6mm x 3.6mm thick due to plate materials supplied by ORNL. Crack length was monitored via the d.c. potential drop method. Calibration curves were created relating crack length to potential drop by optically measuring the crack length with a traveling microscope. The R-ratio (minimum to maximum stress) was 0.5 in order to minimize crack closure effects and the frequency was 20Hz.

### Experimental Results

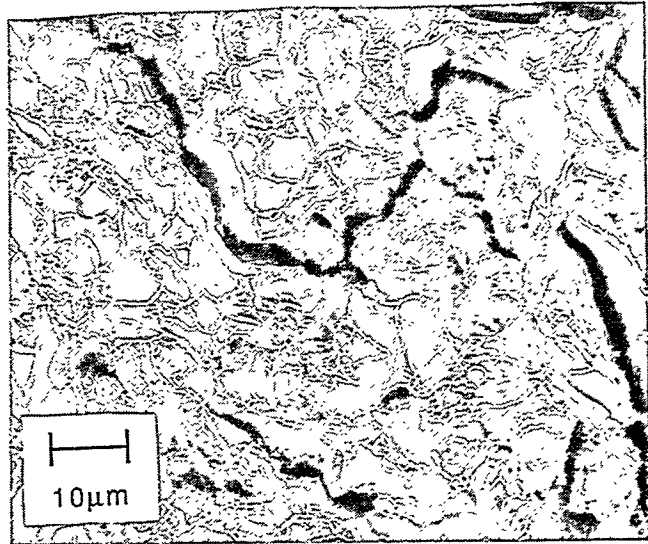
#### *Tensile Experiments*

Tensile data for the iron aluminides examined are listed in Table 2. Alloy 0.5%ZrC had the highest ductility and UTS of all alloys tested. Oxygen provided the highest ductility and UTS for the Ternary alloy while 0.5%ZrC had the same values of ductility and UTS in air and oxygen. Increasing the amount of Zr to 1a% resulted in a decrease of both the ductility and UTS, while the removal of C also decreased the ductility and UTS, but not as severely.

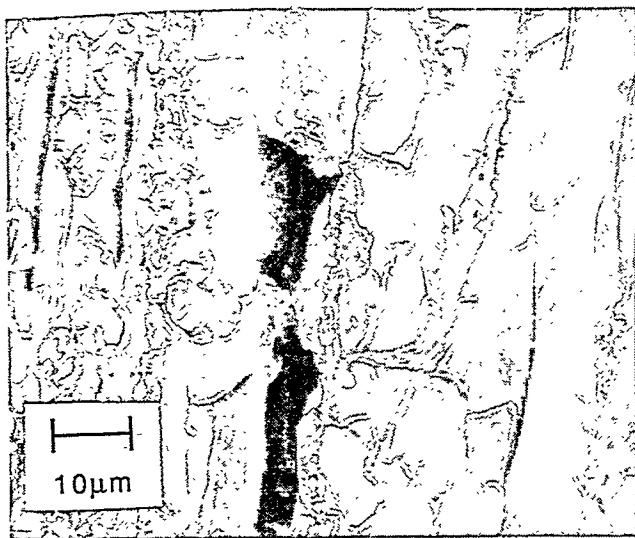
Figures 1(a) - 1(d) show the fracture surfaces of all the alloys tested in air. Fractographic features were found to be insensitive to environment in both the ternary and the 0.5%ZrC alloys. The fracture mode was observed to be mixed transgranular



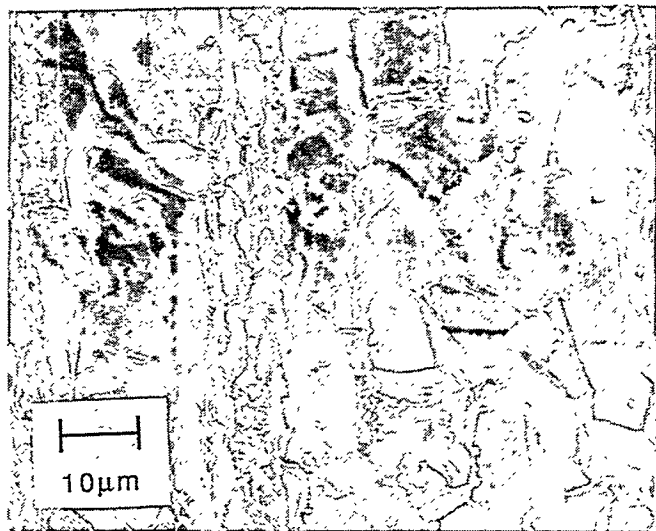
(a)



(b)



(c)



(d)

Fig. 1. Fracture Surfaces of the (a) Ternary Alloy, (b) 0.5%ZrC Alloy, (c) 0.5%Zr Alloy and (d) 1%ZrC Alloy Tested in Tension at 25°C in Air

cleavage and intergranular fracture in the ternary alloy with a switch to transgranular cleavage and dimpled rupture in the 0.5%ZrC and 0.5%Zr alloys. The fracture mode reverted back to mixed transgranular cleavage and intergranular fracture in the 1%ZrC alloy.

Table 2. Tensile Properties of the Iron Aluminides

Alloy	Air			O <sub>2</sub>			H <sub>2</sub>		
	YS (MPa)	UTS (MPa)	Ductility (%)	YS (MPa)	UTS (MPa)	Ductility (%)	YS (MPa)	UTS (MPa)	Ductility (%)
Ternary	500	980	10.2	510	1180	12.8	500	740	4.2
0.5%ZrC	690	1460	13.8	680	1460	13.1	680	1200	6.1
0.5%Zr *	670	1000	8.2	-	-	-	-	-	-
1%ZrC *	510	880	5.3	-	-	-	-	-	-

\* Average of three tests

#### *Fatigue Crack Growth Experiments*

Fatigue crack growth curves are shown in Figures 2, 3, 4, and 5 for the iron aluminides studied. Table 2 lists the threshold and critical stress intensities, as well as the stress intensity necessary to produce a crack growth rate of  $10^{-7}$  m/cycle. The slope in the Paris regime is not reported since a linear region in the  $da/dN$  vs.  $\Delta K$  curves could not always be defined.

Table 2. FCG Data for the Iron Aluminides

Alloy	Environment	$\Delta K$ ( $10^{-7}$ )	$\Delta K_{TH}$	$\Delta K_C$
		(MPa $\sqrt{m}$ )	(MPa $\sqrt{m}$ )	(MPa $\sqrt{m}$ )
Ternary	Air (30% rH)	20.3	16.9	26.4
Ternary	O <sub>2</sub>	38.4	24.2	42.4
Ternary	Vacuum	32.6	29.2	39.1
Ternary	H <sub>2</sub>	15.1	14.2	19.9
0.5%ZrC	Air (21% rH)	29.0	18.0	59.4
0.5%ZrC	O <sub>2</sub>	42.3	18.6	68.7
0.5%ZrC	Vacuum	29.0	23.2	38.0
0.5%ZrC	H <sub>2</sub>	21.1	19.8	42.8
0.5%Zr	Air (21% rH)	28.1	18.7	39.0
0.5%Zr	O <sub>2</sub>	43.3	20.0	48.9
0.5%Zr	Vacuum	32.6	32.5	46.1
0.5%Zr	H <sub>2</sub>	21.2	20.5	38.9
1%ZrC	Air (21% rH)	22.8	16.2	27.6
1%ZrC	O <sub>2</sub>	35.9	23.0	36.8
1%ZrC	Vacuum	30.4	26.9	35.1
1%ZrC	H <sub>2</sub>	21.2	20.5	38.9

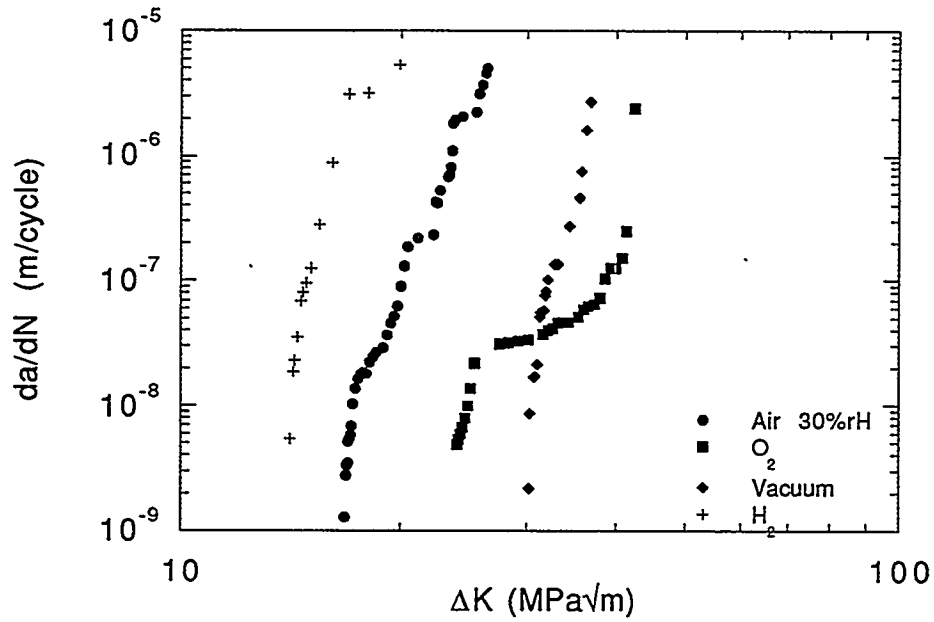


Figure 2. Fatigue Crack Growth Curves for the Ternary Alloy at 25°C.

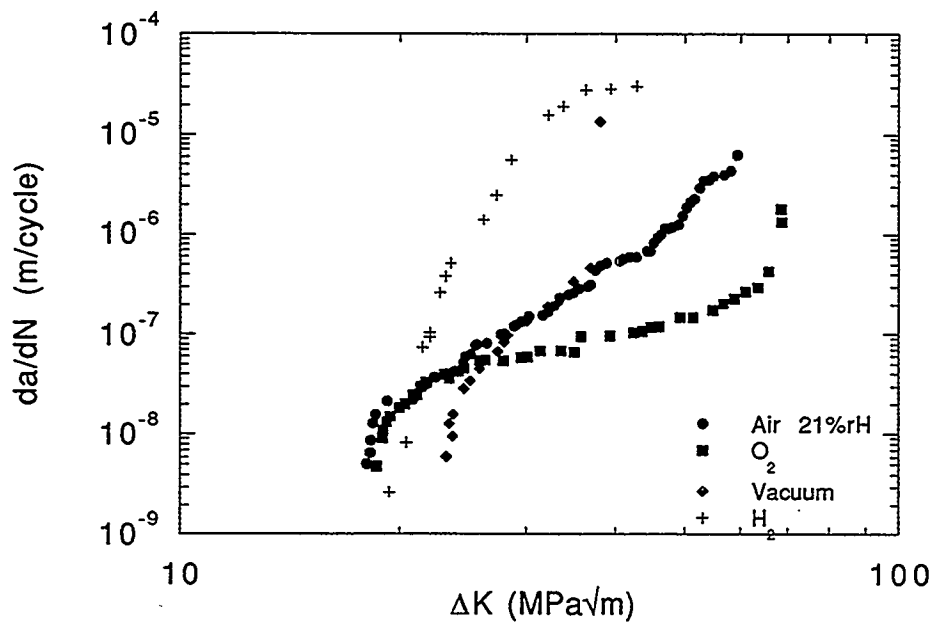


Figure 3. Fatigue Crack Growth Curves for the 0.5%ZrC alloy at 25°C.



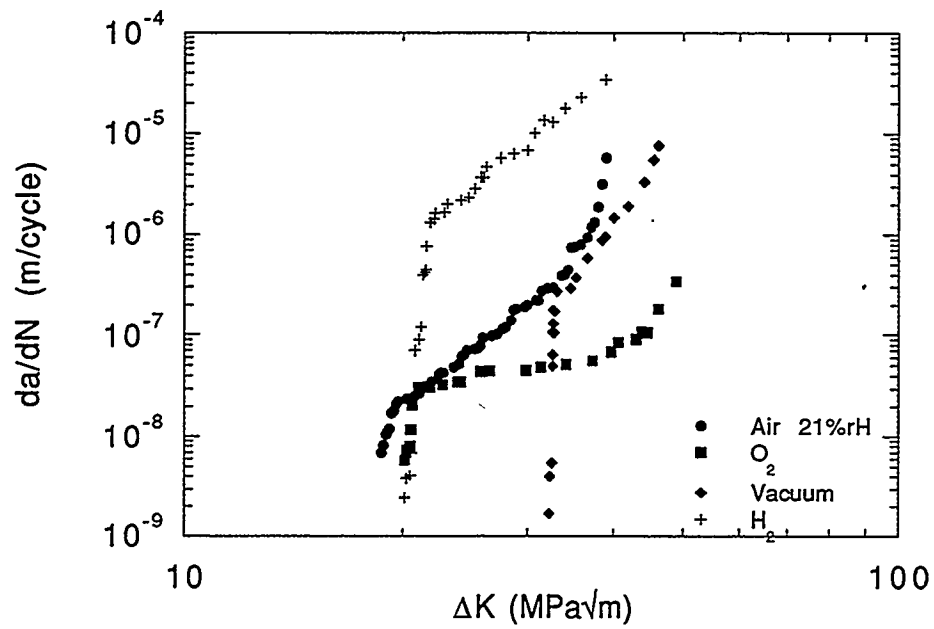


Figure 4. Fatigue Crack Growth Curves for the 0.5%Zr Alloy at 25°C.

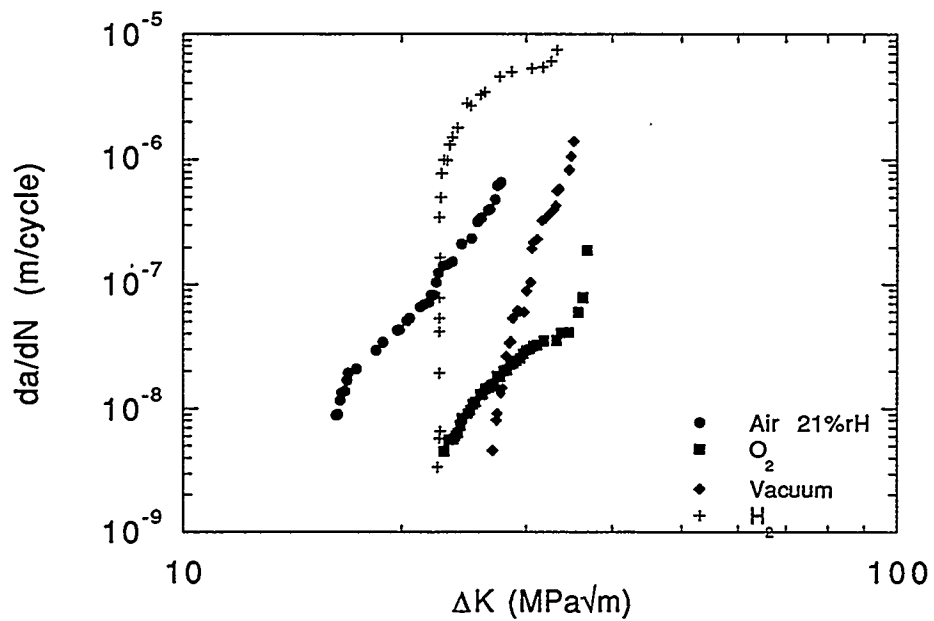


Figure 5. Fatigue Crack Growth Curves for the 1%ZrC Alloy at 25°C.

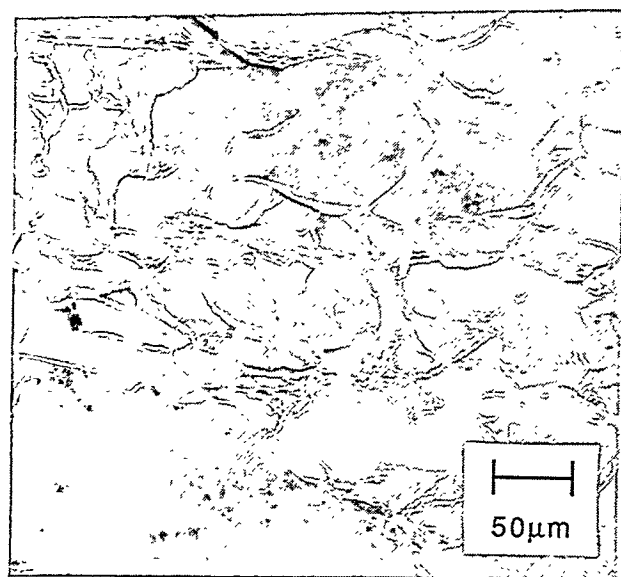
In all alloys tested oxygen provides the lowest crack growth rates. The 0.5%ZrC alloy has the highest critical stress intensity values in all environments, except vacuum, of the alloys studied. The addition of carbon to the 0.5%Zr alloy does not affect the crack growth rates but significantly increases the fracture toughness. The increase in Zr content to 1a% is detrimental to the crack growth resistance while increasing the threshold stress intensities in all environments except air. In all Zr-containing alloys the threshold stress intensity when tested in hydrogen gas was found to be higher than in air.

Figures 6(a) - 6(d) show the fracture surfaces of the fatigued specimens. The fracture surfaces were found to be insensitive to environment for all alloys. The ternary alloy exhibited mixed transgranular cleavage and intergranular fracture, while the fracture mode of the 0.5%ZrC alloy was transgranular, by what appears to be a tearing mechanism. The 1%ZrC alloy failed by a mixed transgranular tearing and intergranular fracture mode, while the 0.5%Zr alloy failed by mostly transgranular tearing.

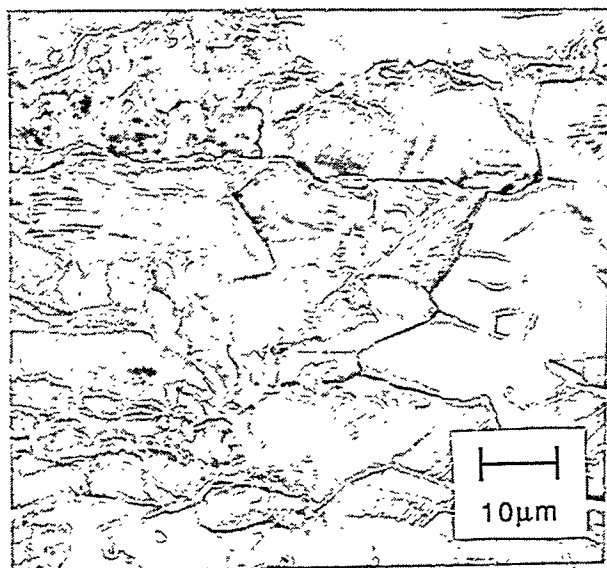
#### Discussion

The increased tensile elongation of the ternary alloy in oxygen as compared to air demonstrates the embrittling effect of moisture in laboratory air, which is consistent with previous findings on Fe<sub>3</sub>Al,Cr (4, 5). The 0.5%ZrC alloy exhibits similar elongations in air and oxygen while the elongation is reduced in hydrogen. For the Zr-containing alloys the elongation is reduced when the C is removed and further reduced when the Zr content is increased to 1a% with the C content maintained at 0.05a%. This suggests that a small amount of Zr can increase the intrinsic ductility of Fe<sub>3</sub>Al,Cr alloys.

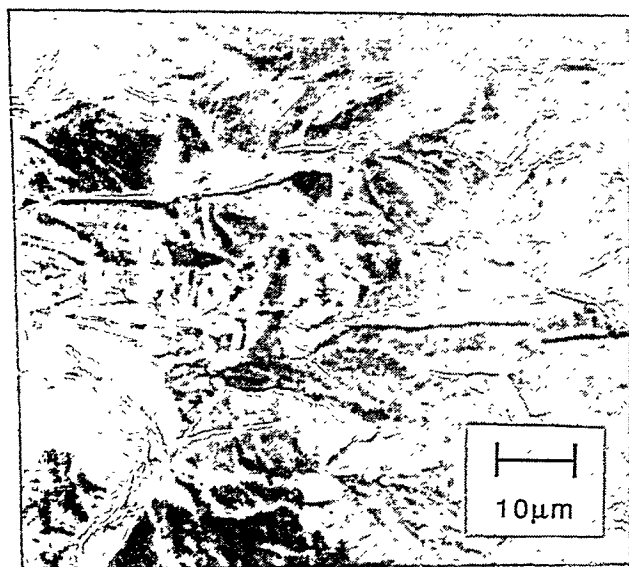
The fatigue crack growth behavior of all alloys clearly show the embrittling effect of hydrogen whether it is present as hydrogen gas or water vapor in air. The lowest crack growth rates were found in oxygen for all alloys. The difference in critical stress intensity in the Zr-containing alloys between air and oxygen (about 21%) was much less



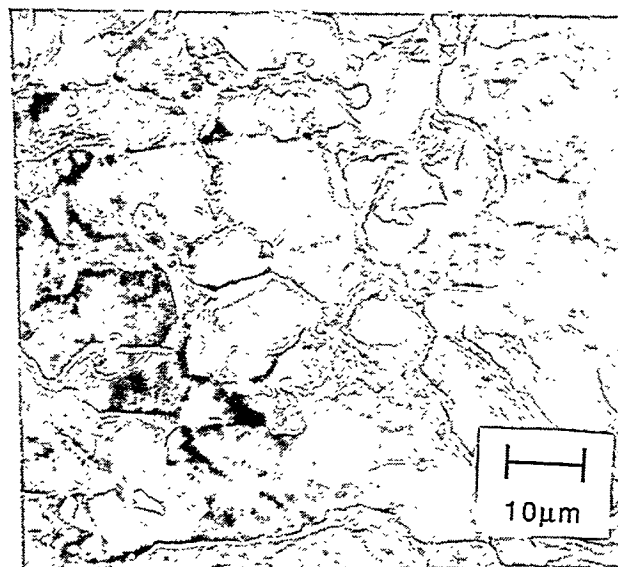
(a)



(b)



(c)



(d)

Fig. 6. Fracture Surfaces of (a) Ternary Alloy, (b) 0.5%ZrC Alloy, (c) 0.5%Zr Alloy and (d) 1%ZrC Alloy Fatigued at 25°C in Air

than in the ternary alloy (36%) which indicates that Zr-containing alloys are less susceptible to moisture-induced embrittlement.

The threshold stress intensities are affected by Zr additions. The addition of 1a% Zr is only beneficial in hydrogen; in all other environments there is no difference when compared to the ternary alloy. In air and in hydrogen 0.5a% Zr raises the threshold stress intensity by 6% and 28% respectively, while in oxygen it lowers the threshold stress intensity by 23% when compared to the ternary alloy.

An interesting effect of the addition of Zr was on the fatigue crack growth resistance in hydrogen. In all Zr-containing alloys the threshold stress intensity is higher in hydrogen gas than in air while the crack growth rate is much higher. The threshold stress intensity also exhibits no change from oxygen to hydrogen for all Zr-containing alloys.

The low crack growth rates in the 0.5%Zr alloys were the most surprising results of this investigation. It has been reported that Zr can influence the oxide formation in iron aluminides at elevated temperatures(6), but it remains to be determined if a similar effect takes place on fresh fracture surfaces at room temperature.

Another explanation by which Zr could affect the crack growth rate is either as a grain boundary strengthener and/or a trap for H so that the later can not reach the crack-tip region. The addition of 0.5a% Zr results in a change from mixed transgranular cleavage and intergranular fracture to transgranular tearing, which could point to both an increase in the strength of grain boundaries as well as trapping of H before it reaches the potential flaw sites of the cleavage planes. Zr additions have been found to increase tensile ductilities in  $\text{Ni}_3\text{Al}$  alloys (7, 8, 9) but the fracture mode was unchanged. Further work is in progress to try to identify the mechanism for improved crack growth resistance of Zr-containing alloys.

### Conclusions

The addition of small amounts of Zr to Fe<sub>3</sub>Al,Cr alloys results in lower crack growth rates. The beneficial effect of Zr is limited, since the addition of 1a% Zr results in higher crack growth rates, similar to those for the ternary alloy. The addition of C appears to only affect the fracture toughness of Fe<sub>3</sub>Al,Cr alloys. Zr additions also result in increased threshold values in hydrogen when compared to air, while the crack growth rate at higher  $\Delta K$  was higher in hydrogen.

### Acknowledgements

The authors are grateful to the Department of Energy, Fossil Energy Program for providing financial support under Martin Marietta Energy Subcontract No. 19X-SF521C. The authors are also grateful for helpful discussions with Dr. V. K. Sikka of ORNL and to Dr. Sikka for providing the alloys.

### References

1. C. T. Liu, E. H. Lee and C. G. McKamey, *Scr. Metall.*, vol. 23, pp. 875-880 (1989).
2. A. Castagna, Ph.D. Thesis, Rensselaer Polytechnic Institute (1995).
3. A. Castagna, P. J. Maziasz and N. S. Stoloff, I. Baker, R. Darolia, J. D. Whittenberger, M. H. Yoo, Eds., *High Temperature Ordered Intermetallic Alloys V* (MRS Symp. Proc., Pittsburgh, 1993), vol. 288, pp. 1043-1048.
4. C. G. McKamey, J. A. Horton and C. T. Liu, *J. Mater. Res.*, vol. 4, pp. 1156-1163 (1989).
5. C. G. McKamey and C. T. Liu, *Scr. Metall.*, vol. 24, pp. 2119-2122 (1990).
6. P. F. Tortorelli, . (Oak Ridge National Laboratory, private communication, 1995),
7. E. P. George, C. T. Liu and D. P. Pope, *Scripta Metall.*, vol. 27, pp. 365-370 (1992).
8. E. P. George, C. T. Liu and D. P. Pope, *Scripta Metall.*, vol. 28, pp. 857-862 (1993).
9. E. P. George, C. T. Liu and D. P. Pope, in *Structural Intermetallics* R. Darolia, J. J. Lewandowski, C. T. Liu, P. L. Martin, D. B. Miracle, M. V. Nathal, Eds. (TMS, Warrendale, PA, 1993) pp. 431-436.



## EFFECTS OF TITANIUM AND ZIRCONIUM ON IRON ALUMINIDE WELDMENTS

R. P. Burt\*, G. R. Edwards\*, and S. A. David\*\*

\*Center for Welding, Joining, and Coatings Research  
Colorado School of Mines  
Golden, CO 80401

\*\*Oak Ridge National Laboratory  
Metals and Ceramics Division  
Oak Ridge, TN 37831

### ABSTRACT

Iron aluminides form a coarse fusion zone microstructure when gas-tungsten arc welded. This microstructure is susceptible to hydrogen cracking when water vapor is present in the welding environment. Because fusion zone microstructural refinement can reduce the hydrogen cracking susceptibility, titanium was used to inoculate the weld pool in iron aluminide alloy FA-129. Although the fusion zone microstructure was significantly refined by this method, the fracture stress was found to decrease with titanium additions. This decrease is attributed to an increase in inclusions at the grain boundaries.

### INTRODUCTION

Iron aluminides have good strength, oxidation resistance, and corrosion resistance at high temperatures. However, using these alloys for structural applications has been limited due to the poor weldability of these materials. Iron aluminides form a coarse fusion zone microstructure which is susceptible to hydrogen cracking when gas-tungsten arc (GTA) welded in the presence of water vapor. Previous research has demonstrated that the resistance to hydrogen cracking can be improved by refining the fusion zone microstructure in iron aluminide weldments.

Fasching used magnetic arc oscillation to refine the fusion zone microstructure in iron aluminide alloy FA-129 weldments<sup>1</sup>. When welded in an inert environment, arc oscillation effectively refined the fusion zone microstructure, and the refined microstructures demonstrated improved fracture stress and ductility when slow strain rate tensile tested in the presence of water vapor. Water vapor was then added to the welding environment to determine if the improved properties of the refined fusion zone decreased the susceptibility to hydrogen cracking. However, each different water vapor concentration present during welding required unique parameters for effective magnetic arc oscillation fusion zone refinement. Recent work has focused on finding a refinement method less sensitive to the welding environment. This paper reports the effect of weld pool inoculation on the properties of alloy FA-129.

## EXPERIMENTAL PROCEDURE

Ingots of alloy FA-129 were melted and cast under vacuum at Oak Ridge National Laboratory with the composition shown in Table 1. The ingots were extruded and then hot rolled at 650°C to a nominal thickness of 760 $\mu$ m. After a 2-hr anneal at 650°C, the sheet was pickled in a solution of 20 parts water, 2 parts nitric acid, and one part hydrofluoric acid to remove the oxide layer.

Table 1 Iron aluminide alloy FA-129 composition

	Fe	Al	Cr	Nb	C
wt. pct.	66.3	28.0	5.00	0.50	0.20
at. pct.	77.7	15.9	5.45	0.97	0.05

Welding coupons were sheared from the sheet to be used for either metallographic analysis (51mm x 51mm) or tensile testing (76mm x 51mm). A groove was machined into the coupons using a bandsaw with no lubrication, and the coupons were then given a final cleaning with methanol prior to welding. Titanium powder (99.5%, <44 $\mu$ m) was deposited in the groove and covered with a 430 $\mu$ m protective cap made of FA-129 as well. The final sample configuration is shown in Figure 1.

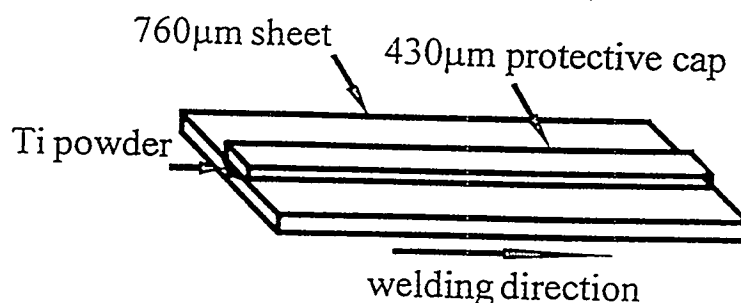


Fig. 1. Schematic diagram of welding coupon used for inoculation study.

A series of GTA welds were made in an argon filled glovebox to determine the effects of heat input and titanium concentration on the fusion zone microstructure. Table 2 summarizes the matrix used.



Table 2 Range of test variables

	Low	High
Heat Input (J/mm)	118	142
Titanium Addition (mg/10mm)	2	6

For metallographic analysis of the weldments, samples were mounted, ground, and polished using standard metallographic techniques. The etchant used to observe the fusion zone microstructure was 60 ml methanol, 40 ml nitric acid, and 20 ml hydrochloric acid. The average fusion zone grain size was determined by using a Leco image analyzer to measure the length, width, and thickness of the fusion zone grains. The average grain size reported is the average of the three measurements.

For inclusion analysis, an etchant of 96 ml water, 2 ml nitric acid, and 2 ml hydrofluoric acid was used. Inclusion fractions were determined by performing point counting on micrographs taken from several locations in the fusion zone. Inclusions were classified as either being located in the matrix or at a grain boundary.

Tensile testing samples were also welded in an inert environment. After welding, the coupons were sheared to a width of 25 millimeters, ground to a uniform thickness across the weldment, and a reduced section was ground into the specimen at the fusion zone (Figure 2). The epoxy beads were added to prevent slipping of the extensometer during tensile testing.

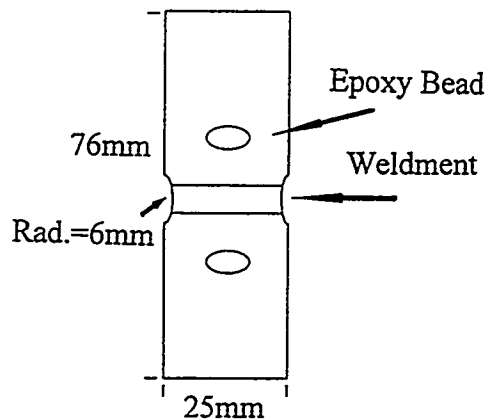


Fig. 2. Schematic of sample used for slow strain rate tensile testing.

Slow strain rate tensile testing ( $2.78 \times 10^{-6} \text{ s}^{-1}$ ) was performed on an M.T.S. fitted with a Plexiglas chamber to control the testing environment. Water vapor was added to the chamber by bubbling argon through deionized water to obtain testing environments which varied the water vapor concentration from 300 to 9000 ppm. A humidity meter was used to measure the actual water vapor concentration in the chamber during the tensile test. The load and strain data were collected on a P.C. during the test. Fracture stress was determined by dividing the maximum load by the cross-sectional area of the fractured sample.

## RESULTS AND DISCUSSION

The addition of titanium to the weld pool effectively refined the fusion zone microstructure. The average grain size in the fusion zone was found to be dependent upon three parameters: travel speed, heat input, and titanium concentration. Initial welding was performed at 4 mm/s. At this travel speed a molten ball was observed to develop in front of the weld pool, which was then pushed ahead of the arc. No fusion zone refinement was observed. When the travel speed was decreased to 2 mm/s, and the welding current was adjusted such that the heat input was not changed, a typical weld pool was formed and the fusion zone was refined.

The lowest heat input used in the study, 118 J/mm, was chosen because it was the minimum value which gave full penetration during welding. However, at the low heat input, fusion zone refinement was not uniform down the weld length and was not consistent from weld to weld. At the higher heat input value, 142 J/mm, fusion zone refinement was uniform throughout the weld and repeatable from weld to weld.

Finally, the fusion zone microstructure was dependent upon titanium concentration. With no titanium addition, the fusion zone microstructure consisted of large columnar grains meeting at a well defined centerline. The average unrefined fusion zone grain size was  $530 \mu\text{m}$ . With the lowest titanium addition, the microstructure was a mixture of columnar grains, located at the edge of the fusion zone, and more equiaxed grains at the weld centerline. With higher titanium additions, the fusion zone was completely uniform with fine, equiaxed grains.

The results of the initial tests are shown in Table 3. Given the more consistent results obtained when the higher heat input of 142 J/mm was used with a travel speed of 2 mm/s, these parameters were used when welding coupons for tensile samples. The high and low titanium additions were kept the same for the tensile sample testing. Using energy dispersive spectroscopy, it was determined that the addition of 2mg/10mm of titanium resulted in 0.8 weight percent titanium in the fusion zone and an average fusion zone grain size of  $370 \mu\text{m}$ . Similarly, a 6mg/10mm titanium addition resulted in 1.2 weight

percent titanium in the fusion zone and an average fusion zone grain size of  $70\mu\text{m}$ . Figure 3 shows the microstructures obtained using the above parameters. These represent the microstructures used for slow strain rate tensile testing.

Table 3 Effect of welding parameters on fusion the fusion zone microstructure with titanium inoculation

Heat Input (J/mm)	Ti Addition (mg/10mm)	Avg. Fusion Zone Grain Size ( $\mu\text{m}$ )	Aspect Ratio (length/width)	Uniform Refinement
118	2	215	2.6	No
118	6	280	2.9	No
142	2	370	3.6	Yes
142	6	70	1.6	Yes

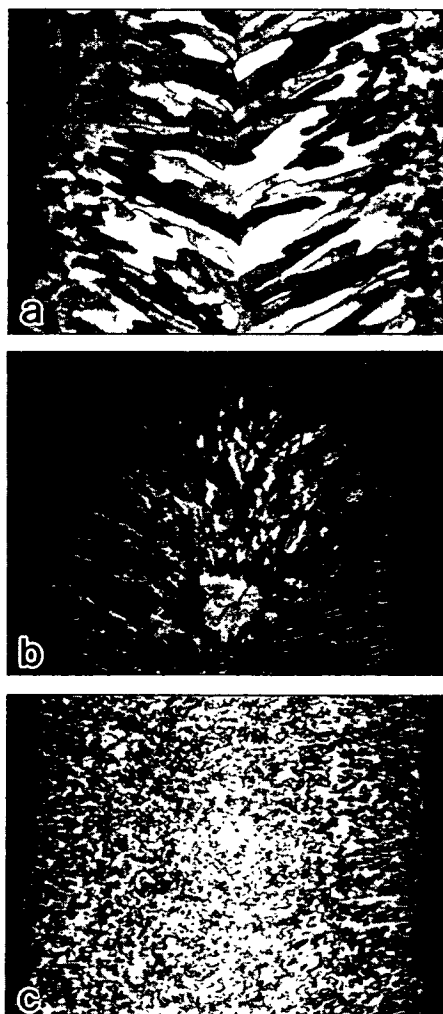


Fig. 3. Fusion zone microstructure of titanium inoculated welds. a) 0% Ti, b) 0.8% Ti, c) 1.2% Ti (14X)

The effects of titanium additions and welding parameters on the fusion zone microstructure are not unexpected. Titanium additions were made with the expectation that the particles would dissolve and precipitate out as carbides and possibly oxides or intermetallics during solidification. These inclusions would then provide heterogeneous nucleation sites in the weld pool. Weld pool conditions are more favorable for these reactions with a slower travel speed. Decreasing the travel speed, while holding the heat input constant by adjusting either the welding current or voltage, gives more time for reactions in the weld pool. If the heat input is increased, the weld pool conditions are also more favorable due to the improved reaction kinetics.

Slow strain rate tensile testing, however, did not give expected results. With increasing titanium concentration, decreasing average grain size, the fracture stress decreased (Figure 4). The fracture stress measured for the unrefined weldments were consistent with Fasching's study<sup>1</sup>, consequently, the decrease does not appear to be a material heat effect or a result of the tensile sample configuration (no reduced section was used in Fasching's study).

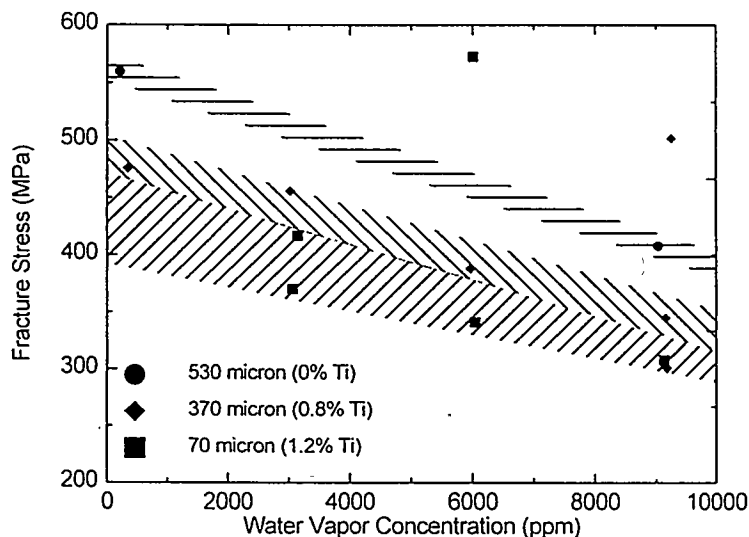


Fig. 4. Fracture stress of titanium inoculated welds as a function of titanium concentration and water concentration.

The effect of titanium on the fusion zone inclusion distribution appears to be the cause of the decrease in fracture stress. The overall fraction of inclusions measured in the fusion zone was independent of titanium concentration. Inclusions constituted approximately 6 percent of the fusion zone microstructure. However, when titanium was added to the weld, the fraction of inclusions at the grain

boundaries increased. In the unrefined weld, 15 percent of the inclusions were located at the grain boundaries. With 0.8 and 1.2 weight percent titanium in the fusion zone, 43 and 50 percent of the inclusions were found at the grain boundaries, respectively. Figure 5 shows the typical inclusion distribution as a function of titanium concentration. At 1.2 weight percent titanium, numerous grain boundaries were almost completely coated with inclusions.

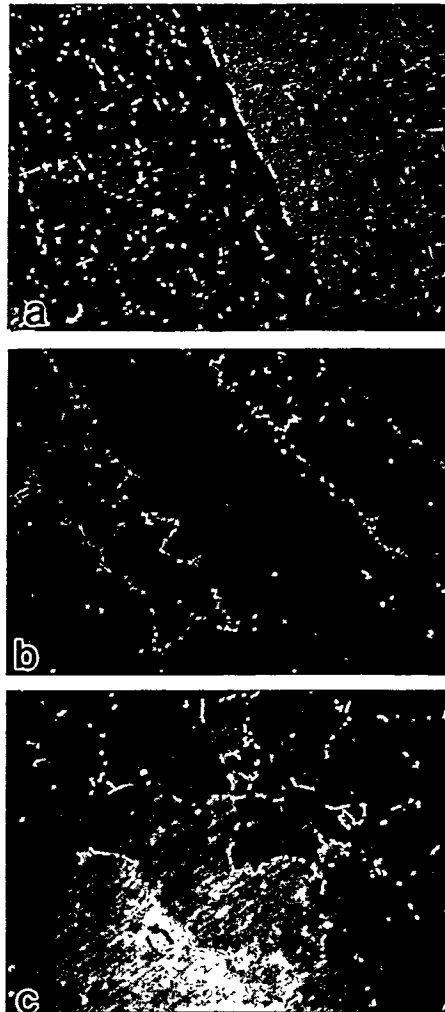


Fig. 5. Inclusion distribution in titanium inoculated welds. a) 0% Ti, b) 0.8% Ti, c) 1.2% Ti (700X)

Given the intrinsically brittle behavior of iron aluminides, fracture initiation is what must be controlled. Fracture is initiated at the weakest point in the weldment and the initiated crack becomes unstable when a critical length is reached. The inclusions located at the grain boundaries may be low stress crack initiation sites. With an applied stress, the interface between the inclusion at the grain boundary and the matrix can be broken, creating a critical crack, which in turn, causes the sample to fail. Inclusions may also be broken by the applied stress, again creating a critical crack. Figure 6 shows both failed interfaces as well as a fractured inclusion observed in an inoculated weldment.



Fig. 6. Weld pool inclusions associated with fracture.  
a) Failed inclusion/matrix interface b) Cracked inclusion (3500X)

A final possible effect of titanium may be an increase in porosity which is related to an increased hydrogen content in the weld pool. At thermodynamic equilibrium, the water, hydrogen, and oxygen concentrations are given by the relationship given in Equation 1.

$$[\text{H}_2\text{O}] = k [\text{H}]^2 [\text{O}] \quad [1]$$

As titanium and aluminum form oxides in the weld pool, the oxygen concentration decreases and the hydrogen concentration increases to maintain the equilibrium equation given in Equation 1. The increased hydrogen could cause higher porosity levels in the fusion zone. Figure 7 shows porosity observed in the area of inclusions in an inoculated fusion zone. Large pores can act as stress concentrators or in an extreme case, the pore diameter may approach the critical crack length.

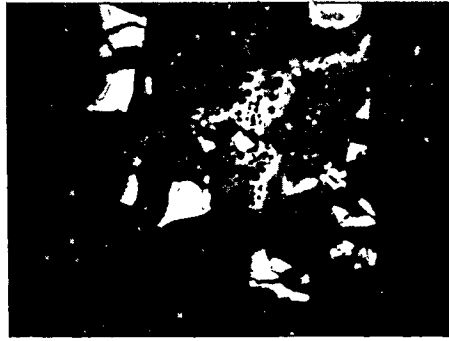


Fig. 7. Porosity in inoculated fusion zone. (2100X)

### CONCLUSIONS

The following conclusions can be reached from the results of the study:

1. Titanium additions effectively refine the fusion zone microstructure in FA-129 weldments.
2. The average fusion zone grain size in FA-129 inoculated welds decreases with increasing titanium concentration.
3. Slow travel speeds, regardless of heat input, are required for titanium inoculation to effectively refine the fusion zone microstructure.
4. Higher heat inputs improve the fusion zone microstructure uniformity when welding with a slow travel speed.
5. Titanium additions change the distribution of inclusions in FA-129 welds.
6. During slow strain rate tensile testing, the fracture stress of the fusion zone decreases with increasing titanium concentration.

### CURRENT WORK

Work currently focuses on determining the weldability and mechanical properties of zirconium-containing iron aluminides. Work done at Oak Ridge National Laboratory has shown that the zirconium and carbon concentration in a base alloy of iron, aluminum, and chromium greatly affect the mechanical properties of the alloy<sup>2</sup>. To determine the effect of zirconium and carbon on weldment properties, two heats of material were cast with the following compositions (all atomic percents): Fe - 28.0% Al - 5.00% Cr and Fe - 28.0% Al - 5.00% Cr - 0.50% Zr - 0.05% C. Welds have been made on tensile samples in an inert environment for slow strain rate ( $2.78 \times 10^{-6} \text{ s}^{-1}$ ) tensile testing in atmospheres of varying water vapor concentration (approximately 0 - 9000ppm).

Preliminary results show that the addition of zirconium and carbon increases the fracture stress of the weldments and that neither the ternary alloy nor the zirconium-containing alloy have shown a fracture sensitivity to the water vapor concentration present during slow strain rate tensile testing. This may indicate less susceptibility of the alloys to hydrogen cracking. With FA-129, the fracture stress decreased with increasing water vapor concentration.

With the zirconium addition, the fracture behavior is the same as seen in alloy FA-129. Once a crack is nucleated, crack growth becomes unstable and the sample completely fractures. In the ternary alloy, however, once a crack is initiated the sample does not fail, allowing the M.T.S. to adjust the applied load. The crack then propagates in a stable manner across the sample. Without a reduced section added to the tensile sample, the ternary alloy fails along the weld centerline, while the zirconium-containing alloy fails in the heat affected zone/fusion line region.

The greatest issue with the zirconium-containing alloy is its weldability. Hot cracking has been observed more frequently than was seen with alloy FA-129 or is currently experienced with the ternary alloy. Future work should therefore focus on determining the effect of zirconium and carbon concentrations on the hot cracking susceptibility of the alloys.

#### REFERENCES

1. A. A. Fasching, "Grain Refinement and Hydrogen Embrittlement in Iron Aluminide Alloy FA-129 Weldments," Thesis #T-4686, Colorado School of Mines, Golden, CO, May 1995.
2. V. K. Sikka, Oak Ridge National Laboratory, Unpublished data.



EVALUATION OF IRON ALUMINIDE WELD OVERLAYS FOR EROSION-  
CORROSION RESISTANT BOILER TUBE COATINGS IN LOW NO<sub>x</sub> BOILERS

J.N. DuPont, S. W. Banovic, and A.R. Marder

Energy Research Center

Lehigh University

Bethlehem, PA 18015

ABSTRACT

Low NO<sub>x</sub> burners are being installed in many fossil fired power plants in order to comply with new Clean Air Regulations. Due to the operating characteristics of these burners, boiler tube sulfidation corrosion is often enhanced and premature tube failures can occur. Failures due to oxidation and solid particle erosion are also a concern. A program was initiated in early 1996 to evaluate the use of iron aluminide weld overlays for erosion/corrosion protection of boiler tubes in Low No<sub>x</sub> boilers. Composite iron/aluminum wires will be used with the Gas Metal Arc Welding (GMAW) process to prepare overlays on boiler tubes steels with aluminum contents from 8 to 16wt%. The weldability of the composite wires will be evaluated as a function of chemical composition and welding parameters. The effect of overlay composition on corrosion (oxidation and sulfidation) and solid particle erosion will also be evaluated. The laboratory studies will be complemented by field exposures of both iron aluminide weld overlays and co-extruded tubing under actual boiler conditions.

## INTRODUCTION

Under new clean air regulations, electric utility companies will be required to operate under boiler conditions which reduce NO<sub>x</sub> emissions. The new operating conditions use a fuel-rich reducing gas to lower NO<sub>x</sub> emissions. The boiler environment created by this approach often inhibits the formation of protective surface oxide scales in localized regions of the boiler and promotes sulfide scale formation, thus accelerating boiler tube corrosion rates. This new operating environment places a greater need on high performance coatings for boiler tube life extension. Through sponsorship of an electric utility consortium, research has been initiated to evaluate commercially available stainless steel and nickel based weld overlay coatings for erosion and corrosion protection in these low NO<sub>x</sub> boiler environments. Recent research on the corrosion and erosion of iron aluminide weld overlays indicates these alloys are also an excellent candidate for this application<sup>1,2</sup>. Therefore, the program was expanded in early 1996 through sponsorship of the Fossil Energy Advanced Research and Technology Development (AR&TD) Program to include the evaluation of iron aluminide weld overlays with deposit aluminum contents from 8 to 16 wt% Al. The main objectives of this research are to: 1) Develop wires for GMAW overlay applications and 2) Develop overlay compositions with good sulfidation resistance that are readily weldable.

## DISCUSSION OF CURRENT ACTIVITIES

### Wire Fabrication

The deposition of weld overlays on boiler tube waterwalls often requires application of very large surface areas under field conditions. Thus, a high deposition rate process such as GMAW must be utilized. Although iron aluminide consumables

can be prepared in rod and powder form for use with the Gas Tungsten Arc Welding (GTAW) and Plasma Arc Welding (PAW) processes, these processes typically operate at low deposition rates due to their inherently low thermal efficiency<sup>3,4</sup>. Therefore, a technique is required for fabricating spooled wire for the GMAW process. Preparation of small diameter iron aluminide wires for GMAW is impractical due to relatively low ductility. A composite wire fabrication technique has been devised and implemented by Stoodly Company of Bowling Green, KY. With this process, a commercially pure aluminum wire is wrapped in a low carbon steel sheath and drawn to the final diameter. Additional alloying elements (e.g., Cr and Zr) can be added between the aluminum core wire and steel sheath during the drawing process. A typical wire prepared with this technique containing 22wt%Al - 8wt%Cr - 0.40wt%Zr is shown in Figure 1. At this early stage in the program, four additional wire compositions are being fabricated (Table 1) for future studies on corrosion, erosion, and weldability.

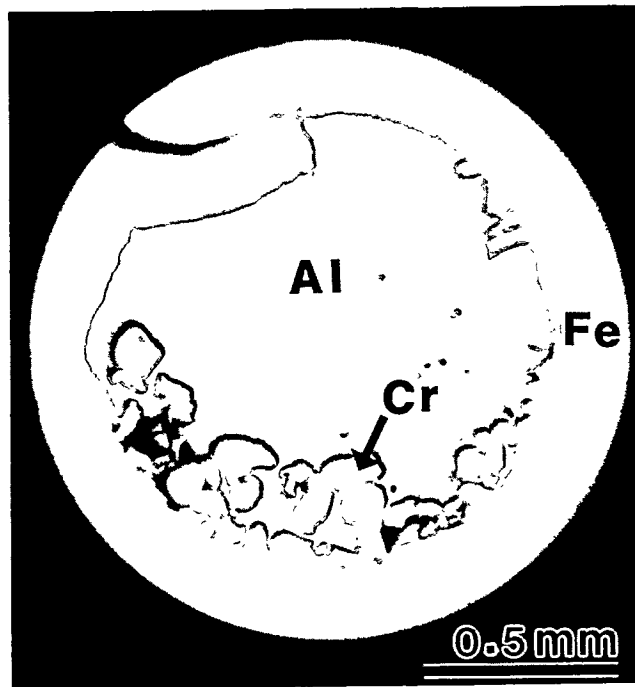


Figure 1. Cross-sectional photomicrograph of composite Fe-Al-Cr-Zr wire used to deposit weld overlays with the GMAW process.

Table 1. Chemical composition of composite iron/aluminum wires selected for weldability and corrosion studies.

Overlay/Wire Number	Al (wt%)	Cr (wt%)	Mo (wt%)	C (wt%)	B (wppm)	Zr (wt%)
Wire-1	21.3	0	0.4	0.1	25-50	0.25
Wire-2	21.3	6.7	0.4	0.1	25-50	0.25
Wire-3	10.5	0	0.4	0.1	25-50	0.25
Wire 4	10.5	6.7	0.4	0.1	25-50	0.25

### FUTURE WORK

The alloys listed in Table 1 will be utilized to prepare GMAW weld overlays with varying compositions. The erosion resistance of each overlay will be evaluated at 500°C using particle impact angles of 30° and 90°. Weldability (resistance to hydrogen cracking) will be evaluated as a function of overlay composition and welding parameters (e.g., preheat, interpass temperature, postweld heat treatment temperature). The corrosion resistance will be evaluated quantitatively using thermo-gravimetric techniques in an H<sub>2</sub>-H<sub>2</sub>S containing gas. Qualitative long term corrosion evaluations will also be conducted in tube furnaces under identical conditions. The results of these studies will be compared to results of similar research being conducted on commercially available stainless steel and nickel based weld overlays.

### REFERENCES

1. S. J.H. DeVan and P.F. Tortorelli, Paper No. 127, Corrosion 92, NACE, 1992.
2. B.F. Levin, J.N. DuPont, and A.R. Marder, Weld Overlay Coatings for Erosion Control, *Proceedings of the TMS Symposium on High Temperature Coatings*, Chicago, Illinois, October 2-6, 1994, pp 325-340.
3. J.N. DuPont and A.R. Marder, Thermal Efficiency of Arc Welding Processes, *Welding Journal*, December, 1995, pp 406s-416s.
4. J.N. DuPont and A.R. Marder, Dilution in Single Pass Arc Welds, accepted for publication in *Metallurgical Transactions B*, June, 1996.

EFFECTS OF SURFACE CONDITION ON AQUEOUS CORROSION AND  
ENVIRONMENTAL EMBRITTLEMENT OF IRON ALUMINIDES

R. L. Perrin and R. A. Buchanan

Dept. of Materials Science and Engineering  
University of Tennessee  
Knoxville, TN 37996-2200

ABSTRACT

Effects of retained high-temperature surface oxides, produced during thermomechanical processing and/or heat treatment, on the aqueous-corrosion and environmental-embrittlement characteristics of Fe<sub>3</sub>Al-based iron aluminides (FA-84, FA-129 and FAL-Mo), a FeAl-based iron aluminide (FA-385), and a disordered low-aluminum Fe-Al alloy (FAPY) were evaluated. All tests were conducted at room temperature in a mild acid-chloride solution. In cyclic-anodic-polarization testing for aqueous-corrosion behavior, the surface conditions examined were: as-received (i.e., with the retained high-temperature oxides), mechanically cleaned and chemically cleaned. For all materials, the polarization tests showed the critical pitting potentials to be significantly lower in the as-received condition than in the mechanically-cleaned and chemically-cleaned conditions. These results indicate detrimental effects of the retained high-temperature oxides in terms of increased susceptibilities to localized corrosion. In 200-hour U-bend stress-corrosion-cracking tests for environmental-embrittlement behavior, conducted at open-circuit corrosion potentials and at a hydrogen-charging potential of -1500 mV (SHE), the above materials (except FA-385) were examined with retained oxides and with mechanically cleaned surfaces. At the open-circuit corrosion potentials, none of the materials in either surface condition underwent cracking. At the hydrogen-charging potential, none of the materials with retained oxides underwent cracking, but FA-84, FA-129 and FAL-Mo in the mechanically cleaned condition did undergo cracking. These results suggest beneficial effects of the retained high-temperature oxides in terms of increased resistance to environmental hydrogen embrittlement.

INTRODUCTION

The overall objective of this project was to study the effects of retained high-temperature surface oxides, produced during thermomechanical processing and/or heat treatment, on the aqueous-corrosion and environmental-embrittlement characteristics of several Fe<sub>3</sub>Al-based iron aluminides, an FeAl-based iron aluminide, and a low-aluminum Fe-Al alloy. Previous aqueous-corrosion studies of these materials by the present authors and colleagues have examined specimens only with cleaned surfaces (i.e., mechanically ground or polished surfaces).<sup>1-4</sup> The high-temperature surface oxides of the present study are not likely to have the same chemistry nor the same morphology (e.g., thermal cracking) as the passive films formed naturally on a clean surface in an aqueous environment. It was hypothesized that

the presence of the high-temperature oxides could modify both the resistance to localized corrosion and the resistance to environmental embrittlement. To address these issues, the project involved cyclic-anodic-polarization testing to evaluate aqueous-corrosion behavior and U-bend stress-corrosion-cracking to evaluate environmental-embrittlement behavior.

In the mild acid-chloride solution employed in this study, which was designed to simulate aggressive atmospheric-corrosion, the alloys evaluated are susceptible, to various degrees, to pitting corrosion. An excellent method for evaluating the relative pitting-corrosion susceptibility involves producing and analyzing cyclic anodic polarization curves. A schematic illustration of such a curve is shown in Figure 1, where certain electrochemical parameters are identified.

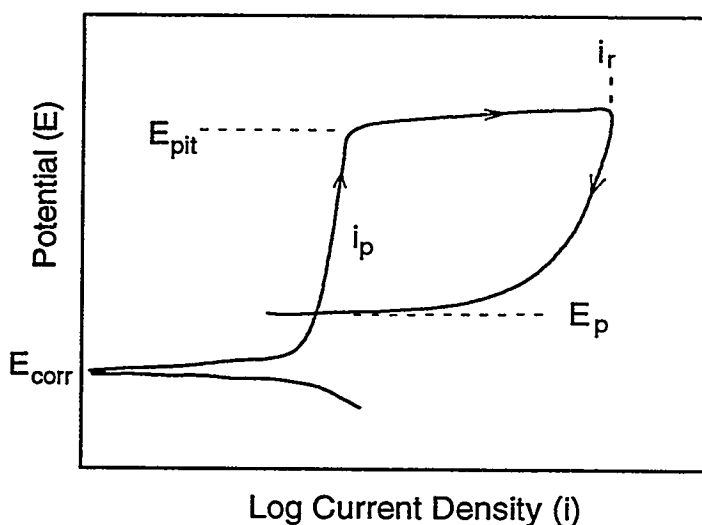


Fig. 1. Schematic illustration of cyclic anodic polarization behavior.

To produce the curve, the corrosion sample first is allowed to stabilize in the electrolyte such that a steady-state, open-circuit, corrosion potential,  $E_{\text{corr}}$ , is established. Next, with a potentiostatic circuit, the potential of the sample,  $E$ , is forced in the positive direction at a given rate while the current density,  $i$ , is continuously measured. After the potential has moved away from  $E_{\text{corr}}$  by a relatively small amount ( $\approx 50$  mV), the current density is directly proportional to the corrosion rate. The potential scan is continued in the positive direction until a predetermined reversing current density,  $i_r$ , is reached. At this point, the potential scan direction is reversed, moving in the negative direction, and continued until a very low current density is achieved. In Figure 1, the nearly vertical region in the up-scan portion of the curve, characterized by an average passive current density,  $i_p$ , is reflective of passivation, where the material has developed a thin protective oxide/hydroxide passive film, and,

therefore, corrodes at a very low rate over a range of potentials. At the critical pitting potential,  $E_{\text{pit}}$ , pitting corrosion initiates, with a sharp increase in current density. The pitting corrosion accelerates to  $i_r$ , and continues during the down-scan portion of the curve until the protection (or repassivation) potential,  $E_p$ , is reached (which corresponds to the cross-over point for the up-scan and down-scan curves). With reference to Figure 1, two of the parameters often used to characterize relative resistance to pitting corrosion are: (1) the magnitude of  $E_{\text{pit}}$ , with higher values corresponding to greater pitting resistance, and (2) the difference between  $E_{\text{pit}}$  and  $E_{\text{corr}}$ , i.e.,  $(E_{\text{pit}} - E_{\text{corr}})$ , with higher values corresponding to greater pitting resistance.

## EXPERIMENTAL PROCEDURES

Cyclic anodic polarization tests were conducted at room temperature in a mild acid-chloride solution ( $\text{pH} = 4$ , 200 ppm  $\text{Cl}^-$ ) on the following materials: the  $\text{Fe}_3\text{Al}$ -based iron aluminides, FA-84 (Fe-28Al-2Cr-0.05B, at. %), FA-129 (Fe-28Al-5Cr-0.5Nb-0.2C, at. %), and FAL-Mo (Fe-28Al-5Cr-1Mo-0.04B-0.08Zr, at. %), a disordered low-aluminum Fe-Al alloy, FAPY (Fe-16.1Al-5.4Cr-1.1Mo-0.1C, at. %), and an FeAl-based iron aluminide, FA-385 (Fe-35.65Al-0.20Mo-0.05Zr-0.11C, at. %). The FA-84, FA-129, FAL-Mo, and FAPY materials, in as-processed sheet form, were kindly supplied by Dr. Vinod Sikka of the Oak Ridge National Laboratory (ORNL); the FA-385 material, in rod form with a cladding, was kindly supplied by Dr. Philip Maziasz of ORNL.

For the FA-84, FA-129, FAL-Mo, and FAPY materials, the surface conditions evaluated were: (1) as-processed (i.e., with the retained high-temperature oxides characteristic of the prior thermomechanical processing methods), (2) mechanically cleaned (ground through 600-grit SiC paper to remove all high-temperature oxides), and (3) chemically cleaned (immersed in an acid solution until all high-temperature oxides were removed (approximately 30 minutes), then immersed in 10%  $\text{HNO}_3$  at 43 °C for one hour as a passivation treatment). Specifically, the thermomechanical processing procedures (accomplished at ORNL) for the as-processed condition were: hot forged 50% at 1000 °C, hot rolled 50% at 800 °C, and warm rolled 70% at 650 °C to a finish thickness of 0.75 mm. The acid solutions employed for chemical cleaning varied with the material, as follows: FA-84, 10%  $\text{HNO}_3$  at 43 °C; FA-129, 10%  $\text{HNO}_3$  plus 2% HF at room temperature; FAL-Mo, 10%  $\text{HNO}_3$  plus 2% HF at 43 °C; and FAPY, no  $\text{HNO}_3$ /HF/temperature combination was found to satisfactorily remove the oxide and produce a smooth surface. Because of the form of the as-received FA-385 material (rods with protective claddings), it did not have the high-temperature oxides. To create the high-temperature-oxide surface condition, the FA-385 samples were annealed in air at 750 °C for one hour, then air

cooled. This condition will be referred to as the "heat treated" condition, not as the as-processed condition. The mechanically-cleaned condition was accomplished in the same manner as described for the other materials.

Cyclic anodic polarization tests were performed with a standard polarization cell and an EG&G Model 273 potentiostat. Each sample was mounted in epoxy, attached and electrically connected to a sample holder, and placed in a polarization cell containing the mild acid-chloride electrolyte. Stabilization was allowed to occur for at least one hour, after which  $E_{\text{corr}}$  was measured. The cyclic polarization curve was then generated at a scan rate of 600 mV/h. The reversing current density was  $1000 \mu\text{A}/\text{cm}^2$ .

U-bend stress corrosion cracking tests were performed on the above alloys (except FA-385). Sheet material was cut into 1 cm by 11.9 cm strips and then the thermomechanical oxide was mechanically removed (600-grit SiC). The strips were heat treated in air at  $750^\circ\text{C}$  for one hour and then quenched in oil. Half of the strips were mechanically cleaned once again to remove the furnace oxide. The strips were bent to a radius of 15.9 mm, thus forming the U-bend specimen geometry illustrated in Figure 2. Each specimen was fastened into the U-bend shape by means of a polyvinyl chloride bolt so as to eliminate galvanic corrosion effects. The total strain in the bend was determined by the relation (ASTM G 30),  $\epsilon = T/2R$ , where  $T$  is the specimen thickness and  $R$  the bend radius. The total strain placed on the U-bend specimens ranged from 0.024 to 0.037 cm/cm. Due to an inability to reliably produce a chemically-cleaned surface for all alloys, this surface condition was not evaluated. Testing of the U-bend specimens was conducted in the same mild acid-chloride solution employed in the polarization tests.

One series of U-bend tests was conducted at the open-circuit corrosion potential,  $E_{\text{corr}}$ , which was monitored continuously for 200 hours. A second series of tests was conducted at a hydrogen-charging potential of -1500 mV(SHE) to enhance the production of hydrogen at the specimen surfaces. In this series of tests, the cathodic current density was monitored continuously.

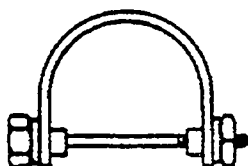


Fig. 2: Schematic geometry of U-bend test specimen.



## RESULTS AND DISCUSSION

The cyclic anodic polarization behaviors of FA-84 (28Al-2Cr) in the as-processed, mechanically-cleaned, and chemically cleaned surface conditions are shown in Figure 3. The as-processed condition, relative to the mechanically-cleaned and chemically cleaned conditions, produced a lower pitting potential ( $E_{\text{pit}}$ ), and a higher corrosion potential ( $E_{\text{corr}}$ ). Both the lower  $E_{\text{pit}}$  value and the lower ( $E_{\text{pit}} - E_{\text{corr}}$ ) value for the as-processed (high-temperature oxide) surface condition indicated reduced resistance to pitting corrosion. The decreased passive current density,  $i_p$ , for the chemically cleaned surface suggested that the chemical cleaning process enhanced the properties of the passive film, most likely by thickening it.

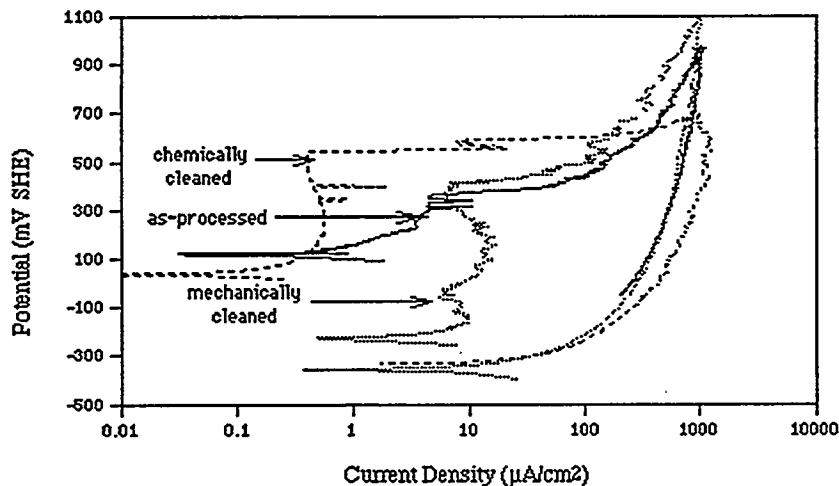


Fig. 3. Cyclic anodic polarization behaviors of FA-84 with as-processed, mechanically-cleaned, and chemically-cleaned surfaces.

As seen in Figure 4 for the FA-129 (28Al-5Cr) alloy, the as-processed surface condition performed poorly with respect to both the mechanically-cleaned and chemically-cleaned surface conditions. The as-processed surface condition showed almost no tendency for passivation. For the as-processed surface, the pitting potential was significantly lower, and the corrosion potential higher, than for the other two conditions which involved removal of the high-temperature oxide. Again, both the lower  $E_{\text{pit}}$  value and the lower ( $E_{\text{pit}} - E_{\text{corr}}$ ) value for the as-processed surface condition indicated reduced resistance to pitting corrosion.

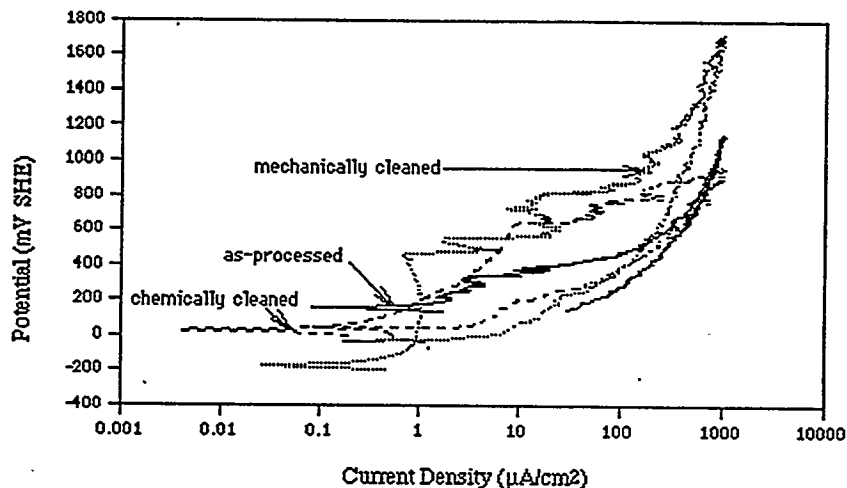


Fig 4. Cyclic anodic polarization behaviors of FA-129 with as-processed, mechanically-cleaned, and chemically-cleaned surfaces.

As seen in Figure 5 for the FAL-Mo (28Al-5Cr-1Mo) alloy, the pitting potential,  $E_{pit}$ , for the as-processed surface condition was significantly lower than the  $E_{pit}$  values for the mechanically-cleaned and chemically-cleaned surfaces. Also, the range of the passive current density,  $i_p$ , was rather small for the as-processed surface condition. It also is noted that the high-temperature oxide on the as-processed surface did not produce a stable  $i_p$ , i.e., current-density fluctuations were obvious. The mechanically and chemically cleaned conditions each had certain advantages. The mechanically-cleaned surface had a slightly higher  $E_{pit}$  and a lower  $E_{corr}$ . However, the chemically cleaned surface had a significantly lower  $i_p$ . The lower  $i_p$  suggested that there was either a thickening of the passive film or possibly a Cr enrichment of the passive film caused by the chemical cleaning process.

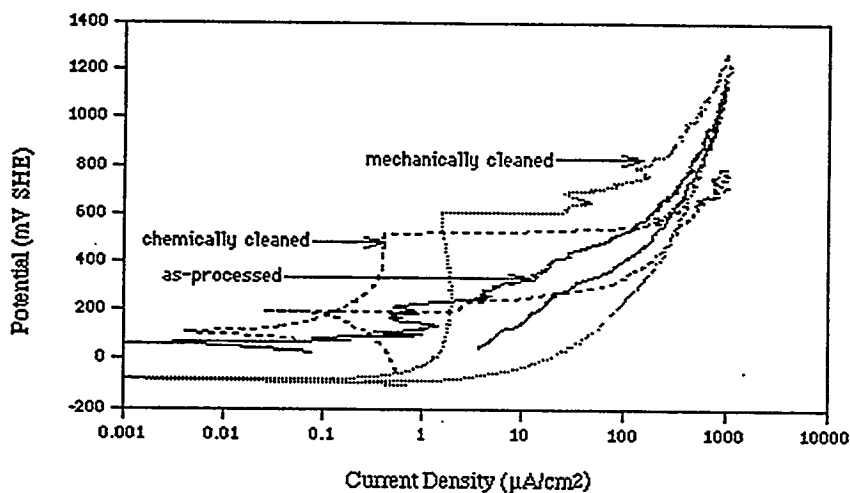


Fig 5. Cyclic anodic polarization behaviors of FAL-Mo with as-processed, mechanically-cleaned, and chemically-cleaned surfaces.

The cyclic anodic polarization behaviors of the disordered alloy, FAPY (16Al-5Cr-1Mo), in the as-processed and mechanically-cleaned surface conditions are shown in Figure 6. A chemically-cleaned surface could not be produced that was sufficiently smooth so as not to promote a surface roughness effect during the polarization test. Once again, the as-processed surface performed poorly in comparison to the mechanically-cleaned surface. The as-processed surface condition produced a much lower  $E_{\text{pit}}$ , with little indication of a passive current density,  $i_p$ , and a much higher  $E_{\text{corr}}$  value.

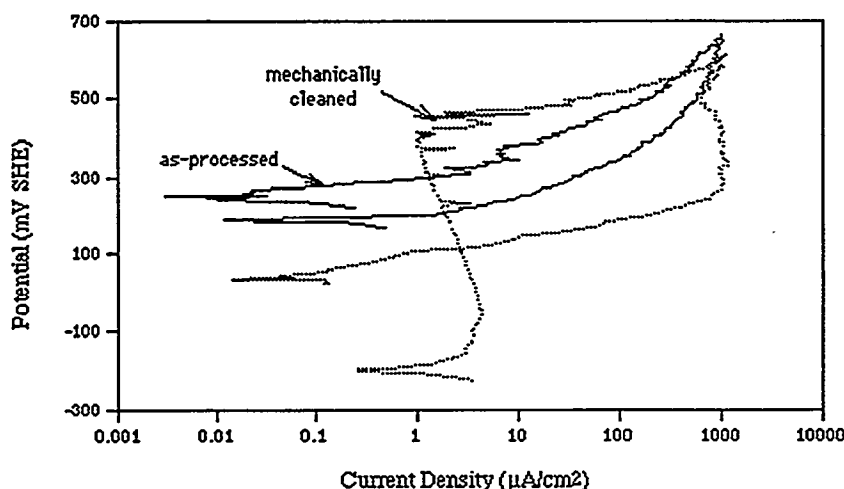


Fig 6. Cyclic anodic polarization behaviors of FAPY with as-processed and mechanically-cleaned surfaces.

As seen in Figure 7 for the FeAl-based iron aluminide, FA-385 (36Al-0.2Mo), the heat-treated high-temperature-oxide surface condition produced a much lower  $E_{\text{pit}}$ , a much lower  $i_p$ , and a higher  $E_{\text{corr}}$  value than the mechanically-cleaned surface condition. Both the lower  $E_{\text{pit}}$  value and the lower  $(E_{\text{pit}} - E_{\text{corr}})$  value for the high-temperature-oxide surface condition indicated reduced resistance to pitting corrosion.

An observation that did not manifest itself directly in the polarization behavior was the appearance of the surfaces of the samples after chemical cleaning. The high-temperature-oxide surfaces of FA-84 and FA-129 were cleaned rather easily in the 10%  $\text{HNO}_3$ , 2% HF solution but also could be cleaned in a solution containing only 10%  $\text{HNO}_3$ . However, the oxide surfaces of FAL-Mo and FAPY were slow to clean in the 10%  $\text{HNO}_3$ , 2% HF solution, and could not be cleaned at all in the 10%  $\text{HNO}_3$  solution. Furthermore, after chemical cleaning, the FA-129 and FA-84 samples had shiny smooth surfaces, whereas the FAL-Mo and FAPY samples had shiny rough surfaces. For the FAL-Mo and FAPY samples, the attack of the 10%  $\text{HNO}_3$ , 2% HF solution was more prominent in areas of exposed base material, i.e., cut faces or where the oxide had flaked off. The difficulties experienced in removal of the

high-temperature oxides apparently can be attributed to the presence of molybdenum in the FAL-Mo and FAPY alloys, which also is partly responsible for the greater aqueous-corrosion resistance exhibited by these alloys.

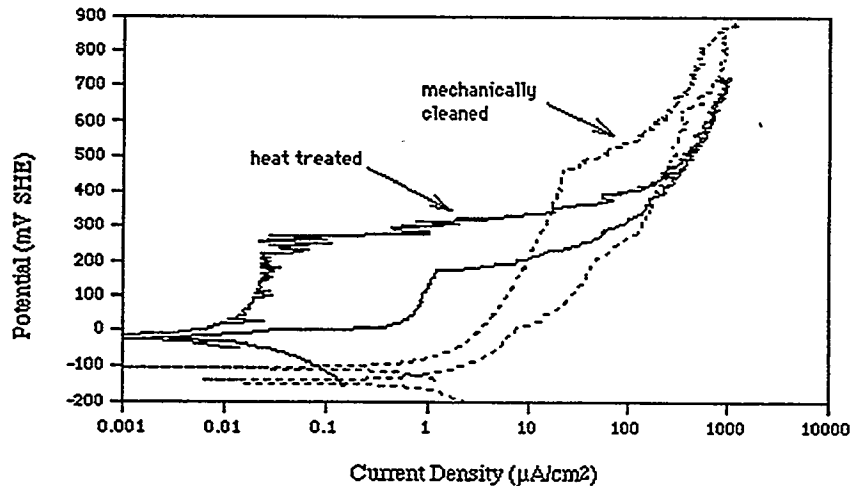


Fig 7. Cyclic anodic polarization behaviors of FA-385 with heat-treated and mechanically-cleaned surfaces.

With regard to the 200-hour U-bend stress-corrosion-cracking tests, the overall results in terms of cracking behavior are shown in Table 1. For the tests conducted at the corrosion potential,  $E_{\text{corr}}$ , none of the mechanically-cleaned nor furnace-oxide U-bend specimens underwent cracking. For the tests conducted at the hydrogen-charging potential,  $-1500 \text{ mV(SHE)}$ , although none of the furnace-oxide specimens underwent cracking, several of the mechanically-cleaned specimens did undergo cracking. Specifically, at the hydrogen-charging potential, specimens of FAL-Mo, FA-129, and FA-84 all experienced cracking in the mechanically-cleaned condition but not in the furnace-oxide condition. These results indicated that under severe hydrogen-producing conditions, the presence of the high-temperature oxides are beneficial in improving the resistance of the materials to environmental embrittlement.

For the U-bend tests conducted at the hydrogen-charging potential, the resultant cathodic current densities for the alloys in the two surface conditions are shown in Table 2 for time periods of 20 and 200 hours. The current densities are directly proportional to the amount of hydrogen cathodically produced at the specimen surfaces, but do not indicate the amount of atomic hydrogen diffusing into the material substrates. Generally (with the exception of FA-84), the cathodic current densities were lower for the furnace-oxide specimens at shorter times, but somewhat higher at longer times. Overall, it appeared that the high-temperature oxides did not prevent, in a major way, the production of

hydrogen at the oxide/solution interface, but rather functioned as barriers in retarding the diffusion of atomic hydrogen through the oxides and into the material substrates, thus reducing the hydrogen-embrittlement effect.

Table 1. 200-hour U-bend-test cracking results.

Alloy	Tests at Corrosion Potential, $E_{\text{corr}}$		Tests at Hydrogen-Charging Potential, -1500 mV SHE	
	Mechanically-Cleaned Surfaces	Furnace-Oxide Surfaces	Mechanically-Cleaned Surfaces	Furnace-Oxide Surfaces
FAL-Mo	No Cracking	No Cracking	Cracked (~190 h)	No Cracking
FA-129	No Cracking	No Cracking	Cracked (~23 h)	No Cracking
FA-84	No Cracking	No Cracking	Cracked (~190 h)	No Cracking
FAPY	No Cracking	No Cracking	No Cracking	No Cracking

Table 2. Cathodic current densities ( $\mu\text{A}/\text{cm}^2$ ) during hydrogen charging.

Alloy	Mechanically-Cleaned Surfaces		Furnace-Oxide Surfaces	
	At 20 hours	At 200 hours	At 20 hours	At 200 hours
FAL-Mo	306	321	217	405
FA-129	445	425	351	435
FA-84	375	430	780	836
FAPY	327	346	323	499

## CONCLUSIONS

Electrochemical aqueous-corrosion studies showed that retained high-temperature surface oxides on iron aluminides (FA-84, FA-129, FAL-Mo, and FA-385) and a related alloy (FAPY), produced during thermomechanical and/or heat treatment processing, caused major reductions in corrosion resistance in a mild acid-chloride electrolyte designed to simulate aggressive atmospheric corrosion. Removal of the oxides by mechanical grinding or chemical cleaning restored the corrosion resistance.

A standard pickling solution employed for stainless steels, nitric plus hydrofluoric acid, worked well for the iron aluminides not containing molybdenum (FA-84 and FA-129), producing a clean, smooth surface. However, for the molybdenum-containing materials (FAL-Mo and FAPY), although this solution was effective in removing the oxide, it produced an unacceptably rough surface.

U-bend stress-corrosion-cracking tests conducted in the mild acid-chloride electrolyte on FA-84, FA-129, FAL-Mo, and FAPY showed that under electrochemical hydrogen-charging conditions, specimens with mechanically-cleaned surfaces underwent cracking, whereas specimens with retained high-temperature furnace-oxide surfaces did not undergo cracking. The results suggest that the high-temperature oxide serves as a hydrogen diffusion barrier and, consequently, is beneficial in terms of improving resistance to environmental embrittlement.

#### REFERENCES

1. R. A. Buchanan and J. G. Kim, "Fe<sub>3</sub>Al-Type Iron Aluminides: Aqueous Corrosion Properties in a Range of Electrolytes and Slow-Strain-Rate Ductilities During Aqueous Corrosion," Final Report, U. S. Dept. of Energy, Fossil Energy AR & TD Materials Program, ORNL/Sub/88-07685CT92/02, National Technical Information Service, Springfield, VA, August, 1992.
2. J. G. Kim and R. A. Buchanan, "Aqueous Corrosion Properties and Slow-Strain-Rate Ductilities of Fe<sub>3</sub>Al-Based and Lean-Aluminum Iron Aluminides," Final Report, U. S. Dept. of Energy, Fossil Energy AR & TD Materials Program, ORNL/Sub/88-07685CT92/03, National Technical Information Service, Springfield, VA, August, 1993.
3. J. G. Kim and R. A. Buchanan, "Pitting and Crevice Corrosion of Iron Aluminides in a Mild Acid-Chloride Solution," Corrosion, Vol. 50, No. 9, pp. 658-668, Sept., 1994.
4. J. G. Kim and R. A. Buchanan, "Localized Corrosion and Stress Corrosion Cracking Characteristics of a Low-Aluminum-Content Iron Aluminum Alloy," Final Report, U. S. Dept. of Energy, Fossil Energy AR & TD Materials Program, ORNL/Sub/88-07685CT92/04, National Technical Information Service, Springfield, VA, October, 1994.

PROCESSING AND PROPERTIES OF LOW-ALUMINUM ALLOY FAPY

V. K. Sikka and C. R. Howell

F. Hall and J. Valykeo

Metals and Ceramics Division  
Oak Ridge National Laboratory  
P.O. Box 2008  
Oak Ridge, Tennessee 37831-6083

Hoskins Manufacturing Company  
10776 Hall Road  
Hamburg, Michigan 48139

## ABSTRACT

This paper deals with the melting, processing, properties, and microstructure of three commercially melted heats of Fe-16 at. % Al alloy FAPY. All of the heats were air-induction melted (AIM), two at Hoskins Manufacturing Company (Hamburg, Michigan) and one at United Defense (Anniston, Alabama). One ingot from each of the heats was used for testing at the Oak Ridge National Laboratory. A 127-mm.-long section from each ingot was used for determining properties and microstructure in the as-cast, cast and hot-processed, and cold-rolled conditions. The fine-grained sheet showed 20% elongation at room temperature.

## INTRODUCTION

The FAPY is an Fe-16 at. % Al alloy of nominal composition given in Table 1. The aluminum content of the alloy is such that it remains single phase ( $\alpha$ ) without the formation of an ordered phase ( $\text{DO}_3$ ). The alloy has good oxidation resistance at temperatures up to 1000°C and has shown significantly superior performance as heating elements when compared to the commonly used nickel-based alloy, NICHROME® (Driver-Harris Company, Harrison, New Jersey). Although wire for the heating elements has been fabricated from small (6.8-kg) laboratory heats, for its commercial applications, the wire needs to be producible from large (545- to 680-kg) air-melted heats. The purpose of this study was to produce commercial-size heats and investigate their mechanical properties and microstructure in the as-cast, hot-worked, and cold-worked conditions. The results of this study are expected to provide: (1) insight into processing steps for large heats into wire under commercial conditions, and (2) the mechanical properties data on commercial-size heats in various product forms.

## ALLOY PREPARATION AND PROCESSING

A total of three commercial-size heats were used in this study. Two heats of 545 kg each were air-induction melted (AIM) at Hoskins Manufacturing Company (Hamburg, Michigan) and cast into standard 203-mm tapered ingots. The third heat was processed by AIM at United Defense (Anniston, Alabama). This heat was primarily cast into various sand molds but was also cast into two ingot molds provided by Hoskins. One ingot each from the heats melted at Hoskins and United Defense were sent to the Oak Ridge National Laboratory (ORNL) for processing, property, and microstructural evaluation. The chemical analysis of each heat and the heat numbers are included in Table 1.

Table 1. Comparison of chemical analysis of two FAPY alloy heats made at Hoskins Manufacturing Company and one heat made at United Defense with the target composition

Element	Target	Weight percent		
		Hoskins Manufacturing Company		United Defense Heat 899-40299
		Heat 899-21689	Heat 899-21690	
Al	8.46	8.69	8.45	9.19
Cr	5.50	5.46	5.49	5.31
Zr	0.20	0.20	0.21	0.21
C	0.03	0.054	0.044	0.022
Mo	2.00	2.06	2.10	2.03
Y	0.10	0.13 <sup>a</sup>	0.16 <sup>a</sup>	0.04 <sup>a</sup>
Mn	—	0.34	0.34	0.19
S	—	0.006	0.007	0.011
Nb	—	0.012	0.01	<0.01
B	—	<0.001	<0.001	<sup>b</sup>
N <sub>2</sub>	—	0.003	0.002	0.003
O <sub>2</sub>	—	0.003	0.003	0.002
Fe	<sup>c</sup>	<sup>c</sup>	<sup>c</sup>	<sup>c</sup>

<sup>a</sup>Estimated.

<sup>b</sup>Not analyzed.

<sup>c</sup>Balance.

A 127-mm-long section of each ingot was cut from the ingot bottom. The macrostructure of the cut sections of each ingot is shown in Fig. 1. The ingots cast at Hoskins were sound but showed a slightly different microstructure. The ingots cast at United Defense showed a crack in the cross section.

A 2-in.-thick slice was cut from the middle section of each of the 127-mm-long ingot sections. The remaining part of the ingot section was used for machining specimens in the as-cast condition. The 51-mm-thick slice was hot-forged 50% at 1150°C. The 25-mm-thick forged plate was hot-rolled at 1000°C to 13-mm-thick plate. This plate was used for machining longitudinal specimens for properties in the hot-rolled condition. A part of the 13-mm-thick plate was hot-rolled at 1000°C to 2.54-mm-thick sheet. This sheet was rolled to 1.3 mm thickness at 600°C, subsequently annealed for 1 h at 800°C, and cold-rolled to 0.76 mm thickness. The cold-rolled sheet was used to punch specimens for testing in the wrought condition.

A square bar of 61- by 61-mm cross section hot-rolled from an ingot at Hoskins was also included for testing.



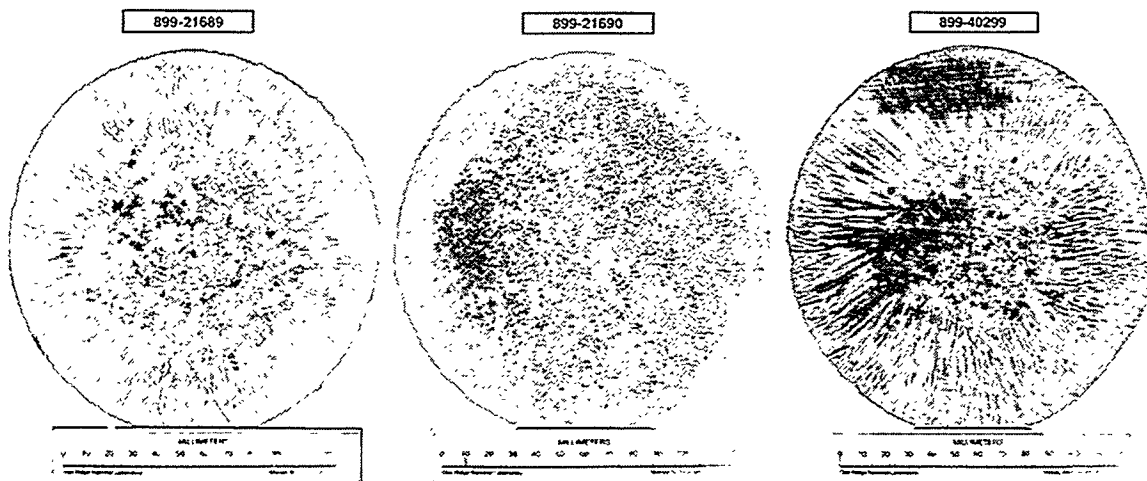


Fig. 1. Macrostructure of sections cut from three ingots of FAPY alloy.

Test bars machined from ingots, hot-rolled plate, hot-rolled bar, and punched from the sheet were all given a 1-h anneal at 800°C in air followed by air cooling prior to testing. In only one case, the sheet specimens were tested in the as-rolled condition, which contained 40% cold-work from the rolling process.

### TENSILE TESTING AND PROPERTIES

Tensile tests (one per temperature) were carried out in air at temperatures varying from room temperature to 800°C. The strain rate for bar specimens was  $2.7 \times 10^{-3}/s^{-1}$  and  $3.3 \times 10^{-3}/s^{-1}$  for sheet specimens. The 0.2% yield strength, ultimate tensile strength, total elongation, and reduction of area for each heat are plotted as a function of test temperature in Figs. 2 and 3. The following observations are made from these figures:

1. The 0.2% yield strength of the as-cast ingot is the lowest from room temperature to 600°C and the highest for the sheet with the hot-rolled plate falling between the two. The cast/forged (bar-rolled) bar from Hoskins showed essentially the same yield strength as the sheet. The yield strength of the as-rolled sheet is significantly higher than the annealed sheet up to 400°C. At 600°C, the difference in yield strength between the cold-worked and annealed conditions is significantly reduced.
2. The ultimate tensile strength showed a clear distinction between the cast, hot-rolled, and cold-rolled sheet. At room temperature, ultimate tensile strength of the cast ingot was the lowest followed by the hot-rolled material and sheet. The cast/forged (bar-rolled) bar was lower in ultimate strength than the sheet. The as-rolled sheet showed substantially higher strength than the annealed sheet. Except for the

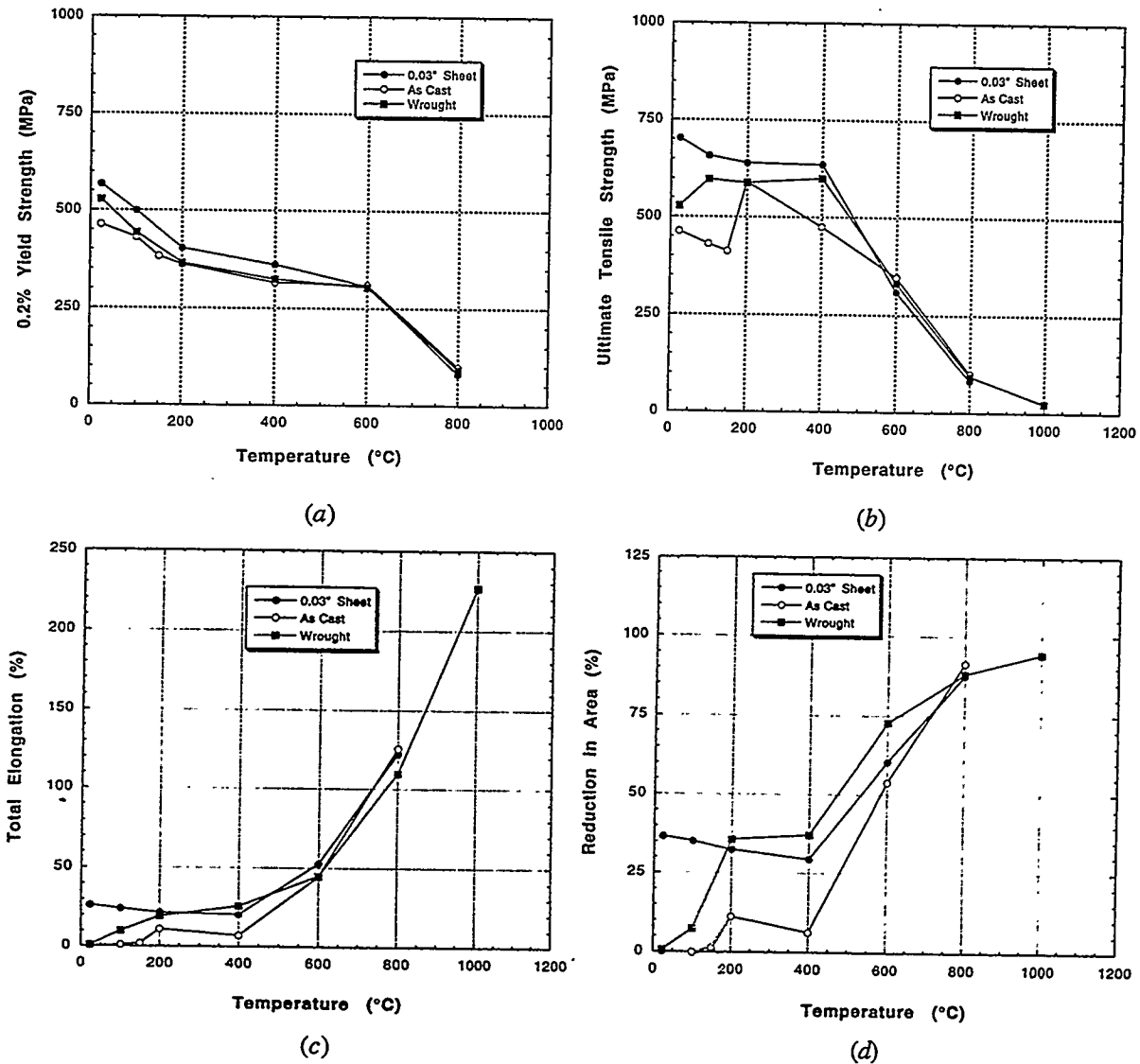


Fig. 2. Plots of tensile properties as a function of test temperature for FAPY heat 899-21690: (a) 0.2% yield strength, (b) ultimate tensile strength, (c) total elongation, and (d) reduction of area.

cast ingot, data for other products were well behaved for the entire test temperature range. The cast ingot data showed an unusual trend with temperature in the range from room temperature to  $< 200^{\circ}\text{C}$ , where the cast ingot was tested in the brittle range [see the ductility data in Fig. 2(c-d)]. Some scatter in the data for the cast ingot may also be due to the variability in grain size from specimen to specimen.

3. The total elongation plots show that the cast ingot has the least ductility at room temperature and remains very low up to  $150^{\circ}\text{C}$ . It only increases to a reasonable level of 10% at  $200^{\circ}\text{C}$ . For the hot-rolled plate, ductility was very low at room temperature but increased to 10% at  $100^{\circ}\text{C}$ , and matched the

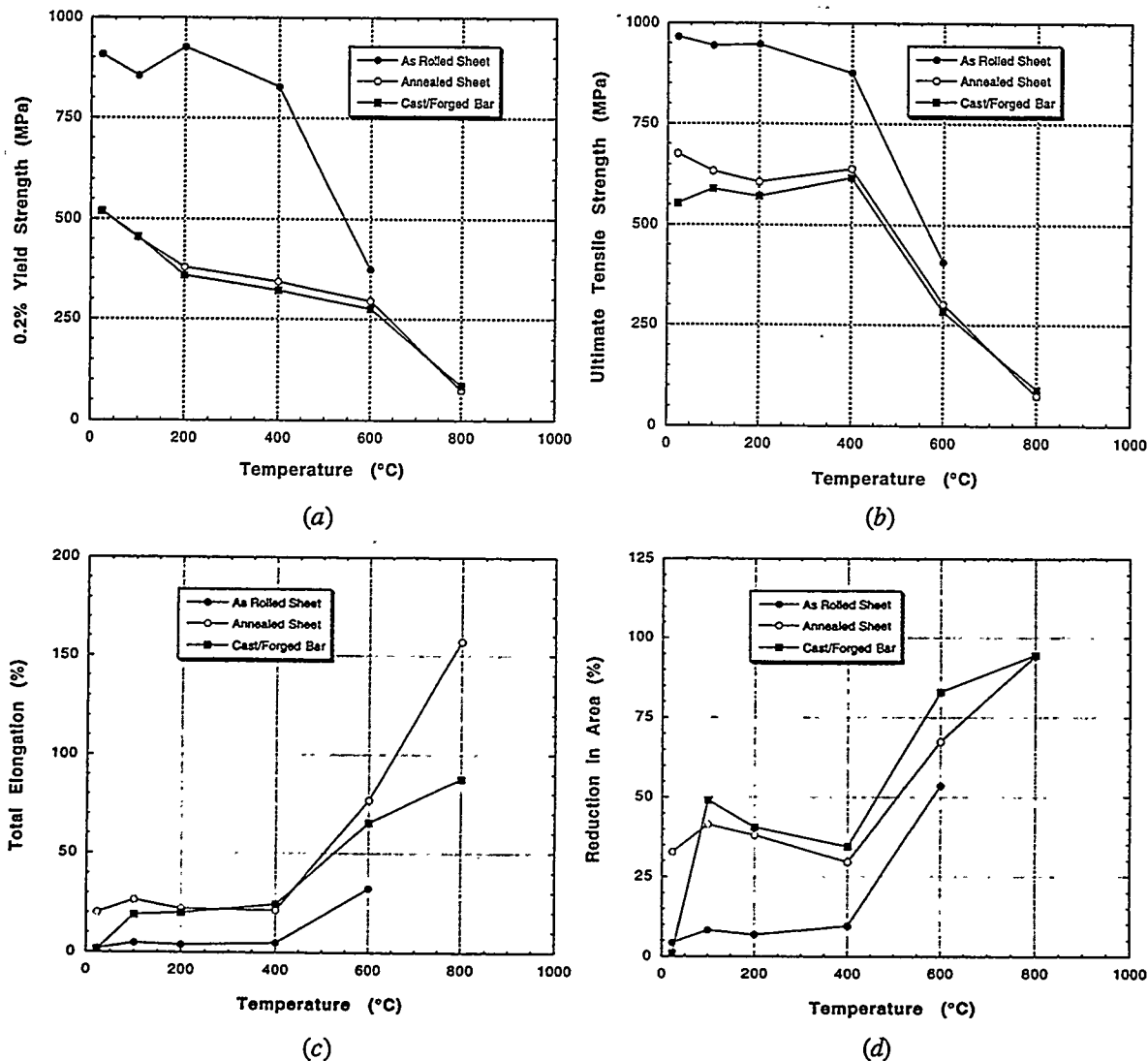


Fig. 3. Plots of tensile properties as a function of test temperature for FAPY heat 899-21689: (a) 0.2% yield strength, (b) ultimate tensile strength, (c) total elongation, and (d) reduction of area.

sheet ductility at 200°C. The cast/forged (bar-rolled) bar processed at Hoskins showed low ductility at room temperature, but it reached 20% at 100°C, which is nearly double the value for the plate hot rolled at ORNL. The annealed sheet showed approximately 20% value at room temperature, with no trends of brittle- (ductility of 51%) to-ductile (ductile defined as  $\geq 10\%$  elongation) transition. The as-rolled sheet with 40% cold-work showed values of 5% up to 600°C, where most of the cold-work appears to have recovered. It should be noted that the reduction in ductility of the as-rolled sheet is a consequence of cold-work (ductility exhaustion) and is different than the brittle-to-ductile trend observed for the cast and

## MICROSTRUCTURE

hot-worked conditions. At 800°C, the FAPY alloy is very ductile in cast, hot-worked, and cold-rolled sheet. At 1000°C, the sheet approached the ductility values in the superplastic range ( $\geq 200\%$ ).

4. The reduction of area plots in Figs. 2 and 3(d) show trends very similar to those described above for total elongation with the exception that the brittle-to-ductile trends are clearer in these plots.

Optical microstructures of as-cast, cast and hot-rolled, and cold-rolled sheet are compared for heat 899-21690 of FAPY in Figs. 4 and 5. The microstructures in Fig. 5 are at low magnification, and those in Fig. 5 are at high magnification. These photomicrographs show that processing refines the grain size. The grain size (measured by line intersection method) of the cast ingot of 305  $\mu\text{m}$  was reduced to 254  $\mu\text{m}$  by hot-forging and hot-rolling to 0.5-in.-thick plate. However, hot-rolling to 2.5 mm thickness followed by warm-rolling at 600°C to 1.3 mm thickness and annealing at 800°C for 1 h followed by cold-rolling 40% to 0.76-mm thickness reduced the grain size to 13  $\mu\text{m}$  (23 times finer than that of the cast ingot). The grain refinement is due to recrystallization of warm- and cold-rolled sheet. The as-cast microstructure in the photomicrographs also showed decoration of grain boundaries with precipitates and some particles in the matrix, and hot-forging and hot-rolling removed most of the particles from the grain boundaries, with some precipitates still present in the matrix.

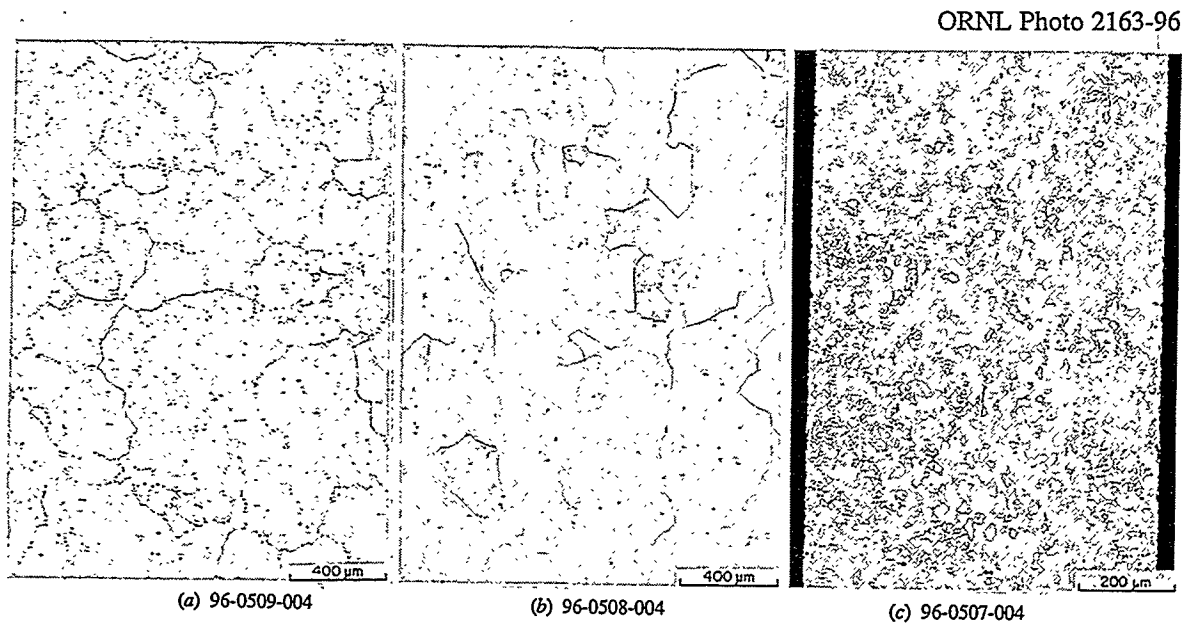


Fig. 4. Comparison of low-magnification optical micrographs of: (a) as-cast, (b) cast and hot-worked, and (c) cold-rolled FAPY samples of heat 899-21690. The grain sizes in three conditions are 305, 254, and 13  $\mu\text{m}$ , respectively.

ORNL Photo 2164-96

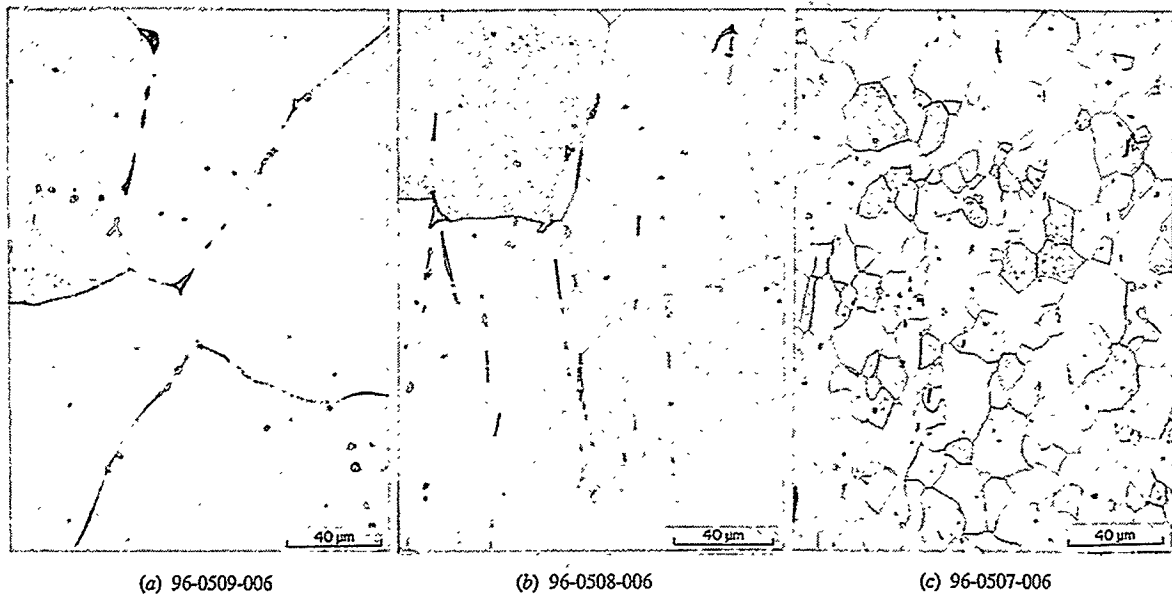


Fig. 5. Comparison of high-magnification optical micrographs of: (a) as-cast, (b) cast and hot-worked, and (c) cold-rolled FAPY samples of heat 899-21690.

ORNL Photo 2181-96

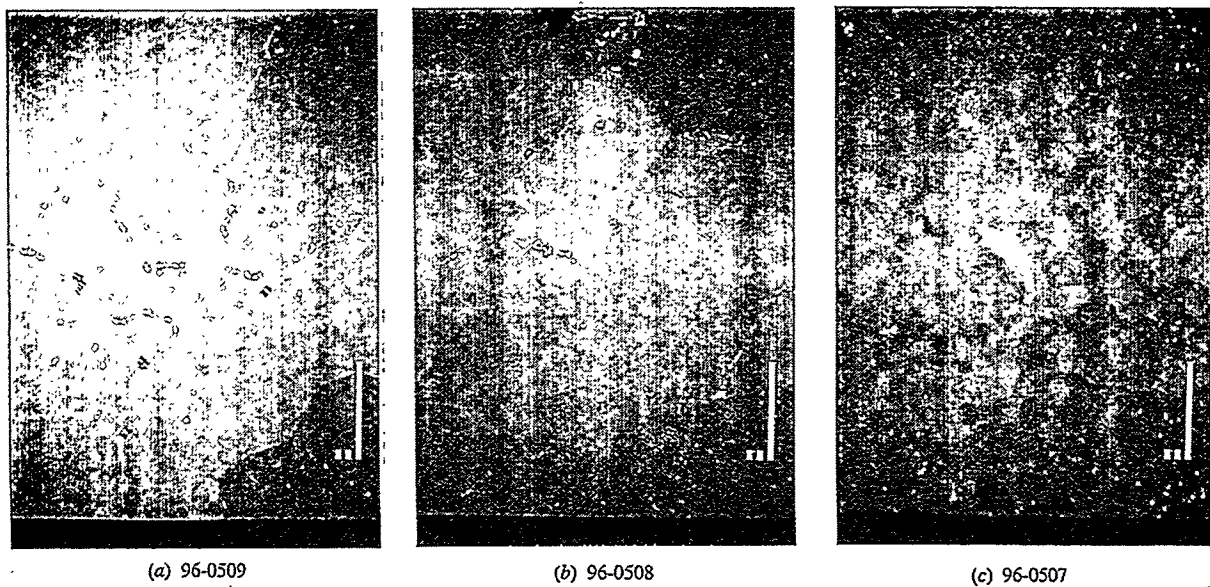


Fig. 6. Backscattered electron images of FAPY alloy in: (a) as-cast, (b) cast and hot-worked, and (c) cold-rolled conditions.

Scanning electron microscope (SEM) analysis was carried out to determine the composition of the precipitates. The back-scattered electron images for the cast, hot-worked, and cold-rolled sheet are compared in Fig. 6. Two types of inclusions {bright [higher atomic number (Z)] and gray in color [intermediate atomic number (Z)]} were observed. Detailed compositional analyses at ten locations in the matrix and the particles are shown in Table 2. Based on these semiquantitative analyses, the bright particles are primarily ZrC with a very small amount of Fe and Y. The darker particles are highly enriched with Y and contain substantial amounts of Fe, Al, Cr, and C. The atomic percentages of various elements suggest that the Y-containing particles may be  $(\text{FeCrC})_3(\text{AlY})$ . The back-scattered electron images in Fig. 6 show that the ZrC- and Y-containing particle sizes become smaller with hot- and cold-processing, but their total estimated amount by area appears to remain nearly the same.

Table 2. Chemical analyses of matrix and precipitates<sup>a</sup> in the as-cast sample of FAPY heat 899-21689

Fe	Al	Cr	Mo	Zr	Y	C	Total
Matrix							
75.8 <sup>b</sup>	15.0	5.5	1.1	0.0	0.0	2.6	101.1
84.6 <sup>c</sup>	8.1	5.7	2.0	0.0	0.0	0.6	
0.5 <sup>d</sup>	0.1	0.1	0.1	—	—	0.2	
High-Z Precipitates							
3.8	0.3	0.4	0.4	42.5	0.4	52.1	104.1
4.6	0.2	0.4	0.8	83.6	0.9	13.5	
2.7	0.2	0.2	0.2	3.6	0.7	0.2	
Intermediate-Z Precipitates							
59.4	16.5	3.7	0.8	0.1	9.0	10.5	101.6
67.9	9.1	4.0	1.5	0.2	16.3	2.6	
0.4	0.1	0.2	0.1	0.1	0.2	0.1	

<sup>a</sup>The same precipitates were observed in the hot- and cold-worked specimens.

<sup>b</sup>Mean composition in normalized atomic percent.

<sup>c</sup>Mean composition in weight percent.

<sup>d</sup>SD = one standard deviation based on ten analyses and expressed in weight percent.

The fracture surface analysis by SEM (see Figs. 7 through 9) of specimens tested at room temperature yielded the following observations:

ORNL Photo 2182-96



(a) 527

(b) 526

Fig. 7. Fracture surface of FAPY heat specimen 899-21690 in as-cast and hot-worked conditions tested at room temperature: (a) low and (b) high magnifications.

ORNL Photo 2183-96



(a) 522

(b) 520

Fig. 8. Fracture surface of FAPY heat specimen 899-21690 in as-cast and hot-worked conditions tested at room temperature: (a) low and (b) high magnifications.

1. As cast: a mixed mode fracture consisting of intergranular separation with some cleavage occurring at the grain faces.
2. Cast and hot-worked: a mixed mode fracture consisting of intergranular separation with possibly more cleavage than the as-cast specimen.

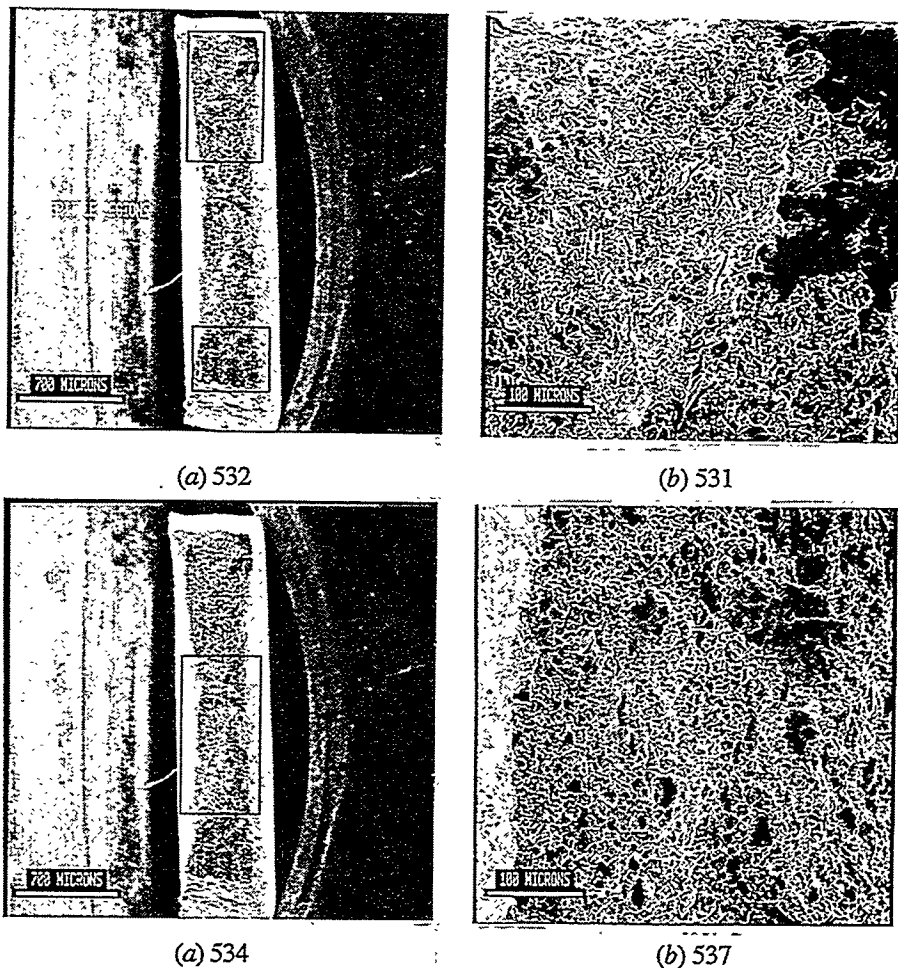


Fig. 9. Fracture surface of FAPY heat specimen 899-21690 in cold-worked condition tested at room temperature: (a) and (b) end location, and (c) and (d) midsection location.

3. Cold-rolled sheet: a mixed mode fracture consisting of brittle regions (cleavage) and a ductile region in the midsection of the tensile specimen.

The energy-dispersive X-ray spectra of the fracture surfaces showed little difference in composition for the three specimens.

#### SUMMARY AND CONCLUSIONS

Two commercial-size heats of the FAPY alloy were processed by AIM at Hoskins and one at United Defense. One ingot from each of the heats was sent to ORNL for processing, properties, and microstructural characterization. A 127-mm-long section was cut from each of the ingots. A 51-mm-thick slab section was cut from each of the 127-mm-long ingot sections for processing. The remaining ingot



section was used to machine specimens in the as-cast condition. The slab was forged and rolled to obtain a plate in the cast and hot-worked condition. Part of the hot-rolled plate was cold rolled into 0.76-mm-thick sheet to obtain a fine-grained wrought microstructure. Tensile tests were conducted from room temperature to 800°C on material in three different conditions. Tests were also conducted on a cast and hot-rolled bar processed at Hoskins. All of the materials were tested after annealing at 800°C for 1 h. One sheet was also tested in the 40% cold-worked condition. The as-cast, cast and hot-worked, and cold-rolled materials were characterized by optical and SEM. The following conclusions are drawn from this work:

1. The fine-grained sheet showed 20% elongation at room temperature. For cast and hot-worked conditions, 20% elongation was reached at 100°C. For the cast condition, the fine-grained sheet reached a value of only 10% at 200°C.
2. While the cast and cast and hot-worked conditions showed a transition from brittle-to-ductile behavior in tensile ductility, the cold-worked material showed only a reduction in ductility.
3. The cast grain size of 305  $\mu\text{m}$  was refined to only 254  $\mu\text{m}$  by hot-working. However, the cold-working refined the microstructure to 13  $\mu\text{m}$ . The grain refinement occurs through recrystallization of warm- and cold-rolled sheet.
4. All three conditions showed the particles believed to be ZrC and FeCrAlY precipitates. Both particles were primarily at the grain boundaries in the as-cast condition. Processing by hot- and cold-working relocated the precipitates from the grain boundaries to matrix and refined their size. However, the total area fraction of the particles appears to remain the same in all three conditions.
5. Based on the ductility data, the fine-grained material can be cold-worked while the hot-worked material can be worked by warming up the work piece to  $\geq 100^\circ\text{C}$ .

#### ACKNOWLEDGMENTS

The authors thank D. C. Harper and K. S. Blakely for cutting and processing the ingots, H. F. Longmire for optical metallography, L. R. Walker for SEM work, C. A. Blue and D. J. Alexander for paper review, K. Spence for editing, and M. L. Atchley for preparing the manuscript.

Research sponsored by the U.S. Department of Energy, Office of Fossil Energy, Advanced Research and Technology Development Materials Program [DOE/FE AA 15 10 10 0, Work Breakdown Structure Element ORNL-2(H)], under contract DE-AC05-96OR22464 with Lockheed Martin Energy Research Corp.



MICROSTRUCTURAL AND MECHANICAL CHARACTERIZATION OF ALUMINA SCALES  
THERMALLY DEVELOPED ON IRON ALUMINIDE ALLOYS\*

K. Natesan, K. L. Klug, D. Renusch, M. Grimsditch, and B. W. Veal  
Argonne National Laboratory  
Argonne, IL 60439

ABSTRACT

An understanding of the underlying phenomena when characterizing material performance requires knowledge in several areas, including the chemistry and physics of the early stages of oxidation, chemistry and bonding at the substrate/oxide interface, effect of segregants on the strength of bonding, transport processes through the scales that are formed during corrosion, mechanisms of residual stress generation and relief, and fracture behavior at the oxide/substrate interface. Specific objectives of the program described here are to (a) systematically investigate the relationships among substrate composition and properties and scale/coating adherence, damage tolerance, and micromechanical properties; (b) use results from the investigation to prevent scale/coating failure at elevated temperatures; and (c) identify conditions that lead to more damage-tolerant coatings and scales that are amenable to legitimate synthesis routes. The paper presents experimental data on microstructural characteristics of alumina scales that have been thermally developed on several Fe-based alumina-forming intermetallic alloys. In addition, adhesion data developed on the scales are presented, along with determinations of strain from data obtained by ruby fluorescence.

INTRODUCTION

Protection from corrosion and environmental effects arising from reactions with gases and condensed products is required to fully exploit the potential of advanced high-temperature materials designed to improve energy efficiency and minimize deleterious environmental impact. This protection is best afforded either by formation of stable surface oxides that are slow-growing, sound, and adherent to the substrate or by deposition of coatings that contain or develop oxides with similar characteristics. The benefits of certain alloying additions on the growth and adherence of protective oxide scales on metallic substrates are well known, but there remains the need for a detailed understanding of the mechanisms by which scale properties and coating integrity are improved by compositional, microstructural, and processing modifications. The ultimate objective of this program is to systematically generate a scientific basis for designing and synthesizing improved protective oxide scales/coatings (slow-growing, adherent, sound) on high-temperature materials without compromising the requisite properties of the bulk materials. Specific objectives are to (a) systematically investigate the relationships among substrate composition and properties and scale/coating adherence, damage tolerance, and micromechanical properties; (b) use such information to predict scale/coating failure; and (c) identify conditions that lead to more damage-tolerant coatings and scales that are amenable to legitimate synthesis routes. The objectives of the ANL program are to correlate actual oxidation performance with stresses, voids, segregants, interface roughness, initial stages of oxidation, and microstructures; study such behavior in growing or as-grown films; and define prescriptive design and synthesis routes to mechanically reliable surface oxides.<sup>1,2</sup> Several techniques are used in the studies, including Auger electron spectroscopy, X-ray diffraction, X-ray grazing incidence reflectance, grazing-angle

---

\*Work supported by the U.S. Department of Energy, Office of Fossil Energy, Advanced Research and Technology Development Materials Program, Work Breakdown Structure Element ANL-4A and Basic Energy Sciences Materials Program, under Contract W-31-109-Eng-38.

X-ray fluorescence, optical fluorescence, and Raman spectroscopy. The project has selected Fe-25 wt.% Cr-20 wt.% Ni and Fe-Cr-Al alloys, which are chromia- and alumina-formers, respectively, for the studies. This paper presents selected results on alumina scale morphologies that develop on several Fe-Al based intermetallic alloys, their adhesion strength, and stresses in scales that can lead to spallation of the scales.

### EXPERIMENTAL PROCEDURE

The experimental study has focused on iron aluminide (Fe-Al) intermetallic alloys, which are of interest for application in coal-gasification and coal-combustion systems. Iron aluminide alloys, which are alumina-formers, are in various stages of development under the sponsorship of the DOE. These alloys can be used as either structural material or cladding to protect structural material against corrosion. Sheets of several Fe<sub>3</sub>Al-based alloys were procured from Oak Ridge National Laboratory. Table 1 lists the compositions of the alloys used in the study. Alloy FA 186 is a ternary alloy that contains Fe, Cr, and Al and is considered a base alloy. Alloy FA 129 is designed to exhibit high ductility at room temperature while retaining its strength at high temperatures, whereas FAL is designed for improved oxidation resistance through addition of Zr. Alloy FAS is designed to resist sulfidation, and FAX is designed for improved resistance in aqueous environments by deliberate addition of Mo. Coupon specimens were cut from sheet material for thermogravimetric oxidation experiments and for spectroscopic studies.

Specimens of the intermetallic alloys were oxidized at 1000°C for up to 100 h in oxygen bubbled through water at room temperature to examine the morphologies of the alumina scales that form on alloys with different bulk compositions. Thermogravimetric experiments were performed with an electrobalance having a sensitivity of 0.1 µg, to evaluate the rate of oxidation in different alloys and to establish the scaling kinetics. Specimens were suspended from the balance in a vertical furnace and held for the desired exposure period. Upon completion of the oxidation test, the furnace was opened and the specimens were rapidly cooled to room temperature. Following thermogravimetric measurement of oxidation, scale surfaces and cross sections of specimens were examined with a scanning electron microscope equipped with an energy-dispersive X-ray analyzer. Further, the oxidized specimens were cooled to liquid nitrogen temperature and fractured to examine the fracture morphologies of the scales and to evaluate the scale/metal interface.

A Sebastian-Five multipurpose tester (from Quad Group Inc.) was used to evaluate the strength of the scale/substrate interface of each oxidized specimen. In this technique, an epoxy-coated pin is attached to the surface of interest at a temperature sufficient to cure the epoxy. The pin is subsequently separated from the sample at room temperature by applying a tensile load. Prior to testing the oxidized samples, the

Table 1. Nominal composition (wt.%) of alloys used in corrosion tests

Material	Cr	Al	Fe <sup>a</sup>	Other
FA 186	2.2	15.9	Bal.	-
FAS	2.2	15.9	Bal.	B 0.01
FA 129	5.5	15.9	Bal.	Nb 1.0, C 0.05
FAL	5.5	15.9	Bal.	Zr 0.1, B 0.05
FAX	5.5	15.9	Bal.	Nb 1.0, Mo 1.0, Zr 0.15, B 0.04

<sup>a</sup>Bal. = balance.

the procedure was evaluated using several flat unoxidized 316 stainless steel samples. This was done to establish the reliability of the technique and the absolute strength of the epoxy. In addition, epoxy-coated pins that had been at room temperature for varying lengths of time (as opposed to being in a freezer, where they are normally held) were used to evaluate the effect of this variable (room temperature degradation of the epoxy) on the strength data. Strength data from these tests were consistent; the maximum strength that could be measured by this procedure was  $\approx 71 \pm 3$  MPa. No significant variation in data was noted for pins exposed to room temperature for up to four days. Adhesion testing was then performed on each of the oxidized Fe-Al specimens.

The oxidized samples were also examined by a ruby luminescence at room temperature. By exploiting the strain dependence of the ruby fluorescence line, strains in the thermally grown oxides were determined for scales that developed on different substrates.<sup>3,4</sup> Fluorescence radiation from unstrained  $\alpha$ -Al<sub>2</sub>O<sub>3</sub>, doped with Cr<sup>3+</sup>, appears as a very sharp doublet, detectable at very low levels of Cr doping, with peaks at 14402 and 14432 cm<sup>-1</sup>. The peak positions are strongly dependent on the state of strain in the sample but very weakly dependent on Cr concentration. Depending on scale-growth conditions, the doublet shifts and broadens, apparently as a consequence of varying strains in the alumina scale. The shifts provide a sensitive measure of strain accumulation in the scales and clearly indicate when strain relief occurs.

## RESULTS AND DISCUSSION

### Oxidation Behavior

Oxidation weight change of the intermetallic alloys was generally parabolic for  $\approx 20$  h, followed by much slower weight change for the rest of the exposure period. However, the scales in FA 186 and FAS exhibited significant spallation during oxidation at 1000°C and therefore, no weight change data could be obtained. For example, FA 186 showed a small weight gain up to 60 h of exposure, after which the weight of the sample decreased and showed a loss after 100 h of exposure. Assuming a parabolic behavior for the alloys with no spallation, rate constants calculated for FA 129, FAL, and FAX at 1000°C were  $6.0 \times 10^{-5}$ ,  $4.2 \times 10^{-5}$ , and  $4.2 \times 10^{-5}$   $\mu\text{g}^2/\text{mm}^4\text{s}$ , respectively. X-ray diffraction data showed  $\alpha$ -Al<sub>2</sub>O<sub>3</sub> as the scale in all of the oxidized samples.

### Microstructures of Oxide Scales

The surfaces of the oxidized samples were examined by scanning electron microscopy (SEM). Subsequently, the specimens were cooled to liquid nitrogen temperature and fractured. The freshly fractured surfaces of scale and substrate were then analyzed by SEM. Figures 1 and 2 show SEM photomicrographs of the fractured and oxidized surfaces of specimens. The fracture microphotograph of FA 186 shows a wavy oxide structure and the oxidized surface of the structure also indicates a fine distribution of oxide crystals or nodules. The fracture photomicrograph of the FAS specimen has an appearance similar to that of FA 186 but the surface shows a few large particles of oxide surrounded by a fine distribution of oxide precipitates. The morphologies in these specimens indicate that the scale is bonded to the substrate, probably at these large particles, and a two-dimensional bonding between the scale and substrate may not be present. In contrast, the fracture surface of the FA 129 alloy shows a dense,  $\approx 2$ - $\mu\text{m}$ -thick oxide scale, bonded well to the

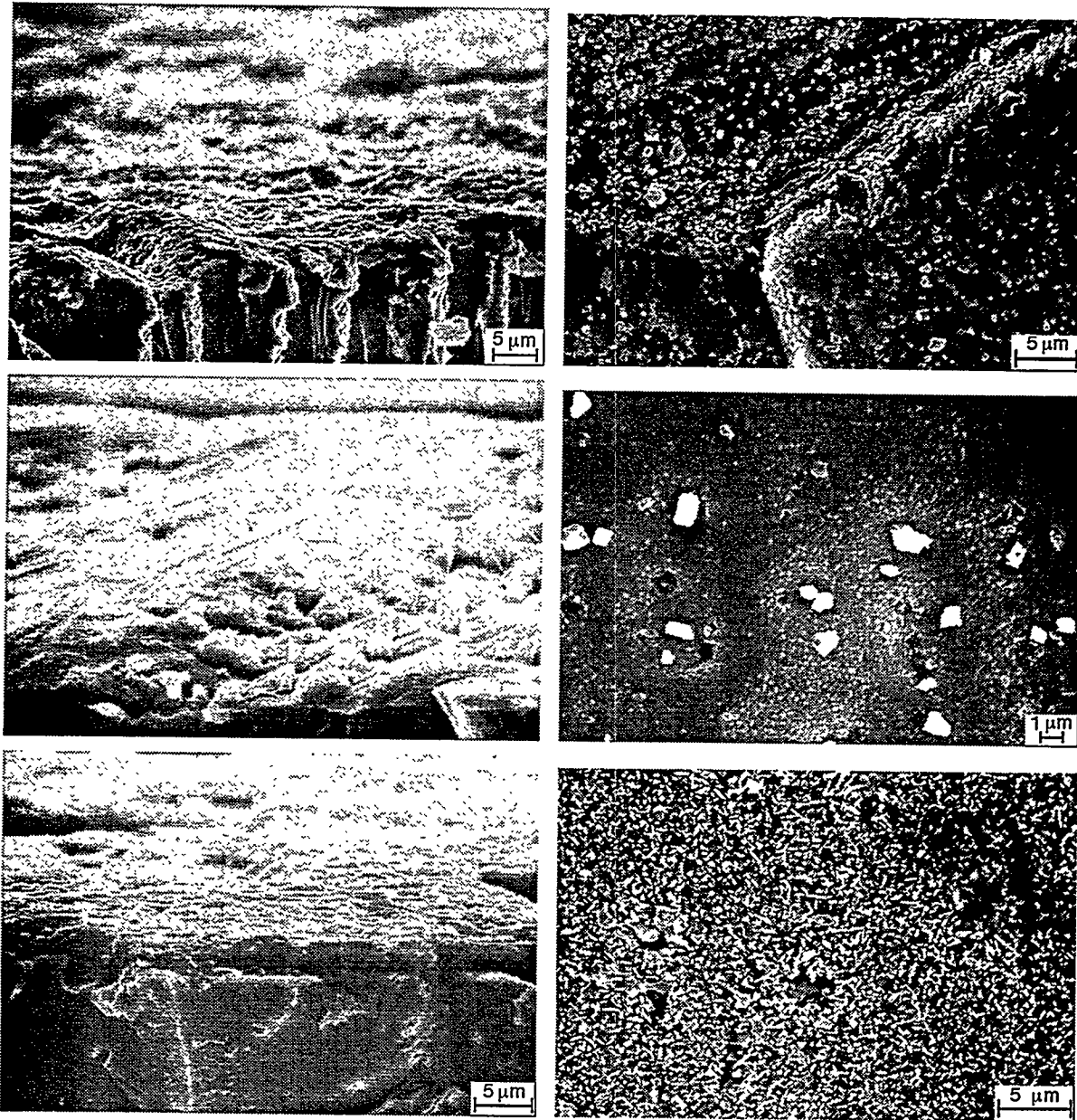


Fig. 1. SEM photomicrographs of (left) fracture surfaces and (right) oxidized surfaces of (top) FA 186, (middle) FAS, and (bottom) FA 129 alloys oxidized for 100 h at 1000°C

substrate. However, the surface of oxide exhibits some clumps of oxide, but not as many as in FAS alloy. The oxide morphology in FAL differs significantly from the morphologies of FA 186, FAS, and FA 129 alloys. Oxide growth is much more uniform and a distribution of fine oxide particles is present rather than spikes or clumps of oxide as observed in other samples. The oxide morphology in the FAX sample is much like that of the FAL sample but the fracture photomicrograph shows some voids at the scale/metal interface, which may be detrimental in the long run from an adhesion standpoint.

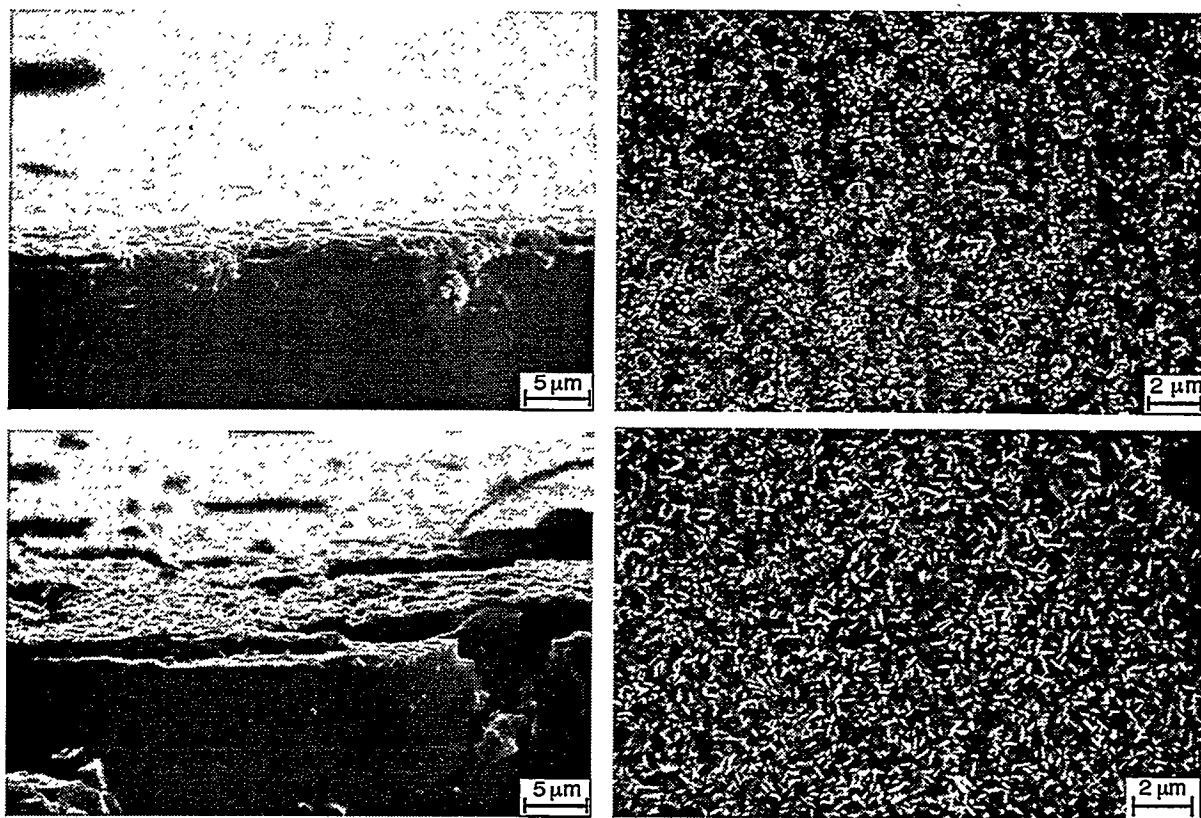


Fig. 2. SEM photomicrographs of (left) fracture surfaces and (right) oxidized surfaces of (top) FAL and (bottom) FAX alloys oxidized for 100 h at 1000°C

#### Adhesion of Scale to Substrate

To examine the adhesion characteristics of the thermally grown scales to the substrate, a Sebastian multipurpose tester was used to apply a tensile pull to separate the scale from the substrate. The surfaces of pulled pins were examined to assess whether the debonding occurred in the scale itself or at the scale/metal interface. Five measurements were taken for each specimen. The highest and lowest values for the load were discarded, and an average of the other three values and deviations from the mean were calculated. Knowing the pin area of contact, the stresses needed to pull the scale from the substrate were calculated. Figure 3 shows plots of the maximum stress endured by scale for the alloys oxidized at 800, 1000, and 1200°C as a function of alloy exposure temperature. The results show that Alloys FAS, FA 186, and FA 129 exhibit a peak in maximum stress value for specimens exposed at 1000°C. On the other hand, maximum stress values for FAL and FAX specimens are almost independent of exposure temperature. Even though the total exposure time of 100 h was used for all the specimens at all temperatures, the rates of disappearance of transient oxides and development of stable alumina scale will be different for different exposure temperatures and may be influenced by the composition of the bulk alloy, especially by the presence of reactive elements such as Zr and Nb.

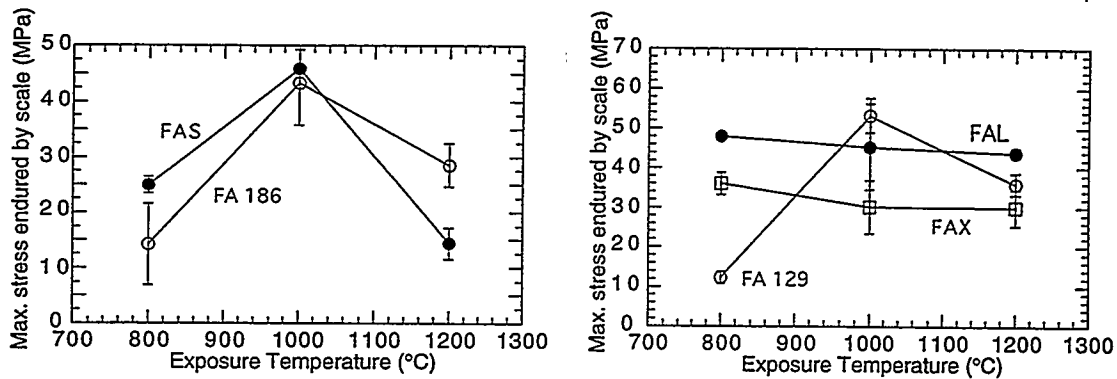


Fig. 3. Maximum stress endured by oxide scales on Fe-Al alloys determined by adhesion tests

#### Fluorescence Spectroscopy - Strain Analysis

Stress determination in thermally grown alumina scales by ruby luminescence has been recently addressed.<sup>3,4</sup> The technique has shown potential to elucidate our understanding of the strains that develop in thermally grown scales. The basic premise is that one can quantitatively assess the shift in the peaks of a relatively sharp fluorescence doublet obtained from the alumina scale, and, assuming a plane strain condition, calculate the strain in the scale. It is difficult to assess the importance of the measured strain values in scale fracture because little or no quantitative data are available for films of alumina in the literature. Nonetheless, the technique can be used to compare the strain values for specimens that have received differing treatment or compare the values obtained for different alloy specimens that have been oxidized under the same conditions. The trends identified in such an approach can shed light on the important variables responsible for the observed microstructure, alloying-element effect, adhesion, and time-dependent variations in the scale and at the scale/metal interface. The frequency shift ( $\Delta\nu$  in  $\text{cm}^{-1}$ ) is related to the in-plane strain by the expression

$$\Delta\nu = 2810 \epsilon_{\text{in}}.$$

Figure 4 shows the fluorescence spectra for various alloys oxidized for 100 h at 1000°C. The three spectra for each alloy are measurements taken at three different locations on the same specimen. The extreme variability in the spectra of FA 186 and FAS specimens indicates that the scale has spalled from various areas of the specimen. The spectra for FA 129, FAL, and FAX are fairly consistent. Figure 5 shows the in-plane strain, calculated from the peak shifts, for the five alloys oxidized for 100 h at 1000°C. The results show low strain values for FA 186 and FAS alloys, indicating significant spallation of the scale. This observation confirms the SEM analysis of the fracture surfaces and thermogravimetric test data for these alloys. The in-plane strain values for FA 129, FAL, and FAX are consistently high and indicate that the scales developed in these alloys can accommodate the deformation, as evidenced by the lack of spalling in the oxidized alloys.

A comparison of the stress needed to pull the scale away from substrate and the strain that was accommodated in the scale of various oxidized specimens is attempted in Fig. 6. It is evident that the maximum stress needed to pull the scale from various alloys is in the range of 30-52 MPa and the



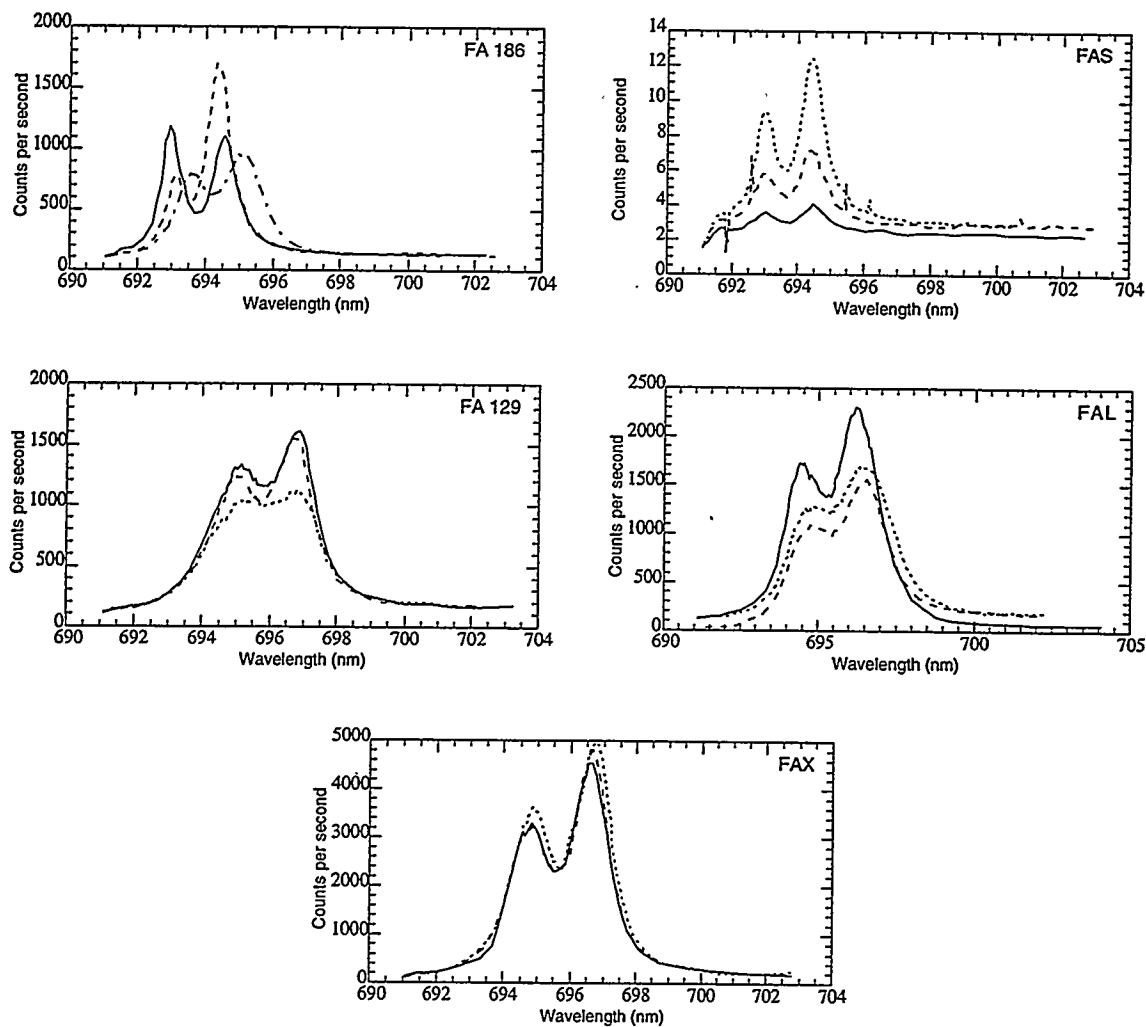


Fig. 4. "Ruby" fluorescence spectra for several Fe-Al alloys after oxidation for 100 h at 1000°C

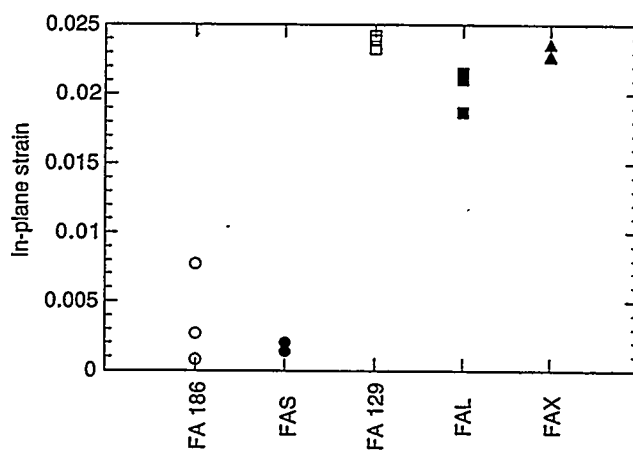


Fig. 5. In-plane strain values for oxide scales calculated from peak shifts in fluorescence spectra

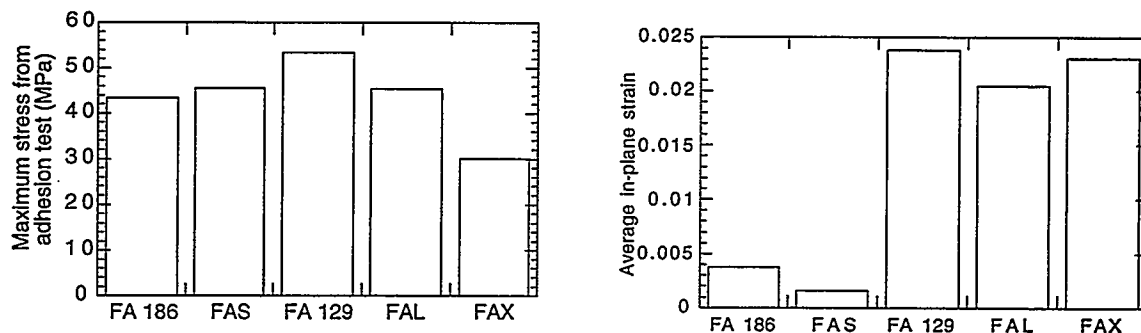


Fig. 6. Comparison of maximum stress needed to pull scale from substrate, and in-plane strain values for oxides that developed on several Fe-Al alloys

microstructural characteristics cannot be correlated with the stress values from the limited adhesion tests. Additional tests are underway with specimens exposed at 800 and 1200°C to develop a better understanding of scaling kinetics, adhesion of scale to substrate, and scale failure.

### SUMMARY

Several alumina-forming Fe-Al intermetallic alloys have been oxidized in oxygen for 100 h at 1000°C to elucidate our understanding of the scaling kinetics, scale morphology, scale adhesion characteristics, and strain accommodation in the scales. Oxidation studies were conducted by the thermogravimetry technique, followed by detailed analyses of the surfaces of oxide scales. In addition, samples were cooled to liquid nitrogen temperature and then fractured; subsequently, their scale/metal interfaces were analyzed. Some of the scales were adhesion-tested by applying a tensile load to pull the scale away from the substrate. Finally, ruby fluorescence was used to measure in-plane strains in the oxide scales and the values were correlated with the scale microstructures.

### REFERENCES

1. K. Natesan, B. W. Veal, M. Grimsditch, D. Renusch, and A. P. Paulikas, "Mechanically Reliable Surface Oxides for High-Temperature Corrosion Resistance," Proc. 9th Annual Conf. on Fossil Energy Materials, CONF-9505204, ORNL/FMP-95/1, p. 225 (1995).
2. K. Natesan, C. Richier, B. W. Veal, M. Grimsditch, D. Renusch, and A. P. Paulikas, "Chemical and Microstructural Characterization of Thermally Grown Alumina Scales," Argonne National Laboratory Report ANL/FE-95/02 (1995).
3. D. Renusch, B. W. Veal, I. Koshelev, K. Natesan, M. Grimsditch, and P. Y. Hou, "Stress Determination in Thermally Grown Alumina Scales Using Ruby Luminescence," Proc. Spring Meeting of MRS Society, San Francisco, CA, April 8-12, 1996.
4. D. M. Lipkin and D. R. Clarke, "Measurement of the Stress in Oxide Scales Formed by Oxidation of Aluminum-Containing Alloys", *Oxid. Metals* (in press), and Q. Ma and D. R. Clarke, "Stress Measurement in Single and Polycrystalline Ceramics using Their Optical Fluorescence", *J. Am. Ceram. Soc.*, 77 (2), 298-302 (1994).

## OVERVIEW OF THE CARBON PRODUCTS CONSORTIUM (CPC)

Caulton L. Irwin (Carl)

Carbon Products Consortium  
P.O. Box 6064  
West Virginia University  
Morgantown, WV 26506

### ABSTRACT

The Carbon Products Consortium (CPC) is an industry, university, government cooperative research team which has evolved over the past seven years to produce and evaluate coal-derived feedstocks for carbon products. The members of the Carbon Products Consortium are UCAR Carbon Company, Koppers Industries, CONOCO, Aluminum Company of America, AMOCO Polymers, and West Virginia University. The Carbon and Insulation Materials Technology Group at Oak Ridge National Laboratory, Fiber Materials Inc., and BASF Corporation are affiliates of the CPC. The initial work on coal-derived nuclear graphites was supported by a grant to WVU, UCAR Carbon, and ORNL from the U.S. DOE New Production Reactor program. More recently, the CPC program has been supported through the Fossil Energy Materials program and through PETC's Liquefaction program. The coal processing technologies involve hydrogenation, extraction by solvents such as N-methyl pyrrolidone and toluene, material blending, and calcination. The breadth of carbon science expertise and manufacturing capability available in the CPC enables it to address virtually all research and development issues of importance to the carbon products industry.

### INTRODUCTION

Section 1304 of the National Energy Policy Act of 1992 authorizes a research and development program on non-fuel uses of coal. The objective is to develop coal-based feedstocks for a wide variety of materials and chemicals. The work of the CPC includes the production of high-value carbon materials from feedstocks derived from coal via solvent extraction and hydrogenation technologies. Tables 1 and 2 summarize the types of carbon products which are being developed by the CPC.

### PARTICIPANTS

Figure 1 shows the feedstock and product linkages within the Carbon Products Consortium. A brief discussion of the CPC membership follows.

UCAR Carbon Company is the world's largest manufacturer of bulk carbon materials, with approximately one-third of the world's market in graphite electrodes, and has the broadest range of commercial carbon products of any domestic carbon company. UCAR is the only domestic carbon

**Table 1.** Feedstock and Product Summary for Intermediate Products.

<u>Intermediate Products</u>	<u>Unit Price</u>	<u>Current Feedstock</u>	<u>Feedstock Status</u>	<u>Domestic Annual Sales</u>	<u>Worldwide Annual Sales</u>	<u>Comments</u>
Binder Pitch	\$300-\$400 per ton	CTP from coke ovens	Declining supply of CT	500,000 T \$175M	1,500,000 T \$525M	SECP could replace CTP
Impregnating Pitch	\$250-\$350 per ton	PP (USA) CTP (elsewhere)	Adequate for demand	30,000 T \$9M	125,000 T \$37M	SECP could replace CTP and PP
Matrix Pitch (D)	\$300-\$400 per ton	75% CTP 25% PP	Declining supply of CT. PP quality declining			SECP could replace CTP and PP
Mesophase Pitch (D)	\$10 per lb. (Japanese prices) No domestic price	PP (USA) CTP (Japan, Korea)	No CT mesophase pitch produced in USA	No domestic sales of mesophase CTP	Japanese production all used internally	SECP could replace CTP and PP
Calcined Coke	\$250 per ton (calcined)	PT (USA) CT (Japan)	Declining quality. 4% annual increase in demand	2,000,000 T \$300M	5,900,000 T \$885M	SECP could replace CT and PT
Isotropic Coke	\$150-\$250 per ton	PT in USA CT in Japan		30,000 T \$6M	100,000 T \$20M	SECP could replace CT and PT
Needle Coke	\$350-\$600 per ton	PT in USA PT & CT in Japan		250,000 T \$106, 250M	1,300,000T \$552.5M	SECP could replace CT and PT

CT: coal tar                      CTP: coal tar pitch  
PT: petroleum tar              PP: petroleum pitch  
T: tons                              SECP: solvent extracted  
D: dual use                        coal pitch

manufacturer that has developed technical expertise in raw materials for the complete scope of carbon products ranging from needle coke for electrodes, isotropic coke for specialty graphite, binder and impregnation pitches, active carbons, and pitches for high performance carbon fibers. UCAR would use precursors developed from coal extracts to produce carbon and graphite end-products. The availability of coal-based cokes with a controllable structure, would allow UCAR to customize graphite properties to fit desired market applications.

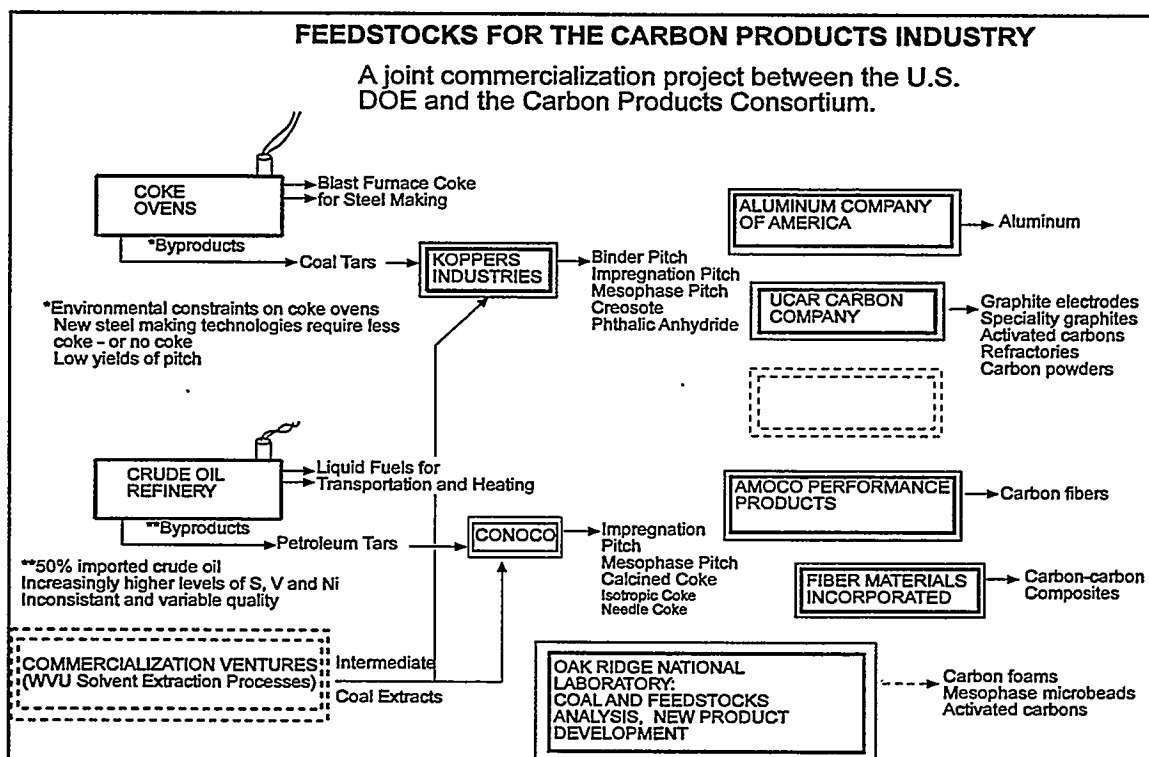
KOPPERS Industries is the largest domestic producer of binder for carbon and graphite used in the production of aluminum and in the production of steel by the electric arc process. The conventional feedstocks for binder pitch are crude tars produced as a by-product during coking of metallurgical coal.

Table 2. Feedstock and Product Summary for Final Products.

<u>Final Products</u>	<u>Unit Price</u>	<u>Current Feedstock</u>	<u>Feedstock Status</u>	<u>Domestic Annual Sales</u>	<u>Worldwide Annual Sales</u>	<u>Comments</u>
Carbon Anodes	\$300-\$400 per ton	Calcined coke binder pitch	Declining quality of petroleum coke	2,300,000 T \$805M	6,900,000 T \$2,415M	Alcoa has 32% of domestic market and 11% of world-wide market
Graphite Electrodes	\$1 per lb.	Needle coke binder pitch impregnating pitch	Electrode Consumption cut in half over last decade	400,000 T \$800 M	1,100,000 T \$2,200M	UCAR has 1/3 of world market
Specialty Graphite (D)	\$5-\$50 per lb.	Cokes binder pitch impregnating pitch	Adequate	\$0.2M	\$0.6M	
Activated Carbon	\$1-2 per lb. (avg) \$80 per lb. (max) \$0.20 per lb. (min)	Various organic precursors including coal and cellulosic material		146,000 T	375,000 T (excluding E. Europe and China)	China exporting up to 25,000 TPY
Carbon Fibers Low Cost CF	\$10-\$12 per lb. (isotropic)	70% PP 30% CTP (Japan)	Isotropic pitch fibers no longer produced in USA	150,000 lbs \$1.65M 400,000 lbs	1,500,000 lbs \$1.65M 650,000 lbs	CTP & SECP fibers show promise for advanced molecular sieves. SECP could replace CTP
High Performance CF (D)	\$500-\$3,000 per lb.	75% PP 25% CTP (Japan)	Only PP feedstocks available in USA from one source	\$400M	\$650M	SECP could replace CTP
Carbon-Carbon Composites (D)	\$150-\$2,000 per lb.	Carbon fibers & matrix pitch		\$100M Brakes \$ 50M Other		

Closure of by-product coke ovens has caused domestic production of coke and tar to decline at 3% to 4% per annum during the first half of the 1990s. By the year 2010, it is projected that domestic coal tar sourcing will have decreased 15% from today, crude petroleum will continue to increase in sulfur and metals, and pitch and coke supply requirements for carbon and graphite will increase by 100%.

Therefore, Koppers is concerned about the United States retaining a dominant worldwide position in key industrial businesses such as aluminum and steel. Koppers' main objective for participating in the CPC is to develop dependable domestic coal-based raw materials for the production of binder pitches for aluminum cell anodes and commercial carbon and graphite products, impregnating pitches for commercial carbon, graphite and specialty materials; oils for wood treatment and carbon black production; feedstock for phthalic anhydride and other chemicals; and metallurgical and foundry grade



**Figure 1.** Feedstocks and Product Linkages within the Carbon Products Consortium.

cokes.

CONOCO is a fully integrated energy corporation with worldwide marketing and production facilities. Today, Conoco has annual worldwide petroleum coke sales in the 2-3 million ton range. Conoco coke is manufactured in five refineries located on three continents and a sixth refining/coking operation is under construction in Malaysia. Conoco is co-owner of a calcining plant in Moundsville, WV. In the petroleum coke area, Conoco is a world market leader, especially in regular coke for aluminum anodes and the  $\text{TiO}_2$  process, and in specialty premium cokes for the graphite industry. Conoco's large, efficient manufacturing plants are technically supported from extensive Research and Engineering facilities in Ponca City, Oklahoma. Conoco believes that coal-based feedstocks being developed through CPC programs offer an abundant, promising alternate source of carbon products for the future.

ALCOA is the largest U.S. aluminum company with approximately one-third market share of the 4,600,000 tons per year domestic production. The aluminum industry is a major user of carbon since approximately 0.43 pounds of carbon are consumed in the production of one pound of aluminum. Reduction cell electrodes are produced from a baked coke and pitch mixture. The cokes and pitches are currently produced as by-products from coke ovens or from oil refining residues. Even a small improvement in carbon electrode quality for this very high volume, competitive industry would result in

considerable savings in aluminum manufacturing and electricity costs. Environmental pressures on coke ovens and the declining quality of imported crude oil (increased sulfur and metals content) have jeopardized existing raw material sources; therefore, ALCOA is highly interested in the development of consistent quality coal-derived carbon products that can improve electrodes and make production more efficient.

AMOCO Polymers has over 20 years experience in the development and commercial production of pitch based carbon fibers and is the only domestic producer of ultra-high thermal conductivity carbon fibers made from petroleum pitch. Ultra-high thermal conductivity carbon fiber and composites are the basis for components which offer unique performance advantages in the electronic packaging and spacecraft business areas. The combination of stiffness, strength, passive thermal management, dimensional stability, and machinability afford the potential to meet the thermal performance and reliability demands imposed by high density electronic packaging and small, high performance satellites. Hence, any innovations in high thermal conductivity carbon fibers directly impact both the commercial and defense industries. Mesophase pitch derived from coal affords AMOCO the opportunity to be more competitive through lower cost and higher quality. A domestic source for coal derived pitch serves defense interests and is consistent with reliability/robust processing goals. Coal-based materials should favorably impact processing costs since they are more graphitizable than petroleum pitches and afford fibers with better crystallinity. Thus, lower costs will result from less demanding furnacing (lower temperatures and shorter times) and improved product quality. Coal-derived precursors would be immediately employed for high thermal conductivity pitch fibers and materials. Cost and performance enhancements, linked with a secure source of raw materials and maintenance of an on-shore technology base, compel industrial and government support for this technology.

West Virginia University (WVU) coal processing technologies, developed in the Department of Chemical Engineering have been tested and proven over the past 10 years with support through the WVU Coal and Energy Research Program, the U.S. DOE's Consortium for Fossil Fuel Liquefaction Science, and the U.S. DOE's New Production Reactor Program. The work is currently supported through the U.S. DOE Advanced Research and Technology Development Materials Program and through PETC's Non Fuel Use of Coal Program. The main focus of the WVU program is to develop an economical process to obtain a high (50% to 80%) yield of ash-free coal-derived extract. The WVU process involves the use of a novel dipolar, aprotic solvent, N-methyl-2-pyrrolidone (NMP) at a mild temperature of 202 deg C and one atmosphere pressure to extract organic coal material selectively and obtain an ultra low ash, low sulfur carbonaceous product. Hydrogenation of coal prior to extraction by NMP substantially increases the yield and alters properties of the extract. A flow chart indicating the three step solvent extraction process developed by WVU is shown in Figure 2. The WVU research team produces a wide

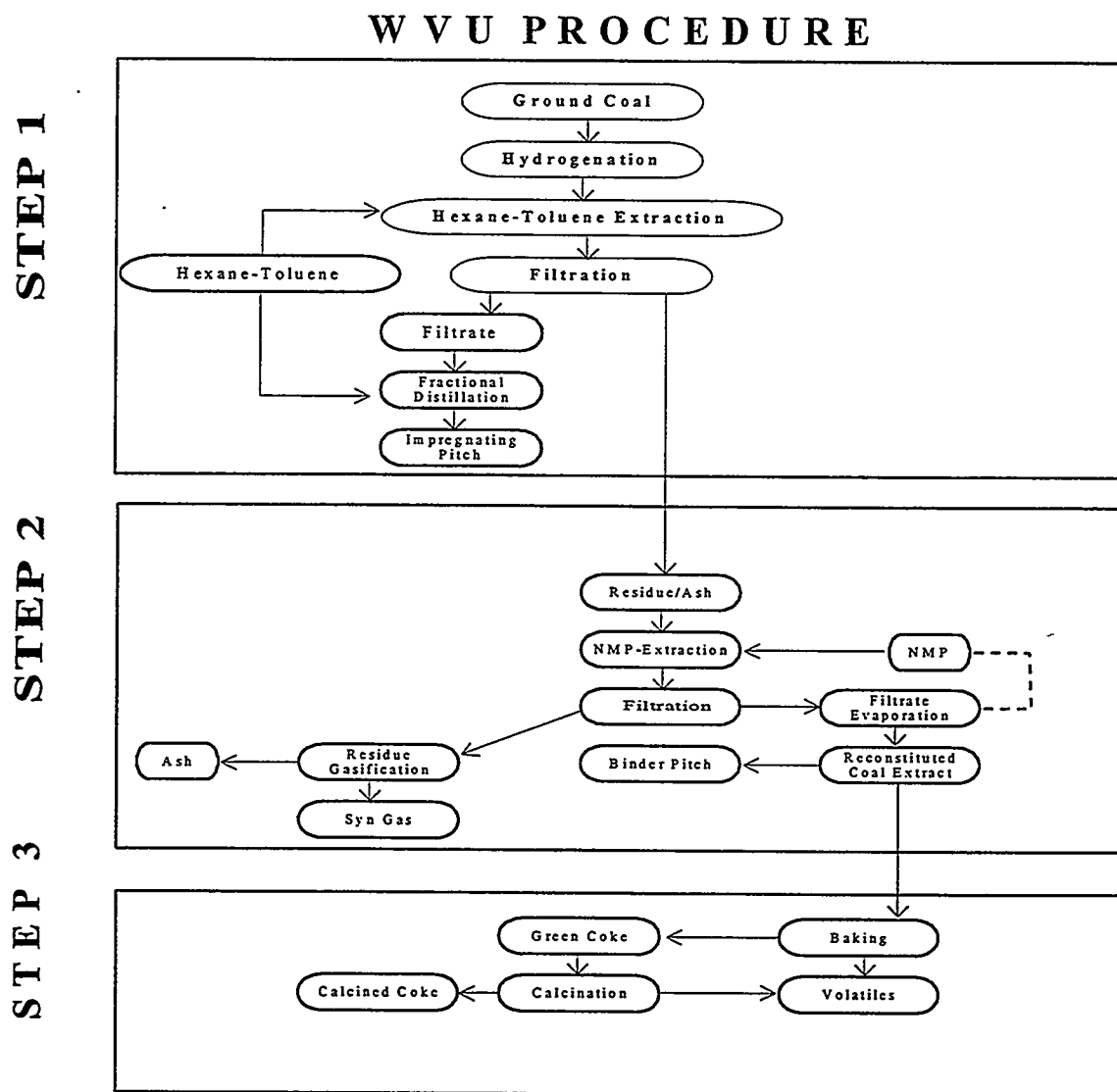


**Figure 2.** WVU Solvent Extraction Procedure

variety of coal extracts. The CPC industrial participants evaluate the suitability of the extracts as feedstocks for their particular product lines, and work with WVU to further optimize the process.

Fiber Materials Inc. (FMI) is a world leader in the manufacture of multidirectional carbon-carbon composites with over 25 years experience using both petroleum and coal tar pitches from companies such as Allied Signal, Ashland, and Koppers. FMI is the largest producer of pitch based carbon-carbon composites in the U.S. and has developed many specialized laboratories and processing techniques. The manufacture of carbon-carbon (C/C) composites for use in the defense industry has relied heavily on petroleum and coal-tar pitches as the matrix material. Over the past decade the properties of pitches have changed, resulting in changes to the composites fabricated. The reason is that



itches come from the residual tars of other manufacturing processes (oil, gas and coke production). Process changes in manufacturing the primary products result in changes to the residual tars. In addition to defense, there are other new applications for C/C composites appearing in the commercial sector, including: biomedical, automotive, fusion and fission energy, and test equipment. It is important that the WVU process be put to practical use in the manufacture of composites for these new applications.

The Carbon and Insulation Materials Technology Group (CMT) at the Oak Ridge National Laboratory (ORNL) has extensive experience in the qualification of high performance graphite and carbon-carbon composite materials and products. ORNL houses many advanced materials testing facilities and CMT personnel have been involved with the analysis of coal structures for many years. The CMT group will develop relations between various coals and solvent extracted coal products and furthermore, is particularly interested in the development of monolithic carbon fiber composite molecular sieves for gas separations and heavy oil upgrading.

## PROGRAMS

The CPC has conducted programs with several agencies and organizations. The participants involved in the project entitled, "Coal-based Nuclear Graphites for the New Production Gas Cooled Reactors", (DOE Grant No. DE-FG02-91NP00159) sponsored by U.S. DOE Office of New Production Reactors, included the West Virginia University Departments of Chemical Engineering, Physics, and Chemistry; West Virginia Geological and Economic Survey; UCAR Carbon Company; and the ORNL Carbon and Graphite Materials Group. The objective was to produce nuclear grade isotropic graphite from coal based feedstocks. During the course of the two and one half year project, UCAR produced 14 CTE graphite test bars using isotropic cokes obtained via the WVU coal extraction process. Conventional binder pitch was used in fabricating the CTE test bars. It was discovered during this project that by varying the extent of hydrogenation prior to extraction, the isotropy of the resultant graphite could be made to range from isotropic ( $CTE \sim 4.5 \times 10^{-6}$ ) to anisotropic ( $CTE \sim 0.5 \times 10^{-6}$ ). Prior to this project, domestic isotropic graphites had only been produced from petroleum cokes.

"Coal-based Precursors for Production of Carbon and Graphite Products", (DOE/PETC Contract No. DE-AC22-95PC94063) sponsored by U.S. DOE Fossil Energy Materials and Pittsburgh Energy Technology Center, initiated a three-phase project in partnership with the CPC to explore and develop the possibilities of making commercially acceptable carbon products from coal. The project is in part a response to a mandate of the National Energy Policy Act of 1992 that the country initiate programs involving research, development, demonstration, and commercial application of technologies for the nonfuel-use of coal rich resources in the United States.

The materials characterization shown in Tables 3 and 4 were developed by the industrial participants during the current U.S. DOE program. As part of this project, the MITRE Center for Environment,

**Table 3.** Comparison of WVU Coal Extract with Commercial Pitches

	WVU Extract	Coal Binder	Petroleum Impregnant
Softening Point (°C)	105	112	120
Modified Conradson Carbon (wt %)	53	58	52
Carbon (wt %)	88.9	93.8	91.5
Hydrogen (wt %)	5.85	3.92	5
Nitrogen (wt %)	2.2	0.7	0.6
Oxygen (wt %)	2.74	0.93	0.5
Sulfur (wt %)	0.45	0.56	2.5
Aromatic Hydrocarbon (%)	45	85	55
Molecular Weight	370	410	500

**Table 4.** Comparison of WVU Pitch with Commercial Impregnation Pitches

	WVU	Ashland A240	Allied 15V
Coking Value (wt %)	49.3	50.2	46.7
Ash Content (wt %)	0.02	0.03	0.17
Quinoline Insoluble (wt %)	0.39	0.15	4.3
Toluene Insoluble (wt %)	1.12	6.52	14.8
Sulfur (wt %)	0.4	2	0.54
Softening Point (°C)	117	117	88
Specific Gravity	1.22	1.26	1.28
Viscosity (sec)	****	16	19

Resources, and Space conducted a review and cost analysis of the WVU coal extraction process. Preliminary conclusions and recommendations include: (1) the extract is a suitable precursor for production of isotropic anode coke, (2) the product cost of the coal extract is estimated by MITRE to be

\$77 per ton at a scale of 500,000 tons per year, and after further coking and calcining the estimated cost of calcined coke is \$173 per ton, (3) it is extremely important that the unhydrogenated coal extract be further evaluated by the CPC for production of anode coke, (4) research on the production of isotropic carbon fibers (\$8 to \$10 per pound) from the coal extracts is recommended, and (5) it is recommended to examine the economics of dual production of both hydrotreated and unhydrotreated coal extracts simultaneously. Such an integrated process could be a significant process development for maximizing value added products from domestic coal.

As part of its DOE sponsored program, UCAR has recently produced an all coal-based CTE graphite test bar, i.e. the anisotropic coke, binder and impregnation pitch were all derived from WVU coal extracts. Some properties of the test bar are shown in table 5.

**Table 5.** Properties of All Coal-Based CTE Graphite Test Bar.

CTE ( $10^{-6}/^{\circ}\text{C}$ )	0.26
Specific Resistance ( $\mu\text{ohm-m}$ )	9.55
Density	1.376

The CPC is co-organizer of a workshop entitled, "Applications of Carbon Products for Efficient Operation of Heavy Trucks, Buses, and Other Commercial Vehicles", (DOE Contract No. DE-AF05-96OR22500) sponsored by the U.S. DOE Office of Heavy Vehicle Technologies, which will be held on September 4 - 5, 1996. The objective of the workshop is to explore the various ways in which carbon products can improve productivity, safety, fuel efficiency, and cost effectiveness of heavy vehicle operations.

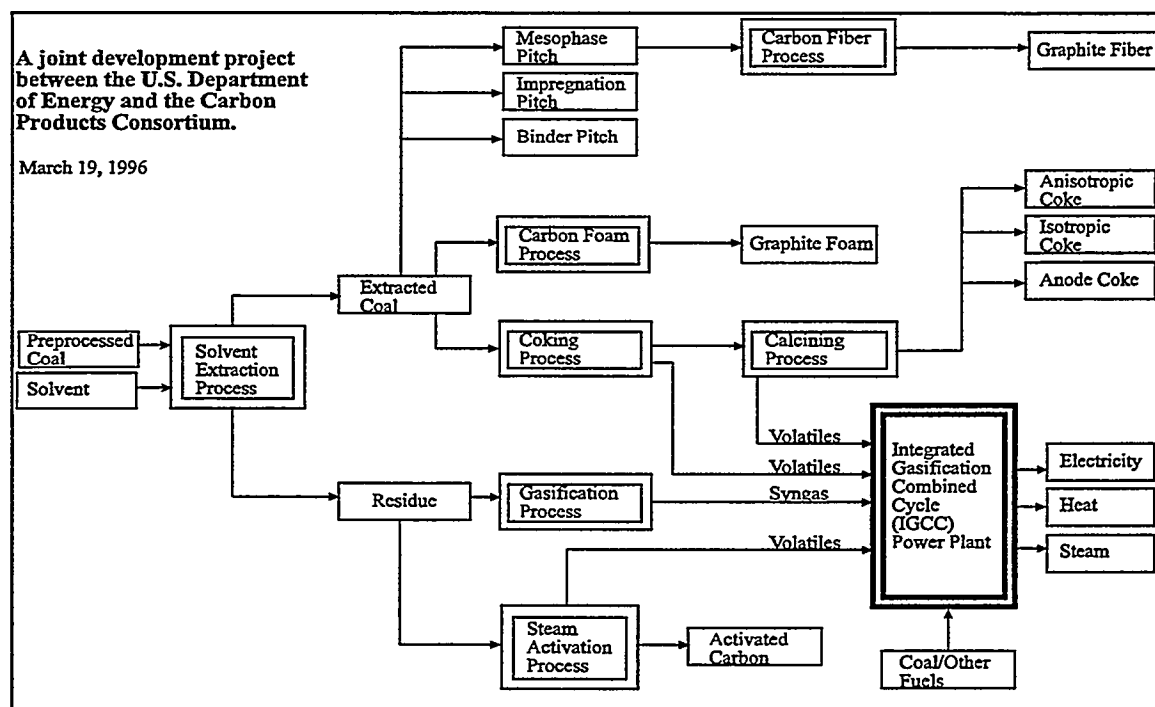
The CPC is pursuing the role of carbon products in the Industries of the Future program with the U.S. DOE Office of Industrial Technologies. Table 6 indicates some of the carbon products which have applications in the seven industries of the future.

The CPC in cooperation with the Pittsburgh Energy Technology Center is pursuing a coal refinery scheme which would co-produce advanced materials from coal and fuel for IGCC power plants. Figure 3 illustrates this coal refinery concept.

#### ACKNOWLEDGMENTS

The contributions of Irwin Lewis and John Chang of UCAR, Ron McHenry of KOPPERS, Ken Tucker and Gene Harlacher of CONOCO, David Belitskus of ALCOA, Mike Michno and Girish

**Table 6.** Role of Carbon Products in the U.S. DOE Industries of the Future

[illegible]

**Figure 3.** Coal Refinery Scheme To Co- Produce Carbon Products and Fuel for IGCC Power Plants

Deshpande of AMOCO, Cliff Baker of FMI, Tim Burchell of ORNL, and John Zondlo and Al Stiller of WVU to this article and to the CPC programs are gratefully acknowledged.

## CARBON-FIBER COMPOSITE MOLECULAR SIEVES FOR GAS SEPARATION

M. Jagtoyen and F. Derbyshire

University of Kentucky, Center for Applied Energy Research,  
3572 Iron Works Pike, Lexington KY 40511-8433, USA

### ABSTRACT

This report describes continuing work on the activation and characterization of formed carbon fiber composites. The composites are produced at the Oak Ridge National Laboratory (ORNL) and activated at the Center for Applied Energy Research (CAER) using steam,  $\text{CO}_2$ , or  $\text{O}_2$  at different conditions of temperature and time, and with different furnace configurations. The general aims of the project are to produce uniformly activated samples with controlled pore structures for specialist applications such as gas separation and water treatment.

In previous work we reported that composites produced from isotropic pitch fibers weighing up to 25g can be uniformly activated through the appropriate choice of reaction conditions and furnace configurations. We have now succeeded in uniformly activating composites of dimensions up to 12x7x6 cm, or up to about 166 gram- a scale-up factor of about six. Part of the work has involved the installation of a new furnace that can accommodate larger composites. Efforts were made to achieve uniform activation in both steam and  $\text{CO}_2$ . We have also succeeded in producing materials with very uniform and narrow pore size distributions by using a novel method involving low temperature oxygen chemisorption in combination with heat treatment in  $\text{N}_2$  at high temperatures. Work has also started on the activation of PAN based carbon fibers and fiber composites with the aim of producing composites with wide pore structures for use as catalyst supports. So far activation of the PAN fiber composites supplied by ORNL has been difficult which is attributed to the low reactivity of the PAN fibers. As a result, studies are now being made of the activation of the PAN fibers to investigate the optimum carbonization and activation conditions for PAN based fibers.

Activated samples of pitch fiber composites have been characterized for the adsorption and desorption of  $\text{CO}_2$ , and to determine the butane (working capacities).  $\text{CO}_2$  working capacities were also determined to further elucidate the function of the composites in the separation of  $\text{CO}_2 / \text{CH}_4$  mixtures. The maximum  $\text{CO}_2$  working capacity occurs at low burn-off (around 10 wt%) which is in the same region where maximum  $\text{CO}_2 / \text{CH}_4$  separation is attained.

The activated carbon fiber composites have also been tested for possible water treatment applications by studying the adsorption of sodium pentachlorophenolate, PCP (a common herbicide/wood preservative). In preliminary tests, a composite specimen has shown superior performance to a commercial water treatment carbon.

## INTRODUCTION

This project involves collaborative research between the ORNL and the CAER, for the development of novel, rigid, monolithic adsorbent carbon fiber composites that can be produced in single pieces to a given size and shape. The carbon fiber composites are produced at the ORNL and activated at the CAER using steam or  $\text{CO}_2$  under different conditions, with the aims of producing a uniform degree of activation, and of closely controlling pore structure and adsorptive properties. The principal aims of the work to date have been to produce uniformly activated samples with narrow porosity for use in gas separations, although numerous other areas of application are envisaged. So far, it has been shown that the composites have excellent capacities for gas separation e.g methane and  $\text{CO}_2$  separation and for adsorption of  $\text{CO}_2$ <sup>5-12</sup>.

The project originated in research conducted at the ORNL in the 1980s<sup>1</sup>, when carbon fiber composite material was developed as a low-density, mechanically strong thermal insulator for a radioisotopic heat source on spacecraft for the Galileo and Ulysses Missions. The basis for the present project was to adapt the process to produce high surface area materials through the activation of similar composites, in which porosity is developed in the carbon fibers to produce high surface areas for adsorption. One of the principal changes, compared to the original work, is to utilize lower cost carbon fibers that are produced from isotropic pitches (other types of fiber will also be included in the studies). In recent years, a great interest has developed in the activated forms of such isotropic carbon fibers, where high surface areas can be produced by partial gasification in steam or other oxidizing gas<sup>2,3</sup>. Moreover, while porosity can be generated in most types of carbon fiber, low-modulus fibers produced from isotropic pitch are particularly suited for activation due to their unique structure in which the random packing of small crystallites allows the development of an extensive pore structure.

Activated carbon fibers are of interest in several areas of adsorption and environmental protection due to their novel properties that make them more attractive than conventional forms (powder or large-size carbons) for certain applications<sup>1,2</sup>. Among the possible applications, activated carbon fiber composites are of interest for the adsorption and recovery of organic vapors; the removal of  $\text{SO}_x$  and  $\text{NO}_x$  from flue gases; the improvement of air quality; and water treatment<sup>2-5</sup>. The incorporation of the fibers into composites surmounts the difficulties in handling and utilizing activated fibers.

The specific objectives of the research described in this report have been to examine the activation of large composites, and to ascertain the uniformity of activation through the body of the materials. Previously, specimens have been activated as plates of dimensions of 12 x 1.5 x 4 cm, and sample weights of about 25 grams. In the present report we have activated composites of dimensions up to 12 x 7 x 6 cm, which corresponds to about 166 gram per sample- a scale-up factor of about six. Part of the work has involved the installation of a new furnace that can accommodate the larger composites. The report provides an account of studies of composite activation, the uniformity of porosity development, and the measurement of physical properties (dimensional changes during activation, gas permeability). The composites have been further characterized for their efficiency in gas separation ( $\text{CH}_4/\text{CO}_2$  mixtures) as well as determinations of their butane and  $\text{CO}_2$  working capacities, and their performance in water treatment applications, specifically adsorption of herbicides.

## DISCUSSION OF CURRENT ACTIVITIES

### Experimental

#### Composite Preparation

Carbon fiber composites are prepared at ORNL<sup>9,10</sup> by vacuum molding from water slurries containing powdered phenolic resin and chopped isotropic petroleum pitch fibers, (P-200, ~ 17.5  $\mu\text{m}$  diameter, average length 380 $\mu\text{m}$ , supplied by courtesy of Ashland Carbon Fibers Division, Ashland Inc.). The slurry is vacuum molded into tubular, plate or rod configuration, followed by drying, curing, and carbonization to about 650°C. The carbon fiber composites are supplied to the CAER usually in the form of plates (28x12x1.5cm).

#### Activation

The formed carbon fiber composites were activated at the CAER<sup>11,12</sup>. The specimens have been activated as plates of dimensions ranging from 12 x 1.5 x 4 cm (about 25 grams) to 12 x 7 x 6 cm (about 166 grams). The reactor furnace used for the activation of composite samples has been described in an earlier report<sup>11</sup>. A new furnace has now been installed that can activate larger pieces. The furnace is a Lindberg Blue M laboratory box furnace with chamber size 12x12x18 inches and maximum operating temperature 1100°C. The specimen is contained in a sealed stainless steel cylindrical chamber of diameter 6", and height 6". The activating agent, steam, CO<sub>2</sub> or O<sub>2</sub>, is distributed into the stainless steel chamber through a perforated plate positioned 1 cm above the bottom of the container. The materials have been activated using three different techniques, steam activation, CO<sub>2</sub> activation, and oxygen activation. For steam activation, the composite samples are activated in an atmosphere of steam mixed with nitrogen. Water is pumped into the reaction chamber at a flow rate ranging from 60-150cc/hr and is vaporized in the bottom of the chamber. The flow rate of N<sub>2</sub> is varied between 2-3 l/min. The reaction temperature is varied from 800-900°C, and reaction times from 0.5-3 hrs. As CO<sub>2</sub> activation is significantly slower than steam, the CO<sub>2</sub> activation is carried out at temperatures from 850-950°C, for reaction times of 1-3 hours. The flow rate of CO<sub>2</sub> is varied from 2-3 l/min. A third method of activation involves the chemisorption of oxygen onto the carbon at low temperatures, from 225-250°C, and subsequent heat treatment in nitrogen to 850-925°C when the oxygen is removed as CO<sub>x</sub>. It is believed that this method can create a uniform pore structure.

#### Characterization

Porosity. Surface area and pore size distributions were measured on a 10 port automated surface area analyzer, OMNISORB 610. The high efficiency of the instrument allows the measurement of surface areas, as well as the characterization of pore sizes down to 4 Å, using nitrogen at 77K as the adsorbate. Surface areas were determined from the isotherms by the BET method, and pore volumes by the D-R method and BJH method.

Butane and CO<sub>2</sub> Working Capacity Test. The butane working capacity (BWC) was developed as a measure of the effectiveness of activated carbons that are used to trap hydrocarbons released by evaporative losses from vehicle fuel systems (used in evaporative loss control devices, or ELCDs). However, it is also

a useful indication of the properties of activated carbons with respect to other applications. Essentially, the BWC is the difference between the saturation adsorptive capacity of butane, and the amount retained upon the carbon after purging under specified conditions. The retained butane is too strongly adsorbed to allow facile desorption.

The tests were performed according to ASTM method D5228-92 for the determination of the Butane Working Capacity of Activated Carbon. The activated carbon sample is outgassed under vacuum at 150°C for 4 hours, and packed in a constant volume bed according to a standard procedure (ASTM D 2854) immersed in a constant temperature water bath at 25°C. Butane is then passed through the activated carbon sample at a flow rate of 250cc/min for 900 seconds. The sample is then weighed, and gas is adsorbed for another 600 seconds. When the sample has reached constant weight, the bed is desorbed with dry air that is passed through the sample at a flow rate of 300mL/min for 2400 seconds. The difference in mass is the BWC and is expressed as mass of butane per unit volume of carbon. In this report we also report CO<sub>2</sub> working capacities that were determined using the same procedure for the butane working capacity.

Permeability of Composites to Liquid Flow. Previously we have reported on the high permeability of the composites to the flow of gases. We have now extended these measurements to include the flow of liquids. Specimens for permeability testing were cut from a composite sample using a hole cutter with 1/2 inch diameter. The samples were about 5.7 cm long, giving a total specimen volume of about 12.5cc. A simple apparatus was used for the permeability test, where water flowed through the cylindrical specimen that was sealed on the outside using heat shrink tubing. The water flow was varied between 8-170 ml/min or 4-90 gpm/ft<sup>2</sup>. The differential pressure was measured using a digital pressure gauge upstream of the sample. The pressure drop was determined as the difference between this pressure and atmospheric pressure.

Adsorption of Herbicides from Water. The adsorptive capacity of an activated carbon composite sample for sodium pentachlorophenolate (PCP) was measured by sealing a 2.0 g sample of carbon into polyolefin tubing to create a column of volume 8 cm<sup>3</sup> and length 6 cm. Plugs of quartz wool were fitted at the column ends to contain the bed. A peristaltic pump, Pulsafeeder - Mec-o-matic VSP-20, located downstream of the column continuously drew a 40 ppm solution of sodium pentachlorophenolate (NaC<sub>6</sub>Cl<sub>5</sub>O) from a reservoir and through the column. The concentration of PCP in the column effluent stream was monitored via a UV-Vis spectrophotometer (Varian, Series 634) fitted with a 10 mm path length flow-through quartz cell, at a wavelength of 317.5 nm. Column breakthrough was determined as the point where the ratio of effluent to inlet PCP (C/Co) was equal to 0.3. The flow rate of PCP solution through the column was held constant at 1 mL·min<sup>-1</sup>. An equivalent experiment was conducted using a granular Norit commercial water treatment carbon to provide a basis for comparison.

## Results and Discussion

### Uniformity of Steam and CO<sub>2</sub> Activation

The focus of this part of the work has been to scale up the activation of carbon fiber composites supplied by ORNL. In previous work we reported that composites weighing up to 25 g can be uniformly activated through the appropriate choice of reaction conditions and furnace configurations. We have now examined the activation of composites with dimensions up to 12 cm x 7 cm x 6 cm and weighing 166 g. The uniformity of activation was determined by measuring BET surface areas and micropore volumes on samples taken from 3 or 6 different positions in the composite, as indicated in Figure 1. The results are shown in Table 1. Three different activating methods were used; steam, CO<sub>2</sub>, and a procedure involving activation in steam for 1 hour and then in CO<sub>2</sub> for one hour. The uniformity of activation appears to be similar for all three methods. The standard deviation of BET surface area for steam activated samples ranged from 0.5-18%, and



for CO<sub>2</sub> activation from 5-8%. The combination of activating agents gave a standard deviation of 9%. The spread in surface area through the samples produced at different burnoffs under the conditions summarized in Table 2 are shown in Figure 2.

**Dimensional Changes.** There is an overall shrinkage of the composites during activation. The effects of burnoff on dimensional change have been discussed earlier<sup>7</sup>. However, we have now generated additional data that confirm the earlier findings. Generally, the volume decreases with burn-off. A linear relationship exists to about 35% burnoff, but at higher burnoff there is a steeper increase in shrinkage. Moreover, above a certain temperature (~850°C) and only in steam, the extent of contraction induces sufficient stress to split the composite and destroy its physical integrity. Another interesting phenomenon is that while CO<sub>2</sub> activation gives the same relationship between burnoff and dimensional change as steam activation, it does not lead to sample cracking, even at high burn-offs.

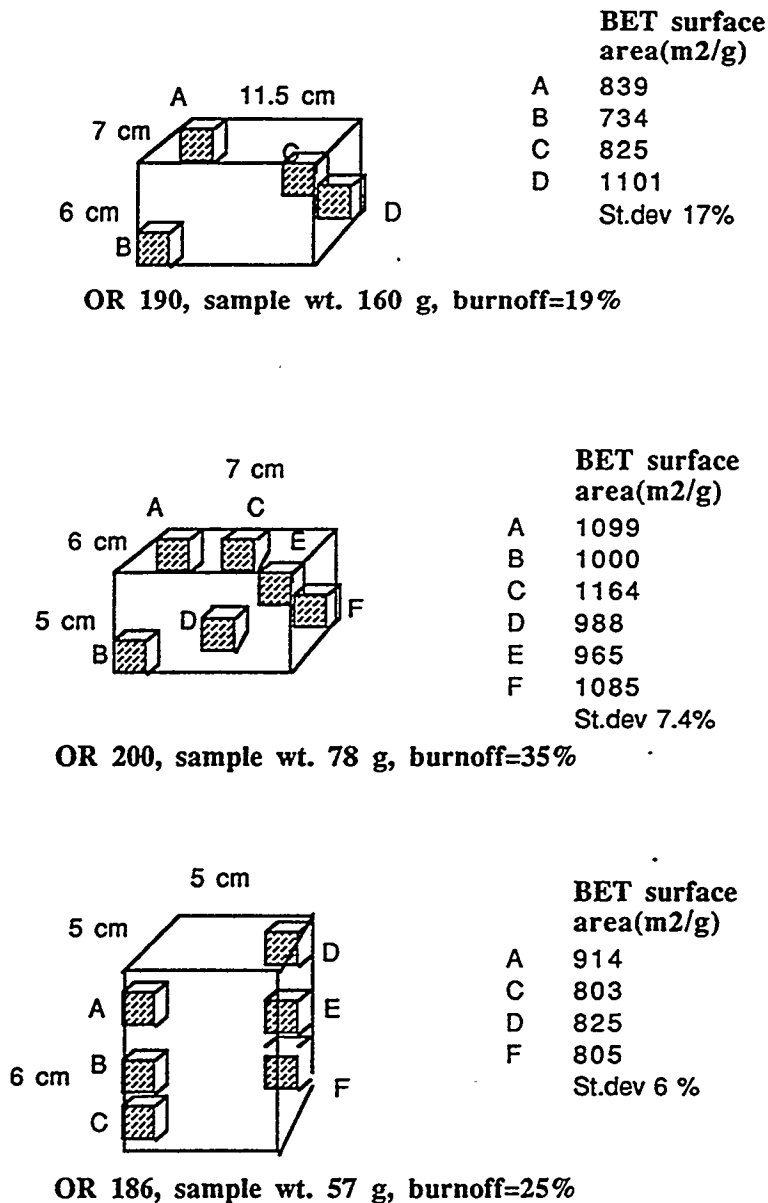
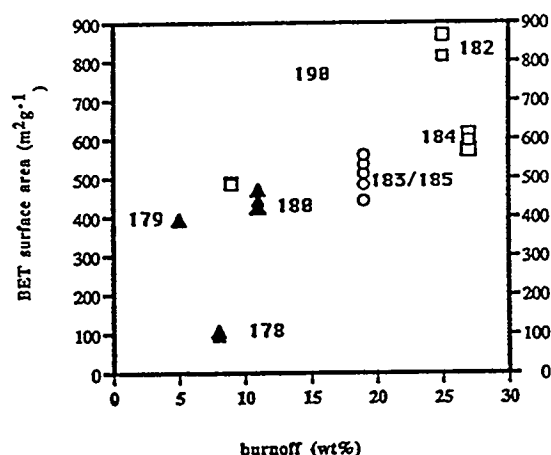


Figure 1: Uniformity of Activation of Carbon Fiber Composites

**Table 1: Uniformity of activation of carbon fiber composites**

ID	B. off	HTT	Time	BET surf. area	pore width, L	W <sub>0,micro</sub> pore vol.	st.dev in BET
(SA-)	(%)	(°C)	(hr)	(m <sup>2</sup> /g)	(Å)	(cc/g)	(%)
<i>Activating Agent</i>							
<i>Sample ID</i>							
<i>Steam</i>							
181	9	850	1	484-487	6.4-6.5	0.23-0.24	0.5
185	19	877	1	465-568			10.0
190	19	877	2	734-1101			18.0
182	25	900	2	812-867	7.3-7.6	0.41	4.6
186	25	877	2	803-914			6.3
106	27	800	4	762-865			9.0
109	41	877	2	1089-1109			1.3
<i>CO<sub>2</sub></i>							
179	5	850	3	390-431	6.7-8	0.19-0.21	5.7
180	11	900	3	426-469	6.2-6.9	0.21-0.23	4.9
126	20	900	3	632-578	6.6-6.3		6.3
<i>Steam/CO<sub>2</sub></i>							
183	19	850	1/1	442-559	5.8-6.4	0.26-0.27	8.9

SA<178 sample weight 20 gram, SA>178 sample weight 50-60 gram, SA=190 sample weight 166 gram  
 \* sample was physically disrupted, and split along plane perpendicular to settling direction during formation of composite



**Figure 2: BET surface area of sample from specimens produced at different burnoffs. (Sample numbers shown on graph).**

### Uniformity of Oxygen Activation

Oxygen chemisorption at low temperature combined with heat treatment at high temperatures was tried as an alternative to steam or CO<sub>2</sub> activation in order to produce uniform activation and a narrow pore size distribution in the carbon fiber composites. Oxygen is chemisorbed onto the composites at 225-250°C, and the samples are subsequently heat treated in nitrogen to 850-925°C. It is believed that the slow chemisorption of O<sub>2</sub> can create a uniform distribution of surface oxygen groups that are later released as CO and CO<sub>2</sub>. It is known that CO<sub>2</sub> is released at temperatures from 300-800°C with a maximum at about 350°C while CO is released at temperatures from 500-900°C with a maximum at

700°C. The surface area development in the composites was very uniform, with a variation in surface area within the samples of only 3-6%, Table 2. Increasing the chemisorption temperature from 225 to 250°C gave sufficient uptake of oxygen to triple the BET surface area upon heat treatment to 900°C. Heat treatment to 850°C is not sufficient to achieve significant microporosity, and heat treatment to 925°C also give low surface area. The optimum upper temperature for maximizing the production of narrow micropores appears to be around 900°C. The influence of repeated chemisorption/heat treatment cycles will be examined in continuing studies.

**Table 2: BET surface area in petroleum based carbon fiber composites activated by oxygen chemisorption/heat treatment at high temperature (single heat treatment cycle).**

Sample#	Oxidation		Heat treatm.		Burnoff (wt%)	Surface area (m <sup>2</sup> /g)		Pore vol	
	T(°C)	t(hr)	T(°C)	t(hr)		BET	mesopore	micro	meso
221	225	3	900	2	4	183	24	0.11	0.03
						107	22	0.04	0.04
						111	24	0.05	0.03
216	250	3	850	2	5	298	50	0.11	0.07
						263	30	0.16	0.03
						384	19	0.18	0.02
218	250	3	900	2	6	408	7	0.21	0.0
						391	5	0.20	0.0
						362	8	0.18	0.0
219	250	3	925	2	6	225	20	0.13	0.03
						227	14	0.12	0.02
						238	23	0.14	0.03

#### Activation of PAN-Based Carbon Fibers and Composites.

A further objective of the work during this period has been to activate PAN-based carbon fibers and PAN based carbon fiber composites in order to produce composites with wider pore size distributions than the petroleum pitch based fibers that have been used so far. PAN-based Fortafil P-200 composites were supplied by ORNL. The composites were first activated in steam at 850°C at the CAER. However, the surface areas developed in the PAN composites were very low, Table 4. The mechanical strength of the composites was also low, and they were extremely weak after burnoff to 29%. It is believed that the PAN fibers had been heat treated to a temperature in excess of 1000°C prior to incorporation into the composites, which would explain the low response to activation. If the fibers are relatively inert, the binder will be preferentially activated which could account for the poor strength.

New PAN fibers were obtained from Dr. Novis Smith with RK Carbon. These fibers had not been heat treated above 600°C. The fibers were carbonized in nitrogen at 800-850°C and subsequently steam activated at temperatures from 800-877°C. Carbonization resulted in yield loss of 15%. Steam activation to burnoffs from 15-95% at temperatures of 800 and 877 respectively produced very low surface areas. The surface area was only 149 m<sup>2</sup>/g at a 40% burnoff, Table 3. The high weight loss is attributed to external burning of the carbon fibers, and not micropore development. In future runs, carbonization and activation will be performed at temperatures from 600- 700°C.

**Table 3: Activation of PAN fibers by steam activation**

Sample#	Carboniz.		Activation		Burnoff (wt%)	Surface area (m <sup>2</sup> /g)		Pore vol	
	T(°C)	t(hr)	T(°C)	t(hr)		BET	mesopore	micro	meso
222	800	1	850	1	40	149	10	0.21	0.05
229	700	2	750	4	46				

### CO<sub>2</sub> Working capacity

It has already been reported that the activated composites have the ability to separate mixtures of CO<sub>2</sub> and CH<sub>4</sub>. The optimum separation was found for samples with a burnoff of 8-10%, Figure 3.

To further investigate this separation, we have measured CO<sub>2</sub> working capacities of the composites, using a test similar to the standard test for butane working capacity. Interestingly, the specimen with the highest CO<sub>2</sub> working capacity has a burnoff of only 9% and a BET surface area of 484 m<sup>2</sup>g<sup>-1</sup>, while a sample with 25% burnoff and a surface area of 850m<sup>2</sup>g<sup>-1</sup> has a significantly lower CO<sub>2</sub> working capacity. The relationship between pore size distribution and CO<sub>2</sub> working capacity is not so straightforward, but again the samples with narrow pore size distribution show the highest CO<sub>2</sub> working capacity. These results are in excellent agreement with our earlier reported results for the separation of CO<sub>2</sub> from CH<sub>4</sub>. The maximum CO<sub>2</sub> working capacity occurs with samples at a burnoff of around 10% which is also the optimum burn-off for the separation of CO<sub>2</sub> and CH<sub>4</sub>.

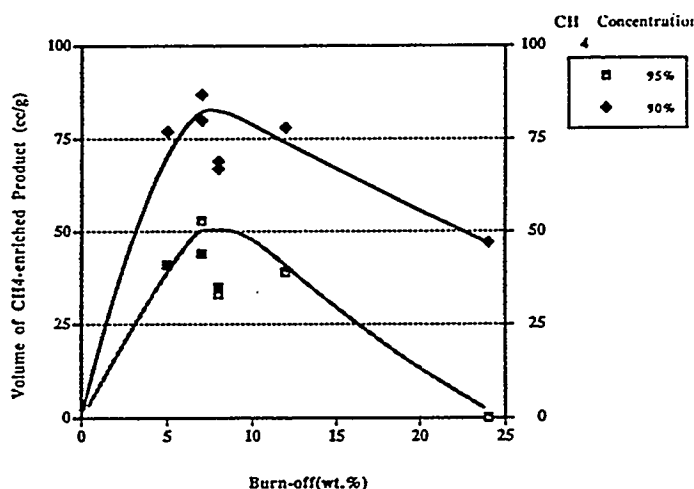


Figure 3: Volume of CH<sub>4</sub> produced at 95 and 90% concentration from a mixture of 75% CH<sub>4</sub>/25% CO<sub>2</sub>.

### Butane working capacity, BWC

The purpose of the BWC test is to investigate how the adsorptive properties of the activated composites compare to those of commercial granular carbons that are currently used in ELCD devices. These commercial carbons have a BWC of around 15 g/100 mL. Two samples were tested, SA182 with a surface area of 850m<sup>2</sup>g<sup>-1</sup> and SA 177 with a surface area of 1411 m<sup>2</sup>g<sup>-1</sup>. The results are shown in Table 4. Sample SA 177 had about twice the BWC of 182, which corresponds to its higher surface area. The same sample had a high uptake of butane (40% by weight and 10% by volume: note the low volumetric capacity, due to the low composite density). However, the retentivity of butane was high, (4.5% by volume) giving a butane working capacity of only 5.5 g/100mL. This is significantly lower than that of the commercial carbons including the wood-based sample, Te-7, produced at CAER, shown in Table 4. One reason for the low performance of the pitch based carbon fiber composite is the narrow pore size distribution that gives high retentivity of butane. The average pore size for wood based carbons is usually around 20-50Å, allowing much more effective desorption. The pitch based activated carbon fibers are therefore not suitable for butane or gasoline vapor storage. However, if the composites were made from a different fiber, like PAN or rayon, the butane working capacity should be much higher as these fibers would develop wider micropores.

**Table 4: Butane working capacities of activated carbon.**

Sample	SA177 <sup>1</sup>	SA182 <sup>1</sup>	TE-7 <sup>2</sup>
Apparent density(g/cc)	0.249	0.29	0.27
Burn-off (%)	56.0	25.0	-
BET surface area(m <sup>2</sup> g <sup>-1</sup> )	1411.0	850.0	1569.0
Average pore size(A)	9.6	7.4	15.0
Butane working capacity,W/W(%)	22.1	9.4	39.8
Butane working capacity,W/V (g/100mL)	5.5	2.8	10.7

1: activated composites, 2: wood based extrudate, prepared in-house

#### Adsorption of Herbicides from Water

The breakthrough plot for PCP in the carbon fiber composites and a commercial carbon specifically designed for water treatment (Norit Hydarco) is shown in Figure 4<sup>13</sup>. The breakthrough time for the composite was found to be almost 1400 column volumes, whereas it was closer to 150 column volumes for the granular carbon - a factor of about nine. At first sight, the difference in the performance of these carbons is surprising, since they are of comparable surface area. However, we believe that the superior performance of the carbon fiber composite is due to the narrow diameter of the fibers (15 - 20  $\mu\text{m}$ ) that essentially minimizes mass transfer limitations, and allows much faster rates of adsorption (and desorption) than is possible over large granules. A second factor is that the composites have a very open architecture (approximately 90% is free volume), which means that the contacting fluid enjoys free access to the adsorbent surfaces. Essentially, the composite can be viewed metaphorically as a situation in which the granules have been "peeled open" to allow the adsorbent to readily access all of the inner adsorbent surface, which can otherwise only be approached by diffusion through an extensive pore network.

#### Liquid Phase Pressure Drop of Activated Composites

One of the most important parameters when considering a carbon for water treatment applications is the pressure drop that is developed over the adsorbent. We have previously reported pressure drops for gas flow, and in this report we have determined the pressure drop developed due to the flow of a liquid. The pressure drop over a 12.5 cc bed of composite at different flow rates of water is shown in Figure 5 along with data from the literature on pressure drop for a granular bed of activated carbon. The composite samples shown have comparable pressure drops to that for the bed of granular carbon, over the range of flow for which it was tested. The differences in pressure drop for the two composite specimens are due to differences in the density of the precursor composite.

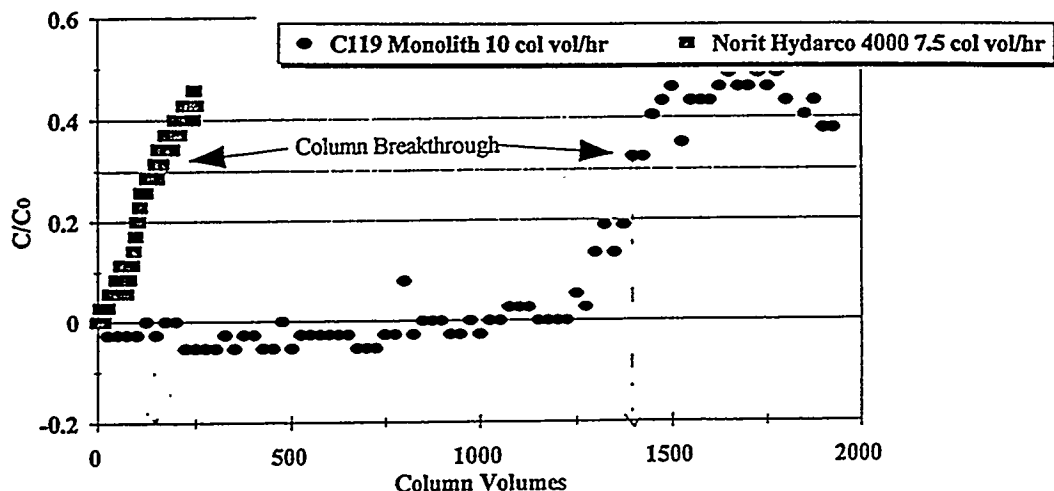


**Figure 4: Adsorption of the herbicide sodium pentachlorophenolate, PCP from water for a composite sample and a commercial granular activated carbon.**

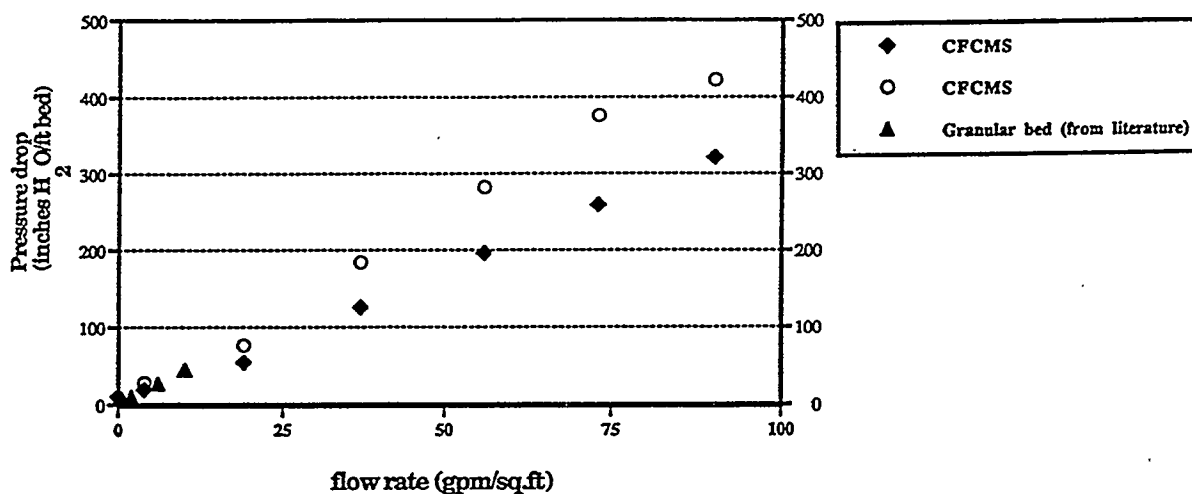


Figure 5: Pressure drop of water over composite samples

#### REFERENCES

- 1) K. OKUDA, *Petrotech*, 5(1) (1982) 37.
- 2) Y. MATSUMURA, *Seikiyu Gakaishi*, 30(5) (1987) 291.
- 3) M. W. THWAITES, M. L. STEWART, B. E. McNEESE, and M. SUMNER, *Fuel Proc.Tech.*34 (1993)137.
- 4) M.SUZUKI, *Proc. Biennial Carbon Conference*, Buffalo (1993)
- 5) F. DERBYSHIRE, M. JAGTOYEN, Y. Q. FEI and G. KIMBER, *Am. Chem. Soc., Div. Fuel Chem. Preprint*, 39(1) (1994) 113-120.
- 6) T. D. BURCHELL, J. W. KLETT AND C. E. WEAVER, *Proceedings of the Ninth Annual Conference on Fossil Energy Materials*, Fossil Energy AR&TD Materials Program, for USDOE, Oak Ridge National Laboratory, May 16-18, (1995) 447-457.
- 7) M. JAGTOYEN, F. DERBYSHIRE, G. KIMBER, Y. Q. FEI, *Proceedings of the Ninth Annual Conference on Fossil Energy Materials*, Fossil Energy AR&TD Materials Program, for USDOE, Contract DE-ACo5-84OR21400, Oak Ridge National Laboratory, May 16-18(1995) 457-467.
- 8) M. JAGTOYEN, F. DERBYSHIRE, N. CUSTER, T. BURCHELL, 1994 Spring Meeting, *Materials Research Society*, San Francisco, April 4-8, 1994, *Symposium Proceedings*, 344, (1994) 77.
- 9) T. D. BURCHELL, F. DERBYSHIRE, Y.Q. FEI AND M. JAGTOYEN, C. E. WEAVER, *Proceedings of Eighth Cimtec World Ceramics Conference*, 6/28, Florence, Italy (1994) 120.
- 10) G. C. WEI, and J. M. ROBBINS, *Ceramic Bull.*, 64(5) (1985)691.
- 11) F. DERBYSHIRE, Y.Q. FEI AND M. JAGTOYEN, G. KIMBER, T. D. BURCHELL, C. E. WEAVER, *Proceedings of CARBON'94*, 3-8 July, Granada, Spain, (1994) 654-5.
- 12) F. DERBYSHIRE, T. BURCHELL, Y. Q. FEI, M. JAGTOYEN, C. WEAVER, *Conference on Applications of Microporous Carbons*, The British Carbon Group, 28-29 Sep, Leeds, UK (1994).
- 13) M. JAGTOYEN, C. LAFFERTY, F. DERBYSHIRE AND G. KIMBER, *Proceedings for the Kentucky Water Resources Annual Symposium*, Holiday Inn, Lexington, KY, Feb13(1996)41-42.

#### ACKNOWLEDGEMENTS

The authors wish to acknowledge G. Kimber D. Turner and C. Lafferty of the CAER, the Commonwealth of KY and Rod Judkins of the ORNL for financial support of this work. This work is sponsored by the Fossil Energy AR&TD Materials Program, US Department of Energy, under contract no.SC19X-SN719C.

## STABILITY OF SOLID OXIDE FUEL CELL MATERIALS<sup>1</sup>

T. R. Armstrong, J. L. Bates, G. W. Coffey, L. R. Pederson,  
P. J. Raney, J. W. Stevenson, W. J. Weber, and F. Zheng

Pacific Northwest National Laboratory  
P.O. Box 999  
Richland, WA 99352

Chromite interconnection materials in an SOFC are exposed to both highly oxidizing conditions at the cathode and to highly reducing conditions at the anode. Because such conditions could lead to component failure, we have evaluated thermal, electrical, chemical, and structural stabilities of these materials as a function of temperature and oxygen partial pressure. The crystal lattice of the chromites was shown to expand for oxygen partial pressures smaller than  $10^{-10}$  atm, which could lead to cracking and debonding in an SOFC. Highly substituted lanthanum chromite compositions were the most susceptible to lattice expansion; yttrium chromites showed better dimensional stability by more than a factor of two. New chromite compositions were developed that showed little tendency for lattice expansion under strongly reducing conditions, yet provided a good thermal expansion match to other fuel cell components. Use of these new chromite interconnect compositions should improve long-term SOFC performance, particularly for planar cell configurations.

Thermodynamic properties of substituted lanthanum manganite cathode compositions have been determined through measurement of electromotive force as a function of temperature. Critical oxygen decomposition pressures for Sr and Ca-substituted lanthanum manganites were established using cells based on a zirconia electrolyte. Strontium oxide and calcium oxide activities in a lanthanum manganite matrix were determined using cells based on strontium fluoride and calcium fluoride electrolytes, respectively. The compositional range of single-phase behavior of these  $ABO_3$ -type perovskites was established as a function of A/B cation ratios and the extent of acceptor doping. Before this work, very little thermodynamic information was in existence for substituted manganite compositions. Such information is needed to predict the long-term stability of solid oxide fuel cell assemblies.

## INTRODUCTION

Acceptor-doped lanthanum chromites are used as the electrical interconnect in solid oxide fuel cells (SOFC) operating at high temperatures because of their high electrical conductivity, chemical stability in oxidizing and reducing environments, high thermal conductivity, and good thermal expansion match to other fuel cell materials.<sup>1</sup> Calcia-substituted yttrium chromite also show promise for this purpose.

The electrical interconnect in an SOFC is exposed to both oxidizing conditions at the air electrode and reducing conditions at the fuel electrode. In a reducing environment, many

---

<sup>1</sup> Research sponsored by the U. S. Department of Energy, Fossil Energy AR&TD Materials Program. Pacific Northwest National Laboratory is operated by Battelle for the U. S. Department of Energy under Contract DE-AC06-76RLO 1830.

chromite compositions undergo a lattice expansion.<sup>2-6</sup> The extent of this lattice expansion depends on several factors, including oxygen partial pressure, temperature, and dopant concentration. The observed expansion is well-correlated with the defect structure of the chromites, particularly the reduction of  $\text{Cr}^{4+}$  to  $\text{Cr}^{3+}$  and the concomitant formation of oxygen vacancies. In the present work, we show that small additions of both acceptor and donor substitutions can be used to control the magnitude of this dimensional instability of interconnect materials when exposed to reducing conditions.

Acceptor-doped lanthanum manganite perovskites are used as the cathode in SOFCs due to high electrical conductivity in oxidizing atmospheres, high electrocatalytic activity for the reduction of molecular oxygen to oxygen anions, and good thermal expansion match to other fuel cell components.<sup>1</sup> Interactions between the cathode and the electrolyte are among the causes of long-term performance losses in SOFCs, the extent of which may be predicted from thermodynamic properties of fuel cell components.<sup>7,8</sup> While undoped lanthanum manganite has been well-studied, very little thermodynamic information on doped compositions is known. In this study, solid electrolyte galvanic cells were utilized to evaluate the chemical activity of strontium oxide in doped lanthanum manganite and to determine the free energy of formation of doped lanthanum manganite from the base oxides.

## EXPERIMENTAL METHODS

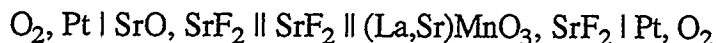
Doped lanthanum and yttrium chromite powders were prepared using the glycine-metal nitrate combustion synthesis method, with a stoichiometric glycine to nitrate ratio.<sup>9</sup> The powders were calcined at 650°C to remove any residual carbon, coarsened at 1000°C, uniaxially pressed into bars (55 MPa), and isostatically pressed (140 MPa). Similar procedures were followed to prepare doped lanthanum manganite samples.

Dilatometry measurements were used to evaluate dimensional changes in oxidizing and reducing environments at 800, 900, and 1000°C. The oxygen partial pressure was controlled in the  $10^{-5}$  to  $10^{-18}$  atm. range using a buffered carbon dioxide/hydrogen gas system equipped with mass flow controllers. The initial oxygen stoichiometry of each of the chromite compositions was determined by potentiometric titration, where the sample was first dissolved in a concentrated solution of sulfuric acid and vanadium sulfate, and then titrated with ferrous ammonium sulfate.<sup>10</sup> Changes in oxygen stoichiometry on heating were determined thermogravimetrically.

Galvanic cells were utilized to determine the activity of strontium and calcium oxide in doped lanthanum manganite cathode materials and to evaluate the critical oxygen

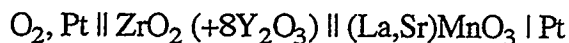


decomposition pressure for these materials. Strontium oxide activities were evaluated using the cell:



For calcium-doped lanthanum manganite compositions, calcium fluoride served as the electrolyte rather than strontium fluoride. Such cells have been found to yield accurate thermochemical data, although establishment of equilibrium is slow.<sup>11</sup>

Critical oxygen decomposition pressures were also measured as a function of temperature using the galvanic cell approach for strontium-doped lanthanum manganite compositions. Yttria-stabilized zirconia served as the electrolyte in the cell:



Small zirconia tubes (5mm dia. x 50 mm length) were fabricated by slip casting. Two areas were platinized on the surface of the tubes, one of which served as an oxygen pump while the other served as an oxygen sensor. The zirconia tubes were sealed to an alumina support using an alumina-based cement. Oxygen was electrochemically pumped from the small zirconia tubes to a residual oxygen pressure of less than  $10^{-22}$  atm at the beginning of each test. The oxygen pump was then turned off and the system allowed to achieve a steady state oxygen partial pressure.

## RESULTS AND DISCUSSION

### Dimensional Stability of Chromite Interconnects

In a reducing environment encountered at the fuel electrode (below  $\approx 10^{-10}$  atm oxygen partial pressure), lattice oxygen vacancies may be formed in chromite interconnects.<sup>2-6</sup> Accompanying the formation of oxygen vacancies are changes in thermal expansion behavior, loss of mechanical strength, and a lowering in the electrical conductivity in these materials. In this work, we have characterized the extent of isothermal linear expansion as a function of oxygen partial pressure for a wide range of chromite compositions to better understand and control these effects. A series of acceptors, donors, and isovalent dopants have been added to base compositions and their stability evaluated. Multicomponent compositions were developed that show very good dimensional stability over a wide range of oxygen partial pressures and provide a good match to other fuel cell components.

The extent of isothermal linear expansion was found to increase significantly with increases in the extent of strontium substitution for lanthanum in the lanthanum strontium chromites, as shown in Figure 1. Calcium-substituted lanthanum chromites behaved in a manner very similar to the strontium-substituted compositions. Undoped lanthanum chromite showed no tendency to expand under very low oxygen partial pressures, expected since there is no tetravalent chromium present that could be reduced to the trivalent state. The onset of lattice expansion for doped compositions was approximately  $10^{-10}$  atm oxygen. A good correlation was developed between the extent of isothermal linear expansion and oxygen stoichiometry, established through thermogravimetry and potentiometric titration measurements.

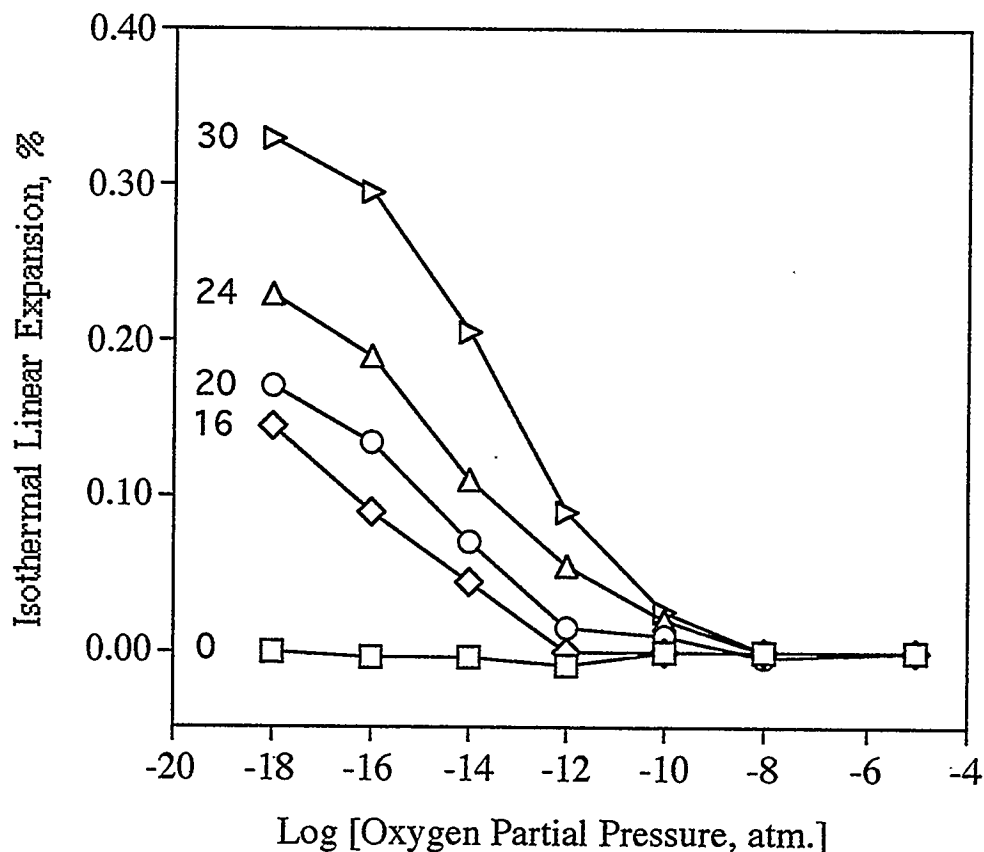


Figure 1. Isothermal linear expansion of lanthanum strontium chromite compositions at 1000°C as a function of the oxygen partial pressure. The indicated values refer to the percent of strontium that has been substituted for lanthanum in the structure.

Lattice dimensions of yttrium calcium chromites also expanded when exposed to reducing environments. The extent of expansion was approximately 40 percent less than the corresponding lanthanum chromites, however. Isothermal linear expansion for several yttrium calcium chromite compositions are given in Figure 2 as a function of oxygen partial pressure at 1000°C. The onset of isothermal linear expansion moved to higher oxygen partial pressures for more highly substituted yttrium chromite compositions. Sample expansion was dependent on not only the concentration of the acceptor dopant ( $\text{Ca}^{2+}$ ) but also on the formation of a secondary phase,  $\text{CaCrO}_4$ , which formed in compositions containing more than 25 mole percent calcium oxide. The unit cell dimensions of yttrium chromite compositions are approximately 6 percent smaller than corresponding lanthanum chromites, due primarily to the smaller size of the yttrium ion.

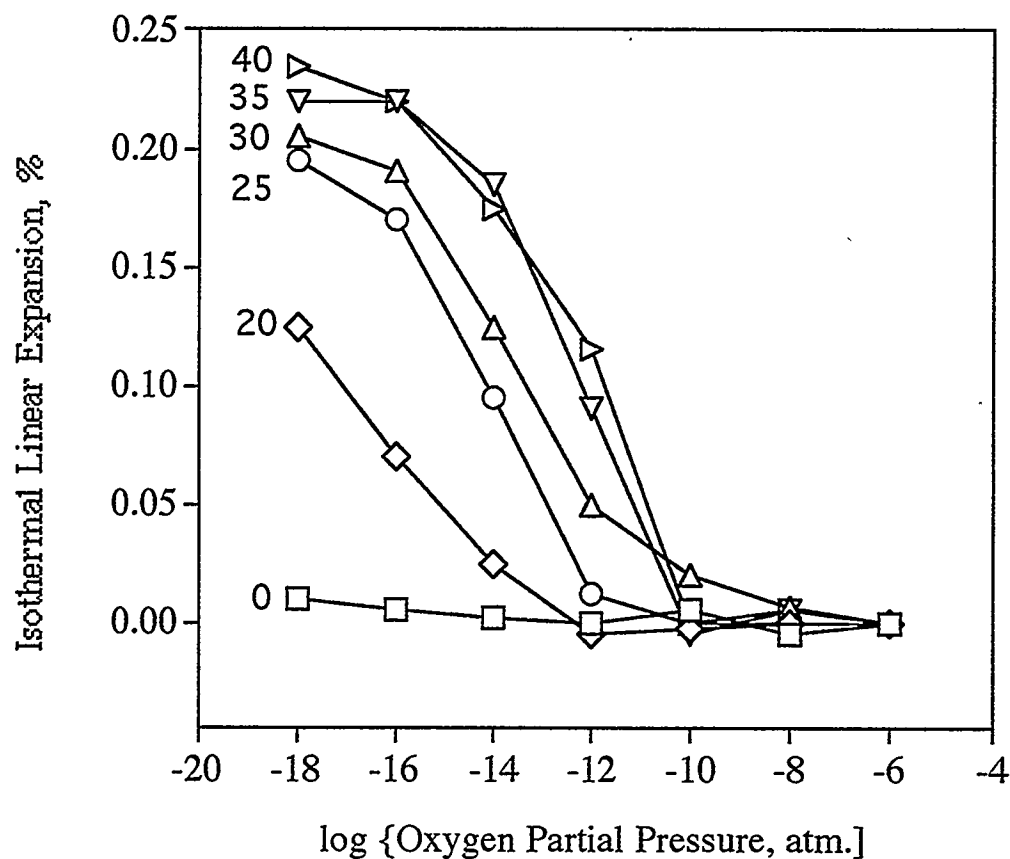


Figure 2. Isothermal linear expansion of yttrium calcium chromite compositions at 1000°C as a function of oxygen partial pressure. The indicated values refer to the percent of calcium that has been substituted for yttrium in the structure.

Interconnect compositions containing various donor, acceptor, and isovalent dopants were prepared as part of an effort to control the dimensional instability of these materials in reducing environments. Donor dopants were expected to be the most effective, by suppressing the initial concentration of  $\text{Cr}^{4+}$  in the chromite lattice that could be eventually reduced to  $\text{Cr}^{3+}$ . Acceptor dopants were also found to be quite effective. Through doping on both the A- and B-sites of these  $\text{ABO}_3$  perovskites, compositions were developed that showed little tendency to expand under conditions expected at the fuel electrode. Isothermal linear expansion behavior for two of these compositions are given in Figure 3; included also in Figure 3 are results for undoped yttrium chromite and 30 mole percent calcia-substituted yttrium chromite. The tailored chromite compositions retained properties of high electrical conductivity as well as a good thermal expansion match to other fuel cell components.

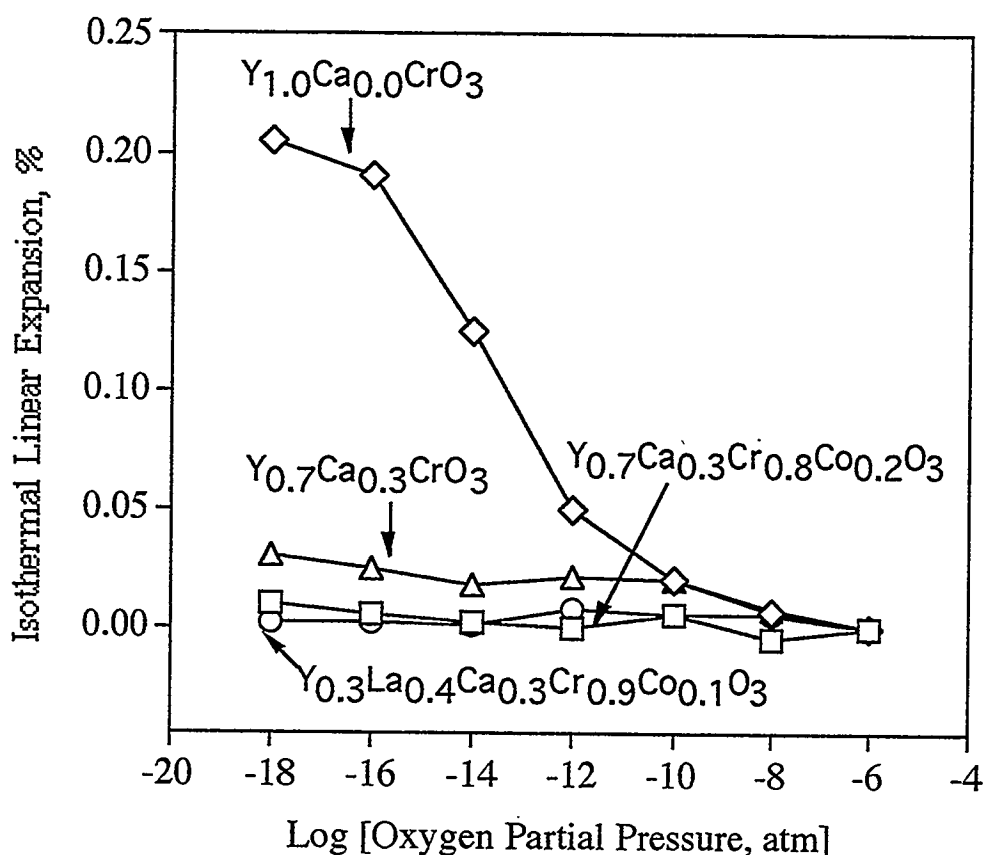


Figure 3. Isothermal linear expansion of chromite interconnection compositions that show little tendency to expand under reducing conditions typical of the fuel electrode side of a fuel cell. Results for undoped yttrium chromite and for 30 mole percent calcium-substituted yttrium chromite are shown for comparison.

### Thermochemical Properties of Lanthanum Manganite Cathodes

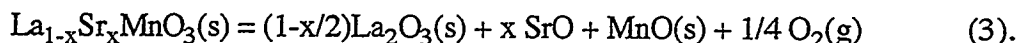
Thermodynamic parameters for doped lanthanum manganite cathode compositions were established as a function of temperature using the galvanic cell approach. Such information is needed to predict the long-term stability of materials and interfaces in SOFCs. Strontium and calcium oxide activities and critical oxygen decomposition pressures were determined as a function of temperature using cells constructed with strontium fluoride and calcium fluoride electrolytes, respectively. The relation between strontium oxide activity in a doped lanthanum manganite matrix and cell voltage is given by

$$E \text{ (volts)} = RT/2F \ln [a(\text{SrO in sample})/a(\text{SrO in reference})] \quad (1)$$

$$\Delta G^\circ = -RT \ln a(\text{SrO}) \quad (2),$$

where R is the gas constant, F is the Faraday constant, and T is temperature, K. The free energy of formation for strontium oxide in several substituted lanthanum manganite compositions is given in Figure 4 as a function of temperature. These materials become progressively less stable as the extent of strontium substitution is increased. These results predict that lanthanum oxide will be displaced by the addition of excess strontium oxide in the manganite structure, confirmed by extensive characterization of phase relations in this system by x-ray diffraction. The formation of a separate lanthanum oxide phase is to be avoided, due to its tendency to readily hydrate and swell.

Critical oxygen decomposition pressures determined by zirconia-based galvanic cell methods showed a lowering in stability of the lanthanum manganites with increased temperature and with increased levels of strontium substitution for lanthanum, as shown in Figure 5. These decomposition pressures correspond to the reaction:



Substituted lanthanum manganites decomposed at oxygen partial pressures one to two orders of magnitude higher than the unsubstituted lanthanum manganite at temperatures typical of an operating SOFC. Unlike galvanic cells based on alkaline earth fluoride electrolytes, thermodynamic equilibrium was established very rapidly in zirconia-based galvanic cells - within an hour in most cases compared to days with fluoride electrolytes. The principal disadvantage is the requirement for a virtually perfect seal between the electrolyte and base.

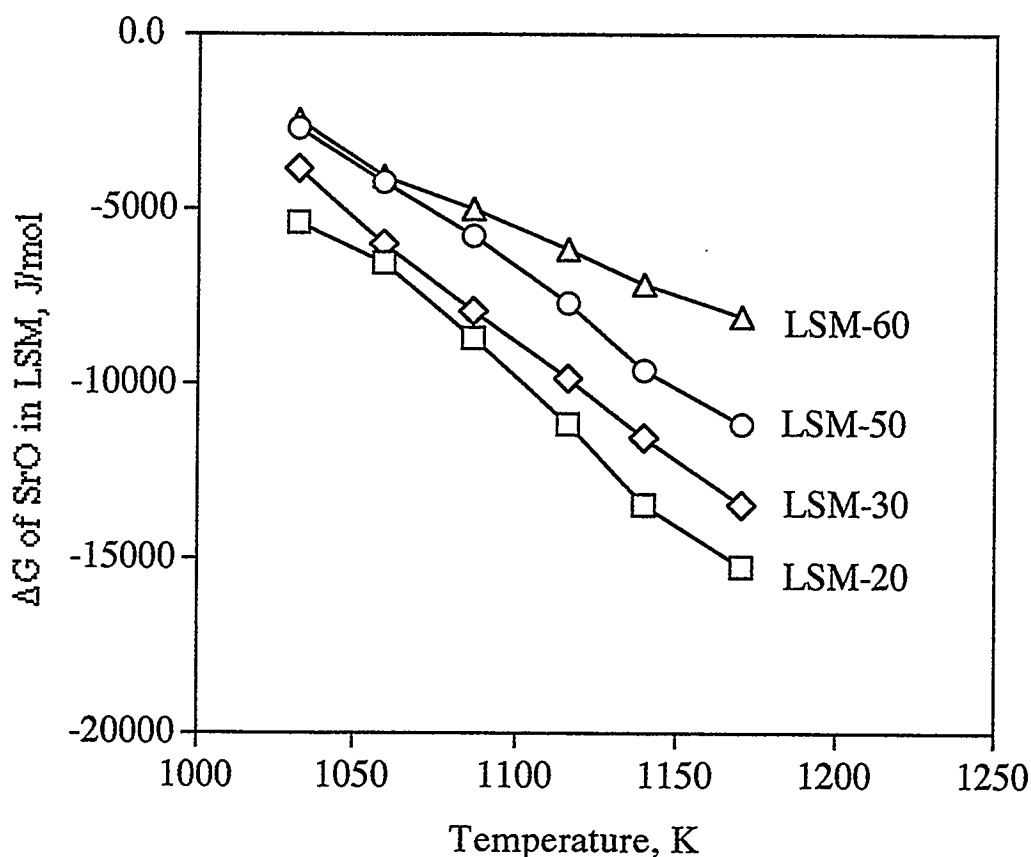


Figure 4. Free energy of formation for strontium oxide substitution in doped lanthanum manganite cathode compositions as a function of temperature, determined using the galvanic cell approach.

Phase relationships in the lanthanum manganite system has been investigated, with the purpose of establishing the compositional range of single-phase behavior. Series of samples where the A/B cation ratio was varied from 0.9 to 1.1 were prepared, heated to 1450°C, quenched into an oil or water bath, and examined by x-ray diffraction. Single phase perovskites were found for A/B cation ratios varying from 0.98 to 1.00 for all levels of strontium substitution for lanthanum. A-site enriched compositions typically contained lanthanum oxide as a second phase, which is easily hydrated to form the hydroxide. B-site enriched compositions contained lanthanum strontium manganite spinel phases plus  $\text{Mn}_3\text{O}_4$  for compositions with an A/B cation ratio smaller than 0.98. The presence of either the spinel phase or manganese oxide is not particularly problematic. Impedance spectroscopy measurements showed that excess manganese oxide actually improved the electrocatalytic

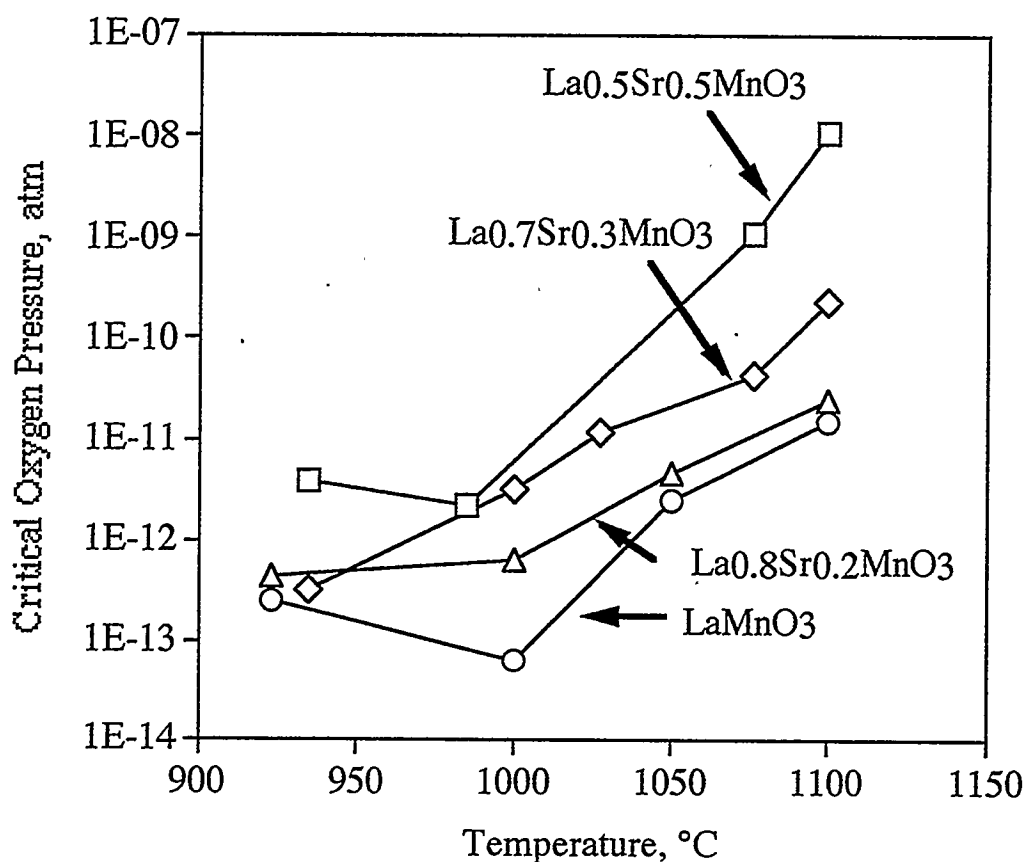


Figure 5. Critical oxygen decomposition pressure for lanthanum manganite compositions versus temperature determined by the galvanic cell method.

activity of the cathode composition. In consideration of ease of sintering and overall phase stability, an A/B cation ratio of 0.98 appears to be optimum for the lanthanum strontium manganite system.

### SUMMARY

The dimensional instability of lanthanum and yttrium chromite interconnect materials has been evaluated as a function of oxygen partial pressure and temperature. Highly substituted lanthanum chromites were the most susceptible to lattice expansion under reducing conditions. Corresponding yttrium chromite compositions were dimensionally more stable by more than a factor of two. New chromite compositions were developed that showed little tendency for lattice expansion even under severely reducing conditions, while retaining high electrical conductivity and a good thermal expansion match to other fuel cell components.

Thermodynamic properties of substituted lanthanum manganite cathode materials have been evaluated using the galvanic cell approach. Activities of strontium and calcium oxide in lanthanum manganite were determined using corresponding fluoride electrolytes, while critical oxygen decomposition pressures were determined using zirconia electrolytes. The thermodynamic stability of these materials was shown to decrease with the degree of A-site substitution. Such thermodynamic information is needed to predict the long-term stability of fuel cell assemblies.

## REFERENCES

1. N. Q. Minh and T. Takahashi, *Science and Technology of Ceramic Fuel Cells* (Elsevier, Amsterdam, 1995).
2. W. J. Weber, C. W. Griffin and J. L. Bates, *J. American Ceramic Society* 70, 265 (1987).
3. M. M. Nasrallah, J. D. Carter, H. U. Anderson, and R. Kroc, in *Proc. 2nd Int. Symp. Solid Oxide Fuel Cells*, Athens, Greece, eds. F. Grosz, P. Zegers, S. C. Singhal, and O. Yamamoto (Commision of the European Communities, Luxembourg, 1991) p. 637.
4. G. F. Carini, H. U. Anderson, D. M. Sparlin, and M. M. Nasrallah, *Solid State Ionics* 49, 233 (1991).
5. T. R. Armstrong, J. W. Stevenson, P. E. Raney, and L. R. Pederson, in *Fuel Cell Seminar Abstracts* San Diego, CA (Courtesy Associates, 1994) p. 105.
6. T. R. Armstrong, J. W. Stevenson, L. R. Pederson, and P. E. Raney, in *Proc. 4th Int. Symp. Solid Oxide Fuel Cells*, Yokohama, Japan, ed. S. G. Singhal (The Electrochemical Society, Pennington, NJ 1995) p. 944.
7. H. Yokokawa, N. Sakai, T. Kawada, and M. Dokiya, *Solid State Ionics* 52, 43 (1992).
8. H. Yokokawa, T. Horita, N. Sakai, T. Kawada, and M. Dokiya, *Solid State Ionics* 78, 203 (1995).
9. L.A. Chick, L.R. Pederson, G.D. Maupin, J.L. Bates, L.E. Thomas, and G.J. Exarhos, *Materials Letters* 10, 6 (1990).
10. R. Nadalin and W. Brozda, *Analytica Chimica Acta* 28, 282 (1963).
11. C. B. Alcock, *High Temperature Science* 28, 183 (1990)
12. R. Hildrum, M. Brustad, W. Changshen, and O. Johannesen, *Materials Research Bulletin* 29, 851 (1994).



## PROTON-CONDUCTING CERATE CERAMICS<sup>1</sup>

L. R. Pederson , G. W. Coffey, J. L. Bates, and W. J. Weber

Pacific Northwest National Laboratory  
P.O. Box 999  
Richland, WA 99352

Single-cell solid oxide fuel cells were constructed using strontium cerate as the electrolyte and their performance tested. Like certain zirconates, hafnates, and tantalates, the cerate perovskites are among a class of solid electrolytes that conduct protons at elevated temperatures. Depending on the temperature and chemical environment, these ceramics also support electronic and oxygen ion currents. A maximum power output of  $\approx 100$  mW per  $\text{cm}^2$  electrolyte surface area was obtained at  $900^\circ\text{C}$  using 4% hydrogen as the fuel and air as the oxidant.

A series of rare earth/ceria/zirconia were prepared and their electrical properties characterized. Rare earth dopants included ytterbia, yttria, terbia, and europia. Ionic conductivities were highest for rare earth/ceria and rare earth zirconia compositions; a minimum in ionic conductivity for all series were found for equimolar mixtures of ceria and zirconia.

Cerium oxysulfide is of interest in fossil energy applications because of its high chemical stability and refractory nature. An alternative synthesis route to preparing cerium oxysulfide powders have been developed using combustion techniques.

### INTRODUCTION

Protonic conductivity has been observed in both cerate and zirconate ceramics including doped  $\text{SrCeO}_3$ ,  $\text{BaCeO}_3$ ,  $\text{CaZrO}_3$ ,  $\text{SrZrO}_3$ , and  $\text{BaCeO}_3$ .<sup>1-3</sup> The presence of water is necessary for protonic conduction; water reacts with oxygen vacancies to produce sites for conduction.<sup>1</sup> Depending on temperature and on the partial pressures of oxygen and water, protons, oxygen ions, and electrons contribute to the overall current.<sup>4,5</sup> In this work, we have constructed single-cell SOFC assemblies using Yb-doped  $\text{SrCeO}_3$  as the electrolyte, and evaluated cell performance. While ceria-based compositions generally give higher overall conductivities than the zirconates, the zirconates are chemically more stable. To take advantage of the good conductivity properties of the cerates and chemical durability of the zirconates, ternary rare earth/zirconia/ceria compositions were also prepared and electrical properties examined.

---

<sup>1</sup> Research sponsored by the U. S. Department of Energy, Fossil Energy AR&TD Materials Program. Pacific Northwest National Laboratory is operated by Battelle for the U. S. Department of Energy under Contract DE-AC06-76RLO 1830.

Certain rare earth oxysulfides are well known for their refractory nature and good stability towards metallic melts and slags.<sup>6,7</sup> Cerium oxysulfide,  $\text{Ce}_2\text{O}_2\text{S}$ , has been used to lower the concentration of sulfur in steel and to remove sulfur from gaseous fuels through an equilibrium involving cerium oxide, cerium oxysulfide, and sulfur.<sup>7</sup> The stability of this material under coal slagging conditions has not been tested to date, partially due to difficulty in preparing appropriate test coupons. We have applied combustion synthesis techniques to preparing cerium oxysulfides and are examining sintering characteristics.

### STRONTIUM CERATE-BASED FUEL CELL

Because the strontium cerates conduct both protons and oxygen ions, there may be significant advantages in using such materials as the electrolyte in an SOFC.<sup>1-3,5</sup> There are two potential-determining ions rather than one. Water is produced at both the cathode and the anode in an SOFC constructed using a strontium cerate electrolyte. In contrast, water is produced only at the anode in an SOFC that utilizes an oxygen ion-conducting zirconia electrolyte.

The open cell potential of a single-cell SOFC with a strontium cerate electrolyte showed a distinctly non-Nernstian behavior at temperatures greater than  $\approx 500^\circ\text{C}$ , as shown in Figure 1. Porous platinum served as both the cathode and the anode in this test cell. Air was supplied to the cathode in this test, while 4% hydrogen/argon was supplied to the anode. The open cell potential was nearly constant in the temperature range 600 to  $900^\circ\text{C}$ . Non-Nernstian behavior is attributed to losses associated with an increased electronic conductivity in this temperature range.<sup>4,5</sup> Higher cell potentials would have resulted if pure hydrogen were used rather than 4% hydrogen; the latter was chosen because the hydrogen concentration is below the lower flammability limit.

Current/voltage curves were determined for cerate-based, single-cell SOFC assemblies. Typical results obtained at  $910^\circ\text{C}$  are shown in Figure 2 using a 4% hydrogen/argon fuel and an air oxidant. At low cell currents, the cell potential approached the open cell voltage of Figure 1. A maximum in the cell power of approximately  $100 \text{ mW/cm}^2$  was obtained, corresponding to a cell potential of  $\approx 0.5 \text{ V}$ . A power level of  $80 \text{ mW/cm}^2$  at a cell potential of  $0.6 \text{ V}$  was sustained for several days with no obvious loss in performance. While open cell potentials remained essentially constant in the temperature range 600 to  $900^\circ\text{C}$ , cell power output fell with decreased temperature due to lower ionic conductivities, as expected. However, the electronic contribution to the overall cell current also decreased,<sup>4,5</sup> partially offsetting the effects of lowered ionic conductivity.

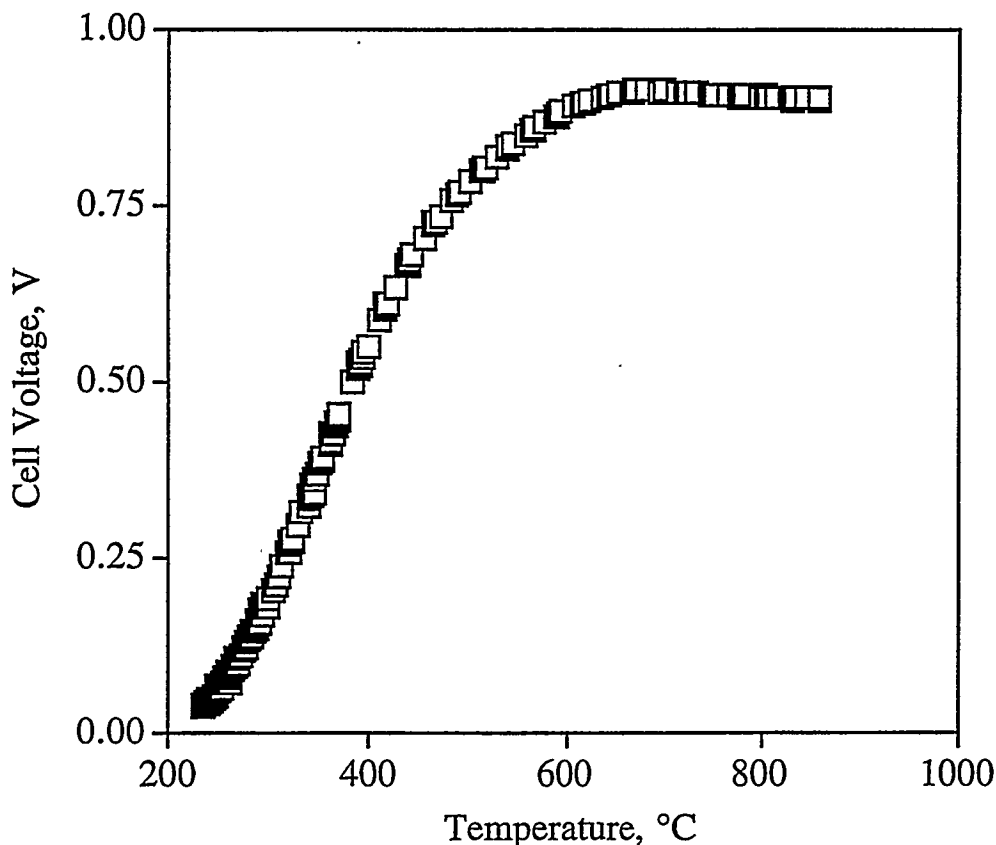


Figure 1. Open cell voltage versus temperature for a single-cell SOFC using a strontium cerate electrolyte. Air was supplied to the cathode and 4% hydrogen/argon was supplied to the anode.

#### RARE EARTH-ZIRCONIA-CERIA ELECTROLYTES

A series of rare earth/ceria/zirconia compositions were prepared and their electrical and structural properties characterized. The purpose was to attempt to combine the high conductivities associated with cerate compositions with high chemical durabilities associated with the zirconates. The glycine-nitrate combustion synthesis method was used to prepare the ternary rare earth/zirconia/ceria compositions  $(\text{MO}_{1.5})\text{O}_2(\text{ZrO}_2)_{0.8-x}(\text{CeO}_2)_x$ , with  $\text{M} = \text{Yb}, \text{Y}, \text{Tb}, \text{and Eu}$ .<sup>6</sup> For the zirconia/ceria compositions, the chosen dopants all exhibit ionic radii in the trivalent state on an octahedral site that are larger than either tetravalent zirconium or cerium ions, and stabilize the cubic structure. Electrical conductivities were measured using a four-probe, pulsed dc technique with platinum knife-edge contacts at about 25 K intervals. Measurements were made in air, during both heating and cooling cycles.

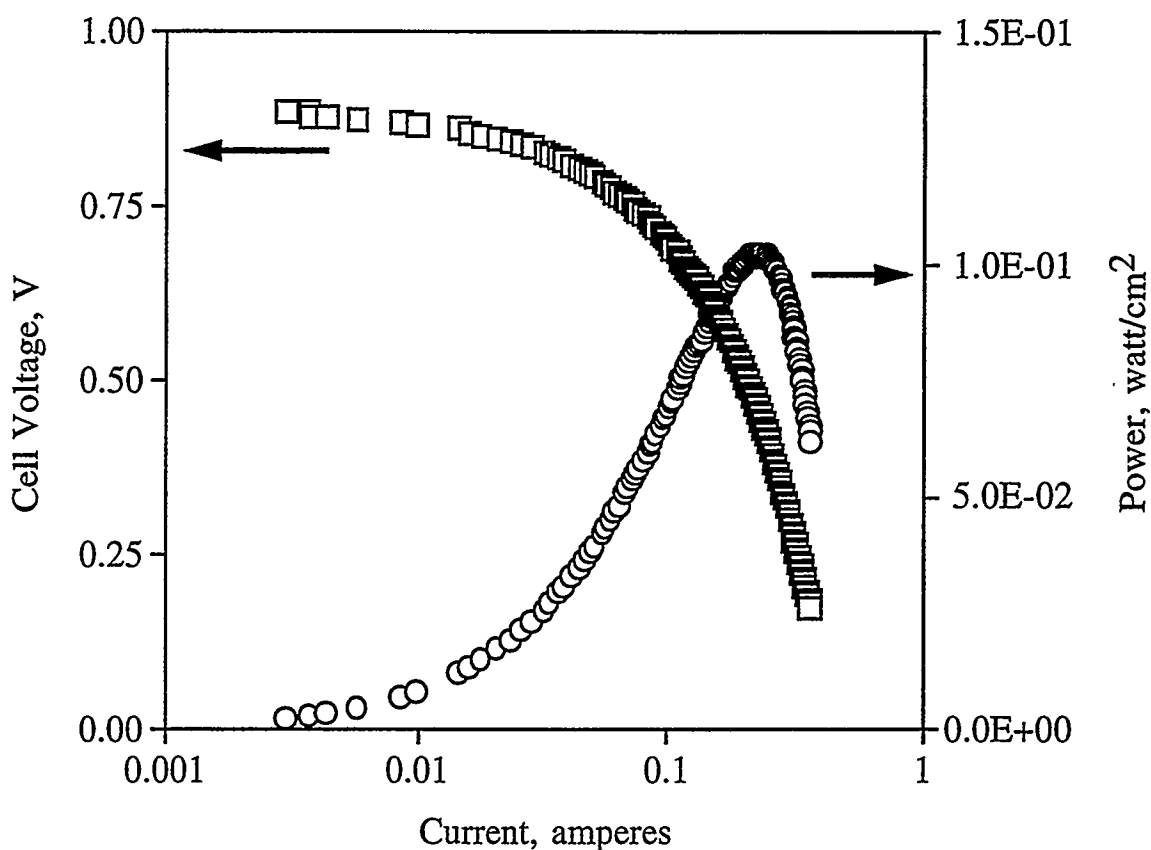


Figure 2. Performance of a single-cell SOFC assembly at 910°C using argon/4% hydrogen as the fuel and air as the oxidant. The open-cell voltage at 910°C was  $\approx 0.9$  V.

In all of the compositions tested, the electrical conductivity was found to decrease with increased cerium substitution for zirconium until an equimolar concentration of each was reached ( $\text{Ce}=\text{Zr}=0.4$ ). Conductivities increased with increased cerium concentration above that point, with highest conductivities observed for full zirconium replacement by cerium. Conductivities obtained at 1000°C are given in Figure 3. There was no clear trend in conductivity with changes in the ionic radius of the dopant. Lattice parameters increased linearly with the ceria content and with the ionic radius of the dopant, however.

Activation energies for ionic conduction were maximized for equimolar ceria and zirconia contents, as shown in Figure 4. Compositions high in zirconia gave activation energies for ionic conduction higher than analogous compositions high in ceria. While improved chemical durability may well result from the addition of zirconia to cerate ceramics, there appears to be no advantage to such compositions when considering the resultant ionic conductivities.

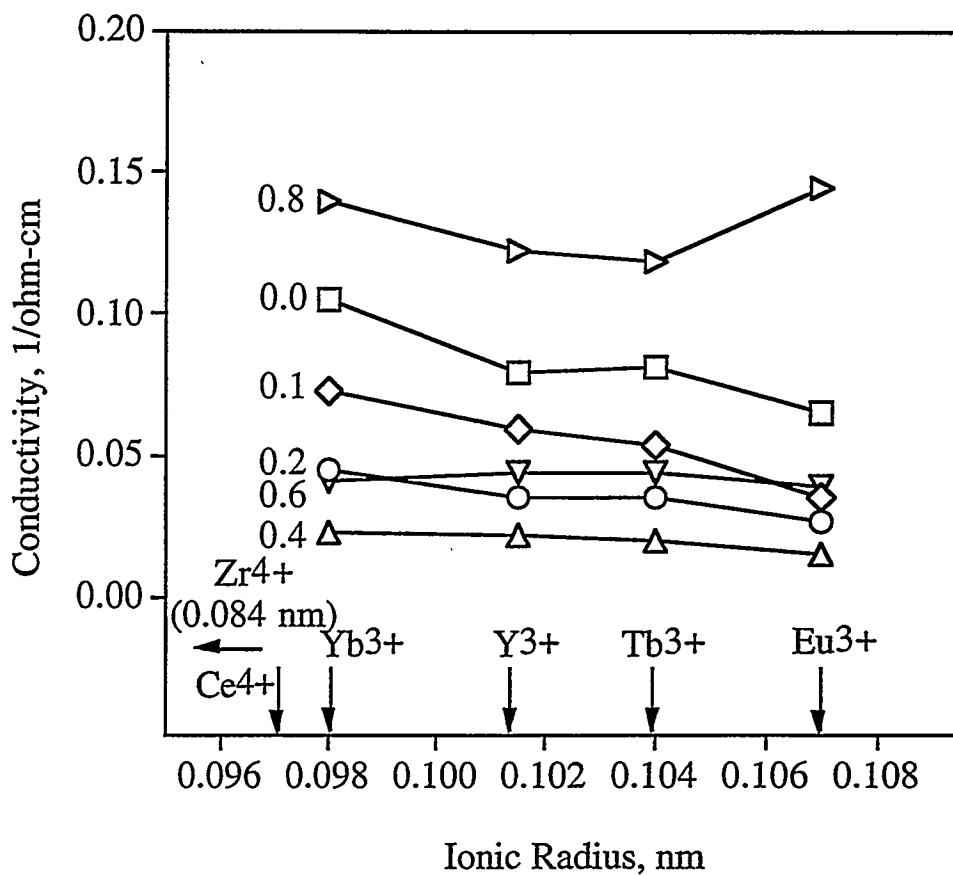


Figure 3. Conductivity of rare earth/zirconia/ceria compositions at 1000°C. Values given are the cerium content in  $(\text{MO}_{1.5})\text{O}_2(\text{ZrO}_2)_{0.8-x}(\text{CeO}_2)_x$ , with  $M = \text{Yb}, \text{Y}, \text{Tb}, \text{and Eu}$ . A minimum in the conductivity was apparent for an equimolar mixture of ceria and zirconia.

### SYNTHESIS OF CERIUM OXYSULFIDE

Cerium oxysulfide is of interest in fossil energy applications because of its expected high stability when exposed to coal slags. The material is typically prepared from the sulfate in flowing hydrogen sulfide at temperatures above 1000°C or by the solid state reaction of cerium oxide and cerium sulfide.<sup>7,8</sup> As traditional synthesis methods are time-consuming and slow, alternate synthesis routes were developed.

Cerium sulfide was precipitated from an aqueous solution of cerium nitrate plus thiourea and triethanolamine. Sulfur is displaced from thiourea to yield urea under these conditions. Thioacetamide was also used with success as the source of sulfur. The cerium sulfide was collected by filtration, washed, and dried in flowing, dry nitrogen. This material was

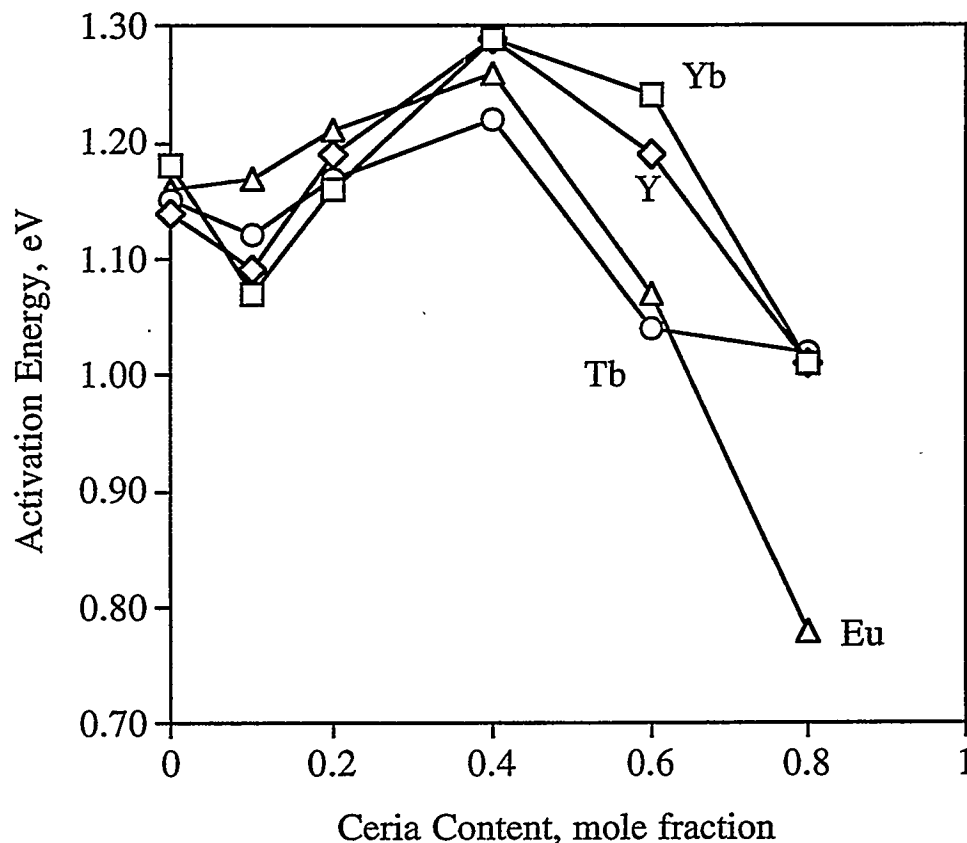


Figure 4. Activation energies for ionic conduction in  $(\text{MO}_{1.5})\text{O}_2(\text{ZrO}_2)_{0.8-x}(\text{CeO}_2)_x$  compositions as a function of ceria replacement of zirconia. Equimolar zirconia/ceria mixtures resulted in the highest activation energies for each of the dopants.

partially oxidized at 600°C and then converted to the oxysulfide in flowing argon/4 percent hydrogen at 1000°C.

Because of the ease by which the cerium sulfide could be formed in an aqueous solution using thiourea, a combustion synthesis route based on the glycine-nitrate method<sup>6</sup> was utilized, where part of the glycine fuel was replaced with thiourea. Ceric ammonium nitrate, glycine, and thiourea were combined in an aqueous precursor, heated with evaporation to the point of autoignition, and the ash collected. Sulfur was displaced from thiourea prior to combustion, resulting in the formation of fine elemental sulfur particles that partially oxidized during combustion. Precursor mixtures contained a stoichiometric mixture of fuel and oxidant, though the ratio of glycine to thiourea was varied. The combustion reaction yielded finely divided cerium oxysulfide plus cerium sulfate powders.

The cerium oxysulfide plus cerium sulfate powders were pressed into pellets approximately 2 cm. in diameter and 0.2 cm. in thickness uniaxially (50 MPa) and isostatically (140 Mpa). Samples were sintered for 1 hour in the temperature range 1000 to 1650°C in flowing 4% hydrogen/argon or in argon. X-ray diffraction analysis showed only the presence of cerium oxysulfide for sintering temperatures below 1400°C, but sintered densities were smaller than 70% of theoretical. Approximately 80% of theoretical density was achieved at a sintering temperature of 1650°C. A sintered density of at least 90% of theoretical is desired for specimens intended for corrosion testing. Samples sintered in argon yielded cerium oxide as a minor component.

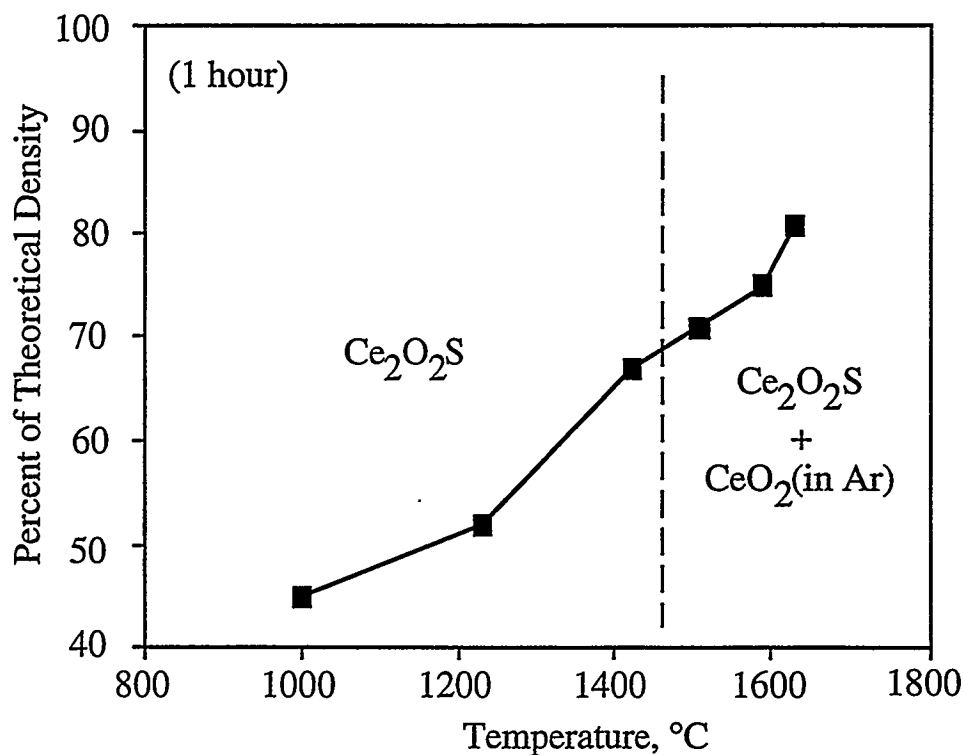


Figure 5. Sintered density versus temperature for cerium oxysulfide, for a sintering time of one hour.

## SUMMARY

Single-cell solid oxide fuel cells were constructed using ytterbium-doped strontium cerate as the electrolyte and their performance tested. Using 4% hydrogen as the fuel and air as the oxidant, maximum power output of  $\approx 100$  mW per  $\text{cm}^2$  electrolyte surface area was obtained at  $900^\circ\text{C}$ . Both oxygen ions and protons are potential-determining ions in this electrolyte. Water was produced at both the cathode and at the anode.

A series of rare earth/ceria/zirconia were prepared and their electrical properties characterized. Rare earth dopants included ytterbia, yttria, terbia, and europia. Ionic conductivities were highest for rare earth/ceria and rare earth zirconia compositions; a minimum in ionic conductivity for all series were found for equimolar mixtures of ceria and zirconia.

An alternative synthesis route to preparing cerium oxysulfide powders have been developed using combustion techniques. The powders consisted of a single crystalline phase. Once sintered to full density, these materials are expected to show good chemical durability in the presence of coal slags.

## REFERENCES

1. T. Norby, *Solid State Ionics* 40/41, 857 (1990).
2. H. Iwahara, T. Yajima, T. Hibino, and H. Ushida, *J. Electrochem. Soc.* 140, 1687 (1993).
3. N. Bonanos, *Solid State Ionics* 53-56, 967 (1992).
4. I. Kosacki and H. L. Tuller, *Solid State Ionics* 80, 223 (1995).
5. G. W. Coffey, L. R. Pederson, and W. J. Weber, *Proc. Mater. Res. Soc.* Vol. 369, 395 (1995).
6. L.A. Chick, L.R. Pederson, G.D. Maupin, J.L. Bates, L.E. Thomas, and G.J. Exarhos, *Materials Letters* 10, 6 (1990).
7. W. Krahle and T. Reetz, *Materials by Powder Technology PTM-93*, ed. F. Aldinger, DGM Informationsges, Oberursel, Germany, p. 563 (1993).
8. R. K. Dwivedi and D. A. R. Kay, *J. Less Common Metals* 102, 1 (1984).



## Ceramic Catalyst Materials

A. G. Sault

Fuel Science Department  
Sandia National Laboratories  
Albuquerque, NM 87185-0710

and

J. Reardon and A. K. Datye

Department of Chemical and Nuclear Engineering  
University of New Mexico  
Albuquerque, NM 87131

### ABSTRACT

This project focuses on the modification of silica and alumina surfaces by titania and hydrous titanium oxide ion-exchange films, and the use of these modified materials as supports for MoS<sub>2</sub> catalysts. Fourier transform infrared spectroscopy (FTIR) studies of molybdena interaction with  $\gamma$ -Al<sub>2</sub>O<sub>3</sub> demonstrate that at low loadings molybdenum interacts with the most basic hydroxyl groups, and that these hydroxyls are associated with tetrahedrally coordinated aluminum. Furthermore, hydrodesulfurization (HDS) activity as a function of Mo loading shows a maximum in specific activity with loading. The Mo species bound to tetrahedrally coordinated Al sites are therefore believed to be inactive for the HDS reaction. Only after the tetrahedral Al sites have completely consumed does molybdena adsorb on the alumina in a manner that leads to an active catalyst. According to this scheme, the activity of alumina supported MoS<sub>2</sub> catalysts could be greatly improved by either titrating the tetrahedral Al sites with a modifier, or by using  $\alpha$ -Al<sub>2</sub>O<sub>3</sub> which contains no tetrahedrally coordinated Al. HDS tests over MoS<sub>2</sub> supported on both  $\alpha$ -Al<sub>2</sub>O<sub>3</sub> and  $\gamma$ -Al<sub>2</sub>O<sub>3</sub> modified by a titania film confirm this hypothesis. Neither support material gives rise to a maximum in activity with Mo loading, but rather exhibits a smooth decrease in activity with loading. Furthermore, for equivalent Mo loadings the activity of both of these support materials exceeds that of unmodified  $\gamma$ -Al<sub>2</sub>O<sub>3</sub> due to the fact that no Mo is tied up in the inactive form. FTIR, X-ray photoelectron spectroscopy, and transmission electron microscopy are currently being used to determine whether our model can indeed account for the observed activity trends. Although the surface area of  $\alpha$ -Al<sub>2</sub>O<sub>3</sub> is too low ( $\sim 10$  m<sup>2</sup>/g) for use as a commercial catalyst, the titania coated  $\gamma$ -

$\text{Al}_2\text{O}_3$  represents an important, practical improvement in support materials for hydrotreating catalysts.

## INTRODUCTION

In previous years, this project has focused on the deposition and characterization of titania films on high surface area substrates, such as silica and alumina. In order to determine the effects that these films have on catalyst activity, we have focused efforts in the current fiscal year on depositing  $\text{MoS}_2$  onto modified and unmodified alumina substrates, and measuring the resulting activity for hydrodesulfurization (HDS) of dibenzothiophene (DBT). On unmodified  $\gamma$ -alumina or silica supports it is known that the specific activity of  $\text{MoS}_2$  goes through a maximum with molybdenum loading, while on titania or zirconia the activity appears to decrease monotonically with coverage<sup>1</sup>. Unfortunately, due to the low surface area of the titania and zirconia supports, and to the fact that a flow reactor was employed for the activity measurements, the data reported on these two supports did not extend to low enough Mo loadings to confirm the absence of a maximum in activity. Assuming, however, that no maximum occurs for titania and zirconia, the different behavior of  $\gamma$ -alumina and silica relative to titania and zirconia has been attributed to differing morphology of the  $\text{MoS}_2$  active phase. For supports that exhibit no maximum with loading,  $\text{MoS}_2$  is proposed to lie flat with the basal plane parallel to the support surface, while for supports that exhibit a maximum the  $\text{MoS}_2$  is proposed to bond perpendicular to the surface in a so-called "bookend" morphology. The evidence for the bookend morphology is indirect, relying on transmission electron microscopy (TEM) images that show  $\text{MoS}_2$  platelets lying parallel to the direction of viewing and perpendicular to the  $\gamma$ -alumina crystallites which preferentially align with the TEM grid. These  $\text{MoS}_2$  platelets could easily be located on the sides of  $\gamma$ -alumina particles, however, and therefore appear to be bound in a bookend morphology even though bonding is primarily through interaction of the basal plane with the sides of the particles. Recent TEM images of  $\text{MoS}_2$  bound to low surface area silica and  $\gamma$ -alumina particles, where the uncertainty introduced by the possibility of bonding at crystallite edges is eliminated, show no evidence

for a bookend morphology, but show ample evidence for basal plane bonding of MoS<sub>2</sub> (ref. 2).

Given the difficulties arising from a morphological explanation of the activity trends, it seems prudent to explore possible chemical differences between the supports that could explain the data. It is known that at very low loadings molybdena binds to the  $\gamma$ -alumina surface as isolated monomeric species that are very difficult to reduce and convert to the sulfide<sup>3,4</sup>. As coverage increases, polymeric molybdena species begin to form ultimately resulting in bulk MoO<sub>3</sub> particles. Since at low loadings ( $<1$  Mo/nm<sup>2</sup>) most of the molybdenum is tightly bound in the inactive form, specific activity for HDS is expected to be very low. As more easily reduced polymeric species form at higher loadings, the specific activity rises, ultimately reaching a maximum at the point at which MoS<sub>2</sub> platelet growth begins to compensate for the increase in the fraction of the molybdenum that is reducible to MoS<sub>2</sub>. In order to explain why a similar phenomenon does not operate on titania and zirconia, one must explore the specific interactions that give rise to the inactive Mo species on  $\gamma$ -alumina.

Fourier transform infrared (FTIR) studies of molybdena adsorption on  $\gamma$ -alumina demonstrate that the initial mode of interaction is through the most basic (highest frequency) hydroxyl groups<sup>5</sup>. These hydroxyl groups are associated with tetrahedrally coordinated aluminum cations in the  $\gamma$ -alumina support<sup>6</sup>. It is therefore postulated that the presence of tetrahedrally coordinated cations in the support material can give rise to strongly bound, inactive molybdena species. Comparing silica and  $\gamma$ -alumina with titania and zirconia in this context reveals that supports that give rise to a maximum in activity with coverage do indeed possess tetrahedrally coordinated cations, while supports that show only a monotonic decrease in activity with coverage contain only octahedrally coordinated cations.

Given this excellent correlation, activity studies and spectroscopic and TEM characterization of supported molybdena as a function of loading were performed to verify this explanation of activity trends. Accordingly, we report here the results of activity studies that confirm the published activity trends over a wider range of Mo coverages, and also

explore the potential of titania films to modify  $\gamma$ -alumina substrates such that the unfavorable, highly basic OH groups are consumed prior to molybdena loading.

## RESULTS AND DISCUSSION

Based on the information and suppositions presented above, it is informative to compare the HDS activity of  $\text{MoS}_2$  measured on several different supports. Mo was loaded onto various supports by aqueous incipient wetness impregnation of ammonium heptamolybdate followed by calcining at  $500^\circ\text{C}$  to disperse the molybdenum. Sulfiding was performed *ex situ* at  $400^\circ\text{C}$  in a flowing mixture of 10%  $\text{H}_2\text{S}$  in hydrogen. Kinetic measurements were made using a batch reactor rather than the flow reactor employed in earlier studies. This arrangement allows activity measurements to be made with low Mo loadings on very low surface area supports by simply extending the reaction time until measurable conversions are achieved. The advantage of being able to measure activity on such catalysts is offset to a certain degree by the need to account for poisoning of the reaction by competitive adsorption of product  $\text{H}_2\text{S}$ , and for a finite heat up time at the start of the reaction. A method for accounting for these factors is presented elsewhere<sup>7</sup>. The result of the analysis is a psuedo-first order rate constant that provides a measure of the specific activity (per g Mo) for a wide range of Mo loadings.

Results of this analysis are presented in figure 1, which shows the first order rate

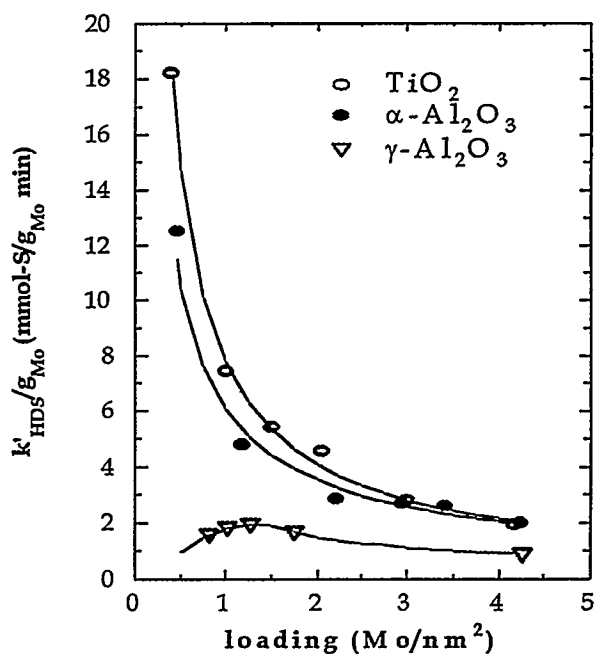


Fig. 1. Activity of  $\text{MoS}_2$  on different supports as a function of Mo loading.

constant as a function of Mo coverage. First, note the maximum in activity for  $\text{MoS}_2/\gamma$ -alumina at  $\sim 1.0 \text{ Mo/nm}^2$ , in excellent agreement with previous measurements of thiophene HDS<sup>1</sup>. Second, when the data for titania supports is extended below  $1.0 \text{ Mo/nm}^2$  the monotonic trend of decreasing activity with loading is maintained, unambiguously confirming a fundamental difference between the activity trends on  $\gamma$ -alumina and titania. Finally, and most significantly,  $\alpha$ -alumina exhibits an activity trend closely resembling that of titania, with no apparent maximum. This result is entirely consistent the hypothesis that isolated molybdate species, formed by reaction with basic hydroxyl groups bound to tetrahedrally coordinated aluminum cations, give rise to the low activity of  $\text{MoS}_2/\gamma$ -alumina at coverages below  $1.0 \text{ Mo/nm}^2$ . Since no tetrahedrally coordinated aluminum cations are present in  $\alpha$ -alumina<sup>8</sup>, the possibility of forming the inactive species is precluded and a normal activity trend is observed. While this result alone does not confirm the validity of the proposed explanation for the maximum observed with  $\gamma$ -alumina, it does demonstrate that the effect is related to the structure of the support and not to the specific chemical identity of the support cations.

In order to verify the nature of the chemical interactions leading to the different activity trends for  $\alpha$ - and  $\gamma$ -alumina, spectroscopic evidence for the presence or absence of

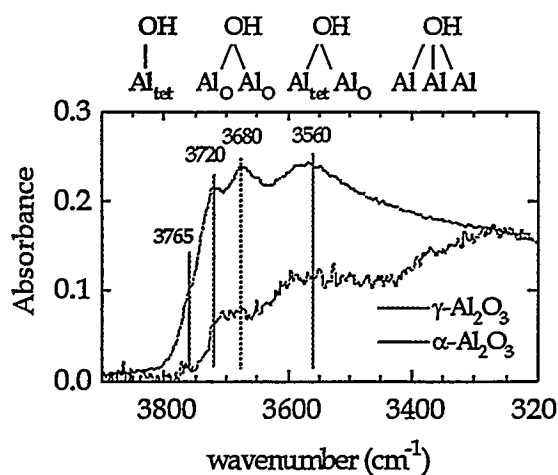


Fig. 2. comparison of FTIR spectra of hydroxyl stretching region on  $\alpha$ -alumina and  $\gamma$ -alumina.

certain molybdena species on each support is required. This evidence is presented in figures 2 and 3. Figure 2 shows FTIR spectra of both  $\alpha$ - and  $\gamma$ -alumina in the hydroxyl stretching regions. The spectrum of  $\gamma$ -alumina agrees well with literature spectra<sup>5,9</sup>, showing multiple bands corresponding to various binding sites and coordinations<sup>6</sup>. The spectrum of

$\alpha$ -alumina is of much poorer quality due to the very low surface area, but it is nevertheless apparent that little intensity is present at the high frequencies characteristic of the most basic hydroxyl groups on  $\gamma$ -alumina. Further evidence for a difference in chemical behavior of Mo loaded on the two supports comes from X-ray photoelectron spectroscopy (XPS) measurements of the percent reduction of Mo on  $\alpha$ - and  $\gamma$ -alumina after treatment in pure  $H_2$  at 500°C for 12h (figure 3).  $\gamma$ -alumina shows an increase in reducibility with loading as

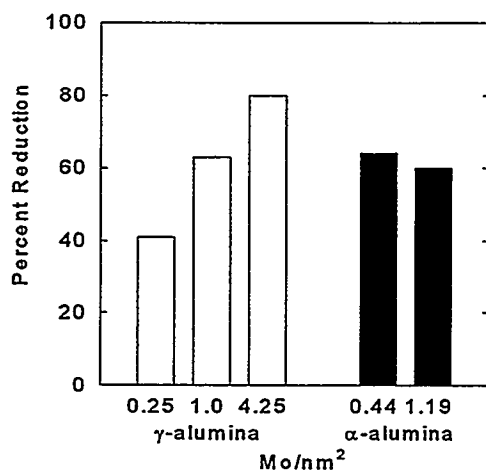


Fig. 3. Extent of Mo reduction at 500°C in hydrogen for 12h, measured by XPS.

reported elsewhere<sup>4a</sup>, consistent with formation of an unreducible, and therefore inactive Mo species at low loadings.  $\alpha$ -alumina, on the other hand, shows no variation of reducibility with loading, consistent with the absence of any changes in the bonding mode of molybdena with loading. The constant reducibility therefore gives rise to a monotonic decrease in activity with loading due to the growth of  $MoS_2$  islands and consequent loss of edge sites.

While the results for  $\alpha$ -alumina are encouraging, and demonstrate the potential of supports without tetrahedrally coordinated

cations for improving supported  $MoS_2$  catalysts, the low surface area of  $\alpha$ -alumina renders it unsuitable for practical use. In other words, although the activity per gram of Mo is quite high on  $\alpha$ -alumina, the activity *per gram or unit volume of catalyst* is very low. In order to apply the knowledge gained so far to the development of an improved practical catalyst, a method must be found to block the adsorption of Mo species at the most basic hydroxyls on  $\gamma$ -alumina. As alluded to earlier, one possible method for accomplishing this result is preadsorption of an additive to consume these basic hydroxyls prior to Mo adsorption. Since a major focus of this program has been the formation of titania films on various supports,

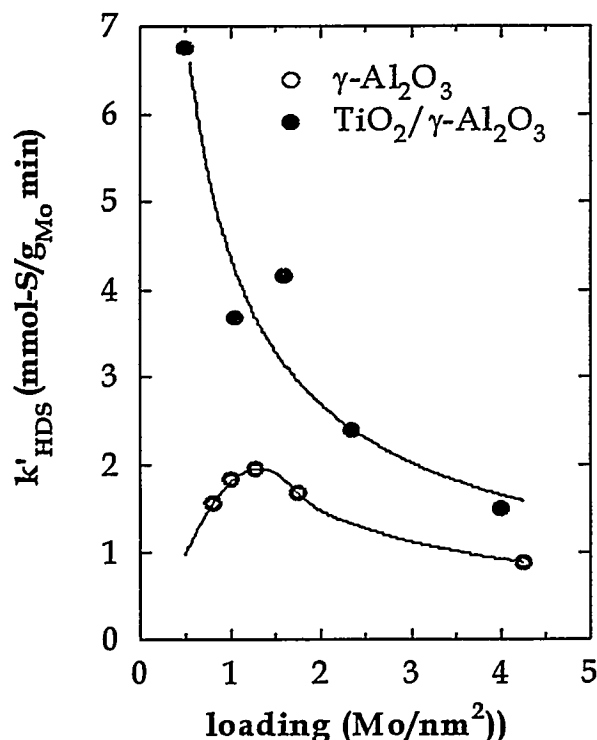


Fig. 4. Comparison of activity trends on  $\gamma$ -alumina vs. titania coated  $\gamma$ -alumina.

titania was chosen as the additive. Measurements were made of the activity of  $\text{MoS}_2$  supported on titania coated  $\gamma$ -alumina, and figure 4 shows the results for a support coated with 16 wt% titania, an amount sufficient to cover approximately two thirds of the  $\gamma$ -alumina surface. Clearly, the presence of the titania alters the specific activity trends associated with  $\gamma$ -alumina and results in behavior closely resembling that of bulk titania or  $\alpha$ -alumina. FTIR spectra show that the titania film indeed preferentially consumes the most basic, high frequency hydroxyls, thereby preventing the formation of inactive Mo species.

A final important result arises from analysis of TEM images of  $\text{MoS}_2$  supported on coated and uncoated  $\gamma$ -alumina samples. Figure 5 shows that the two samples are indistinguishable based on  $\text{MoS}_2$  morphology alone. Even the presence of titania cannot be detected indicating excellent dispersion of this additive. Thus, even if one concedes that the presence of  $\text{MoS}_2$  platelets perpendicular to the viewing direction, as observed in figure 5, is evidence for a bookend morphology, one cannot use this morphology as an explanation for the different activity trends observed on uncoated and titania coated  $\gamma$ -alumina. Instead, a chemical explanation must be sought. Based on the evidence presented here, the formation of an inactive Mo species on  $\gamma$ -alumina associated with tetrahedrally coordinated aluminum cations, and the absence of this species on supports that do not contain tetrahedrally

coordinated cations, must be considered a strong candidate for explaining the observed activity trends.

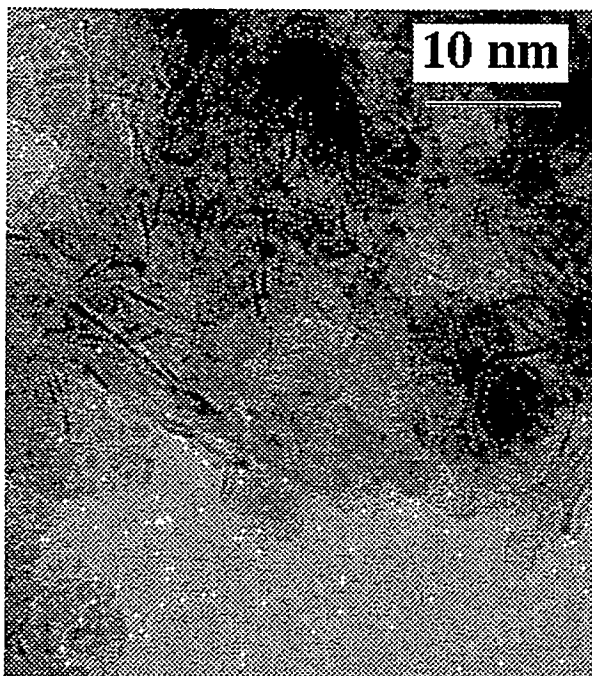


Fig. 5a. TEM image of MoS<sub>2</sub>/γ-alumina.

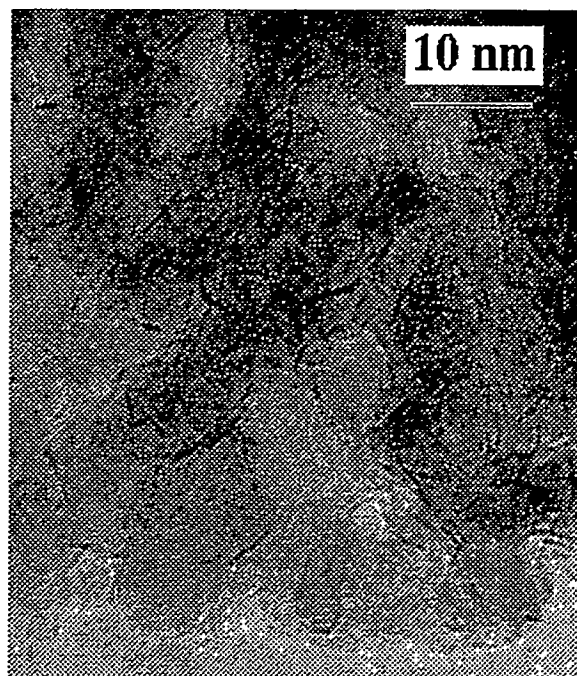


Fig. 5b. TEM image of MoS<sub>2</sub>/titania/γ-alumina

## CONCLUSIONS

The widely diverging activity trends observed for MoS<sub>2</sub>/γ-alumina vs. MoS<sub>2</sub>/TiO<sub>2</sub>/γ-alumina, coupled with the extreme similarity in MoS<sub>2</sub> morphologies, clearly rules out a morphological explanation for the behavior of different supports. Furthermore, the differences observed between α- and γ-alumina indicate that the activity trends are related to the specific structure of the support surface and not to the chemical identity of the oxide support cations. These conclusions, coupled with spectroscopic data on the nature of hydroxyl groups and Mo reducibility lend strong support to an explanation of activity trends involving the formation of inactive Mo species at low loadings on γ-alumina. These species



result from interaction of molybdena with highly basic hydroxyls associated with tetrahedrally coordinated aluminum cations. As coverage increases, a greater fraction of the molybdenum atoms becomes associated with other sites and the extent of Mo reducibility increases, causing a concomitant increase in activity. Ultimately, growth of MoS<sub>2</sub> platelets with coverage decreases the fraction of Mo atoms located at the active edges of the platelets and activity begins to fall. For supports which lack tetrahedrally coordinated cations, formation of unreducible Mo species does not occur and activity trends are dominated by MoS<sub>2</sub> platelet growth over the entire range of coverages studied. A monotonic decrease of activity with coverage results. By using a titania overlayer to consume the basic hydroxyls that lead to unreducible molybdate species, the activity of  $\gamma$ -alumina can be increased significantly at all Mo loadings, and the activity trends can be made similar to those of  $\alpha$ -alumina and titania. This result provides a simple, practical method for increasing the overall activity of supported MoS<sub>2</sub> catalysts.

#### REFERENCES

1. K. C. Pratt, J. V. Sanders, and V. Christov, *J. Catal.*, **124** (1990) 416.
2. S. Srinivasan, A. K. Datye, and C. H. F. Peden, *J. Catal.*, **137** (1992) 513.
3. H. Hu and I. E. Wachs, *J. Phys. Chem.*, **99** (1995) 10911.
4. a) D. S. Zingg, L. E. Makovsky, R. E. Tischer, F. R. Brown, and D. M. Hercules, *J. Phys. Chem.*, **84** (1980) 2898; b) C. P. Li and D. M. Hercules, *J. Phys. Chem.*, **88** (1984) 456.
5. a) N.-Y. Topsøe and H. Topsøe, *J. Catal.*, **139** (1993) 631; b) Y. Okamoto and T. Imanaka, *J. Phys. Chem.*, **92** (1988) 7102.
6. H. Knözinger and P. Ratnasamy, *Catal Rev. Sci. Eng.*, **17** (1978) 31.
7. J. R. Reardon, A. K. Datye, and A. G. Sault., in preparation.

8. Cotton, F. A. and Wilkinson, G., "Advanced Inorganic Chemistry," 4th ed., John Wiley and Sons, New York, 1980; p. 329.

9. T. H. Ballinger and J. T. Yates, Jr., *Langmuir*, 7 (1991) 3041.

NANOPARTICLE SYNTHESIS IN PULSED LOW TEMPERATURE DISCHARGES

R. J. Buss

Sandia National Laboratories  
Albuquerque, NM 87185-0367

## ABSTRACT

Silicon nitride powders with an average size as low as 7 nm are synthesized in a pulsed radio frequency glow discharge. The as-synthesized silicon nitride powder from a silane/ammonia plasma has a high hydrogen content and is sensitive to oxidation in air.

Post-plasma heating of the powder in a vacuum results in nitrogen loss, giving silicon-rich powder. In contrast, heat treatment at 800°C for 20 minutes in an ammonia atmosphere (200 Torr pressure) yields a hydrogen-free powder which is stable with respect to atmospheric oxidation.

Several approaches to synthesizing silicon carbide nano-size powders are presented. Experiments using silane/hydrocarbon plasmas produce particles with a high hydrogen content as demonstrated by Fourier transform infrared analysis. The hydrogen is present as both CH and SiH functionality. These powders are extremely air-sensitive. A second approach uses a gas mixture of methyltrichlorosilane and hydrogen. The particles have a low hydrogen content and resist oxidation. Particle morphology of the silicon carbide is more spherical and there is less agglomeration than is observed in the silicon nitride powder.

## INTRODUCTION

There has been much effort in recent years to develop methods for producing materials with nanometer scale substructure. The desire is to control the macroscopic material properties such as toughness, elasticity and porosity by tailoring the microstructure. For ceramic materials, one approach is to synthesize nano-scale particles and develop methods for compressing and sintering these powders. A wide variety of approaches to manufacturing nano-particles of ceramics have been explored with various degrees of success. Thermal plasma techniques<sup>1</sup> in which precursors are atomized and allowed to condense in the afterglow have been highly successful for many materials including

metals and oxides. For thermal plasmas, however, the chemistry of the powder is typically controlled by thermodynamics and some compounds have been especially difficult to make including silicon nitride. Other approaches to synthesizing nano-particulate materials include direct nitridation of silicon, carbothermic reduction of silica, gas phase reaction of  $\text{SiCl}_4$  and  $\text{NH}_3$ , laser pyrolysis of gaseous reagents, and thermal pyrolysis.

Almost a decade ago, Buss and Ho patented a process<sup>2</sup> for synthesizing ultrafine particles of ceramic, metal and polymer materials in a low-temperature, non-thermal, radio frequency (rf) plasma. The method involves flowing gaseous precursors at low pressure through a glow discharge. Electron-molecule collisions in the plasma result in fragmentation of the starting gases into reactive free radicals which undergo complex gas-phase chemistry leading to particle nucleation. Properties of the powder were thoroughly characterized by a variety of techniques<sup>3</sup>. In particular, the average particle size and size-dispersion were found to be large, and only weakly controllable. The average particle size was typically 100-200 nm.

During the past decade, particle formation and transport in plasmas has become an area of intense interest and activity<sup>4</sup>. It has developed that these particles, occurring in the plasmas used to manufacture microelectronic devices, can result in serious loss of wafer yield. Stimulated by this economic urgency, many laboratories worldwide have begun investigating the mechanisms governing particle nucleation, growth, trapping and agglomeration. One important discovery by Boufendi and Bouchoule<sup>5</sup> in France was that by pulsing the rf plasma, very tight control of the particle size and dispersion was achieved in the case of silicon particles from silane.

We applied the pulsed plasma technique to the synthesis of silicon nitride powder and achieved reasonable control of particle size as low as 7 nm<sup>6</sup>. The particles made in this way are rich in hydrogen-containing functionalities and the resulting powder is air-sensitive making subsequent handling difficult.

We report here the successful post-plasma heat treatment of the powders to render them air-insensitive. Also discussed are the results of applying the pulsed plasma technique to the synthesis of silicon carbide particles. Several chemical approaches including silane/hydrocarbon plasmas and methyltrichlorosilane (MTS)/hydrogen plasmas are compared.

#### EXPERIMENTAL

The plasma apparatus used to synthesize the nano-particles has been described previously<sup>6</sup>. Briefly, a vacuum chamber (base pressure 1 mTorr), is equipped with an electrode assembly consisting of a 15 cm diameter powered electrode, perforated with holes to allow gas flow in a showerhead configuration. The plasma region is enclosed by a grounded copper sheet with a grounded high transparency screen across the bottom. The pumping port is located 15 cm beneath the electrode assembly, and is fitted with a single sheet of filter paper.

In a typical experiment, eg. gas flow 2 sccm  $\text{SiH}_4$ , 12 sccm  $\text{NH}_3$ , at 200 mTorr pressure, the plasma is pulsed with a square wave on/off cycle (0.1 second on/1.0 second off) for 100 periods. Particle morphology is determined from a transmission electron microscope (TEM) grid placed on the collection filter. By running the plasma for an hour, sufficient powder is accumulated to obtain Fourier transform infrared (FTIR) transmission spectra. In order to obtain large quantities of powder for bulk analysis, the plasma is pulsed for several hours and the filter with accumulated powder is removed.

The post-plasma heat treatment of powders is tested by venting the plasma apparatus with dry nitrogen. The powder is transferred with minimal air exposure to a second vacuum chamber and immediately evacuated. Powders are exposed to air for a maximum of 15 seconds. The powder is then heated in vacuum or in an ammonia atmosphere in a resistively heated tantalum crucible. FTIR spectroscopy is used to study the susceptibility of the powder to oxidation in air. A sample is placed in the spectrometer and spectra are periodically acquired. The

growth of silicon oxide is readily measurable at 1100 wavenumbers ( $\text{cm}^{-1}$ ). The decomposition of the powder heated in vacuum is studied using thermogravimetric analysis with mass spectral analysis of the desorbing gas. Samples of powder weighing 100-200 mg are placed in an alumina crucible and the temperature is ramped at a rate of 10  $^{\circ}\text{C}/\text{min}$  with flowing argon as the carrier gas.

Experiments to study the synthesis of silicon carbide use several chemical approaches. Mixtures of silane and methane or ethylene produce powder over a wide range of plasma power (5-50 Watts). Particles are also generated from gas mixtures of argon and hydrogen containing MTS vapor.

#### RESULTS AND DISCUSSION

The silicon nitride powder synthesized in the pulsed rf glow discharge (0.1 second on-time, 10 sccm  $\text{SiH}_4$ , 60 sccm  $\text{NH}_3$ ) is rich in hydrogen<sup>3</sup>. The FTIR spectrum (Fig. 1a) shows strong absorptions at the SiH stretch ( $2100 \text{ cm}^{-1}$ ), and the NH stretch ( $3400 \text{ cm}^{-1}$ ) as well as the NH bending mode ( $1550 \text{ cm}^{-1}$ ). When exposed to ambient water vapor in the air, the SiH absorption decreases while the strong SiO absorption ( $1100 \text{ cm}^{-1}$ ) grows in as seen in the difference spectrum Fig 1b. Although the rate of oxidation can be slowed by storing the powder in a dry atmosphere, handling of the powder during preparation for sintering is difficult.

Thermogravimetric analysis (Fig 2) of the plasma synthesized powder shows that between 100  $^{\circ}\text{C}$  and 250  $^{\circ}\text{C}$ , weakly bound ammonia desorbs. From 250  $^{\circ}\text{C}$  to 500  $^{\circ}\text{C}$ , a second ammonia desorption occurs which may be associative recombination of  $\text{NH}_2$  and H from different silicon sites. From about 250  $^{\circ}\text{C}$  to 900  $^{\circ}\text{C}$ ,  $\text{H}_2$  gas desorbs (but note that there is some contribution to the mass 2 signal from cracking of ammonia which has not been corrected). Above about 900  $^{\circ}\text{C}$ , the powder ceases to evolve gas. The total weight loss is 8-10%.

Figure 1

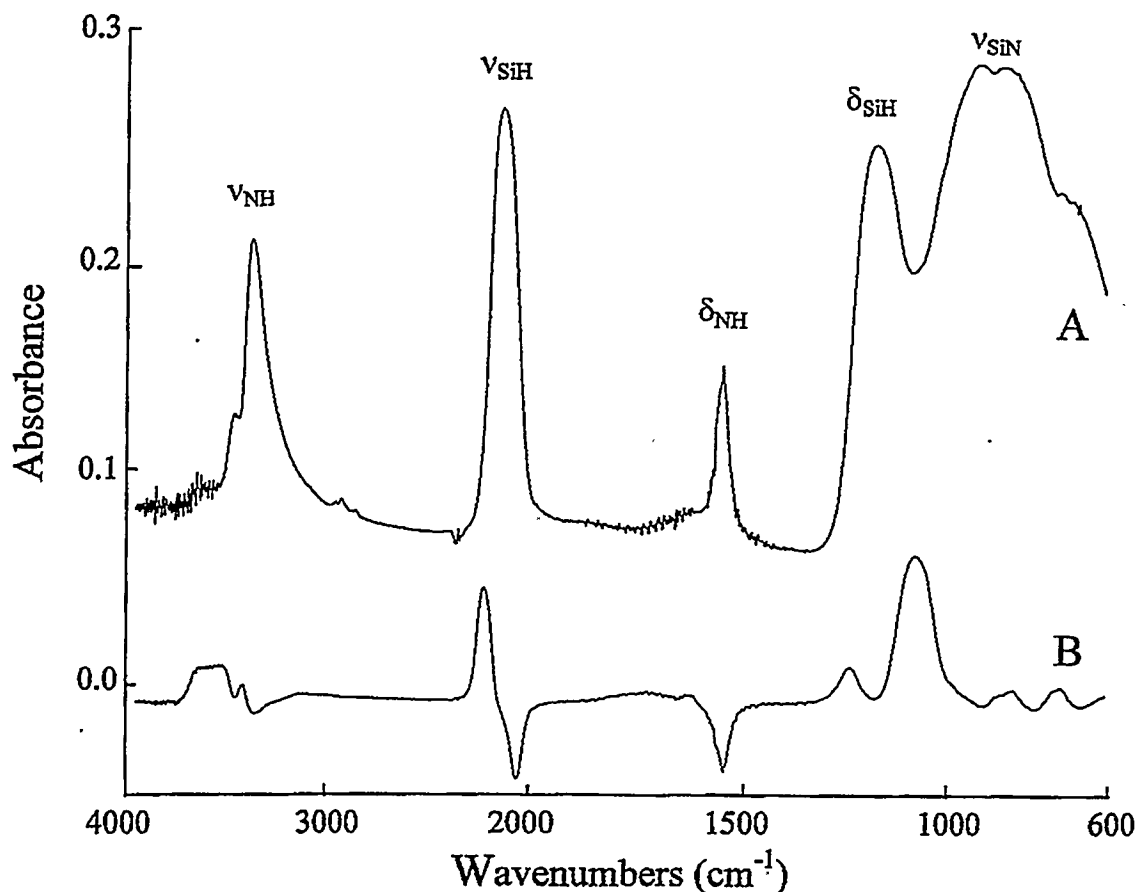


Fig. 1. FTIR spectra of silicon nitride powder a) as synthesized, b) the difference spectrum after 48 minutes exposure to air.

When gram quantities of pulsed plasma synthesized silicon nitride are heated to 800 °C for 20 minutes, the powder changes from pure white to a deep brown. This color is characteristic of silicon-enriched powder. Although the powder is synthesized stoichiometrically rich in nitrogen<sup>3</sup>, it is apparent that excessive nitrogen is evolved during heating in vacuo and silicon-rich powder results. This color change was only observed for the powder from pulsed plasmas, with 15 nm or less average diameter. The larger particles, averaging 150 nm, from a continuous discharge remained white on heating in vacuo. This suggests

Figure 2

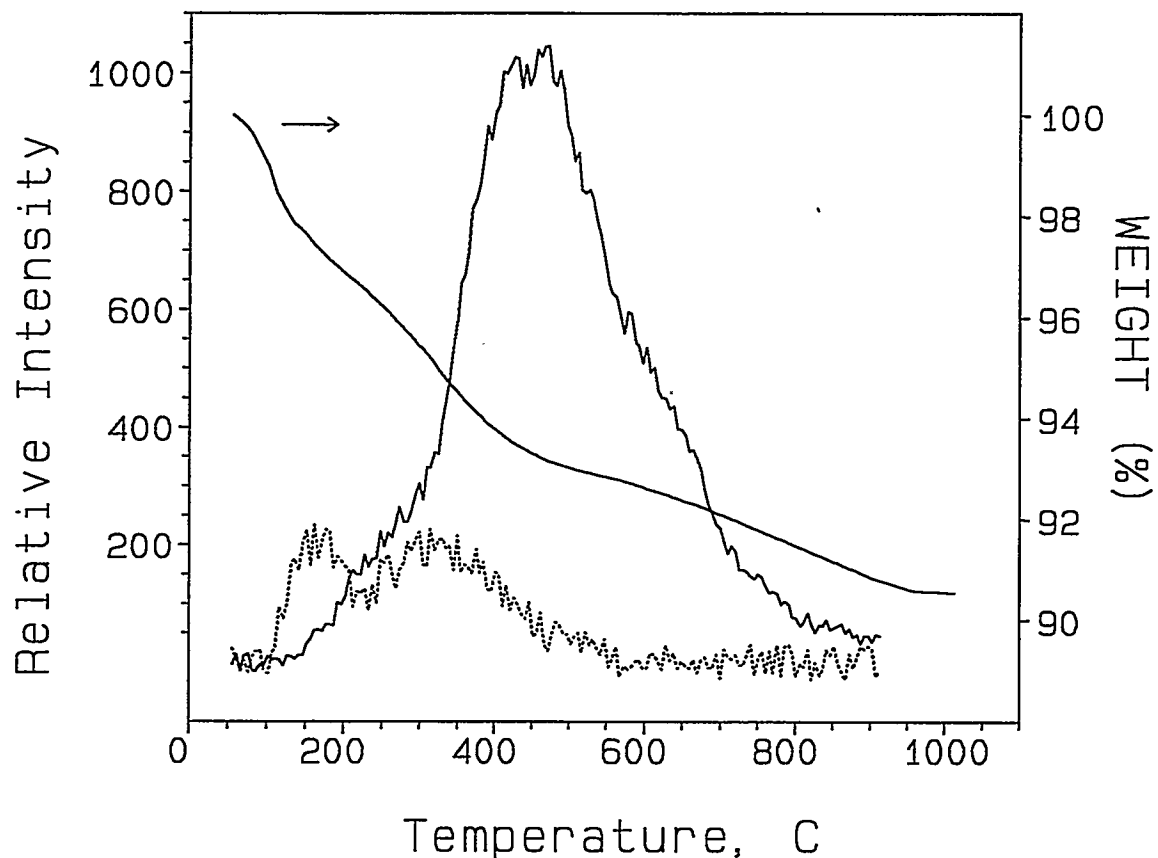


Fig. 2. TGA of plasma-generated silicon nitride powder. The weight loss curve is referred to the right. The mass spectral data for  $H_2$  (solid curve) and  $NH_3$  (dashed curve) are referred to the left.

that the extra loss of nitrogen may occur predominately from the near surface regions of the particles.

The freshly synthesized nano-powder is heated at 800 °C in various pressures of ammonia. At an ammonia pressure of 200 Torr or above, the powder retains its white color. FTIR spectra of these heat-treated samples (Fig. 3a) show the complete elimination of SiH functionality. This powder is resistant to oxidation (or hydrolysis) in atmosphere



Figure 3

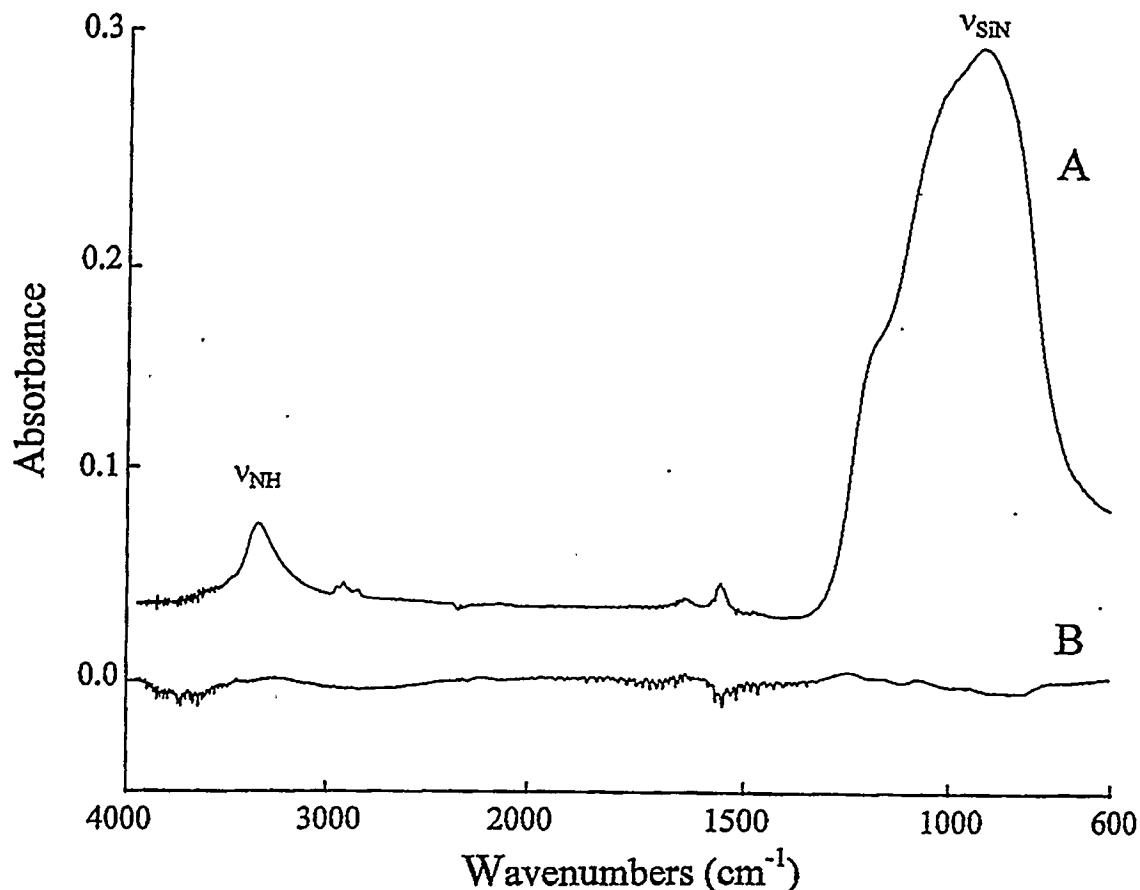


Fig. 3. FTIR spectrum of silicon nitride powder after heating at 800 °C for 20 minutes. A) Fresh from oven, B) Difference spectrum after 24 hour air exposure.

(Fig. 3b); no detectable appearance of SiO functionality is observed after 3 days of atmosphere exposure.

We apply the rf plasma technique to the synthesis of silicon carbide using gas mixtures of silane and methane in analogy with the successful silicon nitride technique. Powder is readily generated from such mixture over a wide range of gas mixtures (10-90% silane) and rf powers (5-50 Watts). The powders formed are extremely sensitive to air-oxidation, making it difficult to obtain FTIR spectra without

significant oxide formation. In fact, on venting the plasma apparatus to air, the powder spontaneously combusted in some instances. The FTIR spectrum (Fig. 4a) shows very significant content of SiH ( $2100\text{ cm}^{-1}$ ), and  $\text{CH}_n$  ( $2900\text{ cm}^{-1}$ ), functionality. Powder generated from silane/ethylene gas mixtures is indistinguishable from silane/methane mixtures.

Powder is also produced from plasmas containing gas mixtures of MTS and hydrogen, with or without added argon. The FTIR spectrum (Fig. 4b) shows significantly reduced CH and SiH features compared to Fig. 4a. A large feature at  $3200\text{ cm}^{-1}$  is probably the result of adsorbed HCl.

Particle morphology of the MTS/ $\text{H}_2$  powders is studied with TEM of samples produced from the pulsed plasmas. The morphology is similar to that of silicon nitride, roughly spherical particles with a significant fraction of the mass occurring in large agglomerates. A larger fraction of individual particles exhibit spherical shape, and the degree of hard agglomeration of SiC particles appears to be reduced relative to silicon nitride, but experiments are underway to investigate potential sampling bias. The fluid flow in the plasma apparatus is laminar through the showerhead and through the collection filter. Calculations suggest that the small particles,  $<100\text{ nm}$  diameter, will be significantly depleted by diffusion to the walls compared to the larger particles and agglomerates. TEM grids placed on the plasma walls appear to confirm this, collecting relatively more of the smaller particles. Large agglomerates are, however, also observed on these wall-mounted TEM grids. Since the fluid flow should prevent the more massive agglomerates from reaching the walls, it is probable that the agglomerates on the sidewalls grow in place by charge dipole induced attraction of incoming small particles at the surface.

Figure 4

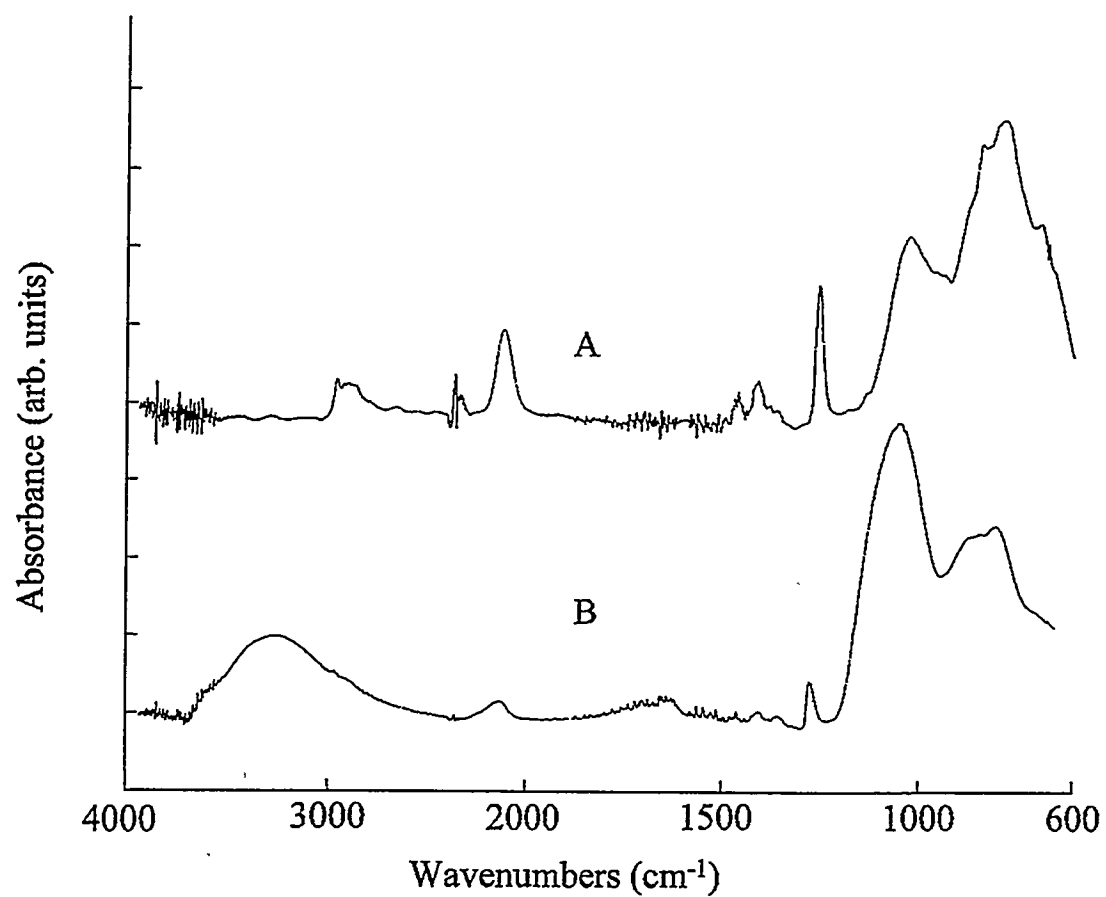


Fig. 4. FTIR of powder from a continuous silane/methane plasma, 50/50 gas mixture, 30 Watts power.

## CONCLUSIONS

The silicon nitride powders synthesized by pulsed rf plasma discharge can be stabilized with respect to air-oxidation by post-plasma heat treatment in an ammonia atmosphere at 800 °C. Heating the powder drives off the labile hydrogen, and the ammonia atmosphere prevents excessive loss of nitrogen. Particles can be generated from silane/hydrocarbon mixtures, but they are extremely sensitive to air oxidation. Particles from an MTS/H<sub>2</sub> plasma look promising as a precursor to silicon carbide.

## ACKNOWLEDGEMENTS

The author gratefully acknowledges the valuable assistance of Dr. Celeste Drewien for performing the TEMs and Michael Smith for excellent technical support. Also this work was supported by the United States Department of Energy under Contract DE-AC04-94AL85000.

## REFERENCES

1. G. J. Vogt and L. R. Newkirk, in *Proc. of the Symp. on High Temperature Materials-III*, edited by Z. A. Munir and D. Cubicciotti (The Electrochemical Society, Pennington, NJ, 1985), p. 164.
2. R. J. Buss and P. Ho, US Patent No. 4,769,064.
3. P. Ho, R. J. Buss, and R. E. Loehman, *J. Mater. Res.*, **4**, 873 (1989).
4. see for example, *Plasma Sources. Sci. Technol.*, **3**, (1994). Entire volume devoted to the topic.
5. L. Boufendi, A. Plain, J. Ph. Blondeau, A. Bouchoule, C. Laure, and M. Toogood, *Appl. Phys. Lett.* **60**, 169 (1992).
6. R. J. Buss and S. V. Babu, *J. Vac. Sci. and Technol.*, **14**(2), 582 (1996).

## SESSION III

# WORKSHOP ON MATERIALS RESEARCH AND DEVELOPMENT NEEDS FOR THE SUCCESSFUL DEPLOYMENT OF ADVANCED POWER GENERATION TECHNOLOGIES



## WORKSHOP ON MATERIALS RESEARCH AND DEVELOPMENT NEEDS FOR THE SUCCESSFUL DEPLOYMENT OF ADVANCED POWER GENERATION TECHNOLOGIES

The 1995 workshop identified several material needs for pressurized fluidized bed combustion (PFBC), integrated coal gasification combined cycle (IGCC), and indirectly fired cycles. The 1996 workshop focused on resolution of some of those issues through the definition or redefinition of projects under way.

**KEYNOTE ADDRESS:** John Stringer, Executive Scientist,  
Electric Power Research Institute,  
Palo Alto, California.

### SESSION A. WORKSHOP ON CERAMIC COMPOSITE INTERFACE COATINGS.

Rapporteurs: R. G. Smith, 3M Company  
R. E. Tressler, Pennsylvania State University  
Moderator: D. P. Stinton, ORNL

Ceramic composites are critical to high-temperature components for fossil energy systems both as hot-gas filters for IGCC and PFBC systems and as structural components, such as heat exchangers, for the indirectly fired cycles, externally fired combined cycle (EFCC), and Combustion 2000 systems. The development of ceramic composites with oxidation resistant interface coatings is extremely important to NASA, the Air Force, and DOE programs. Applications of these composites were summarized during the workshop and different approaches for oxidation resistant interface coatings will be discussed.

### SESSION B. WORKSHOP ON HIGH-TEMPERATURE MATERIALS BASED ON LAVES PHASES.

Rapporteurs: K. S. Kumar, Brown University  
J. H. Perepezko, University of Wisconsin  
D. J. Thoma, Los Alamos National Laboratory  
Moderator: C. T. Liu, ORNL

The Offices of Fossil Energy and Basic Energy Sciences of the Department of Energy jointly sponsored this review of critical issues related to alloy development of new high-temperature structural materials based on Laves phases. Laves phase materials, such as the high-temperature Cr-Nb alloys, are of interest because, characteristically, they are high-melting intermetallics that are extremely hard and strong, although brittle. These metallic, rather than ceramic, materials could provide high strengths up to 2300°F for systems such as the IGCC, PFBC, EFCC, and Combustion 2000.

### **SESSION C. WORKSHOP ON ALLOYS FOR VERY HIGH-TEMPERATURE APPLICATIONS.**

Rapporteurs: N. Birks, University of Pittsburgh  
 T. B. Gibbons, ABB Combustion Engineering  
 Q. J. Mabbutt, British Gas  
 Moderator: I. G. Wright, ORNL

Systems capable of operating at higher efficiencies, such as the low-emission boiler system (LEBS), require materials with higher temperature capabilities, in particular, higher creep strength and environmental resistance. A range of alloys developed from the best of the currently used wrought ferritic and austenitic alloys have improved high-temperature capabilities, and oxide dispersion-strengthened alloys are targeted for extremely high-temperature applications. This workshop examined the temperature capabilities of these alloys compared to current alloys and to the needs of advanced systems to identify their appropriate applications, information and actions required or under way to qualify them for such use, and their limitations.

### **SESSION D. WORKSHOP ON MATERIALS ISSUES ASSOCIATED WITH LOW NO<sub>x</sub> COMBUSTION CONDITIONS IN FOSSIL FUEL-FIRED BOILERS.**

Rapporteurs: J. L. Blough, Foster Wheeler  
 J. N. DuPont, LeHigh University  
 S. Kung, Babcock & Wilcox  
 J. Nava, ABB-Combustion Engineering  
 Moderator: I. G. Wright, ORNL

Some cases of severe corrosion of the furnace wall tubes are being experienced in utility boilers fitted with modern, low-NO<sub>x</sub> burners. It has been anticipated for some time that reducing conditions created as part of the low-NO<sub>x</sub> combustion process might result in sulfidation attack, but initial experience with such burners did not reveal such problems. The intent of this workshop was twofold: first, to better define the situation in terms of the form and rate of attack and to examine what is known about its root causes, and second, to review the potential for using corrosion-resistant materials as part of the solution. In particular, if the corrosion is due to sulfidizing conditions, the application of an iron aluminide as an overlay coating may prove a viable option.

### **WRAP-UP SESSION**

Workshop attendees gathered for summaries of deliberations from Sessions A through D.



## SUMMARY OF WORKSHOP ON CERAMIC COMPOSITE INTERFACE COATINGS

Wednesday, May 15, 1996  
Radisson Hotel  
Knoxville, Tennessee

Commercialization of fiber-reinforced composites has been limited because of the stability of the interface coatings that control the mechanical properties of the composites. Typical materials are currently manufactured with pyrolytic carbon interface coatings that perform well in inert atmospheres or when stresses are kept very low ( $<70$  MPa). Unfortunately, carbon coatings are not stable at high temperatures in air or oxidizing conditions which results in degradation of the mechanical properties of the composites. The problem of oxidation resistant interface coatings is not unique to the Fossil Program. Such coatings are also a concern to the United States Air Force, the Continuous Fiber-reinforced Ceramic Composites Program, the Fusion Energy Materials Program, and to the European Community. This workshop was organized to compare and discuss the need for and development of oxidation-resistant interface coatings in each of these programs.

### STATUS OF COMPOSITE FILTERS: A CURRENT APPLICATION (Robert Smith, 3M Company)

A novel type of hot-gas filter based on a ceramic fiber-reinforced ceramic matrix composite was developed and extended to full-size, 60-mm OD by 1.5-meter-long, candle filters. A commercially viable process for producing the filters was developed and the filters are undergoing testing and demonstration throughout the world for applications in pressurized fluidized-bed combustion (PFBC) and integrated gasification combined cycle (IGCC) plants. 3M Company ceramic composite filters performed well for 200 hrs in PFBC simulation tests at Westinghouse STC and for 1600 hrs in the Tidd demonstration plant. They have also functioned for thousands of hours in IGCC plants around the world. Both the simulation tests and the plant tests are providing data for the use of these filters. Each step in the development process has resulted in insights into the development of superior filters. One area of particular interest in the interface coatings. These materials must be stable in PFBC and IGCC conditions to sustain the mechanical properties of the filters. It is quite possible that different interface coatings will be required for the different combustion conditions.

### INTERFACE CONCEPTS FOR AIR FORCE APPLICATIONS

(Sankar Sambasivan, BIRL-Northwestern University)

Easy cleaving oxides are perhaps the only interface concept that draws a direct analogy to C and BN which has proven to be functional in SiC-based composites. The idea is to design a highly anisotropic oxide coating that has inherent low toughness planes which are preferentially aligned along the fiber axis such that interfacial debonding can occur through cleavage along these planes. The first candidate in the oxide family that was tested was mica-based phlogopites. These materials reacted extensively with the fiber and matrix such that their use was limited to low temperatures. Since then, several layered oxides have emerged that show promise for high temperature use. Among them, the family of beta aluminas and magnetoplumbites of several compositions are currently being examined. The alkali stabilized beta aluminas are attractive but are plagued with alkali loss problems at elevated temperatures (above 1000°C). The most recent and perhaps the most encouraging result was reported recently by Cinibulk where oriented coatings of hibonite ( $\text{CaAl}_{12}\text{O}_{19}$ ) were deposited on sapphire fibers. A TEM section of the coated fiber in alumina matrix showed cracks forming parallel to the basal planes of the hibonite. While this was encouraging, no push out for the fiber was observed in these composites presumably due to residual clamping stresses at the interface. A new family of layered perovskites have been proposed by Sambasivan and Petuskey that show highly anisotropic fracture behavior and seem to be well suited for CMC interfaces. Bulk samples of potassium calcium niobate have been prepared and tested for their anisotropic properties. Vickers indents placed on single grains of this material show extensive cracking in the basal direction with no apparent crack initiated in the normal direction. Development of coatings of potassium calcium niobate on to sapphire fibers for subsequent crack deflection tests and identification of other suitable compositions in the family of layered perovskites are in progress.

### INTERFACE CONCEPTS AT THE UNIVERSITY OF BORDEAUX

(Dick Tressler, Pennsylvania State University)

Researchers at the Laboratoire Composite Thermostructureaux (LCTS) at the University of Bordeaux in France are developing multi-layer SiC/C interface coatings where equivalent total thicknesses of carbon and SiC are deposited as alternating layers. Results indicate that the multilayer interfaces provide for similar behavior to that of equivalent monolayer total carbon thicknesses. A surface treatment has been developed at LCTS that removes the native silica layer from Nicalon fibers so that a carbon rich layer mates with the deposited carbon interface. These materials exhibit greater fiber-interface bonding, resulting in shorter pullout lengths and higher strengths. The tensile curves, however, reveal equivalent strain-to-failure to untreated Nicalon and therefore the material prepared with treated fibers is considered superior. Other work at LCTS focuses on layer-lattice

oxide interface materials. These include the phyllosiloxides developed by them based on phlogopites and fluorophlogopites. Great difficulty was encountered in depositing these phases on fibers.

### INTERFACE CONCEPTS FOR THE CFCC PROGRAM

(Rick Lowden, Oak Ridge National Laboratory)

The selection of the appropriate fiber coating composition and deposition technique is one of the most important tasks required for the development of reliable fiber reinforced ceramic composites for elevated temperature applications. The development of improved interface layers is being explored in the Continuous Fiber Ceramic Composite Program's Supporting Technologies Task. The thermochemical and thermomechanical aspects of potential fiber coatings for composite systems of interest have been examined. Vapor deposition, sol-gel, polymer precursors, and other deposition techniques are being evaluated to apply thin layers to fiber tows, cloth, or fibrous preforms for composite fabrication. Techniques developed and refined earlier in the program are being utilized for the characterization of the microstructure and composition of the coatings. Mechanical properties of as-fabricated composites, and specimens exposed to corrosive environments have been evaluated to assess the stability and reliability of new interlayer compositions. Instruments such as the Interfacial Test System have been used to examine the effects of processing, composition, microstructures, and environmental exposure on the properties of the fiber-matrix interface.

Much of the success in the development of improved fiber coatings has paralleled efforts to protect carbonaceous materials. Boron-containing materials such as boron-doped carbon and boron nitride provide improved oxidation resistance as compared to carbon through the formation of a glass layer that forms upon oxidation and seals the surfaces of the exposed interface. There are many questions concerning the performance and reliability of boron-containing layers. For example, there is little information about the relationships between the properties, microstructure, composition, and performance of boron nitride. The effects of processing conditions and contaminants on the microstructure, properties, and oxidation behavior of BN are being examined. The results of the effort will be used to provide input into the successful processing and utilization of BN as an interface coating for CFCCs.

It has been hypothesized that the ideal interface layer for a SiC/SiC composite would be a modified form of SiC. The fiber, interlayer, and matrix would be thermochemically and thermomechanically stable with respect to each other, and the constituents would exhibit similar stability at any operating temperature. An "all SiC" composite would be protected by a silica surface layer, adding to the life of the material in corrosive environments. The interlayer of choice would be a soft or low modulus SiC that would ensure debonding at the fiber-matrix interface and controlled fiber sliding to produce toughness and gradual failure. Silicon carbide interface coatings with controlled composition, microstructure, and

properties are being deposited employing chemical vapor deposition and liquid infiltration techniques. The goal is to develop a "porous" or low modulus SiC material to be used as a fiber coating. Composites fabricated from coated fabric are being characterized and tested.

The performance of multilayer coatings for controlling mechanical interactions at the fiber-matrix interface have been of growing interest in recent years. At least two multilayer systems for use in SiC/SiC composites are being explored in the CFCC Program. Systems consisting of alternating layers of carbon and SiC, and alumina and BN are being deposited by chemical vapor infiltration by Hypertherm and Amercom, Inc., respectively. Composition, microstructure, and properties are being characterized, and the results being used as feedback to the suppliers for future improvements.

#### INTERFACE CONCEPTS FOR FUSION APPLICATIONS

(Lance Sneed, Oak Ridge National Laboratory)

Fiber-reinforced SiC-matrix composites are being evaluated as a potential first wall material for fusion reactors. Interface coatings are also a significant concern to the Fusion Energy Program but for a very different reason. The Nicalon fibers and the SiC matrix are ideal materials for this application because they do not interact with neutrons during irradiation and become highly radioactive. Therefore, the materials can be much more easily handled, stored, or disposed of after irradiation. Unfortunately, carbon interface coatings swell during irradiation causing the matrix to crack and spall. The Fusion Energy Program is therefore exploring interface concepts that utilize materials that don't interact with neutrons and do not contain carbon. The most promising material at this time is the porous SiC coatings being developed jointly by the Fossil Energy Materials and CFCC Programs. Composites consisting of High-Nicalon fibers (ultra low oxygen), a porous SiC interface, and a SiC matrix have been fabricated for irradiation testing. Mechanical property characterization of the composites revealed high quality materials with flexure strengths of nearly 400 MPa. These materials will be thoroughly characterized after irradiation.

## **SUMMARY OF WORKSHOP ON HIGH TEMPERATURE MATERIALS BASED ON LAVES PHASES**

Wednesday, May 15, 1996  
Radisson Hotel  
Knoxville, Tennessee

The Offices of Fossil Energy and Basic Energy Sciences of the Department of Energy jointly sponsored the Workshop on High Temperature Materials Based on Laves Phases in conjunction with the Tenth Annual Conference on Fossil Energy Materials held at the Radisson Summit Hill Hotel in Knoxville, Tennessee on May 14-16, 1996. The objective of this workshop was to review the current status and to address critical issues in the development of new-generation high-temperature structural materials based on Laves phases. The one-day workshop included two sessions of overview presentations and a session of discussion on critical scientific and technological issues.

The Laves phases represent an abundant class of intermetallic alloys with possible high-temperature structural applications. Laves phases form at or near the  $AB_2$  composition, and there are over 360 binary Laves phases. The ability of these alloys to dissolve considerable amounts of ternary alloying additions provides over 900 combined binary and ternary Laves phases. Many Laves phases have unique properties which make them attractive for high-temperature structural use. At half their homologous temperature, they retain  $>0.85$  of their ambient yield strength, which is higher than all other intermetallics. Many of the Laves phases also have high melting temperatures, excellent creep properties, reasonably low densities, and for alloys containing Cr, Al, Si or Be, good oxidation resistance. Despite these useful properties, the tendency for low-temperature brittleness has limited the potential application of this large class of alloys.

The possible mechanisms governing the plastic deformation of Laves phases are discussed extensively at the Workshop. Because of complex crystal structures, Laves phases have limited active slip systems. Theoretically, Laves phases can deform by synchro-shear at ambient temperatures; however, the operation of this mechanism needs to be confirmed experimentally. It is important to point out that monolithic Laves phases such as  $HfV_2$  are deformable at room temperature.  $HfV_2$  can be cold worked extensively without fracture. Effort should be placed on comparison of the different deformation behaviors of  $HfV_2$  and other Laves phases. Twinning is possibly operative in Laves phases. Both theoretical and experimental work is needed in order to define the conditions required for such microtwinning in Laves phases.

Although experience indicates that monolithic Laves phases are generally brittle, dual-phase alloys containing bcc phases demonstrate encouraging deformability. Multilayers

of HfV<sub>2</sub>+Nb have been cold-rolled up to 30% without fracture. In addition, dual-phase NbCr<sub>2</sub>/Nb and NbCr/Cr alloys indicate promising ambient-temperature fracture toughness, with values ranging from 7 to 15 MPam<sup>1/2</sup>.

To fully develop the potential of Laves phases, three main issues need to be addressed: (1) alloy design, (2) structural stability, and (3) property evaluations. Alloy design is required to fully recognize the enormous base of alloying potential in Laves phases, and the role of defects, stacking faults, and bond strengths needs to be better understood. Structural stability is governed by both the atomic size and electronic structure of the Laves phases, and a structural instability may give rise to the tendency for twinning at ambient temperatures. Different sample quality may have resulted in the spread of the literature values for the physical and mechanical properties of Laves phases, and there is a need for full characterization. Moreover, the deformation modes and mechanisms require better definition to couple with the mechanical behavior of the material. In dual-phase bcc/Laves alloys, the deformability of these alloys has been observed, and the role of the bcc phase on the Laves phase deformation needs more attention.

## SUMMARY OF WORKSHOP ON ALLOYS FOR VERY HIGH-TEMPERATURE APPLICATIONS

Wednesday, May 15, 1996  
Radisson Hotel  
Knoxville, Tennessee

In current fossil energy systems, the maximum operating temperatures experienced by critical metal structures do not exceed approximately 732°C (1350°F), and the major limitation on the use of the alloys typically is corrosion resistance. In systems intended for higher performance and higher efficiency, increasingly higher working fluid temperatures will be employed, which will require materials with higher-temperature capabilities, in particular, higher creep strength and greater environmental resistance. There have been significant developments in alloys in recent years, from modifications of currently-used wrought ferritic and austenitic alloys with the intent of improving their high-temperature capabilities, to oxide dispersion-strengthened alloys targeted at extremely high-temperature applications.

The aim of this workshop was to examine the temperature capability these alloys compared to current alloys, and compared to the needs of advanced fossil fuel combustion or conversion systems, with the goals of identifying where modified/new alloys would be expected to find application, their limitations, and the information/actions required or that are being taken to qualify them for such use. The questions that were addressed, and a synopsis of the answers, were as follows:

- (1) *What are the temperature capabilities and limitations of current high-temperature alloys, and of advanced alloys?*

Several of the new or improved alloys are capable of meeting the needs of applications such as the Low-Emissions Boiler System (LEBS); the requirements of the High-Performance Power System (HIPPS) cycle are more difficult to meet with conventional alloys, although oxide dispersion-strengthened (ODS) alloys have properties that match some of the needs. Although the property data produced for these alloys are very interesting, they usually are available for relatively short times. The real need, especially for creep, is for long-term data such as are required for ASME Boiler and Pressure Vessel Code qualification; however, such data generation is expensive. A further limitation is that there usually are no data available on the effects of corrosion on strain, and vice-versa; these considerations assume increased importance as metals are applied at higher fractions of their melting temperatures. There is a need for a better method for extrapolating short-term data to speed up the ability to use new alloys; an associated problem is that the ASME Code is overly conservative.

- (2) *How do these capabilities match the apparent needs of current and planned power generation cycles, and what are the likely applications of current and new high-temperature alloys?*

Neil Birks of the University of Pittsburgh presented a methodology for matching the stress and strain criteria for a given component in a given cycle to the capabilities of available alloys. This approach appears to have great merit since it provides in diagrammatic form the first step in selecting alloys that could be considered for specific applications. This approach is based on the mechanical property requirements, and must be supplemented by considerations of environmental compatibility, fabricability, and repairability. Of concern in higher-temperature applications is the problem resulting from the differences in coefficient of thermal expansion when joining ferritic and austenitic alloys. A case can be made for eliminating austenitic alloys in some applications by using improved ferritic steels to their maximum temperature (which is approaching that of some austenitic alloys), and then changing to superalloys, or ceramics.

- (3) *What are the pacing alloy properties required for the various advanced cycle scenarios? Can we prioritize the needed property-temperature-environment combinations?*

The desired mechanical properties are highly dependent on the particular component and cycle being considered. In addition, using improved alloys to upgrade the temperature capabilities of a given component necessitates consideration of the impact on the materials used for components downstream. In the case of advanced steam boilers, for instance, higher-temperature steam capability from the use of improved superheater/reheater alloys results in a need for improved alloys for the main steam lines and the steam turbine. If such alloys are not available for fabrication of those components, the improved superheater/reheater alloys will not be used. Considerations of weldability and repairability also are important, especially with complex systems. Overall, materials selection is governed by the ASME Boiler Code which, unfortunately, is in need of updating since the maximum temperature considered is approximately 900°C (1650°F), and 816°C (1500°F) for some materials, and many of the newer alloys have not been Code-qualified.

- (4) *Where do ODS alloys fit into the overall need for high-temperature materials in advanced power generation cycles?*

As indicated by the ranking of alloy properties by system/component requirements in (2), ODS alloys have useful creep strength at temperatures significantly higher than for advanced, conventional structural alloys. For instance, the stress to cause rupture in 10,000 hr. at 1300°C (2372°F) is approximately 20 MPa (2.9 ksi; in the axial direction). This strength, combined with the excellent environmental resistance up to at



least 1300°C, suggests that ODS alloys are alternative candidates for a number of applications for which ceramics are targeted. If ODS alloys were used in advanced cycles to handle working fluid temperatures up to, for instance, 1200°C (2200°F) or so, the very high-temperature duty ceramic heat exchanger part of the circuit could be relatively small, and possible more readily designed and fabricated. Such alloys are also candidates for handling high-temperature steam in advanced steam cycles.

- (5) *At what stage of development is commercial ODS-alloy heat exchanger tubing? And, given the specialized nature of ODS alloy processing, what is its near-term availability? What practical experience is available for processing, forming, and joining ODS alloys?*

Processing of ODS alloys has progressed so that reproducible properties are achieved. The strength in the transverse direction (hoop strength in tubes) is lower than in the axial direction, but improvements are being made continually. ODS-FeCrAl alloys are available in rod, sheet, foil and tubular forms. The maximum size currently available of seamless tubes is 3 in OD (0.2 in wall) x 11 ft long. There are two major suppliers. Since the alloys have highly-directional properties, fabrication and joining require special considerations. The alloys can be bent (after preheating to 300°C), and can be joined. However, fusion welding creates weak zones since it redistributes the oxide dispersion. Joining of ODS-to-ODS and ODS-to-conventional alloys by diffusion bonding, explosive bonding, and friction bonding has been demonstrated. The friction bonding techniques also are applicable to joining ODS alloys to ceramics. There is experience in fabricating ODS tube-to-header joints; British Gas has produced and tested a harp-design heat exchanger that consists of 36 ODS tubes each 3.7 m (12 ft) long. Although these alloys have excellent resistance to corrosive gases, information is needed on their resistance to ash and slag deposits, such as are found in coal-combustion and conversion environments.



## **SUMMARY OF WORKSHOP ON MATERIALS ISSUES ASSOCIATED WITH LOW- NO<sub>x</sub> COMBUSTION CONDITIONS IN FOSSIL-FIRED BOILERS**

Wednesday, May 15, 1996  
Radisson Hotel  
Knoxville, Tennessee

It was anticipated by some members of the high-temperature corrosion community that the fitting of low-NO<sub>x</sub> burners to coal-fired power plants would lead to an increase in furnace wall corrosion, as a result of the relatively substoichiometric conditions created by the staged combustion process. These expectations were not borne out by initial experience. Recently, however, cases of severe furnace wall corrosion have been reported by some U.S. utility boilers retrofitted with modern low-NO<sub>x</sub> burners.

There is extensive experience of furnace wall corrosion in utility boilers in the U.K., which indicates that excessive fireside corrosion rates (>100 nm/hr; 34 mil/yr.) are experienced when tubes are exposed simultaneously to substoichiometric gaseous environments (CO>3.0 percent) and high radiant heat fluxes. Such conditions may be generated when flame impingement occurs. Where such conditions persist, increases in fuel chlorine content will exacerbate the rate of metal loss. In the absence of either circumstances, corrosion rates are much reduced and little influence of coal chlorine content is anticipated. Although the corrosion is essentially sulfidation caused by H<sub>2</sub>S in the flue gas, the contribution of fuel sulfur in the corrosion experience by U.K. boilers is unresolved, partly because of the relatively small range in sulfur content of coals burned in U. K. utility boilers.

The intent of this workshop was three-fold:

- to better define the problem in terms of the form and rate of attack,
- to examine what is known about its root causes, and
- to review the potential for using corrosion-resistant materials as part of the solution.

The questions that were addressed, and the responses were:

- (1) *Is the fireside corrosion being experienced in boilers retrofitted with low-NO<sub>x</sub> burners a significant problem?*

The overwhelming opinion of the workshop was that boilers retrofitted with low-NO<sub>x</sub> burners are experiencing significant corrosion of the furnace walls. The rates of metal loss are in the range 96 to 226 nm/hr (33 to 78 mil/yr.), compared to the 49 to 87 nm/hr (17 to 30 mil/yr.) experienced before retrofitting low-NO<sub>x</sub> burners.

- (2) *Is the problem actually associated with low-NO<sub>x</sub> operation? Or is the cause a combination of changes made in boiler operation that coincided with the installation of low-NO<sub>x</sub> burners?*

The observation of all of the boiler manufacturers represented at the workshop (ABB-Combustion Engineering; Babcock & Wilcox, and Foster Wheeler) was that the problem was directly linked to the operation of low-NO<sub>x</sub> burners. Boilers with historically high furnace wall corrosion rates have exhibited increased corrosion with low-NO<sub>x</sub> burners. Further, this form of attack has occurred in eight tangentially-fired boilers that are burning coal with a sulfur content in excess of 1.5 percent, and that have a history of furnace wall corrosion. The corrosion occurs in locations on the back walls where the flame pattern apparently is distorted as the gas flows toward the furnace 'nose.' Higher than usual heat fluxes are measured in those areas.

- (3) *Can we define the rate of material wastage and the type of attack in such a way that direct comparisons can be made with existing understanding of possible corrosion mechanisms?*

Where detailed measurements have been made, the flue gas in contact with the walls in areas where the accelerated corrosion is observed has levels of CO > 5 percent, and H<sub>2</sub>S up to 500 ppm, which indicates highly-sulfidizing conditions. In addition, carbon-rich deposits (up to 8 percent loss on ignition) containing FeS (pyrites), ZnS, and FeC are found. The corrosion scales consist of an outer layer of iron sulfides, with an inner layer consisting mostly of iron oxides but containing some sulfides adjacent to the metal surface. The corrosion morphologies appear consistent with gas-phase sulfidation attack.

- (4) *What is needed to allow the root cause of the corrosion to be assessed: are available failure analysis data suitable for more extensive study? Do we know enough to simulate the attack in the laboratory? Are field probe tests needed?*

Laboratory simulation (EPRI project at Babcock & Wilcox) reproduced the corrosion morphologies found in actual boilers but, for the same metal temperature and gas CO and H<sub>2</sub>S levels, the rate of corrosion was significantly lower than found in the boiler. Comparing the corrosion rates and conditions measured in the U.S. boilers with the U.K. criteria for excessive furnace wall corrosion suggests that a high heat flux, i.e. flame impingement, also is experienced in the boilers, but was not simulated in the laboratory tests. The same laboratory tests suggested that 300-series stainless steels are extremely resistant to the simulated conditions. It was considered that there is a need for field testing of alloys and coating compositions known to exhibit resistance to sulfidation attack, applied by coating methods with the potential for depositing non-porous, crack-free layers.

- (5) *What remedial measures are being used? How effective are they?*

The main approach to overcome this corrosion problem appears to have been to use high-alloy coatings. In some cases, affected areas have been coated, in others, test panels of different coatings have been installed in boilers. Commercial plasma sprayed coatings appear to be less effective than, for instance, high-velocity oxy-fuel and weld overlay coatings because of coating porosity. Cracking of coatings of austenitic alloys also has led to loss of protection. The best approach was thought to be to use a high-chromium ferritic alloy together with an application method that produces a dense coating. The best reported performance from coatings monitored by LeHigh University was an increase in life to 18 months, from 6 months for bare tubes. Other suggested remedial measures were to avoid high-sulfur coal, and to employ air blanketing of the affected areas.

- (6) *Is there a role for materials/coatings to mitigate this problem?*

Although it was expected that the problem could be mitigated by proper tuning of the low-NO<sub>x</sub> burners for a given boiler operating at a given output on a given coal, it was considered unlikely that this would be achieved in all cases. Therefore, there is a continuing need for the application of more resistant alloys or coatings locally in the affected regions. The desired coating appears to consist of an alloy capable of reliably forming a protective scale of chromium or aluminum oxide, that could be deposited in a non-porous, crack-free condition, at a low cost. In addition to the high-Cr austenitic alloys usually associated with good sulfidation resistance, high-Cr and high-Al ferritic alloys (for instance, Fe<sub>3</sub>Al) should be considered as candidates.



**SESSION IV**

**NEW ALLOYS**





## ODS IRON ALUMINIDES

I. G. Wright, B. A. Pint, E. K. Ohriner, and P. F. Tortorelli

Oak Ridge National Laboratory  
P. O. Box 2008  
Oak Ridge, Tennessee, 37831-6156.

### ABSTRACT

The overall goal of this program is to develop an oxide dispersion-strengthened (ODS) version of  $\text{Fe}_3\text{Al}$  that has sufficient creep strength and resistance to oxidation at temperatures in the range 1000 to 1200°C to be suitable for application as heat exchanger tubing in advanced power generation cycles. The program has two main thrusts: (a) alloy processing, which involves mechanical alloying and thermomechanical processing to achieve the desired size and distribution of the oxide dispersoid, as well as the desired alloy grain size and shape, and (b) optimization of the oxidation behavior to provide increased service life compared to ODS-FeCrAl alloys intended for the same applications. Control of the grain size and shape in the final alloy is very dependent on the homogeneity of the alloy powder, in terms of the size and distribution of the dispersed oxide particles, and on the level of strain and temperature applied in the recrystallization step. Studies of the effects of these variables are being made using mechanically-alloyed powder from two sources: a commercial powder metallurgy alloy vendor and an in-house, controlled environment high-energy mill. The effects of milling parameters on the microstructure and composition of the powder and consolidated alloy are described. Comparison of the oxidation kinetics of ODS- $\text{Fe}_3\text{Al}$  alloys with commercial ODS-FeCrAl alloys in air at 1000-1300°C indicated that the best  $\text{Fe}_3\text{Al}$ -based alloys oxidized isothermally at the same rate as the ODS-FeCrAl alloys but, under thermal cycling conditions, the oxidation rate of ODS- $\text{Fe}_3\text{Al}$  was faster. The main difference was that the ODS- $\text{Fe}_3\text{Al}$  experienced significantly more scale spallation above 1000°C. The differences in oxidation behavior were translated into expected lifetimes which indicated that, for an alloy section thickness of 2.5 mm, the scale spallation of ODS- $\text{Fe}_3\text{Al}$  leads to an expected service lifetime similar to that for the INCO alloy MA956 at 1100 to 1300°C.

### INTRODUCTION

Interest in advanced cycles that involve indirectly-fired gas turbines, in which coal- or gas-fired high-temperature heat exchangers are used to heat a working fluid in a closed system, has led to investigation of materials for heat exchangers capable of operation at temperatures on the order of 1200 to 1300°C. The candidate materials are ceramics and, possibly, oxide dispersion-strengthened (ODS) alloys. An ODS

FeCrAl alloy was found to meet the strength requirements for such an application in which the working fluid at 0.9 MPa was to be heated from 800 to 1100°C over a tube length of 4 m [1].

The oxidation life of ODS FeCrAl alloys is determined by their ability to form or reform a protective alumina scale, and can be related to the time for the aluminum content of the alloy to be depleted to some minimum level [2]. As a result, the service life is a function of the available aluminum content of the alloys and the minimum aluminum level at which breakaway oxidation occurs. Hence there is a limit on the minimum cross section which can be safely employed at temperatures above 1200°C. Because of their significantly higher aluminum content ( $\geq 28$  atom %/ $\geq 16$  wt. percent compared to  $\approx 9$  atom %/5 wt. percent), alloys based on  $\text{Fe}_3\text{Al}$  afford a potentially larger reservoir of aluminum to sustain oxidation resistance at higher temperatures and, therefore, offer a possible improvement over the currently-available ODS FeCrAl alloys, providing they can be strengthened in a similar manner.

The main thrusts of this program are to develop the alloy processing parameters that are required to achieve the typical ODS alloy structure that confers creep strength at extreme temperatures, and to optimize the alloy oxidation behavior to provide increased service life compared to ODS-FeCrAl alloys intended for the same applications. Development of the desired alloy microstructure involves control of the size and distribution of the oxide dispersoid, as well as the desired alloy grain size and shape. The ability to control the recrystallization of ODS alloys is very dependent on the homogeneity of the initial alloy powder, in terms of the size and distribution of the dispersed oxide particles, and on the level of strain and temperature applied in the recrystallization step.

## DEVELOPMENT OF MECHANICAL ALLOYING PARAMETERS FOR ODS $\text{Fe}_3\text{Al}$

### Experimental Procedures

A two-liter size horizontal attritor mill (Zoz GmbH, Kreustal, Germany) was installed at ORNL in order to perform mechanical alloying of iron aluminide powder while maintaining oxygen contents comparable to those in commercial mechanically alloyed materials. The grinding media consisted of high-carbon alloy steel balls of 5 mm diam. The rotational speed of the mill was maintained at 900 rpm, and the milling atmosphere was a static vacuum. The mill was operated by placing the media and powder in the mill, evacuating with a mechanical pump to a pressure of about  $5 \times 10^{-2}$  torr over several hours, and sealing the mill by use of a vacuum valve.

The starting powder was (in weight percent) Fe-15.9Al-2.2Cr-0.02B (FAS), which was screened to -100/+400 mesh. An addition of 0.47%  $Y_2O_3$  powder was made to each run. Two sources of  $Y_2O_3$  were used: one was a powder of nominal size of 5  $\mu m$ , and the second was a colloidal suspension of  $Y_2O_3$  in water with a reported particle size of 0.1  $\mu m$ . This material was dried and heated at 500 °C for 1 hour to produce a powder which had a typical particle size of 0.5 to 1  $\mu m$ . After conditioning the mill and grinding media by running the mill with FAS powder for 4 hr, an initial milling run was made using the 5  $\mu m$  size  $Y_2O_3$  addition. The mill contained 2 kg of grinding media and 200 g of powder. Samples were taken of the powder after total milling times of 1, 2, 4, 8, and 16 hr. Samples were taken through a sampling tube which allowed the milling chamber to remain under vacuum until the end of the total 32 hr run time. The samples were analyzed for oxygen and nitrogen content, and the powder characterized by scanning electron microscopy (SEM). Samples were also polished metallographically and viewed by SEM.

Three additional mill runs were made, each for 24 hr, using colloidal  $Y_2O_3$  with 2 kg of grinding media. The powder weights were 200, 300, and 400 g, corresponding to 10, 15 and 20% of media weight. Two runs were also made using 3 kg of media and powder weights of 450 and 600 g, corresponding to 15 and 20% of media weight, respectively. About 60 g of powder was typically found compacted against the corner of the chamber wall, and this material was segregated from the loose powder recovered from the mill.

The powders were placed in mild steel cans (5 cm OD and about 3 cm ID), evacuated and sealed. Prior to extrusion at a ratio of 10:1, the cans were preheated to 1100°C for 1 hr. An additional extrusion of the 600 g lot of milled powder was made at an extrusion ratio of 16:1. The extruded material from the 200 g powder lot (10:1 extrusion ratio) and the materials from the 600 g powder lot (10:1 and 16:1 ratios) were examined by optical metallography and chemically analyzed for oxygen, nitrogen and carbon. Metallographic analyses were performed on as-extruded material and also on samples heated at 1275°C for 8 hr in an evacuated quartz tube. Transmission electron microscopy (TEM) was performed on the alloy extruded at the 16:1 ratio.

## Results and Discussion

The average particle size of the initial milled powder samples was found to increase for up to 4 hr of milling, then decrease to 16 hr, after which time it remained constant. Also, the particle size of the milled powder and SEM showed no obvious changes after 24 hr milling at loadings of 2 or 3 kg of media and 200

to 600 g of powder. The polished powder samples when viewed by SEM contained a distribution of light-colored streaks, which were shown by energy dispersive X-ray analysis to be essentially pure iron. These regions apparently were associated with wear particles from the steel balls which became distributed in the milled powder. The oxygen content of the milled powder as a function of milling time is shown in Fig. 1. The calculated starting oxygen content consists of 1,000 ppm from the addition of 0.47% of  $Y_2O_3$  and 60 ppm in the FAS powder. The increase in oxygen content up to 1,700 ppm after 32 hr was attributed to leakage of air into the mill. The attritor mill when running empty had a leak-up rate of about 0.03 torr/min, as compared to a leak-up rate of about 0.005 torr/min when idle. The increase in oxygen content with time was consistent with the measured leak-up rate. An effort was made to determine the source of the increased leak rate while the mill was operating. Helium leak detection was not successful in measuring any transport of helium into the mill.

A weight gain was measured as a result of the milling process, apparently due to wear of the media; its dependence on the milling parameters (after 24 hr of milling) is shown in Fig. 2. The trend was to a significant decrease in weight gain at higher ratios of powder:media weight. The weight gains ranged from 3% at a 10% ratio to about 1% at a 20% ratio. The effect of changing the media weight from 2 to 3 kg appeared to have a minimal effect on the relative weight gain in milling.

The microstructures of the extrusions examined to date are shown in the optical micrographs in Figs. 3 (a) and (b). All the materials showed oxide stringers elongated in the extrusion direction. The extrusion produced from material milled with 200 g of powder and 2 kg of media had a uniform microstructure, whereas the extrusions produced with higher mill loading exhibited regions of large grains, which were

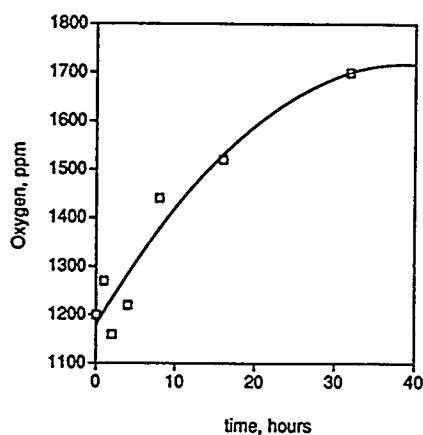


Fig. 1. Oxygen pickup during vacuum attritor milling.

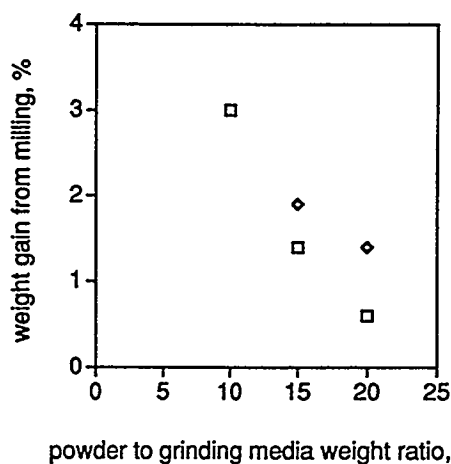


Fig. 2. Effect of milling parameters on weight gain from milling media wear.

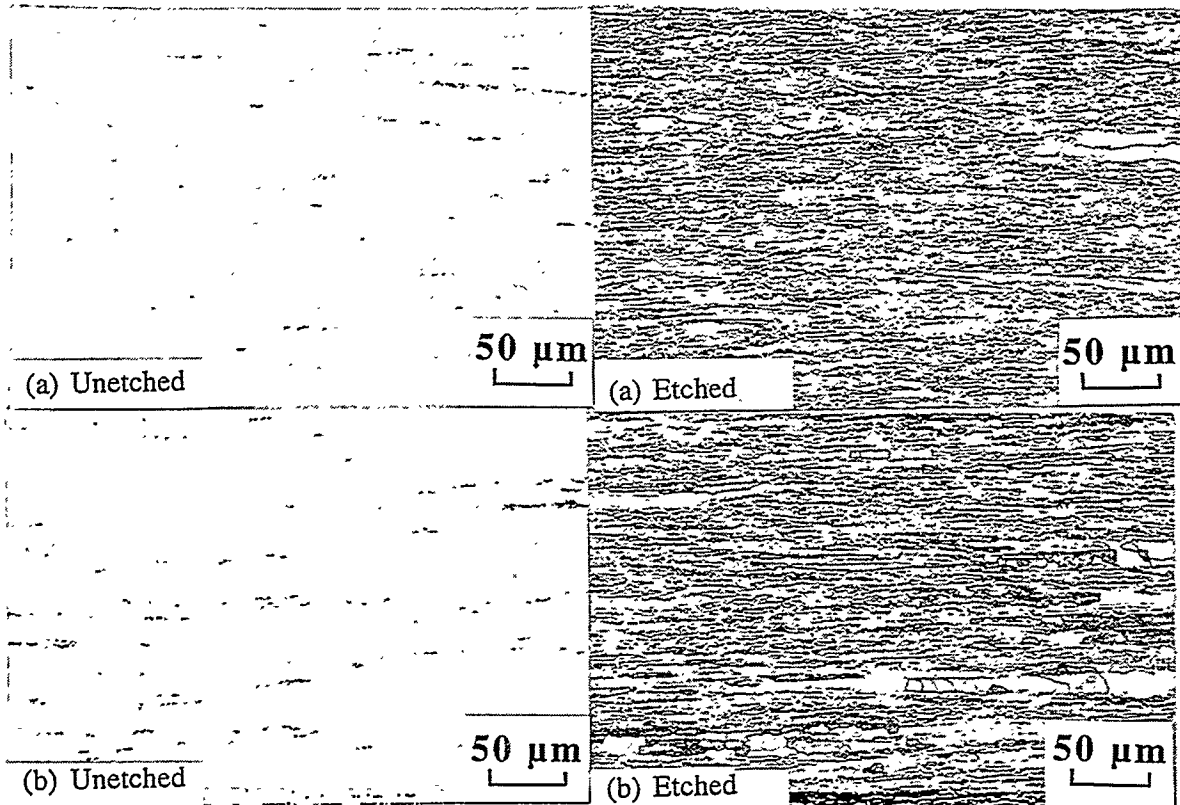


Fig. 3. Microstructures of extruded alloy powders (a) 200 g powder:2 kg media; extrusion ratio 10:1 and (b) 600 g powder:3 kg media; 16:1.

attributed to inadequate mixing of  $Y_2O_3$  particles during the milling. Transmission electron microscopy of the material milled with a powder load of 600g and extruded at a ratio of 16:1 indicated a bimodal distribution of oxide particles with the larger particles in the range of 0.2 to 1  $\mu m$ . The smaller particles were mostly in the range of 0.01 to 0.03  $\mu m$ . Preliminary analysis showed that all of the particles were complex oxides containing both yttrium and aluminum. The matrix was the ordered B2 phase.

Table 1. Chemical Analysis of Extruded Bars

Sample Powder		Extrusion Ratio	Concentration, ppm			
<u>Lot No.</u>	<u>Size, g</u>		<u>Oxygen</u>	<u>Nitrogen</u>	<u>Carbon</u>	<u>Sulfur</u>
220	200	10:1	1,620	160	740	20
360B	600	10:1	1,640	180	370	20
360A	600	16:1	1,760	100	400	20

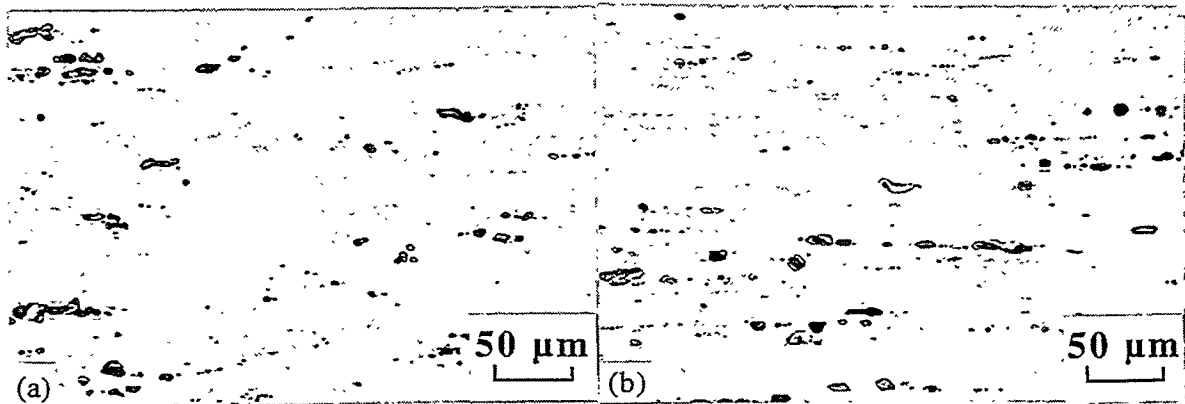


Fig. 4. Stringers of a second phase (possibly an oxide) in extruded alloys (600 g mill load) after recrystallization heat treatment (a) extruded at 10:1, as polished and (b) extruded at 16:1, as polished.

Chemical analysis results of three extruded bars are shown in Table 1. Oxygen content, in the range of 1,620 to 1,760 ppm, and nitrogen contents in the range of 100 to 180 ppm, are consistent with those obtained in an earlier 32 hr milling run; the oxygen contents are significantly lower than those obtained in a smaller attritor mill used in this program (of the order of 1% by weight) and are very similar to those reported for commercial mechanically-alloyed materials. For the 600 g powder lot, carbon contents of 370 and 400 ppm are within, but on the high end of the range of carbon contents measured in previous work and found in commercial ODS materials. The 740 ppm carbon value for the 200 g lot is considered high for this type of material. The carbon content of the steel balls is about 1%; the observed wear of the media would result in a calculated increase in carbon content in the milled powder of 100 to 300 ppm. These values are somewhat lower than the measured carbon contents shown in Table 1, but are within a factor of 2 of the measured values; there may be another source of comparable magnitude.

The microstructure following heating at 1275°C in vacuum was characterized by large quantities of a second phase in all three materials. The phase appeared to be an oxide, and was often strung out in the direction of extrusion. Figure 4 shows these features in as-polished sections; the features appeared to coincide with the location of the much smaller oxide stringers present in the as-extruded materials. The amount of second phase appeared to be higher in regions near the edges of the specimens, near the boundary with the can material. Detailed analysis is in progress to determine the source the second phase.

The material from the 600 g milling lot heat treated at 1275°C showed localized regions of visible grains among large regions with no visible grain boundaries. The material from the 200 g milling lot could

not be etched to show any grain boundaries, which may indicate that very large grains had been achieved by this treatment, although additional characterization is needed to confirm this.

## HIGH-TEMPERATURE OXIDATION BEHAVIOR OF ODS-Fe<sub>3</sub>Al ALLOYS

### Experimental Procedures

The alloys studied included two FeCrAl-based commercially-available oxide dispersion-containing alloys—Kanthal APM and INCO MA956—and an ODS-Fe<sub>3</sub>Al alloy (FAS3Y) made in an earlier phase of the program at ORNL. The compositions of the alloys are shown in Table 2. Kanthal APM is not optimized for high-temperature creep strength, but forms a protective alumina scale that exhibits excellent resistance to spallation [3]; this alloy, therefore, was considered a standard for high-temperature oxidation resistance. INCO MA956 represents the class of ODS alloys available as high-strength, high-temperature tubing. The Kanthal APM was obtained in the form of 1 mm-thick strips [3], whereas the MA956 was a nominally 3 mm-thick plate. The ODS-Fe<sub>3</sub>Al alloy was an as-extruded rod, nominally 1.6 mm (0.0625 in) diameter.

Table 2. Compositions of Alloys (weight percent)

Constituent	FAS3Y	Kanthal APM	INCO MA956*
Dispersoid	Y <sub>2</sub> O <sub>3</sub> -Al <sub>2</sub> O <sub>3</sub>	ZrO <sub>2</sub> -Al <sub>2</sub> O <sub>3</sub>	Y <sub>2</sub> O <sub>3</sub> -Al <sub>2</sub> O <sub>3</sub>
Cr	2.25	20.42	19.22
Al	16.3	5.54	4.32
Y	0.37	<0.01	0.5
Zr		0.10	
Ti	0.07	0.03	0.36
Si	0.10	0.23	
Mn	0.15	0.08	
C	0.03	0.03	0.01
O	0.0533**	0.0526	0.20
S	0.0061	0.001	0.011

\*Analysis for sample of rod stock

\*\*Before mechanical alloying

Specimens of dimensions 1.5 x 1.0 x 0.2 cm thick, or 1.25 cm diameter discs of thickness 1-2 mm from the ODS-Fe<sub>3</sub>Al, were polished to a 0.3  $\mu$ m alumina surface finish, and ultrasonically cleaned in acetone and methanol before exposure. Each specimen was placed in individual lidded, cylindrical alumina crucibles, which were then exposed in air for 500 hr intervals to 5,000 hr at 1000°C, and at 1100, 1200 and 1300°C at 100 hr intervals up to 1,500 hr. The alumina crucibles were baked at 1400°C for 8 hr prior to

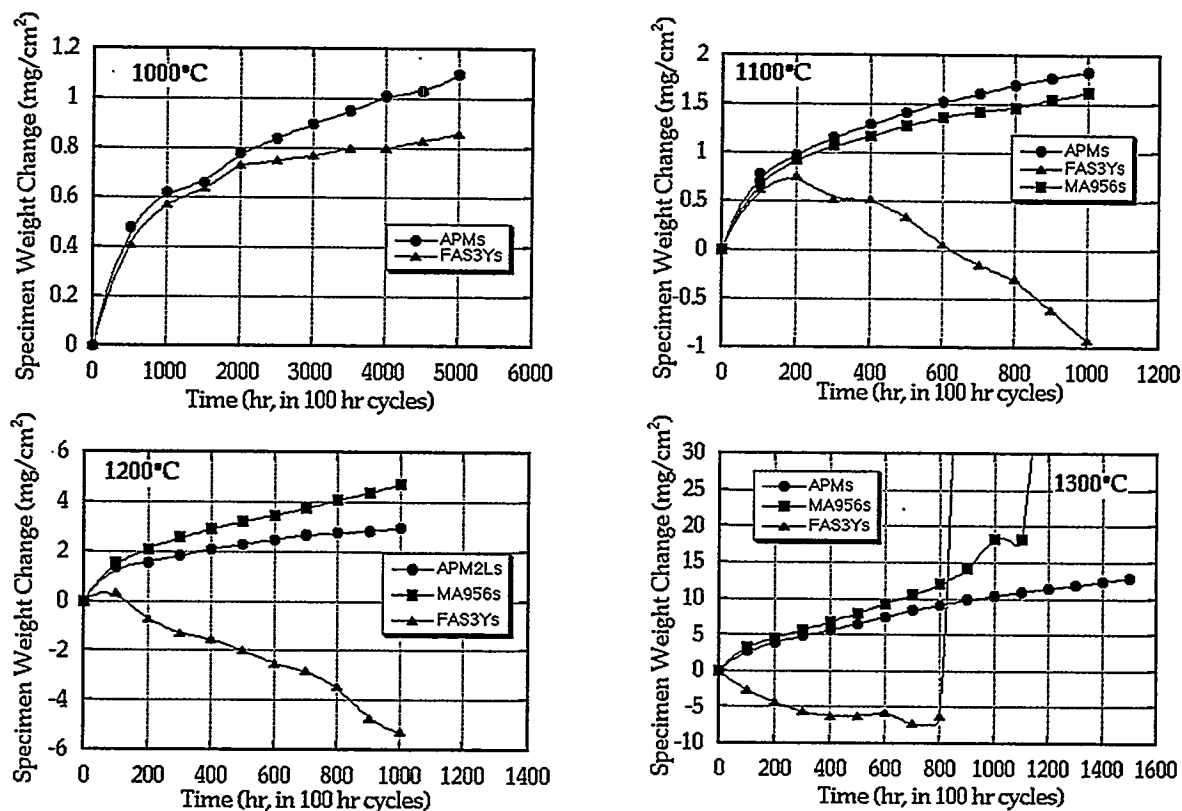


Fig. 5. Specimen weight change data after exposure to thermal cycling conditions.

use. Separate weighing of the specimens and crucibles allowed the total weight gain and the extent of scale spallation to be measured. The specimens and the crucibles (containing any spalled oxide) were weighed after cooling to room temperature on a Mettler model AE 240 balance.

## Results and Discussion

The trends in specimen weight change are shown in Fig. 5. The ODS-FeCrAl alloys exhibited net weight gains at all four temperatures, whereas the ODS-Fe<sub>3</sub>Al showed a net weight loss, following an initial gain, at 1100°C and higher. The overall oxidation rates (rate of oxygen uptake), from the sum of the specimen weight change and the spalled scale, as well as the weight of spalled scale, showed that, at 1000°C, the oxidation rate of the ODS-Fe<sub>3</sub>Al alloy was essentially the same as that of APM, with slightly more spallation from the ODS-Fe<sub>3</sub>Al. With increasing temperature, the overall rate of oxygen uptake of the ODS-Fe<sub>3</sub>Al increased faster than that for APM as a result of the increasing rate of scale spallation. The oxidation behavior of MA956 was intermediate between these two alloys. Log-log plots



of these data were made to determine the values of the parameters  $k$  and  $n$  in the oxidation rate equation, expressed as:

$$\Delta m = k \cdot t^n \quad (1)$$

where  $\Delta m$  is the weight change per unit area due to oxygen uptake,  $t$  is time, and  $k$  and  $n$  are constants. The values of the oxidation rate exponents,  $n$ , are listed in Fig. 6. The excellent oxidation behavior of APM was reflected in values of  $n$  that were consistently less than expected for parabolic scale growth ( $n = 0.5$ ). The  $n$  values for the other two alloys, which suffered increasing degrees of scale spallation with increasing temperature, increased from slower to faster than parabolic as the extent of scale spallation increased.

For ODS-FeCrAl alloys, the lifetime under high-temperature oxidation conditions may be limited by the ability of the alloy to maintain or reform its protective alumina scale [2]. Hence, a major point of comparison between ODS-Fe<sub>3</sub>Al and competing ODS-FeCrAl alloys is the oxidation-governed lifetime for a given thickness of alloy. Using the same considerations as Quadakkers and Bongartz [2,4], the kinetic data reported above were used to construct 'oxidation life diagrams' for the three alloys. As long as oxidation of the alloy involves the formation (and reformation following scale spallation) of an alumina scale, the effective life of the alloy can be calculated from the rate of consumption of aluminum (proportional to  $\Delta m$ , mg/cm<sup>2</sup>), and the total amount of aluminum available. Measurements on specimens oxidized to the point of breakaway oxidation, where an alumina scale no longer forms, have shown that the aluminum concentration profile in the alloy remains essentially flat [4,5], so that the aluminum reservoir available for use in protective scale formation can be calculated from:

- the initial aluminum content of the alloy ( $C_o$ , weight percent),
- the aluminum level at which a protective alumina scale can no longer be formed ( $C_b$ ), and
- the thickness of the section being oxidized ( $d$ , cm).

Hence:

$$k \cdot t^n \cdot M = (C_o - C_b)/100 \cdot d/2 \cdot \rho \quad (2)$$

where  $M$  is the weight fraction of aluminum reacted as Al<sub>2</sub>O<sub>3</sub> corresponding to the oxygen uptake,  $\rho$  is the density (mg/cm<sup>3</sup>) of the alloy, the units of  $k$  are mg/cm<sup>2</sup>.hr, and  $t$  is in hours. Rearranging, the time at which a protective alumina scale can no longer be formed, or the time to breakaway oxidation ( $t_b$ ), becomes:

$$t_b = [4.44 \times 10^{-3} \cdot (C_o - C_b) \cdot r \cdot d/k]^{1/n} \quad (3)$$

Values of  $C_b$  have been determined to be of the order of 1.15 wt. percent for APM [4] (the same value was assumed here for MA956), and 1.8 to 2.4 wt. percent for Fe<sub>3</sub>Al [5]. The resulting diagrams relating lifetime ( $t_b$ ) to wall thickness ( $d$ ) are shown in Fig 6. Figure 7 summarizes the effect of temperature on the oxidation-governed lifetime of the three alloys for a section thickness of 2.5 mm (0.1 in.). Overall, at 1000°C when the extent of scale loss from FAS3Y by spallation is small, its larger usable aluminum reservoir (16.3 vs 4.65 wt. percent) results in a longer life than for APM. As the proportion of the aluminum

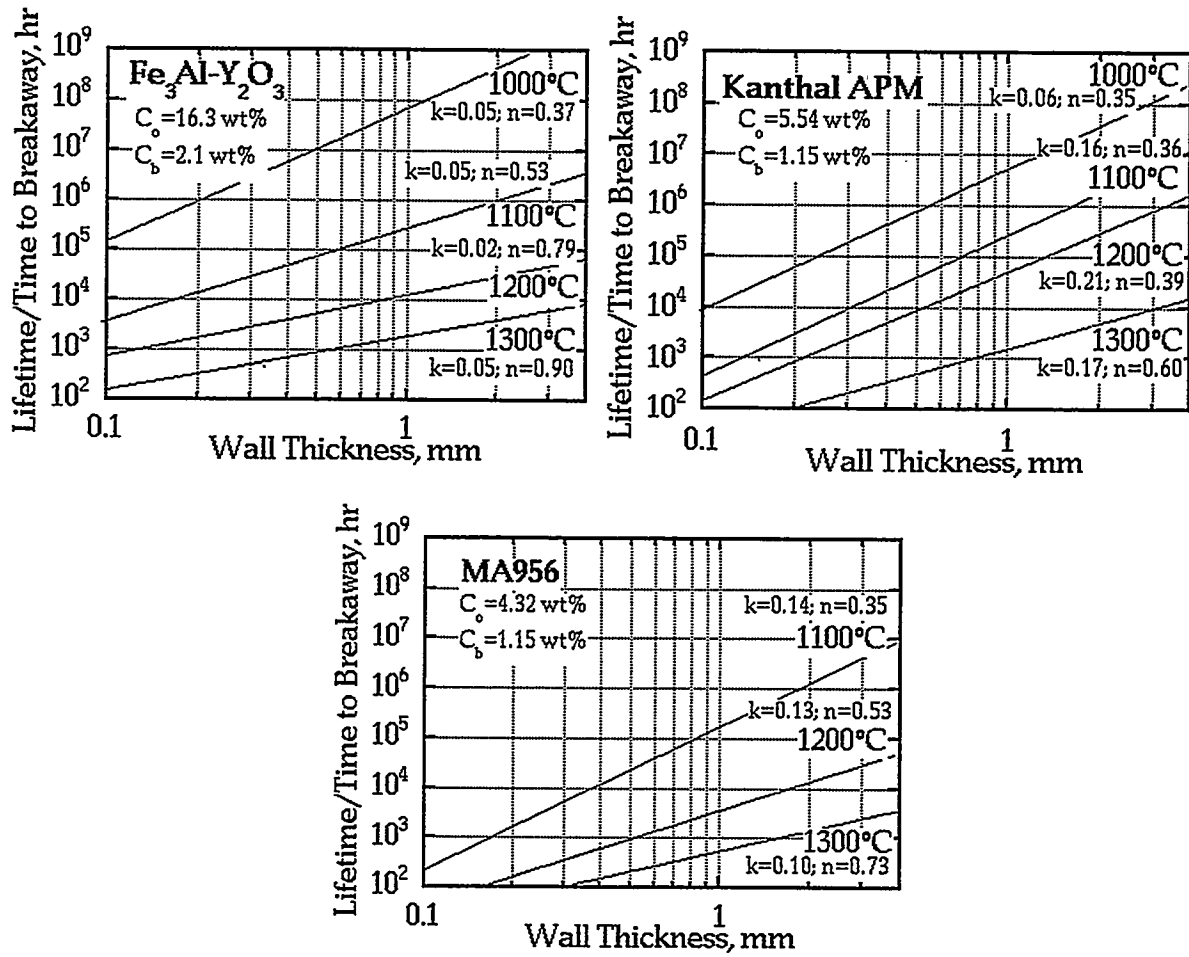


Fig. 6. Calculated oxidation-governed lifetimes as a function of wall thickness

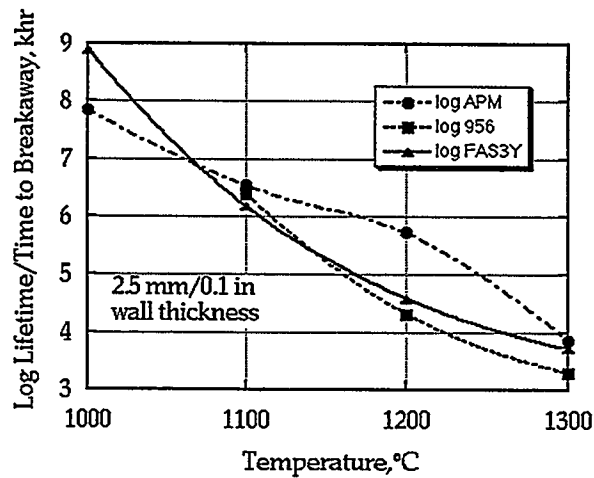


Fig. 7. Comparison of calculated lifetimes for a 2.5 mm thick alloy section.

reservoir consumed to replace scale lost by spallation increases with increasing temperature, the advantage of the large initial reservoir of FAS3Y compared to APM is lost as the temperature is increased to 1300°C, whereas at 1300°C all three alloys exhibited essentially the same calculated lifetimes. The effect of increasing scale spallation on the oxidation-governed life of APM becomes apparent only above 1200°C. In contrast, the moderate scale spallation of MA956 results in calculated lifetimes similar to those of FAS3Y. These oxidation exposures are continuing to determine if scale spallation eventually plays a role in limiting the oxidation lifetime of APM, and to generate data that can be used to test and refine the approach outlined here.

## CONCLUSIONS

Milling in a static vacuum produced low levels of oxygen contamination in the alloy similar to those found in commercial-scale ball-milled powder. There remains a possibility of achieving even lower levels of oxygen pick-up, below the range of 500 to 700 ppm now obtained, by better understanding of sealing issues associated with the mill.

Wear of the steel grinding media gives rise to several issues associated with the milled powder:

- an increase in the average iron content of the powder, which can readily be compensated for by adjusting the initial powder composition,
- inhomogeneity as evidenced by local iron-rich regions in the milled powder associated with wear particles detached from the grinding media toward the end of the milling run, and
- an increase in carbon content in the milled powder. Use of ceramic media is a possibility, but experience in its use in milling of ductile metal powder has not been good.

The heat treatment of the extruded materials at 1275°C for 8 hr resulted in very large grains in the fully-milled alloy, and etching was unable to reveal any grain boundaries. The  $Y_2O_3$  powder currently available appears to be too coarse to achieve a uniform distribution of very fine particles. An experimental batch of  $Y_2O_3$  having a nominal 30 nm particle size has been ordered from a commercial vendor. Currently the most important issue is the presence in all the materials of large stringers of a second phase following heat treatment at 1275°C. The second phase has the appearance of an oxide; if this is the case, a possible source may be air entrapped or adsorbed on the starting powder particles.

The overall rate of oxidation of an ODS-Fe<sub>3</sub>Al at 1000°C in air under thermal cycling conditions was found to be similar to that of the ODS-FeCrAl alloys Kanthal APM and INCO MA956 whereas, from 1100 to 1300°C, its oxidation rate was faster than those alloys due to a greater tendency to scale spallation. Nevertheless, the larger reservoir of aluminum in the ODS-Fe<sub>3</sub>Al resulted in a longer calculated oxidation-governed lifetime for the ODS-Fe<sub>3</sub>Al at 1000°C, for a given alloy thickness. At 1100 and 1300°C, all three alloys exhibited essentially the same calculated lifetimes but, in the intervening temperature range, APM clearly gave the longest lifetimes, with FAS3Y slightly better than MA956. Exposures are continuing to generate oxidation kinetics for a larger fraction of the alloy lifetimes, to allow the calculations to fully reflect the actual oxidation behavior. Work is in progress with the aim of decreasing the tendency for scale spallation by the ODS-Fe<sub>3</sub>Al alloy, which could result in an obvious lifetime advantage commensurate with its larger aluminum reservoir compared to the ODS-FeCrAl alloys.

#### ACKNOWLEDGMENTS

The authors acknowledge the support of the Fossil Energy Advanced Research and Technology Development (AR&TD) Materials Program, U. S. Department of Energy, under contract DE-AC05-84OR21400 with Lockheed Martin Energy Research, Inc. BAP was supported by the U. S. Department of Energy Distinguished Postdoctoral Research Program administered by the Oak Ridge Institute for Science and Education. The authors thank colleagues at ORNL: A. Duncan, who was responsible for the TEM work, V. K. Sikka, K. S. Blakely, M. Howell, L. D. Chitwood, and J. R. DiStefano for their contributions and invaluable discussions.

#### REFERENCES

1. F. Starr., A. R. White., and B. Kazimierzak., *in* Materials for Advanced Power Engineering 1994, D. Coutsouradis, et al., Eds., (Kluwer Academic Publishers, 1994) pp. 1393-1412
2. W. J. Quadackers, K. Bongartz, F. Schubert, and H. Schuster *in* Materials for Advanced Power Engineering 1994, D. Coutsouradis, et al., Eds., (Kluwer Academic Publishers, 1994) pp. 1533-1542
3. B. A. Pint, A. J. Garratt-Reed, and L. W. Hobbs, *Materials at High Temperatures*, 1 (1995) 3

4. W. J. Quadakkers, and K. Bongartz, *Werkstoffe u. Korrosion*, **45** (1994) 232
5. J. H. DeVan, P. F. Tortorelli, and M. J. Bennett, *Proc. Eighth Annual Conference on Fossil Energy Materials*, Oak Ridge, TN, (CONF-9405143; ORNL/FMP-94/1, 1994) pp. 309-320



THE INFLUENCE OF PROCESSING ON MICROSTRUCTURE  
AND PROPERTIES OF IRON ALUMINIDES

R. N. Wright and J. K. Wright

Idaho National Engineering Laboratory  
Lockheed Idaho Technologies Company  
Idaho Falls, ID 83415-2218

ABSTRACT

An Fe-28%Al alloy containing 5% Cr has been synthesized by reaction of elemental powders, followed by consolidation using hot extrusion. The resulting material is fully dense, homogeneous, and has a grain size of less than 5  $\mu\text{m}$ . Reaction synthesis results in an  $\text{Al}_2\text{O}_3$  dispersion that is uniformly dispersed during hot extrusion. Under some circumstances the hot extruded material undergoes secondary recrystallization, resulting in grain sizes greater than 25 millimeters. The fine grained material exhibits improved yield strength compared to the coarse grained material up to test temperatures of 800°C. Creep testing has shown that the coarse grained material has significantly improved time to rupture compared to fine grained material. The oxide dispersion strengthened material has significantly improved creep resistance compared to conventional powder metallurgy material. With proper heat treatment, the coarse grained material exhibits time to rupture of 425 hours at 650°C and a stress of 75 MPa, compared to 40 hours for conventional material of similar composition.

INTRODUCTION

Recent work indicates the problem of limited ductility exhibited by  $\text{Fe}_3\text{Al}$  may be overcome by small additions (2-5 wt%) of chromium.<sup>1</sup> Tensile elongation of  $\text{Fe}_3\text{Al} + 5\% \text{Cr}$  is found to approach 20% with little sacrifice in resistance to oxidation and sulfidation.<sup>2</sup> Unfortunately, the yield strength of  $\text{Fe}_3\text{Al}$  rapidly decreases above 500°C, thereby reducing the suitability of this material for high temperature applications.<sup>2</sup> Nickel-based materials, suffering from a similar decrease in high temperature strength, are strengthened through the incorporation of oxide particles (oxide-dispersion-strengthened or ODS alloys). The oxide particles impede dislocation motion, prevent grain boundary sliding, and inhibit grain growth at elevated temperatures, thus increasing the high temperature strength and creep resistance of these alloys.<sup>3</sup> Since the oxide dispersion affects the mechanisms of deformation, a similar improvement in high temperature strength is expected by incorporating an oxide dispersion into  $\text{Fe}_3\text{Al}$ .

This work examines the high temperature mechanical properties of fully dense  $\text{Fe}_3\text{Al}$ , produced by reaction synthesis from elemental powders followed by hot extrusion, and ascertains the influence of a dispersion of oxide particles on the observed increase in high temperature strength. In

this work, the surface oxide coating the elemental powders prior to reaction synthesis provide the desired dispersion of oxide particles in the processed material. The results are compared to  $\text{Fe}_3\text{Al}$  processed by hot extrusion of pre-alloyed powders, which lacks a dispersion of oxide particles. High temperature characterization of the various materials includes determination of their high temperature mechanical properties as a function of grain size and oxide particle size.

#### EXPERIMENTAL PROCEDURE

Reaction synthesized material was made using carbonyl iron (8  $\mu\text{m}$  diameter), helium gas atomized aluminum (10  $\mu\text{m}$  diameter) and chromium (1-5  $\mu\text{m}$  diameter) powders, mixed in the proper portions to yield Fe-28%Al-5%Cr. Reaction between the elemental powders occurred during a 2 hour thermal treatment at 1100°C in flowing argon. After canning in mild steel, full density rod was produced by hot extrusion (either 9:1 or 16:1 reduction in area) at extrusion temperatures from 900°C and 1200°C. Consolidated material lacking an oxide dispersion was produced via extrusion of pre-alloyed powder of composition  $\text{Fe}_3\text{Al} + 5\%\text{Cr}$ , made by gas atomizing a mixture of  $\text{Fe}_3\text{Al}$  alloyed with 5% chromium. The extrusion process was carried out at 1000°C with a 9:1 reduction in area.

Grain growth experiments were performed during one hour heat treatments in flowing argon at various temperatures. The mean grain size was determined by the linear intercept method on photomicrographs taken of polished and etched samples. Mechanical properties were evaluated during elevated temperature tensile or creep tests. Round cross section tensile bars, machined by centerless grinding from a portion of each of the materials, were tested in tension at various temperatures in laboratory air or in constant load creep tests.

#### DISCUSSION OF CURRENT ACTIVITIES

##### Characterization of Reaction Synthesized Material

The distribution and nature of the particles in the reaction synthesized material is of particular interest in this study. Characterization of the individual particles and their distribution is possible using transmission electron microscopy (TEM). The iron oxide on the elemental iron particles is reduced to iron by the aluminum during the reaction;<sup>4</sup> the oxygen available from this reduction reacts to form  $\text{Al}_2\text{O}_3$ . Extrusion



causes extensive deformation to the preform, forming stringers of particles. Electron diffraction from larger particles indicates their crystal structure to be that of  $\alpha$ -alumina. EDS and Auger spectroscopy also show the particles to contain small amounts of chromium and possibly iron.

We have demonstrated previously that the extruded oxide dispersion containing  $\text{Fe}_3\text{Al}$  exhibits behavior similar to that of oxide dispersion strengthened nickel.<sup>5,6</sup> Ni-based materials show extreme grain growth at high temperature as a few grains with high mobility boundaries break away from pinning particles and grow rapidly, driven by the reduction in total grain boundary area. The final grain size after secondary recrystallization is determined by the density of nuclei with high boundary mobility.<sup>6</sup> Therefore, the exact nature of the annealing response in the Ni-based materials is a function of the processing history, volume fraction of dispersoid and annealing schedule, and is consistent with the behavior of the material used in this study.<sup>5,6</sup>

In the oxide dispersion containing  $\text{Fe}_3\text{Al}$  when extrusion is carried out in a 9:1 reduction in area, material extruded at 900°C will undergo secondary recrystallization, while that extruded at 1100°C will not. In the current work, extrusion was carried out in a 16:1 reduction in area and material extruded at 900, 1000, and 1100°C underwent secondary recrystallization, while that extruded at 1200° did not. Detailed determination of the mechanisms responsible for the unusual grain growth of extruded, reaction synthesized material remains under investigation. An analysis by Hillert<sup>7</sup> suggests three conditions are necessary:

1. Second phase particles prevent normal grain growth.
2. The average grain size cannot exceed a critical value which is determined by dispersoid size and volume fraction.
3. At least one grain much larger than the average grain size must be present.

The reaction synthesized material has a critical grain size of about 7  $\mu\text{m}$ .<sup>8</sup> Since all of the reaction synthesized materials have approximately the same grain size after primary recrystallization, and all of the grain sizes are below the critical value, it appears differences observed in tendency to undergo secondary recrystallization are a result of differences in grain shape, texture, and/or the distribution of dispersoid.

Changing the extrusion temperature, and heat treatment of the extruded material, leads to significant differences in the average size of the oxide particles. TEM micrographs of the oxide dispersion in material extruded at 900 and 1100°C after heat treatment are shown in Figure 1 a, b and c. The oxides in Figures 1a and 1c represent the extremes observed for the extrusion conditions examined, with average sizes of 120 and 330 nm,

respectively. The effects of altering the oxide particle size on the mechanical properties are shown below.



Fig. 1. TEM micrographs of oxide particles resulting from: a) 900°C extrusion, 900°C 1 hour anneal; b) 900°C extrusion, 1300°C 1 hour anneal; and c) 1100°C extrusion, 1300°C 1 hour anneal.

#### Mechanical Properties

Figure 2 shows the yield strength of ODS Fe<sub>3</sub>Al alloys as a function of grain size. The fine grained material has nearly twice the yield strength of the pre-alloyed P/M material, and is also significantly stronger than coarse grained ODS material. The effect appears most dramatic at room temperature; however, the increment of strengthening has been retained at 800°C where the ODS material is still twice as strong despite severely diminished strength for all of the materials. The 2.7 μm grained material is strongest at all test temperatures while retaining room temperature ductility of approximately 2%; however the yield strengths of the 113 and 1000 μm grained materials do not vary significantly from one another. We have demonstrated previously that grain boundary sliding is not a significant deformation mechanism in the fine grained material for temperatures up to 900°C.

Despite the improved tensile properties in the fine grained material, very large grains are typically necessary in ODS alloys to achieve maximum creep properties. Creep curves are shown in Figure 3 for conventional powder metallurgy Fe<sub>3</sub>Al, fine grained ODS material (900°C extrusion followed by one hour anneal at 900°C) and coarse grained ODS material

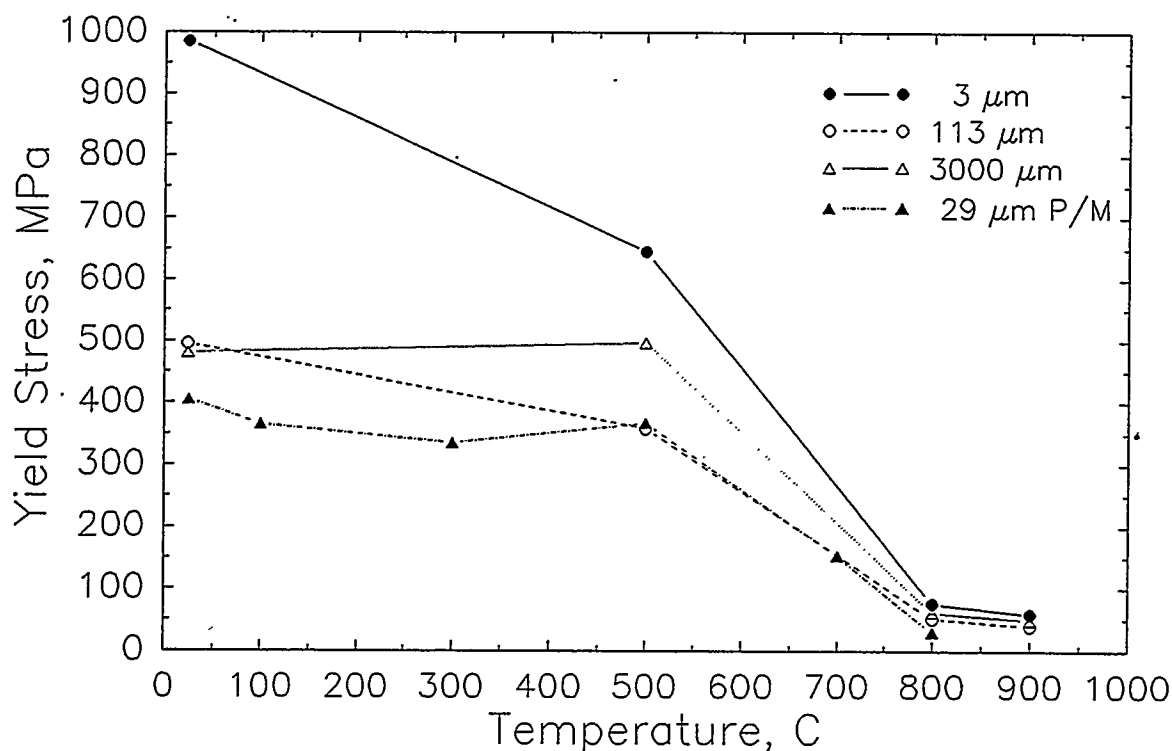


Fig. 2. Tensile properties of ODS alloys as a function of grain size.

(900°C extrusion followed by one hour anneal at 1200°C) tested at 650°C and 75 MPa. It is evident from the figure that both of the ODS materials have significantly reduced minimum creep rates, and greatly increased time to rupture compared to the conventional P/M material. It is also apparent that increasing the grain size increases the time to rupture. The coarse grained ODS alloy shows an order of magnitude increase in time to rupture for the creep conditions examined.

As noted above, heat treatment causes the average oxide size to increase, and because of a fixed volume, this results in increased spacing between particles. While coarsening of the oxide is generally not desirable in application because of expected degradation of properties with time as the oxide spacing increases, it offers the opportunity to quantify changes in creep properties. Several samples with large secondary recrystallized grain size and varying oxide sizes were creep tested at 650°C and 75 MPa and the results are shown in Figure 4. It is apparent that increasing the oxide particle size degrades the creep resistance, such that for the largest oxide particle size (approximately 330 nm) the ODS material essentially has the same properties as the conventional P/M material shown in Figure 3.

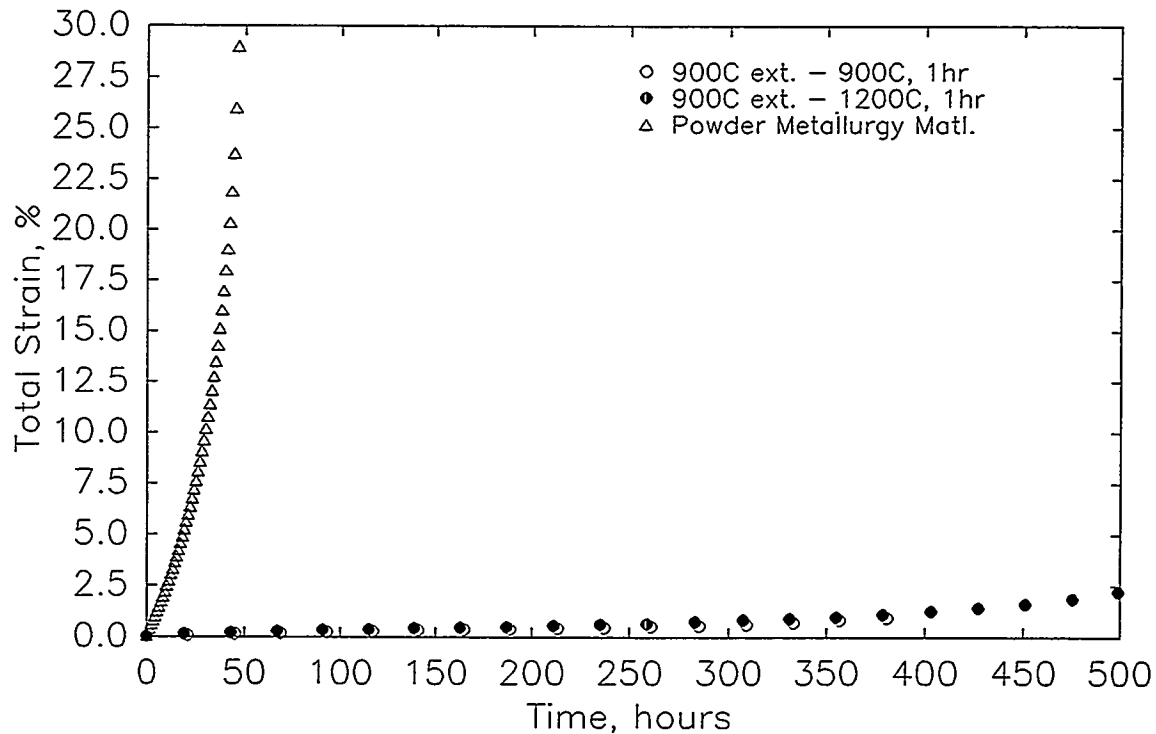


Fig. 3. Creep properties of ODS alloys compared to conventional P/M alloy at 650°C and 75 MPa.

The interaction of the oxide particle dispersion with dislocations during deformation was examined using TEM for both tensile and creep deformation. In tension at temperatures of 25 and 500°C, the particles caused extensive pinning of dislocations, and it appeared that large pile-ups of dislocations occurred around particles. At 800°C, individual dislocations were observed pinned only by the largest particles. In material deformed in creep at 650°C, it appears that individual dislocations and dislocation arrays are pinned by the larger oxide particles. Micrographs of the observed dislocation structures are shown in Figures 5 a and b for tensile deformation at 800°C and creep at 650°C, respectively. In both cases, the interaction between dislocations and particles appears to be attractive, and the dislocation contrast is not evident at the particle-dislocation interface.

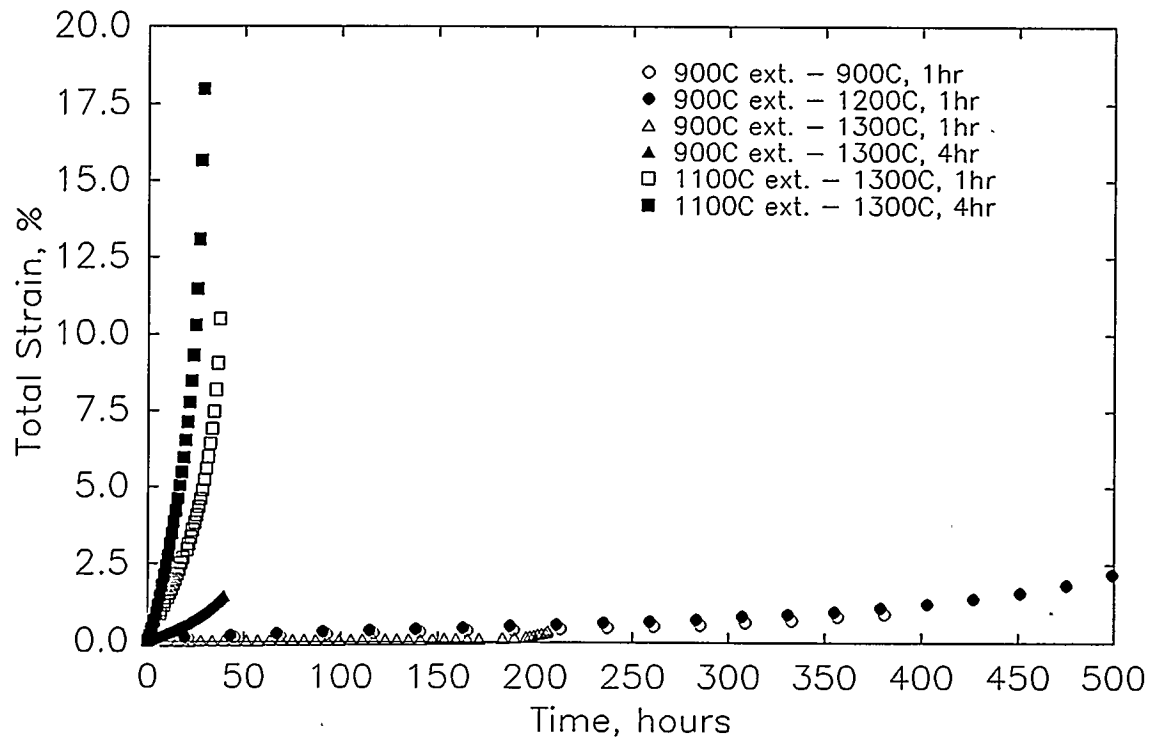


Fig. 4. Creep properties of ODS alloy as a function of heat treatment.

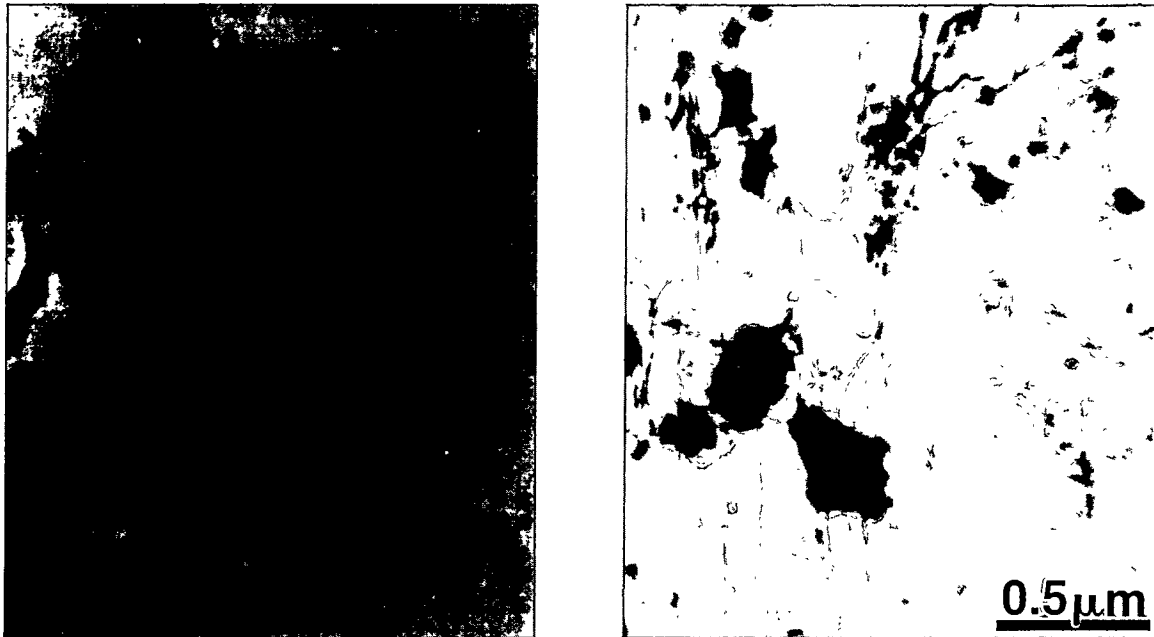


Fig. 5. Dislocation structures in ODS alloy after: a) Tensile test at 800°C; and b) Creep test at 650°C and 75 MPa.

## CONCLUSIONS

Fe<sub>3</sub>Al containing an oxide dispersion has been formed using reaction synthesis followed by extrusion. If the extrusion temperature, reduction ratio, and post-consolidation annealing treatment, are properly controlled secondary recrystallization can result with a final grain size greater than 25 millimeters.

Fine grain size material resulting from primary recrystallization has significantly increased yield strength compared to conventional powder metallurgy material of the same composition, or coarse grained secondary recrystallized material. However, the coarse grained material exhibits greater creep resistance at 650°C and 75 MPa. With proper extrusion ratio and heat treatment, the coarse grained ODS material has time to rupture at 650°C and 75 MPa that is more than an order of magnitude greater than comparable P/M material. Coarsening the oxide dispersion significantly degrades the creep properties.

## ACKNOWLEDGEMENTS

The authors gratefully acknowledge the assistance of T. C. Morris and L. R. Harper in conducting experiments.

## REFERENCES

1. C.G. Mckamey, J.H. DeVan, P.F. Tortorelli, and V.K. Sikka, J. Mater. Res., 6, 1779 (1991).
2. C.R. Clark, R.N. Wright, J.K. Wright, and B.H. Rabin, Scripta Met., 32, 1883 (1995).
3. R.L. Cairns, L.R. Curwick, and J.S. Benjamin, Metall. Trans., 6A, 179 (1975).
4. B.H. Rabin and R.N. Wright, Metall. Trans., 22A, 277 (1991).
5. T. M. Lillo, R. N. Wright, J. K. Wright, and B. H. Rabin. Proc. Inter. Conf. Heat Resistant Alloys II, K. Natesan, et al., eds., ASM International, p. 579, 1995.
6. J.J. Petrovic and L.J. Ebert, Metall Trans., 3, 1131 (1972).
7. M. Hillert, Acta Met., 12, 227 (1965).
8. B. H. Rabin, J. K. Wright, R. N. Wright, and C. H. Sellers, J. Mater. Res., 9, 1384 (1984).

**WELD OVERLAY CLADDING WITH IRON ALUMINIDES****G.M. GOODWIN**

**Oak Ridge National Laboratory  
P.O. Box 2008  
Oak Ridge, Tennessee 37831-6096**

**ABSTRACT**

The hot and cold cracking tendencies of some early iron aluminide alloy compositions limited their use to applications where good weldability was not required. Considerable progress has been made toward improving this situation. Using hot crack testing techniques developed at ORNL and a systematic study of alloy compositional effects, we have established a range of compositions within which hot cracking resistance is very good, essentially equivalent to stainless steel. Cold cracking, however, remains an issue, and extensive efforts are continuing to optimize composition and welding parameters, especially preheat and postweld heat treatment, to minimize its occurrence.

In terms of filler metal and process development, we have progressed from sheared strip through aspiration cast rod and shielded metal arc electrodes to the point where we can now produce composite wire with a steel sheath and aluminum core in coil form, which permits the use of both the gas tungsten arc and gas metal arc processes. This is a significant advancement in that the gas metal arc process lends itself well to automated welding, and is the process of choice for commercial weld overlay applications.

Using the newly developed filler metals, we have prepared clad specimens for testing in a variety of environments both in-house and outside ORNL, including laboratory and commercial organizations.

As a means of assessing the field performance of this new type of material, we have modified several non-pressure boundary boiler components, including fuel nozzles and port shrouds, by introducing areas of weld overlay in strategic locations, and have placed these components in service in operating boilers for a side-by-side comparison with conventional corrosion-resistant materials.

**INTRODUCTION**

Alloys based on the intermetallic compound  $\text{Fe}_3\text{Al}$  exhibit many attractive properties, particularly excellent resistance to high temperature oxidation. Their use in commercial applications has been limited, however, by the limited workability of wrought material and the susceptibility of weldments to both hot and cold cracking. Prior efforts <sup>1-5</sup> have systematically evaluated the effect of alloy composition on hot cracking.

By the use of the Sigmajig test <sup>6</sup>, we have found that hot cracking can essentially be eliminated by the addition of carbon and the control of maximum levels of niobium, zirconium, and other alloying elements. Cold cracking, however, remains an issue, and recent efforts have been aimed at minimizing its occurrence, concurrent with development of welding filler metals, processes, and procedures aimed at commercial applications.

## FILLER METAL DEVELOPMENT

Due to the difficulty in fabricating wrought solid wire of these compositions, the welding development efforts have utilized several alternate forms of filler metal. Early work <sup>1-2</sup> used strip sheared from sheet, which, although useful to investigate compositional effects, could not be considered for commercial applications. Subsequently, aspiration casting, where liquid metal is drawn into a quartz tube producing solid rod, was used as a means for evaluating a number of experimental compositions.<sup>3-5</sup> This technique proved successful, but can only produce rods of limited length (about 12-in. maximum) and diameter (about 1/8-in. minimum), thus restricting its use to the manual gas tungsten arc (GTA) process with relatively high heat input. It was realized from the onset that what was needed was a filler metal of small diameter, (approximately 1/16-in.) available in coil form, which could be used with both the GTA and gas metal arc (GMA) processes, permitting better control of dilution and semi-automatic welding. A novel technique for meeting these needs was found in the form of a composite filler wire, shown in cross-section in Figure 1.

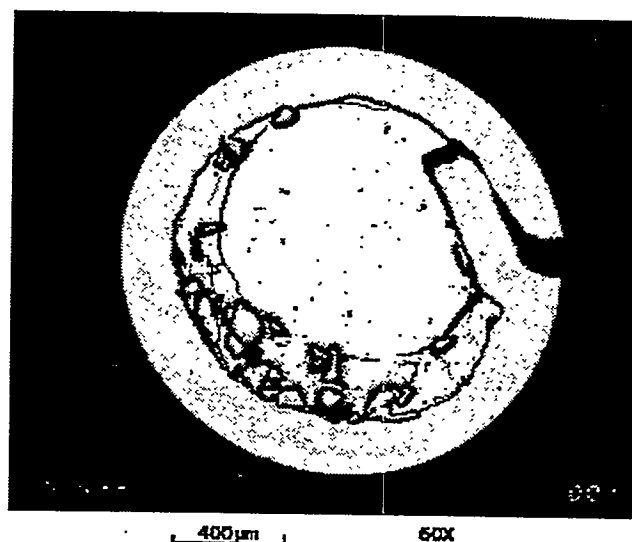


Figure 1. Composite filler wire for producing iron aluminide deposits, consisting of an iron sheath, aluminum core, and other alloying elements in granular form.

The wire consists of an iron sheath of approximately 0.009-in. thickness surrounding a core wire of commercially pure aluminum. Other alloying elements (C, Cr, Mo, Zr, B) are added as granular ferroalloys. After forming and crimping, the composite wire is drawn to eliminate void space and to



arrive at precise final diameter, in this case 0.0625-in. The resulting product is readily produced in coil form and can thus be used with automatic wire feeders for a number of welding processes.

Figure 2 shows a cross-section of a multi-pass weld pad produced using the automatic GMA process on 1-in. thick 2-1/4Cr-1 Mo steel plate.

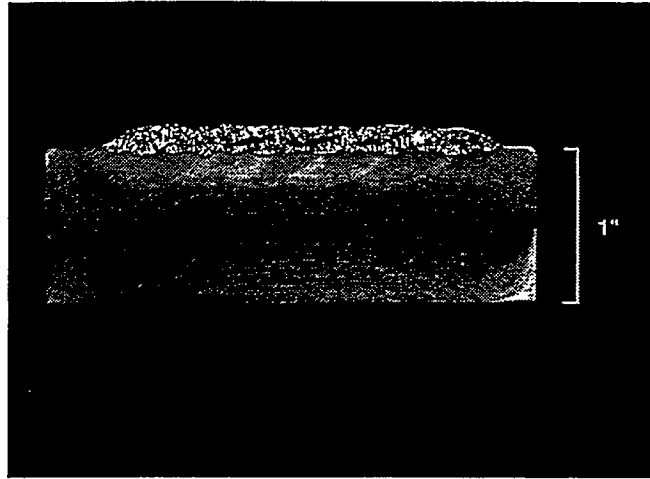


Figure 2. Multipass weld pad produced with composite filler metal using the automatic gas metal arc process on 2 1/4 Cr-1 Mo base plate.

The welding parameters used are summarized in Table 1.

**Table I. Welding Parameters for Gas Metal Arc Weld Overlay Using 1/16-in. Diameter Composite Iron Aluminide Wire**

Current:	245 Amperes, Reverse Polarity (DCEN)
Voltage:	27 volts
Wire Feed:	190 inches/minute
Travel:	13.1 inches/minute
Shield Gas:	Argon, 45 cubic feet/hour
Bead offset:	3/8-in.
Electrode Stickout:	3/4-in.
Preheat:	350° C
Postweld Heat Treatment:	750° C, 1 hour

The weld deposit had approximately 30% dilution and was free of cracks, voids, and porosity. Usability of the wire was found to be excellent and arc spatter was minimal. It was concluded that this form of wire could readily be used in commercial applications with the automatic GMA or GTA processes.

### COMPOSITIONAL EFFECTS

As noted earlier, control of composition of the weld deposit was accomplished to essentially eliminate hot cracking in these alloys.<sup>4</sup> Control of cold cracking, however, has proven to be more elusive, showing a rough correlation with aluminum content<sup>5</sup>, and a clear dependence on geometry, weld preheat, and postweld heat treatment conditions. The dependence on aluminum level is known to be complex, based on the observations of cracking in high and very low aluminum level alloys<sup>7</sup>. In order to clarify this relationship, we are preparing wire compositions which will bracket the range of aluminum levels which can be produced using the composite wire technique with dilution levels consistent with commercial practice. The desired chromium level in the alloy is also debatable, depending on the service conditions to be encountered, so heats of the composite wire have been produced with and without chromium. Table II summarizes the alloy compositions currently under study, and notes two additional heats which have been ordered. The latter heats represent the highest and lowest aluminum levels which can be produced with the composite wire approach, based on the thickness of the iron sheath and the diameter of the aluminum core wire.

As is noted in the table, the weld process, substrate, and dilution substantially affect the composition of the overlay clad deposit, particularly the aluminum level. Note that with an aim of 20 weight % Al for an all weld metal (undiluted) deposit, we actually achieved 21.8 weight % using the GTA process; when this same wire was used on dissimilar substrates (2 1/4 Cr-1 Mo steel and 310 stainless steel) with two weld processes, GMA and GTA, the aluminum levels were 12.6 and 15.3 weight % respectively. The higher aluminum loss with the GMA process is undoubtedly due to higher dilution and vaporization in the arc.

### HEAT TREATMENT EFFECTS

It was established earlier<sup>4,5</sup> that weld preheat and postweld heat treatment were often effective at avoiding cold cracking during welding or upon subsequent cooling from completion of the weld. Optimization of these heat treatment conditions is important for economic and environmental considerations, as heat treatments are expensive, time consuming, and can cause hardship to the operator.

TABLE II: COMPOSITION OF EXPERIMENTAL HEATS  
OF IRON ALUMINIDE ALLOYS

HEAT	WEIGHT %	Al	Cr	C	Zr	Mo
Stoody I	Aim, All weld metal	20	7	0.1	0.25	0.25
	Actual, All weld metal	21.8	7.3	0.06	0.40	NA <sup>c</sup>
	Actual, Clad Deposit <sup>a</sup>	12.6	6.0	0.08	0.20	0.44
	Actual, Clad Deposit <sup>b</sup>	15.3	12.7	0.05	0.22	0.04
Stoody II	Aim, All weld metal	20	--	0.1	0.25	0.25
	Actual, All weld metal	21.5	--	0.08	0.25	NA
Stoody III	Aim, All weld metal	12	--	0.1	0.25	0.25
Stoody IV	Aim, All weld metal	26	--	0.1	0.25	0.25

<sup>a</sup> Single layer automatic gas metal arc on 1-in. thick type 2 1/4 Cr-1Mo steel  
<sup>b</sup> Single layer manual gas tungsten arc on 1/2-in. thick type 310 stainless steel  
<sup>c</sup> NA - Not Analyzed

A series of welds was produced with preheat and postweld heat treatment reduced in 50° C steps starting at 350° C and 750° C respectively. It was found that preheat temperatures as low as 250° C would sometimes yield crack free deposits, but that 350° C was required to completely avoid cracking for a standard test geometry (4x6x1-in. block of 2 1/4 Cr-1 Mo steel). Similarly, reduced postweld heat treatment temperatures would often produce sound deposits which would subsequently crack during liquid penetrant examination. It appears that 350° C and 750° C are minimum temperatures required for the standard geometry with this range of compositions.

### ENVIRONMENTAL TESTING

To establish the corrosion resistance of weld overlay clads in a variety of environments, we have prepared specimens of differing geometries and substrates for testing by several organizations.

In house testing at ORNL (Peter Tortorelli) utilizes strips of overlay deposit removed from different substrates, and tested independent of the substrate. This program has evaluated numerous aluminide filler metals. For gas corrosion tests at Babcock & Wilcox (Steven Kung), we clad twenty plate specimens of Type 310 stainless steel with the Stoody I filler metal using the manual GTA process, and for molten salt characterization at Lawrence Livermore National Laboratory (Donald Stevens), we used the same filler metal to overlay rod and plate specimens of Inconel 600. Results from all the tests will help determine the optimized alloy composition.

### INDUSTRIAL SERVICE TESTING

In order to demonstrate the performance of the iron aluminide compositions in a commercial environment, we have modified several non-pressure boundary components of a paper mill recovery boiler. These components will be placed in service along with others of conventional materials, and will thus give a side-by-side comparison of performance. Figure 3 shows black liquor nozzles of the splash plate type, used to fire the fuel slurry into the boiler. Each is approximately 6-in. long. Figure 3(a) is a new part made of wrought type 316 stainless steel, and Figure 3(b) shows a similar part which has been removed from service and weld repaired using the Stoody I filler metal.

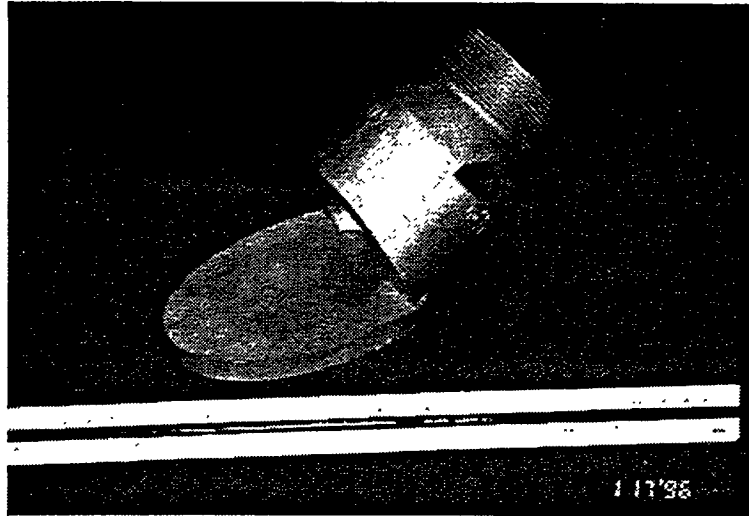


Figure 3. Splash plate type black liquor nozzles:  
(a) new

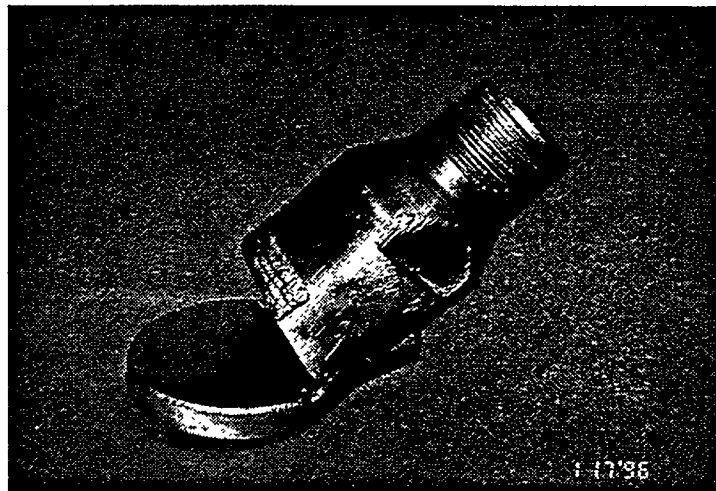


Figure 3. Splash plate type black liquor nozzles:  
b) weld repaired after service by overlay cladding of splash plate (circular plate) and top of nozzle barrel. Each is approximately 6-in. long.

The splash plate (circular plate) has two layers of weld overlay which has subsequently been surface ground, and the leading edge of the nozzle barrel has a patch of overlay in a region where erosion commonly occurs.

Figure 4 shows a swirl cone type black liquor nozzle, after service, (a), and after weld overlay repair, (b). Major erosion/corrosion areas which have been clad are the outlet orifice (top), and the leading edge of the swirl cone [(b), left].

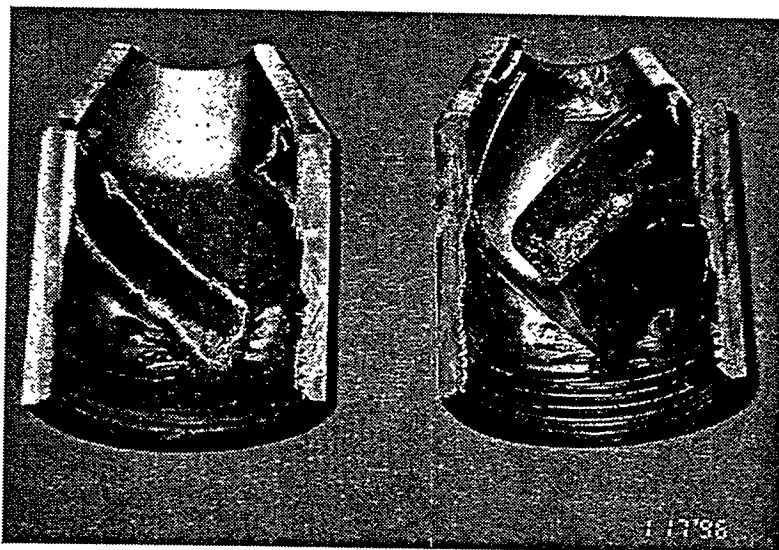


Figure 4. Swirl cone type black liquor nozzles:

(a) After service

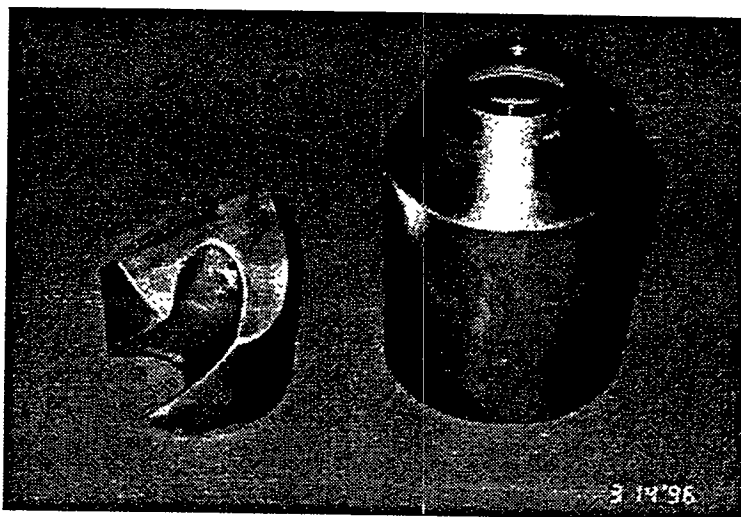
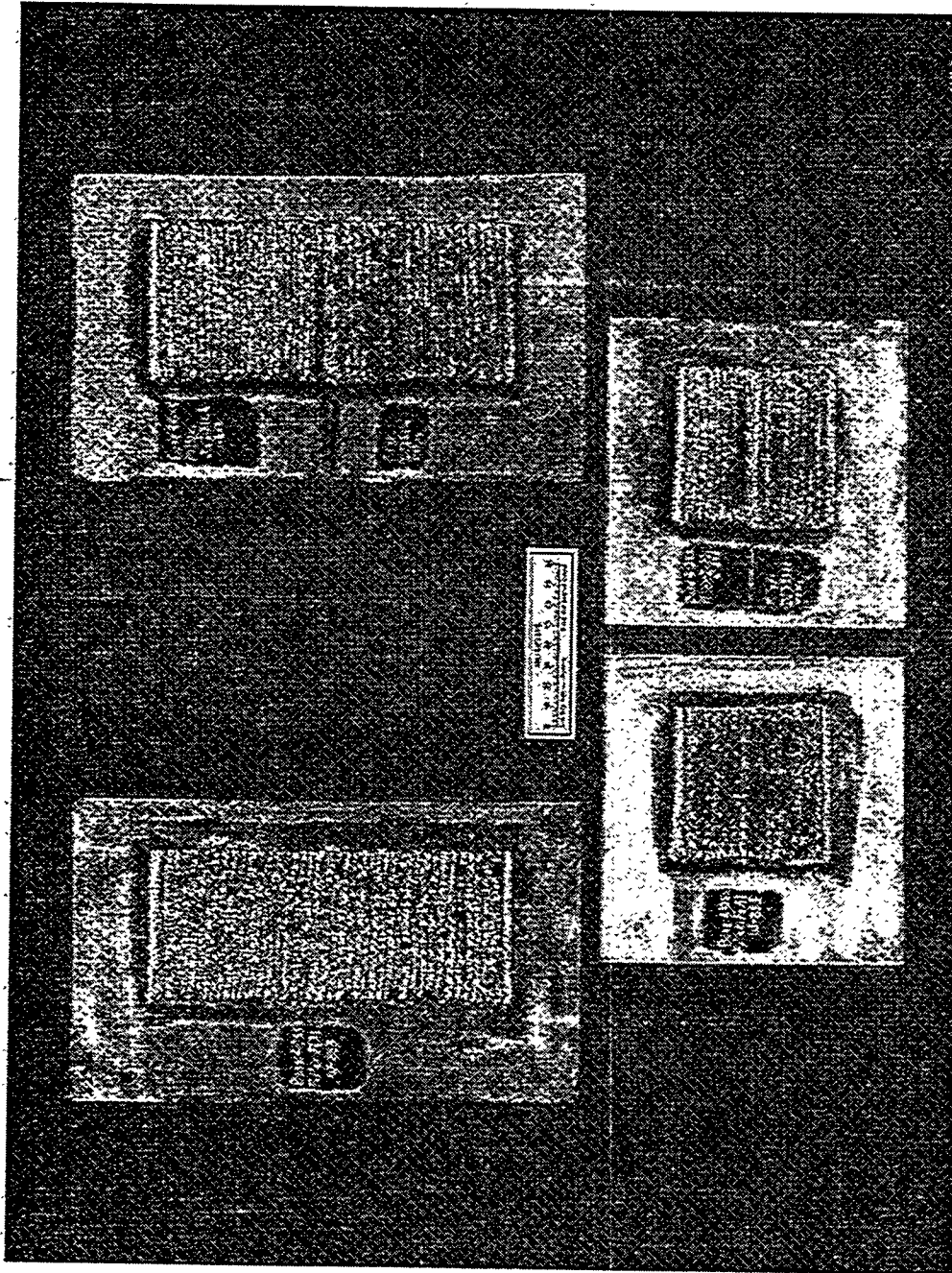


Figure 4. Swirl cone type black liquor nozzles:

(b) Weld overlay repaired at outlet orifice (right, top) and swirl cone leading edge (left, top). Approximately 4-in. long.

Figure 5 shows four sections of a liquor gun port shroud fabricated from 1/2-in. thick type 410 stainless steel plate. These plates are welded into the gun port openings in a hexagonal array (two long plates on the sides, short plates on tops and bottoms) to protect the water wall tubes, and often experience severe erosion/corrosion. The pads of aluminide overlay will give a direct comparison of their performance with that of the standard type 410 plate.

Industrial service testing is seen as an excellent way to rate these new alloys versus conventional alloys, and to guide our development toward additional commercial applications.



YIG-554

Figure 5. Liquor gun port shroud assembly. Weld overlay pads on 1/2-in. thick stainless steel plate will show comparative erosion/corrosion performance.



## SUMMARY

Considerable progress has been made in the development of iron aluminide alloys for weld overlay cladding applications. Filler metals were produced in coil form using a composite approach with an iron sheath and aluminum core wire, permitting the use of automated gas metal arc and gas tungsten arc welding. Compositional modifications were made to essentially eliminate hot cracking, and efforts continue to reduce or eliminate cold cracking by optimizing composition and welding parameters, especially preheat and postweld heat treatment.

Clad specimens were prepared for testing in-house and elsewhere to confirm corrosion performance, and overlay welded components were placed in service in commercial boilers for a side-by-side comparison with currently used materials.

## REFERENCES

1. T. Zacharia and S.A. David, "*Weldability of Iron Aluminides*", proceedings of the Fifth Annual Conference on Fossil Energy Materials, ORNL/FMP-91/1, Oak Ridge National Laboratory, September 1991.
2. T. Zacharia, P.J. Maziasz, S.A. David, and C.G. McKamey, "*Weldability of Fe<sub>3</sub>Al Based Iron Aluminide Alloys*", proceedings of the Sixth Annual Conference on Fossil Energy Materials, ORNL/FMP-92/1, Oak Ridge National Laboratory, July 1992.
3. G.M. Goodwin, C.G. McKamey, P.J. Maziasz, and V.K. Sikka, "*Weldability of Iron Aluminides*", proceedings of the Seventh Annual Conference on Fossil Energy Materials, ORNL/FMP-93/1, Oak Ridge National Laboratory, July 1993.
4. G.M. Goodwin, P.J. Maziasz, C.G. McKamey, J.H. Devan, and V.K. Sikka, "*Weldability of Iron Aluminides*", proceedings of the Eighth Annual Conference on Fossil Energy Materials, ORNL/FMP-94/1, Oak Ridge National Laboratory, August 1995.
5. G.M. Goodwin, "*Weld Overlay Cladding With Iron Aluminides*", proceedings of the Ninth Annual Conference on Fossil Energy Materials, ORNL/FMP-95/1, Oak Ridge National Laboratory, August 1995.
6. G.M. Goodwin, "*Development of a New Hot Cracking Test - The SigmaJig*", Weld J. 66(2) 335-S - 305-S (1987)
7. V.K. Sikka, G.M. Goodwin, D.J. Alexander, and C.R. Howell, "*Welding and Mechanical Properties of Cast FAPY (Fe-16 at % Al-Based) Alloy Slabs*", ORNL/TM-12944, Oak Ridge National Laboratory, May 1995.

HIGH-TEMPERATURE CORROSION BEHAVIOR OF  
COATINGS AND ODS ALLOYS BASED ON Fe<sub>3</sub>Al

P. F. Tortorelli, B. A. Pint, and I. G. Wright

Oak Ridge National Laboratory  
Oak Ridge, Tennessee, U. S. A.

ABSTRACT

Iron-aluminide coatings were prepared by gas tungsten arc and gas metal arc weld-overlay techniques. All the weld overlays showed good oxidation/sulfidation behavior under isothermal conditions, including a gas metal arc deposit with only 21 at.% Al. A rapid degradation in corrosion resistance was observed under thermal cycling conditions when the initially grown scales spalled and the subsequent rate of reaction was not controlled by the formation of slowly growing aluminum oxides. Higher starting aluminum concentrations (>~25 at.%) are needed to assure adequate oxidation/sulfidation lifetimes of the weld overlays. A variety of stable oxides was added to a base Fe-28 at.% Al-2 % Cr alloy to assess the effect of these dopants on the oxidation behavior at 1200°C. A Y<sub>2</sub>O<sub>3</sub> dispersion improved the scale adhesion relative to a Zr alloy addition, but wasn't as effective as it is in other alumina-forming alloys. Preliminary data for powder-processed Fe-28 at.% Al-2% Cr exposed to the H<sub>2</sub>S-H<sub>2</sub>-H<sub>2</sub>O-Ar gas at 800°C showed that the oxidation/sulfidation rate was similar to that of many Fe<sub>3</sub>Al alloys produced by ingot metallurgy routes.

INTRODUCTION

Iron aluminides containing greater than about 20-25 at.% Al have oxidation/sulfidation resistance at temperatures well above those at which these alloys have adequate mechanical strength.<sup>1</sup> In addition to alloying and processing modifications for improved creep resistance of wrought material, this strength limitation is being addressed by development of oxide-dispersion-strengthened (ODS) iron aluminides<sup>2</sup> and by evaluation of Fe<sub>3</sub>Al alloy compositions as coatings or claddings on higher-strength, less corrosion-resistant materials.<sup>3,4</sup> As part of these efforts, the high-temperature corrosion behavior of iron-aluminide weld overlays and ODS alloys is being characterized and compared to previous results for ingot-processed material.

OXIDATION-SULFIDATION OF IRON-ALUMINIDE WELD OVERLAYS AT 800°C

This section contains corrosion data on weld deposits produced by the gas tungsten arc (GTA) process and initial observations of the oxidation/sulfidation behavior of a weld overlay synthesized by gas metal arc (GMA) welding. The development efforts associated with the GTA and GMA processes used to produce the weld overlays are described elsewhere.<sup>3,5</sup>

Rectangular specimens, approximately 18-25 mm x 12 mm, were cut from the weld overlay pads. As in previous oxidation-sulfidation studies,<sup>6,7</sup> coupons were then prepared by grinding away the substrate material so that only weld metal (approximately 1-2 mm thick) remained. Corrosion behavior was characterized by use of a continuous-recording microbalance to measure the weight of these specimens during exposure at 800°C to a flowing (~2 cm<sup>3</sup>/s) mixed gas consisting of 5.4% H<sub>2</sub>S-79.4% H<sub>2</sub>-1.6% H<sub>2</sub>O-13.6% Ar (by volume). The oxygen partial pressure, as determined by a solid-state oxygen cell, was 10<sup>-22</sup> atm, and the sulfur pressure was calculated to be 10<sup>-6</sup> atm. These types of exposures have been used to characterize the sulfidation resistance of iron aluminides and several other alloys.<sup>6-9</sup> In most cases, a specimen was held in the mixed-gas microbalance system at 800°C for a fixed amount of time, cooled to room temperature, and then removed from the system for subsequent examination. However, two specimens underwent thermal cycling, in which they experienced intermediate cooling to below 100°C and more than one hold period at the exposure temperature.

The use of welding to produce iron-aluminide coatings results in a loss of selected elements by vaporization and significant mixing of the filler metal and substrate alloys (dilution) during deposition. The final concentrations of the various elements in the weld deposit will depend on the particular filler metal/substrate combination and, therefore, the actual concentrations of the critical elements were determined using samples taken from the same welded plate as used to make the respective corrosion coupons (Table 1). Because there is essentially no aluminum in the substrates, the concentration of this element in the overlay will be significantly less than that of the weld rod/wire used to produce it. The extent of this dilution in aluminum depends on vaporization losses during welding and the relative amount of substrate material melted and thus is affected by parameters such as current, voltage, polarity, travel speed, etc. Similar dilution/enrichment considerations apply to the other elements. The composition of the weld overlays shown in Table I are consistent with the general dilution/enrichment factors found previously.<sup>3,5-7</sup>

Figure 1 shows the isothermal gravimetric results for corrosion specimens cut from the weld deposits listed in Table 1 and exposed to the H<sub>2</sub>S-H<sub>2</sub>-H<sub>2</sub>O-Ar environment for 70-120 h at 800°C. While all the specimens showed relatively low-to-moderate weight gains, there were

Table 1. Weld Deposit Compositions

Weld Deposit	Process	Sub- strate	Concentration (at. %) <sup>a</sup>							
			Al	Cr	Nb	Si	Ni	Mo	Zr	C
H1	GTA	304L	30.4	9.0	0.1	0.3	2.5	0.1	0.2	0.08
H2	GTA	Cr-Mo	37.3	6.2	<0.01	0.1	0.2	0.3	0.1	0.1
S1	GMA	Cr-Mo	21.3	6.0	<0.01	0.1	0.1	0.4	0.2	0.1

<sup>a</sup> Determined by spark source mass spectrometry. Balance is Fe.

distinct differences in their gravimetric behavior. These differences were also apparent visually. The surfaces of the specimen which exhibited the greatest sulfidation rate (H1) were almost completely covered with a dark corrosion product, while those of the H2 coupon showed a thin gray scale. The specimen cut from the S1 weld

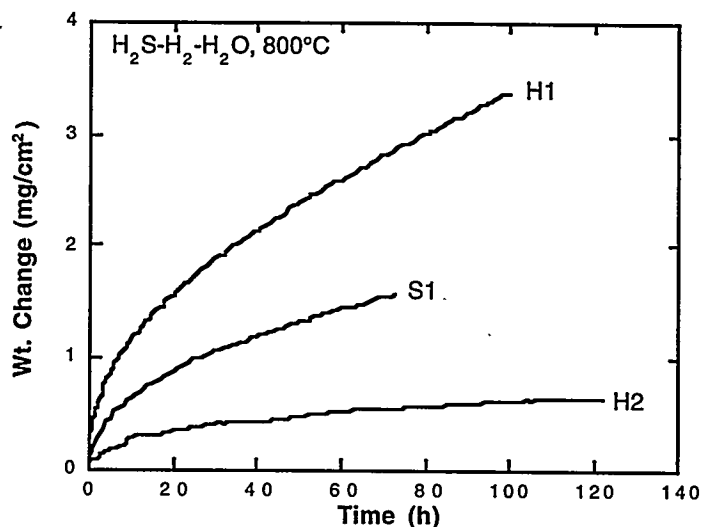


Fig. 1. Weight change versus time for specimens cut from iron-aluminide weld overlays and isothermally exposed to  $\text{H}_2\text{S-H}_2\text{-H}_2\text{O-Ar}$  at  $800^\circ\text{C}$ . The compositions of the weld overlays are shown in Table I.

deposit exhibited a weight gain intermediate between H1 and H2 and developed a gray scale over most of its surface area with only some dark corrosion products along one edge. Some spallation of the scales formed on the H1 and S1 specimens occurred during cooling from the exposure temperature. Despite the differences in gravimetric behavior among the various weld overlays, each deposit composition showed substantially better isothermal oxidation/sulfidation resistance than that of conventional Fe-Cr-Ni and Fe-Cr-Al alloys.<sup>8</sup>

Two more specimens of the S1 weld deposit were individually exposed in the microbalance system and held isothermally at  $800^\circ\text{C}$  in the mixed gas for about 72-74 h, after which they were allowed to cool to below  $100^\circ\text{C}$ . As shown in Fig. 2, the measured weight gains of S1-2 and S1-3 over this time period matched those measured for the first S1 coupon discussed above (S1-1). After its temperature fell to about  $35^\circ\text{C}$ , S1-2 was reheated to  $800^\circ\text{C}$  for several more hours, then cooled and removed from the system. In

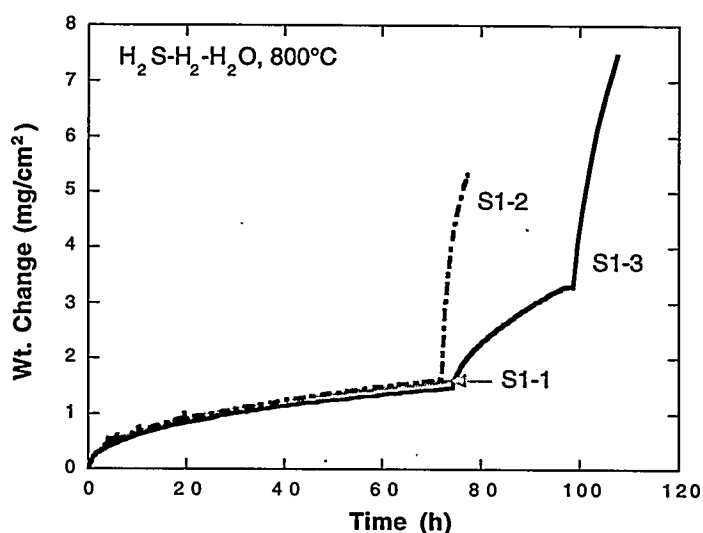


Fig. 2. Cumulative weight gain versus time for three individual specimens cut from weld-overlay S1 and then exposed to  $\text{H}_2\text{S-H}_2\text{-H}_2\text{O-Ar}$  at  $800^\circ\text{C}$ . The breaks in the curves represent reheating to exposure temperature after cooling to below  $100^\circ\text{C}$ . S1-1 was not reheated.

the case of S1-3, the coupon was cycled to below 100°C and back to the exposure temperature twice. For both of these specimens, significant increases in the rate of weight gain relative to the previous isothermal exposure periods were observed. Spallation occurred during the cooling cycles, but the data in Fig. 2 represent cumulative weight gains during the isothermal exposures and do not reflect any of this mass loss. At the end of the cyclic exposures, the specimen surfaces were

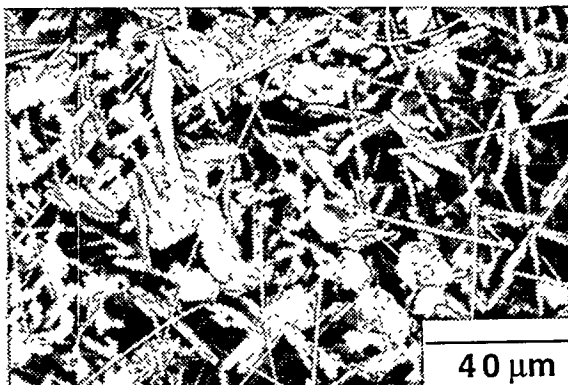


Fig. 3. Scanning electron micrograph of specimen S1-3 after three isothermal exposure periods in  $\text{H}_2\text{S-H}_2\text{-H}_2\text{O-Ar}$  at 800°C.

covered with loosely adherent flakes of a dark corrosion product. Scanning electron microscopy (SEM) revealed a variety of product morphologies (Fig. 3); the platelets and needles resembled what has previously been identified as chromium and iron sulfides.<sup>8,9</sup> Subsequently, the loose scale was removed from the surfaces of the specimens. In both cases, it was combined with the material which had spalled during cooling or came off during handling to produce a powder that was analyzed by x-ray diffraction (XRD) and energy dispersive x-ray fluorescence (EDX). The corrosion products from S1-3 were a mixture of aluminum, iron, and chromium sulfides with a small amount (<1%) of oxide. Based on the most likely forms of these sulfides as determined by XRD, it appeared that the dominant ones were those incorporating aluminum ( $\text{Al}_2\text{S}_3$ ) or iron ( $\text{Fe}_7\text{S}_8$ ), with each composing about 45 - 48% of the total analyzed sample. For S1-2,  $\text{Al}_2\text{O}_3$  was present in the scale in a greater concentration, in addition to iron, chromium, and chromium-iron sulfides. Little  $\text{Al}_2\text{S}_3$  was detected. (It was not possible to determine the relative abundance of the various sulfides formed on S1-2 by EDX.)

The excellent high-temperature corrosion resistance of bulk iron aluminides can be related to the rapid establishment and stability of a protective alumina scale and the absence or inhibited growth of iron and aluminum sulfides.<sup>8</sup> The inclusion of chromium in iron aluminides at levels greater than 2 - 3 at.% promotes more rapid reaction and increases weight gain due to the formation of chromium and iron sulfides.<sup>8,9</sup> On the other hand, little difference in isothermal gravimetric behavior was observed for variations in Al concentration (22-28% Al).<sup>9</sup> The isothermal weight gain behavior of the S1 specimen exactly matched that of  $\text{Fe}_3\text{Al-5% Cr}$ . Furthermore, the gravimetric data for the S1 composition were reproducible; three separate specimens cut from this weld deposit exhibited nearly identical weight changes over the equivalent isothermal time period (compare the first 72 h of exposure of S1-1, -2, and -3 in Fig. 2). However, these data are at variance with previous results from weld overlays:<sup>6</sup> a

coupon with the S1 composition (21% Al-6% Cr) would have been expected to have greater weight gains than those measured in the present study. Variations in minor alloying additions between the present and previous 21-23% Al weld overlays cannot explain the difference in gravimetric behavior; such elements were found to have minimal influence on overall oxidation/sulfidation resistance.<sup>8</sup> More likely, the discrepancy in results is probably due to higher than normal weight gains previously reported for weld overlays with lower aluminum levels<sup>6</sup> because of inadequate mixing during welding and/or rough initial surfaces that allowed localized regions to retain a composition like that of the substrate steel. In this sense, the GMA process, which involves a substantially higher energy input into the weld, may promote more complete mixing of the deposit and therefore result in more reproducible and better corrosion resistance at high temperatures.

As shown in Fig. 1, the S1 specimen (21.3% Al, 6% Cr) showed somewhat better isothermal oxidation/sulfidation behavior than the alloy containing 30% Al and 9% Cr (H1). This can again be explained on the basis of what is known from studies of the corrosion of bulk iron aluminides in this mixed gas. These studies<sup>8,9</sup> have shown that, under isothermal conditions, variations in chromium concentration have a greater effect on the corrosion behavior of Fe-(20-30%) Al alloys than changes in the aluminum concentration. Therefore, the higher weight gains for H1 (9% Cr) vis-à-vis S1 (6% Cr) are not unexpected. The H1 specimen showed a higher density of the black corrosion products associated with chromium (and iron) sulfides consistent with its higher chromium concentration.

The low rate of corrosion for the 37% Al composition (H2) agrees very well with previous results from weld overlays of similar composition.<sup>6</sup> Compared to gravimetric data for bulk Fe-28% Al-2% Cr and Fe-40% Al-6% Cr,<sup>8</sup> H2 showed a higher initial weight gain, but only a slightly greater longer-term corrosion rate. However, the high aluminum concentration of this deposit led to substantial cracking of the coating. While chemically resistant to this environment, the flaws in this weld overlay would have allowed the corrosive species access to the more susceptible substrate.

As described above, previous results from surface analysis of products formed on bulk iron aluminides and weld overlays revealed that  $\text{Al}_2\text{O}_3$  and, under certain conditions,  $\text{Al}_2\text{S}_3$  are predominant corrosion products when there is a higher aluminum content in the alloy, but faster growing sulfides of iron and chromium can form at lower concentrations of this element (< 18-22% Al).<sup>6,8,9</sup> These considerations are important in understanding why the specimens of the S1 weld overlay composition (21% Al, 6% Cr) showed low oxidation/sulfidation rates under isothermal conditions, but suffered substantial degradation when subjected to thermal cycling (Figs. 2 and 3). Results from cyclic exposures of bulk iron aluminides (28% Al,  $\leq 2\%$

Cr ) in this mixed-gas environment showed that, despite some spallation of the corrosion products, the subsequent corrosion rate of alloys upon re-exposure was about the same as that measured initially.<sup>8,9</sup> For these aluminides,  $\text{Al}_2\text{O}_3$  was able to reform following cooling and re-exposure, but this does not appear to be the case for the S1 weld overlay, where iron and chromium sulfides subsequently form at the expense of aluminum-containing products after a thermal cycle. The XRD and EDX data and SEM observations (Fig. 3) showed that, while  $\text{Al}_2\text{O}_3$  appeared to be present initially, a substantial fraction of the corrosion products formed after two and three cycles (S1-2 and S1-3, respectively) were iron, chromium, and chromium-iron sulfides. The formation of these products are associated with the steep increases in weight gain with time shown in Fig. 2. This difference in thermal cycling behavior can be attributed to the lower initial aluminum concentration of the S1 composition (21%) compared to the typical  $\text{Fe}_3\text{Al}$  alloys (28% Al). As mentioned above, the Al concentration of the S1 overlay is close to the critical concentration necessary for good sulfidation resistance of binary Fe-Al alloys.<sup>9</sup> Therefore, any decrease in aluminum level will lead to more rapid corrosion associated with predominant growth of iron and chromium sulfides. Such aluminum depletion can occur by formation of aluminum-containing corrosion products followed by spallation during cooling. Upon further exposure, there is insufficient aluminum remaining in the surface regions to maintain the preferential development of the more slowly growing aluminum-containing products, and a higher rate of weight gain is observed, as in the present case. Indeed, the rates of accelerated weight gain after the initial exposures (S1-2 and -3, Fig. 2) are similar to those measured for alloys that form scales preferentially composed of transition-metal sulfides.<sup>8</sup>

The present results indicate that the aluminum concentration of the S1 weld overlay (21.3%) appears to be sufficient to maintain corrosion resistance in an aggressive oxidizing/sulfidizing environment under isothermal conditions, but that a greater amount of aluminum is required in the deposit to assure acceptable corrosion behavior of such coatings under thermal cycling conditions. Higher concentrations would not only delay any onset of accelerated reaction caused by aluminum depletion but would also improve the corrosion behavior of iron aluminide coatings containing substrate elements that are deleterious to sulfidation resistance (such as chromium and nickel).<sup>6</sup> However, as noted previously, weld deposits containing high aluminum concentrations are very sensitive to hydrogen-induced cracking which would allow corrosion of the substrate by ingress of reactive species. Therefore, the development of iron-aluminide coatings must involve an optimization of the composition and welding parameters such that good corrosion and cracking resistance are attained.



OXIDATION AND OXIDATION-SULFIDATION OF ODS Fe<sub>3</sub>Al ALLOYS

Powders of gas-atomized Fe-28% Al-2% Cr (FAS) and various submicron oxides were mechanically blended in a flowing Ar atmosphere using a high-speed attritor and stainless steel balls.<sup>2,10</sup> The blended powder was canned, degassed, and extruded at 1100°C. For comparison, a FAS powder extrusion without an oxide addition (FASN), ingot-processed Fe-28% Al-5% Cr-0.1% Zr (FAL), and a commercial ZrO<sub>2</sub>-dispersed (0.06% Zr) Fe-20% Cr-10% Al alloy (Kanthal alloy APM) were also tested. Cyclic oxidation experiments were conducted at 1200°C in air using procedures described in ref. 2. Oxide additions were normally made at a standard 0.2 cation % level.

Initial oxidation evaluation used twenty 2-h cycles at 1200°C as a way to assess the performance of the different dopants. The weight change data are shown in Fig. 4. As a reference, Kanthal APM showed almost no spallation and had a weight change almost identical to that measured isothermally.<sup>11</sup> Oxide additions of Ce, La and Sc accelerated the oxidation rate and, in the case of CeO<sub>2</sub>, led to FeO formation.<sup>10</sup> This detrimental influence has been observed for a number of oxide additions, such as CeO<sub>2</sub> in FeCrAl,<sup>12</sup> and can be an effect of over-doping. In order to test this explanation, smaller amounts of La<sub>2</sub>O<sub>3</sub> (0.05%La) and CeO<sub>2</sub> (0.1%) were added to FAS. This approach reduced the negative effects, but did not eliminate them; during longer-term testing (10 x 100 h cycles, see Fig. 5), these alloys exhibited accelerated and breakaway oxidation.

The short-term cyclic oxidation behavior of FAS was similar regardless of whether the added dopant was an oxide of Y, Nd, Yb, Hf or Zr (Fig. 4). In each case, after an initial specimen weight gain, each subsequent cycle resulted in monotonic decreases in weight signifying some spallation after each thermal cycle. As such, these results did not sufficiently differentiate the effects of the various dopants and longer-term cyclic exposures were required to examine the influence of

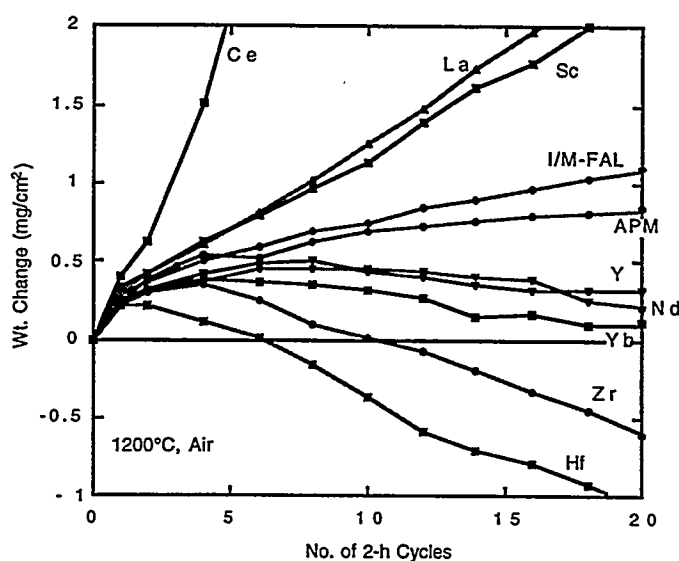


Fig. 4. Specimen weight change versus number of 2-h oxidation cycles of Fe - 28% Al - 2% Cr (FAS) with various cation oxide dispersions (0.2 at.%) in air at 1200°C.

different oxide additions on oxidation behavior. Data from these exposures showed that  $Y_2O_3$ -dispersed FAS performed better than any of the other iron-aluminide alloys (Fig. 5), including the ingot-processed alloy containing Zr (FAL), which has improved scale adhesion relative to other wrought iron aluminides.<sup>13</sup>

Because there were only small differences in the parabolic rate constants of the various alloys,<sup>14</sup> the lower rate of

weight gain of  $Y_2O_3$ -dispersed FAS reflected a reduced degree of scale spallation rather than an effect on scale growth kinetics. (More extensive cyclic oxidation results for  $Y_2O_3$ -dispersed FAS can be found in ref. 2.) The Hf, Nd, Yb and Zr additions did produce some beneficial effect compared to an  $Al_2O_3$  dispersion (which is always present in the as-fabricated ODS FAS alloys); in long-term cyclic exposures, breakaway oxidation was observed for FAS doped only with  $Al_2O_3$ .<sup>14</sup>

Although  $Y_2O_3$  has a positive influence on the spallation resistance of FAS, the present results indicate that this dopant is not as effective in iron aluminides as when it is added to FeCrAl and  $\beta$ -NiAl.<sup>14</sup> Likewise,  $ZrO_2$  in FAS did not replicate the effect of this dopant in commercial APM (Fig. 5). There are several possible reasons for the variations in a dopant's effectiveness, including alloy substrate strength and its effect on scale buckling and void formation.<sup>14</sup> Additionally, while 0.2% Y appeared to be an optimum doping level,<sup>14</sup> this may not be true for the other additions. For example, assuming that the APM alloy has an optimized  $ZrO_2$  content of 0.06 at.% Zr, the 0.2% Zr addition used in this study may not produce the best effect that could be achieved. Lower (0.05%) dopant levels of Zr and Hf are currently being investigated.

As noted in the previous section,  $Fe_3Al$  alloys produced by conventional ingot metallurgy (I/M) procedures, and FAS in particular, have excellent sulfidation resistance in  $H_2S$ -containing environments.<sup>8,9</sup> Therefore, it is of interest to learn whether ODS iron aluminides show similar corrosion behavior. Preliminary data in this regard were obtained by exposing FASN and FAS-

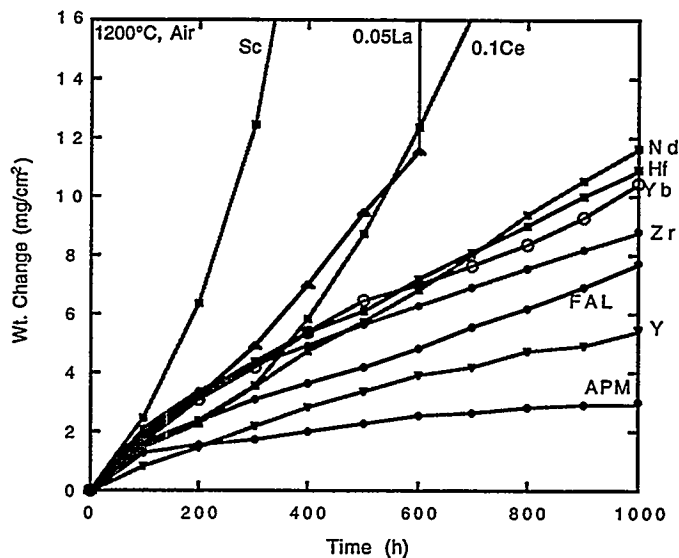


Fig. 5. Total weight change (specimen plus spalled scale) versus time for specimens cyclically oxidized in air at 1200°C (100-h cycles). Except where shown, all cation concentrations were 0.2%.

$Y_2O_3$  (0.2 cation %) to  $H_2S$ -79.4%  $H_2$ -1.6%  $H_2O$ -13.6% Ar in similar experiments to those described above for the weld overlay specimens. The results are shown in Fig. 6, which also contains data for FAS, a Fe-28% Al-5% Cr-1% Nb-0.5% C iron aluminide, and a FeCrAl-type Fe-18% Cr-12% Al alloy produced by ingot processing (FAS-I/M, FA129-I/M, and Fe-18Cr-12Al-I/M, respectively). Note that the isothermal weight gains of the powder metallurgy-processed alloys were somewhat greater than the I/M FAS, but less than the  $Fe_3Al$ -5Cr alloy (FA129-I/M). Much of the difference in the weight gains was established in the early stages of exposure to the oxidizing/sulfidizing environment; at extended times the rates of weight gain are quite similar for the ingot- and powder-processed FAS alloys. The reason for the more rapid initial weight gains of the P/M alloys is not yet known, but it doesn't seem to be related to increases in the chromium levels during the milling process; the chromium concentrations in FASN and FAS- $Y_2O_3$  after extrusion were just 2.0 and 2.4%, respectively. Rather, the fine grain size of these as-extruded alloys (about 1  $\mu m$ ) may allow a more rapid diffusion of chromium to the reaction front<sup>15</sup> and result in higher weight gains due to formation of chromium sulfides. As noted above, the presence of chromium in

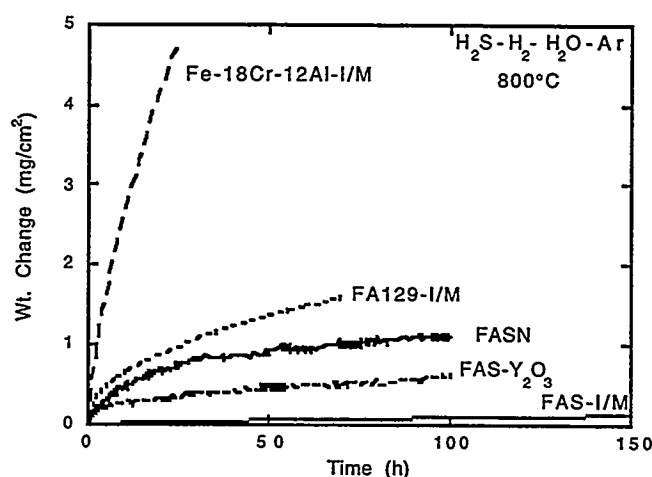


Fig. 6. Weight change versus time for specimens isothermally exposed to  $H_2S$ - $H_2$ - $H_2O$ -Ar at 800°C.

$Fe_3Al$  in excess of about 2% leads to higher corrosion rates in this mixed-gas environment. Nevertheless, these preliminary results for ODS  $Fe_3Al$  alloys indicate good overall sulfidation resistance. The weight gains for these materials are significantly less than for a FeCrAl-type alloy (Fig. 6) and are dramatically better than those measured for a stainless steel.<sup>8</sup>

## SUMMARY AND CONCLUSIONS

The high-temperature strength limitations of  $Fe_3Al$  alloys are being addressed by evaluation of these compositions as coatings or claddings on higher-strength, less corrosion-resistant materials and by development of oxide-dispersion-strengthened (ODS) iron aluminides with oxidation and sulfidation resistance that match or exceed that of ingot-produced versions of these materials. Iron-aluminide coatings were prepared by gas tungsten arc and gas metal arc

weld-overlay techniques. All the weld overlays showed good oxidation/sulfidation behavior under isothermal conditions, including a gas metal arc deposit with only 21 at.% Al. A rapid degradation in corrosion resistance was observed under thermal cycling conditions when the initially grown scales spalled and the subsequent rate of reaction was not controlled by the formation of slowly growing aluminum oxides. Higher starting aluminum concentrations ( $>25$  at.%) are needed to assure adequate oxidation/sulfidation lifetimes of the weld overlays. A variety of stable oxides was added to a base Fe-28 at.% Al-2 % Cr alloy to assess the effect of these dopants on the oxidation behavior at 1200 and 1300°C in air and O<sub>2</sub>. A Y<sub>2</sub>O<sub>3</sub> dispersion improved the scale adhesion relative to a Zr alloy addition, but wasn't as effective as it is in other alumina-forming alloys. Preliminary exposures of ODS Fe-28 at.% Al-2% Cr in the H<sub>2</sub>S-H<sub>2</sub>-H<sub>2</sub>O-Ar gas at 800°C showed that the oxidation/sulfidation resistance of these alloys was good.

#### ACKNOWLEDGMENTS

The authors thank M. Howell for experimental support and J. R. DiStefano, G. M. Goodwin, and C. G. McKamey for their reviews of the manuscript. This research was sponsored by the Fossil Energy Advanced Research and Technology Development (AR&TD) Materials Program, U.S. Department of Energy, under contract DE-AC05-96OR22464 with Lockheed Martin Energy Research Corporation. B. A. Pint is supported by the U. S. Department of Energy Distinguished Postdoctoral Research Program administered by the Oak Ridge Institute for Science and Education.

#### REFERENCES

1. C. G. McKamey, J. H. DeVan, P. F. Tortorelli, and V. K. Sikka, *J. Mater. Res.* **6** (1991) 1779-1805.
2. I. G. Wright, B. A. Pint, E. K. Ohriner, and P. F. Tortorelli, "ODS Iron Aluminides," these proceedings.
3. G. M. Goodwin, P. J. Maziasz, C. G. McKamey, J. H. DeVan, and V. K. Sikka, pp. 205-10 in *Proc. Eighth Annual Conf. Fossil Energy Materials*, N. C. Cole and R. R. Judkins (comp.), CONF-9405143, U. S. Department of Energy, August 1994.
4. K. Natesan, pp. 591-99 in *Heat-Resistant Materials II*, K. Natesan, P. Ganesan, and G. Lai (eds.), ASM International, August 1995.
5. G. M. Goodwin, "Weld Overlay Cladding with Iron Aluminides," these proceedings.
6. P. F. Tortorelli, J. H. DeVan, G. M. Goodwin, and M. Howell, pp. 203-12 in *Elevated Temperature Coatings: Science and Technology I*, N. B. Dahotre, J. M. Hampikian, and J. J. Stiglich (eds.), The Minerals, Metals, and Materials Society, Warrendale, PA, 1995.
7. P. F. Tortorelli, G. M. Goodwin, M. Howell, and J. H. DeVan, pp. 585-90 in *Heat-Resistant Materials II*, K. Natesan, P. Ganesan, and G. Lai (eds.), ASM International, August 1995.
8. J. H. DeVan, pp. 107-115 in *Oxidation of High-Temperature Intermetallics*, T. Grobstein and J. Doychak (eds.), The Minerals, Metals, and Materials Society, 1989.
9. J. H. DeVan and P. F. Tortorelli, *Mater. at High Temp.* **11** (1993) 30-35.
10. B. A. Pint, K. B. Alexander, and P. F. Tortorelli, pp. 1315-20 in *High-Temperature Ordered Intermetallic Alloys VI*, J. A. Horton, I. Baker, S. Hanada, R. D. Noebe, and D. S. Schwartz (eds.), The Materials Research Society, Pittsburgh, PA, 1995.
11. B. A. Pint, A. J. Garratt-Reed, and L. W. Hobbs, *Mater. High. Temp.* **13** (1995) 3.

12. B. A. Pint, "Study of the Reactive Element Effect in ODS Iron-Base Alumina-Formers," submitted for publication in Mater. Sci. Forum, March 1996.

13. P. F. Tortorelli and J. H. DeVan, pp. 257-70 in Processing, Properties, and Applications of Iron Aluminides, J. H. Schneibel and M. A. Crimp (eds.), The Minerals, Metals, and Materials Society, Warrendale, PA, 1994.

14. B. A. Pint, P. F. Tortorelli, and I. G. Wright, "The Oxidation Behavior of ODS Iron Aluminides," submitted for publication in Werst. Korros., March 1996.

15. G. J. Yurek, D. Eisen, and A. J. Garratt-Reed, Metall. Trans. A 13A (1982) 473-85.



EVALUATION OF THE INTRINSIC AND EXTRINSIC FRACTURE  
BEHAVIOR OF IRON ALUMINIDES

Bruce S. Kang<sup>1</sup>, Qizhou Yao<sup>2</sup> and Bernard R. Cooper<sup>3</sup>

<sup>1,2</sup>Mechanical and Aerospace Engineering Department

<sup>3</sup>Physics Department

West Virginia University

Morgantown, WV 26506

ABSTRACT

Comparative creep crack growth tests of FA-186 and FA-187 iron aluminides under either dry oxygen or air environment showed that both alloys are susceptible to room temperature hydrogen embrittlement. Test results also revealed that FA-187 is intrinsically a more brittle material than FA-186. Atomistic computational modeling is being undertaken to find the preferred geometries, structures and formation energies of iron vacancies and vacancy pairs (Fe-Fe) in FeAl and Fe<sub>3</sub>Al. An indication of vacancy clustering in Fe<sub>3</sub>Al, with consequences for dislocation behavior, may be important for understanding the role of dislocation assisted diffusion in the hydrogen embrittlement mechanism.

INTRODUCTION

Because of their excellent corrosion resistance in high temperature oxidizing-sulfidizing environments in combination with low cost and other advantages, iron aluminides are of great potential use in fossil energy technology, however, there are problems at room and medium temperatures with hydrogen embrittlement as related to exposure to moisture.<sup>1,2</sup> In this research, a coordinated computational modeling/experimental study of mechanisms central to mechanical and fracture behavior in these materials from room to medium temperatures under either air or moisture-free environment is undertaken. Some preliminary results of our first year research effort are presented in this paper. The initial computational modeling is focused on the study of iron vacancy and divacancy behavior which may be important for understanding how dislocation assisted diffusion may enter the hydrogen embrittlement mechanism. A fully quantum mechanical full-potential LMTO technique, including force calculations, is being applied to find the preferred geometries, structures

and formation energies of iron vacancies and vacancy pairs (Fe-Fe) in FeAl and Fe<sub>3</sub>Al. As for the experimental research, four iron aluminides with various alloy additives such as Zr, C, Nb, or B are selected to study the effect of alloy additives to fracture behavior, in particular, the improvement of resistance to hydrogen embrittlement. Four crack growth test results of iron aluminides (FA-186 and FA-187) subjected to constant tensile loading in air or dry oxygen environment are discussed in this paper. Moire interferometry is used to obtain full-field crack-tip deformations which will be used to determine crack tip plastic yield zone and fracture parameters such as J-integral or stress intensity factor. Post mortem fractography evaluation is also carried out to correlate the measured crack tip deformations to microstructural characteristics.

## COMPUTATIONAL MODELING

The iron vacancy distribution is central to understanding mechanisms controlling the strength of iron aluminides generally, and may also play a key role in the mechanisms by which hydrogen penetrates and embrittles iron aluminides, such as dislocation-assisted diffusion.<sup>2</sup> For these reasons the initial focus in our computational modeling study of iron aluminides is on the tendency of iron vacancies to cluster. To investigate this question we are first looking at the energetics favoring the formation of a divacancy compared to the energy of two isolated vacancies. This calculation will include the effects of lattice relaxation. The method being used is our well established fully quantum mechanical full potential linear combination of muffin-tin-orbitals (LMTO) technique.<sup>3,4</sup> This is an *ab initio* all-electron technique with full relativistic corrections included. To assure high accuracy we have implemented an augmented basis through use of multiple  $\kappa$ 's and energy windows.<sup>4,5</sup> Initially we have found the preferred unrelaxed geometry through use of total energy minimization. For FeAl this gives a formation energy of 4.6eV, and a calculated lattice constant of 2.82 Å and bulk modulus of 165.39 GPa. This value for the lattice constant compares favorably to the experimental value<sup>6</sup> of 2.90 Å and the value of 2.83 Å calculated earlier by Fu and Yoo<sup>7</sup>; while the bulk modulus compares to Fu and Yoo's calculated value of 187.84 GPa.

Our initial calculation of vacancy formation energy is for FeAl, prior to proceeding to the study of Fe<sub>3</sub>Al, the system of greater practical interest. We find the unrelaxed formation energy of a single iron vacancy in FeAl is 1.0eV. This compares favorably to the experimental value<sup>8</sup> of 0.98±0.07eV and the value of 0.97eV calculated by Fu et al.<sup>9</sup> Judging from the behavior in aluminum,<sup>10</sup> we expect



relaxation effects to lower this by an amount of at most 0.1eV, which would correspond to the lower part of the experimental range. To treat relaxation effects for this transition metal system, we have implemented a force methodology based on our full-potential LMTO total energy technique and will apply this to vacancy and divacancy formation energies in both FeAl and Fe<sub>3</sub>Al. As a test of this methodology, we have calculated the formation energy of a fully relaxed vacancy in aluminum and obtained a value of 0.56eV in comparison with the experimental value of 0.60-0.67eV and the value of 0.66±0.03eV calculated by Chetty et al<sup>10</sup> using a pseudopotential-based technique.

## EXPERIMENTAL PROGRAM

### Materials

Alloys used in this study were fabricated at Oak Ridge National Laboratory (ORNL) by vacuum induction melting and casting into graphite molds. The ingots were then hot forged (two passes, 25% per pass) at 1000°C followed by hot rolled at 800°C for seven passes (15% per pass) to produce finished plate thickness of 6.35 mm. The finished plates were either heat treated at 900°C for one hour then air quenched to produce partially ordered B2 structure or heat treated at 900°C for one hour followed by 550°C for 72 hours then air quenched to produce DO<sub>3</sub> structure. Four alloys (FA-186, FA-187, FA-188, and FA-189) were received, however, only test results of FA-186 and FA-187 are presented in this paper. Table 1 shows the alloy composition of FA-186 and FA-187.

Singe-edge-notched (SEN) specimens were cut from the plates using EDM machine and specimen surfaces were hand-polished with fine grid sandpapers. Figure 1 shows the test specimen geometry. The notch of each specimen was cut using 0.1 mm diameter EDM wire with notch direction parallel to the rolling direction.

### Moire Interferometry

Moire interferometry was developed in the 1980's<sup>11</sup> and has been used to examine a variety of problems in composite materials, interface mechanics and fracture mechanics. Moire interferometry is capable of high sensitivity full-field surface deformation measurement (typical measurement sensitivity can range from 0.1 µm/fringe to 1.6 µm/fringe). Recently, we have demonstrated that moire interferometry can be applied to study environmental assisted cracking problems.<sup>12,13</sup> In this research, an environmental chamber was constructed to conduct crack growth tests of iron

aluminides under controlled gas content (air, argon, hydrogen gas or dry oxygen) environments. Figure 2 shows schematic drawing of the optical setup for moire interferometry test with the environmental chamber mounted on the optical bench.

## RESULT AND DISCUSSION

Table 2 shows the test matrix. As shown in the table, four tests of FA-186 and FA-187 SEN specimens were conducted under constant tensile loading condition in either dry oxygen or air environment. Figures 3 to 6 shows typical recorded moire fringe patterns at different time intervals. Specimen 186#1 was tested in dry oxygen under initial applied  $K_I$  value of 25 MPa $\sqrt{m}$  for nineteen hours with little change of crack tip deformation fields (as shown in Fig. 3). At  $t = 1124$  minutes, the applied  $K_I$  value was increased to 28.7 MPa $\sqrt{m}$  and we observed steady increase of crack tip damage zone (dark region), after 21 minutes ( $t = 1145$  minutes), the specimen failed. As for specimen 186#2, it was tested in air with the same initial applied  $K_I$  value of 25 MPa $\sqrt{m}$ . The recorded moire fringes showed slowly increased creep crack tip deformations (Fig. 4). We also observed the existence (pop-in) of secondary micro cracks at notch tip region right after the 25 MPa $\sqrt{m}$   $K_I$  load was applied; these micro cracks may be caused by the stress-assisted localized crack tip hydrogen embrittlement. At  $t = 95$  minutes, the applied  $K_I$  value was increased to 28.3 MPa $\sqrt{m}$  and quickly (within 20 seconds), the bottom portion of the micro cracks coalesced to trigger unstable crack propagation to failure. Figure 7 shows the corresponding SEM fractographs which indicated transgranular cleavage failure for both FA-186 specimens, however, the one tested in air had rougher cleavage facets (i.e. more tilt and twist boundaries). Since in hydrogen-free environment, cleavage generally takes place along crystallographic planes with the lowest packing density and thus resulted in larger cleavage facets. While in hydrogen-containing environment, hydrogen embrittlement is proposed to be associated with dislocation transport of hydrogen<sup>2</sup>, which occurred along crystallographic planes with the highest packing density, i.e. more rougher cleavage facets for specimen 186#2.

As for the FA-187 specimens which contain small amount of Zr and C, the same initial loading condition ( $K_I = 25$  MPa $\sqrt{m}$ ) was applied (see Table 2) and, as shown in Figs. 5 and 6, the one tested in dry oxygen lasted for about 18 minutes and the one tested in air lasted for only 2 minutes. For both specimens, initial steady crack extension was observed. Figure 8 shows representative

SEM fractographs in areas 1, 2 and 3. Based on the moire fringes, we observe that specimen 187#1 had slow crack extension from initial notch to the beginning portion of area 3 followed by unstable crack propagation, and specimen 187#2 had slow crack extension from initial notch up to the mid-section of area 2 followed by unstable fracture. From Fig. 8, it is noted that the slow crack extension of FA-187 SEN specimens is characterized by intergranular fracture. For specimen 187#2 tested in air, the effect of hydrogen embrittlement is evident and resulted in shorter crack extension and time duration. Our test results indicated the FA-187 is intrinsically more brittle than FA-186. As discussed in ref. 14, the level of zirconium addition needs to be carefully controlled; some amount of zirconium addition (say about 0.1%) is beneficial to promote scale adhesion for protection against corrosion in harsh environment, however, too much zirconium addition (such as 0.5% Zr in FA-187) may produce intrinsically brittle iron aluminide alloy.

### CONCLUSION

Comparative creep crack growth tests of FA-186 and FA-187 SEN specimens under either dry oxygen or air environment showed substantial difference of crack-tip deformation profile and evidence of hydrogen embrittlement for both the FA-186 and FA-187 iron aluminides. Test results also revealed that FA-187 is intrinsically a more brittle material than FA-186.

Additional comparative tests are planned for FA-188 and FA-189 alloys. Evaluation of crack tip plastic yield zone (or damage zone) and fracture parameters such as J-integral or stress intensity factor based on the measured moire fringes is currently undertaken. Research collaboration with ORNL researchers on computational modeling and microstructural analysis should elucidate the intrinsic and extrinsic fracture behavior of the Fe-28Al-5Cr series iron aluminides.

### ACKNOWLEDGMENT

This research is sponsored by the U.S. Department of Energy, Office of Fossil Energy, Advanced Research and Technology Development (AR&TD) Materials Program at the Oak Ridge National Laboratory under contract no. SUB-19X-ST547C with Lockheed Martin Energy Systems, Inc. Technical assistance of Dr. C.T. Liu at ORNL is gratefully acknowledged.

## REFERENCES

1. N.S. Stoloff and C.T. Liu, "Environmental Embrittlement of Iron Aluminides - Review," *Intermetallics*, 2, pp.75-87, (1994).
2. A. Castagna, D.A. Alven and N.S. Stoloff, "Environmental Embrittlement of Iron Aluminides under Cyclic Loading Condition," *Proceedings of the Ninth Annual Conference on Fossil Energy Materials*, Oak Ridge, TN, pp. 377-386, May 16-18 (1995).
3. D.L. Price and B.R. Cooper, *Phys. Rev. B* 39, 4945 (1989).
4. D.L. Price, B.R. Cooper and J.M. Wills, *Phys. Rev. B* 46, 11, 368 (1992).
5. D.L. Price, J.M. Wills, and B.R. Cooper *Phys. Rev. B* 48, 15, 301 (1993).
6. M.H. Yoo, T. Takasugi, S. Hanada, and O. Izumi, *Mater. Trans. Japan Inst. Metals* 31, 435 (1990).
7. C.L. Fu and M.H. Yoo, *Acta, Metall, Mater*, 40, 703 (1992).
8. R. Wurschum, C. Grupp, and H.E. Schaefer, *Phys. Rev. Lett*, 75, 97 (1995).
9. C.L. Fu, Y.Y. Ye, M.H. Yoo, and K.M. Ho, *Phys. Rev. B* 48, 6712 (1993).
10. N. Chetty, M. Weinert, T.s. Rahman, and J.W. Davenport, *Phys. Rev. B* 52, 6313 (1995).
11. D. Post, *Moire interferometry*, Chapter 7 in *SEM, Handbook on Experimental Mechanics*, ed. A.S. Kobayashi. Prentice-Hall, Englewood Cliffs, NJ, pp.314-387, (1987).
12. F.X. Wang and B.S.-J. Kang, *Moire Interferometry in Liquid Medium, SEM, Proceeding of the VII International Congress on Experimental Mechanics*, PP.1711-1716, Las Vegas, NA, June 8-11 (1992).
13. B.S.-J. Kang, G. Zhang, P. Liu and M. Ellathur, *Stress Accelerated Grain Boundary Oxygen Embrittlement on Creep Crack Growth of Ni-base Superalloys*, 1995 ASME Winter Conference, San Francisco, CA, November, 20-24 (1995).
14. C.G. McKamey, P.J. Maziasz and Y. Marrero-Santos, *Effects of Composition and Heat Treatment at 1150°C on Creep-Rupture Properties of Fe<sub>3</sub>Al-based Alloys*, *Proceedings of the Ninth Annual Conference on Fossil Energy Materials*, Oak Ridge, TN, pp. 369-376, May 16-18 (1995).

Table 1 Chemical Composition of Fe-Al Alloys (at%)

Composition	Fe	Al	Cr	Zr	C
FA - 186	balance	28	5		
FA - 187	balance	28	5	0.5	0.05

Table 2 Test Matrix

Specimen	a/W	Structure	Applied K (MPa√m)	Environment	Lasting Time
186 #1	0.65	DO <sub>3</sub>	25 28.7	Dry Oxygen Dry Oxygen	19 hrs 21 min
186 #2	0.65	DO <sub>3</sub>	25 28.3	Air Air	94 min 1 min
187 #1	0.4	DO <sub>3</sub>	25	Dry Oxygen	18 min
187 #2	0.4	DO <sub>3</sub>	25	Air	2 min

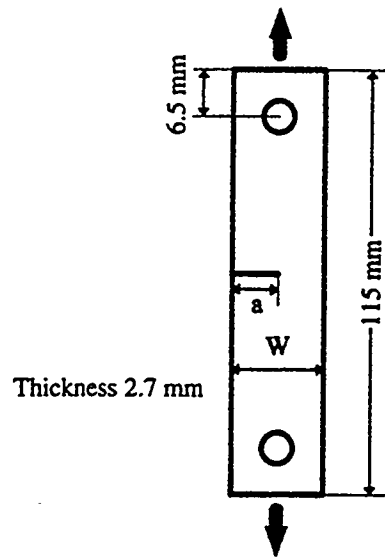


Fig. 1 Test specimen geometry.

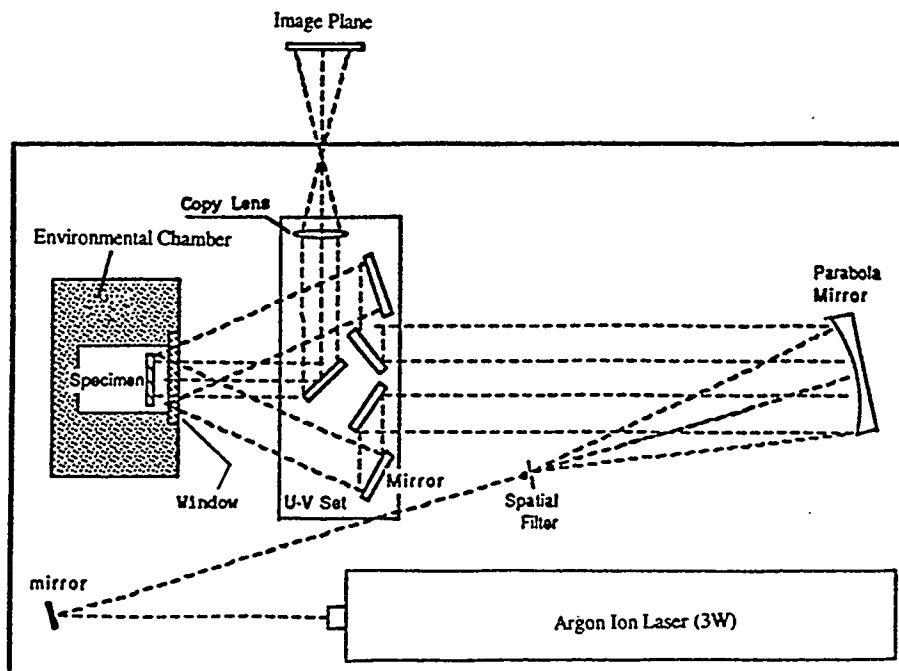
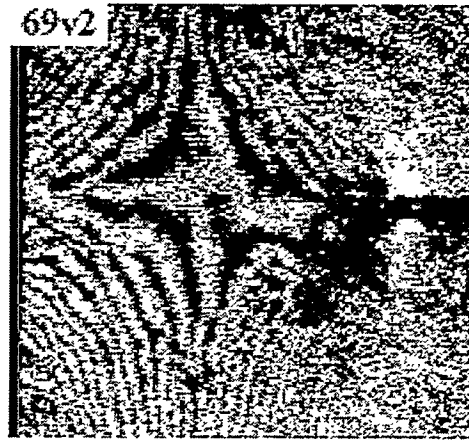
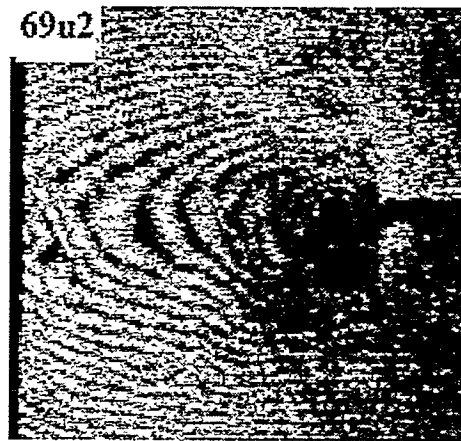


Fig. 2 Optical setup for moiré interferometry test.

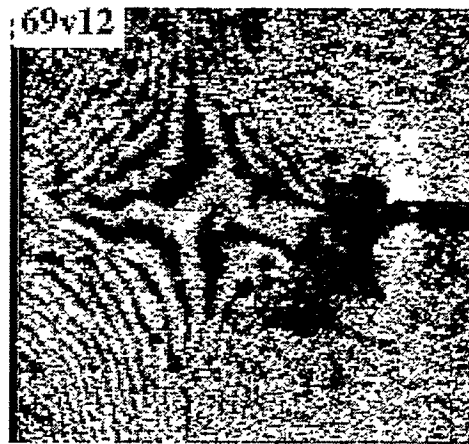
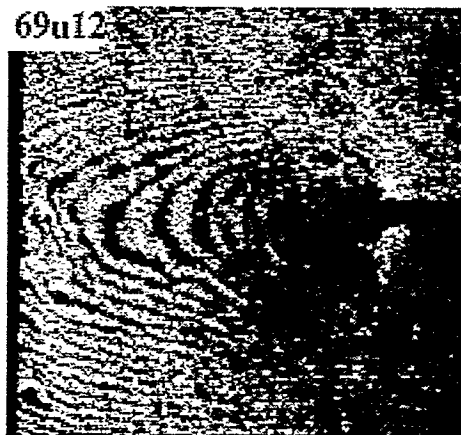
Alloy 186  
Room Temp, Oxygen

U field

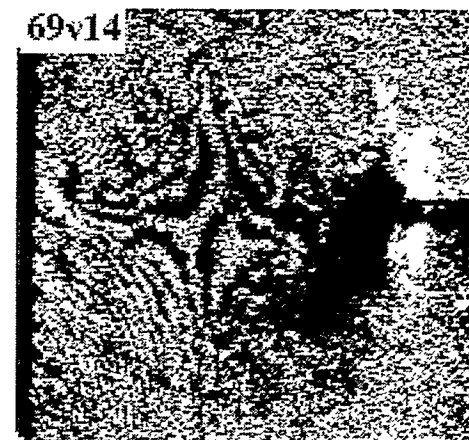
V field



$K = 25$   
 $t = 4 \text{ min}$



$t = 1104 \text{ min}$



$(K = 28.7)$   
 $t = 1124 \text{ min}$

(break)  
 $(t = 1145 \text{ min})$

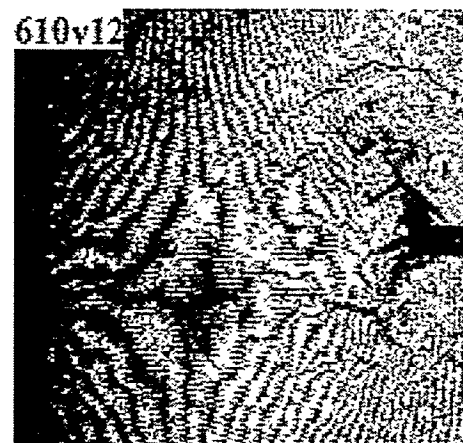
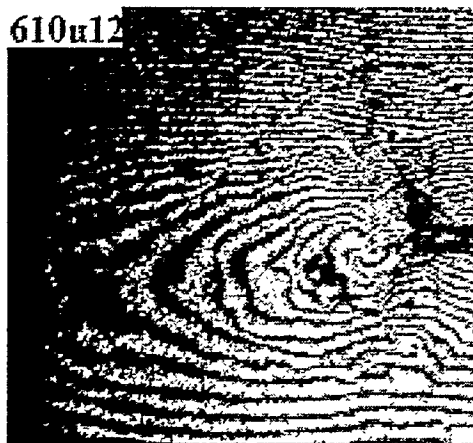
5 mm

Fig. 3 U and V displacement fields of alloy FA-186 SEN specimen tested in dry oxygen.

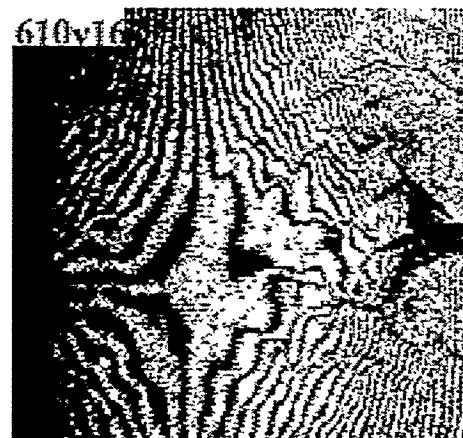
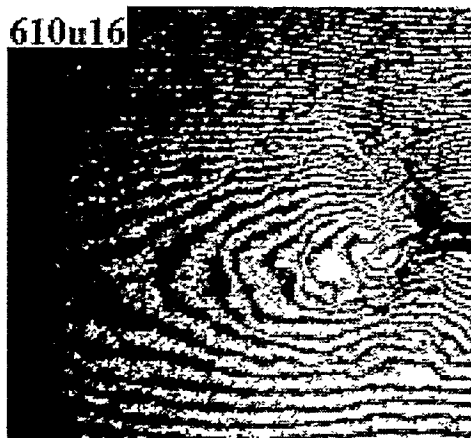
Alloy 186  
Room Temp, Air

U field

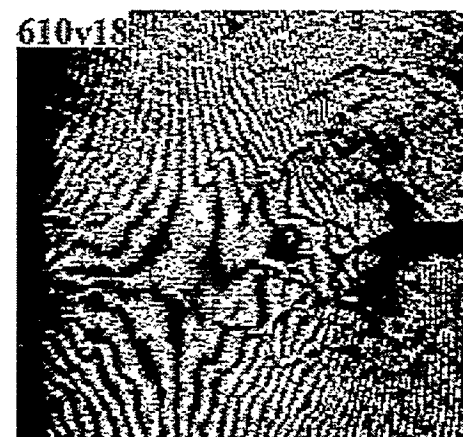
V field



$K = 25$   
 $t = 18 \text{ min}$



$t = 64 \text{ min}$



$t = 92 \text{ min}$

$(K = 28.3)$   
(break)  
 $(t = 95 \text{ min})$

5 mm

Fig. 4 U and V displacement fields of alloy FA-186 SEN specimen tested in air.

**Alloy 187**  
**Room Temp, Oxygen**

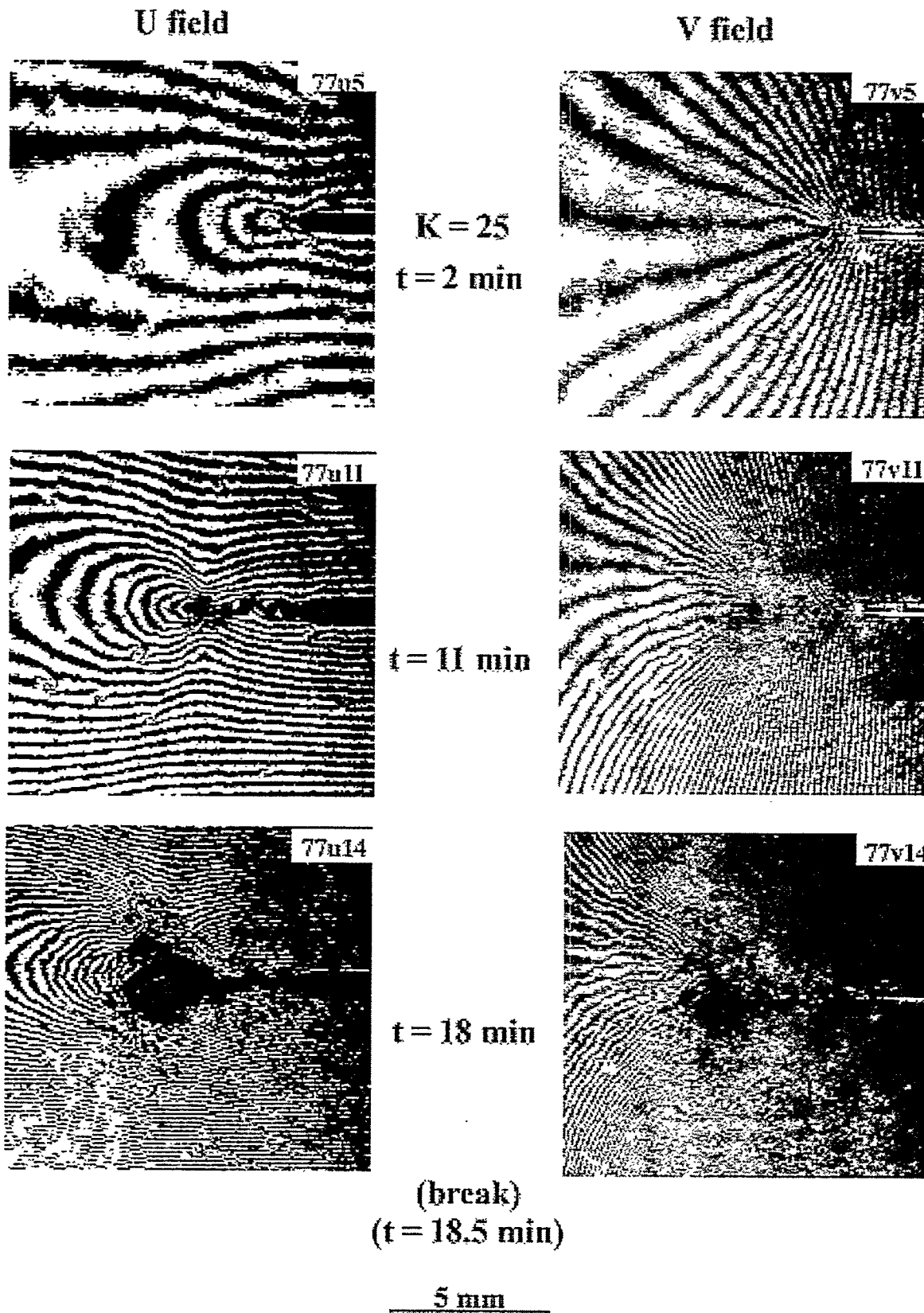


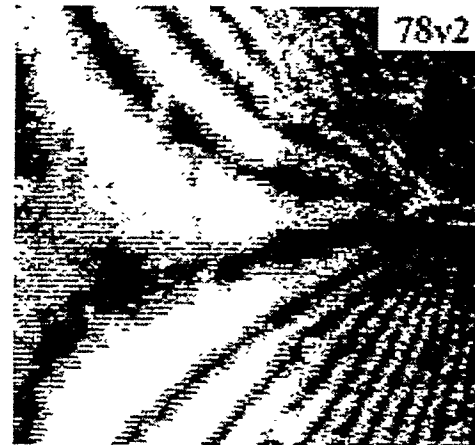
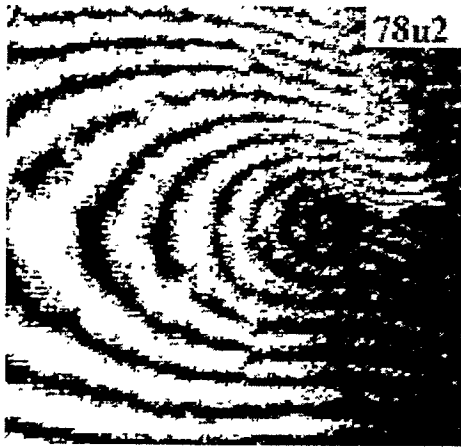
Fig. 5 U and V displacement fields of alloy FA-187 SEN specimen tested in dry oxygen.



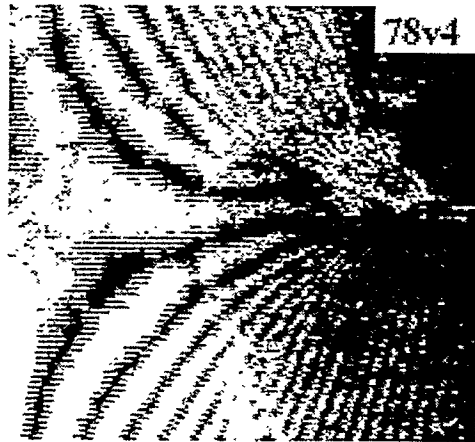
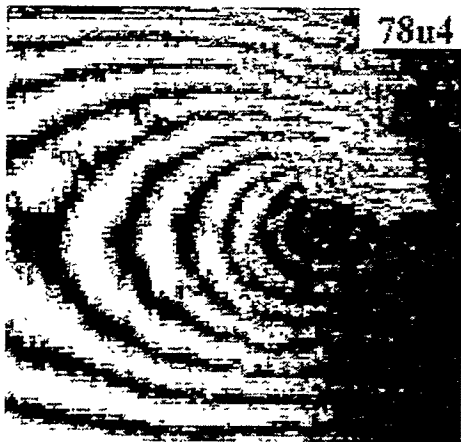
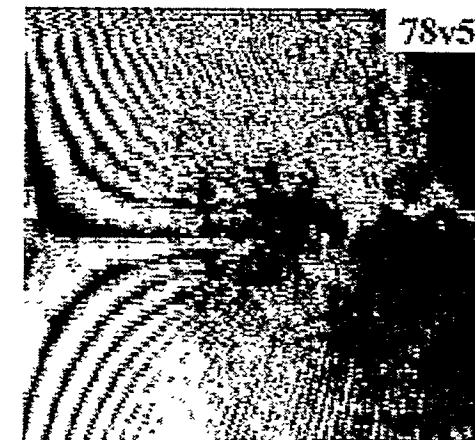
Alloy 187  
Room Temp, Air

U field

V field



$K = 25$   
 $t = 0.5 \text{ min}$

 $t = 1 \text{ min}$  $t = 1.5 \text{ min}$ 

(break)  
( $t = 2 \text{ min}$ )

5 mm

Fig. 6 U and V displacement fields for alloy FA-187 SEN specimen tested in air.

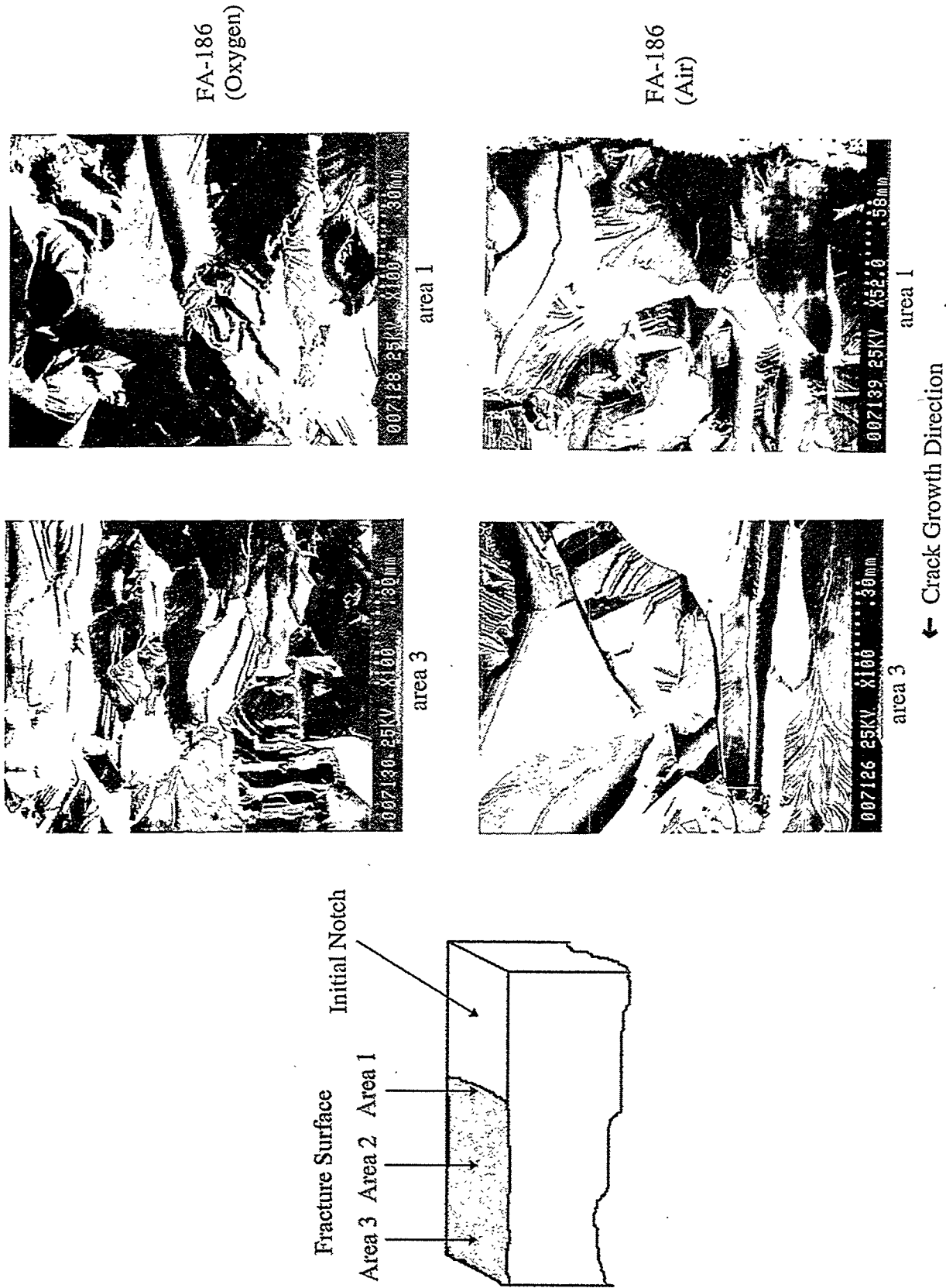


Fig. 7 SEM fractographs of alloy FA-186 SEN specimen.



Fig. 8 SEM fractographs of alloy FA-187 SEN specimen.



## THE MECHANICAL RELIABILITY OF ALUMINA SCALES AND COATINGS

K. B. Alexander, K. Prüßner and P. F. Tortorelli

Oak Ridge National Laboratory  
P. O. Box 2008  
Oak Ridge, Tennessee 37831-6376

### ABSTRACT

The mechanical integrity of oxide scales ultimately determines their ability to protect materials from corrosion and other environmental effects arising from deleterious reactions with gases and condensable products. The microstructure and mechanical behavior of alumina products thermally grown or deposited on Fe-28 at.% Al intermetallic alloys are being characterized in order to develop the knowledge and means to control the mechanical reliability of alumina scales by microstructural manipulation through design and processing.

Mechanical characterization involved gravimetric data from cyclic oxidation experiments, in-situ observation of oxidized specimens undergoing flexural loading in a scanning electron microscope, and measurements of hardness, elastic modulus and cracking resistance by nanoindentation. Values of cracking thresholds for  $\text{Al}_2\text{O}_3$  scales were consistent with other measurements for surface and bulk alumina.

The oxidation behavior of  $\text{Fe}_3\text{Al}$  alloys coated with a thin (0.5 - 1  $\mu\text{m}$ ) alumina film deposited by plasma synthesis has been studied. During exposure in the oxidizing environment, new oxide was formed between the coating and the substrate. The presence of the deposited amorphous oxide inhibited the subsequent thermal oxidation of the metal. Because the thermally grown alumina forms under the deposit, the adherence of the coating is controlled by the strength of the metal/oxide interface that develops during oxidation.

### INTRODUCTION

In many high-temperature fossil energy systems, corrosion and deleterious reactions with gases and condensable products in the operating environment often compromise materials performance. The presence of a stable surface oxide (either as thermally-grown scales or deposited coatings) can effectively protect the materials from these reactions if the oxides are slow-growing, dense and adherent to the substrate. The protection these brittle oxide films provide has long been a critical issue, particularly for applications involving severe high-temperature thermal cycles or very aggressive (for example, sulfidizing) environments. The various factors which control the scale/coating integrity and adherence are not well understood. The present multilaboratory collaborative work is intended to define the relationships between substrate characteristics (composition, microstructure, and mechanical behavior) and the

structure and protective properties of deposited oxide coatings and/or thermally grown scales. Through such studies, the ultimate goal is to assure environmental protection through effective processing and materials selection leading to the development of corrosion-resistant, high-temperature materials for improved energy and environmental control systems.

The Oak Ridge National Laboratory (ORNL) work described in this paper is being conducted in collaboration with work sponsored by the Department of Energy's Office of Fossil Energy at Argonne National Laboratory (ANL) and Lawrence Berkeley National Laboratory (LBNL) as well as in concert with on-going interactions that are part of the Office of Basic Energy Sciences' Center of Excellence for the Synthesis and Processing of Advanced Materials. The Center of Excellence on Mechanically Reliable Surface Oxides and Coatings includes participants from ORNL, ANL, LBNL, Idaho National Engineering Laboratory (INEL) and Lawrence Livermore National Laboratory (LLNL). Each of these laboratories has appropriate expertise in areas of materials characterization, modeling, and coating/deposition techniques relevant to studies of oxide scales and coatings.

The initial work is focusing on several model systems, all of which form stable, slow-growing alumina scales at elevated temperatures. Systems were chosen which were relevant to ongoing technological interests as well as to represent a range of both "soft" and "stiff" substrates in order to explore the role of the substrate on the mechanical reliability of the oxide scale. This paper will discuss work on the initial system chosen: alumina scales on iron-aluminum alloys with and without zirconium.

## EXPERIMENTAL PROCEDURES

Three iron aluminide alloys have been studied to date. Their compositions and common designations are listed in Table 1.

Table 1. Compositions of iron-aluminum alloys used in this study.

Alloy Designation	Concentration <sup>a</sup> (at. %)				
	Al	Cr	Zr	Nb	Other
FA186	28	5			
FA129	28	5	-	0.5	0.2 C
FAL	28	5	0.1	-	0.05 B

<sup>a</sup> Balance is Fe.

Ingots of these alloys were prepared by arc melting and casting. These were then rolled to a final thickness of between 0.8 and 1.3 mm. Rectangular specimens (typically 12 x 10 mm) were prepared from these sheets. Details of the magnetically-filtered cathodic-arc plasma-synthesis process used to deposit alumina coatings on FA186 and FAL alloys are described elsewhere.<sup>1</sup>

Gravimetric measurements under thermal cycling conditions were used to establish overall corrosion behavior at 1000°C. These cyclic oxidation experiments were conducted in static air by exposing coupons in individual pre-annealed alumina crucibles to a series of 24-h exposures. Scanning electron microscopy (SEM) was performed on oxidized coupons as well as on polished cross-sections through the scale.

A Nanoindenter<sup>TM</sup> was used to evaluate the mechanical properties of the oxide scales. Hardness and modulus measurements were obtained using a pyramidal Berkovitch indenter. Cracks were generated within the scale for cracking threshold measurements using a cube-corner indenter.<sup>2</sup> For these experiments, a series of indents at different loads were generated across a polished cross-section of a scale. The cracks were subsequently imaged in an SEM.

Room temperature four-point bend testing of oxidized coupons was performed *in situ* in a scanning electron microscope. The geometry of the bending rig is such that the tensile surface of the specimen is continuously observed during loading. The load is continuously monitored and both still and video images of the tensile surface during loading and unloading can be acquired.

## RESULTS AND DISCUSSION

The oxidation rate was significantly reduced for the iron-aluminide alloy containing zirconium (FAL) as shown by the thermal-cycling weight gain data in Fig. 1. Distinctive differences were also observed in the morphology of the oxide scales formed on the two alloys. As described previously,<sup>3</sup> the FAL alloy exhibited flat, uniform oxide surfaces with no evidence of spallation during thermal cycling, whereas a significant amount of spallation was observed after thermal cycling of the FA129 alloy, Fig. 2. Cross-sections through the scale on the FAL alloy showed that the scale was completely adherent but exhibited some porosity, Fig. 3. Zirconium-rich particles were also observed at the metal/oxide interface after oxidation of FAL alloys (Fig. 3).

The beneficial effect of zirconium on the oxidation resistance of Fe<sub>3</sub>Al alloys is now well-documented over a temperature range of 900-1300°C.<sup>3-5</sup> However, its role in improving oxidation behavior is not well-defined. The present results show that zirconium-rich particles

form at the oxide-metal interface and there is also some evidence that zirconium ions accumulate in the alumina scale.<sup>6</sup> This is consistent with the dynamic segregation behavior observed for reactive-element additions in many alumina-forming systems.<sup>7</sup> Other work has shown that the presence of Zr in the Fe-28Al-5Cr system suppresses segregation of sulfur to the metal-oxide interface.<sup>8</sup>

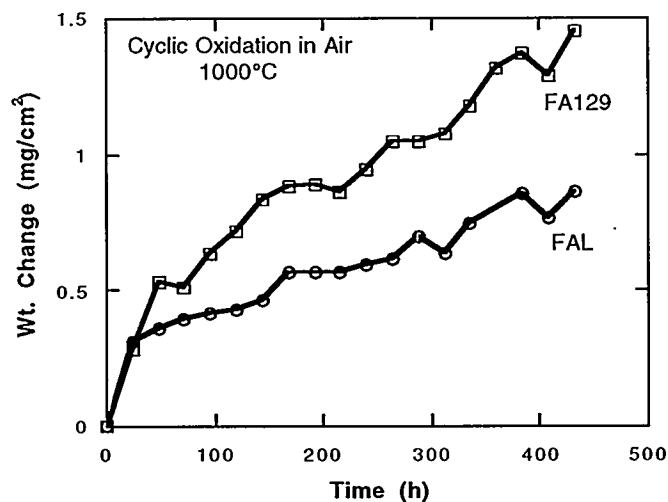


Fig. 1 Total weight gain (specimen + spall) as a function of time for FAL and FA129 cyclically oxidized in air at 1000°C. Each point is a single thermal cycle.

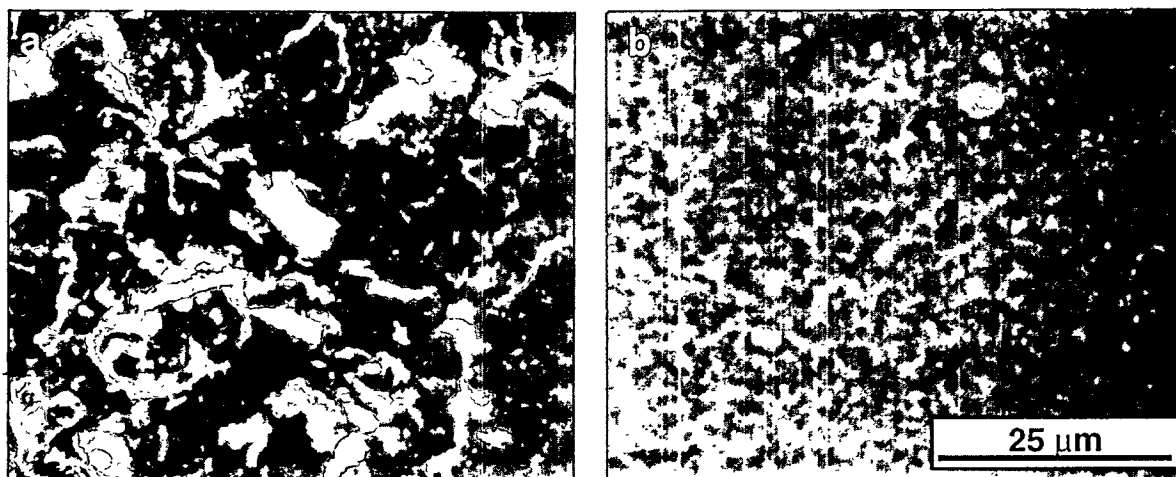


Fig. 2. SEM micrographs of iron-aluminide alloys that were oxidized for 48 h (2 - 24 h cycles) in air at 1000°C. (a) FA129 and (b) FAL. (From Ref. 3)



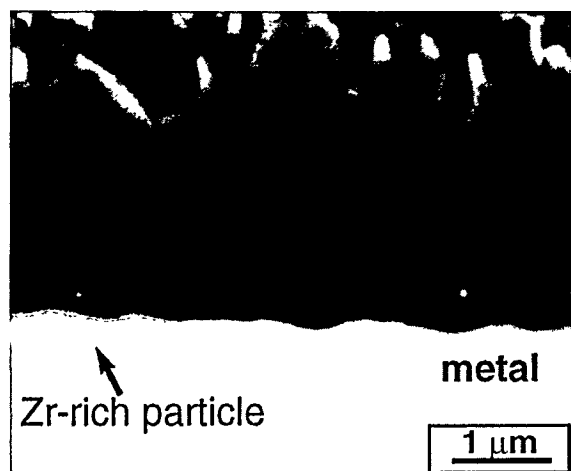


Fig. 3. Back-scattered electron image of oxide scale (2 x 24 h cycles at 1000°) in air) formed on FAL. Porosity within the scale is obvious. Zirconium-rich particles were observed at the metal/oxide interface.

The mechanical reliability of scales depends not only on their intrinsic characteristics such as adherence and defect structure, but also on their response to residual and imposed stresses. For the cracking threshold experiments, performed on an alumina scale grown on FAL, no cracking was detected at 2- $\mu$ m-wide indents generated with a load of 10mN (1g). Higher loads generated much larger indents and extensive cracking from the corners of the pyramidal indents. The indentation size-indentation load relationship obtained from these experiments is shown in Fig. 4, along with nanoindentation data obtained from single crystal sapphire (indicated as a range).<sup>2</sup>

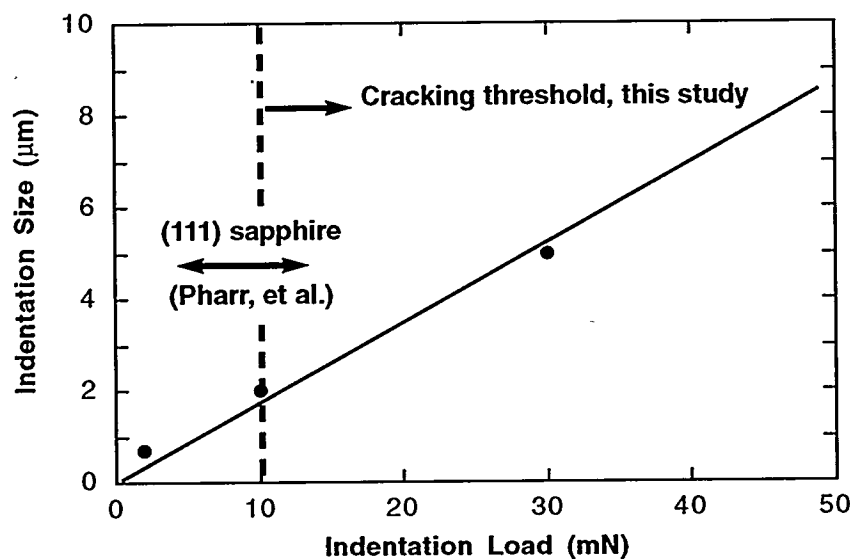


Fig. 4. Indentation size (full width) as a function of indentation load for indents in alumina scale on iron-aluminide. A cube-corner indenter was used for these experiments to attain higher stresses at a given indentation depth and thus induce cracking. Cracks were not observed below the indicated cracking threshold.

Note that the approximate cracking threshold measured for the alumina scale is in agreement with that measured for bulk single crystal  $\alpha$ - $\text{Al}_2\text{O}_3$ . Since cracking was not observed during nanoindentation until the indent was larger than 2  $\mu\text{m}$ , fracture toughness measurements will be problematic since the oxide scale dimensions are typically smaller than the dimensions required to obtain valid indentation crack length measurements. However, the ability to precisely position and create small cracks within the microstructure, especially at or near the metal/oxide interface is encouraging. Such experiments will allow the examination of how crack propagation occurs within the scale and the role of the microstructure on this process.

The four-point-bending experiments also provide information as to how the scale/substrate system responds to imposed stresses. During loading of an FAL coupon with a thin (submicron) oxide scale, sets of parallel, regularly-spaced cracks were observed to spontaneously form on the tensile surface of the specimen after a critical load was reached, Fig. 5. Little growth of the cracks occurred during further loading. Although two sets of nearly orthogonal cracks were observed, the cracking was not perpendicular to the tensile axis. Despite the metal substrate being plastically deformed approximately  $30^\circ$  over approximately 1 cm, the oxide scale remained fully intact with no spallation. Since the scale remained adherent, and cracking was so fine and occurred nearly  $45^\circ$  to the tensile axis, it is suspected that the substrate played a larger role in the deformation process than would be observed for thicker scales. Residual stresses in the oxide may also play a role. The crack spacing and critical load behavior was qualitatively similar to previous bend testing of alumina scales.<sup>9</sup>

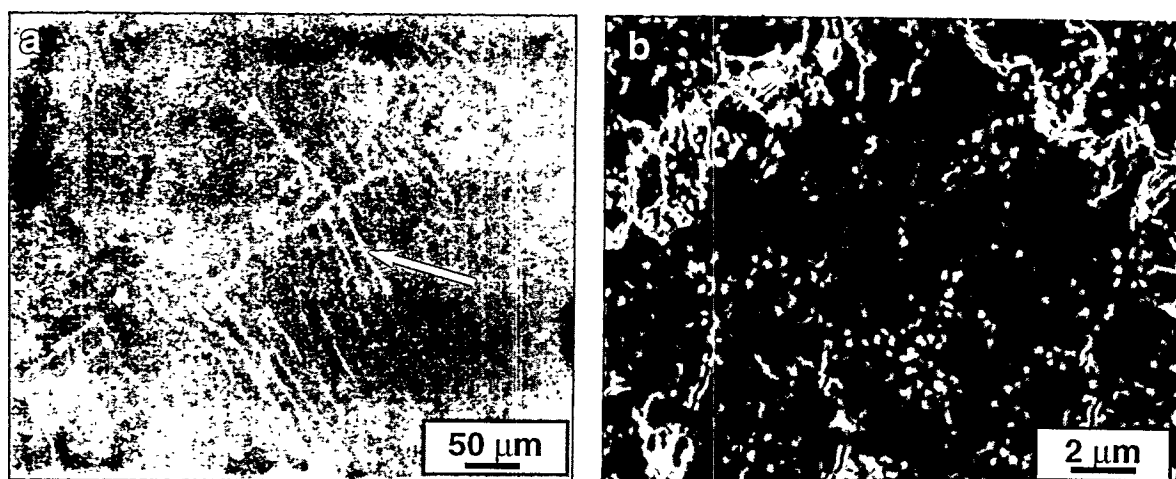


Fig. 5. SEM micrographs of cracking that occurs spontaneously within the scale during four-point-bend loading. The tensile loading direction is horizontal.

The microstructure of the plasma-deposited alumina coatings on FAL was examined in cross-section in the as-deposited condition as well as after exposure for 96 h at 1000°C in air. The surfaces of the deposited films were highly reflective. A comparison between the plasma-deposited alumina film and a thermally-grown scale is shown in Fig. 6. Both the surface and the metal/oxide interface are considerably smoother for the plasma-deposited film. Transmission electron microscopy<sup>10</sup> and X-ray diffraction studies<sup>11</sup> have shown that the as-deposited film is fully amorphous.

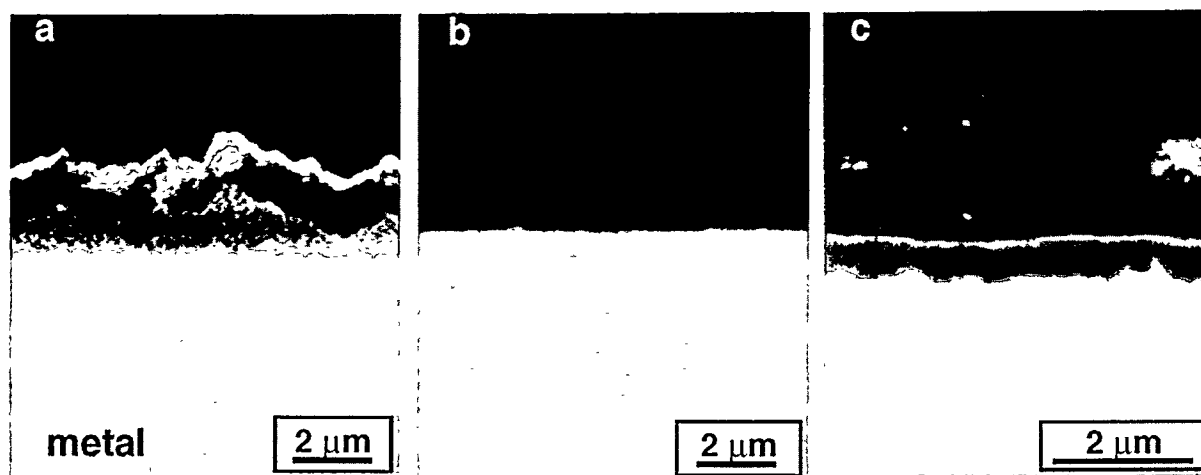


Fig. 6. SEM micrographs of alumina scales on FAL (a) thermally-grown alumina (2 x 24 h cycles at 1000°C), (b) plasma-deposited amorphous alumina, and (c) plasma-deposited film which has subsequently been oxidized for 96 h at 1000°C.

After oxidation (96 h at 1000°C in air), the uncoated FAL specimen exhibited an approximately 2- to 2.5- $\mu\text{m}$ -thick oxide scale. The total alumina thickness after oxidation on a specimen which had been coated with a 0.6- $\mu\text{m}$ -thick plasma-deposited coating prior to oxidation was about 1  $\mu\text{m}$ , as shown in Fig. 7. Zirconium-rich particles were observed at the metal/oxide interface in the case of the uncoated FAL, but not for the coated FAL specimen. A comparison between an as-deposited coating and a coated specimen which had been oxidized is shown in Figs. 6b and 6c. Note that the roughness of the metal/oxide interface has increased, whereas the smoothness of the gas interface has been retained. Auger electron spectroscopy experiments have indicated that the new thermally-grown oxide forms at the metal/oxide interface, beneath the deposited film.<sup>11</sup> Additional experiments on FA186 have confirmed this growth location, since the oxide film (plus thermally-grown oxide) completely spalls from the

metal substrate on cooling consistent with a new thermally-grown oxide/metal interface forming during oxidation and subsequently controlling the adherence in these coated systems after oxidation.<sup>11</sup> These observations are all consistent with the growth of new oxides beneath the deposited film being controlled by the transport of oxygen through the film, rather than by the outward diffusion of aluminum. The presence of the amorphous alumina film obviously diminishes the oxidation rate for the coated FAL alloys, most probably by affecting the transport rate of oxygen and/or by suppressing the formation of the rapidly-growing transition oxides that form initially on bare metal surfaces during oxidation. The absence of zirconium-rich particles at the oxide/metal interface probably reflects diminished oxygen transport through the deposited film.

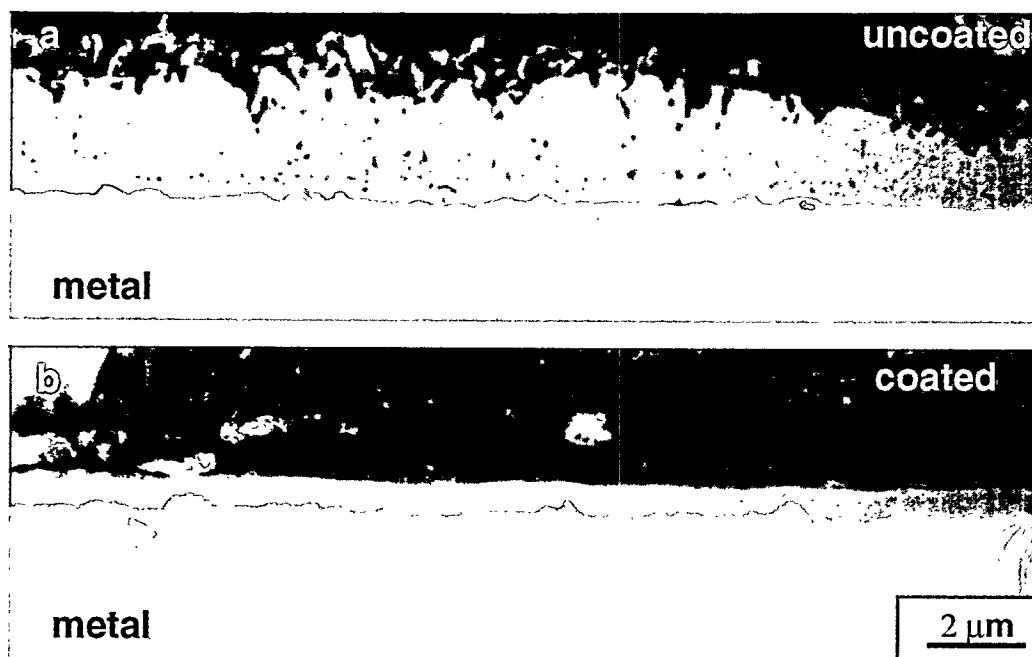


Fig. 7. SEM micrographs showing the effect of an amorphous plasma-deposited coating on the subsequent oxidation behavior of FAL. Cross-sections through oxide scales formed after 96h at 1000°C in air for (a) uncoated FAL and (b) FAL coated with 0.6-μm-thick amorphous alumina prior to oxidation.

## SUMMARY AND CONCLUSIONS

The mechanical reliability of scales and coatings can be assessed by traditional means such as gravimetric experiments and observations of adherence (or spallation) during thermal cycling. Other means to establish and study scale adherence such as measurements of the

mechanical properties of scales and their response to stress and/or cracking as a function of processing, composition, and microstructure can also yield important insights into the mechanisms controlling the long-term reliability of protective scales. The adherence of the metal/oxide interface is clearly of the utmost importance as demonstrated by the oxidation experiments on the plasma-deposited coatings. Despite the fact that the oxidation rate was significantly diminished by the presence of the coating, the reliability of the coating was determined by the properties of the thermally-grown oxide/metal interface; which in turn is controlled (in this case) by the substrate composition. This multilaboratory project seeks to further explore and understand the fundamental relationships among properties, structure, and mechanical reliability of surface oxides that provide corrosion protection at high temperatures.

#### ACKNOWLEDGMENT

The authors thank M. Howell for experimental support. This research was sponsored by the Fossil Energy Advanced Research and Technology Development (AR&TD) Materials Program and the Division of Materials Science, U.S. Department of Energy, DE-AC05-96OR22464 with Lockheed Martin Energy Research Corp. Research was performed in part with the SHaRE User Facilities at ORNL.

#### REFERENCES

- 1 I. W. Brown and Z. Wang, pp. 239-46 in *Proc. Ninth Annual Conf. Fossil Energy Materials*, N. C. Cole and R. R. Judkins (comp.), CONF-9505204, U. S. Department of Energy, August 1995.
2. D. S. Harding, W. C. Oliver, and G. M. Pharr, *Mater. Res. Soc. Symp. Proc.* **356** (1995) 663-68.
3. P. F. Tortorelli and K. B. Alexander, pp. 247-56 in *Proc. Ninth Annual Conf. Fossil Energy Materials*, N. C. Cole and R. R. Judkins (comp.), CONF-9505204, U. S. Department of Energy, August 1995.
4. J. H. DeVan, P. F. Tortorelli, and M. J. Bennett, "Environmental Effects on Iron Aluminides," pp. 309 - 20 in *Proc. Eighth Annual Conf. Fossil Energy Materials*, N. C. Cole and R. R. Judkins (comp.), CONF-9405143, U. S. Department of Energy, August 1994.
5. P. F. Tortorelli and J. H. DeVan, pp. 257-70 in Processing, Properties, and Applications of Iron Aluminides, J. H. Schneibel and M. A. Crimp (eds.), The Minerals, Metals, and Materials Society, Warrendale, PA, 1994.
6. J. A. Horton, Oak Ridge National Laboratory, unpublished results.
7. B. A. Pint, *Oxid. Met.* **45** (1996) 1-37.
8. P. Y. Hou, Lawrence Berkeley National Laboratory, unpublished results.
9. M. M. Nagl, S. R. J. Saunders, and V. Guttman, *Mater. High Temp.* **12** (1994) 163-168.
10. K. B. Alexander and K. Prüßner, Oak Ridge National Laboratory, unpublished results.
11. P. Y. Hou, K. B. Alexander, Z. Wang, and I. G. Brown, "The Effect of Plasma Synthesized Alumina Coatings on the Oxidation Behavior of Iron Aluminides", accepted for publication in High Temperature Coatings II, The Minerals, Metals, and Materials Society, Warrendale, PA, 1996.



## ELECTRO-SPARK DEPOSITION TECHNOLOGY

Roger N. Johnson

Battelle, Pacific Northwest National Laboratory

P.O. Box 999, K3-59

Richland, Washington 99352

### ABSTRACT

Electro-Spark Deposition (ESD) is a micro-welding process that uses short duration, high-current electrical pulses to deposit or alloy a consumable electrode material onto a metallic substrate.

The ESD process was developed to produce coatings for use in severe environments where most other coatings fail. Because of the exceptional damage resistance of these coatings, and the versatility of the process to apply a wide variety of alloys, intermetallics, and cermets to metal surfaces, the ESD process has been designated as one of the enabling technologies for advanced energy systems. Protective coatings will be critical to the life and economy of the advanced fossil energy systems as the higher temperatures and corrosive environments exceed the limits of known structural materials to accommodate the service conditions.

Developments include producing iron aluminide-based coatings with triple the corrosion resistance of the best previous  $\text{Fe}_3\text{Al}$  coatings, coatings with refractory metal diffusion barriers and multi layer coatings for achieving functionally gradient properties between the substrate and the surface. One of the most significant breakthroughs to occur in the last dozen years is the discovery of a process regime that promises an order of magnitude increase in deposition rates and achievable coating thicknesses. Since this regime borders on and exceeds the normal operating limits of existing ESD electronic equipment, development is in progress to produce equipment that can consistently and reliably achieve these conditions for a broad range of materials. Progress so far has resulted in a consistent 500% increase in deposition rates, and greater rates still are anticipated.

Technology transfer activities are a significant portion of the ESD program effort. Notable successes now include the start-up of a new business to commercialize the ESD technology, the incorporation of the process into the operations of a major gas turbine manufacturer, major new applications in gas turbine blade and steam turbine blade protection and repair, and in military, medical, metal-working, and recreational equipment applications.

## INTRODUCTION

The objective of this program is to develop an advanced coating process capable of meeting the surface treatment requirements for the next and future generations of advanced fossil energy systems. This includes the development and testing of new materials and coatings with the ability to operate in severe environments beyond current materials limits, and to provide improvements in performance, durability and cost effectiveness for both new and existing power systems. Ultimately new materials performance limits can enable new systems concepts.

A corollary objective is to further advance the Electro-Spark Deposition (ESD) technology and equipment, and to develop broad commercial applications through technology transfer activities.

Just as high performance jet engines would not be possible today without protective metallurgical coatings, so also does the next generation of high efficiency energy systems depend on protective coatings to survive the necessarily higher temperatures and more corrosive environments. The ESD coating process has been designated as one of the enabling technologies for such future systems. One of the reasons for this is that the exceptional structure produced in these metallurgically-bonded coatings makes them virtually immune to damage or spalling under severe service conditions and temperatures that destroy most other coatings. Additional attractions are that the process is portable (allowing coatings or surface treatments to be performed in the field), environmentally benign (creates no noxious wastes, fumes or effluents), and highly cost-effective.

## BACKGROUND

The ESD process was developed to provide exceptionally robust coatings for use in nuclear reactor environments when all other commercially available coatings either failed to survive the severe conditions or failed to meet the performance requirements. The Fossil Energy Program leveraged on that success to begin further developing the ESD process,



coatings and applications to meet the demands of advanced fossil energy systems.

Electro-spark deposition is a pulsed-arc micro-welding process that uses short-duration, high-current electrical pulses to weld a consumable electrode material to a metallic substrate. The short duration of the electrical pulse allows an extremely rapid solidification of the deposited material and results in an extremely fine-grained, homogeneous coating that may be amorphous for some materials. The microstructures thus produced are believed to be responsible for the superior corrosion and wear performance usually exhibited by the ESD coatings when compared to similar coatings applied by other processes.

The ESD process is one of the few methods available by which a fused, metallurgically-bonded coating can be applied with such a low total heat input that the bulk substrate material remains at or near ambient temperatures. This eliminates thermal distortions or changes in metallurgical structure of the substrate. Not only is the coating metallurgically-bonded, but it exhibits a functional gradient in composition and properties through the coating thickness. This eliminates the "metallurgical notch" associated with coatings that have an abrupt property change at the coating/substrate interface. The elimination of this notch and the metallurgical bond makes ESD coatings inherently more resistant to damage and spalling than the mechanically-bonded coatings produced by most other low-heat-input processes such as detonation gun, plasma spray, electro-chemical plating, etc. Nearly any electrically-conductive metal, alloy, intermetallic, or cermet can be applied by ESD to metal substrates.

Further background information on the ESD process is provided in Ref. 1 and 2.

## DISCUSSION OF PRIOR ACTIVITIES

### Chromium Carbide Experiments

ESD coatings usually show lower corrosion rates in most environments than the same material would in either bulk form or as a coating applied by other processes. For example, ESD-applied coatings of chromium carbide-15% Ni exhibit significantly lower corrosion rates in aqueous and liquid metal environments than similar detonation-gun applied coatings.<sup>3</sup> The

superior performance of the former is attributed to the extremely fine-grained, nearly amorphous structure inherent to the ESD coatings compared to the larger-grained, more heterogenous thermal spray coatings.

In tests at Argonne National Laboratory (ANL), this same ESD chromium carbide-15% Ni coating showed (unexpectedly) four times better sulfidation resistance than Type 310 stainless steel at 875 C.<sup>4</sup> Normally, this composition would not be expected to perform that well because of the strong susceptibility of a nickel matrix to sulfidation attack. Again, the near amorphous structure is believed to be a major factor in the corrosion resistance. This observation is in agreement with other Fossil Energy Program work that indicates one mechanism of improving lifetimes of protective oxide films and scales is to maintain as fine a grain structure as possible.<sup>5</sup>

### Iron Aluminide Coating Development

One of the most significant advances in ESD coatings for use in sulfidation environments has been the successful development of  $\text{Fe}_3\text{Al}$  as a coating material. Oak Ridge National Laboratory (ORNL) has demonstrated the exceptional corrosion properties of  $\text{Fe}_3\text{Al}$  in bulk form, but alloying to achieve acceptable mechanical properties while maintaining optimum corrosion resistance appears to be a challenge. One alternative is to use the most corrosion-resistant compositions as coatings. ORNL supplied us with various  $\text{Fe}_3\text{Al}$ -based alloys for use in ESD coating development. The iron aluminide compositions proved to be nearly ideal for use in the ESD process. Consistent, defect-free coatings over 100  $\mu\text{m}$  were applied rapidly, uniformly and economically.

Sulfidation corrosion tests on these initial coatings, however, showed that although the corrosion performance was significantly improved compared to the stainless steel substrate, the corrosion resistance was still inferior to that of the aluminide alloy in the plate form. Further investigation showed that weld-dilution effects with the substrate material had reduced the aluminum content at the surface below the threshold 12% Al that appears to be necessary for good sulfidation resistance.<sup>6,7</sup>

Three methods for increasing the aluminum content ultimately were tried. In the first, a simple process of alloying of the surface by ESD using an aluminum electrode was successful in producing aluminum enrichment, but the resulting structure was excessively cracked.<sup>8</sup> The second technique involved a preliminary coating (by ESD) of the substrate with a refractory metal, such as niobium or molybdenum. The higher melting material serves as a barrier to diffusion of the substrate material into the coating during subsequent ESD coating. This resulted in achieving a surface composition undiluted with substrate elements, and doubled the corrosion resistance.<sup>7</sup> The third method became possible when ORNL produced experimental electrode compositions based on FeAl.<sup>9</sup> This material also proved to be well-suited to the ESD process. Excellent quality, crack-free coatings using the higher Al content material were developed and tested.

## DISCUSSION OF CURRENT ACTIVITIES

### Improved Iron Aluminide Coatings

Corrosion tests completed at ANL showed that the iron aluminide coatings using the FeAl electrode materials were superior in corrosion resistance to all versions of the Fe<sub>3</sub>Al coatings and to the reference 304 and 316 stainless steels.<sup>6</sup> The corrosion conditions included simulated coal gasification and simulated coal combustion environments at 650°C for 1000 hours, both with and without the presence of HCl, as shown in Table 1.

Table 1. Chemistries of gas mixtures used for coating evaluation at 650°C<sup>6</sup>

Test Condition	pO <sub>2</sub> (atm)	pS(atm)	pCl <sub>2</sub> (atm)	pSO <sub>2</sub> (atm)	pHCl(atm)
Gasification	1.5 x 10 <sup>-23</sup>	5.6 x 10 <sup>-10</sup>	-	1.3 x 10 <sup>-11</sup>	-
Gasif. w/HCl	1.2 x 10 <sup>-23</sup>	5.2 x 10 <sup>-10</sup>	1.5 x 10 <sup>-16</sup>	9.1 x 10 <sup>-12</sup>	2.1 x 10 <sup>-3</sup>
Combustion	6.7 x 10 <sup>-3</sup>	1.4 x 10 <sup>-35</sup>	-	1.2 x 10 <sup>-3</sup>	-
Comb.w/HCl	4.9 x 10 <sup>-3</sup>	1.6 x 10 <sup>-35</sup>	3.6 x 10 <sup>-4</sup>	9.1 x 10 <sup>-4</sup>	1.7 x 10 <sup>-3</sup>

Coated and uncoated specimens were exposed in the above atmospheres for times up to 1000 hr and were periodically retrieved to measure weight changes at intermediate exposures. Figures 1A and B show the weight change data for Types 304 and 316 stainless steels and for  $\text{Fe}_3\text{Al}$ - or  $\text{FeAl}$ -coated Type 316 stainless steel after exposure at 650 C to simulated gasification environments with or without  $\text{HCl}$ . The uncoated alloys exhibited general corrosion and significant sulfidation and localized pitting corrosion. The weight gains and scaling rates were much lower for all the aluminide-coated specimens than for the uncoated alloys. The figure shows two curves for  $\text{Fe}_3\text{Al}$ -coated specimens that were fabricated at different times using somewhat different deposition parameters and tested in the same environments but at different times. The data for the two specimens are similar, indicating that the corrosion performance of these coated alloys is reproducible and that substantial improvement in corrosion resistance can be achieved by the surface coating of structural alloys. The best performance was achieved with the specimens having the highest aluminum content in the surface, i.e. those coated with the  $\text{FeAl}$ .

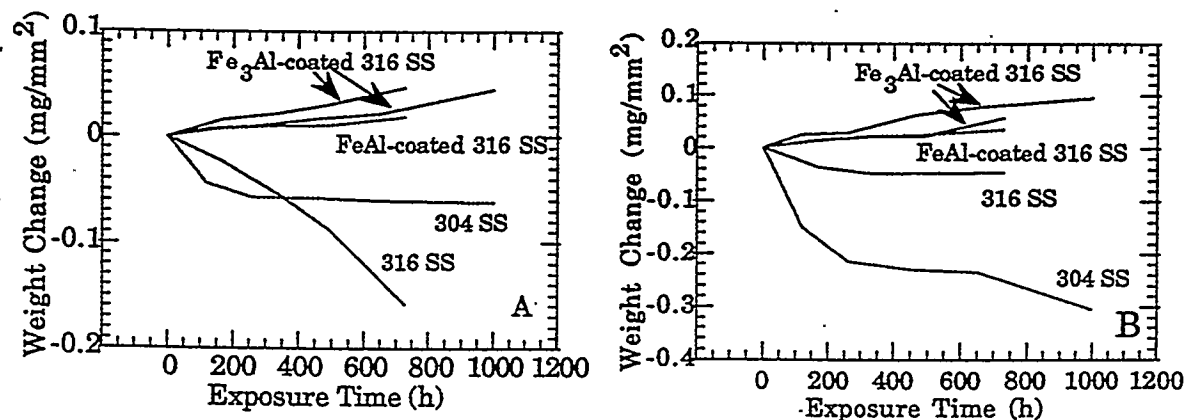


Figure 1. Weight change data for base and aluminide coated alloys tested at 650 C in simulated gasification atmospheres (A) without and (B) with  $\text{HCl}$ .<sup>6</sup>

Figures 2A and B show weight change data for Types 304 and 316 stainless steels and for  $\text{Fe}_3\text{Al}$ - or  $\text{FeAl}$ -coated Type 316 stainless steel after exposure at 650 C to simulated combustion environments with or without  $\text{HCl}$ . In the absence of  $\text{HCl}$ , the uncoated alloys developed scales of  $(\text{Fe}, \text{Cr})$  oxide or  $\text{Fe}$  oxide and tended to crack and spall, as evidenced in

the weight loss in Fig. 2A. The aluminide-coated alloys showed a small weight gain due to the development of a thin, adherent alumina scale. In the presence of HCl, both the uncoated and coated alloys showed increasing weight loss at 650 C. The attack was most notable in the  $\text{Fe}_3\text{Al}$ -coated alloy, indicating that a threshold Al concentration is necessary to protect structural alloys in these environments. The attack was less on the uncoated alloys, but was least on the FeAl-coated alloy.

The success of using FeAl as a coating material now opens the potential of not only improving the corrosion resistance of the structural alloys now used in fossil energy systems, but also of even further improving the performance of the  $\text{Fe}_3\text{Al}$  alloys used in structural applications.

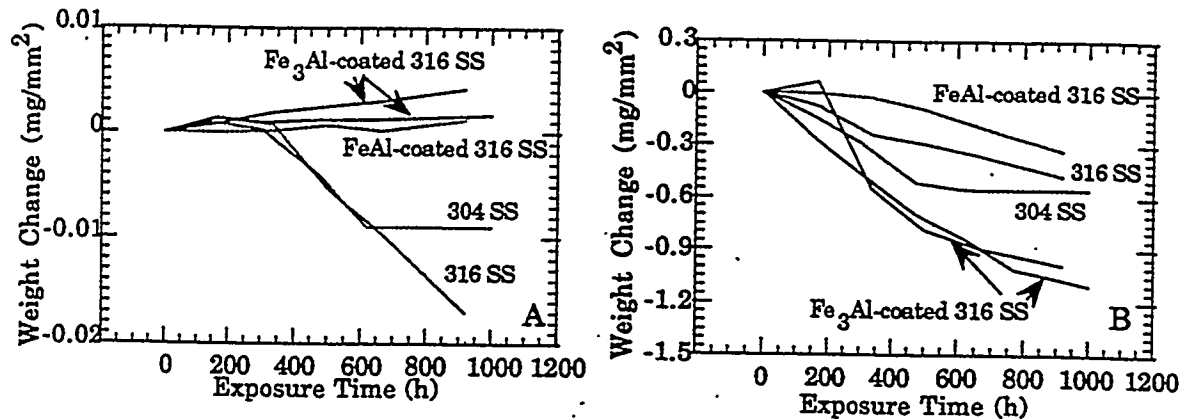


Figure 2. Weight change data for base and aluminide-coated alloys tested at 650 C in simulated combustion atmospheres (A) without and (B) with HCl. <sup>6</sup>

### Process and Equipment Development

Exploration of ESD welding parameters at and near the limits of our power supply capabilities has revealed a distinctly different deposition regime for some materials. When this regime is achieved, deposition rates increase by as much as an order of magnitude. The coating thickness limitations usually inherent to most ESD deposits appear to be eliminated. Whereas 100 microns (0.004 in) is normally considered a practical maximum under most circumstances, we have achieved coatings as thick as 1 mm (0.04 in).

This discovery has sparked an effort to develop a next generation power supply that can consistently exploit this regime of deposition parameters without damage to the supply or its reliability. Initial trials showed that in order to achieve the control we believe will provide the desired capabilities, an advanced switching technology most likely will be necessary. However, the particular current and pulse duration requirements that will be needed are beyond the capabilities of all the commercial electronic components so far identified. Until such components become available, we are working to modify the electrical circuits to allow the use of the available state-of-the-art components so far found.

The first prototype of this advanced ESD power supply is now in test. Although the advanced switching technology we had hoped to use still does not meet our requirements, we have succeeded in developing significant increases in deposition rates, typically on the order of 500% increases. This opens further opportunities where the ESD process will be economically attractive for significant commercial applications. Meanwhile, we continue to aim for even greater capabilities that appear to be achievable once adequately robust switching components become available.

### Technology Transfer Highlights

A major manufacturer of commercial gas turbine engines is now preparing to incorporate the ESD process into their production line for applying wear-resistant coatings to turbine blades and components. This is the second manufacturer of gas turbine engines to adopt the ESD process, not only because of the cost savings, but also because of the unmatched damage resistance achievable.

ESD coatings on extrusion dies, forging dies and metal working tools are providing life improvements of 300 to 800% in tests at another engine manufacturer. The cost savings reportedly range from \$1000 to over \$25,000 per die coated.

Test coatings of mixed refractory metal carbides were applied to paper drills for evaluation at a major printing and publishing company. Preliminary indications are that the ESD coated drills are increasing the time between sharpenings by about a factor of six. We

applied the coating in such a way that resharping can be done without need for recoating. Commercialization of this application appears assured.

## REFERENCES

1. R.N. Johnson, "Principals and Applications of Electro-Spark Deposition," *Surface Modification Technologies*, T.S. Sudarshan and D.G. Bhat, eds., The Metallurgical Society, January 1988, p. 189-213.
2. R.N. Johnson, "Electro-Spark Deposited Coatings for High Temperature Wear and Corrosion Applications," *Elevated Temperature Coatings: Science and Technology I*, N. B. Dahotre, J.M. Hampikian, and J.J. Stiglich, eds., The Metallurgical Society, October 1994, p. 265-277.
3. R.N. Johnson, "Coatings for Fast Breeder Reactors," in *Metallurgical Coatings*, Elsevier Sequoia, S.A., New York, 1984, p. 31-47.
4. K. Natesan and R.N. Johnson, "Corrosion Resistance of Chromium Carbide Coatings in Oxygen-Sulfur Environments," *Surface and Coatings Technology*, Vol. 33, 1987, p. 341-351.
5. I.G. Wright and J.A. Colwell, "A Review of the Effects of Micro-Alloying Constituents on the Formation and Breakdown of Protective Oxide Scales on High Temperature Alloys at Temperatures Below 700 C," ORNL/Sub/86-57444/01, September 1989.
6. K. Natesan and R.N. Johnson, "Corrosion Performance of Fe-Cr-Al and Fe Aluminide Alloys in Complex Gas Environments," presented at *2nd Int. Conf. On Heat-Resistant Materials*, Gatlinburg, TN, September 1995 (to be published in the proceedings).
7. K. Natesan and R.N. Johnson, "Development of Coatings with Improved Corrosion Resistance in Sulfur-Containing Environments," *Surface and Coatings Technology*, Vol. 3/44, 1990, p. 821-835.
8. R.N. Johnson, "Electro-Spark Deposited Coatings for Fossil Energy Environments," in *Proceedings of the Seventh Annual Conference on Fossil Energy Materials*, ORNL/FMP-93/1, July 1993, p.289-295.
9. R.N. Johnson, "Electro-Spark Deposited Coatings for Protection of Materials," in *Proceedings of the Ninth Annual Conference on Fossil Energy Materials*, ORNL/FMP-95-1, August 1995, p. 407-413.





INVESTIGATION OF AUSTENITIC ALLOYS FOR ADVANCED HEAT RECOVERY  
AND HOT GAS CLEANUP SYSTEMS

R. W. Swindeman and W. Ren

Oak Ridge National Laboratory  
P.O. Box 2008  
Oak Ridge, TN 37831

ABSTRACT

Materials properties were collected for the design and construction of structural components for use in advanced heat recovery and hot gas cleanup systems. Alloys systems included 9Cr-1Mo-V steel, modified 316 stainless steel, modified type 310 stainless steel, modified 20Cr-25Ni-Nb stainless steel, modified alloy 800, and two sulfidation resistant alloys: HR160 and HR120. Experimental work was undertaken to expand the databases for potentially useful alloys. Types of testing included creep, stress-rupture, creep-crack growth, fatigue, and post-exposure short-time tensile tests. Because of the interest in relatively inexpensive alloys for service at 700°C and higher, research emphasis was placed on a modified type 310 stainless steel and a modified 20Cr-25Ni-Nb stainless steel. Both steels were found to have useful strength to 925°C with good weldability and ductility.

INTRODUCTION

The objective of the research is to provide databases and design criteria to assist in the selection of optimum alloys for construction of components needed to contain process streams in advanced heat recovery and hot gas cleanup systems. Typical components include: steam line piping and superheater tubing for low emission boilers (600 to 700°C), heat exchanger tubing for advanced steam and topping cycle systems (650 to 800°C), foil materials for recuperators on advanced turbine systems (700 to 750°C), and tubesheets, plenums, liners, and blowback systems for hot gas cleanup vessels (850 to 1000°C).

STEELS FOR LOW EMISSION BOILERS

Alloys such as vanadium-modified 2 1/4 Cr-1 Mo, 2 1/4Cr-1.5W, 9Cr-1Mo, 9Cr-1.5W and 12Cr-1.5W steels are candidates for the construction of piping, headers, and tubing in the low emission boiler (LEB) project supported by the Pittsburgh Energy Technology Center. However, these classes of steels exhibit a complex metallurgical constitutions that

are not fully understood, and concerns exist about long-term embrittlement due to Laves phase precipitation, degradation of weldments due to cavitation cracking, and susceptibility to creep-fatigue damage. Methods for on-line damage assessment are needed as an assurance against component failures. To assist the LEB project contractors in addressing these issues, damage accumulation mechanisms in 9Cr-1Mo-V steel are being studied. These studies involve the continuation of long-time creep testing on aged 9Cr-1Mo-V steel and the examination of correlation methods to relate mechanical behavior time-temperature-stress history. In collaboration with Wright Patterson Air Force Base, a database was assembled to assess the applicability of new deformation and damage accumulation models. Temperature cycling, relaxation, and compression creep tests were performed to expand the database. Good correlations with the new model were developed. Assistance was provided to standards writing groups to assess the acceptability of accelerated cooling for heavy-section components. Creep testing of air-cooled and water-quenched samples was undertaken, and it was found the water quenching was acceptable in terms of the effect of creep strength. Curves for the two metallurgical conditions are compared in Fig. 1.

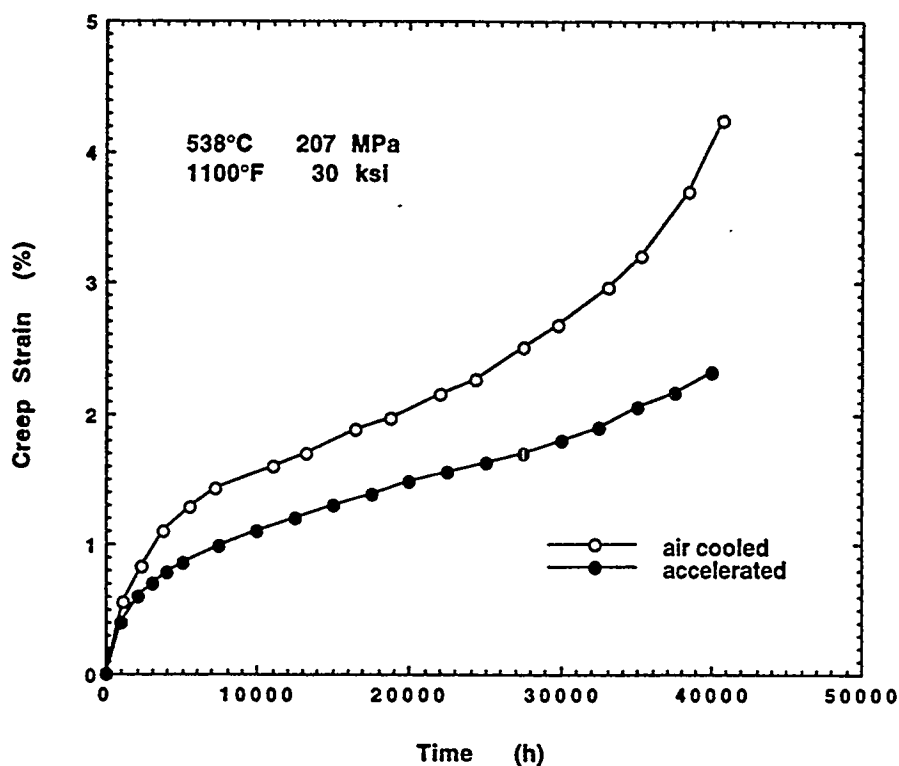


Fig. 1. Comparison of long-time creep curves for 9Cr-1Mo-V steel showing that the creep strength at 538°F is improved by accelerated cooling.

## STEELS FOR ADVANCED HEAT RECOVERY SYSTEMS

In the LEB, austenitic stainless steels will be used for tubing in the hotter, more corrosive sections of the superheater and reheater. Candidate steels including niobium-modified 310 stainless steel and titanium-zirconium-modified 20Cr-25Ni-Nb stainless steel. Both steels are limited to approximately 730°C, due in part to a lack of long-time data at higher temperatures. Both steels are candidates for other advanced heat recovery applications, such as low-cost heat exchanger tubing in an advanced topping cycle system or as recuperator foil materials for an advanced turbine system. For both applications, long-time strength, stability, and oxidation resistance are required. Creep testing of modified 25Cr-20Ni-Nb and modified 20Cr-25Ni-Nb stainless steels was started for temperatures in the range of 700 to 815°C, and efforts were begun to examine after-test microstructures. Creep curves for two developmental alloys are compared in Fig. 2 for tests at 760°C and 69 MPa. Both steels have similar rupture lives but the 310TaN stainless steel exhibited a longer period at the minimum creep rate. For components that are strain limited, the 310TaN stainless steel would be preferred.

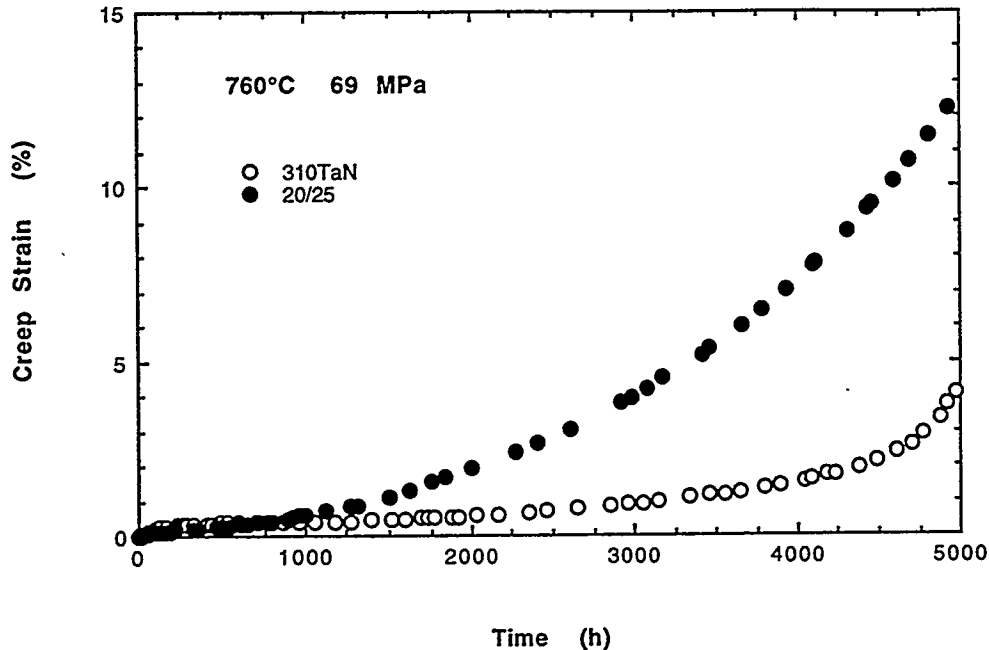


Fig. 2. Comparison of creep curves for 310TaN stainless steel and modified 20Cr-25Ni-Nb stainless steel at 760°C and 70MPa showing the difference in the portion of time spend at low creep rates relative to the rupture life.

## ALLOYS FOR HOT-GAS CLEANUP

Components in several advanced fossil energy systems are expected to experience very high temperatures, and the potential for creep damage, fatigue, thermal-fatigue, and creep-fatigue crack growth are significant. For both "code" alloys and developmental alloys, data for design at very high temperatures are often lacking. For these reasons, exploratory research on creep, creep-fatigue, fatigue, and crack growth of several candidate alloys has been in progress.

Earlier work on alloy for hot-gas cleanup involved studies of alloy 333, alloy 556, and alloy 160, which were candidates for use in pressurized fluidized bed (PFBC) hot-gas cleanup systems at temperature above 815°C. More recently, evaluation was begun of the heat of alloy 120 that is the tubesheet material in the hot-gas cleanup vessel installed at the Wilsonville PFBC facility. Testing of alloy 120 includes creep, creep-crack growth, fatigue, and fatigue-crack growth. Fatigue data for alloy 120 are shown in Fig. 3 where they may be compared to other alloys tested at 871°C. Alloy alloys show similar behavior.

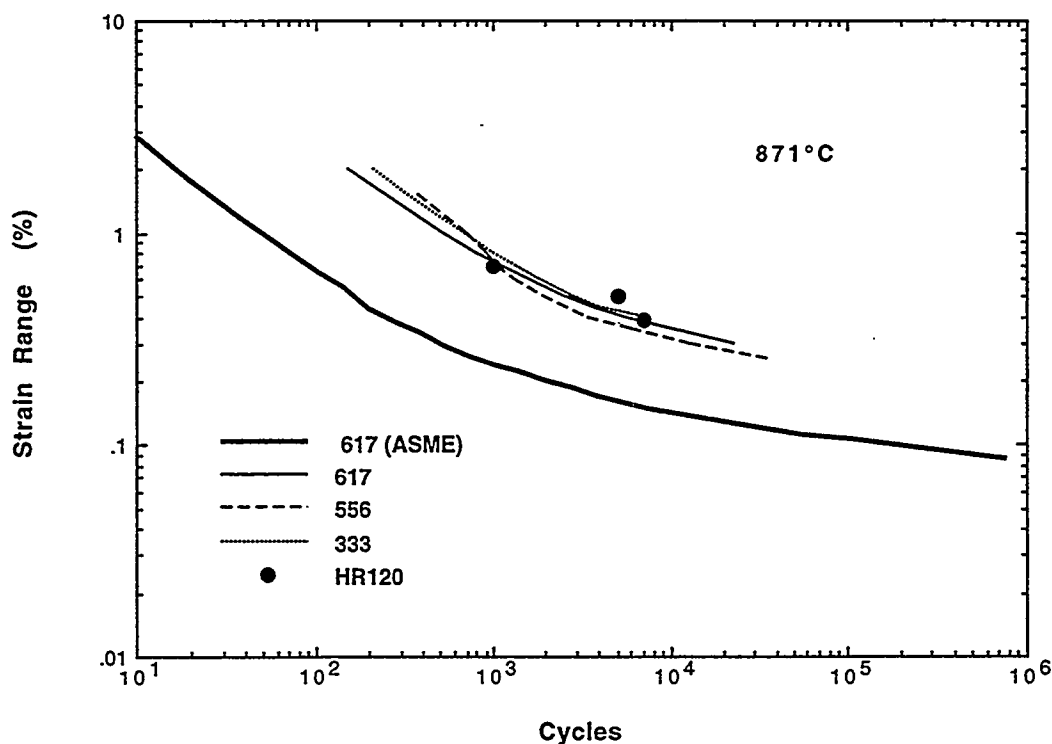


Fig. 3. Comparison of low cycle fatigue data for alloy 120 with other alloys at 871°C.

The modified 25Cr-20 (310TaN) and 20Cr-25Ni-Nb steels are being evaluated for service above 815°C. A comparison of the two steels is shown in Fig. 4 on the basis of the Larson-Miller parameter for rupture. Short-time data indicate that the modified 20Cr-25Ni-Nb steel has slightly better rupture strength properties, but testing of the 310TaN stainless steel has exceeded 30,000 h at 871°C and the performance is excellent relative to standard grades of stainless steels including alloy 800H.

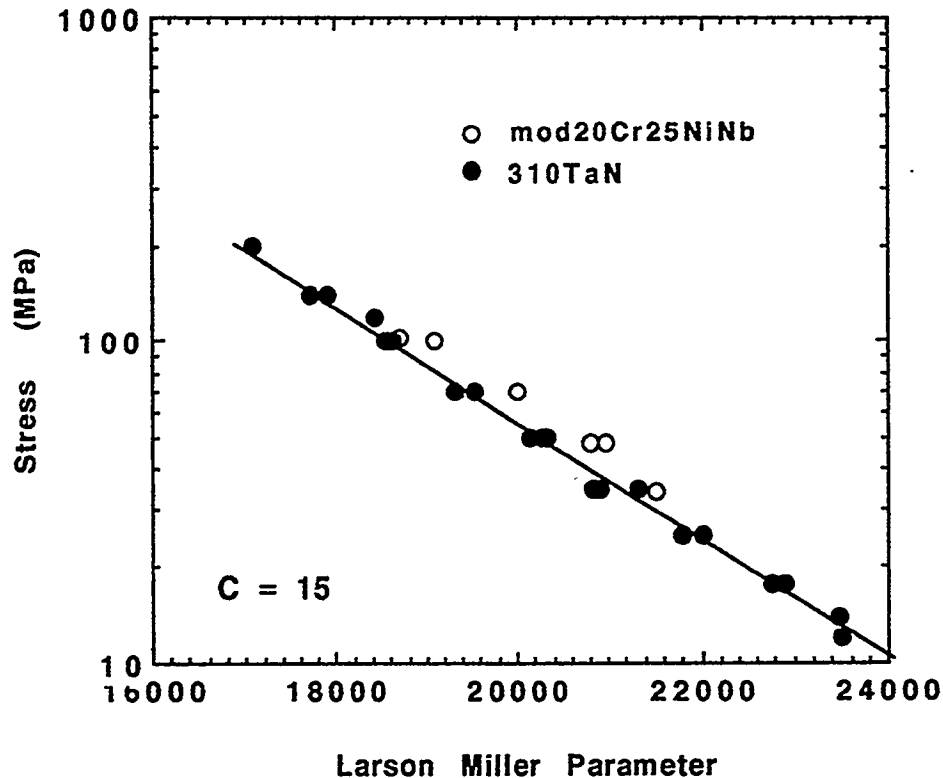


Fig. 4. Comparison of the rupture strength of 310TaN stainless steel with modified 20Cr-25Ni-Nb steel on the basis of the Larson-Miller parameter.



## MICROSTRUCTURAL AND WELDABILITY EVALUATION OF 310TaN

C.D. Lundin and C.Y.P. Qiao

Materials Science and Engineering Department  
The University of Tennessee  
Knoxville, TN 37996

R.W. Swindeman

Metals and Ceramics Division  
Oak Ridge National Laboratory  
Oak Ridge, TN 37831

### ABSTRACT

Excellent weldability and good microstructural stability of 310TaN, in terms of the formation and growth of secondary phases at elevated temperature, was revealed in this investigation. The intergranular stress corrosion resistance of 310TaN is superior to modified 800H and 310HCbN evaluated previously due to the fact that TaC, TaN and Ta(C,N) particles are more stable compared to Nb-rich or Ti-rich carbides, nitrides and carbonitrides presented in the other advanced alloys. Using resistance spot welding technique for which extremely fast cooling is a characteristic, it was found that a very minor amount of grain boundary liquation takes place during welding thermal cycling. The limited grain boundary liquation is of the eutectic type i.e., a low tendency to weld HAZ hot cracking.

### INTRODUCTION

310TaN, one of the elite candidates and the newest version of the advanced austenitic alloys, shows excellent mechanical properties at both ambient and elevated temperature. Weldability evaluations have been carried out in terms of weld hot cracking and weld HAZ microstructural stability. This investigation reveals a superior hot cracking resistance for 310TaN compared to other advanced austenitic alloys (including some alloys which are in commercial use).

310TaN exhibits a low weld HAZ softening tendency compared to the other advanced austenitic alloys [1]. Due to the fact that the advanced austenitic alloys exhibit a good general corrosion resistance, the localized corrosion resistance (HAZ), especially for welded fabrication, is of primary importance. The weld HAZ corrosion resistance of 310TaN was examined and it was shown that 310TaN possesses the highest HAZ intergranular corrosion/stress corrosion cracking resistance contrasted to the other advanced austenitic alloys.

It was revealed by metallographic assessment, that the high stability of the Ta-rich carbides and nitrides significantly contributes to the good corrosion resistance and good weldability. The conclusions from this investigation indicate that 310TaN is a very promising alloy for high temperature applications, i.e. for reheater tubing. An evaluation of the long term mechanical property degradation tendency and an optimum filler metal development for 310TaN is a necessity.

## MATERIALS AND EXPERIMENTAL PROCEDURES

The 310TaN alloy was prepared at ORNL as plate. The material was cold rolled with the wall thickness reduced from 0.5" to 0.124" and then annealed in an argon atmosphere at 1200°C for one hour. The chemical composition was analyzed at ABB-CE Metallurgical Laboratories and the results are documented in Table 1. Clearly, it is one of the 25Cr-20Ni alloy systems with relatively low S and P (0.001 and 0.003, respectively). With the exception of Ta, the content of all other active carbide/nitride/carbonitride forming alloying elements (Mo, V, Nb, and Ti) is relatively low compared to the advanced austenitic alloys previously studied. Therefore, it was not unanticipated that the Ta-rich carbide/nitride/carbonitride precipitates would be the predominant type in this alloy.

Table 1. Chemical Composition of 310TaN (Heat Number : EJF23-3624).

C	Mn	P	S	Si	Ni	Cr	Mo	V	Nb
0.044	1.56	0.003	0.001	0.25	20.78	24.15	0.01	0.01	<0.01
Ti	Co	Cu	Al	B	N	O	Ta	Ca	Fe
<0.01	0.04	0.06	0.044	0.001	0.19	0.004	1.10	<0.002	Bal.

Varestraint hot cracking tests, Gleeble hot ductility tests, Gleeble simulation techniques and electric resistance spot welding techniques were employed to assess weldability. Only a limited number of tests were performed for each evaluation due to the small amount of material available.

The intergranular corrosion resistance for base metal and weld HAZ was evaluated using two ASTM standard testing methods namely; A262 Practice A and Electrochemical Potentiokinetic Reactivation (EPR). Both testing methods assess the tendency for intergranular corrosion and intergranular stress corrosion cracking.

Aging studies were carried out in order to assess the mechanical and metallurgical behavior for long term service at elevated temperature. Two groups of samples were utilized in



the aging effect study. The first group of samples was extracted from creep tested specimens (creep tests were conducted at ORNL) for which the thermal parameters (time and temperature) were available. The materials in the second group of the aging samples were prepared using the 3 mm 310TaN sheet for thermal aging. The sample surface was carefully cleaned and the material was placed in a quartz tube evacuated and backfilled with argon. A photomicrograph showing the quartz encapsulated samples is exhibited in Figure 1. The aging temperatures selected were: 600°C, 800°C, 1000°C and 1200°C combined with aging times of 1, 10, 100 and 1,000 hours.

Microhardness measurements and metallographic evaluations using OLM, SEM and TEM were conducted in order to provide an explanation for the weldability, aging and corrosion resistance evaluations.

## RESULTS AND DISCUSSION

The common weldability issues for structural materials can be classified into two major categories namely, weld metal weldability, which is directly associated with the weld fusion zone chemistry and solidification behavior and the weld HAZ weldability issues (base metal weldability) which are significantly related to the initial base metal composition and conditions. As addressed in the introduction, the base metal weldability of 310TaN is discussed in terms of liquation cracking tendency, weld HAZ softening tendency, microstructural stability, and intergranular corrosion/intergranular stress corrosion cracking resistance. All of the above issues are a function of microstructural changes, such as formation of a partially melted zone, grain growth, and precipitate redistribution (including both precipitate dissolution and re-precipitation during welding thermal history). Recrystallization is not of concern with this alloy because the material was solution heat treated and not cold worked subsequently.

### Weldability Evaluation of 310TaN

#### Varestraint Hot Crack Testing

In the V restraint hot cracking test, information from all three weld regions (BM HAZ, FZ and WM HAZ) is generated in a single hot cracking test specimen and thus, base metal hot cracking tendency is fully characterized. A summary of the V restraint hot cracking results is presented in Table 2. According to the V restraint hot cracking testing criteria [3], the hot cracking tendency in all three zones is low. The cracked HAZ length (CHL) values for two samples tested at 4% augmented strain are 0.70 mm and 0.84 mm which is much smaller than

for 310HCbN (1.25), NF709 (1.36), and modified 800H (1.09). Compared to 310HCbN, the major difference in these alloy systems is that Ta is used in 310TaN while Nb is used in 310HCbN as the MC type carbide forming element. However, a great improvement was found for 310TaN over 310HCbN in terms of hot cracking resistance and weld HAZ softening. It is to be noted that the Fe-Nb and Fe-Ta phase diagrams are similar. However, the eutectic reaction temperature near pure Fe in the Fe-Ta system is 50 C° higher than that in Fe-Nb system and this difference may have contributed to the improved weldability of 310TaN.

Table 2. Summary of Varestraint Hot Cracking Test Results for 310TaN.

Augmented Strain (%)	Weld Metal HAZ		Fusion Zone		Base Metal HAZ		
	MCL (mm)	TCL (mm)	MCL (mm)	TCL (mm)	MCL (mm)	TCL (mm)	CHL (mm)
4	0.16	0.46	0.50	4.71	0.04	0.06	0.77
2	0.10	0.36	0.41	4.62	0.04	0.04	-

\* MCL: maximum crack length, TCL: total crack length, CHL: cracked HAZ length.

#### Gleeble Hot Ductility Testing

The hot ductility behavior of 310TaN is indicated in Figure 2 and clearly, a good ductility recovery is noted on-cooling from the ZDT. Therefore, a good correlation between the Varestraint hot cracking and Gleeble hot ductility tests is apparent for 310TaN.

#### Grain Boundary Liquation Morphology Study

From the work performed in earlier stages [5] of this alloy evaluation program, a HAZ liquation cracking tendency criterion was developed based upon the grain boundary liquation morphologies in a fast cooled resistance spot weld. According to these liquation cracking criteria, if a material exhibits an eutectic reaction related grain boundary liquation it generally possesses a good HAZ liquation cracking resistance. The OLM microstructural morphology in a sample prepared using the resistance spot welding technique is shown in Figure 3. Clearly, the length of liquated grain boundaries is limited in addition to the fact that the grain boundary liquation type is typical of an eutectic reaction related liquation. The HAZ grain boundary liquation study clearly defines why 310TaN possesses excellent HAZ liquation cracking resistance. The grain boundary liquation study also agrees with the weldability predictions from the physical tests.

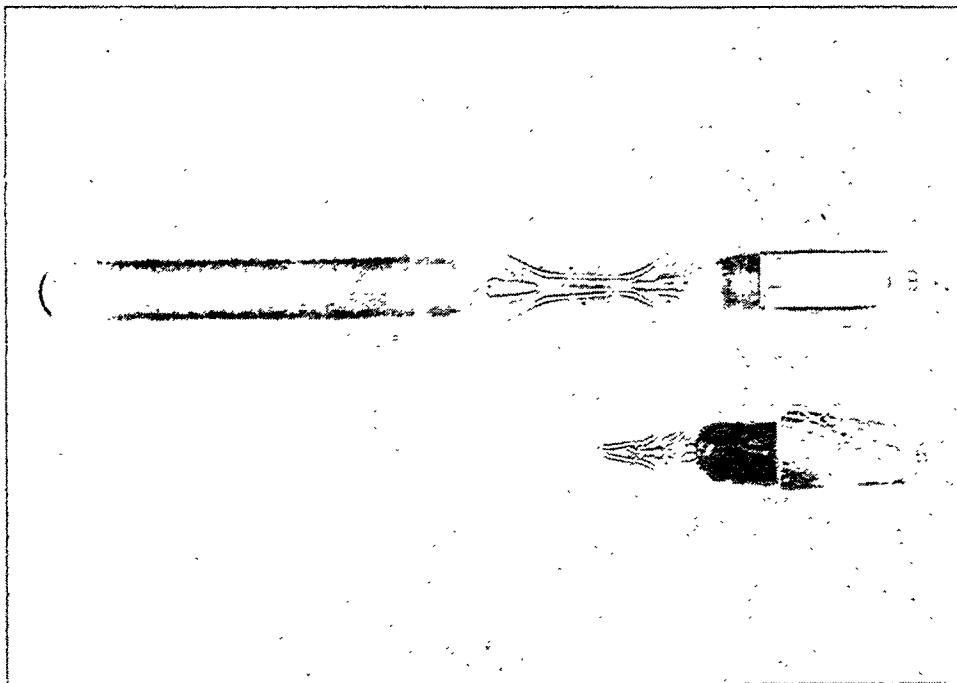


Figure 1. Sealing of sample in quartz tube.

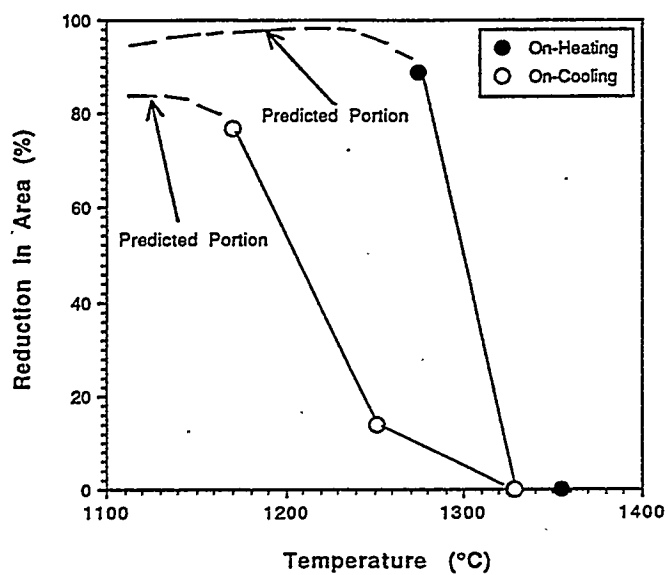


Figure 2. Hot ductility behavior of 310TaN.

## Aging Study

### Microstructural Characterization

Two groups of samples were used in the aging study, including creep tested samples and virgin aged samples. For the creep tested samples, the material was at elevated temperature for a relatively long time, hence, an extensive amount of secondary phases were formed along the grain boundaries are compared to the average base material. It should be pointed out that strain induced secondary phase formation may have played a role in these aged samples (depending upon the thermal and mechanical conditions of the creep tests). The OLM microstructural morphologies in the base metal and the creep tested material (982°C, 17.5 MPa for 1794 hours) are indicated in Figures 4a and 4b, respectively.

The virgin aging sample is similar in microstructure to the creep tested samples. Three major secondary phases were found and are categorized in terms of shape and evolution processes and the accuracy of this observation was further confirmed by SEM/EDS.  $M_{23}C_6$  type carbides which predominant along the grain boundaries reach a maximum precipitation rate at approximately 950°C for 310TaN. In addition, long term aging at elevated temperature, for instance, at 1000°C for 1000 hours,  $\sigma$  phase starts to form in the 310TaN and thus this may degrade the mechanical properties of 310TaN in the long term. Therefore, a complete solution treatment is important to minimize "harmful" secondary phase evolution.

### Hardness Measurements

Hardness measurements were conducted on the creep tested samples as well as annealed base material. The hardness of the creep tested samples is directly related to the type and amount of secondary phases. The harnesses for these aged samples are within a range of 170 to 240HV. If a Larson-Miller parameter is used to assess the thermal effect, the relationship between the hardness and Larson-Miller parameter ( $^{\circ}R (C+\log t)$ ) is presented in Figure 5. While this is scatter in this limited data set, with an increase in the thermal aging parameter, the hardness of 310TaN increases.

### Localized Corrosion Resistance Evaluation

#### ASTM A262 Practice A

As a screening test, A262 Practice A was conducted on the Gleeble simulated HAZ samples. The basic information from A262 Practice A reveals the tendency and level of the

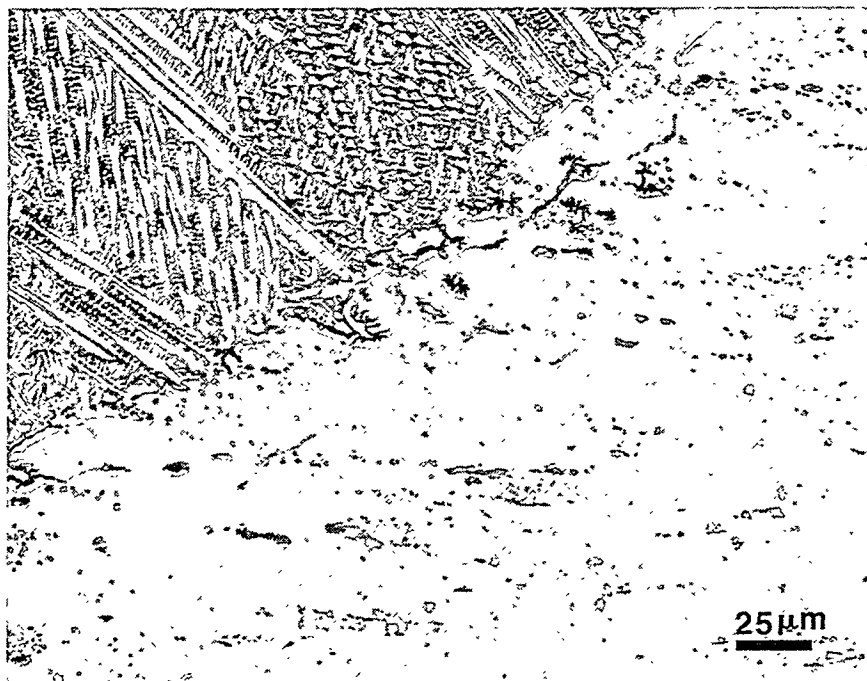


Figure 3. Microstructural morphology in the HAZ of a resistance spot weld in 310TaN.

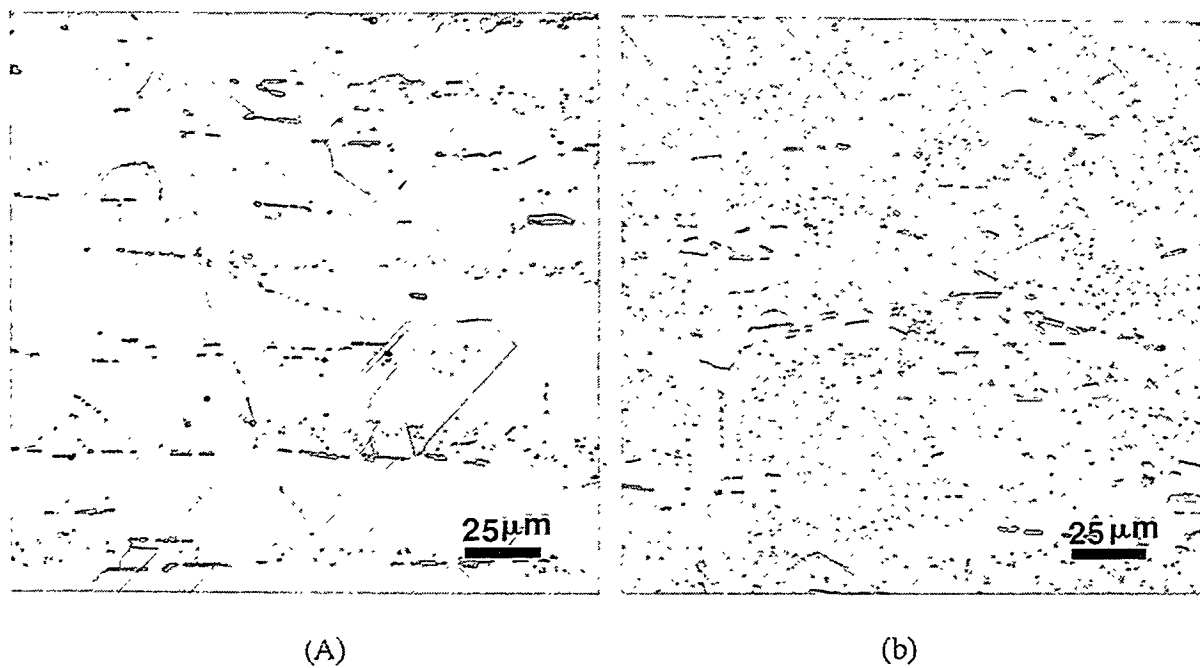


Figure 4. Microstructural morphologies in (a) the base metal and (b) a creep tested sample (982°C, 17.5 MPa for 1794 hours).

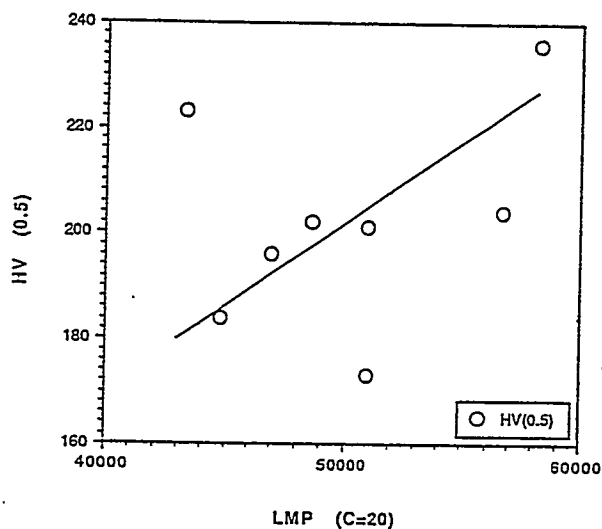


Figure 5. Relationship between the hardness and Larson-Miller parameter ( $^{\circ}\text{R} (C+\log t)$ ).

sensitization. A262 Practice A is applicable not only for the weld HAZ but also for base metal. The test results indicate that all samples passed the A262 A screening corrosion test. The sensitization tendencies for the 310TaN base metal and simulated weld HAZ samples are ranked in order: HAZ (PT:900°C), base metal (solution treated at 1200°C for one hour), HAZ (PT:1320°C), HAZ (PT:1200°C), HAZ (PT:1250°C) and HAZ (PT:1100°C). Among them, only the HAZ (PT:900°C) and base metal samples exhibited any ditched grain boundaries although the ditching did not completely surround any entire grain.

#### ASTM G108 (EPR) Evaluation

The results from electrochemical potentiokinetic reactivation (EPR) evaluations of 310TaN agree with those of ASTM A262 Practice A. All samples used for this evaluation showed only a small weld HAZ sensitization tendency. The EPR test results of the Gleeble simulated samples for 310TaN are presented in Table 3.

Table 3. Summary of EPR Test Results for 310TaN.

Sample	Pa (Test 1) (Coulombs/cm <sup>2</sup> )	Pa (Test 2) (Coulombs/cm <sup>2</sup> )	Pa (Average) (Coulombs/cm <sup>2</sup> )
Base Metal *	0.074	0.044	0.059
HAZ (PT:900°C)	0.038	0.158	0.098
HAZ (PT:1100°C)	0.000	0.035	0.018
HAZ (PT:1200°C)	0.002	0.059	0.031
HAZ (PT:1250°C)	0.006	0.039	0.023
HAZ (PT:1320°C)	0.022	0.069	0.046

\* Solution treated at 1200°C for 1 hour.

The Gleeble simulated HAZ (PT:900°C) sample showed the highest sensitization level among this group of samples. This result is understandable since the  $M_{23}C_6$  type carbide possesses the highest precipitation rate at about 800 to 850°C for 25Cr-20Ni-Fe alloys. For the case of the weld HAZ, the highest precipitation rate temperature range shifts to higher temperatures due to non-equilibrium heating. Therefore, at a peak temperature of approximately 900°C, the simulated 310TaN weld HAZ possesses the highest tendency to sensitization. It should be noted from this study, that the solution treatment temperature (1200°C) used for the 310TaN is considered slightly low. In order to completely dissolve the secondary phases formed during material fabrication, a higher temperature, such as 1280°C is suggested for the solution treatment. It is expected that the sensitization tendency will be reduced using a higher solution treatment temperature.

## CONCLUSIONS

1. The weldability evaluation indicates that the 310TaN alloy exhibits an excellent hot cracking resistance compared to the other advanced austenitic alloys such as 310HCbN, NF709 and modified 800H.
2. Intergranular corrosion resistance of 310TaN is superior to the other advanced austenitic alloys including 310HCbN and modified 800H.
3. Good stability of the TaC, TaN and Ta(C,N) in 310TaN was revealed in the aged and the physically simulated weld HAZ samples and the good thermal stability of these Ta-rich precipitates present in 310TaN is the one of the reasons for the good weldability, intergranular corrosion resistance as well as improved mechanical properties.

## ACKNOWLEDGMENTS

This research was financially sponsored by DOE, through the Fossil Energy Materials Program operated at ORNL managed by Martin Marietta Energy Systems, Inc. The great assistance received from DOE/ORNL managers of R.R. Judkins, N.C. Cole, P.T. Carlson during the course of the investigation is deeply appreciated. The authors also would like thank Professor R.A. Buchanan of the Materials Science & Engineering Department of the University of Tennessee for allowing us to use the corrosion laboratory facilities.

## REFERENCES

1. Lundin, C.D., and Qiao, C.Y.P., "Comparative Evaluation of the Weldability of Modified 800H and Other Advanced Austenitic Stainless Steels," pp. 341-351, Proceedings of the Seventh Annual Conference on Fossil Energy Materials, May 1993.
2. Lundin, C.D., and Qiao, C.Y.P., "Preliminary Metallographic Examination of Service Exposed SA 213 (Grade HR3C) Hot Reheat Tubing at TVA Gallatin Unit 2," Technique Report, The University of Tennessee, 1995.
3. Lundin, C.D., and Qiao, C.Y.P., "Standard Varestraint Testing Parameters, Procedures and Criteria," Technical Report, The University of Tennessee, 1993.
4. Swindeman, R.W., "The Potential of Modified 310 Stainless Steel for Advanced Fossil Energy Application," ORNL/TM-12057, March 1992.
5. Lundin, C.D., and Qiao, C.Y.P., "Weldability of Modified 800H Alloy," DOE/ORNL Technical Report, ORNL/Sub/88-07685/04, June 1994.
6. Forde, P.T., "Tantalum in Superalloys," pp. 39-40, Advanced Materials & Processes, Vol. 149, No.4, April 1996.
7. Hansen, M., and Anderko, K., Constitution of Binary Alloys, McGraw-Hill Book Company, Inc., New York, 1958.



FIRESIDE CORROSION TESTING OF CANDIDATE SUPERHEATER  
TUBE ALLOYS, COATINGS, AND CLADDINGS - PHASE II

J. L. Blough  
G. J. Stanko

Foster Wheeler Development Corporation  
12 Peach Tree Hill Road  
Livingston, NJ 07039

ABSTRACT

In Phase I a variety of developmental and commercial tubing alloys and claddings were exposed to laboratory fireside corrosion testing simulating a superheater or reheater in a coal-fired boiler. Phase II (in situ testing) has exposed samples of 347, RA-85H, HR3C, 253MA, Fe<sub>3</sub>Al + 5Cr, 310 modified, 800HT, NF 709, 690 clad, and 671 clad for over 10,000 hours to the actual operating conditions of a 250-MW coal-fired boiler. The samples were installed on an air-cooled, retractable corrosion probe, installed in the reheater cavity, and controlled to the operating metal temperatures of an existing and advanced-cycle coal-fired boiler. Samples of each alloy will be exposed for 4000, 12,000, and 16,000 hours of operation.

The results will be presented for the metallurgical examination of the corrosion probe samples after 4000 hours of exposure.

INTRODUCTION

High-temperature fireside metal wastage in conventional coal-fired steam generators can be caused by gas-phase oxidation or liquid-phase coal-ash corrosion. Gas-phase oxidation is usually not a problem if tube and support materials are selected for their oxidation resistance at operating temperatures and for spalling, flaking, or other reactions to their environment. Coal-ash corrosion, on the other hand, usually results in accelerated attack and rapid metal wastage—even of stainless steels. The cause of this type of corrosion is generally accepted as the presence of liquid sulfates on the surface of the metal beneath an overlying ash deposit<sup>1-4</sup>.

While substantial progress has been achieved through laboratory testing, actual utility service exposures are evidently necessary to verify any conclusions drawn from laboratory testing. A number of important environmental parameters cannot be fully simulated in the laboratory<sup>5</sup>:

- The actual composition of the deposits formed on the tubes is more complex than the composition of the simulated ash.
- The SO<sub>3</sub>, formed by heterogeneous reaction on cooled surfaces, is variable.
- Very large temperature gradients occur within the ash deposits.
- The ash and fuel gas move past tubes at high velocity; the rate varies with design.
- The composition of the corrosive deposits changes with time.
- Metal and flue gas temperatures fluctuate.

- Fly-ash erosion removes the protective oxides, exposing a clean surface to fresh ash.

Foster Wheeler Development Corporation (FWDC) has performed a number of literature reviews and recent updates discussing the variables affecting the corrosion mechanism<sup>6-8</sup>. Additionally, Foster Wheeler is conducting two sizable research projects—one a laboratory and in situ field testing at three utilities of commercially available alloys<sup>5,9-15</sup> and this program (ORNL-FW2), combining laboratory and field testing to more completely cover the controlling variables for a longer duration<sup>10</sup>.

In Phase I of this ORNL program, "Fireside Corrosion Testing of Candidate Superheater Tube Alloys, Coatings, and Claddings," 20 commercial and developmental alloys were evaluated<sup>10</sup>. The coupons of the metals were exposed to synthetic coal ash and synthetic flue gases at 650 and 700°C (1202 and 1292°F) for up to 800 hours.

## PHASE II CORROSION PROBE TESTING

In this project, the field tests comprise corrosion probe testing, coal characterization, and deposit/corrosion product analysis. The coals have been analyzed to provide fuel characterization, a deposit analysis data bank, and possibly a corrosivity index for predicting corrosivity under various combustion conditions. The equipment and the procedures for this phase have been previously used and perfected at three different utilities for over 3 years of in situ testing at each station.

The utility for test exposures should be burning an aggressive fuel to adequately evaluate the candidate alloys. The coal being burned at Tennessee Valley Authority's (TVA's) Gallatin Station had been previously analyzed, and numerous corrosion indices predicted high corrosivity in addition to the fact that installed T22 and Type 304SS tubing experienced about 7 years of life in the superheaters and reheaters of Units 1 and 2.

### Selection of Materials for Corrosion Probes

FWDC laboratory-tested 20 different materials<sup>10</sup>. Because this quantity was impractical from both an economic and a probe-length standpoint, fewer (the ten listed in Table 1) had to be selected for the field tests. These materials provide a range of compositions and cost for both the commercially available and developmental alloys and claddings.

### Field Corrosion Probe Design

The corrosion probes were designed to provide realistic exposures of metal samples to both actual boiler environments and also at the higher anticipated metal temperatures of an advanced plant. The probes are independent from the main boiler, removable without a boiler outage, and have a fail-safe design, one that removes

Table 1. Chemical Composition of Candidate Alloys (%)

Alloy	Cr	Ni	Others
Type 347	17-19	9-13	$(Nb + Ta) = 10 \times C \text{ (min.)}$
85H	18	15	Al = 1, Si = 3.9
NF 709	20	25	Mo = 1.5, Mn = 1.0, Si = 0.6
690 Clad	30	58	
671 Clad	48	52	
Fe <sub>3</sub> Al + 5% Cr	5	—	Al = 17
HR3C	25	20	Nb = 0.4
253MA	21	11	Si = 1.7
310 modified	25	20	Ta = 1.5
800HT	21	32	Al + Ti = 1

them from the boiler if there are any malfunctions. With these features, years of testing will not be compromised with a sudden system overheating.

The probes are being exposed for 4000, 12,000, and 16,000 hours. This is being accomplished by utilizing two probe test locations. At one test location, the probe is being exposed for 16,000 hours. At the other test location, the probe will be removed after 4000 hours and a new probe inserted for the remaining 12,000 hours. The design and operation of the retraction system has been discussed in previous years at this conference<sup>16</sup>.

The locations in this plant (shown in Figure 1) were chosen because of cavity access and because they best represent the locations for the reheater or superheater outlet on the "Advanced Cycle" unit.

The ideal coal-ash corrosion probe exposure is if only one coal is being burned at the plant. This practice is not common at many utilities; in fact, many are buying coal on the spot market. Gallatin burns a number of eastern high-sulfur coals, mainly Island Creek, Warrior, Dotiri, and Pattiki, which are known to be corrosive and prone to alkali-iron-trisulfate formation. The Borio Index<sup>17</sup> for these coals typically range from 2.0 to 4.1, and the chloride level is 450 to 3000 ppm.

#### Post-Exposure Analysis

##### Exposure Results to Date

The 4000-hour probe was removed and shipped to the laboratory for analysis. The 12,000- and 16,000-hour corrosion probes continued to be exposed in the reheater cavity of the TVA Gallatin Station Unit 2.

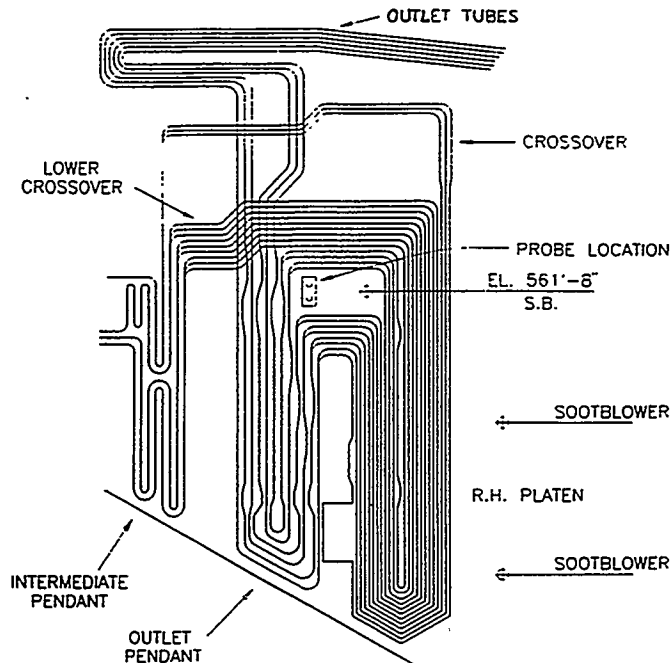


Fig. 1. Side elevation of reheater at TVA Gallatin Unit 2

#### Macroscopic Examination

The appearance of the transverse cross sections used for the wall thickness measurements is shown in Figure 2. As illustrated, the middle of the sections is approximately the 135-deg location. [Note: Axially oriented grooves, evident at the 180-deg location, are artifacts believed to have been caused by a roller in the guide assembly.] Shallow pitting or surface irregularity is apparent in Samples 1 (85H), 2 (347), and 4 (253MA) in the lower temperature group, and Samples 12 (347) and 14 (253MA) in the high-temperature group. Post-exposure wall-thickness readings were made at the 45-, 135-, and 270-deg locations and the wall loss calculated at the three locations. [Note: Subsequent microscopic examination revealed most of the wall loss in the clad 671 and 690 (Samples 6, 7, 16, and 17) resulted from oxidation of the inside surface which contained a lower alloy concentration from the modified 316 base metal and not corrosion of the outside surface. Oxidation of the inside surface also contributed to the wall loss in Sample 12 (347) and 14 (253MA).] Discounting the high values in Samples 6, 7, 16, and 17 because of oxidation of the I.D. surface, the wall loss values of the specimens in each group were relatively minor. Samples 2 (347) and 4 (253MA) in the lower-temperature group and Samples 12 (347) and 14 (253MA) in the higher-temperature group exhibited higher values than most of the other alloys.

#### Microscopic Examination

Short sections from the 45-, 135-, and 270-deg locations of the samples were prepared for microscopic and SEM/EDX examination. A summary of the examination follows.

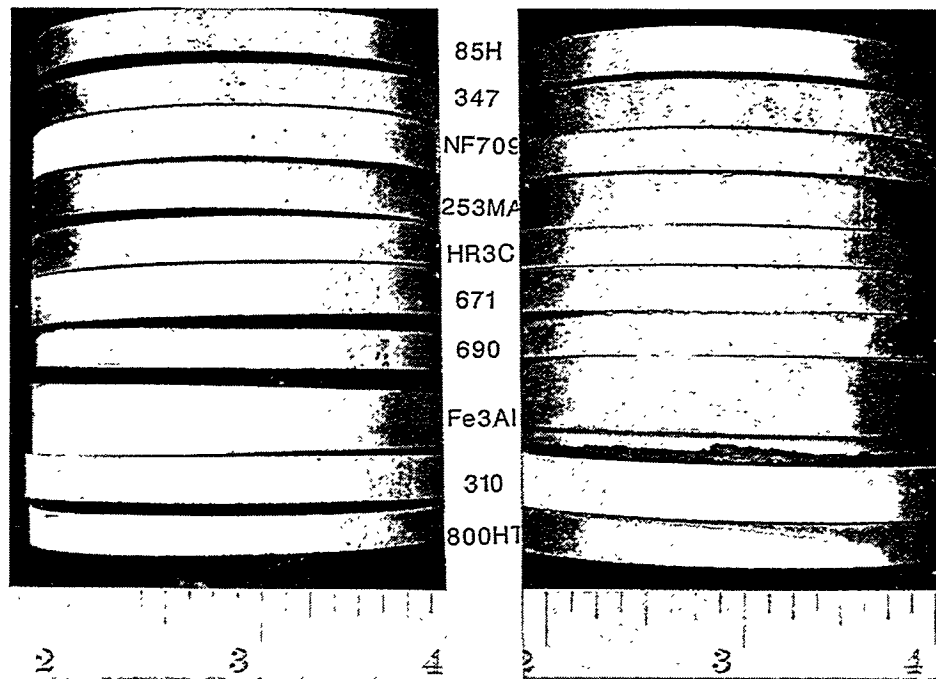


Fig. 2. Cleaned 4000-hour probe.

**85H** — Both 85H samples exhibited intergranular penetration in the outside surface to a depth of approximately 2.5 mils. Sample 1, which operated at a lower temperature than Sample 11 (1156 vs. 1260°F), displayed more areas of subsurface attack (which is consistent with the observation of the shallow pitting in this sample). Energy dispersive x-ray (EDX) analysis revealed the light gray material in the grain boundaries and pits in Sample 1 was chromium-rich oxide with varying amounts of sulfur. The material at similar locations in Sample 11 was also a chromium-rich oxide but appeared to have less sulfur than the material in Specimen 1. Interestingly, the outside surface at the 270-deg location in Sample 11 also exhibited intergranular penetration to a depth of 2 mils.

Both samples also displayed intergranular penetration in the inside surface. The depth of penetration was 2 mils in Sample 1 and 2.5 mils in Sample 11. This type of penetration is not anticipated to have affected the wall-thickness measurements.

**347** — Both 347 samples contained a scale/deposit in the corroded areas. Sulfide penetration to a depth of approximately 0.5 mils below the scale/deposit was also evident in each sample. The outer layer of the scale/deposit was predominantly iron oxide with embedded fly ash particles; the inner layer was a chromium-rich oxide and contained a small amount of sulfur. The sulfides contained iron, manganese, and chromium.

The inside surface of Sample 12 contained a thin oxide with an average thickness of approximately 0.5 mils.

**253MA** — The 253MA sample in the hotter section (Sample 14) contained a two-layer scale/deposit, with subjacent sulfide penetration to a depth of approximately 1 mil below the scale/deposit. The outer layer was iron oxide, while the inner layer was chromium oxide with notable additions of silicon and sulfur. The sulfides contained iron, manganese, and chromium. The inside surface contained oxide that was approximately 0.8 mils thick.

The outside surface of the sample in the cooler section (Sample 4) also exhibited a two-layer scale/deposit, although it was thinner and present in fewer areas compared to the O.D. scale/deposit on Sample 14. EDX analysis revealed the elemental makeup of the scale layers was similar to those in Sample 14. The degree of internal sulfidation was also lower in Sample 4 and the inside surface was free of scale.

**800HT** — Both 800HT samples exhibited a two-layer scale/deposit with some minor internal oxidation and sulfidation. The depth of the internal penetration was approximately 1 mil in each sample. The outer scale layer was iron rich and contained embedded fly ash particles. The inner layer was predominantly chromium oxide. The sulfides contained iron, manganese, and chromium.

**Modified 310** — The modified 310 sample in both sections contained a thin, chromium-rich scale with embedded fly ash particles. No internal oxidation or sulfidation was noted.

**HR3C** — For the most part, both HR3C samples exhibited a thin, chromium-rich scale on the outside surface. In a few localized areas on the hotter section (Sample 15), a thicker scale/deposit with subjacent internal oxidation to a depth of approximately 1 mil was noted. The outer layer of the scale/deposit was primarily iron oxide and contained fly ash.

**NF 709** — Most areas in both samples contained a thin, chromium-rich scale on the outside surface. One localized area in the hotter section (Sample 13) exhibited internal oxidation and sulfidation to a depth of approximately 1 mil. The sulfides contained iron, manganese, and chromium.

**671** — Both samples contained a scale/deposit comprised predominantly of the deposit in the outer layer and a thin, chromium-rich oxide on the metal surface. No internal oxidation or sulfidation was evident. The inside surface (which consisted of Modified 316 stainless steel material) contained a 4-mil-thick oxide in the hotter section (Sample 16) and a 1-mil-thick oxide scale in the cooler section (Sample 6). On the basis of the microscopic examination, the large calculated wall loss from the wall thickness measurements for these samples appears to be the result of the internal scaling. The wall loss from the outside surface is estimated to be less than 1 mil.

**690** — Similar to the 671 samples, both 690 samples displayed a thin, chromium-rich oxide on the outside surface. In a few areas in the hotter section internal oxidation was noted to a depth of approximately 1 mil. No sulfidation was detected in either sample. The inside surface (which also consisted of Modified 316 stainless steel material) contained a 2-mil-thick oxide scale in the hotter section (Sample 17) and a 1-mil-thick scale in the cooler section (Sample 7). On the basis of the microscopic examination, the calculated wall loss

from the wall-thickness measurements for these samples also appears to be the result of the internal scaling. The wall loss from the outside surface is estimated to be less than 1 mil.

$\text{Fe}_3\text{Al}$  — The outside surface of both  $\text{Fe}_3\text{Al}$  specimens was essentially free of any scale/deposit. Shallow pits were noted in isolated areas in the hotter section (Sample 18). The material in the pits was predominantly aluminum oxide. Numerous cracks that initiated from the outside surface were evident in both samples. The oxide in the cracks was rich in iron and contained some aluminum.

#### Wastage Determination

Wastage is considered the sum total of wall loss and metal rendered ineffective because of internal penetration of corrosive species (e.g., oxides, sulfides). Since only the wastage from the outside surface is of concern, wall loss from oxidation of the inside surface must be discounted. On this basis, the wastage of the specimens determined from the macroscopic and microscopic examinations is given in Table 2. In Figure 3 the total wastage is plotted vs. the different alloys in the order of increasing percent of chromium. The 690 and 671 wastage, which is microscopically determined to be less than 1 mil, is plotted as 0.5 mils. With the exception of  $\text{Fe}_3\text{Al}$ , the total wastage decreases with increasing chromium levels. The iron aluminide with only 5 percent chromium has zero wastage. Also, the modified 310 alloy with tantalum has a lower wastage than HR3C with a similar chromium level. Future long-term corrosion probes (12,000- and 16,000-hour) will determine whether this is correct or within the data scatter. Also shown in Figure 3, some of the alloys (85H, NF 709, and HR3C) indicate an increase in wastage rate with increasing temperature while other alloys (347 and 253MA) indicate a peak in the wastage at a lower temperature.

### CONCLUSIONS

The air-cooled retractable corrosion probes are working successfully and are providing exposure of each of the ten alloys to two different temperatures. The wastage measurements from the 4000-hour exposure indicate a wastage for 347 of about 2.5 mils. The field measurements indicate the same benefit of chromium in providing corrosion resistance (i.e., the higher the chromium level, the lower the corrosion) as the previous Phase I laboratory testing. The exception to this is the iron aluminide with only 5 percent chromium showed no evidence of measurable corrosion. Also, the 310 modified with tantalum performed better than the same 25-percent chromium HR3C with niobium. The data from the future 12,000- and 16,000-hour probes will further evaluate whether these preliminary findings are true. The mode of attack for most of the samples is oxidation and sulfidation. All of these alloys have considerable coal ash corrosion resistance, and the general metal wastage by a fluxing action is therefore minimal.

Future metallographic and corrosion deposit analyses will verify the wastage rates and corrosive attack mechanisms (i.e., coal ash, erosion-assisted oxidation, etc.).

Table 2. Total Wastage of Specimens

Sample	Material	Total Wall Loss (mils)	I.D. Wall Loss From Oxidation (mils)	O.D. Penetration (mils)	Total Wastage (mils)
1	85H	0	0	2.5	2.5
2	347	2.7	0.5	0.5	2.7
3	NF 709	0	0	0.5	0.5
4	253 MA	1.9	0	0.5	2.4
5	HR3C	0.3	0	0	0.3
6	671	4.0	1.0	0	<1.0*
7	690	1.1	1.0	0	<1.0*
8	Fe <sub>3</sub> Al	0	0	0	0
9	310†	0	0	0	0
10	800HT	0.5	0	1.0	1.5
11	85H	0.5	0	2.5	3.0
12	347	2.0	0.5	0.5	2.0
13	NF 709	1.6	0	(1.0)§	1.6 (2.6)§
14	253 MA	1.2	0.8	1.0	1.4
15	HR3C	0.8	0	(1.0)§	0.8 (1.8)§
16	671	9.7	4.0	0	<1.0*
17	690	4.9	2.0	(1.0)§	<1.0* (1.0)§
18	Fe <sub>3</sub> Al	0	0	0	0
19	310†	0.1	0	0	0.1
20	800HT	0.5	0	1.0	1.5
*Estimated from microscopic examination. †ORNL modified. §Localized areas.					



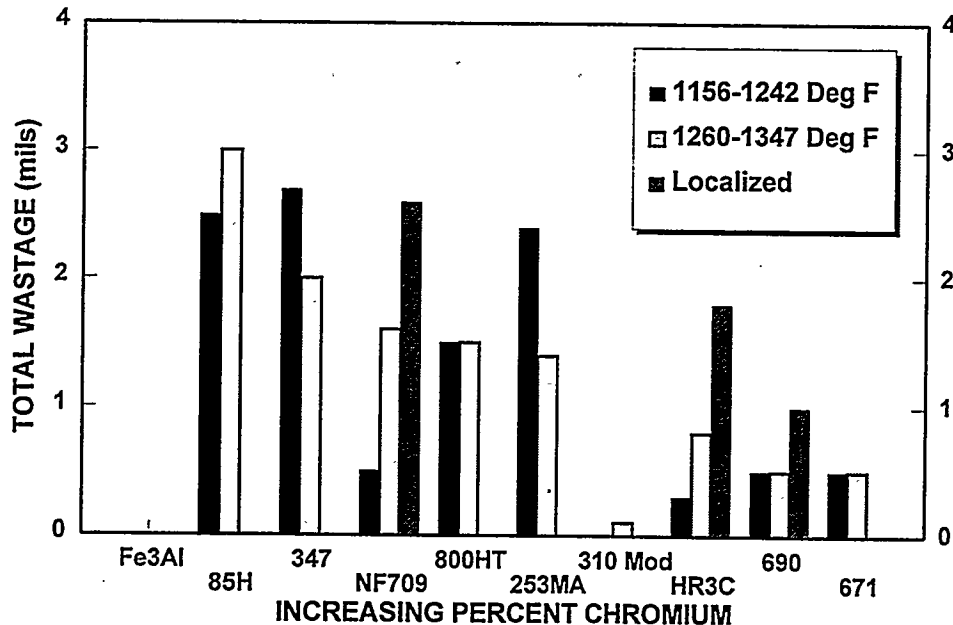


Fig. 3. Total wastage vs. chromium

#### REFERENCES

1. W. Nelson and C. Cain, Jr., "Corrosion of Superheaters and Reheaters of Pulverized-Coal-Fired Boilers," *Transactions of the ASME, Journal of Engineering for Power*, July 1960, pp. 194-204.
2. W. T. Reid, "Formation of Alkali Iron Trisulphates and Other Compounds Causing Corrosion in Boilers and Gas Turbines," Project Review July 1, 1966-June 30, 1968, prepared by Battelle Memorial Institute, Columbus, OH, June 1968.
3. W. T. Reid, *External Corrosion and Deposits: Boilers and Gas Turbines*, American Elsevier Publishing Company, New York, 1974.
4. G. J. Hills, "Corrosion of Metals by Molten Salts," *Proceedings of the Marchwood Conference: Mechanism of Corrosion by Fuel Impurities*, Johnson and Littler, eds., Butterworths, London, 1963.
5. J. L. Blough, G. J. Stanko, M. Krawchuk, W. Wolowodiuk, and W. Bakker, "In Situ Coal Ash Corrosion Testing for 2 Years at Three Utilities," International EPRI Conference on Improved Technology for Fossil Power Plants New and Retrofit Applications, Washington, DC, March 1-3, 1993.
6. I. M. Rehn, "Fireside Corrosion of Superheater and Reheater Tubes," Palo Alto, CA: Electric Power Research Institute, 1980. CS-1653.
7. I. M. Rehn, "Fireside Corrosion of Superheater Alloys for Advanced Cycle Steam Plants," Palo Alto, CA: Electric Power Research Institute, 1987. EPRI 5195.
8. S. Van Weele and J. L. Blough, "Literature Search Update—Fireside Corrosion Testing of Candidate Superheater Tube Alloys, Coatings, and Claddings," Livingston, NJ: Foster Wheeler Development Corporation, September 1990. FWC/FWDC/TR-90-11.

9. W. Wolowodiuk, S. Kihara, and K. Nakagawa, "Laboratory Coal Ash Corrosion Tests," Palo Alto, CA: Electric Power Research Institute, July 1989. GS-6449.
10. S. Van Weele and J. L. Blough, "Fireside Corrosion Testing of Candidate Superheater, Tube Alloys, Coatings, and Claddings," Livingston, NJ: Foster Wheeler Development Corporation, August 1991. ORNL/SUB/89-SA187/02.
11. S. Kihara, K. Nakagawa, A. Ohtomo, H. Aoki, and S. Ando, "Simulating Test Results for Fireside Corrosion of Superheater & Reheater Tubes Operating at Advanced Steam Conditions in Coal-Fired Boilers, *High Temperature Corrosion in Energy Systems*, TMS/AIME, M. F. Rothman, ed., 1984, pp. 361-376.
12. W. Wolowodiuk, et al., "Coal-Ash Corrosion Investigations," *Proceedings of the First International Conference on Improved Coal-Fired Power Plants*. Palo Alto, CA: Electric Power Research Institute, November 1986.
13. J. L. Blough, M. T. Krawchuk, G. J. Stanko, and W. Wolowodiuk, "Superheater Corrosion Field Test Results," Palo Alto, CA: Electric Power Research Institute, November 1993. TR-103438.
14. J. L. Blough and W. T. Bakker, "Measurement of Superheater Corrosion Caused by Molten Alkali Sulfates," First International Conference on Heat-Resistant Materials, to be presented at the ASM International, Lake Geneva, WI, September 22-26, 1991.
15. T. Hammond, W. Wolowodiuk, J. L. Blough, J. Brooks, "Replacement of Reheater at TVA's Gallatin Station Unit 2," presented at the Third International Conference on Improved Coal-Fired Power Plants (ICPP), San Francisco, April 1991.
16. J. L. Blough, M. T. Krawchuk, and S. F. Van Weele, "Fireside Corrosion Testing of Candidate Superheater Tube Alloys, Coatings, and Claddings — Phase II," Oak Ridge, TN: Oak Ridge National Laboratory, August 1995. CONF-9505204, ORNL/FMP-95/1.
17. R. W. Borio and R. P. Hensel, "Coal-Ash Composition as Related to High-Temperature Fireside Corrosion and Sulfur-Oxides Emission Control," *Transactions of the ASME, Journal of Engineering for Power*, Vol. 94, 1972, pp. 142-148.

PACK CEMENTATION COATINGS FOR ALLOYS

Yi-Rong He Minhui Zheng and Robert A. Rapp

Department of Materials Science and Engineering  
The Ohio State University  
Columbus, OH 43210-1179

## ABSTRACT

The halide-activated pack cementation process was modified to produce a Ge-doped silicide diffusion coating on a Cr-Cr<sub>2</sub>Nb alloy in a single processing step. The morphology and composition of the coating depended both on the composition of the pack and on the composition and microstructure of the substrate. Higher Ge content in the pack suppressed the formation of CrSi<sub>2</sub> and reduced the growth kinetics of the coating. Ge was not homogeneously distributed in the coatings. In cyclic and isothermal oxidation in air at 700 and 1050°C, the Ge-doped silicide coating protected the Cr-Nb alloys from significant oxidation by the formation of a Ge-doped silica film.

The codeposition and diffusion of aluminum and chromium into low alloy steel have been achieved using elemental Al and Cr powders and a two-step pack cementation process. Sequential process treatments at 925°C and 1150°C yield dense and uniform ferrite coatings, whose compositions are close to either Fe<sub>3</sub>Al or else FeAl plus a lower Cr content, when processed under different conditions. The higher content of Al in the coatings was predicted by thermodynamic calculations of equilibrium in the gas phase. The effect of the particle size of the metal powders on the surface composition of the coating has been studied for various combinations of Al and Cr powders.

## INTRODUCTION

The search for better high-temperature structural materials has led to the investigation of intermetallic compounds of refractory metal components because of their high melting point, relatively low density, and excellent high-temperature strength<sup>1-5</sup>. Numerous studies have focused on aluminides, silicides, chromides and beryllides. Recently Laves phase intermetallics have received attention.<sup>5,6</sup> Liu and his colleagues<sup>7-13</sup> at Oak Ridge National Laboratory (ORNL) have examined the Cr-Cr<sub>2</sub>Nb (Laves phase) alloys. The effects of material processing, heat treatment, and alloying additions on the microstructure and mechanical and oxidation properties of the Cr-Nb (CN) alloys have been evaluated. Hot extrusion at 1480°C was found most effective in repairing casting defects and refining the Cr-Cr<sub>2</sub>Nb eutectic structure. Several other beneficial alloying elements have also been identified. However, the oxidation resistance of the CN alloys was not adequate for high temperature application significantly above 1000°C.

To satisfy this need for improved oxidation resistance, silicide coatings on Cr-Cr<sub>2</sub>Nb are being investigated in this project. Grabke and Brumm<sup>14</sup> studied the oxidation behavior of CrSi<sub>2</sub> in pure oxygen of 0.003-0.66 bar at 900-1200°C; CrSi<sub>2</sub> was protective below 1100°C. Douglas et al.<sup>15</sup> concluded that alloys containing Fe, Co,

Ni, Ti and Ta oxidized rapidly at and above 1000°C, but that  $\text{Cr}_3\text{Si}$  was highly oxidation resistant below 1200°C.

The pack cementation method to convert a substrate surface to an oxidation-resistant diffusion coating has the advantages of low cost, good coating adhesion and wide versatility<sup>16</sup>. Previous studies by Mueller, et al.<sup>17,18</sup> showed that a Ge-doped  $(\text{MoW})\text{Si}_2$  coating on Nb greatly improved its isothermal and cyclic oxidation resistance. As introduced by Fitzer et al.<sup>19</sup> and Schlichting and Neumann<sup>20</sup>, the  $\text{GeO}_2$  solute formed upon oxidation decreases the viscosity of the protective silica scale. The Ge solute in  $\text{MoSi}_2$  diffusion coatings, as well as the presence of a residual NaF salt contamination on the coating surface, protects the coating from pesting oxidation at low-temperature exposure<sup>21,22</sup>. Cockeram and Rapp<sup>23</sup> have recently developed an oxidation-resistant Ge-doped Ti-silicide diffusion coating on commercially pure Ti, Ti-22Al-27Nb and Ti-20Al-22Nb alloys in a single step coating process. Therefore, the goal for this work was to develop Ge-doped silicide coatings on the CN alloys.

Prior research at Oak Ridge National Laboratory has led to the development and commercialization of alloys based on the  $\text{Fe}_3\text{Al}$  and FeAl compositions. While these alloys exhibit excellent resistance to oxidation and corrosion, especially sulphidation, at high temperatures, the fabrication of the alloys is difficult and their mechanical properties are problematic. However, these compositions show promise as coatings on strong low alloy steels commonly used in fossil energy applications. The *in situ* CVD process known as pack cementation has the advantages of creating a coating with a true metallurgical bond at the surface of steel components. The pack cementation process involves placing the parts to be coated in a pack of reactive powders, and heating this pack in a retort to an elevated temperature for given time, during which treatment the deposition of a diffusion coating is produced.

A high aluminum content can significantly increase the service life of the components made of FeCrAl-base alloys used at very high temperatures<sup>24</sup>. An aluminum content in excess of 10 wt.% is needed for adequate corrosion resistance in sulfur-containing atmospheres<sup>25</sup>. Geib and Rapp have demonstrated pack cementation Cr-Al coatings for low alloy steel<sup>26</sup>, as well as for  $\text{Fe}_3\text{Al}$ <sup>27</sup>, using Cr-Al masteralloy powder as the pack constituent.

Economically, it would be beneficial to codeposit Al and Cr in a single batch process to reduce the labor, energy and material costs. The current study is intended to develop a Cr-Al coating on carbon-containing steel surfaces (e.g. T11: C 0.15, Cr 1.0-1.5, Mo 0.44-0.65) by using pure Cr and Al elemental powders instead of a Cr-Al masteralloy, and to avoid the formation of a blocking Cr carbide at the surface. During the sequential process, a substrate is aluminized first at lower temperature and then chromized at higher temperature. During the use of mixed pure Al and Cr powders, alloying of the powders occurs during the processing. Because the finer metal particles have higher surface, the particle sizes have been found to be an important variable in deciding the surface composition.

## EXPERIMENTAL PROCEDURES

The CN87 alloy provided by Liu et al.<sup>13</sup> contains 61.5Cr, 8Nb, 1.5Al, 5Mo, 4X2 and 20Fe (at.%) and consists of a Cr-rich phase and the Laves  $\text{Cr}_2\text{Nb}$  phase.

Nominally pure elemental powders of Si (99%) and Ge (99.999%) were used in the cementation pack. The halide salt activator was NaF (99.7%). Alumina (98%) was used as the inert filler. As the primary means to vary the Ge content in the silicide diffusion coating, variable amounts of Si and Ge were used in various packs. Prepurified Ar gas flowed through the furnace tube to protect the sealed crucible from oxidation. After holding at the coating temperature for a given time, the coupons were retrieved from the pack at room temperature and prepared for metallurgical study.

Cyclic oxidation studies were performed in air in a vertical electric furnace. A K-type thermocouple was used to monitor the temperature. Coupons were placed on an  $\text{Al}_2\text{O}_3$  mat inside a quartz boat supported by a quartz post, which was moved up and down by a motor. The one hour cycle consisted of 45 minute heating (inside furnace) and 15 minute cooling (outside the furnace).

## RESULTS AND DISCUSSION

Figure 1 (a) shows the cross-section of a CN87 alloy coated at 1030°C for 12 hours in a NaF-activated pack containing 20Si-4Ge (wt.%). X-ray diffraction analysis on the coupon surface revealed the existence of  $\text{Cr}_3\text{Si}$  and  $\text{Cr}(\text{SiAl})_2$ . The transitions in phase morphology and distribution are shown in Fig. 1(b). EDS analysis shows that the bright phase in the coating near the surface has the composition 16.3Cr, 13.2Nb, 3.4Mo and 63.8Si with 3.3Ge (at.%), indicating the formation of  $(\text{CrNbMo})(\text{SiGe})_2$ ; the dark phase consists of 28.9Cr, 3.3Mo, 66.8Si plus 0.9Ge, thus a form of  $(\text{CrMo})(\text{SiGe})_2$ ; the gray phase is composed of 26.4Cr, 20.8Fe, 51.3Si plus 1.5Ge, indicating  $(\text{CrFe})(\text{SiGe})$ .

Figure 2(a) shows the surface morphology of CN-87 alloy coated at 1000°C for 12 hours in a pack containing 16Si-8Ge. The externally deposited nodule phase consisted of 50.2O, 15.0Na, 13.1Al, 12.5Si, 8.5F and 0.6Cl, i. e. an oxide residue from the pack coating process. The bright flakes had the composition of 33.8Na, 27.8F, 21.5O, 10.2Al, 6.3Si and 0.4Cr, i.e. another salt residue. The flat area consisted of 31.7Cr, 4.6Fe, 3.6Al and 60.1Si, indicating the phase of  $(\text{CrAlFe})\text{Si}_2$ . Figure 2(b) shows the cross-section of the coated coupon. A crack traverses the coating but does not enter the substrate; some small voids exist at the substrate/coating interface. Again, the morphology and phase compositions in the coating are closely related to those of the substrate, as expected for dominant inward diffusion of Si and Ge. In the outer part of the coating, the bright phase is  $(\text{NbCrMoFe})(\text{SiGe})_2$ , the dark phase is  $(\text{CrFeMoNb})(\text{SiGe})_2$  and the gray phase is  $(\text{CrFeMo})(\text{SiGe})$ .

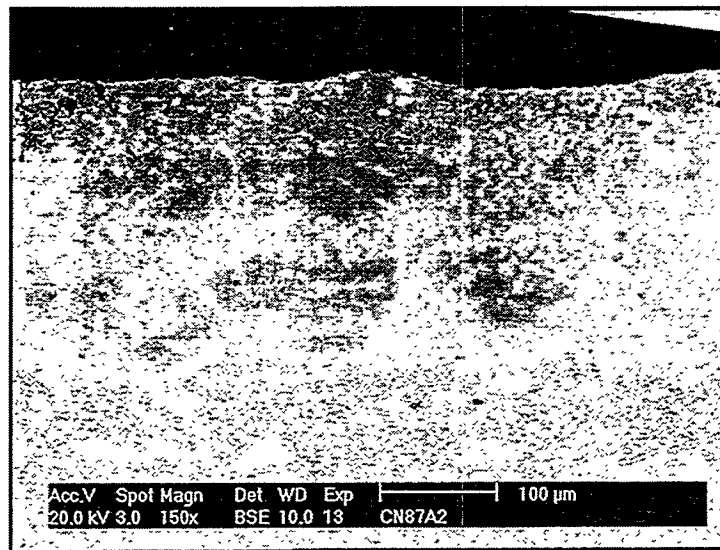


Fig. 1(a) Cross-section of a CN87 alloy coated at 1030°C for 12 hours in a pack containing 20Si-4Ge

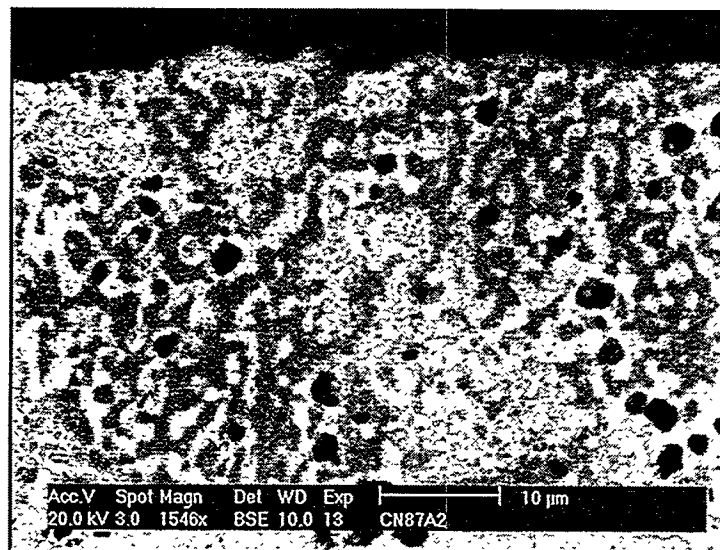


Fig. 1(b) High magnification image of outer part of 1(a)

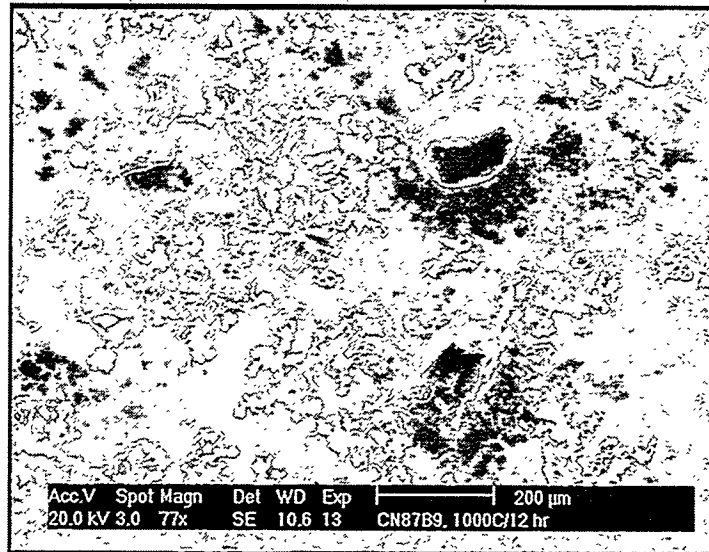


Fig. 2(a) Surface morphology of a CN87 alloy coated at 1000°C for 12 hours in a pack containing 16Si-8Ge

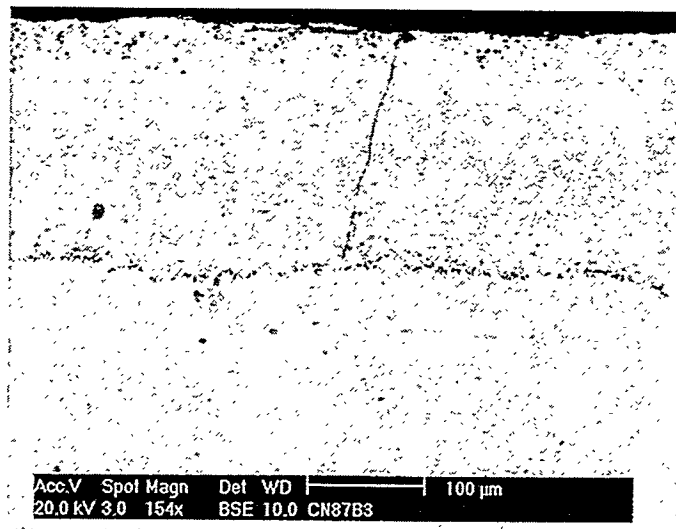


Fig. 2(b) Cross-section of a CN87 alloy coated at 1000°C for 12 hours in a pack containing 16Si-8Ge

Similar characterizations of coatings were made for coatings produced from other packs involving different Si/Ge ratios. Table 1 summarizes the coating characteristics as a function of the Si/Ge ratio in the pack: coating thickness, phases observed, and the highest Ge content and where it was detected.

Table 1 Summary of the characteristics observed in coatings grown from the NaF-activated packs

Si/Ge Ratio	5:1	2:1	1:1	0.5:1	0.2:1
Phases surface to substrate	M(SiGe) <sub>2</sub> M(SiGe)	M(SiGe) <sub>2</sub> M(SiGe) M <sub>11</sub> (SiGe) <sub>8</sub> M <sub>5</sub> (SiGe) <sub>3</sub>	M(SiGe) M <sub>11</sub> (SiGe) <sub>8</sub> M <sub>5</sub> (SiGe) <sub>3</sub>	M(SiGe) M <sub>11</sub> (SiGe) <sub>8</sub> M <sub>5</sub> (SiGe) <sub>3</sub>	M(SiGe) M <sub>11</sub> (SiGe) <sub>8</sub> M <sub>5</sub> (SiGe) <sub>3</sub>
Coating thickness	233 $\mu$ m (1030°C)	200 $\mu$ m (1000°C)	80 $\mu$ m (1000°C)	83 $\mu$ m (1000°C)	52 $\mu$ m (1000°C)
Ge content Region	3.27 (at. %) outer region	2.9 outer region	4.03 inner layer	4.07 inner layer	3.85 inner layer
M represents metal elements					

In general, the morphology and structure of the coatings are complex, which is attributed to the two-phase structure of the substrate and its multiple alloying additions. During the pack cementation treatment, the new phases formed depend on their chemical stability and the diffusion kinetics. Alloying elements partially redistribute among the phases. Therefore, silicides are formed with nominally the same chemical formula but different contents of constituent elements, such as the bright phase of (NbCrMoFe)(SiGe)<sub>2</sub> and the dark phase (CrFeMoNb)(SiGe)<sub>2</sub> in the same layer.

EDS showed that Ge was not homogeneously distributed in the coatings. As summarized in Table 1, when the pack Si/Ge ratio was less than 1, the highest Ge content was found in the M(SiGe)<sub>2</sub> phase in the outermost part of the coatings. When the Si/Ge pack ratio was greater than 1, Ge was concentrated in the M<sub>11</sub>(SiGe)<sub>8</sub> phase of the inner layers. The Ge tended to concentrate in phases with higher Nb content, perhaps because of the larger lattice constants for the high-Nb-content phases. Both CrSi<sub>2</sub> and NbSi<sub>2</sub> have the same hexagonal structure; the lattice constants of CrSi<sub>2</sub> are  $a = 4.43 \text{ \AA}$ ,  $c = 6.37 \text{ \AA}$ <sup>28</sup>, while for NbSi<sub>2</sub>  $a = 4.797 \text{ \AA}$ ,  $c = 6.592 \text{ \AA}$ <sup>29</sup>. Higher Ge content in the pack suppressed the formation of the CrSi<sub>2</sub> phase and tended to retard coating growth. A similar effect was observed for the (MoW)(SiGe)<sub>2</sub> coating<sup>17</sup> and the Ge-doped Ti-silicide coating<sup>23</sup>. The number of voids formed by vacancy condensation in the inner layer of the coatings also increased with increasing Ge content in the pack, because the coating growth involved more outward diffusion with increasing Ge content in the pack. Cracks were also observed in these coatings. Oxidation attack occurs preferentially



along these pre-existing cracks, but they are sealed by a protective glass formation which prevents penetration to the substrate<sup>17,18</sup>.

Two coated CN coupons were subjected to cyclic oxidation in air at 700°C after coating in a pack containing 16Si-8Ge. The residual salt present on the as-coated surface is known to be beneficial in the elimination of pesting for MoSi<sub>2</sub><sup>21,22</sup>. To study the effect of the residual salt on the cyclic oxidation behavior, the surfaces of one coated coupon were slightly abraded preliminarily. Figure 3 shows the cyclic oxidation kinetics after 912 cycles at 700°C. Neither coupon exhibited spalling during cyclic oxidation and the weight gains were low: 0.43 mg/cm<sup>2</sup> and 0.32 mg/cm<sup>2</sup> for the unabraded and abraded coupon, respectively. Oxidation propagated along cracks in the coating but stopped at the coating /substrate interface.

Two coupons coated in a pack of 16Si-8Ge were oxidized cyclically at 1050°C in air. After 325 one-hour cycles, the weight gains were 4.9 and 4.6 mg/cm<sup>2</sup>. For comparison, a CN87 coupon was coated in a pack of 20Si-4Ge, and then tested cyclically for the same conditions. The weight gain was 3.98 mg/cm<sup>2</sup> after 287 cycles. Figure 4 presents the kinetics of these cyclic oxidation tests. X-ray diffraction analysis on the surfaces of the oxidized coupons indicated the existence of Cr<sub>2</sub>O<sub>3</sub> (JCPDS 38-1479) and amorphous SiO<sub>2</sub> (JCPDS 29-85). Internal oxidation of Al was also observed in the substrate of the cyclically oxidized coupons.

For the T11 steel samples used in this study of Al/Cr coating, the phase transformation from ferrite (bcc) to austenite (fcc) occurs at 888°C. At a temperature lower than about 920°C, the steel substrate loses weight by FeCl<sub>2</sub> evaporation and is not coated well because the vapor pressure of aluminum halide in the pack is not sufficiently high. But for the first treatment step at 920°C or higher, Al diffuses into the surface, serves as a ferrite stabilizer, and pushes carbon into the T11 substrate, as shown in Fig. 5. After the low-carbon ferrite case is formed, Cr can be deposited in the second sequential treatment step at higher temperature, without forming a blocking carbide layer on the surface. The second process step at 1150°C results in a thicker coating as aluminum and chromium diffuse into the substrate. The coatings are aluminum-rich, because of the higher vapor pressure of the Al halide compared to Cr halide. Decarburization was not observed for the substrates with good Al-Cr coatings.

Both the Al and Cr concentrations gradually decrease from the surface to the boundary between the coating layer and the substrate as shown by the EDS results in Fig. 6. Twelve T11 coupons coated in this way were sent to ABB Research Lab. for corrosion testing. After 500 h exposure to simulated boiler gases at 500°C, the coatings were essentially not attacked. Forty more test samples and an steel tube segment have also been coated and are being subjected to extended corrosion testing at ABB.

The reactions of the halide activator(s) with the mixed Cr and Al pure powders in the pack result in volatile metal halides which diffuse and deposit metals on the substrates in the pack. In addition, the volatile species effect an alloying of the Al and Cr pack powders themselves. Kinetically, the transfer of the metal halides is affected by the particle size of pure Al and Cr powders. Consequently, the coating composition was found to vary with the particle sizes of the metal powders in the pack.

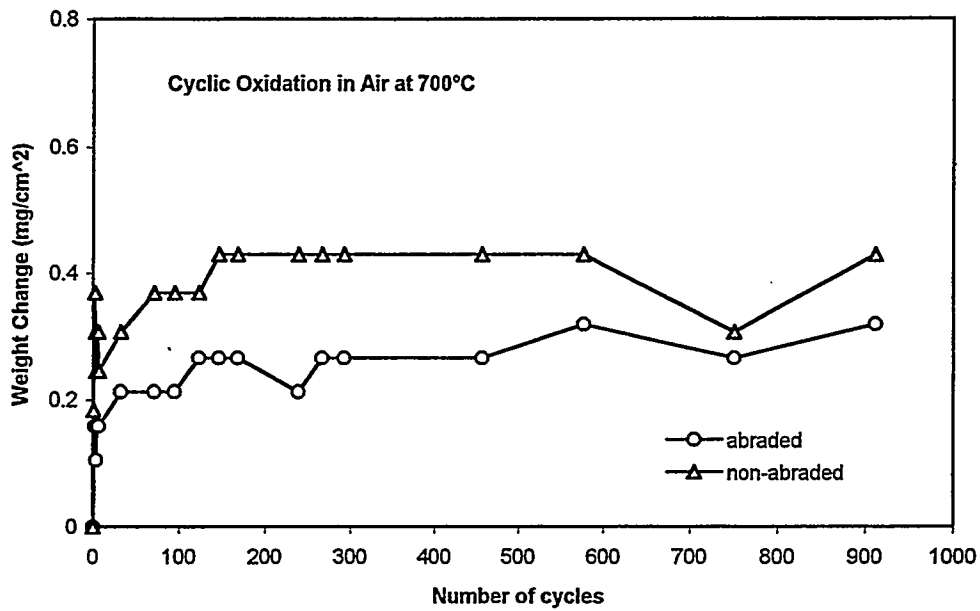


Fig. 3 The cyclic oxidation kinetics at 700°C for duplicate coupons of CN87 coated for 12 hours at 1000°C in a NaF-activated pack with 16Si-8Ge.

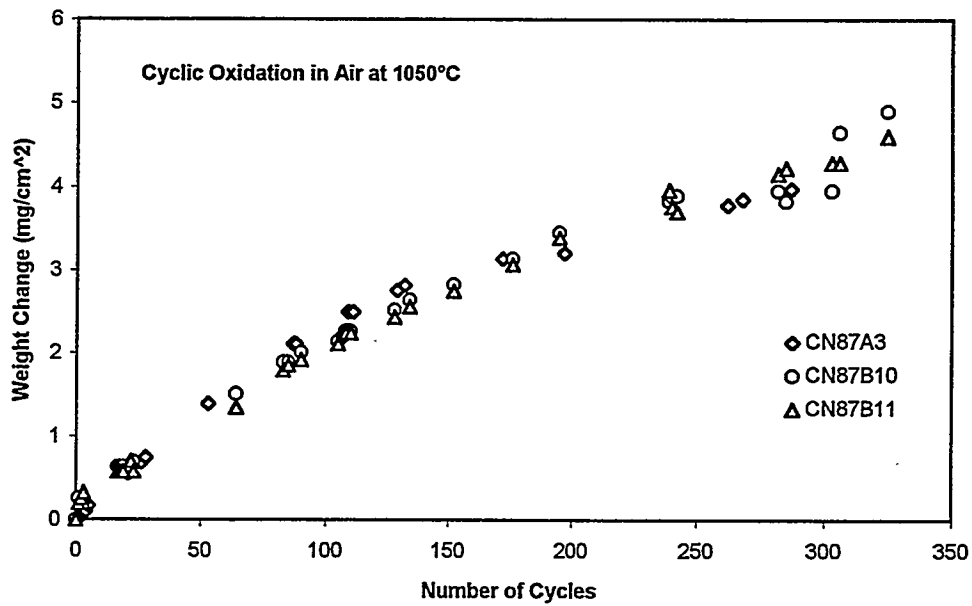


Fig. 4 The cyclic oxidation kinetics of Si-Ge coated CN87 alloy at 1050°C

Figure 7 shows that when fine (20 $\mu$ m) Al powder was used, the Al composition decreased, while the Cr composition increased, with an increase of the particle size of the Cr powder. For some coating runs, chromium carbide layers were produced with a pack using the finest Cr powder. Beneath the carbide, the alloy composition approximated Kanthal. When coarse (-100 mesh) Al powder was used, less extensive variation in Al and Cr concentrations resulted from variation in the particle size of Cr powder, as shown in Fig. 8. Thus the particle sizes of the metals to be used in a codeposition pack cementation process influence importantly the composition of the coating.

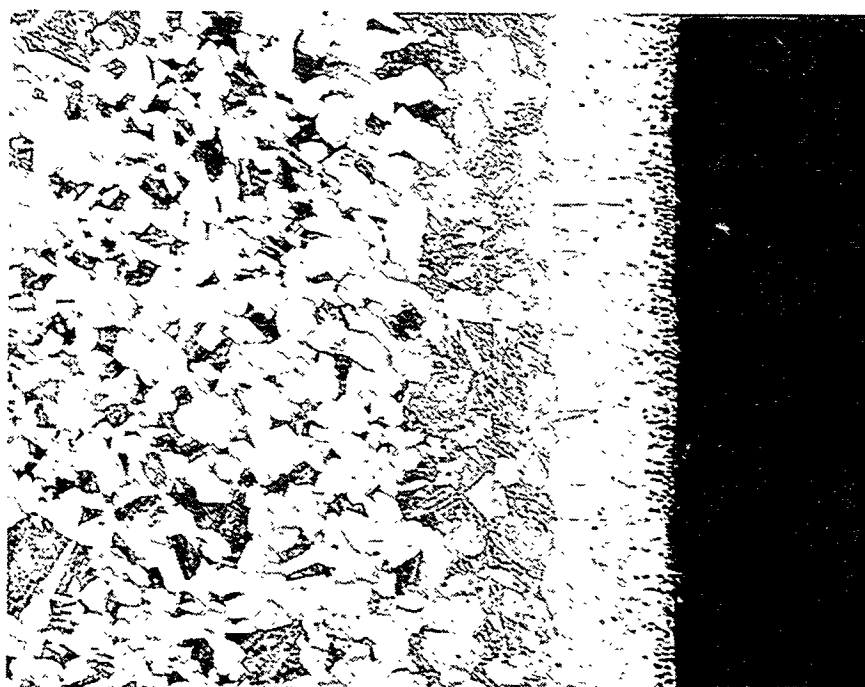


Fig. 5 Photomicrograph of a T11 Substrate with Al and Cr Coating Grown at 920°C for 12 hours Using Pure Cr and Pure Al Powders and Halide Activator (50 $\times$ )

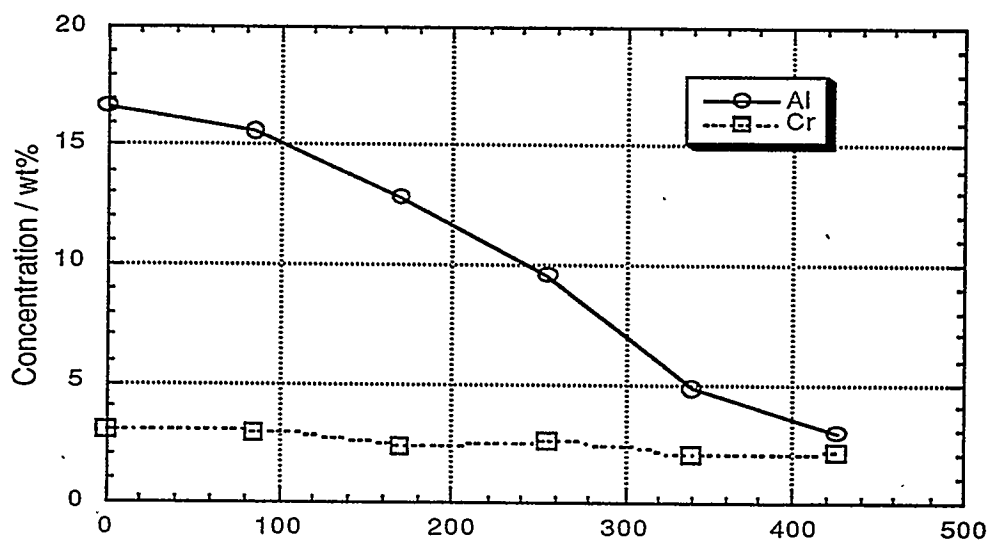


Fig. 6 Concentration Profiles for the Coating on T11 Steel Coated Sequentially at 925°C and 1150°C Using Pure Cr and Al Powders with Halide Activator(s)

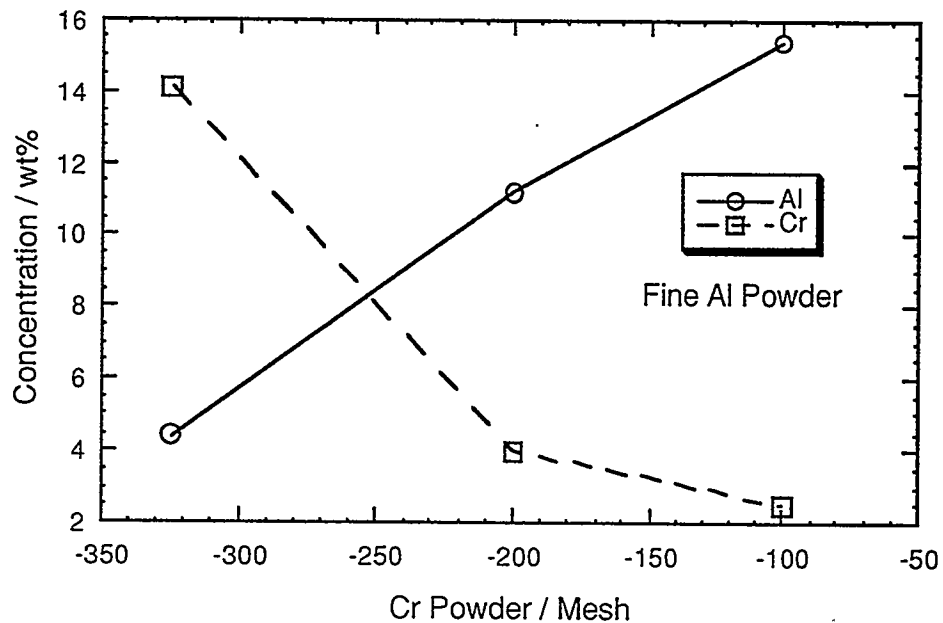


Fig. 7 Surface Compositions of Coatings on T11 Steel Samples vs. Particle Size of Cr Powder in the Pack.

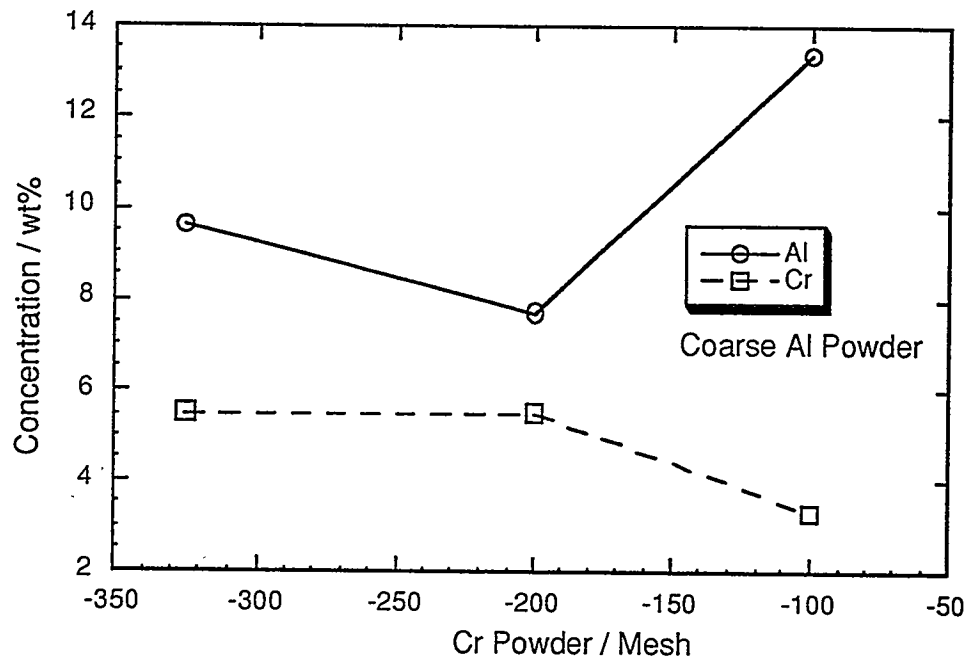


Fig. 8 Surface Compositions of the Coatings on T11 Steel Samples vs. Particle Sizes of Cr Powder in the Pack

### CONCLUSIONS

Ge-doped silicide diffusion coatings were developed for the Cr-Nb alloys in a single-step pack cementation process. The morphology and composition of the coating depended both on the composition of the pack, and on the composition and microstructure of the substrate. Higher Ge content in the pack favored  $\text{NbSi}_2$  formation and suppressed the formation of  $\text{CrSi}_2$ . The thickness of the coating decreased with an increase of Ge in the pack. The Ge-doped silicide coatings minimized the kinetics of cyclic oxidation in air for the Cr-Nb alloys.

The codeposition and diffusion of aluminum and chromium into low alloy steel have been achieved using elemental Al and Cr powders and a two-step pack cementation process. Sequential process treatment at 925°C and 1150°C yields dense and uniform ferrite coatings. The higher content of Al in the coatings was predicted by thermodynamic calculations of equilibrium in the gas phase. The effect of the particle size of the metal powders on the surface composition of the coating has been studied for various combinations of Al and Cr powders.

## REFERENCES

1. D. M. Dimiduk, D. B. Miracle, Y-W. Kim and M. G. Mendiratta, *ISIJ International*, Vol. 31, No. 1, p.1223, 1991.
2. C. T. Liu and K. S. Kumar, *JOM*, May, p. 38, 1993.
3. K. S. Kumar, C. T. Liu, *JOM*, June, p. 28, 1993.
4. E. P. George, M. Yamaguchi, K. S. Kumar, C. T. Liu, *Ann. Rev. Sci.*, vol. 24, p. 409, 1994.
5. G. Sauthoff, "Intermetallics", VCH Verlagsgesellschaft, New York, 1995.
6. D. L. Anton and D. M. Shah, *Materials Science and Engineering*, A153, p. 410, 1992.
7. M. Takeyama and C. T. Liu, *Materials Science and Engineering*, A132, p. 61, 1991.
8. C. T. Liu, J. A. Horton and C. A. Carmichael, *Proc. Seventh Ann. Conf. on Fossil Energy Materials*, N. C. Cole and R. R. Judkins (Eds.), DOE, p. 297, 1993.
9. P. F. Tortorelli, L. J. Carson and J. H. DeVan, *ibid*, p. 309, 1993.
10. C. T. Liu, J. A. Horton and C. A. Carmichael *Proc. Eighth Ann. Conf. on Fossil Energy Materials*, N. C. Cole and R. R. Judkins (Eds.), DOE, p. 377, 1994.
11. P. F. Tortorelli and J. H. DeVan, *ibid*, p. 391, 1994.
12. C. T. Liu, P. F. Tortorelli, J. A. Horton, D. S. Easton, J. H. Schneibel, L. Heatherly, C. A. Carmichael, M. Howell and J. L. Wright, *Proc. Ninth Ann. Conf. on Fossil Energy Materials*, N. C. Cole and R. R. Judkins (Eds.), DOE, p. 415, 1995.
13. J. A. Cook, P. K. Liaw and C. T. Liu, *ibid*, p. 335, 1995.
14. H. J. Grabke and M. Brumm, "Oxidation Behaviour of Chromium Disilicide", *Oxidation of High-Temperature Intermetallics*, T. Grobstein and J. Doychak (Eds.), TMS publisher, p. 245, 1988.
15. W. Douglas, M. L. Fleischer and R. L. Fleischer, *Mat. Res. Soc. Symp. Proc.* Vol. 213, p. 969, 1991
16. P. G. Cappelli, "Coating Processes", *High Temperature Alloys for Gas Turbines*, D. Coutouradis, P. Felix, H. Fischmeister, L. Habraken, Y. Lindblom and M. O. Speidel Eds, Applied Science Publ., London, p. 177, 1978.
17. A. Mueller, G. Wang, R. A. Rapp and E. L. Courtright, *J. Electrochem. Soc.*, 139(5), p.1266, 1992.
18. A. Mueller, G. Wang, R. A. Rapp, E. L. Courtright and T. A. Kircher, *Materials Science and Engineering*, A155, p. 199, 1992.
19. E. Fitzer, H. Herbst, J. Schlichting, *Werkst. Korros.* 24, p. 274, 1973.
20. J. Schlichting and S. Neumann, *J. Non-Crystalline Solids*, 48, p. 185, 1982.
21. B. V. Cockeram, G. Wang and R. A. Rapp, *Materials and Corrosion*, 46, p. 207, 1995.
22. B. V. Cockeram, G. Wang and R. A. Rapp, *Oxid. Met.*, Vol. 45, Nos.1/2, p. 77, 1996.
23. B. V. Cockeram and R. A. Rapp, *Oxid. Met.*, Vol. 45, Nos.3/4, p. 375, 1996.
24. W. J. Quadakker, T. Malkow and H. Nickel, *Proc. 2nd inter. Conf. High Temp. Mat.*, p. 91, 1995.
25. K. Natesan and R. N. Johnson, *Proc. 2nd inter. Conf. High Temp. Mat.*, p.591, 1995.
26. F. D. Geib and R. A. Rapp, *Oxidation of Metals*, 40, p. 213, 1993.
27. F. D. Geib and R. A. Rapp, V. A. Ravi and T. S. Srivastan, Eds., TMS Warrendale, PA, p. 347, 1991.
28. J. D. H. Donnay, "Crystal Data Determinative Tables". Third Edition Vol. 4 Inorganic Compounds, NBS/JCPDS International for Diffraction Data, p. H/R-138, 1972.
29. A. Taylor and B. J. Kagle, "Crystallographic Data on Metal and Alloy Structures", Dover Publications, Inc. New York, p. 143, 1963.

Cr<sub>2</sub>Nb-BASED ALLOY DEVELOPMENT

C. T. Liu, P. F. Tortorelli, J. A. Horton, D. S. Easton, and L. Heatherly

Oak Ridge National Laboratory  
Oak Ridge, Tennessee, U. S. A.

## ABSTRACT

Alloys of Cr-Cr<sub>2</sub>Nb with exceptionally high strength at 1200°C have been developed. However, these compositions suffer from limited ductility and toughness at room temperature. Despite improvements from processing modifications, as-fabricated defects still limit room temperature mechanical behavior. In contrast, an alloy system with only a small mismatch of the coefficients of thermal expansion of the two phases, Cr-Cr<sub>2</sub>Zr, showed good fabricability. However, these alloys are weaker than Cr-Cr<sub>2</sub>Nb compositions at high temperatures and have poor oxidation resistance. Silicide coatings can provide high-temperature oxidation and sulfidation protection of these alloys. Improvements in room temperature mechanical properties of Laves-phase-strengthened alloys will rely on further development based on increasing the ductility of the matrix phase by impurity control and compositional modifications.

## INTRODUCTION

The objective of this work is to develop a new generation of structural materials based on intermetallic alloys for use at high temperatures in advanced fossil energy conversion systems. Target applications of such ultrahigh strength alloys include hot components (for example, air heat exchangers) in advanced energy conversion systems and heat engines. However, these materials may also find use as wear-resistant parts in coal handling systems (for example, nozzles), drill bits for oil/gas wells, and valve guides in diesel engines.

One potential class of such alloys is that based on Cr-Cr<sub>2</sub>Nb alloys. The intermetallic phase, Cr<sub>2</sub>Nb, with a complex cubic structure (C-15)<sup>1,2</sup> has been selected for initial development because of its high melting point (1770°C),<sup>2-4</sup> relatively low material density (7.7 g/cm<sup>3</sup>),<sup>5</sup> and excellent high-temperature strength (at 1000 to 1250°C).<sup>6,7</sup> This intermetallic phase, like many other Laves phases, has a wide range of compositional

homogeneity<sup>2,4</sup> suggesting the possibility of improving its mechanical and metallurgical properties by alloying additions.

The major engineering concern with  $\text{Cr}_2\text{Nb}$  and other  $\text{A}_2\text{B}$  Laves phases is their poor fracture toughness and fracture resistance at ambient temperatures.<sup>3,6-9</sup> The single-phase  $\text{Cr}_2\text{Nb}$  is very hard (~800 DPH) and brittle at room temperature.<sup>9</sup> Because of this brittleness, the development effort has concentrated on two-phase structures containing the hard intermetallic phase  $\text{Cr}_2\text{Nb}$  and the softer Cr-rich solid solution phase. Previous studies indicate that the two-phase Cr- $\text{Cr}_2\text{Nb}$  alloys (CN) exhibited significant plastic deformation prior to fracture under compressive tests at room temperature.<sup>6,7,9</sup> The alloys showed excellent compressive strength at room and elevated temperatures, with the yield strength much superior to nickel-base superalloys and  $\text{Ni}_3\text{Al}$  alloys at and above 1000°C. The CN alloys, however, showed poor fracture strength in tension at ambient temperatures. Because tensile properties were sensitive to defects, efforts aimed at reducing as-cast defects and refining the cast Cr- $\text{Cr}_2\text{Nb}$  eutectic structure led to improved ductility.<sup>10</sup> A room-temperature fracture strength of 548 MPa and an ultimate tensile strength of 388 MPa, and 23% elongation, at 1200°C were achieved, while another CN alloy showed a fracture toughness of 7.6  $\text{MPa}\sqrt{\text{m}}$  at room temperature and 24.4  $\text{MPa}\sqrt{\text{m}}$  at 1000°C.<sup>10</sup>

Current studies are focused on enhancement of fracture resistance in tension at ambient temperatures and oxidation resistance above 1000°C. This report summarizes recent progress on controlling microstructure and improving the mechanical and metallurgical properties and the high-temperature corrosion behavior of Cr- $\text{Cr}_2\text{Nb}$  alloys through alloying additions, material processing, and heat treatment.

## ALLOY PREPARATION AND PROCESSING

CN alloys weighing 430 g were prepared by arc melting and drop casting in a copper mold (2.5 cm diam x 7.6 cm long) preheated to 200°C. High-purity niobium, chromium, and other metal chips were used as charge materials. The cast alloy ingots with the compositions listed in Table 1 generally contained oxide inclusions and cast porosity ranging in size from a few to several hundred microns. The cast alloys also exhibited a coarse eutectic structure with interconnected  $\text{Cr}_2\text{Nb}$  plates, which adversely affect mechanical properties.<sup>8</sup> In order to minimize the cast defects and to refine the eutectic structure, selected alloy ingots were clad inside Mo billets and hot extruded at 1480°C at an extrusion ratio of 4:1. Most alloys were successfully hot extruded into 1.3 cm bar stock.

The CN alloys were also prepared by a powder metallurgy (P/M) route. In this case, elemental powders, in ratios that were chosen to yield the target alloy compositions, were mixed



Table 1. Tensile Properties of Cr-Nb Base Alloys Fabricated by Hot Extrusion at 1480°C

Alloy No.	Alloy Composition (at. %) <sup>a</sup>	Tensile Fracture Strength (MPa)	Yield Strength (MPa)	Elongation (%)
<u>Room Temperature</u>				
CN-80	12Nb-6Mo-1.5Al	548		
CN-90	6Nb-5Mo-4X2-2X3-1.5Al	435		
CN-104	10Nb-6Mo-4X2-0.5X3	293		
CN-112	6Nb-5Mo-2X2-1X3-1X4-1.5Al	508		
CN-113	6Nb-5Mo-2X2-1X3-2X4-1.5Al	374		
<u>1200°C</u>				
CN-80		388	290	23.0
CN-90		384	302	13.4
CN-104		473	371	25.7
CN-112		440	345	30.1
CN-113		414	330	26.4

<sup>a</sup>Balance is Cr.

thoroughly in an inert environment and then placed inside molybdenum cans. The filled cans were then degassed in a vacuum chamber and sealed by electron-beam welding. As above, they were hot extruded at 1480°C to produce CN alloys. All the alloys were successfully hot extruded into bar stock without difficulty.

Within the past year, a series of alloys based on Cr-Cr<sub>2</sub>Zr were also prepared by melting and casting. The advantage of these alloys is that they are more resistant to cast and thermally induced cracking because, unlike the Cr-Cr<sub>2</sub>Nb system, there is a reasonable match between the coefficient of thermal expansion of the second phase and that of the matrix. The alloys with the compositions listed in Table 2 were all successfully fabricated into rod stock by hot extrusion in the same way as the Cr-Cr<sub>2</sub>Nb alloys.

### MICROSTRUCTURAL ANALYSIS

Alloying additions, heat treatment, and material processing all strongly affect the microstructure of the CN alloys. Examination of the microstructure produced by hot extrusion revealed micro-porosity and foreign particles in the P/M products. Energy dispersive x-ray spectroscopic (EDS) analysis indicated that these particles were mainly oxides of aluminum or niobium that formed during materials processing. Apparently, this contamination could not be simply eliminated even though the alloy powders were carefully processed in an inert

Table 2. Tensile Properties of Cr-Zr Base Alloys Fabricated by Hot Extrusion

Alloy No.	Alloy Composition (at. %)	Tensile Fracture Strength (MPa)	Yield Strength (MPa)	Elongation (%)
<u>Room Temperature</u>				
CN-107	Cr-12Zr	304		
CN-114	Cr-8Zr	240		
CN-115	Cr-8Zr-5X1	413		
CN-116	Cr-8Zr-5X1-4X2	443		
CN-117	Cr-8Zr-5X1-4X2-2X3	393		
<u>1200°C</u>				
CN-107				
CN-114		138	108	112
CN-115		267	203	46.3
CN-116		386	281	87.7
CN-117		485	344	28.8

atmosphere. Mechanical tests indicated that the P/M CN alloys had poor fracture resistance at room and elevated temperatures.

Figure 1 shows the optical microstructures of the ingot-processed CN-104 alloy with and without hot extrusion at 1480°C. It, as well as the other alloys listed in Table 1, was given a final heat treatment of 1 d at 1200°C for control of Cr<sub>2</sub>Nb precipitation in the Cr-rich phase. The hot extrusion was effective in breaking up the interconnected coarse Cr<sub>2</sub>Nb phase in the eutectic structure. In fact, it became difficult to distinguish the primary and secondary Cr<sub>2</sub>Nb particles in the alloy after this processing step.

Figure 2 compares the optical microstructures of cast CN-114 and CN-115 fabricated by hot extrusion at 1480°C. Both alloys are based on the Cr-Cr<sub>2</sub>Zr composition containing 8 at. % Zr (see Table 2). Alloy CN-114 is a binary alloy, while CN-115 is a ternary alloy containing 5 % of element X1. The comparison of the microstructures indicates that 5% of X1 is quite effective in breaking up the interconnected Cr<sub>2</sub>Zr phase into blocky particles. All the alloys were also given a final heat treatment of 1 d at 1200°C. It is important to note that, unlike the Cr-Cr<sub>2</sub>Nb system, no precipitation of Cr<sub>2</sub>Zr particles was found in the primary Cr-rich patches. This is consistent with the Cr-Zr phase diagram which shows a very low solubility of Zr in the Cr-rich solid solution phase.<sup>4</sup>

Specimens of the Cr-Nb alloy, CN-90, and the binary Cr-Zr alloy, CN-107, were examined by transmission electron microscopy and energy dispersive spectroscopy (EDS). Both specimens were hot extruded at 1480°C and annealed for 1 d at 1200°C. The matrix of the CN-90 alloy contained a very high density of dislocations while the Cr<sub>2</sub>Nb-based second

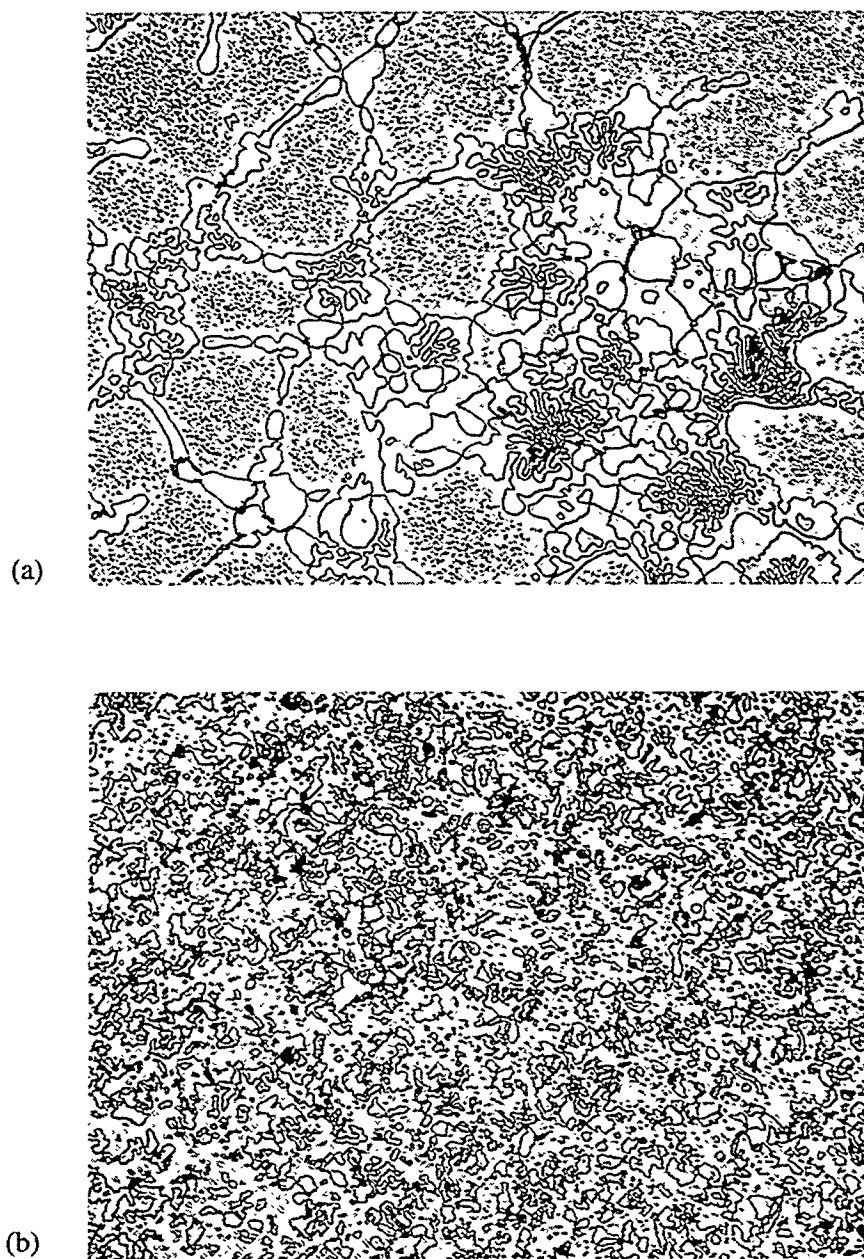


Fig. 1. Optical micrographs of CN-104: (a) as-cast plus annealed for 1 d at 1200°C and (b) hot-extruded at 1480°C plus annealed for 1 d at 1200°C; 625X.

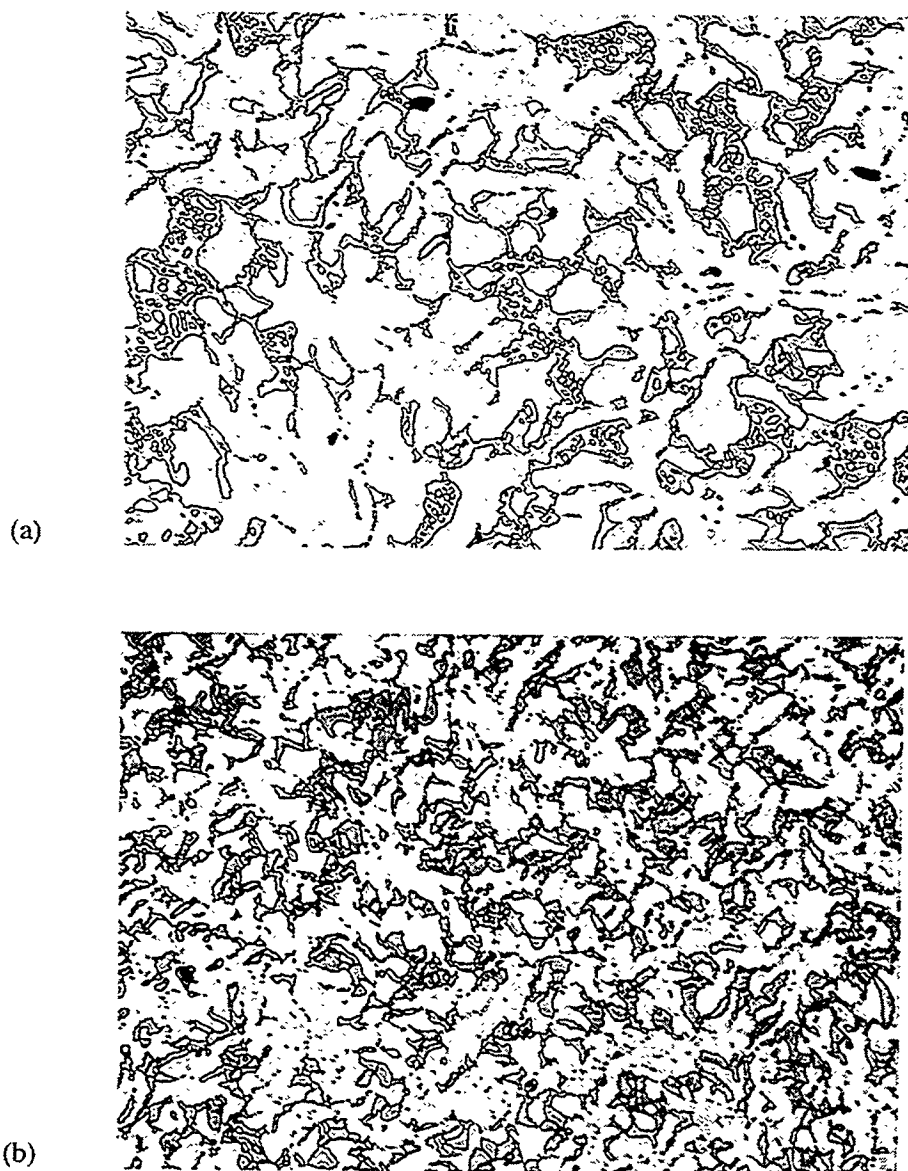


Fig. 2. Micrographs of CN alloys produced by hot extrusion at 1480°C and annealed for 1 d at 1200°C. (a) CN-114 and (b) CN-115; 625X.

phase showed fewer dislocations but some faulting (Fig. 3a). In the CN-107 alloy, (Cr-12% Zr) both the matrix and most of the second phase showed a high density of dislocations even after the 1 d anneal at 1200°C (Fig. 3b). Chemical analyses were performed on very thin areas with the precipitate intersecting the hole and on slightly thicker regions. The analysis of CN-90 showed that the Nb, X2, and X3, elements partitioned strongly to the  $\text{Cr}_2\text{Nb}$  precipitates, while the molybdenum level in the precipitate matched the matrix. In CN-107, the composition of the precipitate was determined to be 68% Cr - 32% Zr, indicating the expected formation of  $\text{Cr}_2\text{Zr}$ . Virtually no zirconium remained in solution. Table 3 summarizes the average compositions determined by EDS.

Table 3. Chemical Analysis of CN-90 and CN-107 (in at. %)

CN-90	Al	X2	X3	Cr	Nb	Mo
Average matrix	1	1	1	90	1	6
Average ppt	0.5	11	4	52	25	7
nominal	1.5	4	2	81.5	6	5

CN-107	Cr	Zr
Average matrix	99	1
Average ppt	68	32
nominal	88	12

## TENSILE PROPERTIES

Button-type tensile specimens with gage dimensions 0.31 diam x 0.95 cm long were machined by electro-discharge machining, followed by grinding and polishing with "0" Emery paper. The tensile specimens were tested in an Instron Testing Machine at room temperature in air and at 1200°C in vacuum. Since the tensile properties of brittle materials are sensitive to microstructure and defects in materials, the CN alloys were tested at room temperature for different fabrication conditions. Table 4 compares the tensile properties of CN-90 processed in different ways. The P/M material, fabricated by hot pressing and isothermal forging of the power compact, had the lowest fracture strength, while the material fabricated by hot extrusion of the cast ingot showed the highest value. As mentioned previously, the low fracture strength of the P/M material is associated with interstitial contamination and the formation of oxide/nitride particles.

Table 1 summarizes the tensile properties of Cr-Nb base alloys fabricated by hot extrusion of cast materials. The CN alloys showed no microscopic yielding prior to fracture, and the two alloys CN-80 and -112 exhibited the best room-temperature fracture strength, >500 MPa. At 1200°C, the CN alloys were very strong and ductile. Yield and ultimate tensile



Fig. 3. TEM micrographs of (a) CN 90 and (b) CN 107 showing a high dislocation density present after extrusion at 1480°C and an anneal for 1 d at 1200°C. The  $\text{Cr}_2\text{Nb}$ -based second phase in (a) has few dislocations while the  $\text{Cr}_2\text{Zr}$  second phase in (b) has a higher location density. Bar is 1  $\mu\text{m}$  long.

Table 4. Room-Temperature Tensile Properties of CN-90<sup>a</sup>

Alloy Preparation and Fabrication	Fracture Strength (MPa)
Hot pressing and forging elemental powders at 1480°C	140
Induction melted ingot	169
Hot extrusion of ingot at 1480°C	435

<sup>a</sup>All materials were given a final heat treatment of 1 d at 1200°C.

strengths were above 340 MPa (50 ksi) and 420 MPa (60 ksi), respectively, for both CN-104 and 112. These values are among the highest ever measured for alloys and meet the strength goal of this alloy development program. Alloy CN-112 appeared to have the best combined properties at room temperature and 1200°C. All the alloys except CN-90 had more than 20% elongation at 1200°C.

Table 2 summarizes the tensile properties of the Cr-Zr base alloys fabricated by hot extrusion. Both binary alloys had a low fracture strength, compared to the more highly alloyed compositions. Among all the alloys, CN-116 had the best tensile fracture strength at room temperature. Both yield and ultimate tensile strengths increased substantially with alloying additions, and the alloy CN-117 had the best strength at 1200°C. All the alloys are ductile at 1200°C, with tensile elongation more than 25%. Alloy CN-117 had the best combination of strengths at room temperature and 1200°C.

## HIGH-TEMPERATURE OXIDATION BEHAVIOR

It has been previously demonstrated that the addition of element X2 to Cr-Cr<sub>2</sub>Nb alloys improves oxidation resistance under isothermal and thermal cycling conditions.<sup>10,11</sup> The beneficial influence of X2 was attributed to improvement in the oxidation resistance of the Cr-rich regions (despite its partitioning to the Cr<sub>2</sub>Nb phase),<sup>11</sup> which otherwise showed preferential susceptibility to degradation upon exposure to high-temperature air.<sup>12</sup> However, despite improvements in the oxidation resistance of Cr-Cr<sub>2</sub>Nb alloys, such materials cannot be used in an uncoated condition in oxidizing environments at the very high temperatures where the superior strength of the CN compositions can be exploited (>1100°C). At these temperatures, thermally grown oxides on Cr-Cr<sub>2</sub>Nb alloys are not protective because chromia volatilizes at a significant rate. Oxidation protection will therefore involve the use of coatings. In this regard, silicide coatings applied by a pack cementation process can substantially improve the oxidation

resistance of Cr-Cr<sub>2</sub>Nb alloys.<sup>10,13,14</sup> Such coatings can also protect these alloys against high-temperature sulfidation. As indicated by the data in Fig. 4, which shows specimen weight gain as a function of isothermal exposure time in a highly-reducing H<sub>2</sub>S-H<sub>2</sub>-H<sub>2</sub>O-Ar gas mixture ( $p_{O_2} = 10^{-22}$  atm,  $p_{S_2} = 10^{-6}$ ), a Cr-12% Nb binary alloy was very susceptible to sulfidation, but a Cr-8% Nb composition (CN-87) coated with a Cr-Si layer produced by pack cementation exhibited very low weight gains. The resistance of the coated alloy was comparable to Fe<sub>3</sub>Al alloys containing > 2% Cr, which are considered to have very good sulfidation resistance compared to stainless steels and FeCrAl-type alloys.<sup>15</sup>

Figure 5 compares the isothermal oxidation rate of two more recent Cr-Cr<sub>2</sub>Nb compositions, CN-90 (see Table 1) and CN-100 (8% Nb-6% Mo-4% X2-2% X3), with that of CN-87, which heretofore showed the best oxidation resistance of the CN alloys.<sup>10,11</sup> (Isothermal air oxidation at 950°C has traditionally served as the initial baseline evaluation of oxidation resistance of the CN alloys.) All three compositions shown in Fig. 5 include the same concentration of X2, which, as noted above, has been shown to significantly improve oxidation resistance.<sup>10</sup> Despite this, CN-90 showed a significantly higher oxidation rate. The reason for this is unknown; all of the alloying elements in this alloy are present in comparable concentrations in CN-87 and/or CN-100, which had similar rates of weight gain that were less than that of CN-90. It is possible that the lower Nb concentration of CN-90, and the accompanying distribution of the matrix and eutectic phases, contributes to its higher oxidation rate as such a trend has been established previously,<sup>12</sup> but a definite explanation awaits chemical and microstructural analyses of these specimens. Examination of the data in Fig. 5 and the respective compositions of CN-87, -90, and -100 indicates that iron and element X3 don't have substantial effects on macroscopic oxidation behavior at 950°C.

Alloys based on Cr-Zr will be susceptible to high-temperature oxidation as Zr forms a very stable oxide that grows very rapidly.<sup>16</sup> It is therefore not surprising that the measured weight changes during isothermal oxidation exposures of alloys CN-107 and -114 (Fig. 6) are significantly higher than what is expected for reactions solely controlled by the growth of Cr<sub>2</sub>O<sub>3</sub> (ref. 16) and than what is measured for certain Cr-Cr<sub>2</sub>Nb alloys (Fig. 5). Interestingly, the addition of alloying elements substantially reduced the weight gains and oxidation rate over those measured for the binary compositions - see the results for CN-117 in Fig. 6. There are at least two possible reasons for the observed beneficial effect of alloying. Element X2 may improve oxidation resistance in a similar manner to its effect in the Cr-Nb system.<sup>11</sup> Secondly, as noted above, element X1 effectively breaks up the network of interconnected Cr<sub>2</sub>Zr (Fig. 2). As this phase is much more susceptible to oxidation than the Cr matrix, creation of a finer distribution of Cr<sub>2</sub>Zr may act to reduce the overall oxidation rate. Experiments specifically designed to examine the effects of volume fraction and distribution of Cr<sub>2</sub>Zr, in the context of



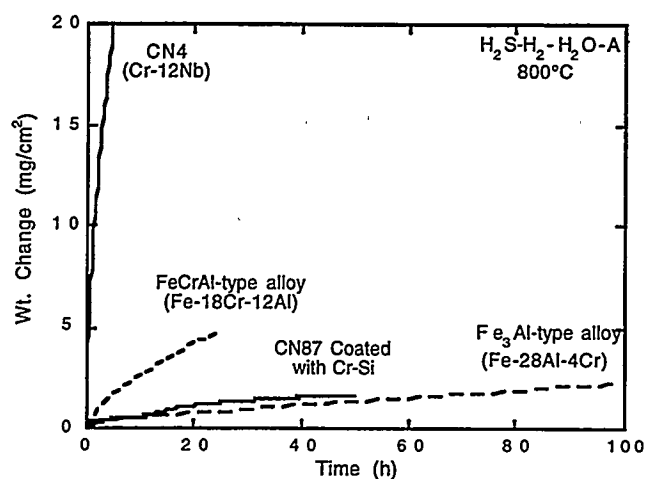


Fig. 4. Weight change as a function of time for alloys isothermally exposed to H<sub>2</sub>S-H<sub>2</sub>-H<sub>2</sub>O-Ar at 950°C. The CN87 alloy consisted of Cr-20%Fe-5%Mo-4%X2-1.5%Al and was coated by a pack cementation process (see ref. 13). Compositions shown are in at. %.

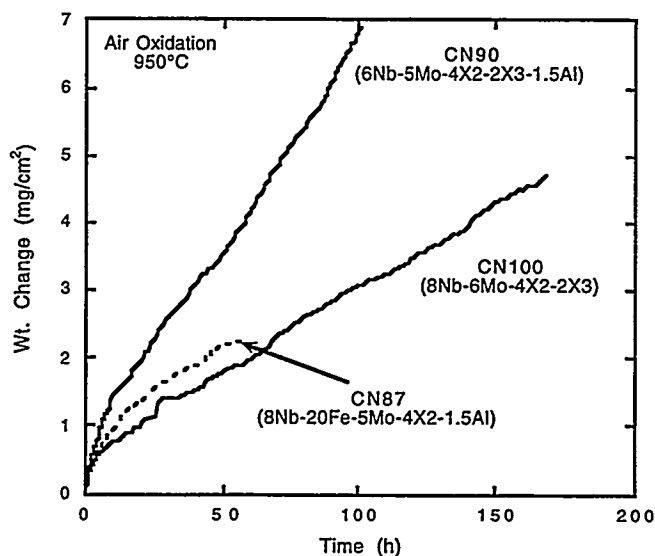


Fig. 5. Weight change as a function of time for Cr-Cr<sub>2</sub>Nb alloys during isothermal exposure to dry air at 950°C. Compositions shown are in at. %.

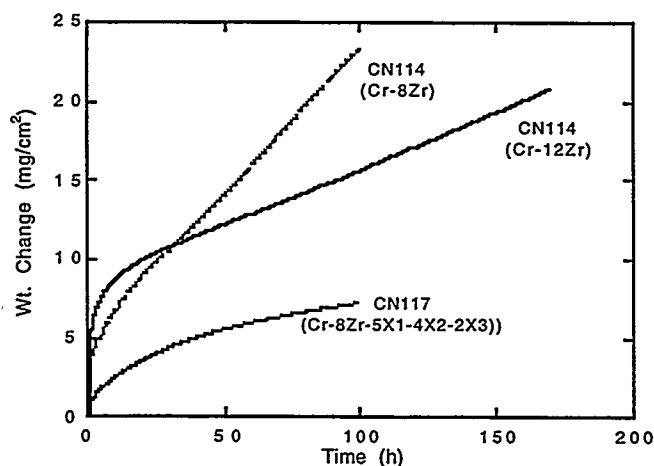


Fig. 6. Weight change as a function of time for Cr-Cr<sub>2</sub>Zr alloys during isothermal exposure to dry air at 950°C. Compositions shown are in at. %.

all the possible processes by which oxide products can grow on two-phase alloys at high temperatures,<sup>17</sup> can best address the validity of this hypothesis.

### FUTURE WORK

The development work on the Cr-Nb system indicates that the alloy CN-112 (Cr-6Nb-5Mo-2X2-1X3-1X4-1.5 Al, at.%) is close to an optimum composition and meets the strength goal of the project. Further studies are required to learn how to scavenge interstitials from the Cr-rich phase in order to achieve good tensile ductility at ambient temperatures. While Cr-Zr alloys show little as-fabricated cracking, there is a need to strengthen the Cr-rich phase by either solid-solution hardening or second-phase precipitation. Oxidation-resistant coatings are needed for the Cr-Zr alloys.

The Cr-rich phase has a limited ductility and fracture resistance at room temperature. In order to significantly improve the room-temperature ductility, the Cr-rich solid solution matrix phase must be substantially modified. Recently, ternary phase diagrams based on the Cr-Nb-X system have been reviewed and new compositions have been identified for alloy development based on a strategy of avoiding as-fabricated cracking and improving the ductility of the matrix in the presence of a Laves phase, which confers the unique high-temperature strength.

### SUMMARY

Alloys of Cr-Cr<sub>2</sub>Nb with exceptionally high strength at 1200°C have been developed. However, these compositions suffer from limited ductility and toughness at room temperature. Despite improvements from processing modifications, as-fabricated defects still limit room temperature mechanical behavior. Alloys based on Cr-Cr<sub>2</sub>Zr show good fabricability because there is only a small mismatch of the coefficients of thermal expansion of the two phases. However, these alloys are generally weaker than Cr-Cr<sub>2</sub>Nb compositions at high temperatures and have poor oxidation resistance. Silicide coatings can provide high-temperature oxidation and sulfidation protection of this alloys. Improvements in room temperature mechanical properties of Laves-phase-strengthened alloys will come from increasing the ductile of the matrix phase by impurity control and compositional modifications.

## ACKNOWLEDGMENTS

The authors thank D. F. Wilson and C. G. McKamey for their reviews of the manuscript. This research was sponsored by the Fossil Energy Advanced Research and Technology Development (AR&TD) Materials Program, U.S. Department of Energy, under contract DE-AC05-96OR22464 with Lockheed Martin Energy Research Corporation.

## REFERENCES

1. F. Laves, p. 124 in Theory of Alloy Phases, American Society for Metals, Metals Park, OH, 1956, .
2. D. J. Thoma and J. H. Perepezko, *Mat. Sci. and Eng.* **A156** (1992) 97.
3. H. J. Goldschmidt and J. A. Brand, *J. Less-Common Met.* **3** (1961) 44.
4. T. B. Massalski, J. L. Murray, L. H. Bennett, and H. Baker (eds.), Binary Alloy Phase Diagram, American Society for Metals, Metals Park, OH, 1986.
5. A. I. Taub and R. L. Fleischer, *Science* **243** (1989) 616.
6. C. T. Liu, pp. 375-383 in *Proc. 6th Annual Conf. Fossil Energy Materials*, N. C. Cole and R. R. Judkins (comp.), U. S. Department of Energy, July 1992.
7. C. T. Liu, J. A. Horton, and C. A. Carmichael, pp. 297-307, in *Proc. 7th Annual Conf. on Fossil Energy Materials*, N. C. Cole and R. R. Judkins (comp.), U. S. Department of Energy, July 1993.
8. C. T. Liu, J. A. Horton, and C. A. Carmichael, pp. 377-390 in *Proc. 8th Annual Conf. on Fossil Energy Materials*, N. C. Cole and R. R. Judkins (comp.), U. S. Department of Energy, August 1994..
9. M. Takeyama and C. T. Liu, *Mat. Sci. and Eng.* **A132** (1991) 61.
10. C. T. Liu, P. F. Tortorelli, J. A. Horton, D. S. Easton, J. H. Schneibel, L. Heatherly, C. A. Carmichael, M. Howell, and J. L. Wright, pp. 415 - 26 in *Proc. Ninth Annual Conf. Fossil Energy Materials*, N. C. Cole and R. R. Judkins (comp.), U. S. Department of Energy, August 1995.
11. P. F. Tortorelli and J. H. DeVan, pp. 391-400 in *Proc. 8th Annual Conf. on Fossil Energy Materials*, N. C. Cole and R. R. Judkins (comp.), U. S. Department of Energy, August 1994.
12. P. F. Tortorelli and J. H. DeVan, pp. 229-236 in *Proc. Symp. on Oxide Films on Metals and Alloys*, B. R. MacDougall, R. S. Alwitt, and T. A. Ramanarayanan (eds.), Proceedings Vol. 92-22, The Electrochemical Society, 1992.
13. Y-R. He, M. H. Zheng, and R. A. Rapp, pp. 311-324 in *Proc. Ninth Annual Conf. Fossil Energy Materials*, N. C. Cole and R. R. Judkins (comp.), U. S. Department of Energy, August 1995.
14. R. A. Rapp, "Pack Cementation Coatings for Alloys," these proceedings
15. P. F. Tortorelli and J. H. DeVan, pp. 257-70 in Processing, Properties, and Applications of Iron Aluminides, J. H. Schneibel and M. A. Crimp (eds.), The Minerals, Metals, and Materials Society, Warrendale, PA, 1994.
16. P. Kofstad, High Temperature Corrosion, Elsevier, London, 1988.
17. F. Gesmundo and B. Gleeson, to be published in *Oxid. Met.* 1996.



STUDY OF FATIGUE AND FRACTURE BEHAVIOR OF NbCr<sub>2</sub>-BASED  
ALLOYS AND INTERMETALLIC MATERIALS: PHASE STABILITY IN  
NbCr<sub>2</sub>-BASED LAVES PHASE ALLOYS

J. H. Zhu and P. K. Liaw

Department of Materials Science and Engineering  
The University of Tennessee, Knoxville, TN 37996

C. T. Liu

Metals and Ceramics Division  
Oak Ridge National laboratory  
Oak Ridge, TN 37831-6115

### ABSTRACT

Phase stability in NbCr<sub>2</sub>-based transition-metal Laves phases is studied in this paper, using data from binary X-Cr, Nb-X, and ternary Nb-Cr-X phase diagrams. It was shown that when the atomic size ratios are kept identical, the average electron concentration factor ( $e/a$  = the average number of electrons per atom outside the closed shells of the component atoms) is the determinate factor in controlling the phase stability of NbCr<sub>2</sub>-based transition-metal Laves phases. The  $e/a$  ratios for different Laves phase structures were determined as follows: with  $e/a < 5.76$ , the C15 structure is stabilized; at an  $e/a$  range of 5.88-7.53, the C14 structure is stabilized; with  $e/a > 7.65$ , the C15 structure was stabilized again. A further increase in the electron concentration factor ( $e/a > 8$ ) leads to the disordering of the alloy. The electron concentration effect on the phase stability of transition-metal A<sub>3</sub>B intermetallic compounds and Mg-based Laves phases is also reviewed and compared with the present observations in transition-metal Laves phases.

### INTRODUCTION

Laves phases are AB<sub>2</sub>-type intermetallic compounds, most of which crystallize in one of the three topologically close-packed structures: cubic C15 — MgCu<sub>2</sub> structure, hexagonal C14 — MgZn<sub>2</sub> structure and dihexagonal C36 — MgNi<sub>2</sub> structure (1). Although Laves phases are in general stabilized by the size-factor principles, that is, the atomic size ratio,  $R_A/R_B$ , is ideally 1.225, with a range of 1.05-1.68 usually observed, the stability of each

crystalline structure is affected by the electron concentration factor. In fact, the electron concentration factor becomes clearly important when the atomic size factors are favorable. The classic work by Laves and Witte (2-3) showed that for several quasi-binary alloy systems involving  $\text{MgCu}_2$  and  $\text{MgZn}_2$ , with increasing valence electron concentration, the three Laves types  $\text{MgCu}_2$ ,  $\text{MgNi}_2$ , and  $\text{MgZn}_2$  exist in that order. For transition-metal Laves phases, average electron concentration was successfully used to correlate the crystal structure by Bardos, Gupta and Beck (4) .

Transition-metal Laves phases have already been in or are being considered for many practical uses, e.g.,  $(\text{Hf,Zr})\text{V}_2$  as superconducting material,  $\text{Zr}(\text{Cr,Fe})_2$  as hydrogen storage material, etc.. More recently,  $\text{HfV}_2$ -,  $\text{HfCr}_2$ - and  $\text{NbCr}_2$ -based two-phase alloys (5-9) are being developed for high-temperature structural uses, because of their good retention of mechanical properties at elevated temperatures. However, their low ductility and brittle fracture characteristics at room temperature are the main concerns for engineering use of these materials.

One attractive way to improve the deformability of complex Laves phases is to control their crystalline structure in the way that stress-assisted phase transformation and/or mechanical twinning can be introduced during plastic deformation (10-11). Thus, it is of uttermost importance to know the factors governing the phase stability in transition-metal Laves phases.

In this study, a number of binary and ternary phase diagrams were surveyed, and the phase stability criteria in the  $\text{NbCr}_2$ -based Laves phase systems X-Cr, Nb-X, and Nb-Cr-X were evaluated. An electron concentration factor ( $e/a$ ) was proposed to control the C14/C36/C15 phase stability in  $\text{NbCr}_2$ -based transition-metal Laves alloys.

## LAVES PHASE IN BINARY X-Cr AND Nb-X SYSTEMS

Since Laves phases are size compounds, we should choose the X elements in the X-Cr systems with an atomic radius close to Nb and X in the Nb-X systems with an atomic radius close to Cr. In this scheme, we can easily separate the  $e/a$  factor with the atomic size factor in controlling the phase stability. According to this scheme, the X elements selected in the X-Cr system are Ti, Ta, and Nb, and X selected in the Nb-X system are Cr, Mn, Fe, Co, Ni, and Cu. The selection of atom size is based on the consideration of

Goldschmidt radius with 12 coordination numbers (CN) (12). With a minimum disturbance of the atomic size factor, the electron concentration factor,  $e/a$ , should become a dominant one in controlling the phase stability of the binary Laves phases. Here, the  $e/a$  ratio is defined as the average number of electrons per atom outside the closed shells of the component atoms. According to this definition, the  $e/a$  ratio of a transition element is the number of electrons ( $s + d$  electrons) outside its inert gas shells.

Table 1. Atomic Size, Electron Concentration Factor ( $e/a$ ) of Alloying Element, and Existing Binary Laves Phase

Element	Goldschmidt Radii ( $\text{\AA}$ )*	$e/a$ <sup>+</sup>	$\text{XCr}_2/\text{NbX}_2$
Nb	1.47	5	$\text{NbCr}_2$
Ti	1.45	4	$\text{TiCr}_2$
Ta	1.46	5	$\text{TaCr}_2$
Cr	1.28	6	$\text{NbCr}_2$
Mn	1.31	7	$\text{NbMn}_2$
Fe	1.27	8	$\text{NbFe}_2$
Co	1.26	9	$\text{NbCo}_2$
Ni	1.24	10	None
Cu	1.28	11	None

\* Data from Reference 12.

<sup>+</sup> The unit of  $e/a$  is number of electrons per atom in this paper.

Table 1 lists the Goldschmidt radii (CN=12) and  $e/a$  ratios of all the alloy components, together with the existing Laves phases observed in the binary X-Cr and Nb-X systems. It is interesting to note that Ti and Ta have the atomic radii close to Nb, thus they are postulated to substitute Nb in the  $\text{NbCr}_2$  Laves phase. Mn, Fe, Co, Ni and Cu atoms with their atom size close to Cr occupy the Cr positions in the  $\text{NbCr}_2$  Laves phase. From the binary X-Cr and Nb-X phase diagrams (13), we can check if the  $\text{XCr}_2$  or  $\text{NbX}_2$  Laves phase exists in the X-Cr and Nb-X systems, as indicated in Table 1. Also, the mutual solubility, or the homogeneity range of  $\text{XCr}_2$  or  $\text{NbX}_2$  Laves phase can be read from the binary phase diagrams. Mutual solubility is defined as the difference between the maximum and minimum atomic percents of A in  $\text{AB}_2$  phase. Corresponding to the homogeneity ranges, we can simply calculate the  $e/a$  ranges for different binary Laves phases, using the  $e/a$  ratios for various

transition elements listed in Table 1. The binary Laves phase,  $R_A/R_B$  ratio, homogeneity range (%A range), e/a range, and corresponding Laves phase structure are tabulated in Table 2. The Laves structure indicated here is the one stabilized at low temperatures if more than one Laves structure occurring in a binary system. Note that no Laves phases were observed in the Nb-Ni and Nb-Cu binary systems, and that the calculation of phase parameters was based on the imaginary "NbNi<sub>2</sub>" and "NbCu<sub>2</sub>" phases.

Table 2. Atomic Size Ratio ( $R_A/R_B$ ), Homogeneity Range (%A Range), Corresponding e/a Range and Laves Phase Structures in XCr<sub>2</sub> and NbX<sub>2</sub> Alloy Systems

Laves Phase	$R_A/R_B$	%A Range	e/a Range	Structure
TiCr <sub>2</sub>	1.133	35-37	5.26-5.3	C15
TaCr <sub>2</sub>	1.141	33-36	5.64-5.67	C15
NbCr <sub>2</sub>	1.148	30-39	5.61-5.7	C15
NbMn <sub>2</sub>	1.122	25.5-40	6.2-6.49	C14
NbFe <sub>2</sub>	1.157	27-38	6.86-7.19	C14
NbCo <sub>2</sub>	1.167	27-33.3	7.67-7.92	C15
"NbNi <sub>2</sub> "	1.185	33.3	8.34	None
"NbCu <sub>2</sub> "	1.148	33.3	9.0	None

### LAVES PHASE IN Nb-Cr-X TERNARY SYSTEMS

As postulated in the previous section, Ti and Ta occupy the Nb sublattice in NbCr<sub>2</sub> Laves phase. From the Nb-Cr-Ta and Nb-Cr-Ti ternary phase diagrams (14), Ti or Ta substitutes for Nb from 0% to 100% without changing the C15 structure of NbCr<sub>2</sub>. This further confirms our above postulation. For Mn, Fe, Co, Ni, and Cu, they are postulated to substitute for Cr in the NbCr<sub>2</sub> phase. There has no Nb-Cr-Mn ternary phase diagram reported so far, and the Nb-Cr-Cu ternary phase diagrams are incomplete, with the reported data mainly concentrated at the copper-rich corner. On the other hand, the Nb-Cr-Co, Nb-Cr-Fe and Nb-Cr-Ni phase diagrams have been reported in literature (14-15). From these phase diagrams, certain common trends are found: Fe, Co and Ni have certain solubility in the NbCr<sub>2</sub> phase without changing the C15 structure. However, above a certain critical amount



of Co, Ni, or Fe added to NbCr<sub>2</sub>, a phase modification from C15 to C14 is observed. The C14 phase is stable over a wide range of X content. For the Nb-Cr-Co system, a further increase in the Co content results in the reappearance of the C15 structure (15).

Table 3. Homogeneity Range (%X) and Corresponding e/a Range of C15/C14 Structures in Ternary Nb-Cr-X Systems

X	C15		C14		C15	
	%X	e/a	%X	e/a	%X	e/a
Ti	0-33.3	5.33-5.67	--	--	--	--
Ta	0-33.3	5.67	--	--	--	--
Fe	0-4	5.67-5.75	9-66.7	5.85-6.69	--	--
Co	0-3	5.67-5.76	8-62	5.91-7.53	66-68	7.65-7.72
Ni	0-2.5	5.67-5.77	5-52	5.87-8.05	--	--

The stability range of C14/C15 phases in the Nb-Cr-X ternary systems at 1000°C are summarized in Table 3, together with the corresponding e/a values. It should be noted that the solubility of Fe, Co, and Ni in NbCr<sub>2</sub> with the C15 structure decreases in the order of Fe, Co, and Ni. However, the e/a ratios corresponding to the change of the NbCr<sub>2</sub> C15 to C14 structure are almost identical for different systems, implying that an average electron concentration may play a key role in determining the C15/C14 phase stability. Note that the maximum e/a ratio for the C15 structure is about 5.76 and the minimum e/a ratio to stabilize the C14 structure is about 5.88.

## GENERAL DISCUSSIONS

Laves phases are size compounds, therefore, the size difference between A and B atoms is predominant in stabilizing the Laves phase. Since we purposely choose some alloying elements with roughly the same atomic size with either Cr or Nb (see Tables 1 and 2), the size difference between A and B is similar in the AB<sub>2</sub> Laves phases we studied. This approach simplifies our analysis, since we can separate the other factors from the size factor in stabilizing different Laves phase structures. Also, we only choose transition metal to form Laves phase, which makes it ideal to study the e/a effect on the Laves phase stability. In transition metals, filling d-band is

important to affect the phase stability. In Laves and Witte's studies (2-3), Mg-based ternary systems were selected, and a valence electron concentration rule was found to control the occurrence of various Laves structures, with C15 stabilized at low  $e/a$  values, C14 stabilized at high  $e/a$  values, and C36 in between. In their study, both non-transition and transition metals are involved in forming some Laves phases, making it difficult to analyze the valence electron concentration in the alloys, since for transition elements, the valence electron number is not a constant value, varying in different systems.

In the present evaluation, all the elements chosen to form Laves phases are transition metals. Instead of using valence electron concentration, average electron concentration is chosen for correlation purposes. This concept of average electron concentration has been successfully used to obtain a good correlation between the  $e/a$  value and the phase stability in a number of transition metal alloy systems (4, 16-21). If we combine the data in Tables 2 and 3, we can clearly demonstrate the  $e/a$  effect on the phase stability (C14/C15) in  $\text{NbCr}_2$ -based Laves alloys, see Fig.1.

At  $e/a$  values lower than 5.76, the C15 structure was stabilized at low temperatures for both binary and ternary Laves alloys. Increasing  $e/a$  to 5.88, the C14 structure was stabilized. Over the  $e/a$  range of 5.88-7.53, the C14 structure is more stable than the C15 structure. This trend is similar to that observed in the Mg-based Laves phases (2-3), where  $\text{C15} \rightarrow \text{C36} \rightarrow \text{C14}$  phase modification was observed with increasing the  $e/a$  value. However, for the Mg-based Laves phases, this should be considered as a tendency, as it is impossible to classify the compounds in terms of their  $e/a$  ratio. In  $\text{NbCr}_2$ -based ternary Laves phases, the  $e/a$  ratio for C15/C14 phase boundaries is very precise, with C15 existing at  $e/a < 5.76$ , and C14 occurring at  $e/a > 5.88$ . This may be associated with the fact, as discussed before, that here all the components of the ternary  $\text{NbCr}_2$ -based Laves phases are transition metals. Also, the C36 phase exists between C15 and C14 ranges, with a certain range of homogeneity for the Mg-based Laves alloys. However, no existence of the C36 phase was indicated in the reported phase diagrams of binary and ternary  $\text{NbCr}_2$ -based systems, probably due to the difficulty in separating C36 from C14. Both C36 and C14 structures are hexagonal close-packed structures, and many of their X-ray diffraction lines overlap. Considering that C36 may exist between C15 and C14 structures (C36 is a transition structure between C14 and C15, in terms of stacking sequence), it is postulated that in

NbCr<sub>2</sub> based Laves phases C36 may exist in the  $e/a$  regime of 5.76-5.88, probably around 5.7-5.9 due to the possible error in the reported data. In fact, a C36 phase was detected in a recent study of the transition metal Nb-Cr-Fe system (11). Even though it is difficult to calculate the exact  $e/a$  value for the C36 Laves phase since that system is basically a Nb solid solution plus Laves phase two-phase alloy, it does indicate that it is possible to stabilize the C36 structure at certain  $e/a$  ratios.

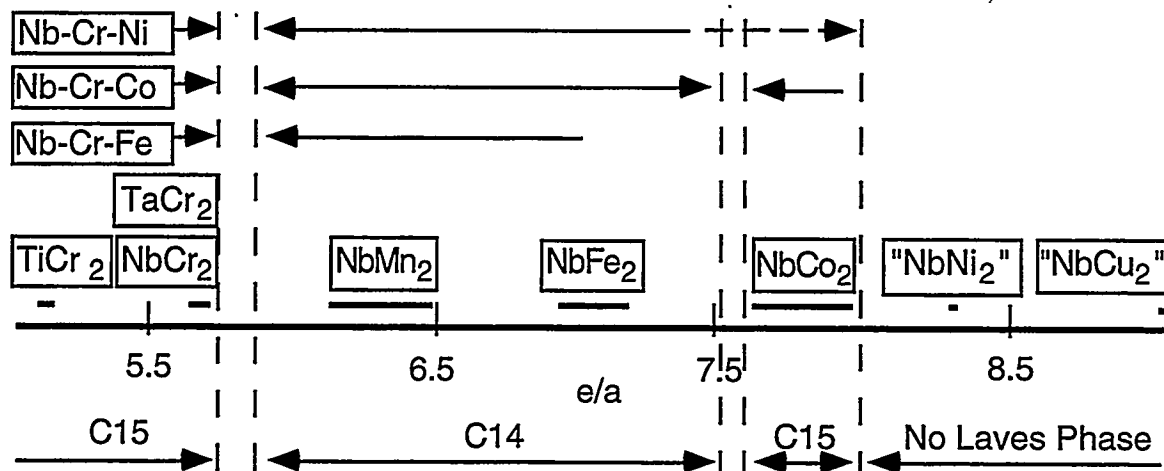


Fig. 1 Effect of electron concentration ( $e/a$ ) on phase stability in NbCr<sub>2</sub>-based binary and ternary systems

The atomic size difference has no effect on the  $e/a$  correlation with the phase stability in both binary and ternary systems. Actually, the solubility of Fe, Co and Ni in NbCr<sub>2</sub> has different values, yet the same critical  $e/a$  value is yielded. These observations may result from the fact that the atomic size difference ( $R_A/R_B$ ) is kept similar in our investigation. However, the size difference may affect the mutual solubility, or homogeneity range of AB<sub>2</sub> Laves phase, as shown in Fig. 2. No good correlation between the  $R_A/R_B$  ratio with the mutual solubility can be inferred from Fig. 2.

The effect of the average electron concentration on phase stability has been shown in many transition-metal A<sub>3</sub>B intermetallic compound systems, usually with a very good correlation obtained (16-18). For example, Liu found that the stacking character of the (Fe, Co, Ni)<sub>3</sub>V ordered alloys can be altered systematically by controlling the  $e/a$  ratio of the alloys (16). Similar to our observation in Laves phase, as  $e/a$  increases, the stacking character changes

from purely cubic to purely hexagonal. However, the critical  $e/a$  ratios for stabilizing the face-centered cubic (f.c.c.) structure ( $< 7.75$ ) and hexagonal close-packed (h.c.p.) structure ( $> 8.54$ ) in  $A_3B$  compounds are different from those for stabilizing the NbCr<sub>2</sub>-based transition-metal Laves phase cubic C15 structure ( $< 5.76$ ) and hexagonal C14 structure ( $> 5.88$ ). The C15/C14

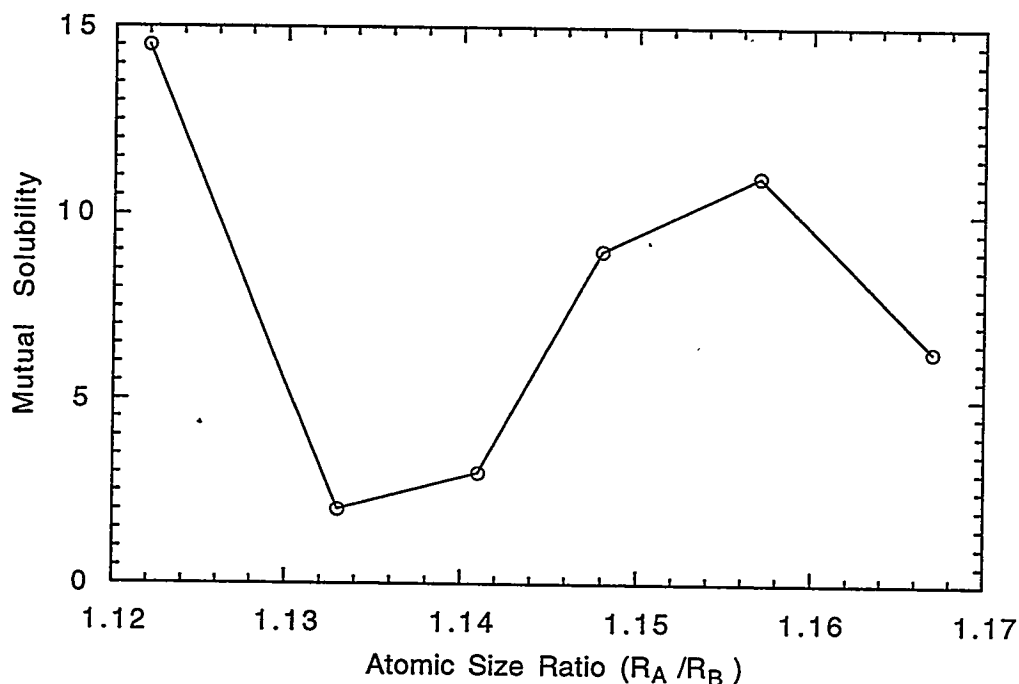


Fig. 2 Effect of  $R_A/R_B$  ratio on the mutual solubility of binary Laves phases

transition in Laves phase systems is sharper than the f.c.c./h.c.p. transition in ordered  $A_3B$  compounds. Also, unlike Laves phase alloys, different ordered mixtures of cubic and hexagonal layers are obtained between the cubic and hexagonal structures for the  $A_3B$  ordered alloys. All the results indicate that the average electron concentration factor has a determinate effect on the phase stability of transition metal intermetallic compounds. The reasons leading to such correlation is not clear now; however, the phase transition in transition metals is known to be related to the filling of an appropriate Brillouin zone.

From Figure 1, we can also see that for the Nb-Cr-Co system, when the  $e/a$  ratio increases further to 7.65, the C15 structure was stabilized again over the C14 structure. This structure modification of C14 to C15 with a further increase in the  $e/a$  ratio has been observed in a number of transition-metal

Laves phases (22). It is a rule, rather than an exception. In ternary Nb-Cr-Mn and Nb-Cr-Fe systems, we can not observe such C14 to C15 transition, since we cannot get  $e/a$  ratio higher than 7.6 in these systems. No NbCu<sub>2</sub> (with  $e/a = 10$ ) and NbNi<sub>2</sub> (with  $e/a = 9.5$ ) Laves phases exist in Cu-Nb and Ni-Nb binary systems, a fact consistent with the observation by Bardos et al. (4) that at  $e/a > 8$ , a disordered structure is stabilized over the Laves phase in transition metal systems. Also in agreement with Bardos et al., the maximum  $e/a$  ratio for the Laves phases in Nb-Cr-Ni system is around 8. However, no C14→C15 transition was reported at  $e/a$  ratio  $> 7.65$ , possibly due to the fact that many ternary phase diagrams containing Laves phases are inaccurate with regard to the identification of C14/C36/C15 structures.

If the electron concentration  $e/a$  correlation with the phase stability is a rule operating in the NbCr<sub>2</sub> based transition-metal alloy systems, it will be possible to modify C15 to C14 and also C14 to C15 by increasingly adding Cu into NbCr<sub>2</sub> to substitute Cr, i.e., by changing the  $e/a$  ratio in the alloy. Systematic work in the direction is being undertaken in our laboratory.

## CONCLUSIONS

Binary X-Cr and Nb-X, and ternary Nb-Cr-X phase diagrams were surveyed, and some interesting phase stability features were identified in these transition metal systems. The average electron concentration factor ( $e/a$ ) has been shown to be a determinate factor in controlling the phase stability of NbCr<sub>2</sub>-based transition-metal Laves alloys. With  $e/a < 5.76$ , the C15 structure is stabilized; at an  $e/a$  range of 5.88-7.53, the C14 structure is stabilized; with  $e/a > 7.65$ , the C15 structure is stabilized again. A further increase in electron concentration ( $e/a > 8$ ) leads to the disordering of the alloy. It is postulated that at  $5.88 > e/a > 5.76$  the C36 structure may be stabilized. The physical background leading to such  $e/a$  correlation with the transition-metal Laves phase stability needs to be further studied.

## ACKNOWLEDGMENTS

This research was sponsored by the Fossil Energy AR & TD Materials Program, U.S. Department of Energy, under subcontract 11X-SP173V to the University of Tennessee with Lockheed Martin Energy Systems, Inc.

## REFERENCES

1. T. B. Massalski, in *Physical Metallurgy Part 1*, R. W. Cahn and P. Hassen, eds., p. 154, North-Holland Physics Publishing, NY (1983).
2. F. Laves and H. Witte, *Metallwirtschaft* 14, p. 645 (1935).
3. F. Laves and H. Witte, *Metallwirtschaft* 15, p. 840 (1936).
4. D. I. Bardos, K. P. Gupta, and Paul A. Beck, *Trans. Met. Soc. AIME* 221, p. 1087 (1961).
5. F. Chu and D. P. Pope, *Mat. Res. Soc. Symp. Proc. Vol.288*, p. 561 (1993).
6. K. S. Kumar and D. B. Miracle, *Intermetallics* 2, p. 257 (1994).
7. M. Takeyama and C. T. Liu, *Mater. Sci. & Eng. A* 132, p. 61 (1991).
8. J. A. Cook, P. K. Liaw, and C. T. Liu, Symposium on "Fatigue and Fracture of Ordered Intermetallics," W. O. Soboyejo, T. S. Srivatsan and R. O. Ritchie, eds., TMS, Warrendale, PA, p. 155 (1995).
9. J. A. Cook, P. K. Liaw, and C. T. Liu, "The Effect of Microstructural Control on the Mechanical Behavior of Cr<sub>2</sub>Nb-Based Intermetallic Alloys," Hans Weertman Symposium, R. J. Arsenault et al., eds., TMS Annual Meeting, Anaheim, CA, Feb.4-8, 1996 (in press).
10. Y. Liu, J. D. Livingston, and S. M. Allen, *Metall. Tran. A* 23, p. 3303 (1992).
11. M. Grujicic, S. Tangrila, O. B. Cavin, W. D. Porter and C. R. Hubbard, *Mater. Sci. & Eng. A* 160, p. 37 (1993).
12. F. Laves, in *Theory of Alloy phases*, American Society for Metals, Metals Park, OH, p. 124 (1956).
13. T. B. Massalski, J. L. Murray, L. H. Bennet, and H. Baker, eds, *Binary Alloy Phase Diagram*, American Society for Metals, Metals Park, OH, 1986.
14. P. Villars, A. Prince, and H. Okamoto, eds, *Handbook of Ternary Phase Diagrams*, ASM International, 1995.
15. N. I. Kaloev, E. M. Sokolovskaya, A. Kh. Abramyan, and R. V. Kalagova, *Soviet Non-Ferrous Metals Research* 14 (6), p. 503 (1986).
16. C. T. Liu, *Inter. Met. Rev.* 29 (3), p. 168 (1984).
17. A. K. Sinha, *Trans. Met. Soc. AIME* 245, p. 911 (1969).
18. A. K. Sinha, *Progr. in Mater. Sci.* 15 ( Part 2), p. 79 (1972).
19. D. I. Bardos, R. K. Malik, F. X. Spiegel, and p. A. Beck, *Trans. Met. Soc. AIME* 236, p. 40 (1966).
20. V. V. Savin, *Phys. Met. Metall.* 68 (1), p. 140 (1989).
21. R. E. Watson and L. H. Bennett, *Acta Metall.* 32 (4), p. 477 (1984).
22. K. Kuo, *Acta Metall.* 1, p. 720 (1953).

APPENDIX A

FINAL PROGRAM





**FINAL PROGRAM**  
**CONFERENCE ON FOSSIL ENERGY MATERIALS**  
**Knoxville, Tennessee**  
**May 14-16, 1996**

**SESSION I - Ceramic Composites and Functional Materials**

**Tuesday, May 14, 1996**

7:00	<b>Registration and Refreshments</b>		
8:00	<i>Welcome and Introductory Remarks, Program Managers, Department of Energy and Oak Ridge National Laboratory</i>	1:00	<i>Corrosion And Its Effect on Mechanical Properties of Materials For Advanced Combustion Systems, K. Natesan, Argonne National Laboratory</i>
8:20	<i>Advanced Research Programs and AR&amp;TD Materials Program Overview - David J. Beecy and James P. Carr, DOE/HQ</i>	1:30	<i>Oxide Coating Development, D. P. Stinton, Oak Ridge National Laboratory</i>
9:00	<i>Fabrication of Fiber-Reinforced Composites by Chemical Vapor Infiltration, T. M. Besmann, Oak Ridge National Laboratory</i>	2:00	<i>Corrosion Protection of SiC Based Ceramics with CVD Mullite Coatings, V. Sarin, Boston University</i>
9:30	<i>Transport Properties of Ceramic Composites, T. L. Starr, Georgia Institute of Technology</i>	2:30	<i>Plasma Deposition of High Temperature Protective Coatings, I. Brown, Lawrence Berkeley National Laboratory</i>
10:00	<b>BREAK</b>	3:00	<b>BREAK</b>
10:20	<i>Joining of SiC Ceramics, B. H. Rabin, Idaho National Engineering Laboratory</i>	3:20	<i>Ceramic Membranes For High Temperature Hydrogen Separation, G. Roettger, Oak Ridge K-25 Site</i>
10:50	<i>Development of Nondestructive Evaluation Methods, W. A. Ellingson, Argonne National Laboratory</i>	3:50	<i>Mixed Oxygen Ion/Electron-Conducting Ceramics for Oxygen Separation, L. R. Pederson, Pacific Northwest Laboratory</i>
11:10	<i>Prediction of Effects of Flaws on Fracture Behavior of Structural Ceramics, J. P. Singh, Argonne National Laboratory</i>	4:20	<i>Preparation and Evaluation of Coal Extracts As Precursors for Carbon and Graphite Products, I. Lewis, UCAR Carbon Company, Inc. and J.W. Zondlo, West Virginia University</i>
11:30	<i>Strength And Corrosion Behavior of SiC - Based Ceramics In Hot Coal Combustion Environments, K. Breder, Oak Ridge National Laboratory</i>	4:50	<i>A Novel Approach to the Removal of Carbon Dioxide, T. D. Burchell, Oak Ridge National Laboratory</i>
12:00	<b>LUNCH</b>	5:20	<b>ADJOURN</b>

**FINAL PROGRAM**  
**CONFERENCE ON FOSSIL ENERGY MATERIALS**  
**Knoxville, Tennessee**  
**May 14-16, 1996**

**SESSION II - Ceramics, New Alloys, and Functional Materials**

**Tuesday, May 14, 1996**  
**6:30 - 8:30 p.m.**

**POSTER PRESENTATIONS - BUFFET RECEPTION**

*Development of Oxidation-Resistant Composite Materials and Interfaces*, D. P. Stinton, Oak Ridge National Laboratory

*Modeling of Fibrous Preforms for CVI Fabrication*, T. L. Starr, Georgia Institute of Technology

*Fiber/Matrix Interfaces for SiC/SiC Composites: Multilayer SiC Coatings and CMZP Oxide Coatings*, W. A. Curtin, Virginia Polytechnic Institute and State University

*Conditions for Testing the Corrosion Rates of Ceramics in Coal Gasification Systems*, J. P. Hurley, University of North Dakota

*Fracture Behavior of Advanced Ceramic Hot-Gas Filters*, J. P. Singh, Argonne National Laboratory

*High Temperature Corrosion of Advanced Ceramic Materials for Hot Gas Filters and Heat Exchangers*, C. E. Crossland, Pennsylvania State University

*Effect of Heat Treatment at 1150°C on Creep-Rupture Properties of Alloy FA-180*, C. G. McKamey, Oak Ridge National Laboratory

*The Influence of Composition on Environmental Embrittlement of Iron Aluminides*, D. A. Alven, Rensselaer Polytechnic Institute

*Effects of Titanium and Zirconium on Iron Aluminide Weldments*, G. R. Edwards, Colorado School of Mines

*Evaluation of Iron Aluminide Weld Overlays for Erosion-Corrosion Resistant Boiler Tube Coatings In Low NO<sub>x</sub> Boilers*, J. N. DuPont, Lehigh University

*Effects of Surface Condition on Aqueous Corrosion and Environmental Embrittlement of Iron Aluminides*, R. A. Buchanan, University of Tennessee

*Processing and Properties of Low-Aluminum Alloy FAPY*, V. K. Sikka, Oak Ridge National Laboratory

*Microstructural And Mechanical Characterization of Alumina Scales Thermally Developed On Iron Aluminide Alloys*, K. Natesan, Argonne National Laboratory

*Overview of the Carbon Products Consortium*, C. Irwin, West Virginia University

*Carbon-Fiber Composite Molecular Sieves for Gas Separation*, M. Jagtoyen, University of Kentucky

*Stability of Solid Oxide Fuel Cell Materials*, L. R. Pederson, Pacific Northwest Laboratory

*Proton-Conducting Cerate Ceramics*, L. R. Pederson, Pacific Northwest Laboratory

*Ceramic Catalyst Materials*, A. G. Sault, Sandia National Laboratories

*Nanoparticle Synthesis in Pulsed Low Temperature Discharges*, R. J. Buss, Sandia National Laboratories

**SESSION III****WORKSHOP ON MATERIALS RESEARCH AND DEVELOPMENT NEEDS FOR  
THE SUCCESSFUL DEPLOYMENT OF ADVANCED POWER GENERATION  
TECHNOLOGIES****WEDNESDAY, MAY 15, 1996**

Last year's workshop identified several material needs for pressurized fluidized bed combustion (PFBC), integrated coal gasification combined cycle (IGCC), and indirectly fired cycles. This year's workshop will focus on resolution of some of those issues through the definition or redefinition of projects under way.

8:00 a.m. **KEYNOTE ADDRESS:** Dr. John Stringer, Executive Scientist,  
Electric Power Research Institute,  
Palo Alto, California

8:30 a.m. **PLENARY SESSION**

9:00 a.m. **SESSION A. WORKSHOP ON CERAMIC COMPOSITE INTERFACE COATINGS.**

Rapporteurs: R. G. Smith, 3M Company  
R. E. Tressler, Pennsylvania State University  
S. Sambasivan, BIRL  
Moderator: D. P. Stinton, ORNL

Ceramic composites are critical to high-temperature components for fossil energy systems both as hot-gas filters for IGCC and PFBC systems and as structural components, such as heat exchangers, for the indirectly fired cycles, externally fired combined cycle (EFCC), and Combustion 2000 systems. The development of ceramic composites with oxidation resistant interface coatings is extremely important to NASA, the Air Force, and DOE programs. Applications of these composites will be summarized during the workshop and different approaches for oxidation resistant interface coatings will be discussed.

9:00 a.m. **SESSION B. WORKSHOP ON HIGH-TEMPERATURE MATERIALS BASED ON  
LAVES PHASES.**

Rapporteurs: K. S. Kumar, Brown University  
J. H. Perepezko, University of Wisconsin  
D. J. Thoma, Los Alamos National Laboratory  
Moderator: C. T. Liu, ORNL

The Offices of Fossil Energy and Basic Energy Sciences of the Department of Energy are jointly sponsoring this review of critical issues related to alloy development of new high-temperature structural materials based on Laves phases. Laves phase materials, such as the high-temperature Cr-Nb alloys, are of interest because, characteristically, they are high-melting intermetallics that are extremely hard and strong, although brittle. These metallic, rather than ceramic, materials could provide high strengths up to 2300°F for systems such as the IGCC, PFBC, EFCC, and Combustion 2000.

**SESSION III - WORKSHOP (Continued)****9:00 a.m. SESSION C. WORKSHOP ON ALLOYS FOR VERY HIGH-TEMPERATURE APPLICATIONS.**

Rapporteurs: N. Birks, University of Pittsburgh  
T. B. Gibbons, ABB Combustion Engineering  
Q. J. Mabbutt, British Gas  
Moderator: I. G. Wright, ORNL

Systems capable of operating at higher efficiencies, such as the low-emission boiler system (LEBS), require materials with higher temperature capabilities, in particular, higher creep strength and environmental resistance. A range of alloys developed from the best of the currently used wrought ferritic and austenitic alloys have improved high-temperature capabilities, and oxide dispersion-strengthened alloys are targeted for extremely high-temperature applications. This workshop will examine the temperature capabilities of these alloys compared to current alloys and to the needs of advanced systems to identify their appropriate applications, information and actions required or under way to qualify them for such use, and their limitations.

**12:00 p.m. LUNCH****1:00 p.m. SESSIONS A & B (Continued)****1:00 p.m. SESSION D. WORKSHOP ON MATERIALS ISSUES ASSOCIATED WITH LOW NO<sub>x</sub> COMBUSTION CONDITIONS IN FOSSIL FUEL-FIRED BOILERS.**

Rapporteurs: J. L. Blough, Foster Wheeler  
J. N. DuPont, LeHigh University  
S. Kung, Babcock & Wilcox  
T. B. Gibbons, ABB Combustion Engineering  
Moderator: I. G. Wright, ORNL

Some cases of severe corrosion of the furnace wall tubes are being experienced in utility boilers fitted with modern, low-NO<sub>x</sub> burners. It has been anticipated for some time that reducing conditions created as part of the low-NO<sub>x</sub> combustion process might result in sulfidation attack, but initial experience with such burners did not reveal such problems. The intent of this workshop is twofold: first, to better define the situation in terms of the form and rate of attack and to examine what is known about its root causes, and second, to review the potential for using corrosion-resistant materials as part of the solution. In particular, if the corrosion is due to sulfidizing conditions, the application of an iron aluminide as an overlay coating may prove a viable option.

**3:30 p.m. WRAP-UP SESSION**

Workshop attendees will gather for summaries of deliberations from Sessions A through D.

**5:00 p.m. ADJOURN**

**FINAL PROGRAM**  
**CONFERENCE ON FOSSIL ENERGY MATERIALS**  
**Knoxville, Tennessee**  
**May 14-16, 1996**

**SESSION IV - New Alloys**

**Thursday, May 16, 1996**

7:30	Registration Desk Opens		
8:00	Welcome and Introductory Remarks	12:00	LUNCH
8:10	ODS Iron Aluminides, I. G. Wright and E. Ohriner, Oak Ridge National Laboratory	1:00	Investigation of Austenitic Alloys for Advanced Heat Recovery and Hot-Gas Cleanup Systems, R. W. Swindeman, Oak Ridge National Laboratory
8:40	The Influence of Processing on Microstructure and Properties of $Fe_3Al$ , R. N. Wright, Idaho National Engineering Laboratory	1:30	Microstructural Stability of Base Metal and Weld Metal in 310TaN, C. D. Lundin, University of Tennessee
9:10	Weld Overlay Cladding With Iron Aluminides, G. M. Goodwin, Oak Ridge National Laboratory	2:00	Fireside Corrosion Testing of Candidate Superheater Tube Alloys, Coatings, and Claddings - Phase II, J. L. Blough, Foster Wheeler Development Corporation
9:40	High Temperature Corrosion Behavior of Coatings and ODS Alloys Based on $Fe_3Al$ , P. F. Tortorelli, Oak Ridge National Laboratory	2:30	BREAK
10:10	BREAK	2:50	Pack Cementation Coatings for Alloys, R. A. Rapp, Ohio State University
10:30	Evaluation of the Intrinsic and Extrinsic Fracture Behavior of Iron Aluminides, B. S. Kang, West Virginia University	3:20	Ultrahigh Temperature Intermetallic Alloys, P. F. Tortorelli, Oak Ridge National Laboratory
11:00	The Mechanical Reliability of Alumina Scales and Coatings, K. B. Alexander, Oak Ridge National Laboratory	3:50	Study of Fatigue and Fracture Behavior of $Cr_2Nb$ -Based Alloys and Intermetallic Materials, P. Liaw, University of Tennessee
11:30	Electro-Spark Deposition Technology, R. N. Johnson, Pacific Northwest Laboratory	4:20	ADJOURN



**APPENDIX B**

**LIST OF ATTENDEES**





LIST OF ATTENDEES

Tenth Annual Conference on Fossil Energy Materials  
 May 14-16, 1996  
 Knoxville, Tennessee

**A** Kathleen B. Alexander  
 Oak Ridge National Laboratory  
 P. O. Box 2008  
 5500, MS 6376  
 Oak Ridge, TN 37831-6376  
 (423) 574-0631  
 FAX 423-574-0641



**B** David Beecy  
 Department of Energy  
 Office of Advanced Research  
 FE-72, B-119  
 19901 Germantown Road  
 Germantown, MD 20585  
 (301) 903-2787  
 FAX 301-903-8350

Dave Bell  
 Electro Physics, Inc.  
 1400 Marshall Street, NE  
 Minneapolis, MN 55413  
 (612) 331-4224  
 FAX 612-331-4230

T. M. Besmann  
 Oak Ridge National Laboratory  
 P. O. Box 2008  
 4515, MS 6063  
 Oak Ridge, TN 37831-6063  
 (423) 574-6852

Neil Birks  
 Materials Science and Engineering  
 Department  
 University of Pittsburgh  
 848 Benedum Hall  
 Pittsburgh, PA 15261  
 (412) 624-9743  
 FAX 412-624-8069

Jeff Blough  
 Foster Wheeler Development  
 Corporation  
 John Blizard Research Center  
 12 Peach Tree Hill Road  
 Livingston, NJ 07039-5701  
 (201) 535-2355  
 FAX 201-535-2242

Kristin Breder  
 Oak Ridge National Laboratory  
 P. O. Box 2008  
 4515, MS 6062  
 Oak Ridge, TN 37831-6062  
 (423) 574-5089  
 FAX 423-574-4913

Ian Brown  
 University of California  
 Lawrence Berkeley Laboratory  
 One Cyclotron Road  
 Bldg 53  
 Berkeley, CA 94720  
 (510) 486-4174  
 FAX 510-486-4374

R. A. Buchanan  
The University of Tennessee  
Department of Materials Science and  
Engineering  
434 Dougherty Engineering Building  
Knoxville, TN 37996-2200  
(423) 974-4858

Tim Burchell  
Oak Ridge National Laboratory  
P. O. Box 2008  
4508, MS 6088  
Oak Ridge, TN 37831-6088  
(423) 576-8595

Richard Buss  
Sandia National Laboratories  
Properties of Organic Materials  
Dept. 1812, MS 0367  
P. O. Box 5800  
Albuquerque, NM 87185-0367  
(505) 844-3504  
FAX 505-844-4816



**C**J. P. Carr  
U. S. Department of Energy  
Fossil Energy  
Office of Advanced Research  
FE 72  
19901 Germantown  
Germantown, MD 20874  
(301) 903-6519  
FAX 301-903-8350

Shao Ping Chen  
Los Alamos National Laboratory  
MS B262  
Los Alamos, New Mexico 87545  
(505) 667-7346  
FAX 505-665-3003

Peter Chesney  
Babcock & Wilcox  
Nuclear Equipment Division  
91 Stirling Ave  
P. O. Box 271  
Barberton, OH 44203-0271  
(330) 860-1306  
FAX 330-860-6274

Daniel Y. Chiang  
Georgia Institute of Technology  
School of Materials Science and  
Engineering  
Bunger-Henry Building  
Atlanta, GA 30332-0245  
(404) 894-2881  
FAX 404-894-9140

Nancy C. Cole  
Oak Ridge National Laboratory  
P. O. Box 2008  
4515, MS 6067  
Oak Ridge, TN 37831-6067  
(423) 574-4824  
FAX 423-574-6098

Bernard R. Cooper  
West Virginia University  
Department of Physics  
Morgantown, WV 26506-6315  
(304) 293-3423  
FAX 304-293-3120

Carl E. Crossland  
Pennsylvania State University  
226 Steidle Building  
University Park, PA 16802  
(814) 865-3953  
FAX 814-865-2917

William Curtin  
 Virginia Polytechnic Institute & State  
 University  
 Department of Engineering Science  
 and Mechanics  
 College of Engineering  
 Blacksburg, VA 24061-0219  
 (540) 231-5316  
 FAX 540-231-9187

John N. Dupont  
 Lehigh University  
 Energy Research Center  
 117 Atlss Drive  
 Bethlehem, PA 18015-4729  
 (610) 758-3942  
 FAX 610-758-5959

Glen R. Edwards  
 Colorado School of Mines  
 Center for Welding, Joining and  
 Coatings  
 Research  
 Golden, CO 80401-1887  
 (303) 273-3773  
 FAX 303-273-3795

William A. Ellingson  
 Argonne National Laboratory  
 9700 South Cass Avenue Bldg. 212  
 Argonne, IL 60439  
 (708) 252-5068  
 FAX 708-252-4798

Jonathan Erpenbach  
 Oak Ridge National Laboratory  
 P. O. Box 2008  
 4508, MS 6087  
 Oak Ridge, TN 37831-6087

Douglas Fain  
 Oak Ridge K-25 Site  
 P. O. Box 2003  
 1004-L, MS 7271  
 Oak Ridge, TN 37831-7271  
 (423) 574-9932  
 FAX 423-576-2930

Thomas B. Gibbons  
 ABB Combustion Engineering  
 Power Plant Laboratories  
 2000 Day Hill Road  
 Windsor, CT 06095  
 (860) 285-3593

G. M. Goodwin  
 Oak Ridge National Laboratory  
 P.O. Box 2008  
 4508, MS 6096  
 Oak Ridge, TN 37831-6096  
 (423) 574-4809  
 FAX 423-574-7721

Forrest Hall  
 Hoskins Mfg. Co  
 10776 Hall Rd  
 P. O. Box 218  
 Hamburg, MI 48139-0218  
 (810) 231-1900  
 FAX 810-231-1226

Sophie Hannel  
 Oak Ridge National Laboratory  
 P. O. Box 2008  
 Oak Ridge, TN 37831

Mark Harper  
 Haynes International, Inc.  
 1020 West Park Avenue  
 P. O. Box 9013  
 Kokomo, IN 46902  
 (317) 456-6234  
 FAX 317-456-6925

Linda Horton  
 Oak Ridge National Laboratory  
 P. O. Box 2008  
 4500S, MS 6132  
 Oak Ridge, TN 37831-6132  
 (423) 574-5081  
 FAX 423-574-4066

Joe Horton  
 Oak Ridge National Laboratory  
 P. O. Box 2008  
 4500S, MS 6115  
 Oak Ridge, TN 37831-6115  
 (423) 574-5575

John P. Hurley  
 University of North Dakota  
 Energy & Environmental Research  
 Center  
 P. O. Box 9018  
 Grand Forks, ND 58202-9018  
 (701) 777-5000  
 FAX 701-777-5181

Jonathan W. Hurley  
 Oak Ridge National Laboratory  
 P. O. Box 2008  
 4515, MS 6063  
 Oak Ridge, TN 37831-6063  
 (423) 574-4559

Carl Irwin  
 West Virginia University  
 Department of Physics  
 P. O. Box 6064  
 Morgantown, WV 26506-6064  
 304-293-2867  
 (FAX) 304-293-3749

Marit Jagtoyen  
 The University of Kentucky  
 Center for Applied Energy Research  
 3572 Iron Works Pike  
 Lexington, KY 40511-8433  
 (606) 257-0213

Mark Janney  
 Oak Ridge National Laboratory  
 P. O. Box 2008  
 4508, MS 6087  
 Oak Ridge, TN 37831-6087  
 (423) 574-4281

Roger N. Johnson  
 Pacific Northwest National Laboratory  
 P. O. Box 999, K3-59  
 Battelle Boulevard  
 Richland, WA 99352  
 (509) 375-6906  
 FAX 509-375-3864

Roddie R. Judkins  
 Oak Ridge National Laboratory  
 P. O. Box 2008  
 4508, MS 6084  
 Oak Ridge, TN 37831-6084  
 (423) 574-4572  
 FAX 423-574-5812

**K** Bruce Kang  
West Virginia University  
Department of Mechanical and  
Aerospace  
Engineering  
P. O. Box 6101  
Morgantown, WV 26506-6101  
(304) 293-3111 ext.316  
FAX 304-293-6689

James Kelly  
Rolled Alloys  
125 West Sterns Road  
P. O. Box 310  
Temperance, MI 48182  
(313) 847-0561

Frank Ko  
Advanced Product Development, Inc.  
2500 Pearl Buck Road  
Bristol, PA 19007  
(215) 785-3230  
FAX 215-785-3123

Kris Kozaczek  
Oak Ridge National Laboratory  
P. O. Box 2008  
4515, MS 6064  
Oak Ridge, TN 37831-6064  
(423) 574-6538  
FAX 423-574-4913

K. Sharvan Kumar  
Brown University  
Engineering Department, Box D  
182 Hope Street  
Providence, RI 02912  
(401) 863-2862  
FAX 401-863-7677

Steve Kung  
Babcock & Wilcox  
1562 Beeson Street  
Alliance, OH 44601  
(330) 829-7626  
FAX 330-829-7832

Libby Kupp  
Oak Ridge National Laboratory  
P. O. Box 2008  
4515, MS 6063  
Oak Ridge, TN 37831-6063  
(423) 574-4559

D. M. Kupp  
Oak Ridge National Laboratory  
P. O. Box 2008  
4515, MS 6063  
Oak Ridge, TN 37831-6063  
(423) 574-4559



**L** W. Y. Lee  
Oak Ridge National Laboratory  
P. O. Box 2008  
4515, MS 6063  
Oak Ridge, TN 37831-6063  
(423) 576-2894

Irwin C. Lewis  
UCAR Carbon Company Inc.  
Parma Center  
12900 Snow Road  
Parma, OH 44130  
(216) 676-2203  
FAX 216-676-2423

Peter Liaw  
The University of Tennessee  
Department of Materials Science and  
Engineering  
427-B Dougherty Engineering Building  
Knoxville, TN 37996-2200  
(423) 974-6356  
FAX 423-974-4115

C. T. Liu  
Oak Ridge National Laboratory  
P. O. Box 2008  
4500S, MS 6115  
Oak Ridge, TN 37831-6115  
(423) 574-4459

Rick Lowden  
Oak Ridge National Laboratory  
P. O. Box 2008  
4508, MS 6087  
Oak Ridge, TN 37831-6087  
(423) 576-2769

Carl D. Lundin  
The University of Tennessee  
Department of Materials Science and  
Engineering  
434 Dougherty Engineering Building  
Knoxville, TN 37996-2200  
(423) 974-5336  
FAX 423-974-4115



**M**Quentin Mabbutt  
British Gas, pic  
Gas Research Center  
Ashby Rd  
Loughborough  
Leics. LE11 3QU  
England  
(44) 1509 282485

Rebecca Martin  
P. O. Box 2008  
4515, MS 6063  
Oak Ridge, TN 37831-6063  
(423) 574-4559

Claudette McKamey  
Oak Ridge National Laboratory  
P. O. Box 2008  
4500S, MS 6115  
Oak Ridge, TN 37831-6115  
(423) 574-6917  
FAX 423-574-7659

Theodore J. McMahon  
U. S. Department of Energy  
Morgantown Energy Technology Center  
P. O. Box 880  
3610 Collins Ferry Road  
Morgantown, WV 26507  
(304) 285-4865  
FAX 304-285-4403

Nikhil Miraj  
Virginia Polytechnic Institute & State  
University  
Department of Engineering Science and  
Mechanics  
College of Engineering  
Blacksburg, VA 24061-0219

John N. Mundy  
U.S. Department of Energy  
BES  
Division of Material Sciences  
ER-131, MSG 236  
19901 Germantown Rd  
Germantown, MD 20874-1290  
(301) 903-4271  
FAX 301-903-9513



**N**K. Natesan  
Argonne National Laboratory  
9700 South Cass Avenue  
Argonne, IL 60439  
(708) 252-5103  
FAX 708-252-3604



**O**Evan Ohriner  
Oak Ridge National Laboratory  
P. O. Box 2008  
4508, MS 6083  
Oak Ridge, TN 37831-6083  
(423) 574-8519  
FAX 423-574-4357



**P**L. R. Pederson  
Pacific Northwest Laboratory  
MS K2/44  
P. O. Box 999  
Richland, WA 99352  
(509) 375-2731  
FAX 509-375-2186

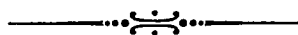
John Perepezko  
University of Wisconsin  
Department of Materials Science and  
Engineering  
1509 University Avenue  
Madison, WI 53706-1595

Art Petty  
Albany Research Center  
1450 Queen Ave. SW  
Albany, OR 97321-2198

David P. Pope  
University of Pennsylvania  
School of Engineering and Applied  
Science  
220 South 33rd Street  
Philadelphia, PA 19104-6391



**Q**Paul Qiao  
The University of Tennessee  
434 Dougherty Engineering Building  
Knoxville, TN 37996-2200  
(423) 974-5310  
FAX 423-974-4115



**R**Barry H. Rabin  
Idaho National Engineering  
Laboratory  
P. O. Box 1625  
MS ILF-2B  
Idaho Falls, ID 83415-2218  
(208) 526-0058  
FAX 208-526-0690

Robert A. Rapp  
Ohio State University  
Department of Materials Science and  
Engineering  
116 West 19th Avenue  
Columbus, OH 43210-1110  
(614) 292-6178  
FAX 614-292-1537

Ravi Ravichandran  
Department of Metallurgical  
Engineering  
University of Utah  
412 Wm. C. Browning Bldg.  
Salt Lake City, UT 84112  
(801) 581-7197  
FAX 801-581-4937

Richard B. Read  
U. S. Department of Energy  
Pittsburgh Energy Technology Center  
P. O. Box 10940  
Pittsburgh, PA 15236  
(412) 892-5721  
FAX 412-892-4604

William Riley  
Albany Research Center  
1450 Queen Ave. SW  
Albany, OR 97321-2198

George Roettger  
Oak Ridge K-25 Site  
P. O. Box 2003  
1004-L, MS 7271  
Oak Ridge, TN 37831-7271  
(423) 574-7539  
FAX 423-576-2930

Grant Rowe  
General Electric Corporate CR&D  
Bldg. K1, MB 265  
P.O. Box 8  
Schenectady, NY 12301  
(518) 387-6154  
FAX 518-387-5576

—•••—  
**S**ankar Sambasivan  
 BIRL

1801 Maple Avenue  
 Evanston, IL 60201  
 (708) 491-4619  
 FAX 708-467-1022

Vinod K. Sarin  
 Boston University  
 College of Engineering  
 15 St. Mary's Street  
 Boston, MA 02215  
 (617) 353-6451  
 FAX 617-353-5548

Allen G. Sault  
 Sandia National Laboratories  
 Department 6211, MS 0710  
 P. O. Box 5800  
 Albuquerque, NM 87185-0710  
 (505) 844-8723  
 FAX 505-845-9500

Otto J. Schwarz  
 Oak Ridge National Laboratory  
 P. O. Box 2008  
 4508, MS 6087  
 Oak Ridge, TN 37831-6087  
 (423) 576-2769

Subu Shanmugham  
 Oak Ridge National Laboratory  
 P. O. Box 2008  
 4515, 6063  
 Oak Ridge, TN 37831-6063  
 (423) 574-7714

David Shelleman  
 Pennsylvania State University  
 110 Steidle Building  
 University Park, PA 16802  
 (814) 865-0634  
 FAX 814-865-2917

Vinod Sikka  
 Oak Ridge National Laboratory  
 P. O. Box 2008  
 4508, MS 6083  
 Oak Ridge, TN 37831-6083  
 (423) 574-5112

Marvin I. Singer  
 U. S. Department of Energy  
 Fossil Energy  
 1000 Independence Ave., SW  
 Washington, DC 20585  
 (202) 586-1577  
 FAX 202-586-7085

J. P. Singh  
 Argonne National Laboratory  
 Bldg. 212  
 9700 South Cass Avenue  
 Argonne, IL 60439  
 (708) 252-5123  
 FAX 708-252-3604

Robert G. Smith  
 3M Company  
 Bldg. 203-1-01, 3M Center  
 St. Paul, MN 55144-1000  
 (612) 733-2564  
 FAX 612-737-5484

Lance Snead  
 Oak Ridge National Laboratory  
 P. O. Box 2008  
 4508 MS 6087  
 Oak Ridge, TN 37831-6087  
 (423) 574-9942

Thomas L. Starr  
 Georgia Institute of Technology  
 School of Materials Science and  
 Engineering  
 Bunger-Henry Building, Room 276  
 Atlanta, GA 30332-0245  
 (404) 894-0579  
 FAX 404-894-9140



David P. Stinton  
Oak Ridge National Laboratory  
P. O. Box 2008  
4515, MS 6063  
Oak Ridge, TN 37831-6063  
(423) 574-4556

N. S. Stoloff  
Rensselaer Polytechnic Institute  
Materials Engineering Department  
Troy, NY 12180-3590  
(518) 276-6371  
FAX 518-276-8554

John Stringer  
Electric Power Research Institute  
3412 Hillview Avenue  
P. O. Box 10412  
Palo Alto, CA 94303  
(415) 855-2472

Ramesh Subramanian  
Oak Ridge National Laboratory  
P. O. Box 2008  
4500S, MS 6115  
Oak Ridge, TN 37831-6115  
(423) 576-7196

Robert W. Swindeman  
Oak Ridge National Laboratory  
P. O. Box 2008  
4500S, MS 6155  
Oak Ridge, TN 37831-6155  
(423) 574-5108  
FAX 423-574-5118

---

**T** Dan Thoma  
Los Alamos National Laboratory  
Center for Materials Science  
MS G770  
Los Alamos, NM 87545  
(505) 665-3645  
FAX 505-667-5268

Peter F. Tortorelli  
Oak Ridge National Laboratory  
P. O. Box 2008  
4500S, MS 6156  
Oak Ridge, TN 37831-6156  
(423) 574-5119  
FAX 423-574-5118

Richard E. Tressler  
Pennsylvania State University  
Department of Materials Science and  
Engineering  
101 Steidle Building  
University Park, PA 16802  
(814) 865-7961  
FAX 814-865-2917

---

**V** Jim Vallykeo  
Hoskins Mfg. Co.  
10776 Hall Rd.  
P. O. Box 218  
Hamburg, MI 48139-0218  
(810) 231-1900  
FAX 810-231-1226

Norman Vaughn  
Oak Ridge National Laboratory  
P. O. Box 2008  
4508, MS 6087  
Oak Ridge, TN 37831-6087  
(423) 576-2769

---

**W** Richard Walters  
Albany Research Center  
1450 Queen Ave. SW  
Albany, OR 97321-2198  
(541) 967-5873  
FAX 541-967-5991

Gerald F. Wheeler  
 U. S. Department of Energy  
 Office of Coal Conversion  
 Fossil Energy (FE-231, GTN)  
 Washington, DC 20545  
 (301) 903-3511  
 FAX 301-903-2406

Jeff Williams  
 Oak Ridge National Laboratory  
 P. O. Box 2008  
 4515, MS 6063  
 Oak Ridge, TN 37831-6063

Ian Wright  
 Oak Ridge National Laboratory  
 P. O. Box 2008  
 4500S, MS 6157  
 Oak Ridge, TN 37831-6157  
 (423) 574-4451  
 FAX 423-574-5118

Richard N. Wright  
 Idaho National Engineering Laboratory  
 P. O. Box 1625  
 Idaho Falls, ID 83415-2218  
 (208) 526-6127  
 FAX 208-526-0690

---

**Z** Jiahong (John) Zhu  
 University of Tennessee  
 420 Dougherty Engineering Building  
 Knoxville, TN 37996-2200  
 (423) 974-5335  
 FAX 423-974-4115

John W. Zondlo  
 West Virginia University  
 Department of Chemical Engineering  
 P. O. Box 6102  
 Morgantown, WV 26506-6102  
 (304) 293-2111 ext. 409  
 FAX 304-293-4139

---

**Y** Jason Yang  
 ABB Power Plant Laboratories  
 Combustion Engineering  
 2000 Day Hill Road  
 P. O. Box 500  
 Windsor, CT 06095-0500  
 (860) 285-3385  
 FAX 860-285-2513

M. H. Yoo  
 Oak Ridge National Laboratory  
 P. O. Box 2008  
 4500S, 6115  
 Oak Ridge, TN 37831-6115  
 (423) 574-5165

## INTERNAL DISTRIBUTION

- |        |                  |        |                                  |
|--------|------------------|--------|----------------------------------|
| 1.     | K. B. Alexander  | 34.    | E. Ohriner                       |
| 2.     | P. Angelini      | 35.    | A. Pasto                         |
| 3.     | R. L. Beatty     | 36.    | B. Pint                          |
| 4.     | T. M. Besmann    | 37.    | G. E. Roettger                   |
| 5.     | R. A. Bradley    | 38.    | G. R. Romanoski                  |
| 6.     | K. Breder        | 39.    | A. C. Schaffhauser               |
| 7.     | T. D. Burchell   | 40.    | J. H. Schneibel                  |
| 8.     | P. T. Carlson    | 41.    | R. Subramanian                   |
| 9-12.  | N. C. Cole       | 42.    | J. Sheffield                     |
| 13.    | K. M. Cooley     | 43.    | V. K. Sikka                      |
| 14.    | J. R. DiStefano  | 44.    | P. S. Sklad                      |
| 15.    | D. E. Fain       | 45.    | D. P. Stinton                    |
| 16.    | G. M. Goodwin    | 46.    | S. Shanmugham                    |
| 17.    | L. L. Horton     | 47.    | R. W. Swindeman                  |
| 18.    | M. A. Janney     | 48.    | T. N. Tiegs                      |
| 19-22. | R. R. Judkins    | 49.    | N. Vaughn                        |
| 23.    | M. A. Karnitz    | 50.    | P. F. Tortorelli                 |
| 24.    | J. R. Keiser     | 51.    | S. Viswanathan                   |
| 25.    | E. R. Kupp       | 52.    | D. F. Wilson                     |
| 26.    | W. Y. Lee        | 53.    | I. G. Wright                     |
| 27.    | C. T. Liu        | 54-55. | Central Research Library         |
| 28.    | R. A. Lowden     | 56.    | Document Reference<br>Section    |
| 29.    | R. L. Martin     | 57.    | ORNL Patent Section              |
| 30.    | P. J. Maziasz    | 58-59. | Laboratory Records<br>Department |
| 31.    | C. G. McKamey    | 60.    | LRD-RC                           |
| 32.    | J. C. McLaughlin |        |                                  |
| 33.    | K. L. More       |        |                                  |

## EXTERNAL DISTRIBUTION

- 61-64. 3M COMPANY, 3M Center, St. Paul, MN 55144  
J. H. Eaton (Bldg 203-1-01)  
M. L. Leitheiser  
D. Pysher  
R. G. Smith (Bldg 203-1-01)
65. A. AHLSTROM CORPORATION, Ahlstrom Pyropower, Kanslerinkatu 14,  
Fin 33720, Tampere, Finland  
J. Isaksson
66. ABB Lummus Crest, 15 Broad St., Bloomfield, NJ 07003  
M. Greene
67. ABB COMBUSTION ENGINEERING, 911 W. Main St.,  
Chattanooga, TN 37402  
D. A. Canonico
- 68-69 ABB COMBUSTION ENGINEERING, 2000 Day Hill Road,  
Windsor, CT 06095  
T. B. Gibbons  
J. Yang
70. ADIABATICS, INC., 3385 Commerce Dr., Columbus, IN 47201  
P. Badgley
71. ADVANCED REFRACTORY TECHNOLOGIES, INC., 699 Hertel Avenue,  
Buffalo, NY 14207  
K. A. Blakely
72. AEA INDUSTRIAL TECHNOLOGY, Harwell Laboratory, Materials  
Development Division, Bldg. 393, Didcot, Oxfordshire,  
OX110RA ENGLAND  
H. Bishop
73. AIR PRODUCTS AND CHEMICALS, INC., 7201 Hamilton Blvd.,  
Allentown, PA 18195-1501  
P. Dyer
- 74-76. ALBANY RESEARCH CENTER, 1450 Queen Ave., SW,  
Albany, OR 97321-2198  
A. Petty  
W. Riley  
R. Walters

- 77. ALBERTA RESEARCH COUNCIL, Oil Sands Research Department,  
P. O. Box 8330, Postal Station F, Edmonton, Alberta,  
CANADA T6H5X2  
L. G. S. Gray
- 78. ALLEGHENY LUDLUM STEEL, Technical Center, Alabama and Pacific  
Avenues, Brackenridge, PA 15014  
J. M. Larsen
- 79. ALLIEDSIGNAL, 2525 W 190th Street, Dept. 93140,  
Torrance, CA 90504-6099  
N. Minh (MS T-41)
- 80. ALLIEDSIGNAL ENGINES, 111 S. 34th Street,  
Phoenix, AZ 85071-2181  
T. Strangman (MS 553-12)
- 81. ALLISON ENGINE COMPANY, Materials Engineering, P.O. Box 420,  
Indianapolis, IN 46206-0420  
L. E. Groseclose
- 82-83. ALLISON GAS TURBINE DIVISION, P. O. Box 420, Indianapolis, IN  
46206-0420  
P. Khandalwal (Speed Code W-5)  
R. A. Wenglarz (Speed Code W-16)
- 84. ALON PROCESSING, INC., Grantham Street, Tarentum, PA 15084  
W. P. Heckel, Jr.
- 85. ALON PROCESSING, INC., 900 Threadneedle, Vista Bldg,  
Houston, TX 77079-2990  
K. A. Wynns
- 86. AMAX R&D CENTER, 5950 McIntyre St., Golden, CO 80403  
T. B. Cox
- 87-88. AMERCOM, Advanced Material Division, Atlantic Research Corporation  
8928 Fullbright Avenue, Chatsworth, CA 91311  
J. O. Bird  
W. E. Bustamante
- 89. AMOCO CHEMICAL COMPANY, P. O. Box 3011, D-2,  
Naperville, IL 60566-7011  
N. Calamur

90. ANSTO, New Illawarra Rd, Lucas Heights NSW 2234 PMB,  
1 Menai NSW 2234, Australia  
A.B.L. Croker
91. APD INC., 2500 Pearl Buck Road, Bristol, PA 19007  
F. Ko
92. A. P. GREEN REFRACTORIES COMPANY, Green Blvd.,  
Mexico, MO 65265  
J. L. Hill
- 93-95. ARGONNE NATIONAL LABORATORY, 9700 Cass Ave.,  
Argonne, IL 60439  
W. A. Ellingson  
K. Natesan  
J. P. Singh
- 96-97. BABCOCK & WILCOX, Domestic Fossil Operations,  
20 South Van Buren Ave., Barberton, OH 44023  
M. Gold  
D. Wasyluk
- 98-101. BABCOCK & WILCOX, Lynchburg Research Center, P. O. Box 11165,  
Lynchburg, VA 24506  
R. Goettler  
J. A. Heaney  
W. Long  
H. H. Moeller
102. BABCOCK & WILCOX INTERNATIONAL, 581 Coronation Blvd.,  
Cambridge, Ontario, Canada N1R 5V3  
R. Seeley
103. BATTELLE COLUMBUS LABORATORIES, 505 King Ave.,  
Columbus, OH 43201  
D. Anson
104. BENNETT, Michael J., Three Chimneys, South Moreton Oxon, United Kingdom
- 105-106. BETHLEHEM STEEL CORPORATION, Homer Research Laboratories,  
Bethlehem, PA 18016  
B. L. Bramfitt  
J. M. Chilton
- 107-108. BIRL, 1801 Maple Avenue, Evanston, IL 60201  
D. Boss  
S. Sambasivan

109. BLACK & VEATCH, 11401 Lamar, Overland Park, KS 66211  
M. Bary
110. BOSTON UNIVERSITY, 44 Washington Street, Boston, MA 02215  
V. K. Sarin
- 111-114. BRITISH COAL CORPORATION, Coal Technology Development Division,  
P. O. Box 199, Stoke Orchard, Cheltenham, Gloucester,  
ENGLAND GL52 4ZG  
J. Oakey  
N. Sims  
M. A. Smith  
I. Summerfield
115. BROWN UNIVERSITY, Division of Engineering, 182 Hope Street,  
Providence, RI 02912  
K. Kumar
- 116-117. CANADA CENTER FOR MINERAL & ENERGY TECHNOLOGY,  
568 Booth St., Ottawa, Ontario Canada K1A 0G1  
R. W. Revie  
M. Sahoo
118. CATERPILLAR INC., Technology Center, P.O. Box 1875,  
Perioria, IL 61656-1875  
D. I. Biehler
119. CERAMEM SEPARATIONS, 952 Eat Fir Street, Palmyra, PA 17078  
J. Vaklyes, Jr.
120. CER-WAT CORPORATION, INC., 1701 Louisville Dr., Suite C,  
Knoxville, TN 37921  
D. Nixdorf
121. CHEVRON RESEARCH & TECHNOLOGY COMPANY, 100 Chevron Way,  
Richmond, CA 94802-0627  
D. J. O'Rear
122. CIEMAT, Avda. Complutense, 22, 28040-Madrid (SPAIN)  
G. M. Calvo
123. COAL & SYNFUELS TECHNOLOGY, 1616 N. Fort Myer Dr., Suite 1000,  
Arlington, VA 22209  
J. Bourbin

- 124-125. COAL TECHNOLOGY CORPORATION, 103 Thomas Road,  
Bristol, VA 24201  
R. A. Wolfe  
R. E. Wright
126. COLORADO SCHOOL OF MINES, Dept. of Metallurgical Engineering,  
Golden, CO 80401  
G. R. Edwards
- 127-139. CONSOLIDATION COAL COMPANY, 4000 Brownsville Road,  
Library, PA 15129  
F. P. Burke  
S. Harding  
D. Nichols
130. CORNING INCORPORATED, SP-DV-1-9, Corning, NY 14831  
P. Bardhan
131. CUMMINS ENGINE COMPANY, Box 3005, MC 50183,  
Columbus, IN 47202-3005  
T. M. Yonushonis
132. DB Riley, Inc., 5 Neponset Street, Worcester, MA 01606  
R. Hallstrom
133. DEVASCO INTERNATIONAL, INC., 9618 W. Tidwell,  
Houston, TX 77041  
J. L. Scott
134. J. DOWICKI, P.E., 19401 Framingham Dr., Gaithersburg, MD 20879
135. DUPONT LANXIDE COMPOSITES, INC., Pencader Plant, Box 6100,  
Newark, DE 19714-6100  
J. K. Weddell
- 136-137. DUPONT LANXIDE COMPOSITES, INC., 1300 Marrows Road,  
P.O. Box 6077, Newark, DE 19714-6077  
A. Z. Fresco  
D. Landini
138. EC TECHNOLOGIES, INC., 3614 Highpoint Dr.,  
San Antonio, TX 78217  
D. J. Kenton



- 139-141. EG&G IDAHO, INC., Idaho National Engineering Laboratory,  
P.O. Box 1625, Idaho Falls, ID 83415  
B. H. Rabin  
R. N. Wright  
J. K. Wright
- 142-146. ELECTRIC POWER RESEARCH INSTITUTE, P.O. Box 10412,  
3412 Hillview Avenue, Palo Alto, CA 94303  
W. T. Bakker  
R. A. Brown  
S. Gehl  
R. Goldstein  
J. Stringer
147. ELECTRO PHYSICS, INC., 1400 Marshall Street, NE,  
Minneapolis, MN 55413  
D. Bell
148. ENERGY AND ENVIRONMENTAL RESEARCH CENTER, Box 8213,  
University Station, Grand Forks, ND 58202  
J. P. Hurley
149. ENERGY AND WATER RESEARCH CENTER, P. O. Box 6064  
West Virginia University,  
Morgantown, WV 26505-5054  
C. L. Irwin
150. ENVIRONMENTAL PROTECTION AGENCY, Global Warming Control  
Division (MD-63), Research Triangle Park, NC 27711  
K. T. Janes
151. ERC, INC., P. O. Box 417, Tullahoma, TN 37388  
Y. C. L. Susan Wu
- 152-153. EXXON RESEARCH AND ENGINEERING COMPANY, Clinton Township,  
Route 2 East, Annandale, NJ 08801  
M. L. Gorbaty  
S. Soled
154. FERRO CORPORATION, Filtros Plant, 603 West Commercial St.  
E., Rochester, NY 14445  
P. S. Way
155. FORSCHUUGS ZENTRUM JÜLICH GmbH, ICT, Postfach 1913, D-5170  
Jülich, Germany  
H. Barnert-Wierner

156. FOSTER WHEELER DEVELOPMENT CORPORATION, Materials  
Technology Dept., John Blizzard Research Center, 12 Peach Tree Hill  
Road, Livingston, NJ 07039  
J. L. Blough
157. FRAUNHOFER-INSTITUT für WERKSTOFFMECHANIK, Wohlerstrass 11,  
79108 Freiburg, West Germany  
R. Westerheide
158. GAS RESEARCH INSTITUTE, 8600 West Bryn Mawr Avenue,  
Chicago, IL 60631  
H. S. Meyer
159. GENERAL APPLIED SCIENCE LABS, 77 Raynor Avenue,  
Ronkonkoma, NY 11779  
M. Novack
160. GENERAL ELECTRIC CORPORATE CR&D, P.O. Box 8, Bldg. K1,  
MB 265, Schenectady, NY 12301  
G. Rowe
161. GEORGIA INSTITUTE OF TECHNOLOGY, Georgia Tech Research  
Institute, 123D Baker Bldg., Atlanta, GA 30332-0245  
T. L. Starr
162. GRI, 8600 W. Bryn Mawr, Chicago, IL 60656  
D. Scarpiello
163. HAYNES INTERNATIONAL, INC., 1020 W. Park Avenue,  
Kokomo, IN 46904  
M. Harper
- 164-165. HOSKINS MANUFACTURING COMPANY, 10776 Hall Rd.,  
Hamburg, MI 48139-0218  
J. Valykeo  
F. B. Hall
166. ILLINOIS INSTITUTE OF TECHNOLOGY, METM Dept., Perlstein Hall,  
IIT, Chicago, IL 60616  
J. A. Todd-Copley
167. INCO ALLOYS INTERNATIONAL, INC., P. O. Box 1958,  
Huntington, WV 25720  
S. Tassen
168. INTECH, INC., 11316 Roven Dr., Potomac, MD 20854-3126  
P. Lowe

- 169-170. IOWA STATE UNIVERSITY, Ames Laboratory, 107 Metals Development,  
Ames, IA 50011  
D. J. Sordélet  
Ozer Unal
171. JET PROPULSION LABORATORY, 4800 Oak Grove Dr., MS-79-21,  
Pasadena, CA 91020  
R. L. Chen
172. LANXIDE CORPORATION, 1 Tralee Industrial Park, Newark, DE 19711  
E. M. Anderson
173. LAVA CRUCIBLE-REFRACTORIES CO., P.O. Box 278,  
Zelienople, PA 16063  
T. Mulholland
- 174-178. LAWRENCE BERKELEY LABORATORY, University of California,  
1 Cyclotron Road, Berkeley, CA 94720  
I. Brown - MS 53  
T. M. Devine  
P. Y. Hou - MS 62-203  
G. Rosenblatt  
S. Visco
179. LAWRENCE LIVERMORE NATIONAL LABORATORY, P.O. Box 808,  
Livermore, CA 94551  
J. H. Richardson (L-353)
180. LEHIGH UNIVERSITY, Energy Research Center, 5 E Packer Avenue,  
Bethlehem, PA 18015  
J. N. DuPont
181. LIQUID CARBONIC INDUSTRIAS S.A, Avenida Rio Branco, 57-6º Andar,  
Centro - 20090-004, Rio De Janeiro, Brazil  
M. Saddy
- 182-184. LOCKHEED MARTIN-KAPL, P.O. Box 1072, MS G2-312,  
Schenectady, NY 12301  
J. J. Letko (MS D2-121)  
G. A. Newsome  
J. Woods
185. E. LORIA, 1829 Taper Drive, Pittsburgh, PA 15241

- 186-190. LOS ALAMOS NATIONAL LABORATORY, P.O. Box 1663,  
Los Alamos, NM 87545  
P. Apen - MS D453  
R. G. Castro - MS G720  
J. D. Katz  
D. Phillips  
D. Thoma - MS K765
191. LURGI LENTJES BABCOCK, Duisburger Strasse 375, D-46041 Oberhausen,  
Germany  
G. von Wedel
192. MALLET TECHNOLOGY, 100 Park Drive, Suite 204, P.O. Box 14407,  
Research Triangle Park, NC 27709  
R. Mallett
- 193-194. MANUFACTURING SCIENCES CORPORATION, 804 Kerr Hollar Road,  
Oak Ridge, TN 37830  
R. Hayes  
T. Muth
195. MASSACHUSETTS INSTITUTE OF TECHNOLOGY, Department of Chemical  
Engineering, Room 66-456, Cambridge, MA 02139  
J. Longwell
196. MER CORPORATION, 7960- S. Kolb Road, Tucson, AZ 85706  
L. Leaskey
- 197-198. MOBIL RESEARCH & DEVELOPMENT CORPORATION,  
P. O. Box 1026, Princeton, NJ 08540  
R. E. Searles  
S. T. Viscontini
- 199-202. NASA LEWIS RESEARCH CENTER, 21000 Brookpark Road,  
Cleveland, OH 44135  
J. P. Gyekenyesi  
N. Jacobson - MS 106-1  
S. R. Levine  
R. Miller - MS 24-1
- 203-205. NATIONAL INSTITUTE OF STANDARDS AND TECHNOLOGY, Materials  
Building, Gaithersburg, MD 20899  
S. J. Dapkunas  
L. K. Ives (Bldg. 220, Rm. A-215)  
S. G. Malghan

206. NATURAL GAS AND OIL TECHNOLOGY PARTNERSHIP,  
12434 Penthshire, Houston, TX 77024  
R. M. Whitsett
- 207-208. NETHERLANDS ENERGY RESEARCH FOUNDATION ECN,  
P.O. Box 1, 1755 ZG Petten, The Netherlands  
P. T. Alderliesten  
M. Van de Voorde
209. NEW ENERGY AND INDUSTRIAL TECHNOLOGY DEVELOPMENT  
ORGANIZATION, 1800 K Street, N.W., Suite 924, Washington, DC 20006  
T. Fukumizu
- 210-212. NEW ENERGY AND INDUSTRIAL TECHNOLOGY DEVELOPMENT  
ORGANIZATION, Sunshine 60 Bldg., P.O. Box 1151,  
1-1 Higashi-Ikebukuro 3-Chome, Toshima-Ku, Tokyo, 170, Japan  
S. Hirano  
H. Narita  
S. Ueda
213. NORCONTROL, Duran Marquina 20, 15080 La Coruna, Spain  
S. Gomez
214. NORTH CAROLINA A&T STATE UNIVERSITY, Department of Mechanical  
Engineering, Greensboro, NC 27411  
J. Sankar
215. OFFICE OF NAVAL RESEARCH, Code 431, 800 N. Quincy St.,  
Arlington, VA 22217  
S. G. Fishman
- 216-217 OHIO STATE UNIVERSITY, Department of Metallurgical Engineering,  
116 W. 19th Avenue, Columbus, OH 43210  
Y. He  
R. A. Rapp
- 218-220. PACIFIC NORTHWEST LABORATORIES, P.O. Box 999,  
Richland, WA 99352  
J. L. Bates  
R. N. Johnson  
L. R. Pederson

- 221-223. PENNSYLVANIA STATE UNIVERSITY, 101 Steidle Building,  
University Park, PA 16802  
K. Spear  
R. Tressler  
M. Trubelja
224. PSI TECHNOLOGY COMPANY, 20 New England Business Center,  
Andover, MA 01810  
L. Bool
225. RENSSELAER POLYTECHNIC INSTITUTE, Materials Engineering  
Department, Troy, NY 12180-3590  
N. S. Stoloff
226. RIBBON TECHNOLOGY CORPORATION, P.O. Box 30758,  
Columbus, OH 43230  
T. Gaspar
227. RILEY STOKER CORPORATION, 5 Neponset Street, Worcester, MA 01606  
D. P. Kalmanovitch
228. RISO NATIONAL LABORATORY, P.O. Box 49, DK-4000, Roskilde,  
DENMARK  
Aksel Olsen
229. ROLLED ALLOYS, 125 West Sterns Road, Temperance, MI 48182  
J. C. Kelly
230. SANDIA NATIONAL LABORATORIES, 7011 East Avenue, P.O. Box 969  
Livermore, CA 94551-0969  
J. E. Smugeresky (MS-9402)
- 231-236. SANDIA NATIONAL LABORATORIES, P.O. Box 5800,  
Albuquerque, NM 87185  
L. L. Baxter  
R. Bradshaw  
R. Buss  
G. Carlson  
G. Samara  
A. Sault
- 237-238. SARGENT AND LUNDY, 55 E Monroe Street, Chicago, IL 60603  
R. J. Kerhin  
D. G. Sloat

- 239-240. SCIENCE APPLICATIONS INTERNATIONAL CORPORATION,  
1710 Goodridge Dr., McLean, VA 22102  
J. T. Bartis  
J. Ward (MS 2-20-1)
241. SFA PACIFIC, INC., 444 Castro Street, Suite 920, Mountain View, CA 94041  
N. Korens
242. SHELL DEVELOPMENT COMPANY, P.O. Box 1380,  
Houston, TX 77251-1380  
L. W. R. Dicks
243. G. SORELL, 49 Brookside Terrace, N. Caldwell, NJ 07006
244. SOUTHERN RESEARCH INSTITUTE, 2000 Ninth Avenue South,  
Birmingham, AL 35202  
H. S. Starrett
245. SOUTHWEST RESEARCH INSTITUTE, 6620 Culebra Road,  
P.O. Drawer 28510, San Antonio, TX 78284  
F. F. Lyle, Jr.
246. SRI INTERNATIONAL, 333 Ravenswood Avenue, Meno Park, CA 04025  
Y. D. Blum
247. STANTON ENERGY INDUSTRY CONSULTANTS, INC., RD #1,  
Liberty Court,  
New Stanton, PA 15672-9621  
R. J. Steffen
248. STATE ELECTRICITY COMMISSION OF VICTORIA, Herman Research  
Laboratory Library, Howard St., Richmond, Victoria, 3121 Australia  
H. Hodgskiss
- 249-250. STRESS ENGINEERING SERVICES, INC., 415 Glensprings Drive, Suite 200,  
Cincinnati, OH 45246  
C. Haynes  
D. Marriott
251. SUNDSTRAND, 4747 Harrison Ave., Rockford, IL 61125  
D. Oakey
252. SUPERKINETICS, 2881 Tramway Place, NE,  
Albuquerque, NM 87122  
J. V. Milewski

- 253.    TECHNIWEAVE, INC., 109 Chestnut Hill Road, Rochester, NH 03868  
          J. A. LeCoustauuec
- 254.    TECHNOLOGY ASSESSMENT AND TRANSFER, 133 Defense Highway,  
          Suite 212, Annapolis, MD 21401  
          J. Hanigofsky
- 255.    TECHNOLOGY MANAGEMENT INC., 9718 Lake Shore Blvd.,  
          Cleveland, OH 44108  
          B. P. Lee
- 256.    TELEDYNE ALLVAC, P.O. Box 5030, Monroe, NC 28110  
          A. L. Coffey
- 257-258.    TENNESSEE VALLEY AUTHORITY, 3N66A Missionary Ridge Place,  
              Chattanooga, TN 37402-2801  
              J. B. Brooks  
              C. M. Huang
- 259.    TEXAS EASTERN TRANSMISSION CORPORATION, P.O. Box 2521,  
          Houston, TX 77252  
          D. H. France
- 260.    THE AMERICAN CERAMIC SOCIETY, INC., 735 Ceramic Place,  
          Westerville, OH 43081  
          L. Sheppard
- 261.    THE CARBORUNDUM COMPANY, Technology Division, P. O. Box 832,  
          Niagara Falls, NY 14302  
          S. K. Lau
- 262.    THE JOHNS HOPKINS UNIVERSITY, Materials Science & Engineering,  
          Maryland Hall, Baltimore, MD 21218  
          R. E. Green, Jr.
- 263.    THE MATERIALS PROPERTIES COUNCIL, INC., United Engineering  
          Center, 345 E. Forty-Seventh St., New York, NY 10017  
          M. Prager
- 264.    THE NORTON COMPANY, High Performance Ceramics Division,  
          Goddard Road, Northboro, MA 01532-1545  
          N. Corbin
- 265.    THE RALPH M. PARSONS COMPANY, 100 West Walnut St.,  
          Pasadena, CA 91124  
          J. B. O'Hara



266. THE TORRINGTON COMPANY, Advanced Technology Center, 59 Field Street, Torrington, CT 06790  
W. J. Chmura
267. THIRD MILLENNIUM TECHNOLOGY, INC., 120 Sherlake Drive, P.O. Box 23556, Knoxville, TN 37933-1556  
C. F. VanConant
268. TRW, 1455 E. 195th Street, Cleveland, OH 44110  
M. Kurup
- 269-271. UNITED TECHNOLOGIES RESEARCH CENTER, Materials Department, 411 Silver Lane, East Hartford, CT 06108  
N. S. Bornstein  
J. E. Holowczak  
D. Seery
272. UNIVERSITY OF CALGARY, 2500 University Dr. NW, Calgary, Canada  
S. X. Mao
273. UNIVERSITY OF CALIFORNIA, Department of Materials Science and Mineral Engineering, University of California, Building 66-Room 247, Berkeley, CA 94720  
R. O. Richie
- 274-275. UNIVERSITY OF KENTUCKY, Center for Applied Energy Research, 3572 Iron Works Pike, Lexington, KY 40511-8433  
F. Derbyshire  
M. Jagtoyen
276. UNIVERSITY OF NORTH DAKOTA, P.O. Box 9018, University Station, Grand Forks, ND 58202  
J. P. Hurley
277. UNIVERSITY OF PITTSBURGH, Materials Science & Engineering Department, 848 Bredum Hall, Pittsburgh, PA 15261  
N. Birks
278. UNIVERSITY OF SOUTH AUSTRALIA, Department of Metallurgy, The Levels SA 5095 Australia  
K. N. Strafford

- 279-282. UNIVERSITY OF TENNESSEE, Department of Materials Science and Engineering, 434 Dougherty Engineering Building, Knoxville, TN 37996  
R. A. Buchanan  
P. Liaw  
C. D. Lundin  
P. Qiao
- 283-285. UNIVERSITY OF TENNESSEE SPACE INSTITUTE,  
Tullahoma, TN 37388  
W. H. Boss  
J. W. Muehlhauser  
M. White
286. UNIVERSITY OF WASHINGTON, Department of Materials Science and Engineering, 101 Wilson, FB-10, Seattle, WA 98195  
T. G. Stoebe
287. UNIVERSITY OF WISCONSIN, Department of Materials Science and Engineering, 1509 University Avenue, Madison, WI 53706-1595  
J. H. Perepezko
288. UOP, 50 E. Algonquin Road, Des Plaines, IL 60017-5016  
G. J. Antos
- 289-290. U.S. BUREAU OF MINES, Tuscaloosa Research Center, P. O. Box L,  
Tuscaloosa, AL 35486  
J. C. Debsikdar  
J. Kwong
291. VEBA OEL, P. O. Box 45, 4650 Gelsenkirchen-Buer, Germany  
D. Fuhrmann
- 292-293. VIRGINIA POLYTECHNIC INSTITUTE AND STATE UNIVERSITY,  
Department of Materials Engineering, Blacksburg, VA 24061  
W. Curtin  
K. L. Reifsnyder
294. WESSEL, James K., 127 Westview Lane, Oak Ridge, TN 37830
- 295-296. WEST VIRGINIA UNIVERSITY, Mechanical & Aerospace Engineering  
Department, P.O. Box 6106, Morgantown, WV 26505  
B. Kang  
B. Cooper
297. WESTERN RESEARCH INSTITUTE, 365 N. 9th Street, P. O. Box 3395,  
University Station, Laramie, WY 82071  
V. K. Sethi

298. WESTINGHOUSE ELECTRIC CORPORATION, 4400 Alafaya Trail,  
Orlando, FL 32826-2399  
S. M. Sabol - MC 303
- 299-303. WESTINGHOUSE ELECTRIC CORPORATION, Research and Development  
Center, 1310 Beulah Road, Pittsburgh, PA 15235-5098  
M. A. Alvin  
G. Bruck  
D. L. Keairns  
T. Lippert  
S. C. Singhal
304. WORCESTER POLYTECHNIC INSTITUTE, 100 Institute Road,  
Worcester, MA 01609  
E. Ma
305. DOE CHICAGO OPERATIONS OFFICE, 9800 S. Cass Ave.,  
Argonne, IL 60439  
J. Jonkouski
306. DOE IDAHO OPERATIONS OFFICE, 765 DOE Place,  
Idaho Falls, ID 83406  
J. B. Malmo
- 307-320. DOE MORGANTOWN ENERGY TECHNOLOGY CENTER,  
P.O. Box 880, Morgantown, W VA 26505  
C. T. Alsup  
R. A. Bajura  
R. C. Bedick  
D. C. Cicero  
F. W. Crouse, Jr.  
R. A. Dennis  
U. Grimm  
J. S. Halow  
N. T. Holcombe  
W. J. Huber  
T. J. McMahon  
H. M. Ness  
J. E. Notestein  
C. M. Zeh
321. DOE OAK RIDGE OPERATIONS OFFICE, Oak Ridge, P. O. Box 2008,  
Oak Ridge, TN 37831-6269  
M. A. Rawlins

- 322-323. DOE OFFICE OF BASIC ENERGY SCIENCES, Materials Sciences Division,  
ER-131, 19901 Germantown Road, Germantown, MD 20874-1290  
A. Dragoo  
J. N. Mundy
324. DOE OFFICE OF COAL TECHNOLOGY, FE-232 GTN,  
Washington, DC 20585  
M. Perlswieg
325. DOE OFFICE OF ENERGY EFFICIENCY AND RENEWABLE ENERGY,  
CE-12, Forrestal Building, Washington, DC 20545  
J. J. Eberhardt
- 326-327. DOE OFFICE OF ENERGY RESEARCH, 14 Goshen Court,  
Gaithersburg, MD 20882-1016  
N. F. Barr  
F. J. Wobber
- 328-337. DOE OFFICE OF FOSSIL ENERGY, Washington, DC 20585  
J. P. Carr (FE-72)  
W. Fedarko (FE-232)  
H. Feibus (FE-23)  
K. N. Frye (FE-13)  
S. C. Jain (FE-231)  
C. E. Pax (FE 73)  
T. B. Simpson (FE-231)  
M. I. Singer (FE-70)  
H. E. Thomas (FE-73)  
G. F. Wheeler (FE-231)
338. DOE OFFICE OF INDUSTRIAL TECHNOLOGIES, 1000 Independence Avenue  
S.W., Washington, DC 20585  
S. Dillich (EE-20)
339. DOE OFFICE OF NAVAL REACTORS, NE-60, Crystal City Bldg.,  
N.C.-2, Washington, DC 20585  
J. Mosquera
340. DOE OFFICE OF PETROLEUM RESERVES, Analysis Division, FE-431,  
1000 Independence Ave., Washington, DC 20585  
D. de B. Gray

- 341-353. DOE PITTSBURGH ENERGY TECHNOLOGY CENTER,  
P. O. Box 10940, Pittsburgh, PA 15236  
A. H. Baldwin  
J. L. Balzarini  
R. A. Carabetta  
R. C. Dolence  
P. Goldberg  
J. D. Hickerson  
J. J. Lacey  
S. R. Lee  
M. E. Mather  
G. V. McGurl  
J. A. Ruether  
L. Ruth  
T. M. Torkos

- 354-355. DOE, OFFICE OF SCIENTIFIC AND TECHNICAL INFORMATION,  
P.O.Box 62, Oak Ridge, TN 37831

For distribution by microfiche as shown in DOE/OSTI-4500,  
Distribution Category UC-114 (Coal Based Materials and Components)